A Combined Study on Earth's Deep Water Cycle using Numerical Modelling and Laboratory Experiments

Doctoral Thesis

submitted to obtain the academic degree of Doctor of Natural Sciences
(Dr. rer. nat.)
of the Bayreuth Graduate School of Mathematical and Natural Sciences
(BayNAT)
of the University of Bayreuth

Enrico Marzotto
from *Vicenza (Italy)*
Bayreuth, 2021

This doctoral thesis was prepared at the department of Bayerisches Geoinstitut (BGI) at the University of Bayreuth from November 2017 until December 2021 and was supervised by Prof. Dr. Gregor J. Golabek.

This is a full reprint of the thesis submitted to obtain the academic degree of Doctor of Natural Sciences (Dr. rer. nat.) and approved by the Bayreuth Graduate School of Mathematical and Natural Sciences (BayNAT) of the University of Bayreuth.

Date of submission: 25.08.2021

Date of defence: 09.12.2021

Acting director: Prof. Dr. Hans Keppler

Doctoral committee:

Prof. Dr. Gregor J. Golabek	(reviewer)
PD Dr. Gerd Steinle-Neumann	(reviewer)
Prof. Dr. Daniel J. Frost	(chairman)
PD Dr. Catherine McCammon	

To my Family: Suchetana,
Alessandro, Francesco
Maria Grazia, Claudio

Summary

A Combined Study on Earth's Deep Water Cycle using Numerical Modelling and Laboratory Experiments. The distinctive feature of Earth's surface compared to other known planets is the abundance of liquid water. This water was delivered during the accretion stage of the planet by rocky asteroids, with minor contributions from comets and protosolar nebular gas. Experimental evidence shows that water can be incorporated into many of the minerals that make up Earth's interior. When water is hosted in the crystalline structures, it alters the physical properties of minerals, thereby enhancing deformation processes. Therefore, water-bearing rocks are less dense and weaker compared to their dry counterparts. Geophysical observations and natural samples reveal that water is indeed present in Earth's mantle, mostly concentrated in the mantle transition zone. The region is bounded by two seismic discontinuities, at $410\ km$ and $660\ km$ depth, and is characterized by the presence of two minerals with high water solubility: wadsleyite and ringwoodite. Water is carried into Earth's interior by the subduction of oceanic lithosphere, i.e. slabs. This water-delivery mechanism is also known as the '*deep water cycle,*' and might represent the key element for the onset of plate tectonics on Earth.

One essential tool to explore the role of water in plate tectonics is numerical modelling. With this technique, it is possible to reproduce many physical phenomena occurring on Earth by self-consistently simulating mantle convection. This is achieved by solving the governing equations of mass, momentum and energy conservation, also known as Stokes equations. The complexity of these equations requires the use of approximation methods, like Finite Difference (FD), to solve the derivatives over time and space. The feedback loop between mineral physics constraints, numerical modelling and geophysical observations represents the best strategy to unravel Earth's interior. However, despite the efforts of geoscientists, many questions regarding the deep Earth water cycle remain so far unanswered.

This thesis focuses on the hydration state of the MTZ, with three aims addressing different aspects of the topic: (1) provide mineral physics measurements on the effect of water on ringwoodite thermal conductivity; (2) produce a model featuring an Earth-like mobile lid while minimizing the effects of numerical parameters; and (3) analyse the parameters that allow for the stagnation of a slab in the MTZ, which may lead to the water enrichment in this region

In project (1), hydrous ringwoodite crystals were synthesized with multi-anvil experiments and characterized by X-ray diffraction, electron-microprobe analysis, and infrared spectroscopy. The samples were loaded into a diamond anvil cell to perform measurements at the high-pressure conditions of the MTZ. The thermal conductivity of ringwoodite, Λ_{Rw} was measured with the time-domain thermo-reflectance method. It was found that the presence of $1.73\ wt\%$ water reduces Λ_{Rw} by 40%. From this analysis, it was possible to derive a parameterized equation to extrapolate Λ_{Rw} as a function of pressure and water content. With this tool, the large-scale thermal evolution of a slab was studied. The calculations were performed by assuming a slab stagnating in the MTZ, then being progressively heated by the warm ambient mantle. A 1D FD numerical code was designed to solve the heat diffusion equation, and the derived equation for Λ_{Rw} was included into the physical model of the slab. The results reveal that hydrous ringwoodite hinders the heating of the slab, thus promoting the survival of water-bearing minerals.

In project (2), a global-scale model to reproduce self-consistently plate-like behaviour was designed. The models were computed with StagYY in a 2D spherical annulus geometry. The tectonic regime of a planet is controlled by the yield strength of the lithosphere τ_y. Four main tectonic regimes can be identified in nature: micro-plate dripping, plate-like, episodic resurfacing, and stagnant lid. It was found that the tectonic regime in the models is heavily influenced by the grid resolution used for the discretization. The modelled lithosphere is weakened by reducing the horizontal grid spacing Δw, while it becomes stronger when reducing the vertical grid spacing Δr. These effects are numerical in nature, and are the consequence of the interpolation of the Stokes equations. It was found that the best results are achieved by accurately resolving the lithosphere, i.e. $\Delta w \leq 40\ km$ and $\Delta r \leq 15\ km$.

In project (3), the interactions between the cold descending slab and the $660\ km$ discontinuity were analysed. The models were computed with StagYY in a 2D spherical annulus geometry. From the models it can be inferred that the stagnation of a slab in the MTZ is controlled by three parameters: (i) the density jump $\Delta\rho$, which enhances the slab pull, and affects the latent heat absorbed by the post-spinel reaction; (ii) the negative Clapeyron slope Υ, which causes a downward deflection of the phase transition; and (iii) the viscosity jump $\Delta\eta$, which decelerates the descent of the slab.

Zusammenfassung

Eine kombinierte Studie über den tiefen Wasserkreislauf der Erde mittels numerischer Modellierung und Laborexperimenten. Die Besonderheit der Erdoberfläche gegenüber anderen Planeten ist der Reichtum an flüssigem Wasser an der Oberfläche. Dieses Wasser wurde während der Akkretionsphase des Planeten von felsigen Asteroiden sowie einem geringen Beitrag von Kometen und protosolarem Nebelgas eingetragen. Experimentelle Beweise zeigen, dass Wasser in viele der das Erdinnere bildenden Mineralien eingebunden werden kann und dass, wenn Wasser in den kristallinen Strukturen enthalten ist, es die physikalischen Eigenschaften von Mineralien verändert und so Deformationsprozesse fördert. Daher sind wasserführende Gesteine im Vergleich zu ihren trockenen Gegenstücken weniger dicht und schwächer. Geophysikalische Beobachtungen und natürliche Proben zeigen, dass Wasser tatsächlich im Erdmantel, hauptsächlich in der Mantelübergangszone (MTZ) konzentriert, vorhanden ist. Diese Region wird von zwei seismischen Diskontinuitäten in 410 und 660 km Tiefe begrenzt und ist durch das Vorkommen von zwei Mineralien mit hoher Wasserlöslichkeit gekennzeichnet: Wadsleyit und Ringwoodit. Durch die Subduktion der ozeanischen Lithosphäre (ozeanischer Platten), wird Wasser ins Erdinnere transportiert. Dieser Wasserabgabemechanismus ist auch als „Tiefer Wasserkreislauf“ bekannt und könnte das Schlüsselelement für den Beginn der Plattentektonik auf der Erde darstellen.

Ein wesentliches Werkzeug zur Erforschung der Rolle von Wasser für der Plattentektonik ist die numerische Modellierung. Mit dieser Technik ist es möglich, viele physikalische Phänomene, die auf der Erde auftreten, durch die selbstkonsistente Simulation der Mantelkonvektion zu reproduzieren. Dies wird durch die Lösung der maßgebenden Gleichungen der Massen-, Impuls- und Energieerhaltung, auch bekannt als Stokes-Gleichungen, erreicht. Die Komplexität dieser Gleichungen erfordert die Verwendung von Näherungsverfahren wie der Finite Differenzen (FD), um die Ableitungen über Zeit und Raum zu lösen. Die Rückkopplungsschleife zwischen mineralphysikalischen Einschränkungen, numerischer Modellierung und geophysikalischen Beobachtungen stellt die beste Strategie dar, um das Erdinnere zu enträtseln. Dennoch bleiben trotz anhaltender Bemühungen der Geowissenschaft viele Fragen zum tiefen Wasserkreislauf der Erde unbeantwortet.

Diese Arbeit konzentriert sich auf den Hydratationszustand der MTZ. Ihr Ziel ist die Behandlung dreier verschiedener Aspekte des Themas, nämlich: (1) Mineralphysikalische Messungen zur Ermittlung des Einflusses von Wasser auf die Wärmeleitfähigkeit von Ringwoodit; (2) Erstellung eines Modells mit erdähnlichen beweglichen Platten unter Minimierung der Auswirkungen numerischer Parameter; und (3) Analyse der Parameter, die eine Stagnation der abtauchenden Platte in der MTZ, welche zur Wasseranreicherung in dieser Region führen kann, ermöglichen.

In Projekt (1) wurden wasserhaltige Ringwoodit-Kristalle mit Multi-Amboss-Experimenten synthetisiert und durch Röntgenbeugung, Elektronenmikrosondenanalyse und Infrarotspektroskopie charakterisiert. Die Proben wurden in eine Diamantambosszelle geladen, um Messungen unter den Hochdruckbedingungen der MTZ durchzuführen. Die Wärmeleitfähigkeit von Ringwoodit, Λ_{Rw}, wurde mit der Zeitbereichs-Thermoreflexionsmethode gemessen. Es wurde festgestellt, dass die Anwesenheit von 1.73 $wt\%$ Wasser Λ_{Rw} um 40% reduziert. Aus dieser Analyse konnte eine parametrisierte Gleichung abgeleitet werden, um Λ_{Rw} als Funktion von Druck und Wassergehalt zu extrapolieren. Mit diesem Werkzeug wurde die großräumige thermische Entwicklung einer Platte

untersucht. Die Berechnungen wurden unter der Annahme einer in der MTZ stagnierenden Platte durchgeführt, die durch den warmen Umgebungsmantel zunehmend erwärmt wird. Ein numerischer 1D-FD-Code wurde entwickelt, um die Wärmediffusionsgleichung zu lösen. Die abgeleitete Gleichung für Λ_{Rw} wurde in das physikalische Modell der Platte aufgenommen. Die Ergebnisse zeigen, dass wasserhaltiges Ringwoodit die Erwärmung der Platte behindert und so die Erhaltung wasserführender Mineralien fördert.

Im Projekt (2) wurde ein globales Modell zur Reproduktion von selbstkonsistentem plattenähnlichem Verhalten entworfen. Die Modelle wurden mit StagYY in einer 2D-Kugelringgeometrie berechnet. Das tektonische Regime eines Planeten wird durch die Bruchfestigkeit der Lithosphäre τ_y bestimmt. In der Natur können vier tektonische Regime identifiziert werden: Mikroplattentropfen, plattenartige und episodische Oberflächenerneuerung und Einzelplatte. Es zeigte sich, dass das tektonische Regime in den Modellen stark von der für die Diskretisierung verwendeten Gitterauflösung beeinflusst wird. Die modellierte Lithosphäre wird durch die Verringerung des horizontalen Gitterabstands Δw geschwächt, während sie durch die Verringerung des vertikalen Gitterabstands Δr stärker wird. Diese Effekte sind rein numerisch und resultieren aus der Interpolation der Stokes-Gleichungen. Es zeigte sich, dass die besten Ergebnisse durch eine genaue Auflösung der Lithosphäre erzielt werden, i.e. $\Delta w \leq 40\ km$ und $\Delta r \leq 15\ km$.

Im Projekt (3) wurden die Wechselwirkungen zwischen kalter, absinkender Platte und der $660\ km$ Diskontinuität analysiert. Die Modelle wurden mit StagYY in einer 2D-Kugelringgeometrie berechnet. Aus den Modellen kann abgeleitet werden, dass die Stagnation der Platte in der MTZ durch drei Parameter gesteuert wird: (i) den Dichtesprung $\Delta\rho$, der den Plattenzug verstärkt und die latente Wärme beeinflusst, die durch die Post-Spinell-Reaktion absorbiert wird; (ii) die negative Clapeyron-Steigung Υ, die eine Ablenkung des Phasenübergangs nach unten bewirkt; (iii) den Viskositätssprung $\Delta\eta$, der das Absinken der Platte verlangsamt.

Chapter Index

Figures

Tables

Equations

List of Abbreviations

BC	Boundary Conditions
BGI	Bayerisches Geoinstitut
BS	Beam Splitter
Br	Bridgmanite
CaPv	Ca-perovskite
Chl	Chlorite
CMB	Core-Mantle Boundary
CR	Crust
DFG	German Research Foundation
DHMS	Dense Hydrous Magnesium Silicates
EOM	Electro-Optical Modulator
EoS	Equation of State
EM	Electro-Magnetic
EMPA	Electron Micro-Probe Analysis
FD	Finite Difference
Fp	Ferropericlase
FTIR	Fourier Transform Infrared Spectroscopy
FV	Finite Volume
FWHM	Full Width at Half Maximum
GDS	Geomagnetic Deep Sounding
GLOSS	Global Subducting Sediments
hpe	heat producing elements
IR	Infrared
IRTG	International Research Training Group
IVCT	Intervalence charge transfer
LLSVPs	Large Low-Shear Wave Velocity Provinces
LM	Lower Mantle
LP	Long Pass filter
LT	Lithosphere
LVZ	Low Velocity Zone
Lws	Lawsonite
Mg	Magnetite
MORB	Mid Ocean Ridge Basalts
MPI	Message-Passing Interface
MTZ	Mantle Transition Zone
NAM	Nominally Anhydrous Minerals
OEL	Octahedral Edge Length
OIB	Ocean Island Basalts
PB	Probe Beam (related to TDTR method)
PBS	Polarized Beam Splitter

PDEs	Partial Differential Equations
PETSc	Portable, Extensible Toolkit for Scientific Computation
Pl	Plagioclase
PP	Pump Beam (related to TDTR method)
PPv	Post-perovskite (i.e. post-bridgmanite)
Px	Pyroxene
Qtz	Quartz
Rw	Ringwoodite
SCO	San Carlos Olivine
SIMS	Secondary-Ion Mass Spectroscopy
SMOW	Standard Mean Ocean Water
SP	Short Pass filter
Srp	Serpentine
St	Stishovite
TDTR	Time-Domain Thermo-Reflectance
TEL	Truncation Edge Length
ULVZ	Ultra-Low Velocity Zones
UM	Upper Mantle
Wd	Wadsleyite
WDS	Wavelength Dispersive Spectrometry
XRD	X-Ray Diffraction

CHAPTER 1 – The Key Role of Water in Earth's Plate Tectonics

1.1. Introduction

From space, Earth can be easily recognized as the '*pale blue dot*' (*Sagan, 1994*) since more than 70% of its surface is covered by water (*Duxbury, 1997*). On Earth's surface, water is abundant in three states of matter (i.e. frozen, liquid, and vapour *Oki et al., 2004*); due to the presence of a permanent atmosphere (*Budyko et al., 1987*) which provides the most temperate climate in the Solar System (*Marlatt et al., 1975*). Moreover, Earth is characterized by an internally generated magnetic field (*Glatzmaier & Roberts, 1995*), which provides an effective shielding against the high-energy cosmic rays (*Dartnell, 2011*). Fostered by this favourable environment, life forms thrive in both oceans and continents (*Boenigk et al., 2015*), with an estimated number of 8– 10 millions species (*Mora et al., 2011*).

These characteristics make Earth the most peculiar planet in the Solar System, since these do not feature simultaneously on any other observable celestial body. For example on Mars, the surface water was lost over the past eons (*Jakosky, 2021*), since the atmosphere was progressively eroded via: (i) photodissociation of H_2O and consequent escape of light H_2 (i.e. Jeans escape), (ii) ions acceleration in the presence of an electric field; (iii) photochemical escape of O atoms heated by chemical reactions in the ionosphere; and (iv) sputtering escape due to the presence of the solar wind (*Catling, 2017*; *Jakosky et al., 2018*). Furthermore, Mars is exposed to the cosmic radiation given the absence of a magnetic field (*Schubert et al., 2000*; *Dartnell, 2011*). Under these conditions, liquid water is barely stable (*Bryson, 2008*) and the search of life forms on Mars is an ongoing challenge (*Joseph et al., 2019*). Although other planets might have a different evolutionary path (e.g. Venus), they still exhibit inhospitable conditions for life (*Jakosky, 1998*). One of the goals in natural sciences is to provide answers to the question: *why is Earth so special*?

1.2. Plate Tectonics

From a geological perspective, the most unique trait of Earth is plate tectonics, i.e. the fragmentation of Earth's outer shell into plates, and their relative motion with respect to each other (*Turcotte & Schubert, 2002*). Plate tectonics on Earth plays a fundamental role in regulating the climate (*Brune et al., 2017*), in controlling the availability of nutrients at the surface (i.e. C, N, P - *Zerkle, 2018*), and in promoting species diversifications by remodelling terrestrial and marine environments (*Descombes et al., 2018*; *Pellissier et al., 2018*). This tectonic activity might have been fundamental in causing the Cambrian life explosion on our planet (*Erwin et al., 2011*; *Lee et al., 2018*). Furthermore, plate tectonics is a very efficient mechanism for cooling Earth's interior and maintaining a stable magnetic field (i.e. geodynamo - *Nakagawa & Tackley, 2010*).

So far, the plate-tectonic regime represents an exception in our Solar System, since Earth is the only known terrestrial planet displaying this feature (*Korenaga, 2013*). Other possible candidates that might be characterized by this tectonic behaviour are Jupiter's moons Europa (*Kattenhorn, 2018*) and Io (*O'Neill et al., 2007*). The rest of the studied terrestrial planets show different tectonic regimes compared to that of Earth (*Fischer et al., 2015*). Therefore, the presence

of a plate tectonic regime might represent a key ingredient for the establishment of life on a planet (*Stern, 2016*).

1.2.1. Theory of Plate Tectonics

The theory of plate tectonics was gradually developed in the first half of the 20^{th} century, starting from the observations of Alfred Wegner and his theory of continental drift (*Wegner, 1915*). Additionally, Frank B. Taylor suggested the idea that mountain building was a consequence of the horizontal motion of continents (*Taylor, 1910*). For both Wegner and Taylor, the driving force of the continental drift was the Coriolis force, and the tidal pull exerted by both the Moon and the Sun. It was Alfred J. Bull who proposed mantle convection as a driving force for the mountain building (*Bull, 1921, 1927, 1931*). At that time, one of the main arguments against this model, was due to the fact that Earth's mantle was assumed to be solid and stiff (*Mallet, 1846*; *Gutenberg, 1925*), hence incapable of flowing. However, the theory of the solid-state creep of the warm mantle (*Holmes, 1931, 1933*), combined with the field observations of the post-glacial rebound (*Haskell, 1935, 1936, 1937*), and first experimental models (*Griggs, 1939*), favoured the idea that continental motion is related to solid-state mantle convection.

After World War II, the major improvements in submarines and magnetometers technology, allowed for extensive bathymetric surveys, and magnetic mapping of the sea floor. In these years, the spreading of the sea floor at the mid ocean ridges, and the magnetic stripes with reversed polarity were discovered (*Dietz, 1961*; *Heezen & Ewing, 1961*; *Vine & Matthews, 1963*; *Morley & Larochelle, 1964*; *Khramov et al., 1966*; *King et al., 1966*; *Caner et al., 1967*; *Ewing & Ewing, 1967*; *Le Pichon, 1968*). These observations indicated that oceans spread over time, and that this evolution is marked by Earth's magnetic reversal (*Hess, 1962*). Finally, the initial continental drift hypothesis evolved into the theory of plate tectonics, after the formalization of mid-ocean ridges (*McKenzie & Parker, 1967*) and the subduction at the trenches (*Morgan, 1968*). This theory was essential for the formulation of the model known as '*Wilson cycle*' (*Wilson, 1968*), which is still used today to explain the evolution of both oceans and continents.

1.2.2. Lithosphere and Plate Margins

As mentioned in the previous section, plate tectonics is a theory employed to describe the behaviour of Earth's outermost shell, i.e. the lithosphere. The lithosphere is formally defined as the solid outer layer of a planet that possesses a high rigidity, along with an elasto-plastic behaviour (*Barrell, 1914*; *Anderson, 1995*). The lithosphere represents the region where conduction is the dominant heat transport mechanism, since solid-state convection requires a viscous creep rheology (*White, 1988*). The definition of the lithosphere is purely thermo-mechanical, hence it includes both the oceanic and continental crust, as well as the shallow upper mantle (i.e. lithospheric mantle), despite their major chemical difference (*Anderson, 1995*).

Despite its stiffness, the lithosphere is far from being intact and is fragmented into a mosaic of plates which float and drift on top of a weak warm layer known as asthenosphere (*Bunge et al., 1996*; *Richards et al., 2001*; *Höink & Lenardic, 2008*). Each plate behaves like a rigid shield in its centre, while accommodating most of the deformation at its boundaries, where the interaction with other plates occurs.

There are three types of plate margins (*Turcotte & Schubert, 2002*):

1. Divergent plate margins (i.e. mid ocean ridges and continental rifts) form when two plates move away from each other, thus allowing the asthenospheric mantle to rise towards the surface. The decompression experienced by the mantle during the ascent causes the partial melting of the rocks and the production of the basaltic oceanic crust in a marine environment (*McKenzie & Bickle, 1988*; *Asimow et al., 1995, 2001*), or rhyolites and flood basalts in the case of continental rifting (*Marzoli et al., 1999*; *Natali et al., 2011*). Divergent margins are also called spreading margins or constructive plate boundaries.
2. Convergent plate margins (i.e. subduction zones and continental collision) form when two plates move towards each other. When this interaction involves two plates with distinct densities (e.g. high–ρ ocean vs. low–ρ continent) the convergent margin evolves into a subduction zone (*Stern, 2002*; *Becker & Faccenna, 2009*; *Stern & Gerya, 2017*). The term '*subduction*' indicates the whole act of sinking into the mantle. During its descent, the oceanic lithosphere is called '*slab*' (*Stern, 2002*). The locations where slabs subduct feature depressions in the ocean floor, and are called '*trenches*'. These areas are characterized by the sinking of the high–ρ lithosphere (i.e. slab) into the mantle, and the further pull of the rest of the plate along with it (*Forsyth & Uyeda, 1975*). Subduction zones represent the key characteristic feature of plate tectonics (*Crameri et al., 2019*), and its major driving force (*Forsyth & Uyeda, 1975*; *Conrad & Lithgow-Bertelloni, 2002, 2004*). The subduction of the lithosphere overcomes the contribution of mantle dragging and it plays a significant role in accelerating the attached plates (*Coltice et al., 2019*).
   When two low–ρ continents collide with each other, the onset of subduction is prevented by the buoyancy of both plates, and this interaction will involve buckling, folding and piling (i.e. orogeny) (*Twiss & Moores, 1992*). Many of the mountain ranges on Earth, e.g. the Alps and the Himalayas are the product of continental collisions.
3. Transform margins form when two plates slide past each other, without producing new crust or consuming the existing one. The most famous transform margin is the San Andreas fault (*Fialko, 2006*) which separates the North American plate from the Pacific Plate.

Furthermore, intra-plate interactions between the lithosphere and the mantle are represented by the activity of the so-called '*hot-spots*', i.e. warm plumes of mantle material that are capable of breaking through the lithosphere, and thus producing volcanic landforms (*Steinberger, 2000*; *Jellinek & Manga, 2004*). The most famous example of intra-plate volcanism is the Hawaii-Emperor chain. Hot-spots activity is not limited to the inner part of the plates, and it can also occur at the plate boundaries, e.g. Iceland hot-spot (*Schilling et al., 1982*).

1.2.3. The Rheology of the Lithosphere

Plate tectonics requires a mechanism to generate plate boundaries (*Solomatov & Moresi, 1997*). The low temperatures that characterize the lithosphere relate to an extremely high viscosity of the plates (i.e. $\eta \gg 10^{23}\ Pa\ s$ - *De Bremaecker, 1977*; *Liu & Hasterok, 2016*), hence the stress is mostly accommodated by brittle failure and plastic yielding (*Kohlstedt et al., 1995*). The brittle rheology of the lithosphere (*Brace & Byerlee, 1966*; *Byerlee, 1970*; *Byerlee, 1978*) is a crucial mechanism for the onset of the plate tectonic regime, since it limits the maximum stress sustainable by the lid, and also reduces the effective resistance of the lithosphere (*Moresi & Solomatov, 1995*). Moreover, the plastic rheology that characterizes the deep warmer portions of the lithosphere allows for the propagation of the weak zones toward the base of the lid (*Karato, 2010*). The strength envelope of the lithosphere is computed by considering the P-dependent resistance to brittle failure, and the $T-\sigma-$dependent resistance to plastic yielding (*Brace & Kohlstedt, 1980*; *Kohlstedt et al., 1995*). The differential stress required to break/yield the oceanic lithosphere at $\approx 40\ km$ and $600\ K$ is $\approx 800\ MPa$ (*Kohlstedt et al., 1995*; *Stern et al., 2018*).

The rheology of the lithosphere, along with the thermal evolution of the mantle, controls the tectonic regime of terrestrial planets (*Bercovici, 2003*; *O'Neill et al., 2007*; *Bürgmann & Dresen, 2008*; *Stern & Gerya, 2018*), hence their habitability (*Bergin et al., 2015*; *Way et al., 2016*; *Javaux, 2019*). The absence of active plate margins on most terrestrial planets might indicate that their lithospheres have a higher threshold to trigger brittle-plastic failure behaviour, coupled with a much lower geological stress (*O'Neill et al., 2007*).

The tectonic style of the Earth evolved and matured into the present-day plate tectonics as a consequence of its cooling history (*McGovern & Schubert, 1989*; *Hawkesworth et al., 2016*). It has been suggested that Earth's tectonic regime switched from a bottom-up plume-driven convection, into a top-down plate-driven convection over the past 4 $Gyrs$ (*Ernst, 2017*). The exact time frame during which the present-day plate tectonics started, is still heavily debated (*Korenaga, 2013*). Modern estimates constrain the onset of plate tectonics between 3.8 $Gyrs$ (*Keller & Schoene, 2018*) and 2 $Gyrs$ (*Holder et al., 2019*).

It is still not clear how plate tectonics started on Earth, and if this behaviour was also present on other planets in the past (*Bürgmann & Dresen, 2008*). However, most hypotheses address the necessity of stress focussing mechanism (*Hall et al., 2003*; *Nikolaeva et al., 2010*; *Thielmann et al., 2015*; *Crameri & Tackley, 2016*) and strain-weakening processes (*Tackley, 2000b*; *Thielmann & Kaus, 2012*; *Gueydan et al., 2014*) in order to break the lithosphere and allowing for the onset of plate tectonics.

From laboratory deformation experiments, it appears that water (H_2O), has a strong effect by reducing the brittle-plastic yield strength of lithospheric minerals (e.g. quartz - *Griggs, 1967*; plagioclase - *Rybacki & Dresen, 2000*; clinopyroxene - *Chen, 2006*; garnet - *Su et al., 2002*; olivine - *Mei & Kohlstedt, 2000a, 2000b*). Water is one of the most common molecules on Earth's surface, representing Earth's peculiar traits to distinguish it among the other planets of the Solar System (*Sagan, 1994*). A fundamental question arises from these considerations: *can water be the key component that accounts for Earth's plate tectonics?*

1.3. Earth and Venus: a Comparison

The importance of water on plate tectonics can be grasped by considering Earth's twin sister Venus (*Malcuit, 2014*). Venus has a planetary radius of 6052 km (Earth, 6371 km), its mass is $4.86 \times 10^{24}\ kg$ (Earth, $5.97 \times 10^{24}\ kg$), leading to an average density of 5240 $kg\ m^{-3}$ (Earth, 5517 $kg\ m^{-3}$) (*Ringwood & Anderson, 1977*). The reduced density, i.e. without considering gravitational compression, of both planets is around 4000 $kg\ m^{-3}$ (*Flamini, 2014*). The moment of inertia I provides information on the internal structure of a planet: $I = 0.4$ indicates an homogenous sphere, $I < 0.3$ indicates the presence of a dense differentiated core (*Flamini, 2014*). Venus's moment of inertia is $I \approx 0.33$, hence is characterized by a metallic core similar to the one of Earth ($I \approx 0.33$). From the analysis of I, *Margot et al., (2021)* predict that Venus has an outer core radius of $\approx 3500\ km$, i.e. 58% of the equatorial radius (Earth, 3480 km, i.e. 55%). The gravity acceleration measured on Venus is 8.87 $m\ s^{-2}$(Earth, 9.81 $m\ s^{-2}$) (*Seiff, et al., 1979a, 1979b*).

Despite all these geophysical similarities, Venus possesses remarkably different climatic conditions. The planet is surrounded by a dense CO_2–rich atmosphere (96% CO_2 *Zasova et al., 2007*) reaching a ground pressure of >90 atm, and a temperature of 660–740 K (*Seiff, et al., 1979a, 1979b*; *Fegley et al., 1992*; *Johnson & Fegley, 2002*). Venus is the hottest planet in the Solar System thanks to the sustained greenhouse effect of its thick atmosphere (*Pollack et al., 1980*). Moreover, Venus's clouds contain a 75 $wt\%$ solution of sulphuric acid H_2SO_4 (*Young, 1973*). This environment presents forbidding conditions to host any known life form on the surface (*Cockell, 1999*), although organic molecules are potentially stable in the uppermost atmosphere (*Limaye et al., 2018*).

Considering its geology, Venus's topography is dominated by flat volcanic planes (80% of the surface has $< 1\ km$ elevation - *Ford & Pettengill, 1992*), and it does not present any divergent or convergent margins (*Nimmo & McKenzie, 1998*). Geophysical measurements on Venus also reveal a weak magnetic field (*Russell, 1980*; *Nimmo, 2002*; *Zhang et al., 2006, 2016*). These observations lead to the conclusion that Venus does not present a plate tectonics regime (*Turcotte, 1993*). As stated above, plate tectonics has a fundamental role in regulating Earth's climate (*Brune et al., 2017*), by sequestrating the CO_2 from the surface (*Duncan & Dasgupta, 2017*). In the absence of CO_2-removal mechanism, present-day Venus is characterized by a heavy greenhouse effects (*Grinspoon, 2013*). Without plate tectonics, Venus evolved extreme surface conditions that made it earn the title of '*hellish planet*' (*Byrne, 2021*).

Currently, it is not clear what could have caused such similar planets to exhibit such different tectonic regimes. However, from spectroscopic analysis it appears that one fundamental compound is heavily depleted in Venus's atmosphere, namely water (*Moroz et al., 1979*; *Hoffman et al., 1980*; *Johnson & Fegley, 2000*). Venus seems to be a very dry planet that exhausted its initial water budget over the past eons (*Kulikov et al., 2006*; *Kurosawa, 2015*). Several authors address the lack of water on Venus as a potential explanation for the absence of plate tectonics on the planet (*Phillips et al., 1981*; *Mian & Tozer, 1990*; *Nimmo & McKenzie, 1998*; *Tikoo et al., 2017*).

This comparison reveals that the presence of water on Earth is important for Earth's geological history and habitability. This topic has been at the centre of many studies in the past decades, all trying to answer several fundamental questions: *Where did Earth's water come from? Can water be hosted in Earth's rocks and minerals? What is the effect of water on Earth's minerals? Is there any water in Earth's interior?*

1.4. Where did Earth's Water Come From?

The origin of water on Earth is a conundrum that has challenged researchers for many decades. Currently, two main models have been proposed to explain the water budget on Earth (*O'Brien et al., 2018*): the impact of icy comets coming from the region beyond Jupiter (*Chyba et al., 1990*; *Owen & Bar-Nun, 1995*), and the heterogeneous accretion of rocky asteroids originating from various regions of the Solar System (*Rubie et al., 2015*). Both scenarios locate the main water delivery event before the so-called *Late Veneer* stage (*Chyba, 1991*), which refers to the late impact of planetesimals after the iron-nickel segregation during core formation (*Dauphas & Marty, 2002*; *Maier et al., 2009*).

1.4.1. Icy Comets as Water Source

In the recent years, the hypothesis of comets as main water carriers has been challenged by the isotopic constraints on the deuterium/hydrogen ratio (*Bockelée-Morvan et al., 2004*). The *in-situ* measurements of ice from Jupiter family comets (e.g. Rosetta mission *Glassmeier et al., 2007*) show a three-times higher D/H ratio compared to the SMOW (i.e. Standard Mean Ocean Water) measured on Earth (*Altwegg et al., 2015*). On the other hand, other authors report a D/H ratio of the same family comets that is comparable with the SMOW (*Hartogh et al., 2011*; *Lis et al., 2013*). Nevertheless, estimates on the efficiency of water delivery through comet impact, predict that only $\approx 10\%$ of Earth's water budget has been accreted in this way (*Morbidelli et al., 2000*). From these observations, it becomes apparent that comet delivery mechanism cannot be solely responsible for Earth's water reservoir.

1.4.2. Rocky Asteroids as Water Source

The second hypothesis identifies the rocky asteroids as Earth's main water source (*Morbidelli et al., 2000*; *Broadley et al., 2020*). Over the years, it has been noticed that the closest proxy to Earth's composition is the chondrite meteorite family (*Birch, 1965*). Among this family, the scientific community identifies two main building blocks of the Earth: carbonaceous chondrites (volatile-rich and oxidized - *Hart & Zindler, 1986*), and dry enstatite chondrites (with similar isotopic ratio to Earth's rocks and heavily reduced - *Javoy et al., 2010*). However, the exact proportion of these two components is still debated. *Fitoussi & Bourdon, (2012)* compared the silicon isotopic signature ($\delta^{30}\mathrm{Si}$‰) of meteorites with terrestrial samples, revealing several inconsistencies in the enstatite chondrite model for the bulk Earth. They propose a chondrite mixing model which includes three chondrite family groups (CI-CO-LL) with a maximum of 15% of enstatite chondrites (EC).

1.4.3. Water Delivery to Earth

The delivery mechanism of carbonaceous chondrites is still debated, and two main scenarios have been proposed (*O'Brien et al., 2018*): (1) the Nice model scenario (*Gomes et al., 2005*; *Morbidelli et al., 2005*; *Tsiganis et al., 2005*) where the majority of carbonaceous-chondrite-like material reached Earth from the asteroid belt between Jupiter and Mars (i.e. 2.5–4 Astronomical Units *Izidoro et al., 2013*); (2) the Grand Tack scenario, where the outward migration of Jupiter and Saturn caused a major input of volatile-bearing material toward Earth's accretion region (*Walsh et al., 2011, 2012*; *O'Brien et al. 2014*).

Scenario (1) assumes that Jupiter and Saturn had a co-planar low-eccentricity orbit during Earth's accretion stage (*O'Brien et al., 2006*; *Raymond et al., 2009*). Additionally, this model requires a large input of carbonaceous chondrites in order to build Earth's water budget. However, this scenario leads to a large discrepancy from Earth's constraints on the volatile elements' abundances, and the oxygen isotopic ratios (*Drake & Righter, 2002*; *Marty, 2012*). Scenario (2) produces a better match with the observable Solar System (in terms of planet size), but it requires the influx of fully oxidized carbonaceous-chondrite material, with $20\ wt\%\ H_2O$, in order to reproduce the Earth's isotopic constraints (*Rubie et al., 2015*).

Scenario (2) seems to be the most promising hypothesis (*O'Brien et al., 2018*). N-body accretion simulations used in *Rubie et al., (2015)* assume a heterogeneous formation of the Earth's water reservoir. In the early stages of its accretion, Earth's feeding zone was primarily the inner Solar System (i.e. within Jupiter's orbit, $0-5\ au$ *Namouni et al., 1996*; *Weidenschilling et al., 1997*), and the major building blocks were the dry, heavily reduced, planetesimals originating close to the Sun ($< 0.9-1.2\ au$ - *Morbidelli et al., 2000*; *Dauphas, 2017*; *Rubie et al., 2011*). In a later stage, a major influx of increasingly oxidized carbonaceous chondrites coming from the region between Jupiter and Saturn ($6-7\ au$ *Alexander et al., 2012*; *Schlichting et al., 2015*), is thought to have delivered most of the Earth's water budget, as predicted by the Grand Tack hypothesis (*Wood et al., 2008*; *Rubie et al., 2011, 2015*). In the N-body simulations, the main hydration pulse occurs after $60-80\%$ of Earth's final mass has accreted, i.e. before the *late veneer* (*O'Brien et al., 2018*). This late stage accretion of material from beyond the snow line (i.e. $\approx 3.2\ au$ - *Martin & Livio, 2012*) represents the best-fit scenario with the current geochemical constraints (*Clayton et al., 1984*; *Dauphas et al., 2002*; *Drake & Righter, 2002*; *Marty, 2012*). On the basis of the data provided by the aforementioned studies, scenario (1) is considered outdated.

Additional planet accretion models that might help explaining the Earth's water budget are: pebble accretion (*Levison et al., 2015*), the inward scattering of planetesimals during the gas giants formation (*Raymond & Izidoro, 2017a*), and the low mass asteroid belt hypothesis (*Raymond & Izidoro, 2017b*).

1.4.4. Protosolar Gas as Water Source

Another source of water on Earth might have been the protosolar nebula gas that surrounded the Earth at the time of its formation. To incorporate this source of volatiles, the fast accretion of the planetary mass is necessary to gravitationally capture the gas before the dissipation of the protosolar nebula (i.e. $< 4\ Myrs$ since the birth of the Solar System - *Wang et al., 2017*). The pebble accretion model represents a potential mechanism to accrete Earth-mass objects in few thousand years (*Johansen et al., 2007*; *Youdin, 2011*; *Lambrechts & Johansen, 2012*; *Kretke & Levison, 2014*). Assuming such fast accretion for the Earth case, the protosolar gas might have been captured, and its volatiles still retained in the present-day Earth (*Wu et al., 2018*). This hypothesis is supported by the H isotopes (*Hallis et al., 2015*), and Ne isotopes (*Yokochi & Marty, 2004*; *Williams & Mukhopadhyay, 2019*) measured in erupted lavas. Present-day estimates of Earth's accretional water budgets vary between $1-4$ ocean masses when only the contribution of planetesimals is considered, and it expands to $7-12$ ocean masses when the protosolar gas is included in the computation (*Ohtani, 2020*).

1.5. Silicate Earth's Layers and their Lithologies

In order to study the effect of water on Earth's plate tectonics, it is fundamental to provide a description of the four main layers of the silicate Earth: the crust (CR), the upper mantle (UM), the mantle transition zone (MTZ), the lower mantle (LM). Each layer is characterized by a distinct mineral assemblage.

The silicate Earth is chemically differentiated from the inner portion of the planet, namely the core (*Rubie et al., 2011*). Earth's core is predominately composed by dense Fe–Ni alloys, and it is subdivided in an outer liquid part (*Jeffreys, 1926*), and an inner solid part (*Lehmann, 1936*). Water can react with the Fe alloys of the core to form hydrated oxides (*Stevenson, 1977*; *Fukai, 1984*). The presence of water in the core changes its physical properties, in particular reduces its density and the solidus temperature (*Fukai, 1992*). *Ab initio* calculations of the partition coefficient between Fe and Si melts reveal the siderophile nature of H_2O (*Li et al., 2020*). According to these studies, the core might represents the largest reservoir of water on Earth (*Li et al., 2020*), containing 2–10 ocean masses (*McDonough, 2003*; *Wu et al., 2018*).

In this thesis, the discussion regarding the role of water in Earth's core is limited to this paragraph. The focus of this thesis is the effect of water on plate tectonics. Therefore, in this chapter, the solely role of H_2O in the silicate Earth will be discussed.

1.5.1. Crust

The crust is the outermost layer of the Earth, which is chemically distinguished from the underlying upper mantle (*Vening Meinesz, 2012*) since it exhibits a variety of different lithologies: metamorphic, igneous, and sedimentary rocks (*Tucker, 2001*; *Winter, 2010*). Earth's crust can be differentiated into two main components (*Hofmann, 1988*): the oceanic crust, exemplified by Mid Ocean Ridge Basalts (i.e. MORB) composition; and the continental crust, exemplified by a granite composition. The mineral assemblage of MOR basalts is characterized by: 50 $wt\%$ plagioclase Pl, 40 $wt\%$ ortho-/clinopyroxenes Px, 10 $wt\%$ accessory minerals (e.g. magnetite, ilmenite, olivine) (*Winter, 2010*). The mineral assemblage of granites features: 65 $wt\%$ Pl, 30 $wt\%$ quartz Qtz, 5 $wt\%$ accessory minerals (e.g. corundum and biotite) (*Winter, 2010*). The oceanic crust is thin ($\approx 6–10\ km$ *White et al., 1992*) and dense ($\approx 2900\ kg\ m^{-3}$ - *Carlson & Raskin, 1984*), characterizing Earth's ocean basins (*Gale et al., 2013*), whereas the continental crust is thick and light ($\approx 15–70\ km$ $\approx 2830\ kg\ m^{-3}$ *Christensen & Mooney, 1995*), characterizing Earth's continents and continental shelves (*Le Fort et al., 1987*; *Schermaier et al., 1997*).

From the available dataset, there is no representative paradigm of a subducting slab (*Syracuse et al., 2010*). However, an idealized slab can be imagined as a $100–km$ thick sheet-like object composed of a $0.5–km$ thick sediment layer (*Straub & Layne, 2003*) which is enriched in carbon (i.e. CO_2) and aluminum (Al_2O_3) (*Tucker, 2001*), an $8\ km$ thick oceanic crust which includes a shallow basaltic layer ($\approx 2\ km$ - *Dilek & Furnes, 2014*), plus a deeper gabbroic complex (i.e. intrusive basalts, $\approx 6\ km$ - *Le Voyer et al., 2019*), and $> 90\ km$ thick harzburgitic mantle layer at its base (*Boudier & Nicolas, 1985*). Harzburgite is the residual rock originating from the partial melting of the upper mantle (pyrolite = 25% basalt + 75% harzburgite - *Ringwood, 1962*), and is made of 80 $vol\%$ of α–olivine Ol, $(Mg, Fe)_2SiO_4$, 15 $vol\%$ of orthopyroxene and 5 $vol\%$ of garnet (*Irifune & Ringwood, 1987*). The definition of a slab is therefore chemo-mechanical, since it includes both the crust and the brittle part of the mantle (*Stern, 2002*).

1.5.2. Upper Mantle

The upper mantle is the layer of the Earth extending from the bottom of the crust down to $\approx 410\ km$ of depth. The upper mantle is bounded at the top by the Mohorovičić seismic discontinuity (*Lovering, 1958*; *Bullard & Griggs, 1961*; *Jarchow & Thompson, 1989*). The '*Moho*' discontinuity is determined by the different lithology that distinguishes the upper mantle from the crust. Mantle lithology is exemplified by the '*pyrolite*' model (*Ringwood, 1962*; *Anderson & Bass, 1984*), which is assumed to be composed of: $\approx 60\ vol\%$ of $\alpha-$olivine, and by $\approx 40\ vol\%$ of a mixture of garnet Grt and ortho-/clinopyroxenes Px the proportion of which varies with depth (*Frost, 2008*).

1.5.3. Mantle Transition Zone

The MTZ is the Earth's layer enclosed by two seismic discontinuities, located at $410\ km$ and $660\ km$ depth. The abrupt velocity increase of both longitudinal and shear waves has been attributed to two phase transformations. First, $\alpha-$olivine transforms into $\beta-$olivine Wd (i.e. wadsleyite) at $\approx 410\ km$ of depth (*Bina & Wood, 1987*; *Frost, 2008*). Second, $\gamma-$olivine Rw (i.e. ringwoodite) breaks down into the lower mantle assemblage (i.e. bridgmanite and ferropericlase) at $\approx 660\ km$ of depth (*Frost, 2008*; *Ishii et al., 2018, 2019*).

The phase transition from wadsleyite to ringwoodite has been experimentally shown to occur at pressure conditions corresponding to $\approx 520\ km$ of depths (*Akaogi et al., 1989*; *Katsura & Ito, 1989*; *Suzuki et al., 2000*; *Frost, 2008*). However, the existence of a $520\ km$ discontinuity is a strongly debated topic in the geosciences community (*Shearer, 1990, 1996*; *Cummins et al., 1992*; *Bock, 1994*; *Sinogeikin et al., 2003*; *Saikia et al., 2008*). The MTZ is composed of $\approx 60\ vol\%$ of β/γ –olivine, $(\mathrm{Mg,Fe})_2\mathrm{SiO}_4$, and by $\approx 40\ vol\%$ of majoritic garnet (*Frost, 2008*).

1.5.4. Lower Mantle and D''

The lower mantle extends from the base of the transition zone down to the Core-Mantle Boundary (CMB), located at $\approx 2890\ km$ of depth (*Gutenberg, 1913*). The pyrolitic LM is assumed to be composed of $\approx 80\ vol\%$ of (Fe,Al)-bearing bridgmanite, Br, $(\mathrm{Mg,Fe})(\mathrm{Si,Al})\mathrm{O}_3$, $\approx 15 vol\%$ of ferropericlase/magnesiowüstite, Fp, $(\mathrm{Mg,Fe})\mathrm{O}$, and $\approx 5\ vol\%$ of Ca–perovskite, CaPv, CaSiO_3 (*Marquardt & Thomson, 2020*).

In the past few decades, the presence of a corrugated topography at the base of the mantle has been noticed (*Olson et al., 1987*), which has been identified as an additional layer of the mantle, named D'' (*Hernlund et al., 2005*; *Hutko et al., 2008*; *Wookey et al., 2005a, 2005b*). The D'' layer is believed to be composed mainly of the post-perovskite phase, PPv, MgSiO_3 (i.e. post-bridgmanite) (*Murakami et al., 2004*; *Oganov & Ono, 2004*; *Tsuchiya et al., 2004*; *Wentzcovitch et al., 2006*).

1.6. Can Water be Stored in Earth's Rocks and Minerals?

As stated in the previous section, Earth is predominantly made of silicate rocks, since the mantle constitutes 67% of Earth's mass ($\approx 4.01 \times 10^{24} kg$), and 84% of its volume (*Anderson, 2007*). The global mass of Earth's oceans is approximately $1.4 \times 10^{21} kg$ (*Eakins & Sharman, 2010*) and, by assuming an initial water budget of 12 ocean masses (upper end member discussed in *Ohtani, 2020*), the estimated total mass of Earth's water is $1.68 \times 10^{22} kg$. Even after considering this upper end member, water represents only $0.004\ wt\%$ of the silicate mantle, therefore making the Earth an essentially dry planet.

Nevertheless, two main conclusions can be drawn: (1) most of the water on Earth is somehow stored in the silicate rocks of the mantle or in the metal alloys of the core; (2) given the size of the mantle, an average water concentration of $300\ ppm$ in mantle rocks (a conservative estimate according to *Ohtani, 2020*) suffices to match the global mass of the oceans. The question now is: *How can water be incorporated into Earth's minerals?*

Natural samples and laboratory experiments reveal that water can be contained in several minerals. Two main families of water-bearing minerals can be distinguished: the nominally hydrous, and the nominally anhydrous minerals.

1.6.1. Water Bearing Minerals in the Mantle: Nominally Hydrous Minerals

The term '*hydrous mineral*' indicates a mineral phase that hosts water in its crystal lattice in the form of hydroxyl groups $(OH)^-$ or as H^+ ions. These ions are chemically bonded with the rest of the mineral, and they constitute an integral part of the crystal unit cell. The presence of hydroxyl groups in a hydrous phase is explicit in the chemical formula (hence '*nominally*'), e.g. chlorite, Chl, $(Mg, Fe)_3(Si, Al)_4O_{10}(OH)_2 \cdot (Mg, Fe)_3(OH)_6$. Some minerals may also contain H_2O molecules directly in their chemical formula, e.g. lawsonite, Lws, $CaAl_2Si_2O_7(OH)_2 \cdot H_2O$.

The pelagic sediments that constitute the upper part of the slab are represented by the $Al_2O_3 - SiO_2 - H_2O$ system (*Plank, 2013*). The $Al - H_2O$–rich phases that characterize slab sediments at high pressure are: diaspore ($15\ wt\%\ H_2O$, $P < 6\ GPa$ - *Ohtani, 2005*), topaz–OH ($10.7\ wt\%\ H_2O$, $P < 11\ GPa$, $T < 1300\ K$ - *Ohtani, 2005*), phase-Egg ($7.5\ wt\%\ H_2O$, $P = 12 - 24\ GPa$ - *Eggleton et al., 1978*; *Schmidt, 1995*), and the δ–phase ($15\ wt\%\ H_2O$, $P > 24\ GPa$ - *Sano et al., 2004*; *Abe et al., 2018*). Given its extended P-T stability field, the δ–phase is considered to be one of the key hydrous minerals of the slab, capable of carrying water down to the lower mantle (*Duan et al., 2018*).

The main hydrous minerals in the oceanic crust are: lawsonite ($11.2\ wt\%\ H_2O$), chlorite ($13\ wt\%\ H_2O$), phyllosilicates ($2 - 4.5\ wt\%\ H_2O$), and amphibole ($1 - 3\ wt\%\ H_2O$) (*Faccenda, 2014*). These mineral assemblage is stable in the blueschist facies, i.e. at depths $< 100\ km$, $P < 3\ GPa$ (*Schmidt & Poli, 1998*). However, after the blueschist to eclogite transformation (*Green & Ringwood, 1972*; *Fukao et al., 1983*), the only stable hydrous minerals are lawsonite, and the K-bearing phyllosilicate phengite. However, none of them can exist at depths larger than $300\ km$ (*Schmidt & Poli, 1998*; *Okamoto & Maruyama, 1999*).

In the harzburgitic lithosphere, the main hydrous minerals are: chlorite, amphiboles, talc ($4.8\ wt\%\ H_2O$), brucite ($31\ wt\%\ H_2O$), and serpentines ($13\ wt\%\ H_2O$) (*Faccenda, 2014*). At pressure higher than $P > 2\ GPa$, only serpentines and chlorite can exist (*Schmidt & Poli, 1998*).

Laboratory synthesis experiments performed by *Ringwood & Major (1967)* demonstrated the existence of a sequence of high pressure polymorphs of serpentines, which were found to be stable at high pressure and low temperatures conditions (*Ohtani et al., 2000*; *Ohtani et al., 2001*). So far, these phases have not been observed in any natural sample, hence they are addressed with their synthesis name, as phase–A, phase–B and phase–C (*Ringwood & Major, 1967*). This nomenclature reflects the pressure synthesis sequence, having phase–A as the lowest pressure polymorph, and phase–C as the highest pressure polymorph. The '*alphabetical phases*' maintain the bulk chemical composition of the serpentine (i.e. Mg, Si, and H_2O) with a $\approx 15\%$ density increase (*Faccenda, 2014*). Given these characteristics, the alphabetical phases are better known as Dense Hydrous Magnesium Silicates (DHMS). The DHMS have overlapping stability fields, and their sequence might represent a relay-run mechanism capable of delivering water down to the lower mantle (*Frost, 1999*). However, these water carrier phases survive only at P-T conditions corresponding to a cold slab geotherm, and require high water saturation conditions in order to form (*Ohtani et al., 2004*; *Ohtani, 2005, 2020*).

Additionally, recent studies have found a promising high-P hydrous phase, i.e. pyrite type FeO_2H_x. This phase is the result of the reaction between iron and water at $P > 70\ GPa$, and $T \approx 1800$ K (*Hu et al., 2016*; *Nishi et al., 2017*; *Yuan et al., 2018*). Thus, the FeO_2H_x phase might be capable of transporting water down to the CMB.

1.6.2. Water Bearing Minerals in the Mantle: Nominally Anhydrous Minerals (NAM)

Some minerals can incorporate relevant quantities of water in the form of defects in the crystal lattice (*Smyth, 1987*). The presence of $(OH)^-$groups or H^+ ions is not explicit in the chemical formula of the mineral, hence the term '*nominally anhydrous*'. Nevertheless, NAM can store up to several $wt\%$ units of water and, given their abundance in the mantle, they represent potential water reservoirs in the deep Earth.

The water solubility in α–olivine increases with pressure, reaching $4000\ ppm$ (i.e. $0.4\ wt\%$) at the base of the upper mantle (*Bolfan-Casanova, 2005*; *Litasov & Ohtani, 2007*).

The main nominally anhydrous minerals in the mantle are the high-pressure polymorphs of olivine: wadsleyite β–$(Mg,Fe)_2SiO_4$, and ringwoodite γ–$(Mg,Fe)_2SiO_4$. The peculiar crystal structure of these two minerals, allows for the incorporation of $(OH)^-$, and H^+ in the defects of the crystal lattice (*Smyth, 1987*; *McMillan et al., 1991*; *Young et al., 1993*; *Jacobsen et al., 2005* for wadsleyite, and *Grüninger et al., 2017, 2018, 2020* for ringwoodite). Initial estimates predicted an H_2O solubility of $3.3wt\%$ for Mg–wadsleyite and $2.5wt\%$ for Mg–ringwoodite (*Kohlstedt et al., 1996*; *Keppler & Smyth, 2006*), although more recent measurements re-evaluated these values, reporting a water solubility of $1.8–2.3wt\%$ and $1.0–1.5wt\%$ (*Inoue et al., 2010*). The lower water solubility in the recent dataset is justified by the fact that the measurements were performed for Fe-bearing minerals ($Mg_{0.8}$, $Fe_{0.2}$), and at higher temperatures $\approx 1600\ K$.

Stishovite, Stv, (i.e. high-P polymorph of SiO_2) may be considered to be a potential NAM depending on temperature, pressure and composition. Water content in pure SiO_2 ranges from $\approx 50\ ppm$ at warm conditions ($\approx 1400\ K$ - *Bolfan-Casanova et al., 2000*) to $1.3\ wt\%$ at cold conditions ($\approx 800\ K$ - *Spektor et al., 2011*). In Al–bearing stishovite, the water content ranges from $\approx 800\ ppm$ at low pressure ($\approx 14\ GPa$ - *Chung & Kagi, 2002*) to $\approx 2500\ ppm$ at high pressure ($\approx 20\ GPa$ - *Litasov et al., 2007*). Stishovite represents $10\ vol\%$ of the meta-basaltic crust in the

MTZ and reaches, after the post-pyroxene reaction ($\approx 18\ GPa$ - *Oguri et al., 1997*; *Akaogi et al., 2004*), $20\ vol\%$ in the lower mantle (*Marquardt & Thomson, 2020*). The water solubility of stishovite might be important for the preservation of water in the meta-basaltic part of the slab.

Regarding the water solubility of lower mantle phases, many studies report contradictory results: $0-1\ ppm$ for pure Mg–bridgmanite (*Bolfan-Casanova et al., 2000*; *Litasov et al., 2003*), $< 10\ ppm$ for Fe–Al–bridgmanite (*Bolfan-Casanova et al., 2003*; *Panero et al., 2015*), $40-110\ ppm$ in Fe–Al–bridgmanite (*Litasov et al., 2003*), $1000\ ppm$ in Fe–Al–bridgmanite (*Fu et al., 2019*), $0.2\ wt\%$ in bridgmanite and magnesiowüstite (*Murakami et al., 2002*), and $20\ ppm$ in magnesiowüstite $(Mg_{0.93}, Fe_{0.07})O$ (*Bolfan-Casanova et al., 2002*). Despite these inconsistencies, all experimental results agree in reporting a much lower water solubility in the lower mantle assemblage compared to the MTZ.

1.7. What is the Effect of Water on Earth's Minerals?

As stated above, the incorporation of water into minerals introduces $H^+$and OH^- into the crystal lattice (*Keppler & Bolfan-Casanova, 2006*). These ions are very light (H^+: 1u, OH^-: 17u) with a relatively large ionic radius (O^-: 1.4 Å) compared to the rest of the ions (masses: Mg^{2+} : 24.3 u, Fe^{2+} /Fe^{3+}: 55.8 u – ionic radii: Mg^{2+}: 0.86 Å, Fe^{2+}: 0.75 Å, Fe^{3+}: 0.69 Å). $H^+$and OH^- ions create local densities of charge which are balanced by the creation of vacancies in the crystal lattice (i.e. point defects - *Grüninger et al., 2020*). The concentration of lattice vacancies is a crucial parameter for most diffusive processes (*Bolfan-Casanova, 2005*). Therefore, the presence of water in a crystal lattice creates larger and less dense minerals, with enhanced kinetic transport properties (*Jung & Karato, 2001*).

1.7.1. Effect of Water on the Sound Velocities

Thermodynamic calculations performed by *Hacker (2003)* confirm that the presence of water in the mafic (i.e. oceanic crust) and ultramafic (i.e. harzburgite) lithologies of the slab causes a density reduction, and slower seismic velocities (reduction of V_P and of the V_P/V_S ratio). Seismic velocities are reduced because of the softening of the ionic bond strength induced by H_2O, and by the fast kinetics of dislocation migration and grain-boundary sliding (*Karato, 1995*). Moreover, the elastic moduli (bulk modulus K and shear modulus G) of water-bearing minerals decrease with increasing H_2O content (*Jacobsen, 2006*). The pressure derivatives of the elastic moduli (K' and G'), on the other hand, show an opposite trend given the high compressibility of the lattice vacancies (*Jacobsen, 2006*).

However, the magnitude of the water effect on seismic velocities is still debated. For example, recent studies on wadsleyite (*Buchen et al., 2018*) and ringwoodite (*Schulze et al., 2018*) argue that, at MTZ pressures, moderate amounts of water ($< 1wt\%$) would be seismologically invisible. Using Brillouin spectroscopy on hydrous samples, they showed that $\approx 1wt\%$ H_2O decreases the wave velocity only by $< 1\%$, which is well below the present-day detection limit. Alternatively, *Buchen et al. (2018)* and *Schulze et al. (2018)* suggest using the seismic impedance contrast at the MTZ discontinuities to infer the hydration state of the region (*Chambers et al., 2005*; *Bagley & Revenaugh, 2008*).

The acoustic (seismic) impedance $z_{P/S}$ is given by the product of the wave velocity $V_{P/S}$ and the density ρ of the medium in which the wave travels ($z = V\rho$) (*Aki & Richards, 1980*). Changes in the impedance contrast at the interface between two media cause changes in reflectivity r, i.e. the amount of energy that is reflected back at the interface.

$$r = \frac{z_2 - z_1}{z_2 + z_1} \tag{1.7.1}$$

Where z_n is the impedance of the relative propagation media, assuming that a ray is travelling from layer 1 into layer 2. Depending on the impedance contrast, three things might happen: (1) no reflection ($z_1 = z_2$), i.e. the wave energy is entirely transmitted through the interface; (2) positive reflection ($z_1 > z_2$), i.e. part of the wave energy is transmitted through the interface, and part is reflected back with the same phase as those of the incoming ray; (3) negative reflection ($z_1 < z_2$) i.e. the wave is reflected with an opposite phase.

In some minerals (e.g. ringwoodite), water affects predominantly only one elastic modulus (e.g. shear modulus G), which leads to a marked difference between the V_P/V_S ratios at high

pressure (*Jacobsen & Van Der Lee, 2013*), and higher impedance contrasts (i.e. Δz_P vs. Δz_S). This feature represents a key element for the seismic detection of water at depth (*Jacobsen & Van Der Lee, 2013*).

The Brillouin spectroscopy measurements of the sound velocities report that DHMS minerals are characterized by $7-16\%$ slower V_P and V_S, compared to the dominant minerals of the ambient mantle (*Sanchez-Valle et al., 2008*; *Mashino et al., 2016*; *Satta et al., 2019*). *Liu et al. (2017)* report also a low seismic velocity for FeO_2H_x, if compared to the ambient lower mantle.

1.7.2. Effect of Water on Rheology

Water enhances the anelastic behaviour of minerals, leading to a higher seismic attenuation, i.e. lower quality factor Q (*Karato, 2006*). Furthermore, H_2O favours any type of creep deformation, by enhancing vacancy diffusion (diffusion creep), defect migration (dislocation climb), and by reducing the Peierls stress barrier (dislocation glide) (*Karato, 2006*; *Kohlstedt, 2006*). This should have a major implication on the plastic deformation of rocks (*Katayama & Karato, 2008*), and on their effective viscosity (*Mei & Kohlstedt, 2000a, 2000b*).

Karato (2006), predicts a viscosity reduction of $O(10^3)$ with just $0.1\ wt\%$ H_2O. However, experiments performed by *Fei et al. (2013)* show that the viscosity reduction is minimal for olivine at upper mantle conditions ($< O(10^1)$ for $100\ ppm$ H_2O), whereas it is relevant for wadsleyite and ringwoodite in the MTZ ($\approx O(10^2)$ for $1\ wt\%$ H_2O - *Fei et al., 2017*).

Moreover, the water expelled by the breakdown of hydrous phases might be accumulated between the grain boundaries and in the pore space (*Huang et al., 2019, 2020*). The increasing pore fluid pressure might counteract the lithostatic pressure, thus triggering earthquakes by reducing the differential stress necessary for brittle failure (*Thielmann, 2018*). This rock-weakening mechanism is called '*dehydration embrittlement*' (*Yamasaki & Seno, 2003*; *Jung et al., 2004*). Several authors address the dehydration embrittlement as the cause of intermediate-deep earthquakes (i.e. $70-300\ km$), and the double-seismic zone within the slab (*Hacker et al., 2003*; *Yamasaki & Seno, 2003*; *Faccenda et al., 2012*; *Campione & Capitani, 2013*). However, the occurrence of this mechanism is still heavily debated, and other processes might be responsible for the intermediate-deep earthquakes (e.g. thermal runaway - *Thielmann, 2018*). Some authors report that the weakening effect of dehydration is related to the dynamic recrystallization of the minerals, following the volume decrease due to the loss water (e.g. *Ferrand et al., 2017*).

1.7.3. Effect of Water on the Electrical conductivity

In recent years, electrical conductivity measurements have provided promising insights into detecting water in the mantle (*Yoshino et al., 2008*). This method is of importance since electrical conductivity is sensitive to small amounts of H^+ and Fe, and it varies by orders of magnitude when a conductive object is present at depth (*Koyama et al., 2006*).

The electrical conductivity $\sigma\ [S\ m^{-1}]$ is related to the concentration of hydrogen $C_H\ [atom\ m^{-3}]$ given by the Nernst-Einstein relationship (*Karato, 1990*).

$$\sigma = \frac{C_H \kappa q^2}{kT} \tag{1.7.2}$$

Where $\kappa\ [m^2\ s^{-1}]$ is the diffusivity, q is the elementary charge of H^+ (i.e. $1.60 \times 10^{-19}\ C$), k is the Boltzmann constant ($1.38064852 \times 10^{-23}\ m^2 kg\ s^{-2} K^{-1}$), and T [K] is the temperature. A possible explanation for this H^+ dependency was suggested by *Huang et al. (2005)*, who proposed

that the hydrogen ions in the crystal lattice act as free protons, thus reducing the activation enthalpy for conduction.

According to *Karato and Dai (2009)*, the electrical conductivity of dry wadsleyite is comparable to that of dry olivine. Therefore, any jump in electrical conductivity detected at 410 km is likely produced by the high water content (i.e. H^+) of the MTZ.

1.7.4. Effect of Water on the Phase Boundary Depths

The most important discontinuities within the mantle are represented by the phase transition of Ol → Wd at 410 km, and the transition of Rw → Br + Fp at 660 km. However, the depth at which these phases transform is not constant, and depends on the temperature of the reacting minerals (*Katsura et al., 2004*; *Suetsugu et al., 2010*). This is due to the nature of the thermodynamic process (either endothermic or exothermic), and the Clausius-Clapeyron slope that characterizes the reaction (see **Chapter 2.6.3**, and **Chapter 7** for further details).

Experimental constraints on the $P-T$ stability field of hydrous wadsleyite reveal that, for increasing water content, the 410 km–discontinuity shifts toward shallower depths, and it broadens the two-phase coexisting region (*Wood, 1995*; *Smyth & Frost, 2002*; *Konstantin et al., 2006*). The 660 km–discontinuity, on the other hand, shows an opposite behaviour, shifting toward larger depths as the water content increases (*Higo et al., 2001*; *Litasov et al., 2006*; *Litasov & Ohtani, 2007*). Furthermore, the post-garnet reaction (720 km) shows a similar deepening for increasing H_2O (*Sano et al., 2006*).

1.7.5. Effect of Water on other Properties of Rocks

Experimental measurements show that water has an effect on the lattice thermal conductivity of olivine (50% reduction with 0.7 $wt\%$ H_2O - *Chang et al., 2017*), and on the radiative thermal conductivity of both wadsleyite and ringwoodite (30– 40% reduction with 1.0 $wt\%$ H_2O - *Thomas et al., 2012*). The effect of water on thermal conductivity will be discussed in **Chapter 5**.

Moreover, many experimental results on different mantle assemblages demonstrate that the presence of free water reduces the solidus temperature T_{melt} of the rocks: 30 $wt\%$ H_2O in natural spinel-bearing lherzolite reduces T_{melt} by ≈ 400– 700 K depending on pressure (*Kushiro et al., 1968*); 10 $wt\%$ H_2O in the pyroxenite assemblage (53 $wt\%$ diopside, 47 $wt\%$ enstatite) reduces T_{melt} by ≈ 100 K (*Kushiro, 1972*); 6 $wt\%$ H_2O in pyrolite reduce the solidus by ≈ 400 K (*Green, 1973*); water-saturated conditions in pyrolite reduce T_{melt} by ≈ 1000 K (*Kawamoto & Holloway, 1997*). More recent calculations performed by *Hirschmann (2006)* predict a 200 K reduction for pyrolite +1000 ppm of water.

Measurements of the C_{H2O} of Al-bearing enstatite (20– 40 $vol\%$ of UM), reveal that the minimum water solubility in the upper mantle coincides with the Low Velocity Zone (LVZ) that characterises the asthenosphere (*Mierdel et al., 2007*). The presence of free water in the shallow lower mantle is believed to trigger the partial melting of the pyrolitic rocks, thus creating a weak layer right beneath the lithosphere (*Green et al. , 2010*).

1.8. Is there any Water in Earth's Interior?

The presence of water in the Earth's interior has been investigated thoroughly over the years by analyzing mantle xenoliths, and by observing the changes in the physical properties of the mantle using geophysical methods.

1.8.1. Water at Depth: Evidence from Natural Samples

The measurements for natural olivine samples from MORB, and ocean island basalts (OIB) reveal a water content C_{H2O} of $0-700\ ppm$ (*Miller et al., 1987*; *Bell & Rossman, 1992*; *Bell et al., 2004*). However, measurements for mantle xenoliths and geophysical observations performed by *Jones et al. (2013)* and *Peslier et al. (2017)* report a rather dry UM with $C_{H2O} < 200\ ppm$, and some local enrichment of $C_{H2O} \approx 400\ ppm$ (*Pommier, 2014*).

A single crystal of ringwoodite of $\approx 40\ \mu m$ size was found as an inclusion, inside an ultra-deep diamond from Brazil (Juína district, Mato Grosso) (*Pearson et al., 2014*). This sample could represent ambient transition zone conditions, provided that it was encapsulated during diamond formation. Analysis of the sample with Fourier-Transform Infrared Spectroscopy (FTIR) showed that it contains $\approx 1.5\ wt\%$ of H_2O, implicating at least a locally water-rich transition zone.

Recently, *Tschauner et al. (2018)* found ice-VII inclusions in diamonds coming from South Africa (Namaqualand) and China (Shandong). Among thirteen samples, only two originated from the transition zone. It was concluded that water was trapped as a complex hydrous melt and crystallized during ascent. These evidences show that a water-rich fluid region occurs around the lower MTZ boundary beneath South Africa and China.

Furthermore, Phase-Egg, $AlSiO_3(OH)$, was found in a diamond Brazil (Juína district, Mato Grosso) (*Wirth et al., 2007*). The inclusion paragenesis is dominated by ultra-high pressure phases corresponding to the lower MTZ. This natural sample suggests that crustal material, possibly corresponding to the H_2O-Al-rich meta-sediment layer of the slab, has been subducted down to the MTZ.

1.8.2. Water at Depth: Evidence from Seismic Studies

The indirect observation of water at depth from the recorded seismic velocities is a rather complex task. The difficulty lies in the fact that water has a negligible effect on NAMs at MTZ conditions (*Buchen et al., 2018*; *Schulze et al., 2018b*), and because of the accuracy required to detect water at depth with a statistical significance (i.e. $\pm 3\ km$ for depth estimates and $\pm 0.2\%$ for velocity anomalies - *Suetsugu et al., 2010*).

In the past years, several seismological studies reported a LVZ region at the base of the upper mantle ($\approx 410\ km$ of depth) in different areas of the world: Europe (*Nolet & Zielhuis, 1994*), Japan and China (*Revenaugh & Sipkin, 1994*), and the western United States (*Song et al., 2004*). More recent seismic observations from *Tauzin et al. (2010)* report evidence for a global LVZ at 410 km depth. *Song et al. (2004)* explain the LVZ at 410 km depth by addressing the presence of a hydrous melt layer, which could be linked to prior subduction of the ancient Farallon plate.

The presence of this ponding melt layer is supported by density measurements at high pressure, which reveal that peridotitic magma has a neutral buoyancy compared to the ambient mantle (*Sakamaki et al., 2009*). The melting of the mantle at that depth might be induced by changes in water solubility between MTZ and UM minerals. This is consistent with the water-filter model (*Bercovici & Karato, 2003)*: (I) subduction of the slab induces the displacement of the

surrounding mantle to accommodate the descent; (II) when the slab crosses the MTZ, part of the water-rich wadsleyite is pushed upwards crossing the 410 km stability depth; (III) the ascending wadsleyite transforms into olivine, and releases water at the base of the upper mantle (*Ohtani et al., 2004*); (IV) the free water reduces the solidus temperature of the pyrolitic mantle, causing dehydration melting of the rocks (*Litasov & Ohtani, 2002*). This mechanism might also be triggered by the ascending plumes which push the material in their path upwards (*Bercovici & Karato, 2003*).

The ponding layer of melt at the base of the UM has also been suggested to be the feeding source of the intraplate volcanism in northeastern China (*Yang & Faccenda, 2020*). This geodynamic structure has been called '*Big Mantle Wedge*' (*Zhao, 2004*; *Ohtani & Zhao, 2009*; *Zhao & Ohtani, 2009*).

An LVZ was also found at the base of the MTZ ($\approx 660\ km$ of depth) beneath the United States (*Schmandt et al., 2014*), which might be explained with the same water-filter mechanism (*Bercovici & Karato, 2003*), by assuming a down-ward expulsion of water-rich ringwoodite from the MTZ. The enhanced seismic attenuation found by *Lawrence & Wysession (2006)* beneath East Asia, might be attributed to the low quality factor Q caused by the presence of hydrous melt at the base of the MTZ.

The seismological observations of the topography variations of the MTZ discontinuities are potentially correlated with the local hydration state of the mantle. *Suetsugu et al. (2010)* report a very deep 660 km-discontinuity at 691 km of depth, due to the presence of the stagnant slab beneath the Philippine Sea. They assumed a Clapeyron slope of $-2.0\ MPa\ K^{-1}$ to calculate the temperature reduction due to endothermic post-spinel reaction, which gave an estimate of $-500\ K$ in the proximity of the slab, and around $-200\ K$ in the surrounding area. This is in good agreement with the seismic anomaly found by *Suetsugu et al. (2010)*, and would create a cold region where water could be easily retained in the slab. The chosen Clapeyron slope of $-2.0\ MPa\ K^{-1}$, would imply the presence of 0.2 $wt\%$ H_2O in the region (*Litasov & Ohtani, 2007*).

A similar study was performed by *Houser (2016)* who performed a global seismic analysis of the topography of the 410/660 discontinuity. These observations suggest a globally dry MTZ ($\approx 0.6\ wt\%$, i.e. less than 1 ocean mass), with a few hydrated areas in the proximity of subducting slabs.

1.8.3. Water at Depth: Evidence from Electrical Conductivity Studies

There are two different ways to determine the electrical conductivity in the mantle: (1) the geomagnetic depth sounding (GDS) technique, and (2) the induced electro-magnetic (EM) method. The GDS technique measures the variations in Earth's magnetic field caused by internal changes of the geodynamo, or by spikes in the solar activity. The EM method, on the other hand, employs electrodes that produce a pulse of current in the ground, thereby generating a magnetic flux (Ampère's law). This magnetic field changes with time and induces eddy currents in conductive materials sampled at depth (Faraday's law). The eddy currents oscillate with the same periodicity of the transmitter electrodes, and produce a secondary magnetic field, which is detected by a receiver. This in turn generates a secondary current in the receiver that can be measured by an amperometer.

To probe the deep and large-scale structures of the Earth's interior, it is necessary to measure the electro-magnetic fields for long time periods (from 100 days up to several years), and with good coverage by observatories around the world. The GDS method, in particular, is heavily constrained

by this limitation, because the vertical geomagnetic variations are very small when sampled for short periods.

EM measurements reveal that Earth's upper mantle is dry (*Jones et al., 2013*; *Pommier, 2014*). Using the GDS method *Koyama et al. (2006)* linked the anomalously high conductivity of the MTZ below the Mariana trench with a high water content in this region (estimated to be $\approx 0.3\ wt\%$). *Utada et al. (2009)* resolved the electrical conductivity distribution in the MTZ below Europe and suggested that the European MTZ is drier than that in the western Pacific even though both regions feature stagnating slabs. Additionally, *Khan and Shankland (2012)* infer that the hydration of the transition zone is only a local feature since the mantle beneath both southwestern North America, and central China, appears to be wetter than that beneath central Europe or Australia. A high water content beneath China was also reported by the electrical conductivity measurements performed by *Karato (2011)* and *Yoshino & Katsura (2013)*.

1.9. Deep Earth Water Cycle

In the past decades, geoscientists have collated a large number of geophysical observations and experimental analyses in the quest to answer the questions posed above. Their results were fundamental in discovering that: (1) water can be hosted in minerals; (2) the presence of water in the minerals alters their physical properties; (3) mantle rocks contain a non-negligible amount of water (mantle xenoliths), and (4) several water-induced features characterize the mantle at depth (i.e. melt ponds and broad phase transitions). This poses additional questions: *How does water reach the mantle? Is there an exchange of water between Earth's mantle and its surface?*

Concerning the latter, spectroscopic investigations on volcanic gases reveal that water is the most abundant volatile species exhaled by volcanoes ($75-95\%$ - *Giggenbach, 1996*; *Gerlach, 2004*; *Kern et al., 2017*). Moreover, indirect estimates on the state of the oceans in the past, indicate that the surface budget of H_2O remained approximately constant over time (*Kendrick et al., 2020*). These studies on oceans are based on: isotopic mass-balance calculations (*Lécuyer et al., 1998*; *Parai & Mukhopadhyay, 2012*), consideration of the continental freeboard (i.e. sea level variations *Galer, 1991*; *Korenaga et al., 2017*), and observations on the salinity of oceans over time (*Marty et al., 2018*). Therefore, since water is constantly outgassed from the mantle, and the surface budget has not changed considerably over eons, there must be a mechanism that removes water from the surface and delivers it to the Earth's interior.

These considerations led to the formulation of the deep Earth water cycle model (*Hirschmann, 2006*; *Ohtani, 2020*; *Bekaert et al., 2021*), which represents an extension of the surface water cycle (*Oki et al., 2004*). This model includes the redistribution of water between the Earth's surface and its deep reservoirs. The deep Earth water cycle is driven by plate tectonics, and intrinsically connected with slab subduction (*Crameri et al., 2019*), without which water would be confined to the surface and the atmosphere.

The deep Earth water cycle can be summarized in four main steps (*Faccenda, 2014*): (1) initial storage of water in the oceanic lithosphere at the seabed; (2) subduction of the slab, and introduction of water into the mantle (*Hacker, 2008*); (3) release of fluids at depth, and redistribution of water over the different mantle regions through solid-state rock convection (*Bercovici & Karato, 2003*); ($4a$) expulsion of water toward the surface via volcanic activity and magma degassing (*Green & Falloon, 2015*), and ($4b$) accumulation of water at depth with consequent hydration of the mantle (*Ohtani, 2004*).

1.9.1. Water Storage Inside the Slab

Water is incorporated into the slab lithologies either as a free fluid in the interstices of the rocks (*Davis & Elderfield, 2004*) or as OH^- / H^+ ions in the mineral structure (*Keppler & Smyth, 2006*). In each layer of the slab, water is distributed differently depending on the porosity of the rocks (*Saffer & Tobin, 2011*; *Eichheimer et al., 2020*), and their chemical composition (*Poli & Schmidt, 2002*).

The average composition of Global Subducting Sediments (GLOSS) indicates a water content of 7 $wt\%$. The water is hosted as free fluid in the unconsolidated sediment and chemically bound in the hydrous minerals (*Plank & Langmuir, 1998*; *Plank, 2013*).

The water content of the oceanic crust is primarily given by the hydrothermal alteration reactions (*Alt et al., 1986*), where the percolating seawater interacts with the dry minerals (i.e. pyroxene, feldspars, olivine), and produces amphiboles and phyllosilicates (i.e. chlorite, talc, clay minerals). The hydrothermal systems are located in proximity of the mid-ocean ridges and are driven by the sustained magmatic activity of the area (*Alt, 1995*; *Coumou et al., 2008*). The alteration of the oceanic crust continues far from the spreading centres as well (*Johnson & Semyan, 1994*). The most efficient alteration reaction to incorporate water into the oceanic crust is the serpentinization reaction (*Janecky & Seyfried, 1986*), where H_2O reacts with pyroxene Px and/or olivine Ol to serpentines Srp (see reaction **(1.9.3)** taken from *Lamadrid et al., 2017*). A common by-product of the serpentinization is magnetite Mgt, which is formed when the iron present in both pyroxene and garnet is oxidized by the water (*Lamadrid et al., 2017*).

(1.9.3)

$$(Mg, Fe)_2SiO_4[Ol] + (Mg, Fe)SiO_3[Px] + 2H_2O \leftrightarrow (Mg, Fe)_3Si_2O_5(OH)_4[Srp]$$

$$3Fe^{2+} + 4H_2O \leftrightarrow Fe_3O_4[Mgt] + H_2 + 6H^+$$

The magnetic susceptibility given by the presence of magnetite, is a key feature that allows for the estimation of the degree of serpentinization of the oceanic rocks (*Oufi, 2002*). The water content of a saturated basaltic oceanic upper crust is approximately $\approx 4-6.5\ wt\%$ (*Jarrard, 2003*), while the underlying gabbroic lower crust contains only $0.4-1.4\ wt\%$ of water (*Poli & Schmidt, 2002*; *Carlson & Miller, 2003*).

The lithospheric mantle is hydrated via serpentinization of the harzburgitic rocks, in particular olivine minerals (*Hacker, 2008*). This process occurs in two specific geodynamic environments: (1) at the mid-ocean ridges (*Ildefonse et al., 2007*), and (2) at the trench-rise systems (*Grevemeyer et al., 2018*; *John et al., 2011*; *Michibayashi et al., 2007*; *Ranero et al., 2003*). An intermediate alteration scenario predicts a 5% serpentinization of the upper $6\ km$ of the harzburgitic mantle layer, which corresponds to approximately $2\ wt\%$ of water (*Barnes & Straub, 2010*; *John et al., 2011*). The same water concentration can be achieved if the upper $3\ km$ of the lithospheric mantle are pervasively altered, i.e. 15% serpentinization (*Faccenda et al., 2012*).

By combining the water content estimates for each layer, it can be determined that a subducting slab could host up to $2-3\ wt\%$ of H_2O. Bearing in mind the scale of subduction processes (*Goes et al., 2017*), this amount of hydration of a slab is sufficient to remove large amounts of water from the Earth's surface.

1.9.2. The Fate of Water at Depth: Subduction Zone and Mantle Wedge

Once the slab sinks into the mantle, major changes in both pressure and temperature cause a redistribution of water in the surrounding area, and in the slab itself.

Most of the water hosted in the pores of the sediments is expelled and transported toward the mantle wedge (*Wilson et al., 2014*), and the shallow forearc (*Saffer & Tobin, 2011*; *Faccenda et al., 2012*). The presence of water at the convergent plate boundaries potentially acts as a fault-lubricating mechanism. This facilitates the sliding of the plates by reducing the internal friction, and promotes a self-feeding subduction zone (*Duarte et al., 2015*; *Diao & Espinosa-Marzal, 2018*).

The water that is trapped as fluid inclusions in the interstices deeper inside the slab (e.g. gabbros and serpentinites - *Chepurov et al., 2012*), and the water that is structurally bonded to the minerals (*Ohtani, 2005*), has a higher chance of being transported deeper into the mantle. The progressive heating of the slab during its descent through the mantle causes the breakdown of the least stable hydrous phases, triggering the hydration melting of the mantle wedge (*Ulmer & Trommsdorff, 1995*; *Schmidt & Poli, 1998*; *Rüpke et al., 2004*; *Rustioni et al., 2019*). The consequence of deep hydration-induced melting can be observed as extensive magmatic processes at volcanic arcs, e.g. Japan, Andes and the Cascade Range (*Tatsumi & Eggins, 1995*), and also causes volatile-rich lavas (*Wallace, 2005*).

1.9.3. The Fate of Water at Depth: Upper Mantle

The hydrous phases are stable only at low temperature conditions, i.e. $T < 1300$ K at $P < 10\ GPa$, and $T < 1700$ K at $P > 10\ GPa$ (*Ohtani et al., 1995*; *Litasov & Ohtani, 2003*; *Ohtani et al., 2004*). Therefore, the only suitable place for the survival of the hydrous phases is the cold lithosphere of the subducting slab (*Van Keken et al., 2011*).

Once the temperatures reaches $T > 1000\ K$ at $P \approx 7\ GPa$, serpentines decompose and most of the water content of the lithospheric slab is lost (*Hacker et al., 2003*). Thermo-petrological simulations performed by *van Keken et al. (2011)*, estimated that only $1/3$ of the initial slab water content is able to pass the "subduction zone filter" at $230\ km$ depth (i.e. serpentine breakdown). The remaining $2/3$ is expelled from the subducting lithosphere through dehydration reactions. In these models, the preserved water is mainly hosted in the lower crust and in the lithospheric mantle. Based on these considerations, it appears that very little quantities of water are retained within the slab at depth, since the major water bearing phases (i.e. serpentines) break down at $P \approx 7\ GPa$.

The breakdown of serpentine at $230\ km$ has been used to explain the intermediate-deep seismicity, and the double-seismic zone corresponding to the most serpentinized regions within the slab (i.e. the outer oceanic crust and the inner harzburgitic lithosphere - *Hacker et al., 2003*; *Yamasaki & Seno, 2003*; *Faccenda et al., 2012*; *Campione & Capitani, 2013*).

However, despite the absence of sound evidence, the existence of DHMS in the slab is often assumed to explain the water delivery deeper into the mantle. The relay-run of water-bearing minerals into the mantle starts with the breakdown of serpentines at $P \approx 7\ GPa$, $T < 1000$ K, which produces phase– A ($12\ wt\%\ H_2O$ *Ringwood & Major, 1967*), and phase– 10 Å (*Fumagalli, et al., 2001*). Phase– A transforms into phase– E ($11.4\ wt\%\ H_2O$, *Kanzaki, 1991*) at $P > 12\ GPa$ and carries the water down to the MTZ.

1.9.4. The Fate of Water at Depth: Mantle Transition Zone

Despite the major breakdown of water-bearing phases, significant quantities of H_2O may be retained in the subducting slab and could reach the deep mantle regions (*Ohtani et al., 2004*). In particular, the MTZ is considered by most authors to be the major water reservoir in the mantle, due to the high water solubility of wadsleyite and ringwoodite (*Kohlstedt et al., 1996; Bercovici and Karato, 2003*). Given the abundance of these two phases in the mantle transition zone (i.e., 80 $vol\%$ in the harzburgitic slab - *Irifune & Ringwood, 1987*, and 60 $vol\%$ pyrolitic mantle - *Frost, 2008*) a fully hydrated transition zone would contain ≈ 2 ocean masses (*Nestola & Smyth, 2016*). Moreover, laboratory experiments report a strong partitioning of water toward the MTZ phases compared to that of the lower mantle (*Bolfan-Casanova et al., 2000, 2003*). This is in agreement with the water filter hypothesis proposed by *Bercovici & Karato (2003)* who infer that most of the water in the mantle would be concentrated in the MTZ.

Despite the capacity of Wd and Rw to retain water even at high temperatures ($\approx 2000\ K$ – *Fei & Katsura, 2020*), these phases cannot survive at high pressure ($> 24\ GPa$ – *Litasov et al., 2005; Ishii et al., 2018, 2019b, 2019c*). Therefore, a slab has to retain some H_2O–bearing minerals capable of sustaining the high pressure conditions in order to deliver water down to the lower mantle.

Assuming the survival of DHMS in the coldest part of the slab, the phase–E coming from the UM decomposes into superhydrous phase–sB (i.e., former phase–C, $5.8\ wt\%\ H_2O$, $P = 15–17\ GPa$ – *Pacalo & Parise, 1992*), which transforms into phase–D ($10–14\ wt\%\ H_2O$ – *Liu, 1987*) at the base of the MTZ. Phase–D has an extended stability field and can survive at lower mantle conditions (up to $1200\ km$ of depth - *Irifune et al., 1998*). High pressure phase–F (*Kanzaki, 1991*) and phase–G (*Ohtani et al., 1997)* has been recently identified as phase–D (*Ohtani, 2020*).

1.9.5. The Fate of Water at Depth: Lower Mantle

The detection of $12–km$–thick seismic reflectors in the shallow lower mantle has been attributed to the presence of oceanic crust (i.e. subducting slabs) at depth (*Kaneshima & Helffrich, 1998*; *Niu et al., 2003*). The estimated density of these reflectors, however, is not compatible with a dry meta-basaltic crust, and the presence of low-density melt layers has been inferred (*Ohtani & Litasov, 2006*). A possible explanation for the presence of melt layers within the slab might be given by the breakdown of DHMS (i.e. phase–sB and phase–D), and the consequent dehydration melting of the rocks (*Xu & Inoue, 2019*).

Despite dehydration phenomena, a slab can still retain H_2O in its most stable water-bearing minerals, i.e. the δ–phase (*Duan et al., 2018*), phase–H ($15\%\ H_2O$ - *Nishi et al., 2014*; *Ohtani et al., 2014*) which is stable up to $60\ GPa$ (i.e. $\approx 1500\ km$), and the pyrite type FeO_2H_x (*Hu et al., 2016*; *Nishi et al., 2017*; *Yuan et al., 2018*). Depending on the thermal evolution of a slab, these phases can reach the CMB (*Mashino, 2016*; *Ohtani, 2018*; *Yuan et al., 2019*).

Seismological studies performed by *Frost & Rost (2014)* suggested the idea that the slabs, at the end of their descent, feed the Large Low-Shear Wave Velocity Provinces (LLSVPs) beneath the African and the Pacific plate (*Ritsema & Lekić, 2020*). They also addressed the hypothesis that part of the water released after the breakdown of the last surviving hydrous phases, triggers dehydration melting and causes the Ultra-Low Velocity Zones (ULVZ) that characterize the CMB (*Garnero & Helmberger, 1996*; *Williams & Garnero, 1996*; *Rost et al., 2005*). Furthermore, part of the water

could also react with the iron alloys present at the CMB forming more iron hydrates FeO_2H_x (*Liu et al., 2017*).

It is believed that the ULVZ may represent the source of the rising mantle plumes (*Rost et al., 2005*; *McNamara et al., 2010*; *Cottaar & Romanowicz, 2012*). If part of the hydrous material that reached the CMB is entrained in the ascending plumes rising from the ULVZ, water can be re-transported upwards, and be released by the surface volcanism (*Mao et al., 2017*). This would make the deep Earth water cycle a closed loop.

1.10. Unresolved Questions

Despite the large number of experimental constraints, geophysical observations, and direct measurements on natural samples, several questions still remain unanswered:

- *What is the total water influx into Earth's interior?*
- *How does the balance between in-/out-flux evolve over the geological history of the Earth?*
- *What is the exact distribution of water among the different reservoirs?*
- *What are the mechanisms that lead to a heterogeneous distribution of water in the mantle?*
- *For how long can the hydrous mantle regions retain their water?*
- *Are there hidden reservoirs in the mantle that we do not know anything about?*
- *Which other physical properties of minerals are influenced by the presence of water and how? Do these properties have an impact on the large-scale evolution of the Earth?*
- *Can water significantly influence the solid-state convection in the mantle, and ultimately control the tectonic regime of the Earth?*
- *Is water a necessary ingredient for the onset of plate tectonics?*

All these questions represent an ongoing challenge for the scientific community. However, they cannot be answered by limiting our studies to analyzing small-scale samples, and observing the present-day structure with geophysical methods. A fundamental tool to unravel these unresolved questions is numerical modelling.

1.11. Numerical Modelling in Geosciences

Numerical modelling is a computational technique employed to reproduce the physical behaviour of a given object in time and space. This method requires the parameterization of the physical properties of the object (experimental constraints), and the comparison of the results with the observations (geophysical measurements). In the absence of solid constraints, these models operate under educated assumptions in order to capture the basic physics behind the given phenomenon. It is often fundamental to reduce the number of variables in the model to disentangle the contribution of each individual parameter, thus allowing to identify the key properties that control the studied phenomenon.

The large uncertainties regarding the Earth's interiors, require a constant re-working of numerical code parameterizations, by incorporating up-to-date mineral physics measurements. Numerical modelling is essential to test hypotheses and link micro-scale experiments to large-scale features observed in the Earth's interior. This feedback loop between observations, experiments, and models constantly refines our knowledge of Earth's evolution.

1.11.1. Deep Water Cycle in Numerical Modelling

Numerical modelling has been extensively employed to study the deep Earth water cycle. The numerical code I2ELVIS (*Gerya & Yuen, 2007*) has been used to study: (i) the path of water during slab unbending and the possible hydrofracturing in the double seismic zone (*Faccenda et al., 2009*; *Faccenda & Mancktelow, 2010*; *Faccenda et al., 2012*) and (ii) the shear wave anisotropy due to the serpentinization of the faults in the subducting slab (*Faccenda et al., 2008*).

Self-written codes have been employed to study: (i) the evolution of the water influx in the mantle driven by plate tectonics (*Korenaga, 2011*); (ii) the extent of lithosphere hydration during the bending of the slab at the trench (*Korenaga, 2017*); (iii) the migration of water in the mantle wedge and the triggering of arc volcanism (*Iwamori, 1998, 2006*); (iv) the temperature field of subducting slabs (*Syracuse et al., 2010*), and (v) the stability field of hydrous phases (*van Keken et al., 2011*); (vi) the deserpentinization of the slab and the retention of water at depth $> 230\ km$ (*Rüpke et al., 2004*); (vii) the diffusion of water between a hydrous slab stagnating in the MTZ and the dry ambient mantle (*Richard, 2006*) and $(viii)$ the effect of water on mantle convection (*McGovern & Schubert, 1989*).

The numerical code Citcom (*Moresi & Solomatov, 1995*) has been employed to study the dehydration of slabs down to 300 km of depth (*Magni et al., 2014*).

The numerical code StagYY (*Tackley, 2008*) has been used to study: (i) the global-scale circulation of water and its effect on mantle rheology (*Nakagawa et al., 2015*); (ii) the low solubility of lower mantle minerals (*Nakagawa, 2017*); (iii) the effect of water on the stability of plate tectonics over geological time (*Nakagawa & Iwamori, 2017*); (iv) the total water budget on Earth (*Nakagawa & Spiegelman, 2017*) and (v) water distribution in the mantle (*Nakagawa & Iwamori, 2019*).

1.12. Thesis Overview

This PhD thesis is part of the IRTG (International Research Training Group) program, funded by the German Research Foundation (DFG). This program is a collaborative research between the Bayerisches Geoinstitut (BGI) for Experimental Geochemistry and Geophysics at University of Bayreuth (Germany), and the Department of Earth Sciences at Tohoku University (Sendai, Japan). The IRTG research program involves, twelve PhD students from around the World to explore the "Deep Earth Volatile Cycle", using experimental or computational methods. The object of these studies is to investigate how volatile components (e.g. H_2O, C, N, O, Cl, noble gases) are transported, stored and expelled from Earth's interior.

1.12.1. Motivation

The current consensus is that water plays a key role for the onset of plate tectonics on Earth. Plate tectonics is considered to be a self-lubricating mechanism related to the presence of water on Earth. The continuous subduction of the oceanic lithosphere removes volatiles from the surface while maintaining an active plate tectonic regime. An understanding of the role of water in deep Earth is fundamental in reconstructing a valid geodynamic model of our planet.

The mantle transition zone is a pivotal region for the studies on the deep Earth water cycle. Its importance is given by the high water solubility of wadsleyite and ringwoodite, and the role that both the 410 km and the 660 km discontinuity have on slab subduction (*Goes et al., 2017*). The best strategy study the hydration of this region, is to perform self-consistent, global-scale mantle convection models, where subducting slabs deliver the water from the Earth's surface down to MTZ.

Recently, *Brändli and Tackley (2016)* implemented water diffusion and advection into the StagYY code (*Tackley, 2008*). This version of the code includes phase-dependent solubility, a water-dependent viscosity law and a wet solidus temperature function. A realistic model of the deep Earth water cycle requires few essential conditions:

1. A parameterization of the physical properties of the slab which is up-to-date with mineral physics data. The parameterization should consider the changes of temperature, pressure and composition during the computation.
2. The self-consistent subduction of the lithosphere, thus minimizing the influence of the parameters chosen by the user (e.g. no prescribed subduction velocity).
3. To constrain the parameters that control the interaction between the slab and the two phase discontinuities at the top and bottom of the MTZ. Two scenarios are feasible: (1) direct penetration of the slab into the LM, and (2) slab stagnation at the 660 km discontinuity. It is still unclear under which conditions slab penetration or slab stagnation is more likely to occur.

Once these features have been thoroughly investigated and benchmarked, the hydration state of the MTZ can be studied in detail.

1.12.2. Objectives

The aim of this thesis is to build a self-consistent model of the deep Earth's water cycle by providing physical and numerical constraints into the three conditions stated above. For this purpose, three projects have been conducted:

1. An experimental study on the effect of water on the thermal conductivity of ringwoodite. Based on these measurements an empirical parameterization of ringwoodite's thermal conductivity as a function of P,T, and water content C_{H2O} was derived. The parameterized equation was implemented into a self-written 1D code to study the thermal evolution of the subducting slab.
2. The effect of the numerical grid resolution on self-consistent tectonic regimes. Numerical codes in geodynamics solve the governing equations on a discretized domain which is defined by a stencil of nodes. A recent study by *Tosi et al. (2015)* reports that the style of convection heavily depends on the number of nodes. The aim of this study is to determine how the grid resolution affects the tectonic regime and to provide an optimal value to be employed in future simulations. A fine grid spacing would be also advantageous to constrain the water influx in the subduction zone.
3. A computational overview on the parameters that control slab stagnation at the 660 km discontinuity. This study focuses in particular on the Clapeyron slope of the endothermic phase transition and the viscosity jump between the MTZ and the LM. The stagnation of the slab may represent the main mechanism to hydrate the MTZ.

1.12.3. Thesis Structure

The workflow of this thesis combines experimental methods with computational techniques. Chapters 2 describe the governing equations of geodynamics, and chapter 3 the finite-difference method. Chapter 4 discusses the experimental techniques. The study on thermal conductivity of hydrous ringwoodite is reported in chapter 5. The influence of grid resolution is reported in chapter 6. The overview on the 660 km discontinuity is reported in chapter 7.

Chapter 5 has been published in open access as: *Marzotto et al. (2020)* Geophysical Research Letters, 47(13). The main manuscript has been modified to adapt it to the style and format of this thesis. Part of the supplementary material from *Marzotto et al. (2020)* has been included in the main text. Several sections of the paper have been expanded with further descriptions of the methods employed in the study. Additional images have been produced and added to this chapter.

CHAPTER 2 - Governing Equations

2.1. Introduction

To physically describe the phenomenon of mantle convection, it is necessary to approximate the solid rock deformation as highly viscous fluid. This approximation is valid on geological time scales, where continuous and long-lasting stresses determine a viscous creep flow. The branch of physics that studies this behaviour is called fluid dynamics.

The motion of a viscous fluid is governed by a set of partial differential equations known as Navier-Stokes equations. These equations take the name after the pioneering work done by the French engineer Claude-Louis Navier, who first described the behaviour of an incompressible viscous fluid, and the Anglo-Irish physicist George Gabriel Stokes who provided an in-depth description of the creeping flow of highly viscous fluids. The Navier-Stokes equations assume the fluid medium as a continuum substance, without any voids or gaps. These equations are based on three cardinal principles of physics: mass, momentum and energy conservation.

The Navier-Stokes equations have a vast range of applications (*Łukaszewicz & Kalita, 2016*), from engineering to medical science, and they are broadly employed in the design of many everyday life tools, like cars (*Hassan et al., 2014*), power plants (*Sangi et al., 2011*), piping (*Priymak & Miyazaki, 1998*), meteorological stations (*Milashuk & Crane, 2011*) and even videogames. Despite their relevance, the existence of a smooth analytical solution in 3D has not been proven, and for this reason are considered one of the seven most important open problems in mathematics (Millennium Prize Problems *Fefferman 2006*).

Given the lack of an universal analytical solution, the Navier-Stokes equations are defined over a finite control volume V, confined by a surface A. This control volume can be expressed with two distinct approaches: Eulerian or Lagrangian. Eulerian control volumes are fixed in space and 'observe' the fluid flux passing through them, whereas the Lagrangian control volumes represent a finite portion of the fluid that moves with the flow. For the present analysis the Navier-Stokes equations will be derived for an Eulerian control volume of fluid δV.

Moreover, for the mantle convection case, the Navier-Stokes equations must be accompanied by an Equation of State (EoS), relating pressure and temperature to density, and by constitutive laws governing the flux-controlling coefficients (i.e. viscosity and thermal conductivity).

2.2. General Continuity Equation

A continuity equation is a conservation relation which states that the variations of a physical property ϕ, defined over a control volume δV, must be caused by the net flux $\varphi_{out/in}$ of that property through the enclosing surface δA, plus its consumption/production quantified by the sink/source term S. This statement can be expressed as an integral equation.

$$\frac{\partial}{\partial t}\int_V \phi\, \delta V = -\int_A \phi \boldsymbol{u} \cdot n\, \delta A - \int_V S\, \delta V \tag{2.2.1}$$

Where $\boldsymbol{u}$ is the flow velocity, and n is the unit-normal vector of the enclosing surface δA. As a convention, the normal vector n is pointing outward, and the term S is positive when it acts as a material property sink. This means that an influx is considered negative $-\varphi_{in}$, and an outflux is considered positive φ_{out}.

By applying the divergence theorem, the flux through the enclosing surface A can be converted into the flux divergence $\nabla\cdot$ over the control volume V:

$$\int_A \phi\boldsymbol{u}\cdot n\,\delta A = \int_V \nabla\cdot(\phi\boldsymbol{u})\,\delta V \tag{2.2.2}$$

In 3D Cartesian coordinates, the velocity field $\boldsymbol{u}$ is defined by its components in three directions (u_x, u_y, u_z), which can be re-named as (u, v, w). The divergence operator $\nabla\cdot$ is defined by the following equation:

$$\nabla\cdot\mathbf{u}(x,y,z) = \frac{\partial u}{\partial x}+\frac{\partial v}{\partial y}+\frac{\partial w}{\partial z} \tag{2.2.3}$$

If the total flux is moving outward (i.e. positive), the flow is diverging away from the volume ($\nabla\cdot\boldsymbol{u} > 0$), whereas if the total flux is moving inward (i.e. negative), the flow is converging into the volume ($\nabla\cdot\boldsymbol{u} < 0$) (**Figure 2.1**). In cases where the amount of inward flux is completely balanced by an outward flux, the divergence is zero ($\nabla\cdot\boldsymbol{u} = 0$) (**Figure 2.1**).

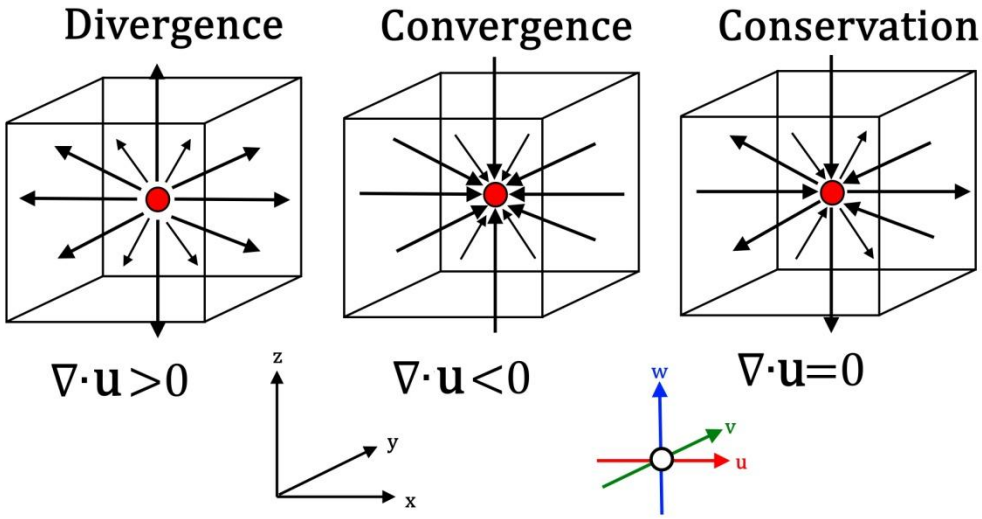

Figure 2.1. Divergence of the flux in an Eulerian control volume

Applying the divergence theorem to equation **(2.2.1)** yields:

$$\frac{\partial}{\partial t}\int_V \phi\,\delta V = -\int_V \nabla\cdot(\phi\boldsymbol{u})\,\delta V - \int_V S\,\delta V \tag{2.2.4}$$

In the special case of the domain volume V remaining constant with respect to time, we can apply the Reynolds transport theorem:

$$\frac{\partial}{\partial t}\int_V \phi\,\delta V = \int_V \frac{\partial\phi}{\partial t}\delta V \tag{2.2.5}$$

and combine the three integrals in equation **(2.2.4)** to a single one:

$$\int_V \left(\frac{\partial\phi}{\partial t} + \nabla\cdot(\phi\boldsymbol{u}) + S\right)\delta V = 0 \tag{2.2.6}$$

This volume integral can only be equal to zero if the integrand equals zero, which results in:

$$\frac{\partial\phi}{\partial t} + \nabla\cdot(\phi\boldsymbol{u}) + S = 0 \tag{2.2.7}$$

This conservation equation forms the base of mass, momentum and energy conservation principles.

2.3. Conservation of Mass

When the conserved physical property ϕ is the mass m $[kg]$, equation **(2.2.7)** defines the mass conservation equation. In fluid dynamics, it makes more sense to define the mass of the fluid as a function of the control volume δV. Therefore, the mass conservation principle is formulated by considering the local density ρ $[kg\ m^{-3}]$ (mass per unit volume) of the fluid.

Lomonosov's (*Lewis 2012*) and Lavoisier's (*Whitaker, 1975*) mass conservation principle states:

'*The mass of an isolated system is neither created nor destroyed.*'

This implies that for the case of mass conservation, the source/sink term S is equal to zero.

$$\frac{\partial \rho}{\partial t} + \nabla \cdot (\rho \boldsymbol{u}) = 0 \tag{2.3.8}$$

Mass conservation equation **(2.3.8)** is a fundamental pillar of continuum mechanics. When applied in fluid dynamics mass conservation principle states:

'The total mass of fluid contained in a fixed control volume remains constant over time'

Mathematically this means $\partial \rho / \partial t = 0$, i.e. the divergence of mass flux is equal to zero (**Figure 2.1**).

$$\nabla \cdot (\rho \boldsymbol{u}) = 0 \tag{2.3.9}$$

This formulation is also known as anelastic approximation of mass conservation (*Ogura & Phillips, 1962*; *Gough, 1969*). The assumption $\partial \rho / \partial t = 0$ ignores the contribution of transient density variations produced by sound waves in the fluid.

On Earth, seismic processes occur at a much smaller time scale compared to mantle convection (i.e. minutes versus millions of years), and thus have a negligible effect on mantle flow. Moreover, their presence in the computation would require very short time steps in the numerical integration, making the calculation of the Navier-Stokes computationally expensive. Given the high value of sound speed in materials $O(km\ s^{-1})$, the anelastic approximation is also employed in meteorological sciences (*Ogura & Phillips, 1962*; *Gough, 1969*).

The continuity equation implies that is not possible to create holes in the domain, since any gap left by the moving fluid has to be filled by the motion of surrounding mass.

$$\frac{\partial (\rho u)}{\partial x} + \frac{\partial (\rho v)}{\partial y} + \frac{\partial (\rho w)}{\partial z} = 0 \tag{2.3.10}$$

2.4. Conservation of Momentum

Momentum is defined as the product of the mass of an object and its velocity $p = m\boldsymbol{u}$ $[kg\ m\ s^{-1}]$. The momentum conservation bases its founding principles on the laws of dynamics, the branch of physics that studies the effect of forces on the motion of objects. These principles were mathematically defined by Sir Isaac Newton (*Newton, 1687*).

2.4.1. Equation of Motion

The first law of dynamics states (*Scheurer & De Brock, 1988*):

'Every object persists in its state of rest or uniform motion in a straight line unless it is compelled to change that state by forces impressed on it.'

$$\sum F = 0 \leftrightarrow a = \frac{\delta \boldsymbol{u}}{\delta t} = 0 \tag{2.4.11}$$

As a consequence of the First Law, in order to cause any acceleration of an object it is necessary to have an imbalance of forces (i.e. $\sum F \neq 0$).

The acceleration gained by an object is proportional to the applied force, as stated by the Second Law of Motion (*Scheurer & De Brock, 1988*):

'*A change in motion is proportional to the motive force impressed and takes place along the straight line in which that force is impressed*'

$$\sum F = ma = m\frac{\delta \boldsymbol{u}}{\delta t} \tag{2.4.12}$$

Where m is the mass of the object. The Second Law can be also expressed in terms of momentum p of a body.

$$\sum F = \frac{\delta p}{\delta t} \tag{2.4.13}$$

Finally, Newton's Third Law of Motion states (*Scheurer & De Brock, 1988*):

'*The reaction is always opposite and equal to the action, or the reciprocal actions of two bodies are always equal and directed in contrary directions*'

This Law is also known as the *Principle of Action-Reaction*, and is expressed mathematically in terms of exchanged momentum between the two bodies A and B.

$$\frac{\delta p_A}{\delta t} = -\frac{\delta p_B}{\delta t} \tag{2.4.14}$$

From the Three Laws of Motion it follows that the total momentum p of an object is a conserved property. The principle of momentum conservation can be applied to an Eulerian control volume of fluid by considering p as the physical property ϕ in the equation **(2.2.7)**. In this case, the source term S represents the source of mechanical motion (i.e. the net external force $\sum F_E$).

$$\frac{\partial}{\partial t}(\rho \boldsymbol{u}) + \nabla \cdot (\rho \boldsymbol{u} \otimes \boldsymbol{u}) = \sum F_E \tag{2.4.15}$$

The dyad tensor product can be expressed as:

$$\nabla \cdot (\rho \boldsymbol{u} \otimes \boldsymbol{u}) = (\boldsymbol{u}\boldsymbol{u} \cdot \nabla \rho) + (\boldsymbol{u}\rho \cdot \nabla \boldsymbol{u}) + (\boldsymbol{u}\rho \nabla \cdot \boldsymbol{u}) \tag{2.4.16}$$

By substituting equation **(2.4.16)** into equation **(2.4.15)**, and by further regrouping for $\boldsymbol{u}$ and ρ, the following equation is obtained:

$$\boldsymbol{u}\left(\frac{\partial \rho}{\partial t} + \boldsymbol{u} \cdot \nabla \rho + \rho \nabla \cdot \boldsymbol{u}\right) + \rho\left(\frac{\partial \boldsymbol{u}}{\partial t} + \boldsymbol{u} \cdot \nabla \boldsymbol{u}\right) = \sum F_E \tag{2.4.17}$$

The sum $(\boldsymbol{u} \cdot \nabla \rho + \rho \nabla \cdot \boldsymbol{u})$ in the first term of the left-hand side of equation **(2.4.17)** gives the divergence of the momentum $\nabla \cdot (\rho \boldsymbol{u})$, which leads to:

$$\boldsymbol{u}\left(\frac{\partial \rho}{\partial t} + \nabla \cdot (\rho \boldsymbol{u})\right) + \rho\left(\frac{\partial \boldsymbol{u}}{\partial t} + \boldsymbol{u} \cdot \nabla \boldsymbol{u}\right) = \sum F_E \tag{2.4.18}$$

Based on the anelastic approximation **(2.3.9)**, we know that the first term on the left-hand side of the equation is equal to zero, thus equation **(2.4.18)** becomes:

$$\rho\left(\frac{\partial \boldsymbol{u}}{\partial t} + \boldsymbol{u} \cdot \nabla \boldsymbol{u}\right) = \sum F_E \tag{2.4.19}$$

This formulation is an expression of Newton's Second Law $F = ma$, where density ρ is the mass m per unit volume V and the acceleration a is the derivative of flow velocity $\boldsymbol{u}$.

$$\rho\left(\frac{\partial \boldsymbol{u}}{\partial t} + u\frac{\partial \boldsymbol{u}}{\partial x} + v\frac{\partial \boldsymbol{u}}{\partial y} + w\frac{\partial \boldsymbol{u}}{\partial z}\right) = \sum F_E \tag{2.4.20}$$

At this point, it is necessary to define the external forces acting on the Eulerian control volume. In continuum mechanics the total net force results from the contribution of body forces F_{Body} (acting through the bulk volume), and surface forces F_{Surf} (acting on the bounding surface). The total amount of forces acting on the control volume V can be expressed in integral form:

$$\int_V F_E \, \delta V = \int_V F_{Body} \, \delta V + \int_A F_{Surf} \, \delta A \tag{2.4.21}$$

The magnitude of body forces is proportional to the volume on which they act: the more material is contained within the control volume, the stronger F_{Body} will be. In Earth's mantle the dominant contribution to the total body force is given by gravity acceleration g ($\approx 9.81 \, m \, s^{-2}$) therefore, for the present analysis $F_{Body} = F_G = \rho g$.

Surface forces F_{Surf}, on the other hand, are proportional to the surface A on which they act: the larger the bounding area, the higher is the cumulative F_{Surf} experienced by the fluid in the control volume. The total surface forces F_{Surf} are described by the stress tensor σ_{ij}.

Total net force **(2.4.21)** can be expressed by considering the contribution of gravity and stress.

$$\int_V F_E \, \delta V = \int_V \rho g_i \, \delta V + \int_A \sigma_{ij} \, \delta A \tag{2.4.22}$$

As for equation **(2.2.2)**, the divergence theorem can be applied to transform the surface integral into a volume one.

$$\int_A \sigma_{ij} \, \delta A = \int_V \nabla \cdot \sigma_{ij} \, \delta V \tag{2.4.23}$$

Total external force thus becomes:

$$\int_V F_E \, \delta V = \int_V \rho g_i \, \delta V + \int_V \nabla \cdot \sigma_{ij} \, \delta V \tag{2.4.24}$$

The general *Equation of Motion* is obtained by substituting equation **(2.4.24)** (external force definition) into **(2.4.20)** (momentum conservation).

$$\rho\left(\frac{\partial \boldsymbol{u}}{\partial t} + \boldsymbol{u}\cdot\nabla\boldsymbol{u}\right) = \rho g_i + \frac{\partial \sigma_{ij}}{\partial x_j} \tag{2.4.25}$$

Where the notation i, j indicates: i the axis along which the stress component is taken (e.g. x for a component parallel to the x axis), and j the surface on which the force is applied (e.g. x for the face orthogonal to the x axis). Equation **(2.4.25)** is valid for any arbitrary control volume.

2.4.2. Stress and Strain Tensor

In order to describe exhaustively the momentum conservation, it is necessary to define a momentum equation for each flow direction (x, y, z). The moving fluid exerts a certain amount of stress on each face of the control volume V (**Figure 2.2**).

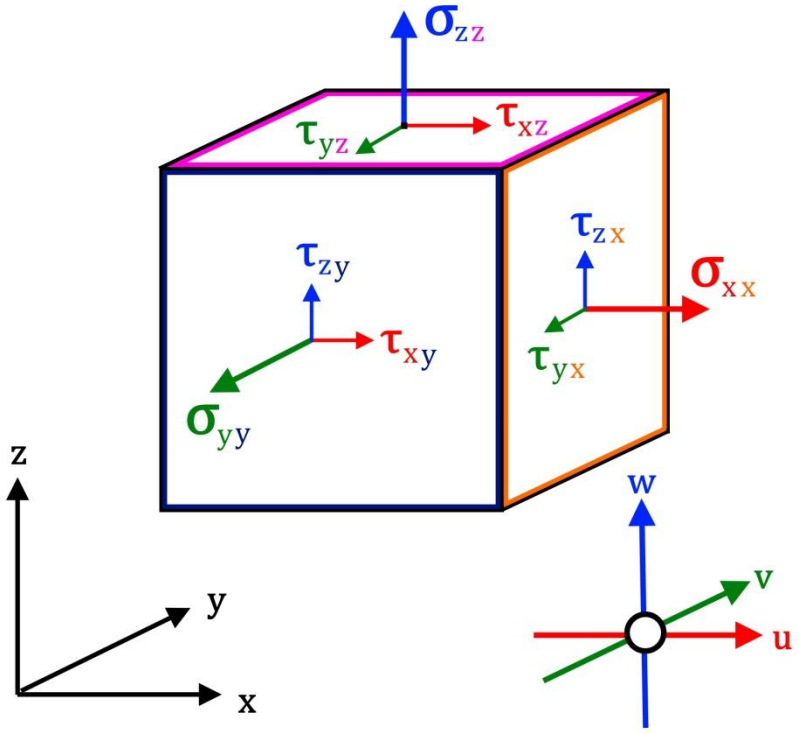

Figure 2.2. Stress field over an Eulerian control volume

Stress is defined as the force per unit area $\sigma = F/A\ [N\ m^{-2}]$ and, in a 3-dimensional body, is represented by the second-order tensor σ_{ij}.

$$\sigma_{ij} = \begin{bmatrix} \sigma_{xx} & \tau_{xy} & \tau_{xz} \\ \tau_{yx} & \sigma_{yy} & \tau_{yz} \\ \tau_{zx} & \tau_{zy} & \sigma_{zz} \end{bmatrix} \tag{2.4.26}$$

When a force is directed perpendicular to a face of the control volume ($i = j$), the resulting stress is called *normal stress* σ_{kk}, whereas the stress resulting from a force applied parallel to a face of the control volume ($i \neq j$), is called *shear stress* τ_{ij}.

In the absence of flow (i.e. hydrostatic condition), the only contribution to the total normal stress σ_{kk} acting on a surface is given by the hydrostatic pressure P, which is defined as:

$$P = \frac{\sigma_{xx} + \sigma_{yy} + \sigma_{zz}}{3} = \frac{\sigma_{kk}}{3} \tag{2.4.27}$$

The pressure experienced by a control volume fully surrounded by fluid is isotropic, meaning that it has the same magnitude independently from the orientation of the surface.

Once fluid flow is established, additional stress (normal and shear) is applied to the surface of the control volume. This flow-induced stress is called '*deviatoric*', since it produces a deviation in the original shape of the control volume (i.e. body distortion). Deviatoric stress is defined as:

$$\acute{\sigma}_{ij} = \sigma_{ij} - P\delta_{ij} \tag{2.4.28}$$

$$\begin{bmatrix} \acute{\sigma}_{xx} & \acute{\tau}_{xy} & \acute{\tau}_{xz} \\ \acute{\tau}_{yx} & \acute{\sigma}_{yy} & \acute{\tau}_{yz} \\ \acute{\tau}_{zx} & \acute{\tau}_{zy} & \acute{\sigma}_{zz} \end{bmatrix} = \begin{bmatrix} \sigma_{xx} & \tau_{xy} & \tau_{xz} \\ \tau_{yx} & \sigma_{yy} & \tau_{yz} \\ \tau_{zx} & \tau_{zy} & \sigma_{zz} \end{bmatrix} - \begin{bmatrix} P & 0 & 0 \\ 0 & P & 0 \\ 0 & 0 & P \end{bmatrix}$$

Where δ_{ij} is the Kronecker delta, which is equal to 1 if $i = j$, and 0 if $i \neq j$. In case of normal deviatoric stress $\acute{\sigma}_{kk}$, the contribution of the hydrostatic pressure has to be removed from the total tensor σ_{ij} , whereas the shear stress τ_{ij} is always deviatoric ($\acute{\tau}_{ij} = \tau_{ij}$).

On Earth, hydrostatic pressure is given by the force per unit area exerted by matter in a gravitational field $P = F_G/A$ $[N\,m^{-2}]$. Pressure increases with depth, since the resulting force is produced by the gravity acceleration of the column of rocks on top of the surface (i.e. lithostatic pressure).

Newton's principles state that, whenever the forces acting on a body are unbalanced ($\sum F \neq 0$) an acceleration occurs. Deviatoric stress represents the amount of force that deviates from the hydrostatic (balanced) conditions, thus producing a displacement of material (i.e. acceleration).

The displacement vector d quantifies the motion of particles from the initial undeformed position (x,y,z) to the final deformed configuration $(\acute{x}, \acute{y}, \acute{z})$. The gradient of the displacement vector ∇d, gives a second order tensor in which the variations of all components in space are considered.

$$\nabla d = \begin{bmatrix} \frac{\partial d_x}{\partial x} & \frac{\partial d_x}{\partial y} & \frac{\partial d_x}{\partial z} \\ \frac{\partial d_y}{\partial x} & \frac{\partial d_y}{\partial y} & \frac{\partial d_y}{\partial z} \\ \frac{\partial d_z}{\partial x} & \frac{\partial d_z}{\partial y} & \frac{\partial d_z}{\partial z} \end{bmatrix} \tag{2.4.29}$$

The displacement tensor contains two components: rigid body displacement ω_{ij} and deformation ε_{ij}. The rigid body displacement consists of the coupled translation and rotation of the body, which does not result in any deformation of the body, and is hence called '*rigid*' (i.e. undeformable). Deformation, instead, implies the change of the original shape of the body. Here the contribution to the total displacement given by the rigid body rotation ω_{ij} will be ignored, since it does not contribute to the total deformation.

The physical property that describes the entire deformation history of a given material is called strain ε_{ij}. Strain is defined as the change in material coordinate $[m]$ over the travelled distance $[m]$, therefore the unit of measure of deformation is null $[/]$. The strain of a body is a second order tensor that relates the initial and the final shape of the body to a transformation caused by the acting stress.

$$\varepsilon_{ij} = \frac{1}{2}(\nabla d - \nabla d^{T}) = \frac{1}{2}\left(\frac{\partial d_i}{\partial j} + \frac{\partial d_j}{\partial i}\right) \tag{2.4.30}$$

$$\varepsilon_{ij} = \begin{bmatrix} \frac{\partial d_x}{\partial x} & \frac{1}{2}\left(\frac{\partial d_x}{\partial y} + \frac{\partial d_y}{\partial x}\right) & \frac{1}{2}\left(\frac{\partial d_x}{\partial z} + \frac{\partial d_z}{\partial x}\right) \\ \frac{1}{2}\left(\frac{\partial d_y}{\partial x} + \frac{\partial d_x}{\partial y}\right) & \frac{\partial d_y}{\partial y} & \frac{1}{2}\left(\frac{\partial d_y}{\partial z} + \frac{\partial d_z}{\partial y}\right) \\ \frac{1}{2}\left(\frac{\partial d_z}{\partial x} + \frac{\partial d_x}{\partial z}\right) & \frac{1}{2}\left(\frac{\partial d_z}{\partial y} + \frac{\partial d_y}{\partial z}\right) & \frac{\partial d_z}{\partial z} \end{bmatrix}$$

Where the diagonal terms indicate the deformation occurring as a consequence of uniaxial compression/extension (i.e. '*pure shear*'), and the lateral terms indicate the deformation produced by shear stress (i.e. '*simple shear*').

As for the stress tensor **(2.4.28)**, pure shear contains also the contribution of pressure-induced displacement, namely hydrostatic strain ε_{Hyd} (i.e. pure compression/extension). This type of deformation is not considered as 'deviatoric' as only the volume of the body changes, not its shape.

$$\varepsilon_{Hyd} = \frac{\varepsilon_{xx} + \varepsilon_{yy} + \varepsilon_{zz}}{3} = \frac{1}{3}\varepsilon_{kk} \tag{2.4.31}$$

Deviatoric strain is calculated by subtracting the hydrostatic component from the total pure shear deformation.

$$\acute{\varepsilon}_{kk} = \varepsilon_{kk} - \varepsilon_{Hyd} \tag{2.4.32}$$

If the fluid is assumed to be incompressible, then the hydrostatic component is equal to 0:

$$\varepsilon_{Hyd} = 0 \leftrightarrow \acute{\varepsilon}_{kk} = \varepsilon_{kk} \tag{2.4.33}$$

The time derivative ∂t of the strain tensor ε_{ij} (which contains displacements d) gives the strain rate tensor $\dot{\varepsilon}_{ij}$ (which contains velocities $\boldsymbol{u}$).

$$\dot{\varepsilon}_{ij} = \frac{1}{2}(\nabla \boldsymbol{u} - \nabla \boldsymbol{u}^{T}) = \frac{1}{2}\left(\frac{\partial \boldsymbol{u}_i}{\partial j} + \frac{\partial \boldsymbol{u}_j}{\partial i}\right) \tag{2.4.34}$$

$$\dot{\varepsilon}_{ij} = \begin{bmatrix} \frac{\partial u}{\partial x} & \frac{1}{2}\left(\frac{\partial u}{\partial y} + \frac{\partial v}{\partial x}\right) & \frac{1}{2}\left(\frac{\partial u}{\partial z} + \frac{\partial w}{\partial x}\right) \\ \frac{1}{2}\left(\frac{\partial v}{\partial x} + \frac{\partial u}{\partial y}\right) & \frac{\partial v}{\partial y} & \frac{1}{2}\left(\frac{\partial v}{\partial z} + \frac{\partial w}{\partial y}\right) \\ \frac{1}{2}\left(\frac{\partial w}{\partial x} + \frac{\partial u}{\partial z}\right) & \frac{1}{2}\left(\frac{\partial w}{\partial y} + \frac{\partial v}{\partial z}\right) & \frac{\partial w}{\partial z} \end{bmatrix}$$

The diagonal terms represent the rate of uniaxial deformation, whereas the off-diagonal terms represent the rate of shear deformation. Strain-rate is defined as the change of material velocity $[m\ s^{-1}]$ over the travelled distance $[m]$, hence the unit of $\dot{\varepsilon}_{ij}$ is $[s^{-1}]$.

Strain-rate $\dot{\varepsilon}_{ij}$ is a direct consequence of the applied stress σ_{ij} (force). Stress and strain-rate are linked to each other through a coefficient of proportionality χ that quantifies the resistance to deformation. The nature of this proportionality ($\sigma_{ij} \propto \chi\dot{\varepsilon}_{ij}$) is studied by the branch of physics called rheology. In continuum mechanics, several proportionality relations χ are possible, and a material can have an elastic, a plastic or a viscous behaviour. Often, complex materials exhibit a combination of the aforementioned rheologies, which results in composite behaviours (visco-elasticity, visco-plasticity etc.).

For simplicity, the constitutive relationship χ between stress σ_{ij} and strain rate $\dot{\varepsilon}_{ij}$ is assumed to be linear viscous creep:

$$\sigma_{ij} = 2\eta\dot{\varepsilon}_{ij} + \left(\eta_B - \frac{2}{3}\eta\right)\dot{\varepsilon}_{kk}\delta_{ij} \tag{2.4.35}$$

Where η is the dynamic viscosity $[Pa\ s]$, η_B is the bulk viscosity $[Pa\ s]$, and δ_{ij} is the Kronecker delta. The first term indicates shear deformation ($i \neq j$), whereas the second term in equation **(2.4.35)** indicates the volumetric deformation. The dynamic viscosity thus represents the resistance of the material to shear deformation, whereas the bulk viscosity indicates the resistance to volumetric deformation.

Equation **(2.4.35)**, describes the effect of the whole strain tensor σ_{ij} to the fluid flow $\dot{\varepsilon}_{ij}$. However, it is necessary to remove the contribution of the hydrostatic component ($P\delta_{ij}$) from this computation, since does not produce any deviatoric effect $\acute{\sigma}_{ij}$.

$$\acute{\sigma}_{ij} = 2\eta\dot{\varepsilon}_{ij} + \left(\eta_B - \frac{2}{3}\eta\right)\dot{\varepsilon}_{kk}\delta_{ij} - P\delta_{ij} \tag{2.4.36}$$

Equation **(2.4.36)** can be expressed in terms of material velocity $\partial u/\partial t$, by applying the strain-rate definition **(2.4.34)**.

$$\acute{\sigma}_{ij} = \eta\left(\frac{\partial \boldsymbol{u}_i}{\partial j} + \frac{\partial \boldsymbol{u}_j}{\partial i}\right) + \left(\eta_B - \frac{2}{3}\eta\right)\frac{\partial \boldsymbol{u}_i}{\partial i}\delta_{ij} - P\delta_{ij} \tag{2.4.37}$$

Which defines the deviatoric surface forces $\left(\sum F_{surf} = \acute{\sigma}_{ij}\right)$ as a function of the material velocity field $\boldsymbol{u}$ and the fluid viscosities η, η_B.

2.4.3. Navier-Stokes Equation

Equation **(2.4.37)** can be substituted into the Equation of Motion **(2.4.25)** to obtain the full *Navier-Stokes Equation*.

$$\rho\left(\frac{\partial \boldsymbol{u}}{\partial t}+\boldsymbol{u}\cdot\nabla\boldsymbol{u}\right)=\rho g_i-\frac{\partial P}{\partial x_i}+\frac{\partial}{\partial x_j}\left[\eta\left(\frac{\partial \boldsymbol{u}_i}{\partial j}+\frac{\partial \boldsymbol{u}_j}{\partial i}\right)+\left(\eta_B-\frac{2}{3}\eta\right)\frac{\partial \boldsymbol{u}_i}{\partial i}\delta_{ij}\right] \tag{2.4.38}$$

In geodynamics, the bulk viscosity η_B of rocks is very low and often assumed to be zero. This assumption is also known as Stokes assumption, and leads to:

$$\rho\left(\frac{\partial \boldsymbol{u}}{\partial t}+\boldsymbol{u}\cdot\nabla\boldsymbol{u}\right)=\rho g_i-\frac{\partial P}{\partial x_i}+\frac{\partial}{\partial x_j}\left[\eta\left(\frac{\partial \boldsymbol{u}_i}{\partial j}+\frac{\partial \boldsymbol{u}_j}{\partial i}\right)-\frac{2}{3}\eta\,\frac{\partial \boldsymbol{u}_i}{\partial i}\delta_{ij}\right] \tag{2.4.39}$$

Moreover, if the fluid is assumed to be incompressible (i.e. hydrostatic deformation $\varepsilon_{Hyd}=\partial \boldsymbol{u}_i/\partial i=0$), equation **(2.4.39)** additionally simplifies to:

$$\rho\left(\frac{\partial \boldsymbol{u}}{\partial t}+\boldsymbol{u}\cdot\nabla\boldsymbol{u}\right)=\rho g_i-\frac{\partial P}{\partial x_i}+\frac{\partial}{\partial x_j}\left[\eta\left(\frac{\partial \boldsymbol{u}_i}{\partial j}+\frac{\partial \boldsymbol{u}_j}{\partial i}\right)\right] \tag{2.4.40}$$

In case of an isoviscous fluid, the coefficient η is constant for the whole domain (i.e. no spatial variation $\partial/\partial x_j$). The isoviscous Navier-Stokes equation takes the form of:

$$\rho\left(\frac{\partial \boldsymbol{u}}{\partial t}+\boldsymbol{u}\cdot\nabla\boldsymbol{u}\right)=\rho g_z-\frac{\partial P}{\partial x_i}+\eta\frac{\partial^2 \boldsymbol{u}_i}{\partial {x_j}^2} \tag{2.4.41}$$

However, this is not the case of Earth's mantle where major viscosity variations occur (*Forte & Mitrovica, 1996*; *Peltier, 1996*; *Mitrovica & Forte, 2004*; *Steinberger & Calderwood, 2006*).

The Navier-Stokes equation represents the balance between inertia (ρa) and the cumulative effect of gravity g_z, pressure P and the viscous flow η. The inertial term represents the amount of force $[N]$ necessary to produce the acceleration a of an object of mass ρ. In planetary convection, flow velocities $\boldsymbol{u}$ are on the order of $O(10^{-9}\ m\ s^{-1})$ (*Silver & Holtz, 2002*), and velocity changes occur over a million year time scale $O(10^{13}\ s)$ (*Colli et al., 2014*). The resulting acceleration ($\partial \boldsymbol{u}/\partial t$) is on the order of $O(10^{-22}\ m\ s^{-2})$, which is an extremely low number. For comparison, even dense rocks at the base of the lower mantle have a density on the order of $O(10^{3}\ kg\ m^{-3})$ (*Ricolleau et al., 2009*). Therefore, the inertial force term can be assumed to be negligible $O(10^{-19}\ N)$.

These assumptions leads to the formulation of slow flow (high viscosity) equation - known as Stokes equation.

$$0=\rho g_i-\frac{\partial P}{\partial x_i}+\frac{\partial}{\partial x_j}\left[\eta\left(\frac{\partial \boldsymbol{u}_i}{\partial j}+\frac{\partial \boldsymbol{u}_j}{\partial i}\right)\right] \tag{2.4.42}$$

2.5. Conservation of Energy

The equation of energy conservation has its roots in the laws of thermodynamics. Thermodynamics is the branch of physics that describes the processes of energy transformation and how these phenomena affect the physical properties of an object (e.g. pressure, temperature, volume). The unit of measure of energy is the Joule [J].

In order to properly define the equation of energy conservation it is necessary to introduce few thermodynamic principles and variables. A thermodynamic system is a physical object containing finite mass and energy, and separated by boundaries from the environment. The environment is everything that is outside of the system. The permeability of the boundaries to a given physical property, determines the type of thermodynamic system. A system is defined as '*isolated*' when its boundaries impede any transfer of mass and energy, '*closed*' when only energy exchange is allowed, and '*open*' when the boundaries are permeable to both mass and energy flow. The energy exchanged between different systems during a thermodynamic process is represented by heat Q and work W.

Heat Q is defined as the amount of energy exchanged as a function of the temperature T. If a temperature difference exists between two objects, they can exchange energy in the form of heat. If two objects have the same temperature, they cannot exchange heat, as they are in thermal equilibrium, as stated by the Zeroth Law of Thermodynamics:

'*If two systems are in thermal equilibrium with a third system, then they are in thermal equilibrium with each other*.'

Work W is defined as the energy exchanged between two objects through the application of a force F along a displacement s. To produce work, the force F must have a non-null component along the direction of displacement ($\cos\theta \neq 0,\ \theta \neq 90°$).

$$W = F\cos\theta * s \tag{2.5.43}$$

Work W is positive when the force F is applied along the direction of motion (driving force), negative when F is applied against the direction of motion (resisting force), and null when F is perpendicular to the direction of motion (neutral force).

The two concepts of heat and work are similar but not equivalent, since both represent a way to exchange energy. The First Law of Thermodynamics states:

'*The total energy E of an isolated system is constant; energy is neither created nor destroyed, but it can be transformed into different forms through heat Q or work W exchange*'.

$$E = Q - W \tag{2.5.44}$$

This means that energy, in the form of heat, can be spent to produce work. Any infinitesimal variation of the internal energy of the system δE, is the balance between the energy lost by performing work δW and the energy gained as heat δQ

$$\delta E = \delta Q - \delta W \tag{2.5.45}$$

In this case the total energy is conserved, since the exchange of Q and W between system and the environment is included. Heat variations δQ are positive when energy flows from the environment toward the system (heating), and negative when energy is escaping from the system (cooling). Work

variations δW are considered negative when the system exert a mechanical energy transfer (pushing, pulling and shearing) to the environment, and positive when the system is subject to mechanical deformation exerted by the environment.

2.5.1. Heat Diffusion

The First Law **(2.5.44)**, relates the capacity of a system to produce work to its capacity to exchange heat. Therefore, if two systems are in thermal equilibrium with each other, they cannot produce any work. Temperature disequilibrium is a necessary condition to establish any energy flow between different systems.

One formulation of the Second Law of Thermodynamics states:

'*Heat can never pass from a colder to a warmer body without some other change, connected therewith, occurring at the same time.*'

This Law states that heat naturally flows from the system with the higher temperature to the system with the lowest. The only way to reverse this process is to perform work on the system and extract heat from it (i.e. refrigerators).

The higher the temperature difference, the more heat can be exchanged between different systems. This process is called heat diffusion and is described by the following equation:

$$\rho Cp\left(\frac{\partial T}{\partial t}\right) = -\nabla \cdot Q = -\left(\frac{\partial Q_{\mathrm{x}}}{\partial x} + \frac{\partial Q_{\mathrm{y}}}{\partial y} + \frac{\partial Q_{\mathrm{z}}}{\partial z}\right) \tag{2.5.46}$$

Equation **(2.5.46)** relates the temperature evolution over time $(\partial T/\partial t)$, with the opposite of the local heat flux divergence $(\nabla \cdot Q)$. When the divergence is positive, the internal heat diffuses from the system and the temperature evolution is negative, whereas when the divergence is negative the external heat converges toward the system and the temperature increases over time. The amount of energy necessary to cause temperature variation in a given material is controlled by its density ρ $[kg\ m^{-3}]$ and its specific heat capacity Cp $[J\ kg^{-1}\mathrm{K}^{-1}]$.

The heat flux Q is defined as a function of the temperature gradient ∇T, and the thermal conductivity Λ $[W\ m^{-1}\mathrm{K}^{-1}]$ of the material. Fourier's Law describes the heat flow Q:

$$Q = -\Lambda \nabla T = -\Lambda\left(\frac{\partial T_{\mathrm{x}}}{\partial x}, \frac{\partial T_{\mathrm{y}}}{\partial y}, \frac{\partial T_{\mathrm{z}}}{\partial z}\right) \tag{2.5.47}$$

Thermal conductivity describes the amount of thermal energy transported per unit of time $(W = J\ s^{-1})$ across a temperature gradient. The negative sign on the right-hand side of the equation **(2.5.47)** follows from the Second Law of Thermodynamics. As for the mass flux, the heat flux is considered positive when it is escaping from the system boundaries, and negative when it is directed inwards (**Figure 2.3**).

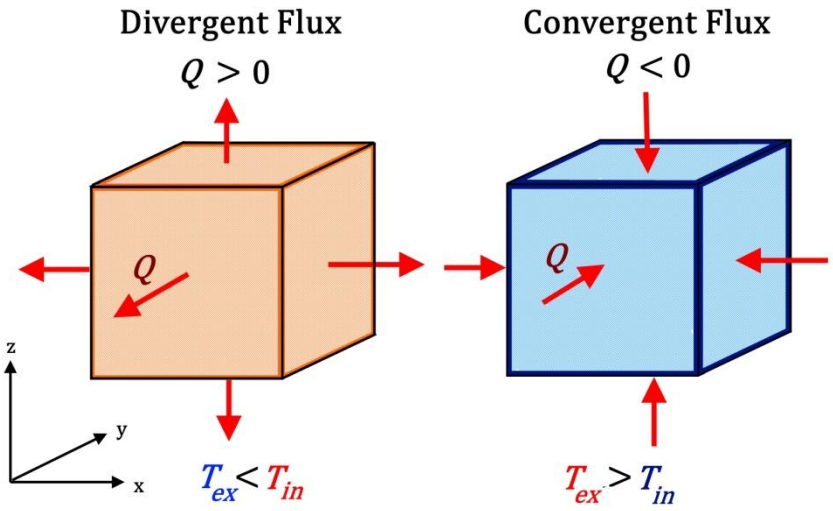

Figure 2.3. Heat flux and temperature gradient in an Eulerian control volume

This means that, if the system is warmer than the environment ($T_{ex} < T_{in}$), the gradient ∇T is negative and the resulting heat flux is positive ($Q > 0$). Vice-versa when the system is colder than the environment ($T_{ex} > T_{in}$), the gradient is positive and the resulting heat flux is negative ($Q < 0$).

Fourier's law can be expressed as a function of the spatial distribution of the temperature field, by substituting Q together with eq. **(2.5.47)** into eq. **(2.5.46)**.

$$\rho Cp\left(\frac{\partial T}{\partial t}\right) = -\nabla \cdot (-\Lambda \nabla T) \tag{2.5.48}$$

By exchanging heat, system and environment vary their respective temperatures over time. This process, however, is often accompanied by mass displacement caused by energy transfer in the form of work.

2.5.2. Volumetric Work and Viscous Dissipation

The second term in eq. **(2.5.45)** (δW), considers the energy lost by the system when it exerts deformation toward the environment, and the energy gained by the system when is deformed by the environment. When a bounded volume of fluid (system) is moving through a liquid (environment), it pushes/pulls the material in front of it/behind it. The force exerted by the moving fluid on its surroundings, depletes it from its energy storage. According to the First Law of Thermodynamics, this energy loss is either transformed into heat **(2.5.45)**, or is transferred to the external environment in different forms. Vice-versa, the volume of fluid can be squeezed or pulled by the environment and increase its internal energy accordingly. The total work variation over time is the result of volumetric and shear work contributions.

$$\frac{\partial W}{\partial t} = W_{vol} - W_{shear} = P\,\frac{\partial V}{\partial t} - \acute{\sigma}_{ij}\frac{\partial \boldsymbol{u}_i}{\partial j} \tag{2.5.49}$$

Volumetric work W_{vol} describes the internal energy variations related to the isotropic volume changes ∂V over time. These volume variations (material displacement) are caused by an applied force, which is represented by the pressure P. Effective pressure results from the balance between the external confining pressure of the surroundings P_{ex}, and the internal pressure exerted by the system on its boundaries P_{in}. In the neutral state, internal and external pressures are equal ($P_{ex} = P_{in}$), therefore no volume change occurs. When the external pressure is higher than the internal one

($P_{ex} > P_{in}$), the fluid is squeezed and the volume shrinks ($\partial V/\partial t < 0$), whereas when the internal pressure is higher than the external one ($P_{ex} < P_{in}$), the fluid pushes its boundaries and the volume expands ($\partial V/\partial t > 0$). In the first scenario, the environment performs work on the system ($\delta W_{vol} < 0$), thus increasing its internal energy ($\delta E > 0$). In the second case, on the other hand, the system exerts work on its surroundings ($\delta W_{vol} > 0$) and thus loses its internal energy ($\delta E < 0$). Since volumetric work is only related to the hydrostatic pressure P, it is always reversible.

The second term in the right-hand side of eq. **(2.5.49)** describes the deviatoric work (W_{shear}), i.e. all energy variations related to shape changes over time. In this case, the applied force is the deviatoric stress $\acute{\sigma}_{ij}$ **(2.4.28)** which stretches and shears the original shape of the body. By considering a linear viscous creep rheology **(2.4.37)**, deviatoric work definition W_{shear} becomes:

$$W_{shear} = 2\eta \left[\frac{1}{2}\left(\frac{\partial \boldsymbol{u}_i}{\partial j} + \frac{\partial \boldsymbol{u}_j}{\partial i}\right) - \frac{1}{3}\left(\frac{\partial \boldsymbol{u}_i}{\partial i}\right)\delta_{ij}\right]^2 + \eta_B \left(\frac{\partial \boldsymbol{u}_i}{\partial i}\right)^2 \tag{2.5.50}$$

The first term on the right-hand side of the equation **(2.5.50)** indicates the dissipation through shear deformation, and is controlled by the dynamic viscosity η. The second term describes the internal friction dissipation caused by volume changes, which is controlled by the bulk viscosity term η_B. Shear work is always dissipative given the presence of frictional resistance to motion, η and η_B (which are always positive). This means that part of the mechanical work ($\partial W/\partial t$) is lost by the system during the deformation process ($-W_{shear}$). Shear work is also known as viscous dissipation ϕ_η. Following the First Principle of Thermodynamics **(2.5.45)** the energy dissipated through friction is transformed into heat and the energy conservation is fulfilled.

2.5.3. Thermal Expansivity and Bulk Modulus

These energy exchanges, in the form of heat and work, alter the physical properties of the system and the environment. At the end of these processes a system might vary its temperature, volume, internal pressure or shape. Several parameters can be defined to relate these changes to the evolving thermodynamic state of the system. The thermal expansivity $\alpha\,[\mathrm{K}^{-1}]$ and the incompressibility modulus $K\,[Pa]$ (also known as bulk modulus) are given as:

$$\alpha = \frac{1}{V}\left(\frac{\partial V}{\partial T}\right)_P = -\frac{1}{\rho}\left(\frac{\partial \rho}{\partial T}\right)_P \tag{2.5.51}$$

The thermal expansivity α quantifies the percentage of the system's volume expansion ∂V, due to temperature increase ∂T, at constant pressure P. This can also be expressed as density reduction ($-\partial\rho$), due to volume increase. Typically thermal expansivity ranges are on the order of $O(\,10^{-5}\,\mathrm{K}^{-1})$. Similarly, the isothermal incompressibility modulus is defined by:

$$K = -V\left(\frac{\partial P}{\partial V}\right)_T = \rho\left(\frac{\partial P}{\partial \rho}\right)_T \tag{2.5.52}$$

The bulk modulus K quantifies the percentage of the system's volume reduction ($-\partial V$), due to increase in external pressure ∂P, at constant temperature T. This shrinkage corresponds to an increase of density $\partial\rho$. Bulk modulus typically ranges $O\ (10^2 - 10^5\ MPa)$.

2.5.4. Entropy and Irreversible Processes

Another fundamental physical parameter is the entropy of the system S. As stated above, a system featuring a temperature difference with its surroundings is capable to exchange heat, and therefore, work. In an ideal process, this transformation is total: all the heat is spent to cause mechanical work without any dissipation ($W = Q$).

This ideal system can be imagined as a tank of fluid heated from the bottom (T_H), and cooled from the top (T_C). In this example, the focus is a control volume of fluid, sitting at the bottom of the tank. As soon as the liquid heats up (Q_H), the control volume starts to expand accordingly to equation **(2.5.51)**, and to float toward the colder upper boundary. Once the control volume reaches the top of the tank, it cools down (Q_C), shrinks, and it sinks back toward the warm bottom. This cycle occurs under the assumption that the motion of the volume in between the two boundaries is adiabatic, i.e. no heat exchange with the surrounding fluid. The work produced by the control volume depends only on the temperature difference ($T_H - T_C$), and not on the nature of the fluid (Carnot's theorem).

Moreover the ratio between heat flux and temperature at the boundaries of the tank remains constant

$$\frac{Q_H}{T_H} = \frac{Q_c}{T_C} \tag{2.5.53}$$

This ratio is called entropy $S\,[J\,\mathrm{K}^{-1}]$. Entropy is a state function, meaning that its value is determined only on the current state of the system (P, T, V), and not on its evolution path. In the case of an ideal (fully reversible) process the entropy is a conserved quantity.

$$S_H = S_C \tag{2.5.54}$$

The entropy variations between two different state of the system ($a \rightarrow b$) is given by:

$$\Delta S = \int_a^b \frac{\delta Q}{T} \tag{2.5.55}$$

Where δQ is the incremental heat variation and T is the current temperature of the system. The entropy of one state can be calculated, provided the entropy of another state is known.

The Third Law of Thermodynamics states:

'The entropy of a system approaches a constant value as its temperature approaches absolute zero'

Thus, at 0 K the entropy of the system is 0. A fully reversible process is the ideal case where entropy of the system is conserved, and the mechanical motion originated by the moving fluid is perfect and it is not dissipated through internal friction ($W = Q$).

In nature, however, this is never the case, and the motion of the fluid always produces frictional heat (Q_F). This means that not all of the exchanged heat is employed to produce work ($W < Q$), but part of it is converted into thermal energy, thus increasing the temperature of the fluid. The heat balance at the boundaries shows an asymmetry, since the heat delivered to the cold boundary ($Q_C = Q_H + Q_F$) is larger than the one added by the warm boundary (Q_H).

$$\frac{Q_H}{T_H} < \frac{Q_C}{T_C} \tag{2.5.56}$$

The fluid in the tank slowly heats up, and after every cycle the system loses part of its capacity to produce work. This type of process is called irreversible, since its initial state cannot be restored without spending energy on it. Another formulation of the Second Law of Thermodynamics states:

'*The total entropy of an isolated system can never decrease over time. Entropy is constant only if all processes are reversible. The Entropy of an irreversible process is always increasing.*'

$$S_H < S_C \tag{2.5.57}$$

These concepts define the irreversibility of natural processes and their tendency to achieve thermal equilibrium. Entropy is the measure of the unused energy of the system, i.e. the mechanical energy not spent for the motion of an object, but dissipated as heat. This heat increases the temperature of the system, bringing it closer to the temperature of the warm reservoir, and thus favouring thermal equilibrium. The higher is the entropy of a system, the lower is the energy useable to produce work. The excess heat produced by a system as a consequence of the increasing entropy is quantified by:

$$\delta Q = T\delta S \tag{2.5.58}$$

2.5.5. Thermodynamic Potentials and Maxwell Relations

In thermodynamics, the state of a system can be represented by the use of potentials. These potentials describe the energy configuration of a system, as a function of the so-called '*natural variables*'. The most commonly used thermodynamic potential are: the internal energy U; enthalpy H; Helmholtz free energy F; and Gibbs free energy G.

Thermodynamic potentials are extensive properties of a system, and they cannot be measured directly. In order to quantify their status, it is necessary to measure the changes in the system's intensive (temperature T, pressure P, chemical potential μ_i) and extensive natural variables (mass m, volume V, entropy S). Each potential is governed by a specific set of natural variables: one thermal (T or S), and one mechanical (P or V).

1. $$U\,(S,V) = \int \left(T\delta S - P\delta V + \sum_i \mu_i \delta N_i \right) \tag{2.5.59}$$

2. $$H(S,P) = U + P\delta V \tag{2.5.60}$$

3. $$F(T,V) = U - T\delta S \tag{2.5.61}$$

4. $$G(T,P) = U - T\delta S + P\delta V \tag{2.5.62}$$

The internal energy U **(2.5.59)**, accounts for all energy gains and losses due to the changes of the internal state of system: heat production ($T\delta S$), expansion work ($-P\delta V$), and chemical energy due to phase transition ($\sum_i \mu_i \delta N_i$). Here, N_i indicates the number of i-*type* particles and their relative chemical potential μ_i. During a phase transition, N_i changes and the chemical energy associated with the reaction can be absorbed/released by the system from/into the environment. The processes involving internal energy potential $U\,(S,V)$, can occur adiabatically (constant S) or isochorically (constant V).

The enthalpy H **(2.5.60)**, considers the balance of all energy included in the internal energy U, plus the expansion work ($P\delta V$). The latter term indicates the amount of work required by

the system to displace its surroundings and create space for the products of the reaction. The processes involving enthalpy potential $H\ (S,P)$, may occur adiabatically or isobarically (constant P of the environment)

The Helmholtz free energy F **(2.5.61)** indicates the energy of a system that can be spent to perform mechanical work (i.e. motion of an object) toward the environment $(-P\delta V)$. Heat production caused by entropy increase is removed from the total balance $(-T\delta S)$. The processes involving free energy potential $F\ (T,V)$, may occur isothermally (constant T) or isochorically.

The Gibbs free energy F **(2.5.62)** indicates the amount of energy of a system that can be spent to perform non-mechanical work (related to chemical potentials). The contribution from expansion work $(P\delta V)$ and heat production $(-T\delta S)$ are removed from the internal energy balance. The processes involving internal energy potential $G\ (P,T)$, occur either isobarically or isothermally.

The relation between the four potentials and their natural variable are summarized in the Maxwell's thermodynamic relations:

1. $$+\frac{\partial^2 U}{\partial S \partial V} = +\left(\frac{\partial T}{\partial V}\right)_S = -\left(\frac{\partial P}{\partial S}\right)_V \tag{2.5.63}$$

2. $$+\frac{\partial^2 H}{\partial S \partial P} = +\left(\frac{\partial T}{\partial P}\right)_S = +\left(\frac{\partial V}{\partial S}\right)_P \tag{2.5.64}$$

3. $$-\frac{\partial^2 F}{\partial T \partial V} = +\left(\frac{\partial S}{\partial V}\right)_T = +\left(\frac{\partial P}{\partial T}\right)_V \tag{2.5.65}$$

4. $$+\frac{\partial^2 G}{\partial T \partial P} = -\left(\frac{\partial S}{\partial P}\right)_T = +\left(\frac{\partial V}{\partial T}\right)_P \tag{2.5.66}$$

With these concepts is possible to derive the energy conservation equation from the ruling principles of thermodynamics.

2.5.6. Energy Conservation Equation

In fluid dynamics the properties of the system are constantly evolving, therefore the energy balance stated in the First Law of Thermodynamics **(2.5.45)** has to be fulfilled over time.

$$\frac{\partial E}{\partial t} = \frac{\partial Q}{\partial t} - \frac{\partial W}{\partial t} \tag{2.5.67}$$

The two terms of heat Q and work W can be substituted by equation **(2.5.48)** (Fourier's law) and equation **(2.5.49)** (volumetric and shear work).

$$\frac{\partial E}{\partial t} = \left[\nabla \cdot (\Lambda \nabla T)\right] - \left[P\ \frac{\partial V}{\partial t}\right] + \left[\phi_\eta\right] \tag{2.5.68}$$

In the assumption of an homogeneous fluid (N_i is constant), the internal energy E of a control Eulerian volume of fluid can be expressed by the potential U **(2.5.59)**.

$$\frac{\partial E}{\partial t} = \frac{\partial U\ (S,V)}{\partial t} = \frac{T\partial S}{\partial t} - \frac{P\partial V}{\partial t} \tag{2.5.69}$$

The entropy of a system cannot be measured directly. Using partial derivatives, it is possible to write the change of one state variable as the correlated change of two other state variables. In this case, the entropy S is expressed as a function of two commonly measured thermodynamic parameters T and P.

$$\delta S = \left(\frac{\partial S}{\partial T}\right)_P \delta T + \left(\frac{\partial S}{\partial P}\right)_T \delta P \tag{2.5.70}$$

Each term in equation **(2.5.70)** can be rearranged using previous concepts and principles. Following the Second Law of Thermodynamics **(2.5.58)** and Fourier's law **(2.5.46)**, the entropy ∂S in the first term can be expressed as:

$$\left(\frac{\partial S}{\partial T}\right)_P = \left(\frac{\partial Q}{T\partial T}\right)_P = \left(\frac{\rho Cp \partial T}{T\partial T}\right)_P = \frac{\rho Cp}{T} \tag{2.5.71}$$

The second term in equation **(2.5.70)** can be re-arranged according to Maxwell's 4^{th} relation **(2.5.66)** and using the definition of thermal expansivity α **(2.5.51)** we obtain:

$$\left(\frac{\partial S}{\partial P}\right)_T = -\alpha V \tag{2.5.72}$$

Combining equations **(2.5.71)** and **(2.5.72)** with equation **(2.5.70)** results in:

$$\delta S = \left(\frac{\rho Cp}{T}\right) \delta T - (\alpha V)\, \delta P \tag{2.5.73}$$

Entropy variation δS **(2.5.73)** can be substituted into the Second Law of Thermodynamics **(2.5.69)**

$$\frac{\partial U\ (S,V)}{\partial t} = \rho Cp \frac{\partial T}{\partial t} - \alpha T V \frac{\partial P}{\partial t} - P \frac{\partial V}{\partial t} \tag{2.5.74}$$

The two laws of thermodynamics can finally be combined, **(2.5.68)** and **(2.5.74)**, to obtain the equation of energy conservation for an Eulerian volume of fluid:

$$\rho Cp \frac{\partial T}{\partial t} = \nabla \cdot (\Lambda \nabla T) + \phi_\eta + \alpha T V \frac{\partial P}{\partial t} \tag{2.5.75}$$

The left-hand term of equation **(2.5.75)** can be rearranged and expressed as energy density $\rho CpT = \boldsymbol{e}\ [J\ m^{-3}]$. Therefore, the variation of energy density in an Eulerian control volume of fluid $\partial \boldsymbol{e}/\partial t\ [J\ m^{-3}\ s^{-1}]$, can be expressed as:

$$\frac{\partial \boldsymbol{e}}{\partial t} = \phi_\Lambda + \phi_\eta + T_W + H_{source} \tag{2.5.76}$$

Where ϕ_Λ is the heat diffusion, ϕ_η is the shear heating **(2.5.50)**, T_W is the adiabatic temperature increase, and H_{source} is the heat source term $[W\ m^{-3}]$.

The term T_W indicates the temperature variations induced by the volumetric work W_{vol} **(2.5.49)**, as a consequence of the hydrostatic pressure changes $\partial P/\partial t$. These temperature variations do not represent a source/sink of heat, since W_{vol} is completely reversible (i.e. adiabatic process).

The latter term H_{source}, represents all the additional heat producing sources within the Eulerian control volume. These components of the Energy Conservation Equation **(2.5.76)** do not arise self-consistently from the principles of Thermodynamics, but are derived from the thermo-chemical history of the fluid.

2.6. Earth's Energy Sources

Earth's internal heat balance is estimated from the heat flux measured at the surface $Q_{surf} \approx 47 \pm 3\ TW$. This heat flux is caused by several heating sources (*Jaupart & Mareschal, 2015*): secular cooling H_S ($\approx 16\ TW$, i.e. ≈ 32 %); radiogenic heat production H_R (crust contribution $\approx 8\ TW$, i.e. ≈ 16 %, and mantle contribution $\approx 12\ TW$, i.e. ≈ 24 %); latent heating H_L(which affects the adiabatic temperature profile T_S) the heat flux across the Core Mantle Boundary H_Q ($\approx 11\ TW$, i.e. ≈ 22 %), and the external energy sources H_ψ ($\approx 3\ TW$, i.e. ≈ 6 %).

2.6.1. Secular Cooling

Secular cooling H_S represents the heat released during Earth's formation and subsequently trapped inside the planet. Secular heat originates from two main contributions: heat released by the impacts of planetesimals during the accretion of the Earth H_{accr}, and the heat produced by chemical differentiation processes H_{diff} (i.e. separation of the iron core from the silicate mantle). Accretion heat H_{accr} is given by (*Schubert et al., 1986*):

$$H_{accr} = -\frac{16}{15}\pi^2 G r^5 \rho_P^2 \tag{2.6.77}$$

Where $G = 6.672 \times 10^{-11}\ N\ m^2\ kg^{-2}$ is the gravitational constant, ρ_P is the mean density of the planet, and r is the radius.

The heat released by the bombardment of planetesimals during Earth's accretion ($\approx 100\ Myrs$, *Chambers, 2004*) produced the so called '*magma ocean*'(*Abe, 1997*; *Karato & Murthy, 1997*). The low viscosity of the magma ocean ($\eta \approx 10^{-1}$–$10^{-2}\ Pa\ s$ *Liebske et al., 2005* ; *Karki & Stixrude, 2010*) allowed the fast segregation of liquid iron-alloys from the bulk silicate melt, and favoured their aggregation at the centre to form the Earth's core (*Wood et al. , 2006*). The potential energy release due to differentiation H_{diff} (*Schubert et al., 1986*) is given as:

$$H_{diff} = -\frac{16}{15}\pi^2 G r^5 \left[\rho_m^2 + \frac{5}{2}\rho_m(\rho_P - \rho_m) + \left(\frac{3}{2}\rho_m - \rho_c\right)(\rho_m - \rho_c)\left(\frac{\rho_P - \rho_m}{\rho_c - \rho_m}\right)^{5/3}\right] \tag{2.6.78}$$

Where ρ_m represents the density of mantle minerals (silicates), and ρ_c represents the density of core iron alloys.

Secular energy source H_S was established over a time span of $\approx 100\ Myrs$, while the planet was dissipating heat through radiation to outer space. However, given the slowness of heat transfer processes, a large amount of the original H_S is still trapped in Earth's interior and it represents the dominant contribution to internal heat budget as it accounts for $\approx 16\ TW$, i.e. $\approx 32\%$ of the total present-day heat flux (*Jaupart & Mareschal, 2015*).

2.6.2. Radiogenic Heating

The radiogenic heat production H_R is generated by the radioactive decay of the so-called '*heat producing elements*' (hpe), predominantly: Uranium (^{238}U, ^{235}U), Thorium (^{232}Th) and Potassium (^{40}K). During a radioactive decay process, an unstable parent nucleus (parent P_R), decays into a daughter atom (D_R), by emitting energetic particles ($\alpha-$, $\beta-$, $\gamma-$) and radiative heat. Over time, the amount of parent atoms declines, whereas the number of stable daughter atoms increases. The initial concentration of a parent atoms ∂P_R^0 diminishes proportionally to its atomic decay constant λ_D:

$$\frac{\partial P_R^t}{\partial t} = -\lambda_D P_R^0 \tag{2.6.79}$$

The exponential decay trend is obtained by integrating equation **(2.6.79)**.

$$P_R(t) = P_R^0 e^{-\lambda_D t} \tag{2.6.80}$$

A common way to express the exponential decay of radioactive elements is through their half-life $t_{1/2}$ (**Table 2.1**), which is the time until half of the initial parent atom concentration decays ($P_R^t = 0.5P_R^0$).

$$t_{1/2} = \frac{ln\,(2)}{\lambda_D} \tag{2.6.81}$$

Isotope	Natural abundance [%]	$t_{1/2}\,[yr]$	$R_H[W\ kg^{-1}]$
^{238}U	99.27	4.46×10^9	95.13×10^{-6}
^{235}U	0.72	7.04×10^8	568.47×10^{-6}
^{232}Th	100	1.40×10^{10}	26.30×10^{-6}
^{40}K	0.0117	1.26×10^9	28.47×10^{-6}

Table 2.1. Here reported are the half-life $t_{1/2}\,[yr]$ and the heat production per unit mass $R_H[W\ kg^{-1}]$ of the principal radioactive elements in Earth's mantle (*Dye, 2012*). Natural abundance refers to the fraction of isotope of a chemical element as naturally found on a Earth.

These elements are strongly incompatible in the mantle rocks, and tend to concentrate in melts (i.e. MORB) (*Saunders et al., 1988*). Furthermore, the hpe content in igneous rock progressively increases through the magmatic sequence that produces continental crust (*Galer & O'Nions, 1985*). Continental hpe reservoirs represent $\approx 75\%$ of the heat flux produced by the radioactive decay of U and Th (*Enomoto et al., 2007*). The high concentration of radioactive elements in the continental crust is responsible for $\approx 17\%$ of the global heat flux ($\approx 8\ TW$) (*Jaupart & Mareschal, 2015*).

The abundance of heat producing elements in Earth's rock is on the order of 10^{-1}– $10^{-2}\ ppm$ (U, Th), and $10^2\ ppm$ (K). Measuring the concentration of radioactive elements in the mantle is a challenging task due to the lack of representative samples. The study of meteorites allows us to constrain the bulk Earth composition, and to provide an estimate on the average hpe concentration (*McDonough & Sun, 1995*). Geochemical analysis provides a current constraint on the amount of radiogenic heating R_H produced by in mantle to be $3.5 - 5.2 \times 10^{-12}\ W\ kg^{-1}$ (see **Table 2.2** from *Palme & O'Neill, 2007*). Radioactive elements are the second-most important source of heat, and they account for $\approx 12\ TW$, i.e. $\approx 24\%$ of the total heat flux (*Jaupart & Mareschal, 2015*).

	U $[ppm]$	Th $[ppm]$	K $[ppm]$	$R_H[W\ kg^{-1}]$
CI-chondrites	0.008	0.030	544	3.5×10^{-12}
Elemental ratios	0.022	0.083	261	5.2×10^{-12}

Table 2.2. Geochemical constraint of the radiogenic heat $[W\ kg^{-1}]$ produced by the mantle (*Palme & O'Neill, 2007*)

Furthermore, the presence of short-lived radioactive elements like ^{26}Al ($t_{1/2} = 7.2 \times 10^5\ yr$) might have represented an important heat source during the early stages of planet formation in the protoplanetary disk (*Diehl et al., 2006*). This radiogenic heat source might have caused significant degassing of CI-chondrites, and also contributing to the secular heating of our planet (*Lichtenberg et al., 2019*). The amount of radiogenic heat produced by a cubic meter of material H_R $[W\ m^{-3}]$ is given by $H_R = R_H \rho_V$ where ρ_V is the density of the control volume of fluid.

2.6.3. Latent Heat

The latent heat H_L term represents the heat produced/consumed during a phase transition reaction. This heat source does not contribute to temperature changes of the reacting substance, but it is used for the reorganization of its molecular configuration. In geosciences, polymorphs are crystals with the same chemical composition, but with different crystallographic configuration (e.g. olivine, wadsleyite, ringwoodite). To pass from one crystallographic phase to the other, some energy (i.e. latent heat) has to be absorbed or released. A phase transitions is *endothermic* when heat is consumed during the reaction, and *exothermic* when heat is produced during the reaction.

In P-T space, the product and the reagent of a given phase reaction are separated by a curve. The relationship that describes the slope $\partial P/\partial T$ of a tangent line in a given point of the phase transition curve is called Gibbs-Duhem relation (*Schubert et al., 1975*), and reads:

$$\frac{\partial P}{\partial T} = \frac{E_H \rho_B \rho_A}{T_d \Delta\rho} \tag{2.6.82}$$

Where E_H $[J\ kg^{-1}]$ is the specific latent energy required to transform a unit mass of phase A into phase B, ρ_A and ρ_B are the densities $[kg\ m^{-3}]$ of the reagent A and the product B, respectively. T_d [K] is the temperature at the given point of the curve, $\Delta\rho = \rho_B - \rho_A$ is the density variation caused by the phase transition. Latent energy E_H can be converted in latent heat L_H $[W\ kg^{-1}]$ provided that is known the rate of the phase transformation $\dot{t}$ $[s^{-1}]$.

The ratio $\partial P/\partial T$ is better known as '*Clausius-Clapeyron-slope*' Υ $[MPa\ K^{-1}]$ and is a fundamental parameter in geosciences. In Earth's mantle, the phase transitions encountered by a sinking particle ($A \rightarrow B$) always involves an increase in density ($\Delta\rho > 0$). Furthermore, densities ρ_A, ρ_B and temperature T are always positive. This means that, when a reaction is endothermic ($L_H < 0$) the Clapeyron slope is negative, whereas when a reaction is exothermic ($L_H > 0$) the Clapeyron slope is positive.

In geosciences a common way to deal with latent heat is by introducing the effective thermal expansivity $\acute{\alpha}$ and the effective heat capacity $\acute{C}p$ (*Schubert et al., 1975* ; *Christensen & Yuen, 1985* ; *Ismail-Zadeh & Tackley, 2010* ; *Tackley, 1998, 2008*). The effective thermal expansivity $\acute{\alpha}$ $[K^{-1}]$ takes into account the latent heat L_H released/absorbed as the temperature changes ∂T at constant pressure P, whereas effective heat capacity $\acute{C}p$ $[J\ kg^{-1}K^{-1}]$ takes into account the latent heat released/absorbed as pressure changes ∂P at constant temperature T (*Schubert et al., 1975*).

$$\acute{\alpha} = \bar{\alpha} + \frac{\Delta\rho}{\bar{\rho}}\left(\frac{\partial \Gamma}{\partial T}\right)_P \tag{2.6.83}$$

$$\acute{Cp} = \overline{Cp} + \left(\frac{\partial \Gamma}{\partial T}\right)_P T\Delta S$$

Where $\Delta\rho$ $[kg\ m^{-3}]$ and ΔS $[J\ K^{-1}]$ are the density and the entropy jump due to phase transition, respectively. Barred terms, $\bar{\alpha}$, $\overline{Cp}$ and $\bar{\rho}$ represent the parameters in the two-phase divariant region of the reaction ($A \rightarrow AB \rightarrow B$).

$$\bar{\alpha} \approx \Gamma^A \alpha^A + (1 - \Gamma^A)\alpha^B \tag{2.6.84}$$

$$\overline{Cp} \approx \Gamma^A Cp^A + (1 - \Gamma^A)Cp^B$$

$$\bar{\rho} \approx \Gamma^A \rho^A + (1 - \Gamma^A)\rho^B$$

The parameter Γ is called phase function, and indicates the amount of products present at a given moment of the reaction, i.e. $[\Gamma^A = 1,\ \Gamma^B = 0]$ when the reaction has not started, and $[\Gamma^A = 0,\ \Gamma^B = 1]$ when it is completed. The phase function Γ smoothly changes with pressure P and temperature T. The effect of P-T can be combined in the '*excess pressure*' parameter π which considers the effect of the Clapeyron slope Υ $[MPa\ K^{-1}]$.

$$\pi = (P - P_{1/2}) - \Upsilon(T - T_{1/2}) \tag{2.6.85}$$

Where $(P_{1/2}, T_{1/2})$ represent the point in P-T space where both phases of the reaction have the same proportion ($\Gamma^A = \Gamma^B = 0.5$). The Clapeyron slope Υ indicates if a given phase transition is endothermic ($\Upsilon < 0$) or exothermic ($\Upsilon > 0$).

Moreover, the Clapeyron slope Υ controls the depth (i.e. pressure) at which a given phase transition occurs as a function of the temperature of the moving fluid (*Faccenda & Dal Zilio, 2017*). In the case of an endothermic phase transition ($\Upsilon, L_H < 0$) warm materials react at low-P, whereas cold materials react at high P. For the case of an exothermic phase transition ($\Upsilon, L_H > 0$) it occurs the other way round: warm materials react at high P, and cold materials react at low P. A detailed discussion on the effect of the Clapeyron slope on mantle convection can be found in *Schubert et al. (1975)*, and in **Chapter 7.1.5**.

Using the method illustrated in eq. **(2.6.83)-(2.6.85)** (*Schubert et al., 1975*; *Ismail-Zadeh & Tackley, 2010*), the latent heat L_H term is included in the reference mantle adiabatic temperature profile (*Tackley, 1998*). The adiabatic temperature gradient of a given domain $\dot{T}_S$ $[K\ m^{-1}]$ is produced by the volumetric work exerted by the hydrostatic pressure of the fluid. The equation that defines $\dot{T}_S$ can be derived starting from Maxwell's 2^{nd} thermodynamic relation **(2.5.64)**, by assuming a linear pressure increase ($P = \rho g z$) and by expressing Maxwell's 4^{th} relation as αV **(2.5.72)**.

$$\left(\frac{\partial T}{\partial z}\right)_S = \dot{T}_S = T_P \frac{\alpha g}{Cp} \tag{2.6.86}$$

This equation shows that the adiabatic temperature profile depends on thermal expansivity α and specific heat capacity Cp. The parameter T_P is the potential temperature, i.e. the adiabatic temperature extrapolated to the surface. Given the presence of a conductive lithosphere on terrestrial bodies in the solar system, it is impossible to measure directly the adiabatic parameter T_P. A current experimental estimate for Earth's potential temperature is $T_P \approx 1600$ K (*Katsura et al.,*

2010). The adiabatic temperature profile of the mantle T_s is derived from equation **(2.6.86)** by using the bulk modulus K **(2.5.52)** and by introducing the Grüneisen parameter γ (*Brugger & Fritz, 1967*).

$$\gamma = \frac{\alpha K}{\rho Cp} \tag{2.6.87}$$

$$T_S = T_P \left(\frac{\rho}{\rho_0}\right)\gamma$$

Where and ρ_0 is the reference density of the fluid at the surface. Equation **(2.6.87)** it is not applicable to derive the Earth's temperature profile at the phase transition given the presence of density jumps.

The adiabatic temperature profile **(2.6.87)** in a multi-phase mantle can be computed by considering the effective parameters $(\acute{\alpha}\ \acute{C}p)$ **(2.6.83)**, and therefore including the latent heat contribution $\Delta T_{A\to B}$ to the total temperature $(T_S + \Delta T_{A\to B})$. The volumetric latent heat $H_L\ [W\ m^{-3}]$ is given by $H_L = L_H \bar{\rho}$ where $\bar{\rho}$ is the density of the fluid in the divariant field **(2.6.84)**. The temperature variations $\Delta T_{A\to B}$ caused by the latent heat H_L depends on the coexisting phases region parameters $(\bar{\alpha}, \overline{Cp}, \bar{\rho})$ **(2.6.84)**, and on the width of the coexisting region, which is a function of the Clapeyron slope Υ **(2.6.85)**. Moreover, the sign of the Clapeyron slope controls the temperature jumps of the adiabat: exothermic reactions $(\Upsilon, L_H > 0)$ will cause positive jumps $(\Delta T_{A\to B} > 0)$, whereas exothermic reactions $(\Upsilon, L_H < 0)$ will produces negative jumps $(\Delta T_{A\to B} < 0)$. This kinked adiabat has an impact on the super-adiabatic temperature term which is the balance between the temperatures of a given convective object T_O, and the adiabatic temperature of the fluid T_S at a given depth $(T_{SA} = T_O - T_S)$. The variations of T_{SA} produced by the phase reactions has an effect on the buoyancy of the convective fluid (*Schubert et al., 1975*).

2.6.4. Core Mantle Boundary Heat Flux

The outer core is composed of liquid (*Oldham, 1906*; *Jeffreys, 1926*) Fe-rich alloys (*Asahara et al., 2007*; *Umemoto & Hirose, 2020*) with an extremely low viscosity $\eta \approx 10^{-2}\text{–}10^{-3}\ Pa\ s$ (*Secco et al., 1997*; *De Wijs et al., 1998*; *Posner & Steinle-Neumann, 2019*). Convection in the outer core is driven by thermo-chemical instabilities (*Bouffard et al., 2019*) that effectively transport heat toward the CMB with estimates in the range $Q_{CMB} \approx 80 \times 10^{-3}\ W\ m^{-2}$ (*Nimmo, 2015*).

The heat flux at the CMB is produced by the contribution of: secular core cooling; latent heat from core crystallization; potential energy release due to chemical separation **(2.6.78)**; and radiogenic heat generation. A detailed description of the governing equations of outer core convection can be found in *Braginsky & Roberts (1995)*. CMB heat flux accounts for $\approx 11\ TW$, i.e. $\approx 22\%$ of the earth's total heat flux (*Jaupart & Mareschal, 2015*).

2.6.5. External Energy Source

External energy H_ψ term represents the heat sources produced by the interaction with external systems, e.g. tidal heating. Tidal heating is produced by the viscous dissipation ϕ_η **(2.5.50)** induced by the gravitational pull by other celestial bodies. For Earth, the tidal heating is induced by the presence of the Moon ($\approx 80\%$) and the Sun ($\approx 20\%$) (*Jaupart & Mareschal, 2015*). Most of the tidal heating is due to the ocean-rock interaction, related to the fast response of low η water to gravitational perturbations ($\approx 90-95\%$ *Lambeck, 1977*). However, also high η mantle rocks are influenced by tidal pull, and the resulting friction contributes to the total heat budget.

Tidal dissipation on a given control volume can be seen as the material dislocation (i.e. strain ε_{ij}) induced by transient stress (σ_{ij}), that is maximum when the volume is the closest to the external gravity source. This perturbation peak occurs rhythmically (i.e. sinusoidal variations) and depends on the angular velocity of the rotating body ω. Since the strain varies with rotation, its fundamental to define tidal heat as a function of the strain rate $\dot{\varepsilon}_{ij}$ **(2.4.34)**. Moreover, the response to this source of stress depends on the viscosity η and elastic shear modulus μ. The average volumetric dissipation heat H_{tide} $[W\ m^{-3}]$ is given by (*Tobie et al., 2003*; *Mitri & Showman, 2008*; *Rozel et al., 2014*):

$$H_{tide} = \frac{2\eta\widetilde{\dot{\varepsilon}_{ij}^2}}{1+\left(\frac{\omega\eta}{\mu}\right)^2} \tag{2.6.88}$$

Where $\widetilde{\dot{\varepsilon}_{ij}^2}$ is the Fourier transform of the strain rate to account for the sinusoidal perturbation.

On Earth, tidal heating H_ψ produces $\approx 3\ TW$ ($\approx 0.07\%$ of Q_{surf}), but the contribution to the solid mantle is only $\approx 0.1\ TW$ ($\approx 0.002\%$ of Q_{surf}). However, this heat source is much more relevant for celestial bodies in close proximity with massive centres of gravity, e.g. Jupiter's moon Io (*Yoder, 1979*; *Moore, 2003*; *Hamilton et al., 2013*; *Tyler et al., 2015*) and Europa (*Ross & Schubert, 1987*; *Sotin et al., 2002*; *Tobie et al., 2003*; *Beuthe, 2015*), and Saturn's moon Enceladus (*Ross & Schubert, 1989*; *Meyer & Wisdom, 2007*; *Mitri & Showman, 2008*; *Rozel et al., 2014*).

2.7. Constitutive Laws

The three Navier-Stokes equations are not sufficient to fully describe the motion of a fluid. These equations contain several parameters that need to be defined in order to determine the solution of the problem. The unknown parameters are constrained by laboratory measurements or geophysical observations, which are used to extrapolate constitutive laws or parameterized equations for the physical properties of interest.

2.7.1. Pressure P and Density ρ

Pressure and density are related to each other by the bulk modulus K **(2.5.52)**, which quantifies how difficult is to cause volume variations with increasing pressure. However, the more the fluid volume is reduced, the higher is the repulsion between the electronic clouds of the constituent atoms. Therefore, the resistance to compression K increases as the volume decreases.

The relations linking K, P and ρ (V_0/V) are called Equation of States (EoS) (*Ballaran, 2010*). There is no universal EoS for solids due to the lack of a general thermodynamic basis. Hence, several assumptions can be used (*Murnaghan, 1937*; *Birch, 1947*; *Vinet et al., 1989*; *Poirier & Tarantola, 1998*). The most widely used formulation is the 3^{rd} order Birch-Murnaghan EoS.

$$P(V) = 3K_0 f_E (1 + 2f_E)^{5/2}\left[1 + \frac{3}{2}(K' - 4)f_E\right] \tag{2.7.89}$$

Where K_0 is the bulk modulus at room pressure, and $K'$is the pressure derivative of the bulk modulus $K' = \partial K/\partial P$. Equation **(2.7.89)** expresses the strain energy of a compressed solid with a Taylor series of finite Eulerian strain f_E (*Birch, 1947*).

$$f_E = \frac{\left[\left(\frac{V_0}{V}\right)^{2/3} - 1\right]}{2} \tag{2.7.90}$$

In geosciences, equation **(2.7.89)** is widely used to calculate the density distribution inside a planet (*Katsura & Tange, 2019*). Density calculations are combined with compositional constraints (i.e. mineral abundances) to infer the aggregate density distribution, and thus extrapolate the pressure trend inside planet interiors.

2.7.2. Gravity Field g_i

Regardless of their origins, density anomalies in the fluid cause buoyancy instabilities only in the presence of a gravitational potential ϕ_G $[J\,kg^{-1}]$. Without gravity, fluid convection is not possible (*Javadi & Kazemi, 2018*), and therefore it is fundamental to define the gravity potential in the domain, in order to solve the Navier-Stokes equations.

In continuum mechanics the gravitational potential ϕ_G, is expressed in the form of the Poisson equation, i.e. $\nabla^2\phi = \mathcal{G}$. Where ∇^2 is the Laplacian operator, ϕ is the given potential, and $\mathcal{G}$ is the source that determines that potential. The Poisson equation, solved for the gravitational potential, reads:

$$\frac{\partial g_x}{\partial x} + \frac{\partial g_y}{\partial y} + \frac{\partial g_z}{\partial z} = 4\pi G \rho_{xyz} \tag{2.7.91}$$

Where $\mathcal{G} = 4\pi G\rho_{xyz}$ is the source of gravity due to the density distribution ρ_{xyz} (i.e. mass) within the continuum body. The term $4\pi G$ arises from the spherical region of influence of the gravitational

attraction. The left-hand side of the equation **(2.7.91)**, represents the divergence of the gravity acceleration field $\nabla \cdot g$.

For a given planet, the reference gravity acceleration g_0 can be an input parameter in the Navier-Stokes equations. At Earth's surface $g_0 \approx 9.81\ m\ s^{-2}$, whereas deep in the mantle is approximately constant $g_0 \approx 10\ m\ s^{-2}$ (*Lowrie, 2007*).

2.7.3. Flux Controlling Parameters (η and Λ)

Flux controlling parameters regulate the propagation of the given material property (mass or energy) as a function of the acting constitutive laws. The two main flux controlling parameters are the viscosity η $[Pa\ s = kg\ m^{-1}\ s^{-1}]$, which controls the flux of matter, and the thermal conductivity Λ $[W\ m^{-1}\ K^{-1} = J\ s^{-1}\ m^{-1}\ \mathrm{K}^{-1}]$, controls the flux of thermal energy.

Viscosity

The rheological behavior of Earth's mantle assumed in section **2.4.2** is linear viscous creep, which correspond to the idealized case of a Newtonian fluid. The diffusion creep mechanism, is characterized by the individual migration (i.e. diffusion) of point defects (e.g. ions, atoms, vacancies) through the grain boundaries (Coble creep - *Coble, 1963*) or through the grain interior (Nabarro-Herring Creep - *Nabarro, 1948*; *Herring, 1950*). These deformation processes are efficient provided that the temperature T of the deforming material is close to its melting point T_{melt}, i.e. mantle rocks possess an high homologous temperature $T_H = T/T_{melt}$ (*Weertman & Weertman, 1975*). Given the high temperatures of Earth's mantle ($\approx 1600 - 2700\ K$ *Katsura et al., 2010*), the homologous temperatures of mantle rocks are sufficiently high to trigger the diffusion creep processes (*Karato, 2008*), i.e. $T_H = 0.65 - 0.75$ for olivine in the upper mantle (*Borch & Green, 1987*), and $T_H = 0.70 - 0.85$ for bridgmanite in the lower mantle (*Heinz & Jeanloz, 1987*). Moreover diffusion creep process are dominant when the applied stress σ is low and the grain size d is small (*Karato, 2008*).

Several other mechanisms contributes to the total deformation of mantle rocks (*Twiss & Moore, 2007*): dislocation creep (1D linear defects, e.g. atom lines), which involves dislocation glide and dislocation climb, and grain boundary sliding (2D planar defects). Dislocation creep mechanisms are dominant in an intermediate-high stress regime, and they show a power law relation between stress and strain rate (*Tsenn & Carter, 1987*). The grain boundary sliding mechanism, instead becomes dominant at high stress regime and at high homologous temperatures (*Hansen et al., 2011*; *Ohuchi et al., 2015*).

The effective viscosity of the rocks results from the contribution of aforementioned mechanisms, which depends on temperature T, deviatoric stress regime $\acute{\sigma}$ (which change with the hydrostatic pressure P), and the grain size d. Furthermore, the presence of impurities such as water or melt, weakens the crystal lattice and reduces the viscosity.

The general equation for rock flow is given by (*Hirth & Kohlstedt, 2003*):

$$\dot{\varepsilon} = \widehat{A}\ \acute{\sigma}^n\ d^m\ C_{H2O}^{-r}\ exp(-\alpha f_{melt})\ exp\left(\frac{E_{act} + PV_{act}}{RT}\right) \tag{2.7.92}$$

Where $\dot{\varepsilon}$ $[s^{-1}]$ is the strain rate (*Brennen, 1974*; *Conrad & Molnar, 1999*; *Becker, 2006*); $\widehat{A}$ $[s^{-1}]$ is a pre-exponential factor (*Hrma, 2008*), e.g. 3.5×10^{22} and 2.0×10^{18} for dry and wet olivine respectively (*Karato & Wu, 1993*); $\acute{\sigma}$ the deviatoric stress; n is the mechanism-dependent stress

exponent (i.e. $n = 1$ for diffusion creep and $n \approx 3$–4 for dislocation creep); d $[m]$ is the rock grain size (*Solomatov, 2001*), m is the mechanism-dependent grain size exponent (i.e. $m = 0$ for dislocation creep, $m = 2$ for Nabarro-Herring creep and $m = 3$ for Coble creep); $C_{H2O}[wt\%]$ is the water content; r is the water content exponent (1.0-2.0 *Mei & Kohlstedt, 2000*; *Korenaga & Karato, 2008*), f_{melt} [%] is the melt fraction in the rocks (*Scott & Kohlstedt, 2006*; *Zimmerman, 2004*); α is a constant (*Hirth & Kohlstedt, 2003*). Furthermore, rock flow dependency on temperature and pressure is controlled by the activation energy E_{act} $[J\,mol^{-1}]$ and volume V_{act} $[m^3\,mol^{-1}]$, of the mineral assemblage (*Ranalli, 1995*). Typically $E_{act} \approx O(10^5\,J\,mol^{-1})$ and $V_{act} \approx O(10^{-6}\,m^3\,mol^{-1})$ (*Karato & Wu, 1993*). The parameter R represents the universal gas constant $R = 8.314\,J\,mol^{-1}\,\mathrm{K}^{-1}$.

Thermal Conductivity

The thermal conductivity Λ of mantle rocks controls the cooling history of planets and therefore their geodynamic regimes (*Zhang et al., 2019*). For non-opaque materials, the total thermal conductivity Λ_{tot} is given by the contribution of lattice thermal conductivity Λ_{lat} and radiative thermal conductivity Λ_{rad}.

The radiative thermal conductivity is expected to become important at high temperatures, since it increases with T^3 (*Brewster, 1972*), provided that the minerals remain optically transparent even at high pressure (*Keppler et al., 2008*). Therefore, radiative heat transfer is more effective in the deepest part of the lower mantle (*Goncharov et al., 2008*; *Goncharov et al., 2009*). The contribution of radiative heat transfer might lead to the formation of super-plumes in the deep lower mantle (*Matyska et al., 1994*; *Matyska & Yuen, 2005*).

For average mantle temperatures, however, the main contribution to Λ_{tot} is given by the phonon-phonon heat transport, i.e. Λ_{lat}. Typically, Λ_{lat} increases with the fourth-power of density (*Anderson, 1987*; *Osako & Ito, 1991*), since with increasing pressure P the bulk modulus increases, and sound velocities are faster (*Aramberri et al., 2017*). The effect of the temperature, however, is opposite and Λ_{lat} diminishes with increasing temperature, following a T^{-1} dependence for homogenous crystals (*Dalton et al., 2013*), and a $T^{-1/2}$ dependence for crystals with impurities (*Xu et al., 2004*; *Deschamps & Hsieh, 2019*; *Zhang et al., 2019*). In particular, the phonon scattering caused by the presence of impurities in the crystal lattice, reduces the mean free-path of thermal energy carriers, and hinders heat conduction (see **Chapter 5.5.2**). This phenomena are enhanced at high pressure where the inter-atomic distance shortens, and the ionic defects may form an interconnected network (*Chang et al. , 2017*; *Hsieh et al., 2017*; *Marzotto et al., 2020*).

The parameterization of P-T-X dependence is fundamental to calculate the thermal diffusivity κ $[m^2 s^{-1}]$.

$$\kappa = \frac{\Lambda}{\rho C p} \tag{2.7.93}$$

This parameter quantifies the thermal diffusion processes, which competes against thermal convection as heat transport mechanism. If a volume of fluid is capable to quickly dissipate the excess heat through conduction, it loses its enhanced buoyancy and it stops moving. Nevertheless, for most materials, κ is on the order of 10^{-5} - 10^{-6} $m^2 s^{-1}$ which indicates that thermal diffusion in Earth's mantle is a rather slow process, thus thermal convection is the dominant heat transport mechanism inside Earth's mantle.

2.8. Nondimensionalization

The reported Navier-Stokes equations are in their dimensional form, meaning that all the parameters have a physical dimension expressed accordingly to the International System of Units (m, s, kg, K). One important use of the Navier-Stokes equation is to study which parameters influence the most a given problem. A method to perform such analysis is to assess each parameter individually, by varying it over a certain range and by keeping all others constant. Given the large amount of coefficients involved in the Navier-Stokes equation, this method is extremely time consuming and often impractical.

A better way to operate is to nondimensionalize each coefficient. Furthermore, several dimensional parameters can be combined into dimensionless numbers to consider several properties of the fluid simultaneously. This approach has the advantage of analysing a given aspect of the fluid flow as a whole contribution of forces, and compare it against a competing mechanism. Once the governing mechanism is constrained, a refined analysis can be performed on the dimensionless group to identify the dominating parameter. In the next subsections, the most common dimensionless numbers used in geosciences will be described.

2.8.1. Rayleigh Number

To establish convection in a given volume of fluid, the system has to possess a certain set of characteristics. In fluid dynamics, the tendency of a system to exchange heat through convection is quantified by the Rayleigh Number Ra. The non-dimensional number Ra, is defined as the ratio between the parameters that drive convection ('*buoyancy forces*') against the parameter that opposes to fluid motion ('*resisting forces*'). The Rayleigh Number is considered the principal dimensionless group of fluid dynamics:

$$Ra = \frac{\rho\, g\, \alpha\, \Delta T\, D^3}{\kappa\, \eta} \tag{2.8.94}$$

Fluid convection is principally driven by the density instabilities within a gravity field $g\ [m\ s^{-2}]$. The temperature-induced density instabilities are a consequence of the action of thermal expansivity $a\ [K^{-1}]$ **(2.5.51)**, whereas the amount of work a system is capable to produce is proportional to the temperature difference between the hot and cold heat reservoirs $\Delta T\ [K]$. The term $D\ [m]$ indicates the thickness of the domain. Against these driving parameters, thermal diffusivity $\kappa\ [m^2 s^{-1}]$ and viscosity $\eta\ [Pa\ s]$ dampen the onset of convection by diffusing the excess heat, and by inhibiting fluid motion.

The balance between these two forces quantifies the tendency of a given fluid to establish convection. The critical Rayleigh Number Ra_{crit} necessary for the onset of convection is calculated to be around ≈ 1000 (*Turcotte & Schubert, 2002*). The higher Ra the more $vigorous$ the convection is.

The Rayleigh Number for Earth's mantle can be calculated by using average physical properties. Average mantle density $\rho = 4200\ kg\ m^{-3}$ and mantle thickness $D = 2.89 \times 10^6\ m$ are estimated from seismology (*Gutenberg, 1913*; *Dziewonski & Anderson, 1981*). Thermal expansivity $\alpha = 2.40 \times 10^{-5}\ K^{-1}$ is estimated from *Katsura et al., 2010*. Gravity acceleration in the mantle is approximately constant $g = 10\ m\ s^{-2}$ (*Dziewonski & Anderson, 1981*; *Lowrie, 2007*). Temperature difference ΔT is estimated to be around 2400 K (*Schubert et al., 2001*), and is calculated considering a CMB temperature of ≈ 4000 K (*Boehler, 2000*; *Price et al., 2004*; *Kawai*

& Tsuchiya, 2009), and a mantle potential temperature of ≈ 1600 K *(Dalton, et al., 2014*; *Hole & Millett, 2016*; *Katsura et al., 2010*; *Sarafian et al., 2017*). Average mantle viscosity of $\eta \approx 3.40 \times 10^{22}\ Pa\ s$ is based on inversion estimates (*Forte & Mitrovica, 1996*; *Peltier, 1996*; *Mitrovica & Forte, 2004*; *Steinberger & Calderwood, 2006*). Thermal diffusivity $\kappa = 1.00 \times 10^{-6}\ m^2 s^{-1}$ is based on measurements for olivine's Λ (*Chang et al., 2017*), ρ (*Zhang & Bass, 2016*) and Cp (*Su et al., 2018*). From this calculation, Earth's mantle $Ra = 1.8 \times 10^6$ which is 3 orders of magnitude higher then Ra_{crit} and indicates that thermal convection is the dominant heat transfer process in the mantle.

2.8.2. Reynolds Number

The nature of Earth's mantle convection is described by the Reynolds Number Re. This value is defined by the ratio of inertial forces (i.e. how difficult is it to change the velocity of the fluid), and the resisting forces (i.e. viscosity).

$$Re = \frac{\rho\, D\, u}{\eta} \tag{2.8.95}$$

The inertial forces are controlled by the mass-per-unit-volume of the fluid $\rho\ [kg\ m^{-3}]$, the flow velocity $u\ [m\ s^{-1}]$, and the domain thickness $D[m]$. Depending on the balance between inertial and viscous terms, a fluid flow can be: $turbulent$ (inertia > viscosity) or $laminar$ (inertia < viscosity). The threshold values for the different flow regime are: $Re > 10^4$ for turbulent flow, and $Re < 10^3$ for laminar flow. Hybrid regimes occurs in between these values, following *Schubert et al., 2001*. The Reynolds number can be calculated for Earth's mantle. Using mantle flow velocity $\boldsymbol{u} = 3.00 \times 10^{-9}\ m\ s^{-1}$ (see section **2.4.3**) we obtain $Re = 1.1 \times 10^{-21}$. Due to the high viscosity of the rocks, the Earth's mantle flows in a laminar regime.

2.8.3. Nusselt Number

Previous estimates of Ra and Re establish the presence of laminar convection in Earth's mantle. However, regardless of its ability to flow, the uppermost part of Earth forms a highly viscous lithosphere ($\eta \gg 10^{23}\ Pa\ s$) (*Walcott, 1970*; *De Bremaecker, 1977*; *Liu & Hasterok, 2016*). This highly viscous layer is unable to convect, therefore it can only transfer heat via conduction and radiation. Given the slowness of heat conduction processes, the lithosphere acts as a thermal insulator, and drastically reduces heat loss from Earth's interior. The efficiency of convection is given by the Nusselt Number Nu.

$$Nu = \frac{Q\, D}{\Lambda\, \Delta T} \tag{2.8.96}$$

This dimensionless number is the ratio of average heat flux measured at the surface Q, and the total heat flux transported by conduction $D/\Lambda\,\Delta T$. If $Nu = 1$, then the heat flux at the surface is established only through conduction. For $Nu > 1$, the measured heat flux is higher than the value expected from pure conduction, and additional processes transport heat to the surface (i.e. mantle convection).

Earth's surface Nusselt Number Nu_{top} can be calculated by using the average heat flux $Q = 91.6 \cdot 10^{-3}\ W\ m^{-2}$, (*Davies & Davies, 2010*) and assuming an average thermal conductivity of the lithospheric rocks of $\Lambda = 3.60\ W\ m^{-1}K^{-1}$ (*Chang et al., 2017*). Mantle thickness, and temperature difference are the same used in section **2.8.1**. From this calculation, $Nu_{top} = 29.4$, it

appears clear that mantle convection is responsible for most of the heat flux budget of Earth's surface.

Theoretically, it would be possible to calculate a Nusselt Number also for the CMB Nu_{bot}. However, Nu_{bot} has much larger uncertainties given the difficulties to constrain the thermal conductivity of CMB rocks Λ_{bot} (*Anderson, 1987*; *Osako & Ito, 1991*), and the heat flux at the bottom of the lower mantle Q_{bot} (*Labrosse, 2014* and reference therein). A simple Nu_{bot} estimate can be calculated by assuming $\Lambda_{bot} = 12\ W\ m^{-1}\ K^{-1}$ (*Osako & Ito, 1991*) and $Q_{bot} = 80 \times 10^{-3}\ Wm^{-2}$ (*Nimmo, 2015*). The outer core thickness $D = 2.26 \times 10^{6}\ m$ is estimated from Earth reference models (*Dziewonski et al., 1975*), whereas temperature difference between CMB ($\approx$ 4000 K) and Inner-Core Boundary ($\approx$ 5000 K *Tateno et al., 2010*) is $\Delta T = 1000\ K$. Core mantle boundary Nusselt Number is $Nu_{bot} = 15.01$.

These calculation shows that $Nu_{bot} < Nu_{top}$, which means that convective heat extraction at the CMB is less efficient than at the surface (*Sotin & Labrosse, 1999*; *Deschamps et al., 2010*). This is due to the high thermal conductivity of deep mantle rocks. Top and bottom Nusselt Number calculations are fundamental to constrain the planetary energy balance and the early planet evolution reconstructions (*Jaupart & Mareschal, 2015*).

2.8.4. Péclet Number

A measure of the effectiveness of convective heat transport through the volume of fluid is given by the Péclet Number Pe.

$$Pe = \frac{u\ D}{\kappa} \tag{2.8.97}$$

The Péclet Number is the ratio between convective velocity $u\ D$ against the speed of heat diffusion processes κ. If the plume is fast enough ($Pe > 1$), the plume does not lose its buoyancy and it effectively transports heat from one boundary to the other. Fast rising velocity u is a necessary condition for adiabatic plume ascend (i.e. without heat exchange). On the other hand, if heat diffusion processes are faster than the flow velocity ($Pe < 1$), the plume thermally equilibrates with the ambient fluid and it loses its ability to float/sink. In this case, heat conduction is more effective than convection. The Péclet Number Pe can be calculated for the Earth case by using the same values reported for Rayleigh Number calculation (section **2.8.1**), i.e. $Pe = 8.7 \times 10^{3}$. This calculation shows that on Earth, mantle convection is $\approx 10^{4}$ faster than heat diffusion.

2.8.5. Prandtl Number

Another dimensionless number used to estimate the effectiveness of convection over conduction is the Prandtl Number Pr.

$$Pr = \frac{\eta}{\kappa\ \rho} \tag{2.8.98}$$

The Prandtl number is defined as the ratio between momentum diffusivity η/ρ against the thermal diffusivity κ. Momentum diffusivity defines how fast a given fluid is capable to relocate its mass under the action of a constant deviatoric stress, i.e. an established fluid flow. Momentum diffusivity on Earth's mantle is much higher than the thermal diffusivity, and the Prandtl Number can be calculated as $Pr = 8.1 \times 10^{24}$ (see section **2.8.1** for the assumptions). The extremely high Pr ($\approx \infty$), shows the dominance of viscous convection over thermal diffusion in Earth's mantle. In

geodynamical modelling, the infinite Prandtl Number assumption is often used to describe the type of convective fluid with high viscosity η and low thermal diffusivity k.

2.8.6. Dissipation Number

When the Navier-Stokes equations are non-dimensionalised using the domain length-scale D and the thermal diffusion time scale $t_k = D^2/\kappa$, a new non-dimensional number appears in the energy conservation equation **(2.5.76)**. This parameter is called dissipation number, and it is defined as the ratio between the mantle depth D and the adiabatic temperature scale h_S $[m]$.

$$Di = \frac{D}{h_S} \tag{2.8.99}$$

The latter term h_S is derived from the adiabatic temperature gradient $\dot{T}_S$ $[K\ m^{-1}]$ **(2.6.86)**, and indicates the height over which the potential temperature T_P increases adiabatically by a factor of e (Euler's number ≈ 2.72) (*Jarvis & McKenzie, 1980*).

$$\frac{\Delta T}{h_S} = \frac{T_P(e-1)}{h_S} = T_P\frac{\alpha g}{Cp} \tag{2.8.100}$$

$$h_S = (e-1)\frac{Cp}{\alpha g}$$

The adiabatic temperature scale h_S for Earth's mantle can be calculated by using the same α and g employed in previous calculations (section **2.8.1**), and by assuming a specific heat capacity of $Cp = 1200\ J\ kg^{-1}\ K^{-1}$ (*Saxena et al. 1993*; *Katsura et al., 2010*): $h_S = 8.60 \times 10^6\ m$, leading to a dissipation number of $Di = 0.34$. Given the thickness of Earth's mantle D, Di shows that a considerable amount of the temperature difference ΔT between the top T_{surf} and bottom T_{CMB} boundary is related to shear heating during plume motion (*Hewitt et al., 1975*), the adiabatic temperature increase, and the latent heat released/absorbed at the phase boundaries (*Christensen & Yuen, 1985*).

2.9. Stokes Equation in Spherical Coordinate

One important aspect that has to be taken into account in mantle convection studies is the sphericity of the modelled domain. In particular, the spherical shape of planets generates an intrinsic asymmetry in the global energy balance (*Sotin & Labrosse, 1999*; *Deschamps et al., 2010*). In a Cartesian box the top and the bottom boundaries of the domain have the same areas ($A_{top} = A_{bot} = \Delta x \Delta y$), whereas in a spherical geometry the domain is contained within an upper and a lower shell with different areas ($4\pi r_{top}^2 > 4\pi r_{bot}^2$).

Assuming a bottom-heated-only mantle ($H_{source} = 0$), the global energy conservation implies that the power balance $\hat{P} = AQ$ at the boundaries is the same, i.e. $\hat{P}_{top} = \hat{P}_{bot}$. In order to maintain this balance in a spherical geometry, the heat flux at the lower boundaries has to be higher than the heat flux at the upper boundary ($Q_{top} < Q_{bot}$), which leads to a different Nusselt number Nu **(2.8.96)**. The Nusselt numbers that describe Cartesian box convection Nu_{box}, and spherical shell convection Nu_{shell} are comparable only if the aspect ratio $\Delta z/\Delta y$ of the convective cell is similar (*Vangelov & Jarvis, 1994*; *Jarvis et al., 1995*). However, with increasing curvature (r_{top}/r_{bot}), the bottom boundary area A_{bot} is reduced as well as the warm plume production (*Deschamps et al., 2010*), thus leading to a different convective cell configuration and a non-comparable Nu.

For an internally heated mantle ($H_{source} > 0$), the cooling rate of a planet is described by the Urey Ratio U_r (*Urey, 1955*), defined as the ratio between the volumetric heat production ($M_m H_r$), and the emitted surface power $\hat{P}_{top}$. Where M_m is the mass of the planet and R_H in the heat production per unit mass (section **2.6.2**). For $U_r = 1$ the planet is in a steady-state mode and all the heat produced is dissipated at the surface by the heat flux. For $U_r > 1$ the planet heats up, whereas for $U_r < 1$ the planet cools down. Mantle convection is very effective in transporting the heat despite the internal production R_H, and therefore $U_r < 1$ for most planets. The rate of cooling is controlled by the surface-area-to-volume ratio (*Planinšič & Vollmer, 2008*), which is the lowest for a spherical object ($3/r$). Hence a sphere has a slower cooling rate compared to a Cartesian box domain ($6/r$). The mass, momentum and energy conservation equations in a spherical domain are reported in *Schubert et al. 2001*.

2.9.1. Spherical Coordinates

The spatial coordinates in a spherical domain are: colatitude θ, longitude φ and radial distance r (**Figure 2.4**).

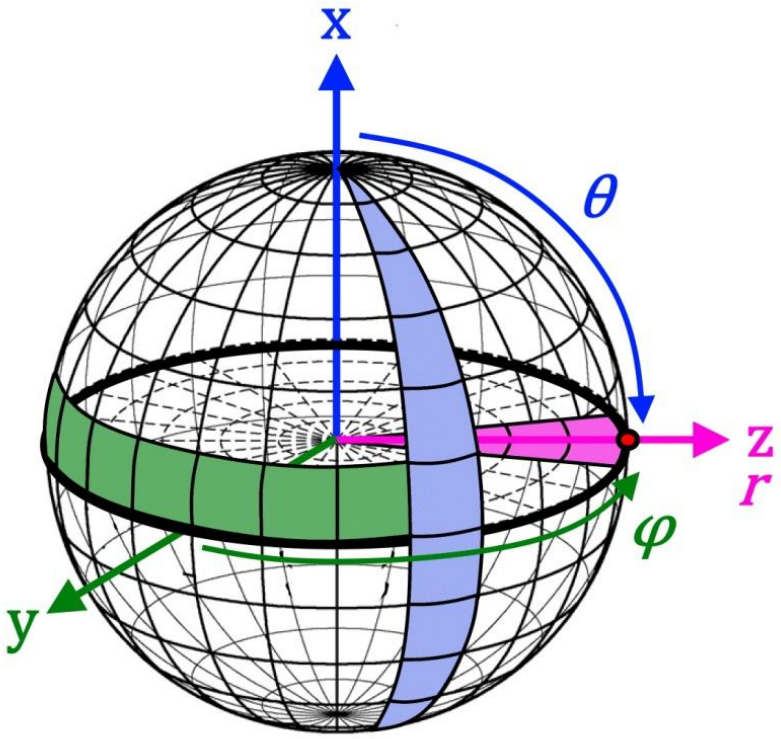

Figure 2.4. Spherical coordinate (modified from *Hernlund & Tackley, 2008*): θ colatitude (blue), φ longitude (green), r radial distance (pink).

This formulation requires the conversion of the Stokes equations from Cartesian (x,y,z) to spherical coordinates:

$$\frac{\partial \phi_x}{\partial x} \rightarrow \frac{1}{r \sin\theta} \frac{\partial}{\partial \theta} (\sin\theta \, \phi_\theta) \tag{2.9.101}$$

$$\frac{\partial \phi_y}{\partial y} \rightarrow \frac{1}{r \sin\theta} \frac{\partial}{\partial \varphi} (\phi_\varphi)$$

$$\frac{\partial \phi_z}{\partial z} \rightarrow \frac{1}{r^2} \frac{\partial}{\partial r} (r^2 \phi_r)$$

The notation ϕ_i indicates the components of the physical property ϕ along the i-direction $\phi = (\phi_\theta, \phi_\varphi, \phi_r)$.

2.9.2. Spherical Annulus Geometry

The computation of the Stokes equation in a 3-dimensional domain is computationally expensive, and therefore, limited to low grid resolutions. The 2D spherical annulus geometry (**Figure 2.5**) represents the best compromise between the curved domain of the 3D sphere, while maintaining a relatively high resolution even for global-scale mantle convection studies (*Hernlund & Tackley, 2008*). The formulation of Mass, Momentum, and Energy conservation equation in a 2D spherical annulus geometry is derived from the 3D spherical formulation (*Schubert et al. 2001*), but by assuming the colatitude as $\theta = 90°$ (i.e. equatorial slice).

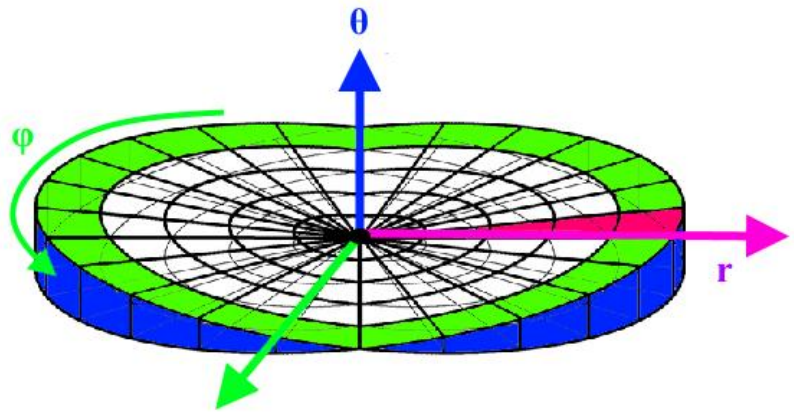

Figure 2.5. Spherical annulus geometry modified from (*Hernlund & Tackley, 2008*): θ colatitude (blue), φ longitude (green), r radial distance (pink).

The mass conservation **(2.3.10)** for $\theta = 90°$ becomes:

$$\left[\frac{1}{r}\frac{\partial}{\partial\varphi}(\rho\boldsymbol{u}_\varphi)\right] + \left[\frac{1}{r^2}\frac{\partial}{\partial r}(r^2\rho\boldsymbol{u}_r)\right] = 0 \tag{2.9.102}$$

The momentum conservation **(2.4.42)**, for $\theta = 90°$ and g acting only in the radial direction reads

$$-\left[\frac{1}{r}\frac{\partial P}{\partial\varphi}\right] + \left[\frac{1}{r^2}\frac{\partial}{\partial r}(r^2\tau_{\varphi r}) + \frac{1}{r}\frac{\partial\sigma_{\varphi\varphi}}{\partial\varphi} + \frac{\tau_{\varphi r}}{\mathrm{r}}\right] = 0 \tag{2.9.103}$$

$$[\rho g] - \left[\frac{\partial P}{\partial r}\right] + \left[\frac{1}{r}\frac{\partial\tau_{r\varphi}}{\partial\varphi} - \frac{\sigma_{\theta\theta}+\sigma_{\varphi\varphi}}{r} + \frac{1}{r^2}\frac{\partial}{\partial r}(r^2\sigma_{rr})\right] = 0$$

The deviatoric stress **(2.4.36)** is expressed as:

$$\sigma_{\theta\theta} = 2\eta\left(\frac{\boldsymbol{u}_r}{r}\right) - 2\eta\left\{\left[\frac{1}{r}\frac{\partial\boldsymbol{u}_\varphi}{\partial\varphi}\right] + \left[\frac{1}{r^2}\frac{\partial}{\partial r}(r^2\boldsymbol{u}_r)\right]\right\} \tag{2.9.104}$$

$$\sigma_{\varphi\varphi} = 2\eta\left(\frac{1}{r}\frac{\partial\boldsymbol{u}_\varphi}{\partial\varphi} + \frac{\boldsymbol{u}_r}{r}\right) - 2\eta\left\{\left[\frac{1}{r}\frac{\partial\boldsymbol{u}_\varphi}{\partial\varphi}\right] + \left[\frac{1}{r^2}\frac{\partial}{\partial r}(r^2\boldsymbol{u}_r)\right]\right\}$$

$$\sigma_{rr} = 2\eta\left(\frac{\partial\boldsymbol{u}_r}{\partial r}\right) - 2\eta\left\{\left[\frac{1}{r}\frac{\partial\boldsymbol{u}_\varphi}{\partial\varphi}\right] + \left[\frac{1}{r^2}\frac{\partial}{\partial r}(r^2\boldsymbol{u}_r)\right]\right\}$$

$$\tau_{\varphi r} = \eta\left[\frac{1}{r}\frac{\partial\boldsymbol{u}_r}{\partial\varphi} + r\frac{\partial}{\partial r}\left(\frac{\boldsymbol{u}_\varphi}{r}\right)\right]$$

The conservation of energy **(2.5.76)** is expressed as

$$\frac{\partial \boldsymbol{e}}{\partial t} + \left[\frac{\boldsymbol{u}_\varphi}{r}\frac{\partial \boldsymbol{e}}{\partial \varphi}\right] + \left[\boldsymbol{u}_r\frac{\partial \boldsymbol{e}}{\partial r}\right] = \phi_\Lambda + \phi_\eta + H \tag{2.9.105}$$

With the heat diffusion term ϕ_Λ **(2.5.46)** expressed as:

$$\nabla\cdot(\Lambda\nabla T) = \left[\frac{1}{r^2}\frac{\partial}{\partial\varphi}\left(\Lambda\frac{\partial T}{\partial\varphi}\right)\right] + \left[\frac{1}{r^2}\frac{\partial}{\partial r}\left(\Lambda r^2\frac{\partial T}{\partial r}\right)\right] \tag{2.9.106}$$

And the viscous dissipation term ϕ_η **(2.5.50)** expressed as:

$$\phi_\eta = 2\eta\left[\left(\frac{\boldsymbol{u}_r}{r}\right)^2\left(\frac{1}{r}\frac{\partial \boldsymbol{u}_\varphi}{\partial\varphi}+\frac{\boldsymbol{u}_r}{r}\right)^2+\left(\frac{\partial \boldsymbol{u}_r}{\partial r}\right)^2\right]+\eta\left[\frac{1}{r}\frac{\partial \boldsymbol{u}_r}{\partial\varphi}+r\frac{\partial}{\partial r}\left(\frac{\boldsymbol{u}_\varphi}{r}\right)\right]^2 \tag{2.9.107}$$

$$-\frac{2}{3}\eta\left[\frac{1}{r}\frac{\partial \boldsymbol{u}_\varphi}{\partial\varphi}+\frac{1}{r^2}\frac{\partial}{\partial r}(r^2\boldsymbol{u}_r)\right]^2$$

CHAPTER 3 - Numerical Methods

3.1. Taylor Series Expansion

A common method to calculate the solution of a continuous function is by employing the Taylor series expansion, which is defined as the infinite sum of derivatives, at a single point of the function, for all the points of the functions.:

$$f_{i+1} = f_i + \frac{\Delta x}{1!}\left(\frac{\partial f}{\partial x}\right)_i + \frac{\Delta x^2}{2!}\left(\frac{\partial^2 f}{\partial x^2}\right)_i + \frac{\Delta x^3}{3!}\left(\frac{\partial^3 f}{\partial x^3}\right)_i + \frac{\Delta x^4}{4!}\left(\frac{\partial^4 f}{\partial x^4}\right)_i \ldots + \frac{\Delta x^n}{n!}\left(\frac{\partial^n f}{\partial x^n}\right)_i \quad (3.1.1)$$

Where the solution of the function in the point $i+1$, is calculated starting from the function in the previous point i, plus an infinite sum of polynomials. Each polynomial term is composed by: an n-order derivative at point i $(\partial^n f/\partial x^n)_i$, the spatial distance Δx between point i and $i+1$, and the factorial term $n!$ The Taylor series expansion can be also applied retroactively to calculate the function at point $i-1$, from the derivatives of the function f_i.

$$f_{i-1} = f_i - \frac{\Delta x}{1!}\left(\frac{\partial f}{\partial x}\right)_i + \frac{\Delta x^2}{2!}\left(\frac{\partial^2 f}{\partial x^2}\right)_i - \frac{\Delta x^3}{3!}\left(\frac{\partial^3 f}{\partial x^3}\right)_i + \frac{\Delta x^4}{4!}\left(\frac{\partial^4 f}{\partial x^4}\right)_i \ldots - \frac{\Delta x^n}{n!}\left(\frac{\partial^n f}{\partial x^n}\right)_i \quad (3.1.2)$$

The solution of the function f progressively improves as the number of polynomials considered in the calculation increases. However, this operation has to include a large number of terms (virtually infinite), and it has to be repeated for each point of the function ($i \to \infty$). This, evidently, is not feasible and usually the solution of the Taylor series is truncated at the desired order of accuracy. The solution, in this case, is an approximation of the original function, and it takes its name from the order employed in the calculation (e.g. cubic approximation for an 3^{rd}-order Taylor expansion). The truncation of the solution at a given polynomial introduces an approximation (truncation) error. This error E, is inversely proportional to the spacing Δx, elevated to the n^{th} power of the n-truncated term (i.e. $E \propto 1/\Delta x^n$). Truncating a high-order polynomial introduces a small error in the computation of the solution, whereas the low-orders polynomials (i.e. $1 \to 4$) have a larger impact on the final solution. The approximated solution of a function is called '*numerical*', whereas the exact solution is called '*analytical*'.

One method to solve a function numerically, is to truncate the Taylor series at the first derivative (linear approximation), and further approximate the derivative as differential quotient.

$$f_{i+1} = f_i + \frac{\Delta x}{1!}\left(\frac{\partial f}{\partial x}\right)_i + \cancel{\frac{\Delta x^2}{2!}\left(\frac{\partial^2 f}{\partial x^2}\right)_i} + \cancel{\frac{\Delta x^3}{3!}\left(\frac{\partial^3 f}{\partial x^3}\right)_i} + \cancel{\frac{\Delta x^4}{4!}\left(\frac{\partial^4 f}{\partial x^4}\right)_i} \ldots + \cancel{\frac{\Delta x^n}{n!}\left(\frac{\partial^n f}{\partial x^n}\right)_i} \quad (3.1.3)$$

$$f_{i+1} \approx f_i + \frac{\Delta x}{1!}\left(\frac{\partial f}{\partial x}\right)_i + O\left(\frac{1}{\Delta x^2}\right) + O\left(\frac{1}{\Delta x^3}\right) + O\left(\frac{1}{\Delta x^4}\right) \ldots + O\left(\frac{1}{\Delta x^n}\right)$$

$$f_{i-1} = f_i - \frac{\Delta x}{1!}\left(\frac{\partial f}{\partial x}\right)_i + \cancel{\frac{\Delta x^2}{2!}\left(\frac{\partial^2 f}{\partial x^2}\right)_i} - \cancel{\frac{\Delta x^3}{3!}\left(\frac{\partial^3 f}{\partial x^3}\right)_i} + \cancel{\frac{\Delta x^4}{4!}\left(\frac{\partial^4 f}{\partial x^4}\right)_i} \ldots - \cancel{\frac{\Delta x^n}{n!}\left(\frac{\partial^n f}{\partial x^n}\right)_i}$$

$$f_{i-1} \approx f_i - \frac{\Delta x}{1!}\left(\frac{\partial f}{\partial x}\right)_i + O\left(\frac{1}{\Delta x^2}\right) - O\left(\frac{1}{\Delta x^3}\right) + O\left(\frac{1}{\Delta x^4}\right) \ldots - O\left(\frac{1}{\Delta x^n}\right)$$

This technique is called Finite Difference method, and is the basic method employed by many codes in the geodynamics community used to solve the Stokes equations (*Gerya, 2019*).

3.2. Finite Difference Method

The Finite Difference (FD) method requires the discretization of the domain, meaning that the continuous function ∫ is sampled in a finite number of locations called nodes (or also grid points). With this approach, the solution to the equation is not continuous field, but a rather a grid of intersecting stencils of nodes (i.e. pattern of points). The higher is the number of nodes that describes the function, the better would be the approximation (**Figure 3.1**).

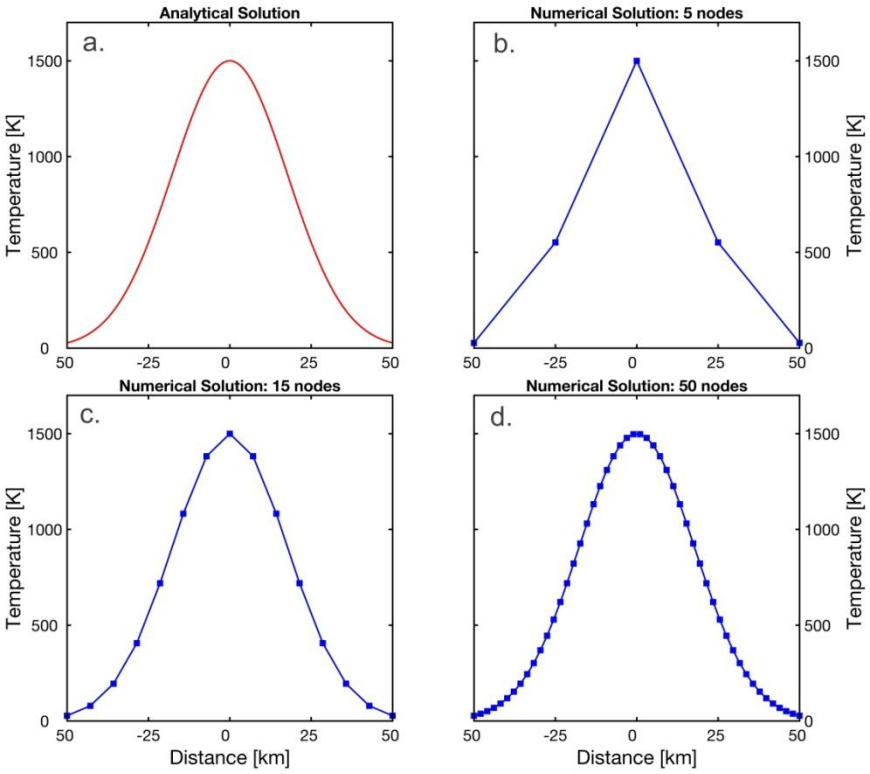

Figure 3.1. Numerical discretization of a Gaussian temperature distribution: continuous function (red line), numerical solution (blue lines), grid nodes (square markers). (a) analytical solution; (b) 5 nodes FD discretization; (c) 15 nodes FD discretization; (d) 50 nodes FD discretization.

The discretization is employed for both time ($\partial t \approx \Delta t$) and space ($\partial x \approx \Delta x$), this approximation is valid provided that Δt and Δx are sufficiently small. It is fundamental to choose an appropriate value for these numerical parameters in order to obtain an accurate solution. To calculate the differential quotients three approaches are possible depending on the nodes considered in the computation:

I. Forward Difference

The node considered to compute the derivative of f_i in the node i is the subsequent one in the stencil of nodes (i.e. $i + 1$).

$$\left(\frac{\partial f}{\partial x}\right)_i \approx \frac{f_{i+1} - f_i}{\Delta x} \tag{3.2.4}$$

This can be visualized as:

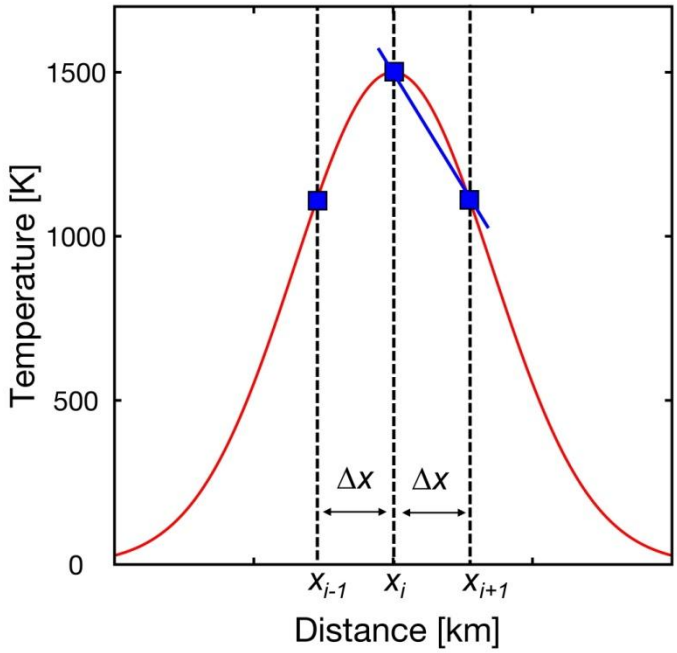

Figure 3.2. Forward Difference. Analytical solution (red line), numerical discretization (blue line), grid nodes (blue squares)

II. Backward Difference

The node considered to compute the derivative of f_i in the node i is the previous one in the stencil of nodes (i.e. $i-1$).

$$\left(\frac{\partial f}{\partial x}\right)_i \approx \frac{f_i - f_{i-1}}{\Delta x} \tag{3.2.5}$$

This can be visualized as:

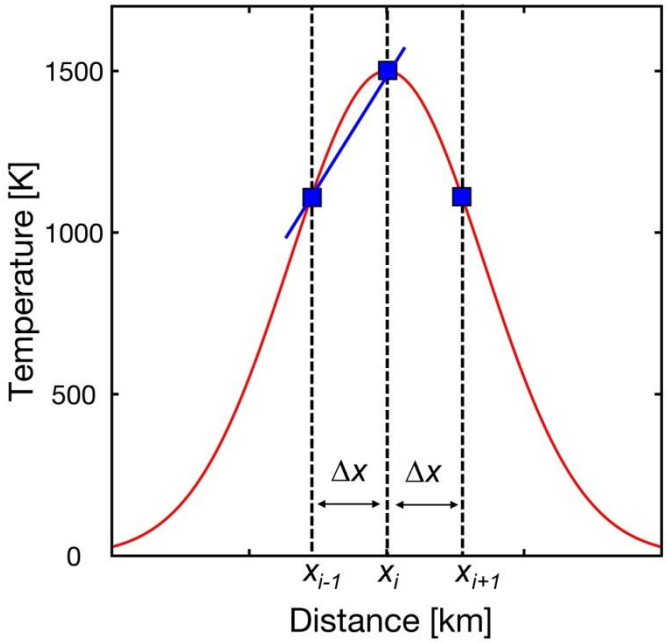

Figure 3.3. Backward Difference. Analytical solution (red line), numerical discretization (blue line), grid nodes (blue squares)

III. Central Difference

The nodes considered to compute the derivative of f_i in the node i are the previous and subsequent ones in the stencil of nodes (i.e. $i-1$ and $i+1$). Following the Taylor series expansion f_{i+1} and f_{i-1} **(3.1.3)**, the difference $f_{i+1} - f_{i-1}$ produces:

$$f_{i+1} - f_{i-1} = \frac{2\Delta x}{1!}\left(\frac{\partial f}{\partial x}\right)_i + \frac{2\Delta x^3}{3!}\left(\frac{\partial^3 f}{\partial x^3}\right)_i \ldots + \frac{2\Delta x^n}{n!}\left(\frac{\partial^n f}{\partial x^n}\right)_i \tag{3.2.6}$$

$$\left(\frac{\partial f}{\partial x}\right)_i \approx \frac{f_{i+1} - f_{i-1}}{2\Delta x} - E\left(\frac{1}{\Delta x^2}\right) \ldots - E\left(\frac{1}{\Delta x^{n-1}}\right)$$

This can be visualized as:

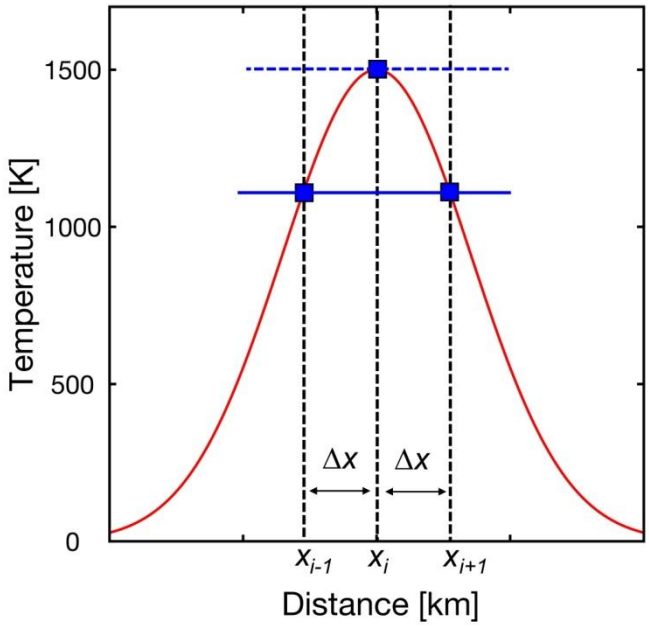

Figure 3.4. Central Difference. Analytical solution (red line), numerical discretization (blue solid line), grid nodes (blue squares). The slope of the function at the point x_i is indicated by the dashed blue line.

Central difference has a higher order of accuracy since the first truncation error scales $E \propto 1/\Delta x^2$. Moreover, the slope of the function is maintained in the derivatives (**Figure 3.4**), thus producing a more reliable approximation.

The second-order derivatives of the function f_i calculated with the FD method is the differential quotient between forward and backward first-order derivatives.

$$\left(\frac{\partial^2 f}{\partial x^2}\right)_i \approx \frac{\left(\frac{\partial f}{\partial x}\right)_i^{forward} - \left(\frac{\partial f}{\partial x}\right)_i^{backward}}{\Delta x} \tag{3.2.7}$$

$$\left(\frac{\partial^2 f}{\partial x^2}\right)_i \approx \frac{\frac{f_{i+1} - f_i}{\Delta x} - \frac{f_i - f_{i-1}}{\Delta x}}{\Delta x}$$

$$\left(\frac{\partial^2 f}{\partial x^2}\right)_i \approx \frac{f_{i+1} - 2f_i + f_{i-1}}{\Delta x^2}$$

The Finite Difference method can also consider higher order approximations in the computation of the solution. This is done by including higher order terms from the Taylor series expansion, which translates in including more neighbouring nodes in the FD computation (e.g. 2^{nd}–order approximation additionally considers these grid points → $i+2$; $i-1$; $i+1$; $i+2$).

3.3. Discretization of the Fourier Law

The present section describes the Finite Difference method to solve Partial Differential Equations (PDE), applied to a simple 1D heat diffusion problem. This case will be used as an example to generally describe how FD works, but also as a detailed explanation of the self-written Matlab code design to study the thermal evolution of the slab as used in **Chapter 5**.

Heat diffusion is described by eq. **(2.5.48)** where the temperature evolution $\partial T/\partial t$ is a function of the second order derivative of the temperature distribution in space $\partial T/\partial x$.

$$\rho Cp\left(\frac{\partial T}{\partial t}\right) = \frac{\partial}{\partial x}\left(\Lambda \frac{\partial T}{\partial x}\right) \tag{3.3.8}$$

Where ρ is the density $[kg\ m^{-3}]$ Cp is the specific heat capacity $[J\ kg^{-1}K^{-1}]$, and Λ is the thermal conductivity $[W\ m^{-1}K^{-1}]$. The 1D domain (x-direction) is discretized by a series of nodes which are spaced by a distance Δx, and identified by an index i. The temperature variations in the node i, are calculated by considering the local heat flux established between the two neighbouring nodes $i-1$ (left), and $i+1$ (right), i.e. central difference ($T_{i-1} - T_i - T_{i+1}$). In the FD method, the second order derivative **(3.2.7)** of temperature in the node i can be approximated as:

$$\left(\frac{\partial^2 T}{\partial x^2}\right)_i \approx \frac{T_{i+1} - 2T_i + T_{i-1}}{\Delta x^2} \tag{3.3.9}$$

When a flux-controlling coefficient (e.g. thermal conductivity Λ, and viscosity η, see **Chapter 2.7.3**) changes with space, a conservative discretization must be used (*Gerya, 2019*). These flux-controlling parameters are extremely important in many physical problems, and in finite difference it should be taken special care to compute them. A sharp discontinuity will result in artificial mass(η)/energy(Λ) flux at the interface, if it is not correctly implemented (**Figure 3.5**).

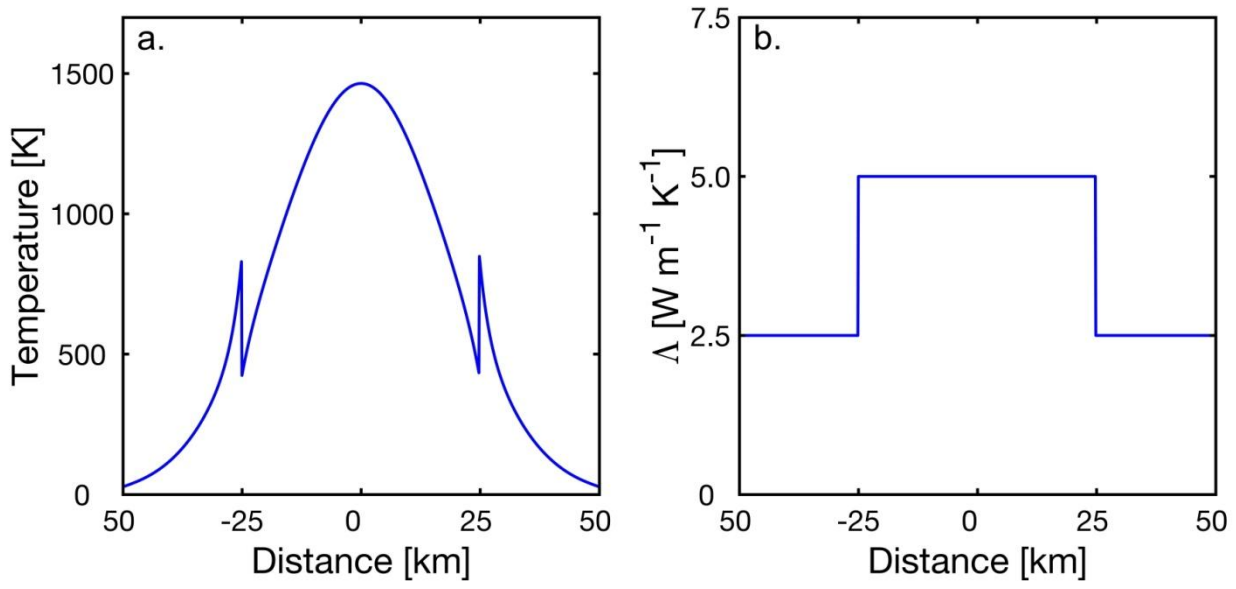

Figure 3.5. Example of a non-conservative discretization. (a) numerical solution of the temperature distribution in space, (b) space-dependent thermal conductivity Λ, featuring two sharp discontinuities at $\pm 25\ km$. The anomalous spikes in the temperature profile (a) are a consequence of the wrong implementation of the numerical solution.

To avoid this issue, the thermal conductivity Λ has to be included in the spatial derivative $\partial/\partial x$, in order to ensure the conservation of fluxes and a correct numerical solution. The conservative formulation requires the use of two intermediate auxiliary nodes (A and B) where the local thermal conductivities Λ_A, and Λ_B are defined as:

$$\Lambda_A = \frac{\Lambda_i + \Lambda_{i-1}}{2} \qquad (3.3.10)$$

$$\Lambda_B = \frac{\Lambda_{i+1} + \Lambda_i}{2}$$

In the conservative FD formulation, density and specific heat capacity are always defined on the target node i ($\rho_i\ Cp_i$) (**Figure 3.6**). This is done to prevent artificial variations of heat fluxes as a consequence of different material properties (*Gerya, 2019*).

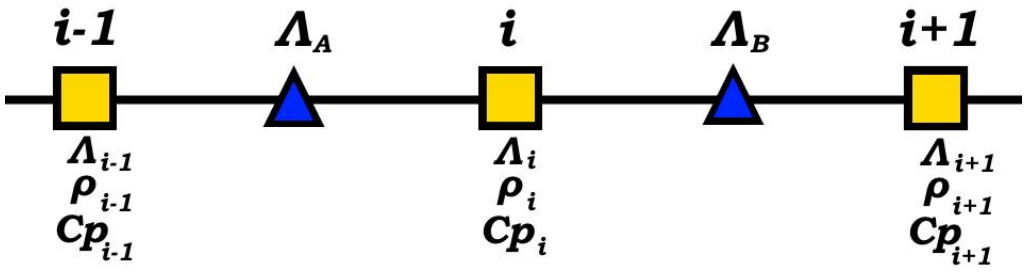

Figure 3.6. 1D node stencil in the i direction. Yellow squares indicate the target grid nodes where temperature is calculated, whereas blue triangles indicate the auxiliary nodes where the thermal conductivities are defined for the conservative FD formulation.

The discretized formulation of the Fourier Law **(3.3.9)** on the target node i is given by:

$$\rho_i Cp_i \left(\frac{\Delta T_i}{\Delta t}\right) = \frac{1}{\Delta x^2}[\Lambda_B(T_{i+1} - T_i) - \Lambda_A(T_i - T_{i-1})] \qquad (3.3.11)$$

This formulation is called conservative because the temperature equations share common quotients. For example, the equations for ΔT_i and ΔT_{i+1} share the common quotient $\Lambda_B(T_{i+1} - T_i)$, thus passing the temperature information from one node to the other through the auxiliary point B.

$$\Delta T_i = \frac{\Delta t}{\rho_i Cp_i \Delta x^2}[\boldsymbol{\Lambda_B(T_{i+1} - T_i)} - \Lambda_A(T_i - T_{i-1})] \qquad (3.3.12)$$

$$\Delta T_{i+1} = \frac{\Delta t}{\rho_{i+1} Cp_{i+1} \Delta x^2}[\Lambda_C(T_{i+2} - T_{i+1}) - \boldsymbol{\Lambda_B(T_{i+1} - T_i)}]$$

By solving for the temperature variation ΔT_i, the equation **(3.3.11)** the equation becomes:

$$T_i^{t+1} - T_i^t = \hat{c}[\Lambda_B(T_{i+1} - T_i) - \Lambda_A(T_i - T_{i-1})] \qquad (3.3.13)$$

Where T_i^{t+1} is the future temperature for node i, T_i^t is the current temperature for node i, and $\hat{c}$ is the coefficient that takes into account the numerical (Δt, Δx) and physical properties (ρ_i, Cp_i) of the target node:

$$\hat{c} = \frac{\Delta t}{\rho_i Cp_i \Delta x^2} \qquad (3.3.14)$$

At this point two different approaches can be followed to compute the solution to this equation: solve it for the current temperature T_i^t (explicit method) or solve it for the future temperature T_i^{t+1} (implicit method). The two formulations present different mathematical implementation and require distinct solver algorithms to be computed. The final structure of the code heavily depends on this choice, although many advanced codes present both solving options.

3.3.1. Explicit Formulation

In the explicit discretization scheme, the time derivative is solved for the temperature at the future time $t + 1$.

$$T_i^{t+1} = \hat{c}[\Lambda_B T_{i+1}^t - (\Lambda_A + \Lambda_B)T_i^t + \Lambda_A T_{i-1}^t] + T_i^t \tag{3.3.15}$$

In each node i, the linear equation defining the temperature evolution from T_i^t to T_i^{t+1} has the form:

$$T_i^{t+1} = \hat{c}\Lambda_A T_{i-1}^t - (\hat{c}\Lambda_A + \hat{c}\Lambda_B - 1)T_i^t + \hat{c}\Lambda_B T_{i+1}^t \tag{3.3.16}$$

This formulation is quite straightforward to implement in the code, since it simply requires to solve equation **(3.3.16)** locally (i.e. just considering nodal points $[i-1, i, i+1]$) and to apply it for the entire domain $[i, n]$. However, this comes at the cost of a strong limitation on the time step length Δt, which has to satisfy the Courant factor:

$$\Delta t < \frac{\Delta x^2}{2\kappa} \tag{3.3.17}$$

Where κ is the thermal diffusivity $[m^2 s^{-1}]$, defined as $\kappa = \Lambda/\rho Cp$ **(2.7.93)**. This mean that the maximum time step employed has to be shorter than the characteristic time scale t_κ for heat diffusion process ($t_k = D^2/\kappa$), otherwise the solution of the PDE degenerates over time (*Gerya, 2019*). The Courant limit is particularly inconvenient for high resolution codes, where the number of time steps increases exponentially with the decreasing Δx.

3.3.2. Implicit Formulation

In the implicit discretization scheme the time derivative is not solved for the future temperature $t + 1$, but for the current time t.

$$T_i^t = \hat{c}[-\Lambda_B T_{i+1}^{t+1} + (\Lambda_A + \Lambda_B)T_i^{t+1} - \Lambda_A T_{i-1}^{t+1}] + T_i^{t+1} \tag{3.3.18}$$

The implicit scheme requires a global system of equations, where Fourier's Law has to be solved simultaneously for all the nodes of the domain (*Gerya, 2019*). In each node i, the linear equation defining the temperature evolution from T_i^t to T_i^{t+1} has the form:

$$T_i^t = -\hat{c}\Lambda_A T_{i-1}^{t+1} + (\hat{c}\Lambda_A + \hat{c}\Lambda_B + 1)T_i^{t+1} - \hat{c}\Lambda_B T_{i+1}^{t+1} \tag{3.3.19}$$

This complex system can be rewritten as a product of matrixes $\hat{C} \cdot L = R$:

(3.3.20)

$$\begin{pmatrix} 1 & 0 & 0 & 0 & 0 \\ -\hat{c}\Lambda_A & (\hat{c}\Lambda_A + \hat{c}\Lambda_B + 1) & -\hat{c}\Lambda_B & 0 & 0 \\ 0 & -\hat{c}\Lambda_B & (\hat{c}\Lambda_B + \hat{c}\Lambda_C + 1) & -\hat{c}\Lambda_C & 0 \\ 0 & 0 & -\hat{c}\Lambda_C & (\hat{c}\Lambda_C + \hat{c}\Lambda_D + 1) & -\hat{c}\Lambda_D \\ 0 & 0 & 0 & 0 & 1 \end{pmatrix}_{\hat{C}} \begin{pmatrix} T_1^{t+1} \\ T_2^{t+1} \\ T_3^{t+1} \\ T_4^{t+1} \\ T_5^{t+1} \end{pmatrix}_{L} = \begin{pmatrix} T_1^{t} \\ T_2^{t} \\ T_3^{t} \\ T_4^{t} \\ T_5^{t} \end{pmatrix}_{R}$$

Where $\hat{C}$ is represents the coefficients matrix, L 'left' is the vector featuring the future temperatures, and R 'right' is the present temperatures vector.

The definition of the coefficient matrix $\hat{C}$ represents the bulk part of many scripts, since it contains the material and numerical properties of the system. The matrix $\hat{C}$ is sparse and quadratic. Sparse means that most of the elements in the matrix are equal to 0, whereas quadratic indicates that the number of rows and columns is the same. Each equation in the system is identified by a row index m, whereas the value assumed by each nodal point in the stencil is identified by the columns index n. It should be noted that, for a specific equation, only the neighbouring nodes (n_{i-1}, n_i, n_{i+1}) are $\neq 0$ and therefore considered in the temperature computation. All the remaining nodes has no influence on the local temperature calculation T_i^{t+1}.

To find the solution of the array R, the implicit formulation requires the simultaneous computation of all the equations in the system. This formulation does not have strict limitations regarding the grid spacing Δx and time stepping Δt (*Gerya, 2019*). Nevertheless, large Δx and Δt do not guarantee an accurate numerical solution, even with the implicit scheme. Therefore, the code should be benchmarked in order to find the optimal values for these two numerical variables.

3.3.3. Boundary Conditions:

In the system **(3.3.20)**, is possible to notice that the first and the last nodes in the L matrix's diagonal, feature different coefficients compared to the rest of the stencil (i.e. $\hat{C}_{1,1} = \hat{C}_{m,n} = 1$). They both represent the boundaries of the domain, since the system is not defined before and after them, and they require special mathematical treatment (i.e. boundary conditions, BC).

In this specific problem setting, the chosen boundary conditions are the so called Dirichlet BC. This type of boundary conditions, imposes a constant value for the given function at both ends of the domain. For the presented case, where the evolving function is the temperature ($\int = T$), the Dirichlet BC denote isothermal boundaries (i.e. $T_i^t = T_i^{t+1}$). In order to fulfil this constraint, the $\hat{c}$ coefficient in Fourier's Law must be equal to 1 (i.e. $T_i^t = \hat{c}T_i^{t+1}$). When the boundaries are set to be isothermal T^k, both ends of the domain act as infinite temperature sinks/source, establishing a heat flux at the limits of the system ($T_1 = T_1^k$ and $T_n = T_n^k$).

(3.3.21)

$$Q_1 = \Lambda_A \frac{T_2 - T_1^k}{\Delta x}$$

$$Q_n = \Lambda_Z \frac{T_n^k - T_{n-1}}{\Delta x}$$

Depending on the temperature gradient at the boundaries (e.g. $T_1 > T_2$ or $T_1 < T_2$) the heat flux can be positive (i.e. entering the domain) or negative (i.e. leaving the domain), see **Chapter 2.5.1**.

Dirichlet BC is not the only type of BC which can be implemented. Another possibility is represented by the Von Neumann boundary condition. This type of BC, instead of prescribing a constant value ($\mathfrak{f} = \mathrm{k}$), they imposed a constant derivative ($\partial\mathfrak{f}/\partial x = \mathrm{k}$) which represent an in-/out-flux. In finite difference this translates as:

(3.3.22)

$$\left(\frac{\partial \mathfrak{f}}{\partial x}\right)_1 \approx \frac{\Delta \mathfrak{f}_1}{\Delta x}$$

$$\left(\frac{\partial \mathfrak{f}}{\partial x}\right)_n \approx \frac{\Delta \mathfrak{f}_n}{\Delta x}$$

A complication intrinsic of the Von Neumann BC, arises from the fact that in FD, the solution of the quotient $\Delta\mathfrak{f} = \mathfrak{f}_{i+1} - \mathfrak{f}_i$ is always located halfway between the two nodes $i+1$ and i. As a consequence of this, if the differential quotient at the boundaries is computed using the first/last two nodes, the derivative will fall in the middle, and not at the limits of the domain.

(3.3.23)

$$\left(\frac{\partial \mathfrak{f}}{\partial x}\right)_{1+0.5} \approx \frac{\mathfrak{f}_2 - \mathfrak{f}_1}{\Delta x}$$

$$\left(\frac{\partial \mathfrak{f}}{\partial x}\right)_{n-0.5} \approx \frac{\mathfrak{f}_n - \mathfrak{f}_{n-1}}{\Delta x}$$

Therefore, the von Neumann BC, requires the introduction of fake auxiliary nodes located beyond the rims of the domains, namely *ghost nodes* ($\mathfrak{f}_0$ and $\mathfrak{f}_{n+1}$).

(3.3.24)

$$\left(\frac{\partial \mathfrak{f}}{\partial x}\right)_1 \approx \frac{\mathfrak{f}_2 - \mathfrak{f}_0}{2\Delta x}$$

$$\left(\frac{\partial \mathfrak{f}}{\partial x}\right)_n \approx \frac{\mathfrak{f}_{n+1} - \mathfrak{f}_{n-1}}{2\Delta x}$$

The von Neumann BC are used to prescribe an entry/exiting flux, of the given physical property, in the system (e.g. mass, momentum, energy etc…). These BC, applied to the case of Fourier's law, allow to establish a given heat flux Q^k at the edges, as a user input parameter. It follows that the value of temperature at the ghost nodes (T_0 and T_n), depends on the prescribed heat flux.

(3.3.25)

$$Q_1^k = \Lambda_A \frac{T_2 - T_0}{2\Delta x}$$

$$T_0 = T_2 - \frac{Q_1^k 2\Delta x}{\Lambda_A}$$

$$Q_n^k = \Lambda_Z \frac{T_{n+1} - T_{n-1}}{2\Delta x}$$

$$T_{n+1} = T_{n-1} + \frac{Q_n^k 2\Delta x}{\Lambda_Z}$$

Where Λ_A and Λ_Z are the thermal conductivities in the auxiliary nodes A and Z, close to the boundaries. The FD temperature evolution at the boundaries follows from the equation **(3.3.19)**.

(3.3.26)

$$T_1^t = -\hat{c}\Lambda_A T_0^{t+1} + (2\hat{c}\Lambda_A + 1)T_1^{t+1} - \hat{c}\Lambda_A T_2^{t+1}$$

$$T_n^t = -\hat{c}\Lambda_Z T_{n-1}^{t+1} + (2\hat{c}\Lambda_Z + 1)T_n^{t+1} - \hat{c}\Lambda_z T_{n+1}^{t+1}$$

The thermal conductivity Λ at the boundaries (i.e. between nodes $0 \rightarrow 2$ and nodes $n-1 \rightarrow n+1$) is assumed to be constant. By substituting the ghost nodes **(3.3.25)** in the finite different computation **(3.3.26)**, for the first node we obtain:

(3.3.27)

$$T_1^t = -\hat{c}\Lambda_A\left(T_2^{t+1} - \frac{Q_1^k 2\Delta x}{\Lambda_A}\right) + (2\hat{c}\Lambda_A + 1)T_1^{t+1} - \hat{c}\Lambda_A T_2^{t+1}$$

$$T_1^t - Q_1^k 2\hat{c}\Delta x = -\hat{c}\Lambda_A T_2^{t+1} + (2\hat{c}\Lambda_A + 1)T_1^{t+1} - \hat{c}\Lambda_A T_2^{t+1}$$

$$T_1^t - Q_1^k 2\hat{c}\Delta x = (2\hat{c}\Lambda_A + 1)T_1^{t+1} - 2\hat{c}\Lambda_A T_2^{t+1}$$

While at the last node the result is:

(3.3.28)

$$T_n^t = -\hat{c}\Lambda_Z T_{n-1}^{t+1} + (2\hat{c}\Lambda_Z + 1)T_n^{t+1} - \hat{c}\Lambda_z\left(T_{n-1}^{t+1} + \frac{Q_n^k 2\Delta x}{\Lambda_Z}\right)$$

$$T_n^t + Q_n^k 2\hat{c}\Delta x = -\hat{c}\Lambda_Z T_{n-1}^{t+1} + (2\hat{c}\Lambda_Z + 1)T_n^{t+1} - \hat{c}\Lambda_z T_{n-1}^{t+1}$$

$$T_n^t + Q_n^k 2\hat{c}\Delta x = -2\hat{c}\Lambda_Z T_{n-1}^{t+1} + (2\hat{c}\Lambda_Z + 1)T_n^{t+1}$$

The system of equations **(3.3.20)** now becomes:

(3.3.29)

$$\begin{pmatrix} (2\hat{c}\Lambda_A+1) & -2\hat{c}\Lambda_A & 0 & 0 & 0 \\ * & * & * & 0 & 0 \\ 0 & * & * & * & 0 \\ 0 & 0 & * & * & * \\ 0 & 0 & 0 & -2\hat{c}\Lambda_Z & (2\hat{c}\Lambda_Z+1) \end{pmatrix}_{\hat{C}} \begin{pmatrix} T_1^{t+1} \\ * \\ * \\ * \\ T_n^{t+1} \end{pmatrix}_L = \begin{pmatrix} T_1^t - Q_1^k 2\hat{c}\Delta x \\ * \\ * \\ * \\ T_n^t + Q_n^k 2\hat{c}\Delta x \end{pmatrix}_R$$

By controlling the heat flux Q^k, the boundaries can behave as: a source ($Q^k > 0$), a sink ($Q^k < 0$) or an insulator ($Q^k = 0$).

The combination of Dirichlet and Von Neumann type, applied to different physical properties (e.g. flow velocity $\boldsymbol{u}$ or stress σ) allows for the creation of several boundary conditions. The most commonly used in geodynamical problems are:

1) Free slip BC:
   It imposes no friction at the boundary, i.e. the fluid is free to flow without losing momentum. This condition requires that the component of the velocity vector perpendicular to the given boundary is equal to 0 (Dirichlet BC), i.e. the flux directed toward the boundary is stopped by it. It also requires that the components of the velocity vector parallel to the boundary do not change along that direction (Von Neumann BC), i.e. the fluid does not lose velocity because of the friction with the boundary (free slip). Mathematically this is formulated as:

$$w = 0 \tag{3.3.30}$$

$$\frac{\partial u}{\partial z} = \frac{\partial v}{\partial z} = 0$$

   Assuming an upper and lower boundary in the z-direction (vertical) and a velocity vector $\boldsymbol{u} = (u, v, w)$. Free slip BC are often used as a velocity conditions at the surface and at the Core-Mantle Boundary in mantle convection problems.
2) No slip BC
   It imposes zero fluid flow at the boundaries (Dirichlet BC). This means that in the proximity of the boundary the fluid is progressively slowed down until it becomes static. No slip BC mimic an adhesive limit where the flowing fluid is stuck at the boundaries. Mathematically this reads as:

$$u = v = w = 0 \tag{3.3.31}$$

3) Free surface
   This condition allows the surface of the domain to be deformed by the vertical push of the flowing fluid (i.e. vertical normal stress σ_{zz}), and consequently to produce a topography. In order to imposed this condition, the shear stresses at the surface must be equal to 0 (Dirichlet BC).

$$\tau_{ij} = 0 \tag{3.3.32}$$

   Free surface conditions are difficult to handle since they require the implementation of a deformable grid (*Duretz et al., 2011*) or the introduction of a low-density low-viscosity layer on top of the model domain (*Schmeling et al., 2008*). This BC might cause several instability in the code which must be handled with care (*Crameri et al., 2012*). However a free surface represents a more accurate representation of a planet, since mantle convection generates dynamic topography and continent collisions can form orogens. The formation of convection-induced topography is important in the formation stress-focused regions (*Thielmann et al., 2015*), and has an influence on the resulting tectonic regime (*Crameri & Tackley, 2016*).

3.3.4. Implementation of Source/Sink Terms in FD

An important component of conservation equations is the source/sink term S **(2.2.1)**. This can be easily included at some specific nodes by adding the term S to the finite difference computation **(3.3.19)**.

$$T_i^t + S_i^{t+1}\Delta t = -\hat{c}\Lambda_A T_{i-1}^{t+1} + (\hat{c}\Lambda_A + \hat{c}\Lambda_B + 1)T_i^{t+1} - \hat{c}\Lambda_B T_{i+1}^{t+1} \tag{3.3.33}$$

Where the term $S_i^{t+1}\Delta t$ produces/removes a given physical property into/from the internal node i at each timestep. In this case, the implementation of the term S follows the implicit formulation. The system of equation becomes:

$$\begin{pmatrix} * & 0 & 0 & 0 & 0 \\ * & * & * & 0 & 0 \\ 0 & * & * & * & 0 \\ 0 & 0 & * & * & * \\ 0 & 0 & 0 & 0 & * \end{pmatrix}_{\hat{C}} \begin{pmatrix} T_1^{t+1} \\ * \\ * \\ * \\ T_n^{t+1} \end{pmatrix}_{L} = \begin{pmatrix} T_1^t \\ * \\ * \\ * \\ T_n^t \end{pmatrix}_{R} + \begin{pmatrix} 0 \\ S_2^{t+1} \\ S_3^{t+1} \\ S_4^{t+1} \\ 0 \end{pmatrix}_{S} \cdot \Delta t \tag{3.3.34}$$

As reported in **Chapter 2.2** and **2.6** the introduction of the sink/source term is fundamental in mantle convection problems (e.g. radiogenic heating, latent heat, tidal heating).

3.3.5. Solvers

The algorithms that allow to compute the solution for $L = \hat{C} \cdot R$ are called '*solvers*'. There are two main types of solvers: (1) iterative and (2) direct. The iterative solver starts from an initial guess to compute a sequence of approximated solutions for the PDEs. This iterative sequence continues until the solutions converges around a certain value. Several algorithms deals with the repeated iterations (e.g. fine grid or multigrid approaches). Iterative methods are relatively fast, but they struggle to converge when large parameter variations occur in the model (e.g. sharp viscosity contrasts of several orders of magnitude). Direct solvers, on the other hand, solves all the equation of the system $L = \hat{C} \cdot R$ at once. Several mantle convection codes employ the algorithm called '*UMFPACK*' (*Davis, 2004*) for solving unsymmetric sparse linear systems of the form $Ax = b$. This algorithm has been implemented in Matlab (operator '\'), and in PETSc (*Balay et al., 2015*). The direct solvers are computationally heavy, given the large amount of equations to solve for each time step, and the execution time scales increases with the number of grid nodes. However, this drawback is compensated by the stability of the solution, and its convergence even for sharp parameter variations.

3.3.6. Benchmarking

A way to attest the reliability of the numerical solution is to benchmark it against an analytical solution. The analytical solutions are extremely useful to test the goodness of numerical discretization and the convergence of the numerical solution. However, given the complexities of most natural phenomena, analytical solutions are available only for few, very simple, problem settings. For fluid convection problems, benchmark problem analysis is substituted with solution comparison, in which the solution to a simple problem setting is compared among different codes (*Blankenbach et al., 1989*; *Tackley & King, 2003*; *Koglin et al., 2005*; *Zhong et al., 2008*; *Kronbichler et al. , 2012*; *Burstedde et al., 2013*). The goodness of the solution is quantified by analyzing a set of diagnostic non-dimensional parameters (**Chapter 2.8**) that has to remain within the error range.

3.4. Staggered Grid:

The discretization of Stokes equations in several numerical modelling codes takes advantage of the staggered grid implementation: e.g. I2ELVIS (*Gerya & Yuen, 2007*), LaMEM (*Popov et al., 2013*), StagYY (*Tackley, 2008*), StreamV (*Samuel & Evonuk, 2010*). This method can be exemplified by performing the discretization of the Mass Conservation Equation in 2D **(2.3.10)**.

$$\frac{\partial u}{\partial x} + \frac{\partial v}{\partial y} = 0 \tag{3.4.35}$$

Where u and v are the $x-$ and $y-$ components of the Stokes flow velocity vector $\boldsymbol{u}$. In a non-staggered 2D grid (see **Figure 3.7**), with indexing i (rows) and j (columns), the FD discretization of the equation **(3.4.35)** in the node (i,j) requires the use of the velocities at the four neighbouring nodes (i.e. $u_{i,j+1}$, $u_{i,j-1}$, $v_{i+1,j}$, $v_{i-1,j}$).

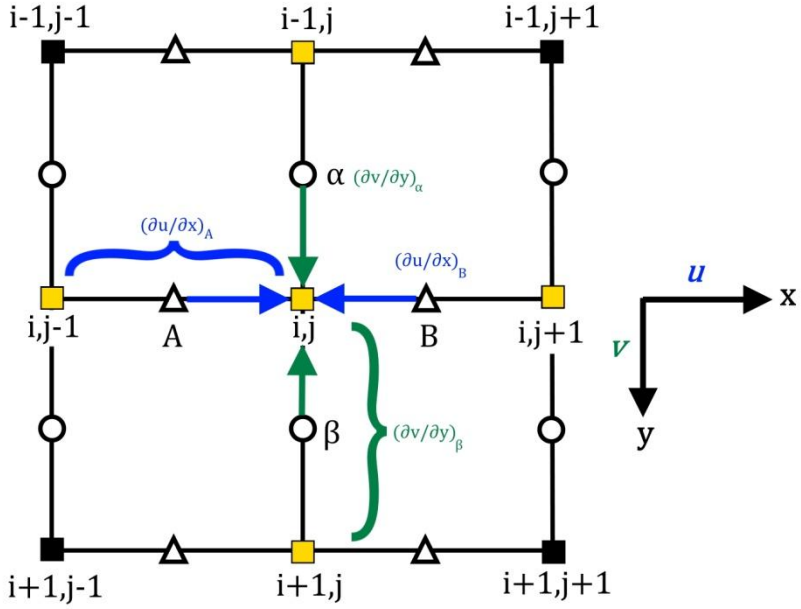

Figure 3.7. Non-staggered grid. Grid nodes are represented by squares, with i, j indexing. Yellow nodes indicate the neighbouring nodes employed to calculate Stokes velocities in the central node (i,j). Auxiliary mid-spacing nodes are represented by empty triangles ($x-$direction), and circles ($y-$direction). The nodes A,B are used to calculate u_{ij} (blue arrows), whereas the nodes α,β are used to calculate v_{ij} (green arrows).

The disadvantage of using a non-staggered grid is given by the articulated calculations of the differential quotients for u_{ij} and v_{ij}, since the quotients fall in the mid points (A,B,α,β)

$$\left(\frac{u_{i,j} - u_{i,j-1}}{\Delta x}\right) = \left(\frac{\partial u}{\partial x}\right)_A \quad \left(\frac{u_{i,j+1} - u_{i,j}}{\Delta x}\right) = \left(\frac{\partial u}{\partial x}\right)_B \tag{3.4.36}$$

$$\left(\frac{v_{i,j} - v_{i-1,j}}{\Delta y}\right) = \left(\frac{\partial v}{\partial x}\right)_\alpha \quad \left(\frac{v_{i+1,j} - v_{i,j}}{\Delta y}\right) = \left(\frac{\partial v}{\partial x}\right)_\beta$$

This requires an additional step to calculate the velocities in (i,j) from the average of the velocities in the midpoints (i.e. u_A, u_B, v_α, v_β).

$$\left(\frac{\partial u}{\partial x}\right)_{i,j} = \frac{\left(\frac{u_{i,j+1} - u_{i,j}}{\Delta x}\right)_B + \left(\frac{u_{i,j} - u_{i,j-1}}{\Delta x}\right)_A}{2} \tag{3.4.37}$$

$$\left(\frac{\partial v}{\partial x}\right)_{i,j} = \frac{\left(\frac{v_{i+1,j} - v_{i,j}}{\Delta y}\right)_\beta + \left(\frac{v_{i,j} - v_{i-1,j}}{\Delta y}\right)_\alpha}{2}$$

The staggered grid is a method design to simplify the formulation of the FD equations by implementing auxiliary grids along with the principal one (see **Figure 3.8**). Each node in the auxiliary grids is shifted, from the respective principal node, by half grid spacing (i.e. $+\Delta x/2$ and $+\Delta y/2$), hence the name *staggered*. In a given staggered grid all Stokes flow components are saved parallel to a certain direction (e.g. x,y,z in Cartesian coordinates or θ, φ, r in spherical coordinates).

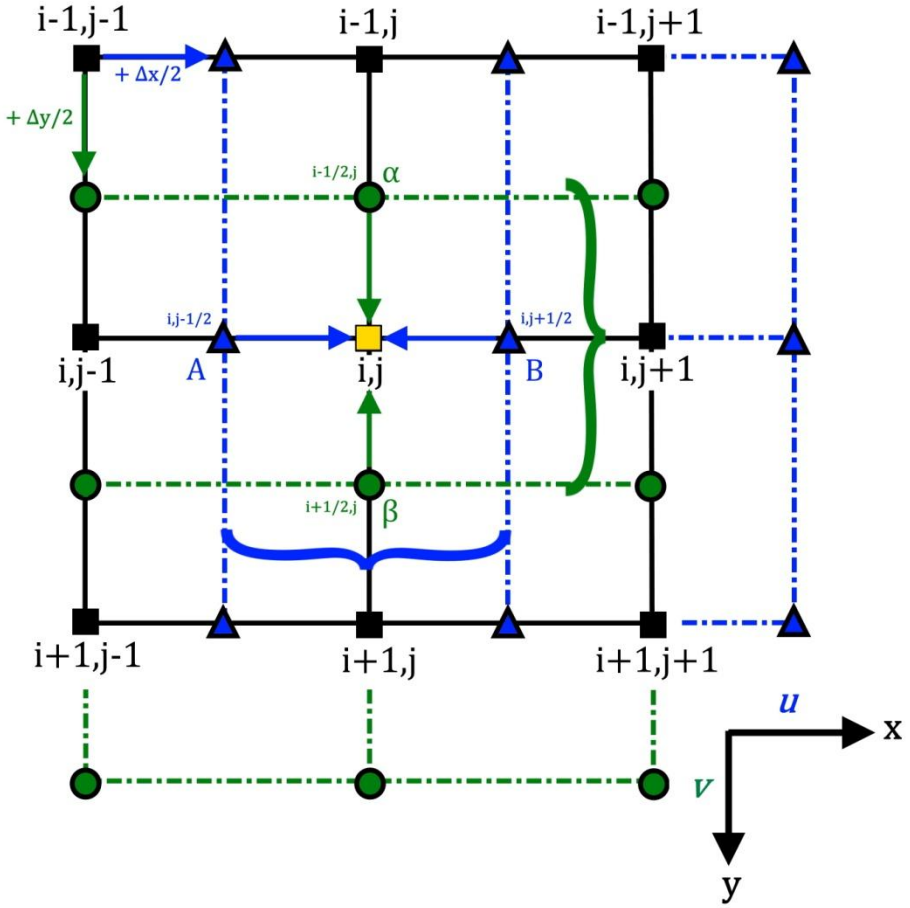

Figure 3.8. Staggered grid. Principal grid nodes are represented by black squares, with i, j indexing and Δx, Δy spacing. Auxiliary x–shifted grid is represented by blue triangles ($+\Delta x/2$), whereas auxiliary y–shifted grid is represented by green circles ($+\Delta y/2$) . The nodes A,B are used to calculate u_{ij} (blue arrows), whereas the nodes α,β are used to calculate v_{ij} (green arrows).

By employing the staggered grids, the auxiliary grid nodes naturally fall in the middle of the stencils. This reduces the calculation of the Stokes velocities on the node (i, j) to a single step, which are simply given by the differential quotients of the velocities in the auxiliary nodes (i.e. u_A, u_B, v_α, v_β).

$$\left(\frac{\partial u}{\partial x}\right)_{i,j} = \frac{u_B - u_A}{\Delta x} = \frac{u_{i,j+1/2} - u_{i,j-1/2}}{\Delta x} \tag{3.4.38}$$

$$\left(\frac{\partial v}{\partial x}\right)_{i,j} = \frac{v_\beta - v_\alpha}{\Delta y} = \frac{v_{i+1/2,j} - v_{i-1/2,j}}{\Delta y}$$

Staggered grids are particularly useful when thermo-mechanical problems involve sharp viscosity variations, which is relevant in Earth and planetary sciences. The advantages arising from staggered grid implementation outclass the inconveniences represented by the additional programming effort, and the resulting geometrical complexities (*Gerya, 2019*). Moreover, the staggered grid approach provides a more accurate numerical solution for the Stokes equations (*Fornberg, 1996*).

3.5. Material Advection in Finite Differences

Advection is the transport of material properties through the bulk motion of the material itself, e.g. a rising mantle plume transports simultaneously heat and mass. When advection is driven by temperature disequilibrium between the two domain boundaries, it takes the name of convection.

3.5.1. Numerical Diffusion

In numerical modelling, handling the advection of fluids is not straightforward, and imprecision result from the merely application of the Finite Differences to the Stokes equations. An example is the discretization of the 1D Mass Conservation equation **(2.3.10)**.

$$\frac{\partial \rho}{\partial t} = -\frac{\partial (\rho u)}{\partial x} \tag{3.5.39}$$

With the FD method, it is possible to express the derivatives of the mass flux (ρu) on the node i with different quotients:

$$central\ difference: \frac{\rho_i^{t+1} - \rho_i^t}{\Delta t} = -\frac{(\rho u)_{i+1}^{t+1} - (\rho u)_{i-1}^{t+1}}{2\Delta x} \tag{3.5.40}$$

$$downwind\ difference: \frac{\rho_i^{t+1} - \rho_i^t}{\Delta t} = -\frac{(\rho u)_{i+1}^{t+1} - (\rho u)_i^{t+1}}{\Delta x}$$

$$upwind\ difference: \frac{\rho_i^{t+1} - \rho_i^t}{\Delta t} = -\frac{(\rho u)_i^{t+1} - (\rho u)_{i-1}^{t+1}}{\Delta x}$$

The best approach for advecting material is the upwind difference, since it computes the mass flux by considering the influx coming from the previous node $(\rho u)_{i-1}$ (*Gerya, 2019*). The other two approaches (central and downwind) tend to have unreliable numerical solutions (*Gerya, 2019*). However, even the upwind difference displays instabilities when used for computing an advecting fluid. In particular, the FD solution of the Stokes equation on the nodes, is unable to advect properly an object with sharp property contrast (e.g. high-ρ slab). Over time, the original sharp gradient

diffuses as an intrinsic consequence of the numerical implementation in the nodes (*Gerya, 2019*). The numerical diffusion term arises from the numerical discretization of Stokes equation. In the case of central discretization, the advection equation reads:

$$\frac{\rho_i^{t+1} - \rho_i^t}{\Delta t} = -\left[\frac{(\rho u)_{i+1}^{t+1} - (\rho u)_{i-1}^{t+1}}{2\Delta x}\right] + \frac{\Delta x}{2}\left[\frac{(\rho u)_{i-1}^{t+1} - 2(\rho u)_i^{t+1} + (\rho u)_{i+1}^{t+1}}{\Delta x^2}\right] \quad (3.5.41)$$

$$\left(\frac{\partial \rho}{\partial t}\right)_i = -\left(\frac{\partial \rho}{\partial x}\right)_i + \frac{\Delta x}{2}\left(\frac{\partial^2 \rho}{\partial x^2}\right)_i$$

Where the first term in the right-hand side is the central difference **(3.5.40)** and the second term represents the second derivative of the mass flux (i.e. the numerical diffusion term). The numerical diffusion is an unwanted consequence of the Finite Difference discretization, and it alters the final solution of the Stokes equations. Some codes apply an anti-diffusion correction to compensate for this problem (e.g. StagYY *Tackley, 2008*). However, even by employing this tool, the numerical solution shows large discrepancies from the analytical solution (*Gerya, 2019*).

3.5.2. Markers-in-Cell Technique

A reliable way to overcome this issue is to employ the so called '*markers-in-cell*' technique (*Harlow & Welch, 1965*). This method take advantage of the implementation of mobile Lagrangian markers (*tracers*/*particles*) to support the static Eulerian nodes framework (*Gerya, 2019*). The FD solution of the Stokes equations is calculated on the Eulerian nodes, whereas the material advection occurs through the motion of Lagrangian markers. The markers-in-cell techniques is computationally heavy to implement since it requires:

a. An interpolation mechanism to transfer information from the nodes to the markers
b. An advection routine to move the markers accordingly to the FD solution on the nodes

a. Interpolation Routine

The physical properties advected by the Lagrangian markers are calculated on the Eulerian nodes. In the following example of a 1D stencil, several markers are present in the space between two nodes Δx (**Figure 3.9**).

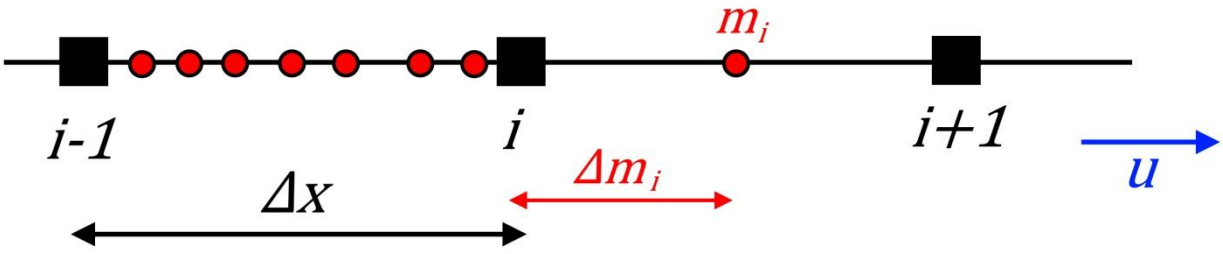

Figure 3.9. Lagrangian markers (red dots) in a 1D Eulerian node stencil (black squares). The markers are advected along the Stokes flow velocity u (blue arrow).

Each marker is positioned at a certain distance Δm_i from the node i. When the materials advect there is a continuous exchange of information between the nodes and the markers. Essentially, this dialog occurs in three steps:

1) The markers surrounding a given node i communicate their physical status to that node. *Example: the marker m has a certain density ρ and temperature T.*
2) The node i uses this information to compute the Navier-Stokes equations employing the Finite difference method. *Example: the solution of the Navier-Stokes predicts a temperature increase and consequent density reduction.*
3) The node transfers the information back to the markers which will move accordingly. *Example: the marker with the updated physical status will be advected upwards as a consequence of its newly enhanced buoyancy (i.e. new ρ, T conditions)*

In order to achieve a synergic work relationship between markers and nodes, it is fundamental to establish: (a) a hierarchy of the information reaching a given node i, and (b) a region of influence of the solution calculated in i. If all markers in the domain would start to communicate their physical status to the nodes, this would slow down the calculation considerably. On the other hand, if the local solution calculated on a given node are valid for all the markers in the domain, the whole calculation would be pointless.

These problems are easily overcome by the introduction of a numerical weight $\mathcal{W}_i$. This parameter assigns a 'weight' to the information contained on the marker m_i, as a function of the marker-node distance Δm_i and the grid spacing Δx.

$$\mathcal{W}_i = 1 - \left(\frac{\Delta m_i}{\Delta x}\right) \tag{3.5.42}$$

From equation **(3.5.42)** it becomes clear that the maximum range of influence of the given node i is the grid spacing Δx. The weight of the information contained on a marker is maximum ($\mathcal{W}_i = 1$), when the marker is located exactly on the node i ($\Delta m_i = 0$), whereas is null ($\mathcal{W}_i = 0$) when the marker location is on one of the neighbouring nodes, i.e. $i-1$ or $i+1$ ($\Delta m_i = \Delta x$). All the information coming beyond that threshold are not considered in the solution of the Navier-Stokes equations for the given node i.

Same reasoning can be applied for the influence that the solution f^{new} has on markers surrounding the node i. In a 1D stencil, the given marker m would be influenced by the solutions that come from the enclosing nodes i and $i+1$ (i.e. interpolation)

$$f_m^{new} = \frac{(f_i^{new}\mathcal{W}_i) + (f_{i+1}^{new}\mathcal{W}_{i+1})}{\mathcal{W}_i + \mathcal{W}_{i+1}} \tag{3.5.43}$$

Several interpolation functions are available to be used in the marker-in-cell technique. One of the most commonly used is the '*linear interpolation*' **(3.5.43)**, i.e. the weight of the information linearly decreases with distance. In this case, the solution in the marker m is the given by the weighted arithmetic mean of the solutions coming from all the surrounding nodes.

$$f_m^{new} = \frac{\sum f_i^{new}\mathcal{W}_i}{\sum \mathcal{W}_i} \tag{3.5.44}$$

In 2D/3D the grid mash forms cells that contains a certain amount of markers, hence the name markers-in-cell. The weight of the solution f^{new} on each marker m within the cell Δx, Δy, Δz, is given by:

$$\mathcal{W}_{ijk} = \left(1 - \frac{\Delta m^x_{ijk}}{\Delta x}\right)\left(1 - \frac{\Delta m^y_{ijk}}{\Delta y}\right)\left(1 - \frac{\Delta m^z_{ijk}}{\Delta z}\right) \tag{3.5.45}$$

$$f^{new}_m = \frac{\sum f^{new}_{ijk}\mathcal{W}_{ijk}}{\sum \mathcal{W}_{ijk}}$$

Interpolation can be performed with other approaches, e.g. harmonic or geometric (*Schmeling et al., 2008*).

b. Marker Advection

Once the information is correctly interpolated from the nodes, a routine has to deal with the material advection of the markers. The new position of the marker can be simply calculated as the trajectory of an object moving with a velocity $\boldsymbol{u}$ (derived from the Navier-Stokes equations). This approach is known as Eulerian scheme, and in 3D this reads:

$$m^{t+1}_{x,y,z} = m^t_{x,y,z} + \Delta t \boldsymbol{u}^t \tag{3.5.46}$$

This formulation, however, is too simplistic and, unless Δt is very small, the numerical calculation diverges rapidly from analytical solutions (*Gerya, 2019*).

One solution to this problem is offered by the Runge-Kutta approach, which employs intermediate 'stations' in between the initial $(x, y, z)^t$ and final $(x, y, z)^{t+1}$ marker position. 1) Instead of moving the markers for the full length of the timestep Δt, the markers are stopped after they travelled half of the timestep, i.e. $1/2\Delta t$.

$$m^{t+1/2}_{x,y,z} = m^t_{x,y,z} + \frac{\Delta t}{2}\boldsymbol{u}^t \tag{3.5.47}$$

2) In the intermediate position reached by the markers $(x, y, z)^{t+1/2}$, the velocity field $\boldsymbol{u}^t$ is re-calculated considering the physical properties of the markers in that point (i.e. $\boldsymbol{u}^{t+1/2}$). 3) Markers are re-located to their initial position $(x, y, z)^t$ and the new velocity field $\boldsymbol{u}^{t+1/2}$ is used to move the marker to their final position $(x, y, z)^{t+1}$.

$$m^{t+1}_{x,y,z} = m^t_{x,y,z} + \Delta t \boldsymbol{u}^{t+1/2} \tag{3.5.48}$$

The velocity field calculate in the intermediate station is an 'explorative' velocity which is used to check the variation of a function within the discrete positions $(x, y, z)^t \rightarrow (x, y, z)^{t+1}$. In the Eulerian formulation, the motion of the markers does not detect any small variation between the two positions, thus the solution progressively diverges from the analytical benchmark. With the Runge-Kutta approach, however, small variations of the parameter fields are detected and incorporated into the FD solution of the Navier-Stokes equations. The higher is the number of intermediate 'stations' the better would be the final approximation. The procedure described above is called 2^{nd}-order Runge-Kutta because the velocity field is calculated 2 times ($\boldsymbol{u}^t$ and $\boldsymbol{u}^{t+1/2}$).

These days, many geodynamical codes employ the 4^{th}-order Runge-Kutta routine to minimize the discrepancies of the FD solution from the analytical benchmark (**Figure 3.10**). This formulation can be exemplified by considering four points: the starting position A $(x, y, z)^t_A$, two intermediate positions B and C $(x, y, z)^{t+1/2}_{B/C}$, and a furthermost position D $(x, y, z)^{t+1}_D$.

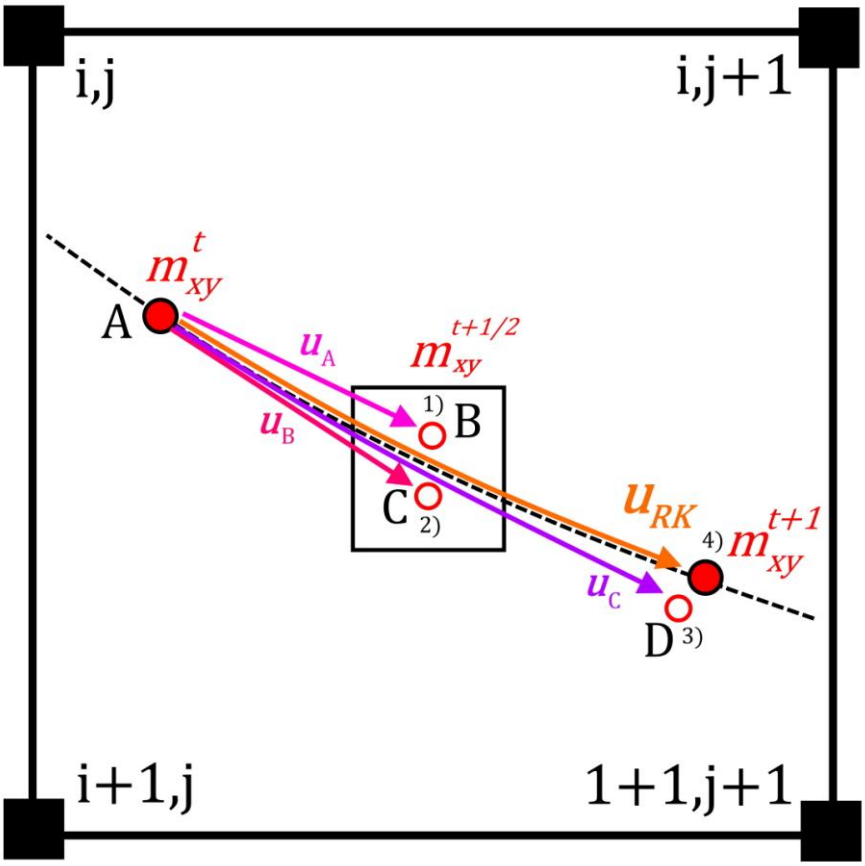

Figure 3.10. Example of the 4^{th}–order Runge-Kutta advection scheme for the Lagrangian marker m (red circles) in a 2D Eulerian cell. The black squares represent the bounding nodes. At the instant t, marker m is located in the position A $[x^t, y^t]$ (solid red circle). The marker m should follow the trajectory computed by the FD solution for the Stokes equations (dashed black line), and reach the point $[x^{t+1}, y^{t+1}]$ at the instant $t + 1$ (solid red circle).
With the 4^{th}–order Runge-Kutta advection scheme the motion occurs in four steps: (1) m moves from A, with the explorative velocity u_A (pink arrow) toward the intermediate point B (open red circle); (2) m moves from A, with the explorative velocity u_B (red arrow) toward the intermediate point C (open red circle); (3) m moves from A, with the explorative velocity u_C (purple arrow) toward the furthermost point D (open red circle), (4) m moves from A, with the cumulative velocity u_{RK} (orange arrow) toward the final position $[x^{t+1}, y^{t+1}]$ (solid red circle). The cumulative velocity u_{RK} is computed as the contribution of all velocities u_A, u_B, u_C , u_D see **(3.5.52)**.

1) As for the 2^{nd}-order Runge-Kutta, the marker leaving point A stops at the intermediate position B after it travelled half of the timestep $1/2\Delta t$. The velocity of the marker in point A is denoted by the subscript $\boldsymbol{u}_A^t$.

$$m_B^{t+1/2} = m_A^t + \frac{\Delta t}{2}\boldsymbol{u}_A^t \tag{3.5.49}$$

2) The velocity field is re-calculated at the position B $\boldsymbol{u}_B^{t+1/2}$, and is used to move the markers from the initial position A to another intermediate position C.

$$m_C^{t+1/2} = m_A^t + \frac{\Delta t}{2}\boldsymbol{u}_B^{t+1/2} \tag{3.5.50}$$

3) Again, same procedure as before: the velocity field is re-calculated in C $\boldsymbol{u}_c^{t+1/2}$, and used to move the markers from A to the furthermost position D, this time moving the whole timestep Δt.

$$m_D^{t+1} = m_A^t + \Delta t\boldsymbol{u}_C^{t+1/2} \tag{3.5.51}$$

4) At point D, the velocity field is re-calculated a 4^{th} time (hence, 4^{th}–order) $\boldsymbol{u}_D^{t+1}$. At the end of these passage, four 'explorative' velocities have been calculated: $\boldsymbol{u}_A^t$, $\boldsymbol{u}_B^{t+1/2}$, $\boldsymbol{u}_c^{t+1/2}$and $\boldsymbol{u}_D^{t+1}$.

5) The final velocity used to calculate the final position of the markers from $m_{xy}^t \rightarrow m_{xy}^{t+1}$ is the average between the four contributions.

$$\boldsymbol{u}_{RK} = \frac{1}{6}\left(\boldsymbol{u}_A^t + 2\boldsymbol{u}_B^{t+1/2} + 2\boldsymbol{u}_c^{t+1/2} + \boldsymbol{u}_D^{t+1}\right) \tag{3.5.52}$$

$$m_{xy}^{t+1} = m_{xy}^t + \Delta t\boldsymbol{u}_{RK}$$

The 4^{th}–order Runge-Kutta advection routine is a reliable method to mobilize the markers and it provides a robust solution of the FD Navier-Stokes equations (*Gerya, 2019*). Once the two routines (interpolation and Runge-Kutta) are implemented, the geodynamical code can make full use of the markers to model material advection without numerical diffusion. Markers are extremely useful to track the spatial variations of physical parameters (density, temperature) and the composition (e.g. heat production elements, mineral phases, and chemical composition) of mantle rocks (*Tackley & King, 2003*).

3.6. StagYY

The main geodynamical code employed for this thesis work is StagYY (*Tackley, 2008*) in a 2D spherical annulus geometry (*Hernlund & Tackley, 2008*). This section describes the general structure of this code along with its main features in detail. All simulations reported in **Chapter 6** and **Chapter 7** were run on parallelized computer clusters: btrzx2 (2016) and btrzx1 (2020) clusters at University of Bayreuth, and the Euler cluster at ETH Zürich.

3.6.1. Numerical Methods

StagYY (*Tackley, 2008*) is a Fortran95 code designed to study geodynamical problems by solving the Stokes equations. The code employs the finite difference (FD) / finite volume (FV) technique to approximate the solution of partial differential equations (PDE). Spatial discretization benefits from a staggered grid setting, hence the name 'Stag', in which the Stokes velocities (u, v, w) are defined at the centre of the face perpendicular to the flow component, whereas pressure P, and scalar parameters (e.g. temperature T, viscosity η etc.) are defined at the centre of the cell. The main advantage of the staggered grid implementation is that the calculation of viscosity derivatives is naturally incorporated in the 2^{nd}–order derivatives of the stress σ components.

Moreover, StagYY makes use of the marker-in-cell technique (*Harlow & Welch, 1965*) to advect the mantle material (*Gerya, 2019*). The main usage of the markers in StagYY is to trace different compositions (i.e. lithologies) and the melt/volatile phases, therefore they are always referred to as '*tracers*'. The temperature field in the Eulerian nodes is advected through the finite-volume MPDATA advection scheme (*Smolarkiewicz, 1984*) with a correction routine to compensate for the numerical diffusion of the upwind donor (*Tackley, 2008*). Lagrangian tracers, on the other hand, are moved following an 2^{nd} to 4^{th}-order (in space) Runge-Kutta scheme (*Gerya, 2019*).

StagYY is a portable software, therefore it can be used in different environments: from a single-processor desktop computer to a parallelized computer cluster. In the latter case, the Message-Passing Interface (MPI) (*Walker, 1994*) is required to establish functional communication between the different computing nodes. Parallel computation of PDE and matrices is supported by the PETSc software library (Portable, Extensible Toolkit for Scientific Computation, *Balay et al., 2015*), which also handles the direct solver available in StagYY (UMFPACK, *Davis, 2004*)

StagYY is the evolution of its predecessor, Stag3D (*Tackley, 1993*), from which it inherits previous geometries (3D/2D Cartesian boxes). The new key feature of StagYY is the implementation of the Yin-Yang grid (*Kageyama & Sato, 2004*), to study 3D spherical mantle convection problems (*Tackley, 2008*). Additional options include the 3D-spherical patch (*Tackley, 2008*) and the 2D spherical annulus (*Hernlund & Tackley, 2008*). The latter geometry in particular, the 2D spherical annulus (see **Chapter 2.9.2**), is widely used by the numerical modelling community, given the fact that it represents the best 2D approximation of the 3D sphere, providing an optimal compromise between light computational models and accurate numerical solution (*Hernlund & Tackley, 2008*). In the $2D$ spherical annulus geometry the conservation equations are computed along two spherical coordinates: the radial distance from the centre r, and the azimuthal angle φ (**Chapter 2.9.2**). The grid resolution is handled by controlling the number of cells in the azimuthal direction R_{azi}, and the number of cells in the radial direction R_{rad}.

3.6.2. Discretization of the Governing Equations

In StagYY, the governing equations are non-dimensionalised using the thermal diffusion scale ($t_\kappa = D^2/\kappa$), and by assuming an infinite Prandtl number approximation, see **Chapter 2.8.5** (*Tackley, 2008*). In Mass conservation equation **(2.3.10)** in StagYY is implemented as:

$$\nabla \cdot (\rho \underline{\boldsymbol{u}}) = 0 \tag{3.6.53}$$

Where ρ is the density and $\underline{\boldsymbol{u}}$ is the velocity vector. Momentum conservation equation **(2.4.42)** reads:

$$\underline{\nabla} \cdot \underline{\underline{\sigma}} - \nabla P_{dyn} = \frac{Ra \cdot \underline{\hat{r}} \cdot \rho(C,r,T)}{\Delta\rho_{thermal}} \tag{3.6.54}$$

Where $\underline{\underline{\sigma}}$ is the deviatoric stress tensor, P_{dyn} is the dynamic pressure (*Tackley, 2008*), Ra is the Rayleigh number **(2.8.94)**, $\underline{\hat{r}}$ is the radius, and $\rho(C,r,T)$ is the density as a function of composition C, radius r, and temperature T. The parameter $\Delta\rho_{thermal}$ represents the temperature-induced density variations ($\alpha_{dimensional}\Delta T_{dimensional}$). The viscosity at the centre of the cell η_{cell} is calculated from the temperature field, while the shear viscosity η_{shear} is calculated from η_{cell} by geometric averaging to the edges of the cell. In StagYY, the geometric interpolation is preferred because it offers a better convergence of the numerical solution (*Schmeling et al., 2008*; *Tackley, 2008*). The geometric interpolation of viscosity reads:

$$\eta_{shear} = \left(\eta_{i,j}\eta_{i+1,j}\eta_{i,j+1}\eta_{i+1,j+1}\right)^{0.25} \tag{3.6.55}$$

Where $\eta_{i,j}$ is the viscosity at the given bounding node $[i,j]$, and the weight of the information is $\mathcal{W}_{i,j} = 0.25$. The energy conservation equation **(2.5.75)** reads:

$$\rho Cp \frac{DT}{Dt} = -Di_s \alpha \rho T w + \underline{\nabla} \cdot (\Lambda \nabla T) + \rho H + \frac{Di_s}{Ra} \underline{\underline{\sigma}} : \underline{\underline{\dot{\varepsilon}}} \tag{3.6.56}$$

$$\rho Cp \frac{DT}{Dt} = -T_\alpha + \phi_\Lambda + H_R + \phi_\eta$$

Where Cp is the specific heat capacity, Di_s the surface dissipation number **(2.8.99)**, α the thermal expansivity, w radial velocity, Λ thermal conductivity, H the internal heating rate, $\underline{\underline{\dot{\varepsilon}}}$ is the strain rate tensor. The different terms of the energy conservation equation (i.e. adiabatic heating T_α, heat diffusion ϕ_Λ, and viscous dissipation ϕ_η) are advanced in time using the FD method with an explicit discretization scheme described in section **3.3.1** (*Tackley, 2008*). The governing equations **(3.6.53)**, **(3.6.54)**, **(3.6.56)** are expressed and implemented in the general form, in order facilitate the use of constitutive laws for the various physical properties. Moreover, in StagYY, governing equations are expressed in polar coordinates as reported in **Chapter 2.9** (*Schubert et al., 2001*; *Hernlund & Tackley, 2008*).

In this thesis, the dimensional formulation of StagYY governing equation is employed. This formulation is simply obtained by substituting $\underline{\hat{r}} \cdot \rho(C,r,T) \cdot g$ in the right hand term of equation **(3.6.54)**, and by removing Di_s/Ra from equation **(3.6.56)**. The parameter $g\ [m\ s^{-2}]$ is gravity acceleration.

3.6.3. Boundary Conditions

The top and bottom boundary conditions available in StagYY include: (1) isothermal boundaries, (2) boundary cooling mode, (3) free slip or rigid boundaries and (4) free surface. The configuration of the side boundaries includes: periodic, reflecting, permeable, or interpolation from one block to the other when yin-yang geometry is used.

3.6.4. Time Stepping

StagYY take advantage of the adaptive time stepping Δt_a feature.

$$\Delta t_{adv} = \alpha_{adv} * \min\left(\Delta d_{\varphi,r}/\boldsymbol{u}\right) \tag{3.6.57}$$

$$\Delta t_{diff} = \alpha_{diff} * \min\left(\Delta {d_{\varphi,r}}^2/\kappa\right)$$

$$\Delta t_a = \min\left[\Delta t_{adv}, \Delta t_{diff}\right]$$

Where Δt_{adv} and Δt_{diff} are the advective and the diffusive time stepping respectively, α_{adv} and α_{diff} are the advective and diffusive courant time steps (in this thesis $\alpha_{adv} = 0.6$ and $\alpha_{diff} = 1 \times 10^{10}$), $\Delta d_{\varphi,r}$ [m] is the grid spacing, $\boldsymbol{u}\,[m\,s^{-1}]$ is the advective velocity and κ the thermal diffusivity $[m^2\,s^{-1}]$. The time stepping is automatically reduced whenever $\boldsymbol{u}$ or κ are high enough to transfer mass or heat over more than one grid spacing within the time step Δt (i.e. Courant factor *El-Kadi & Ling, 1993*). This feature is necessary to avoid instabilities of the numerical solution at the variations of $\boldsymbol{u}$ and κ (*Gerya, 2019*).

3.6.5. Constitutive Laws for Depth-Dependent Parameters

In StagYY, the radial profile of thermodynamic parameters can be computed in three different ways:

1) Boussinesq approximation (*Boussinesq, 1903*), i.e. incompressible mantle. In this approximation, density ρ_0, expansivity α_0, thermal conductivity Λ_0 and specific heat capacity Cp_0 are constant. Temperature-induced density variations $\Delta\rho_{thermal}$ are included in the buoyancy term of the momentum equation **(3.6.54)**. The implementation of Boussinesq approximation favours the onset of a symmetric convection pattern (*Tackley, 1996*). In the Boussinesq approximation viscous dissipation and adiabatic heating are ignored.

2) Extended Boussinesq approximation. In this approximation, density ρ_0 is constant (except for $\Delta\rho_{thermal}$), whereas expansivity α_r, thermal conductivity Λ_r and specific heat capacity Cp_r are depth-dependent. In the extended Boussinesq approximation viscous dissipation and adiabatic heating are included.

3) Compressible mantle (classic anelastic approximation). In this approximation, density ρ_r, expansivity α_r, thermal conductivity Λ_r and specific heat capacity Cp_r are depth-dependent. The implementation of mantle compressibility favours the upwelling of broad hot plumes, and the downwelling of narrow sheet-like cold features (*Tackley, 1996*). Thermodynamic models can be used to calculate the pressure- or depth-dependency of the different parameters.

The depth-dependent density ρ_r can be calculated by using the pressure-dependent bulk modulus K_r **(2.5.52)** obtained from 3^{rd}–order Birch-Murnaghan Equation of State **(2.7.89)**. In this

formulation, the zero-pressure bulk modulus K_0 and its pressure derivative $K'$are treated as input parameters and may vary between different mineral phases. The specific heat capacity is normally assumed to be constant ($Cp_r = Cp_0$), since it might be the case for Earth's mantle, as discussed in **Chapter 4**. The thermal expansivity α_r is calculated from the density ρ_r, and the bulk modulus K_r

$$\alpha_r = \frac{\rho_r Cp_r \gamma_r}{K_r} \tag{3.6.58}$$

Where γ_r is the depth-dependent Grüneisen parameter (*Brugger & Fritz, 1967*).

$$\gamma_r = \gamma_0 \left(\frac{\rho_0}{\rho_r}\right)^q \tag{3.6.59}$$

The zero-pressure gamma γ_0 is normally taken from the literature dataset for the given mineral phase (*Stixrude & Lithgow-Bertelloni, 2005*). The exponent q is normally assumed to be equal to 1, i.e. the product $\alpha_r \cdot K_r$ is constant. The thermal conductivity Λ_r is assumed to vary with the k power of density, given the increase consistent with theory and experimental data (*Anderson, 1987*; *Osako & Ito, 1991*).

$$\Lambda_r = \Lambda_0 \left(\frac{\rho_0}{\rho_r}\right)^k \tag{3.6.60}$$

Where zero-pressure conductivity Λ_0 and the exponent k depends on the mineral phase (*Chang et al., 2017*; *Marzotto et al., 2020*). Finally, the thermal diffusivity κ_r is calculated from previous parameters ($\kappa_r = \Lambda_r / \rho_r Cp_r$).

3.6.6. Chemical Composition

In StagYY, density ρ, thermal expansivity α, thermal conductivity Λ and viscosity η are also dependent on the chemical composition. The bulk chemical composition of the mantle is handled by systems of functions (i.e. phase systems X_i), each one containing a set of equations representing the physical properties of the system. The phase systems X_i represent a given set of phases with a shared bulk chemical composition: e.g. olivine system, pyroxene-garnet system, sialic crust, metal alloys etc. The composite mantle assemblage is computed as the chemical fraction of each system, e.g. pyrolitic mantle is composed by 60% of olivine system X_{ol}, and 40% of the pyroxene-garnet X_{pxgt}. The chemical fractionation of the mantle can change over time when the melting routine is switched on, e.g. fractionation of harzburgite ($X_{harz} = 75\%\ ol + 25\%\ pxgt$) from the basaltic crust ($X_{basalt} = 100\%\ pxgt$) as in *Ballmer et al., (2015)*.

3.6.7. Mineral Phases and Phase Transitions

Each chemical system is characterized by several mineral phases Γ, e.g. for the olivine system olivine → spinel → Mg-perovskite (bridgmanite) + ferropericlase → post-perovskite. The phase boundaries can be implemented following two different approaches (*Faccenda & Dal Zilio, 2017*): 1) parameterized phase boundaries and 2) internally-consistent thermodynamic dataset. For the latter, StagYY employs the PerpleX package (*Connolly, 2005*) to calculate the equilibrium phase assemblages, at the given P-T-X conditions, and their physical properties (*Nakagawa et al., 2009, 2010*).

In this thesis however, the preferred approach was the parameterized phase boundaries (*Tackley, 1996*; *Xie & Tackley, 2004*; *Nakagawa & Tackley, 2005*). With this implementation, it is possible to prescribe in the model: the number of phase boundaries n_X, the reference temperature T_X^Γ, depth D_X^Γ of the phase transition and its Clapeyron slope Υ_X^Γ, density jump $\Delta\rho_X^\Gamma$, and viscosity ratio η/η_X^Γ. Additional input parameters allow for the control the width of the phase transition and the type of transition: fixed boundary (*Tackley, 1993*), smooth phase change, T-induced boundary deflection, or coupled smooth-deflection (*Christensen & Yuen, 1985*; *Solheim & Peltier, 1994*). In the parameterized approach, each mineral phase is identified by a number corresponding to its prescribed stability region, starting from the CMB toward the surface: $\Gamma = 1$ post-perovskite region (PPV), $\Gamma = 2$ lower mantle (LM), $\Gamma = 3$ mantle transition zone (MTZ), $\Gamma = 4$ upper mantle (UM), $\Gamma = 5$ lithosphere (LT).

The latent heat L_H of the phase transition is calculated using the input parameters from equation **(2.6.82)**. The effect of latent heat on the adiabatic temperature profile T_S is calculated by using the effective heat capacity $\acute{C}p$ and thermal expansivity $\acute{\alpha}$ approach (*Schubert et al., 1975*; *Christensen & Yuen, 1985*) as described in **Chapter 2.6.3**.

Phase-dependent activation energy E_X^Γ and activation volume V_X^Γ can be activated with a code switch. These two parameters are taken from a 3-dimensional array where the indices stand for: (i) the deformation mechanism $\varkappa$ (diffusion or dislocation creep), (ii) the given mineral phase Γ, (iii) the phase system X.

3.6.8. Reference State

At the beginning of each simulation, StagYY builds the radial mantle profile for each thermodynamic parameter described in section **3.6.5** (i.e. adiabatic temperature temperature T_S, density ρ, thermal expansivity α, specific heat capacity Cp, thermal conductivity Λ, pressure P). This initial model setting is called reference state (see **Figure 3.11**), and is built for each phase system X, and each mineral phase Γ. The equations defining the physical properties of a given mineral phase (e.g. ρ_X^Γ) can be handled separately without changing the main code (*Tackley, 2008*). The physical properties of each mineral phase Γ are computed for the entire domain depth (CMB → surface). The cumulative radial profile for a given phase system X is computed by considering the stability range of each mineral phase, e.g. $\rho_{ol} = [\rho_{ol}^{PPV}; \rho_{ol}^{LM}; \rho_{ol}^{MTZ}; \rho_{ol}^{UM}]$. Finally, the composite mantle radial profile is given by the fractional contribution of each chemical system X.

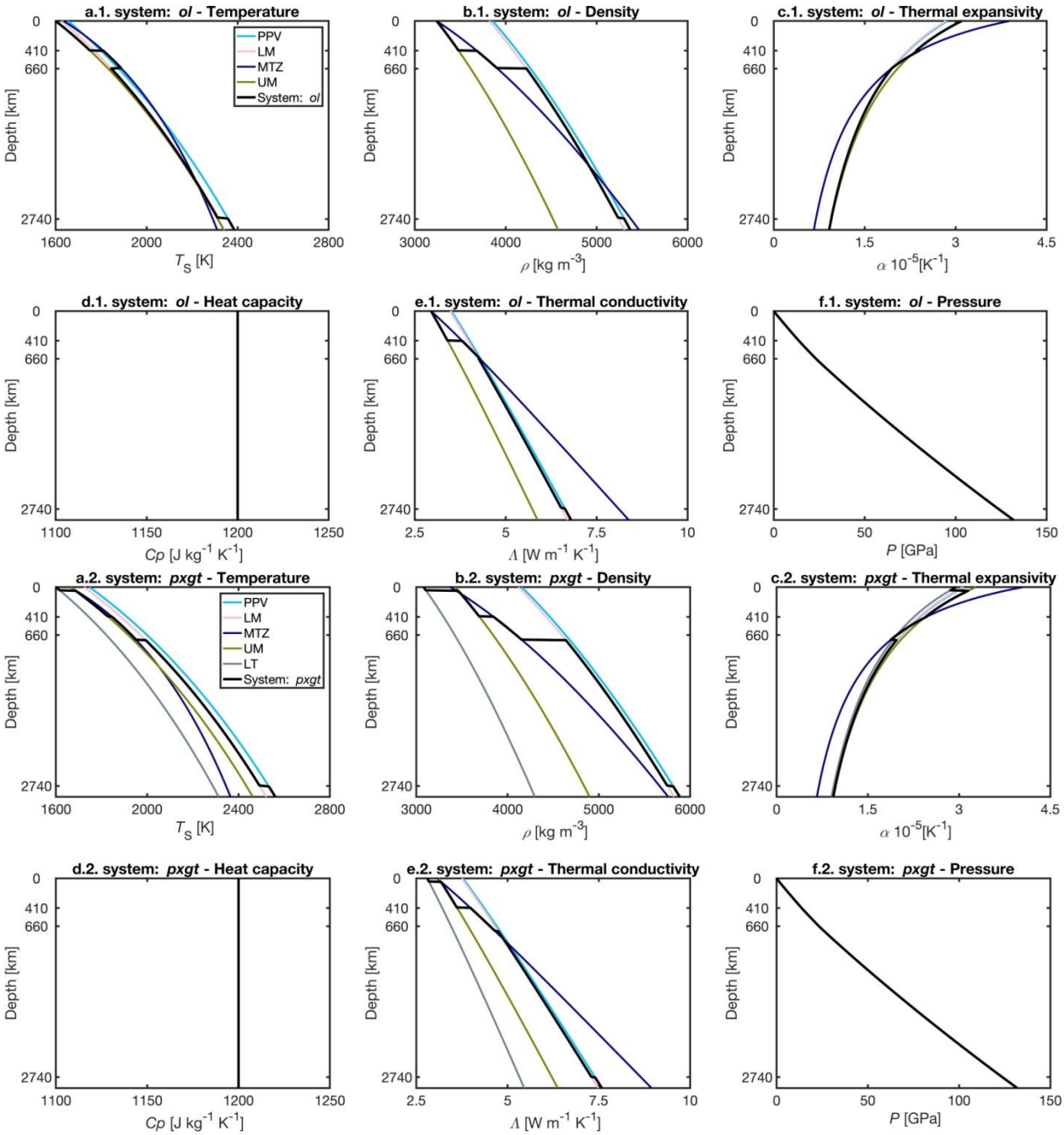
a.1. system: ol - Temperature
PPV
LM
MTZ
UM
System: ol
Depth [km]
T_S [K]
b.1. system: ol - Density
ρ [kg m^{-3}]
c.1. system: ol - Thermal expansivity
α 10^{-5}[K^{-1}]
d.1. system: ol - Heat capacity
Cp [J kg^{-1} K^{-1}]
e.1. system: ol - Thermal conductivity
Λ [W m^{-1} K^{-1}]
f.1. system: ol - Pressure
P [GPa]
a.2. system: pxgt - Temperature
PPV
LM
MTZ
UM
LT
System: pxgt
b.2. system: pxgt - Density
c.2. system: pxgt - Thermal expansivity
d.2. system: pxgt - Heat capacity
e.2. system: pxgt - Thermal conductivity
f.2. system: pxgt - Pressure

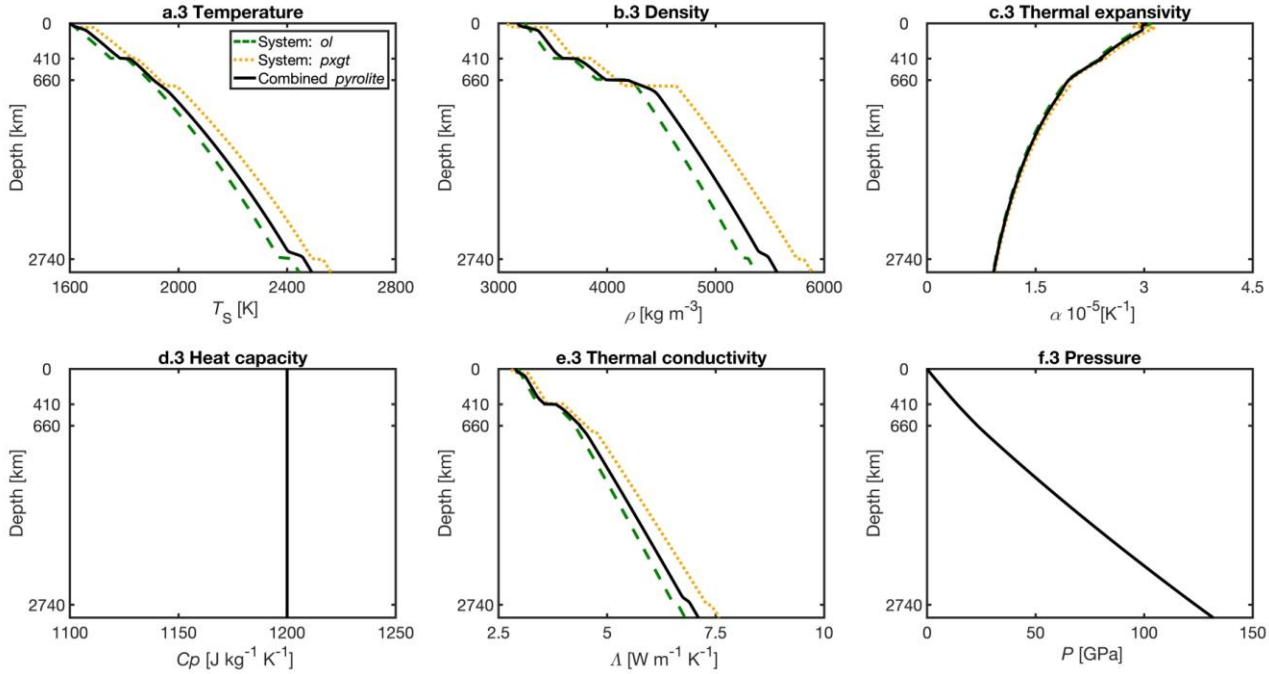

Figure 3.11. Example of a reference state radial profile. In this case the model is composed by two phase systems: *olivine* (ol - plots a.1-f.1) and *pyroxene-garnet* ($pxgt$ - plots a.2-f.2).
The depth-dependent parameters are the ones described in section **3.6.5**: adiabatic temperature T_S (a.1-3), density ρ (b.1-3), thermal expansivity α (c.1-3), specific heat capacity Cp (d.1-3), thermal conductivity Λ (e.1-3), pressure P (f.1-3).
Each phase system (plots a.1-f.1 and a.2-f.2) is characterized by a certain number of mineral phases Γ (coloured lines). Each phase is labelled as its prescribed stability region: lithosphere LT (grey lines), i.e. MORB pyroxenes and garnets ($0-40\ km\ pxgt$ system); upper mantle UM (olive green lines), i.e. olivine ($0-410\ km\ ol$ system) and eclogitic pyroxenes and garnets ($40-400\ km\ pxgt$ system); mantle transition zone MTZ (blue lines), i.e. spinel ($410-660\ km\ ol$ system) and post-pyroxene and majoritic garnets ($400-720\ km\ pxgt$ system); lower mantle LM (pink lines) i.e. Mg-perovskite (i.e. bridgmanite) and ferropericlase ($660-2740\ km\ ol$ system, $720-2740\ km\ pxgt$ system); post-perovskite region PPV (light blue line $2740-2890\ km\ ol-pxgt$ systems).
The cumulative radial profile of the given phase system X (black lines) is computed by considering the contribution of the stable mineral phase Γ at a given depth.
The cumulative parameters profiles of the pyrolitic mantle (plots a.3-f.3, black lines) is computed as the fractional contribution of 60% olivine (green dashed line), and 40% pyroxene-garnet system (orange dotted line).

3.6.9. Viscous Rheology

In StagYY, viscosity η can change as a function of temperature T, pressure P, strain rate $\dot{\varepsilon}$, deviatoric stress $\acute{\sigma}$, grain size d, deformation mechanism $\varkappa$, water content C_{H2O}, mineral phase Γ, and melt fraction f_{melt} **(2.7.92)**.

Different viscosity laws are implemented in the code in order to consider the various contributions separately or in a coupled manner. In this work the employed viscosity follows a strong temperature dependence as described by the Arrhenius Law (*Weertman, 1970*) for a creep diffusion deformation mechanism (*Yamazaki & Karato, 2001*) .

$$\eta_{diff}(P,T) = \eta_0 exp\left[\left(\frac{E_\Gamma + PV_\Gamma}{RT}\right) - \left(\frac{E_\Gamma}{RT_0}\right)\right] \tag{3.6.61}$$

Where η_0 is the reference viscosity for the reference state T_0, P_0, and σ_0 (typically $T_0 = 1600$ K, $P_0 = 0\,Pa$, $\sigma_0 = 1\,MPa$), while E_Γ and V_Γ are the phase-dependent activation energy $[J\,mol^{-1}]$ (*Yamazaki & Karato, 2001*; *Steinberger & Calderwood, 2006*) and activation volume $[m^3\,mol^{-1}]$ (*Ammann et al. , 2009*; *Ammann et al., 2010*). The parameter R represents the universal gas constant $R = 8.314\,[J\,mol^{-1}\,K^{-1}]$. The Arrhenius law **(3.6.61)** causes the formation of a stiff, high viscosity lid at the upper cold boundary of the model (*Tackley, 2000*). This feature is consistent with the experimental viscosity estimates of Earth's lithosphere, i.e. $\eta_{lit} \gg 10^{23} Pa\,s$ (*Walcott, 1970*; *De Bremaecker, 1977*; *Liu & Hasterok, 2016*). For this purpose, it is also necessary to introduce an upper and lower viscosity cutoff η_{min} $(10^{17} - 10^{19}\,Pa\,s)$ and η_{max} $(10^{25} - 10^{28}\,Pa\,s)$.

3.6.10. Plastic Rheology

StagYY also features a plastic rheology law to successfully reproduce the plate tectonic regime of the Earth (*Tackley, 2000*). The ruptures and fault planes (*King, 1983*; *Handy, 1989*) that characterise the Earth's near surface layers (*Brace & Kohlstedt, 1980*), as well as rock porosity (*Eichheimer et al., 2020*), cannot be directly modelled in StagYY, since the codes uses the principles of continuum mechanics (mass and momentum conservation in particular) that do not allow for empty voids. Therefore, brittle failure has to be mimicked by plastic flow, i.e. pseudoplastic behaviour. The effective viscosity η_{eff} of the lithosphere is reduced whenever the surface stress σ_{ij} reaches a certain threshold, namely the *yield stress* τ_y (*Tackley, 2000*). As soon as τ_y is reached, StagYY calculates the apparent viscosity η_{app} as:

$$\eta_{app} = \frac{\tau_y}{2\dot{\varepsilon}_{II}} \tag{3.6.62}$$

Where $\dot{\varepsilon}_{II}$ is the second invariant of the strain rate tensor. At every timestep, the code calculates the effective viscosity of the lithosphere by choosing the minimum value between η_{diff} **(3.6.61)** and η_{app} **(3.6.62)**.

$$\eta_{eff} = \min\left[\eta_{diff}(P,T), \eta_{app}(\tau_y, \dot{\varepsilon}_{II})\right] \tag{3.6.63}$$

This implementation produces self-consistently narrow weak zones in strongly deformed areas of the lithosphere, thus mimicking the gliding of faults at the plate boundaries (*Tackley, 2000*). StagYY features several constitutive laws to control the behaviour of the yield stress. A perfectly plastic material (i.e. no work-hardening) flows under constant stress, and obeys the von Mises equations (*Prager & Hodge, 1952*).

$$\tau_y = \sigma_{ij}\frac{\dot{\varepsilon}_{II}}{\dot{\varepsilon}_{ij}} \tag{3.6.64}$$

With σ_{ij} and $\dot{\varepsilon}_{ij}$ representing the stress and strain rate tensors respectively. When $\sigma_{ij} < \tau_y$ there is no glide along the faults (i.e. no plastic deformation). In natural rocks, however, the yield stress τ_y is not constant and increases with pressure (depth) following the Drucker-Prager plastic yield criterion (*Alejano & Bobet, 2012*).

$$\tau_y = a + bP \tag{3.6.65}$$

Where the pressure P can be expressed as the first invariant of the stress tensor ($P = \sigma_I = 1/3\sigma_{kk}$) **(2.4.27)**, and a, b are experimentally constrained constants. The Drucker-Prager criterion is a generalization of the Mohr-Coulomb failure criterion (*Labuz & Zang, 2012*), and the experimentally derived Byerlee's Law (*Byerlee, 1978*) on the brittle behaviour of rocks.

$$\tau_y = c \cdot \cos\phi + \sigma_{ave} \cdot \sin\phi \tag{3.6.66}$$

Where c $[MPa]$ is the cohesion coefficient, $\sigma_{ave}[MPa]$ is the average between the maximum σ_1 and minimum σ_3 stresses, and ϕ is the angle of internal friction. In StagYY the yield stress τ_y is given by the minimum between the pressure-dependent brittle yield criterion **(3.6.66)** and the depth-dependent ductile yield criterion **(3.6.65)** see **Figure 3.12** and *Crameri & Tackley, (2016)*.

$$\tau_y = \min\left[\tau_y^{brittle}(P), \tau_y^{ductile}(D)\right] \tag{3.6.67}$$
$$\tau_y^{brittle}(P) = c_y + f_\phi P$$
$$\tau_y^{ductile}(D) = \sigma_y + f_\sigma D$$

With c_y as the input cohesion coefficient, f_ϕ the input frictional coefficient (i.e. slope of Byerlee's Law), σ_y the input yield stress limiter, and f_σ the depth gradient of σ_y. These parameters can be set by the user to assign a certain strength profile to the lithosphere. In StagYY, the plastic yielding in the deep mantle is neglected by prescribing a switch that activates when the gradient is $f_\sigma \neq 0$. To avoid this occurrence, the depth gradient is usually prescribed as $f_\sigma = 0.01\ Pa\ m^{-1}$ to maintain an almost constant value of $\tau_y^{ductile}$.

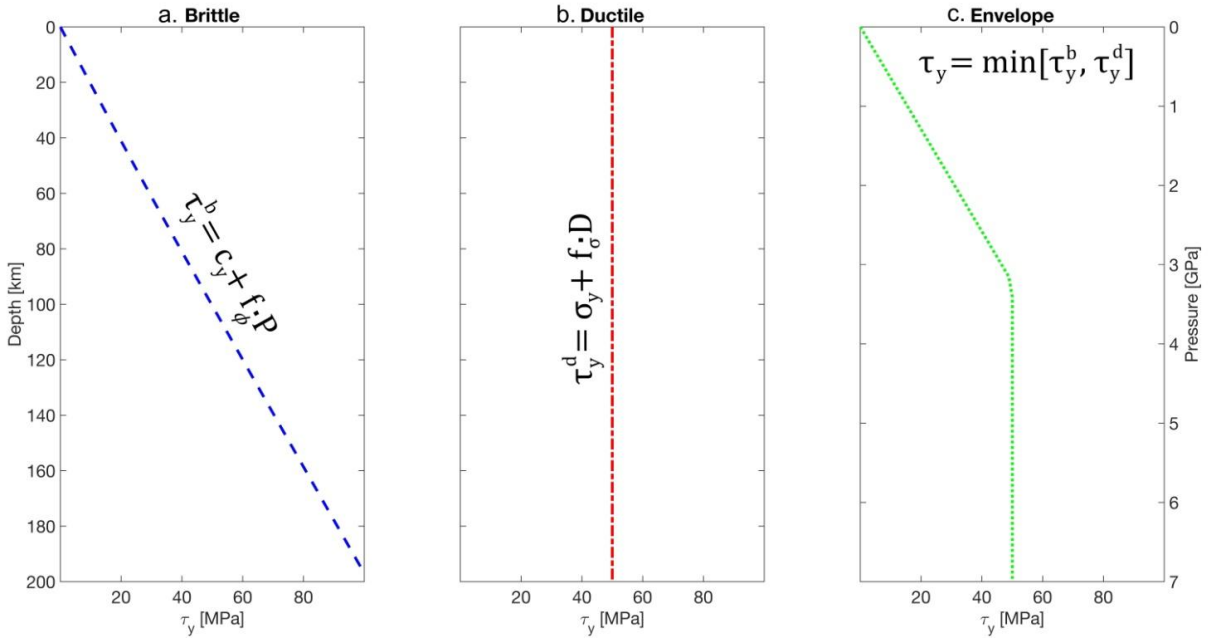

Figure 3.12. Examples of strength envelopes of the lithosphere **(3.6.67)**: (a – left column) brittle criterion τ_y^b (blue dashed line) with $c_y = 0\ MPa$ and $f_\phi = 0.015$ ($\approx 500\ Pa\ m^{-1}$); (b – mid column) ductile criterion τ_y^d (red dash-dotted line) with $\sigma_y = 50\ MPa$ and $f_\sigma = 0.01\ Pa\ m^{-1}$; (c – right column) composite envelope τ_y (green dotted line).

3.6.11. Model Output

During the simulation time span, various outputs are produced by StagYY: 2D field parameters ($T, \eta, \sigma, \dot{\varepsilon}, \boldsymbol{u}, P_{dyn}$), 1D reference state radial profiles ($T_S, \rho, \alpha, Cp, \Lambda$), 1D radial profiles ($T, \eta, \sigma, \dot{\varepsilon}, \boldsymbol{u}, P_{dyn}$), rms time evolution ($T, \eta, \boldsymbol{u}, Q_{top}, Q_{bot}, Nu_{top}, Nu_{bot}$), and rms time evolution of plate analysis parameters (M_o, P_{80}).

The 2D field parameters consist of a $R_{azi} \times R_{rad}$ matrix reporting the value of the cell-centred parameters for a given time output (**Figure 3.13**). The saved time frame t_{frame} is handled by the input parameter '*time print*' t_{print}, i.e. $t_{frame} = n * t_{print}$ (typically $t_{print} = 4.5\ Myrs$). The saved field parameters are: temperature T; viscosity η; stress σ; strain rate $\dot{\varepsilon}$; velocity $\boldsymbol{u}$ (horizontal and vertical), and the dynamic pressure P_{dyn}.

The 1D reference state radial profiles contain all the thermodynamic parameters of the pyrolitic mantle necessary to calculate the adiabatic temperature profile and the latent heat, i.e. density ρ, thermal expansivity α, specific heat capacity Cp, and thermal conductivity Λ. This radial mantle structure is build at the beginning of the simulations and it remains constant overtime. The file consists of a 1D array where the value of a given parameter at cell edges and centre is reported, i.e. $2 * R_{rad} + 1$ entries.

The 1D radial profiles contain the azimuthal (i.e. horizontal) average of the 2D field parameters at the given t_{frame}. The file consists of a 1D array where the value of a given parameter at cell centre is reported, i.e. R_{rad} entries.

The rms time evolution contains the volume-averaged root-mean-square parameters of the whole domain, for each timestep dt of the simulation. Typically, a 4.5 $Gyrs$ simulation has $O(10^4)$ time steps, with increasing values when the adaptive timestep reduces. Some important parameters saved here are: the top and bottom heat fluxes Q $[W\ m^{-2}]$, and the top and bottom Nusselt numbers Nu (see **Chapter 2.8.3**). The rms plate analysis output is similar to the previous file, but it contains parameters like the mobility M_o and the plateness P_{80} (*Tackley, 2000a*).

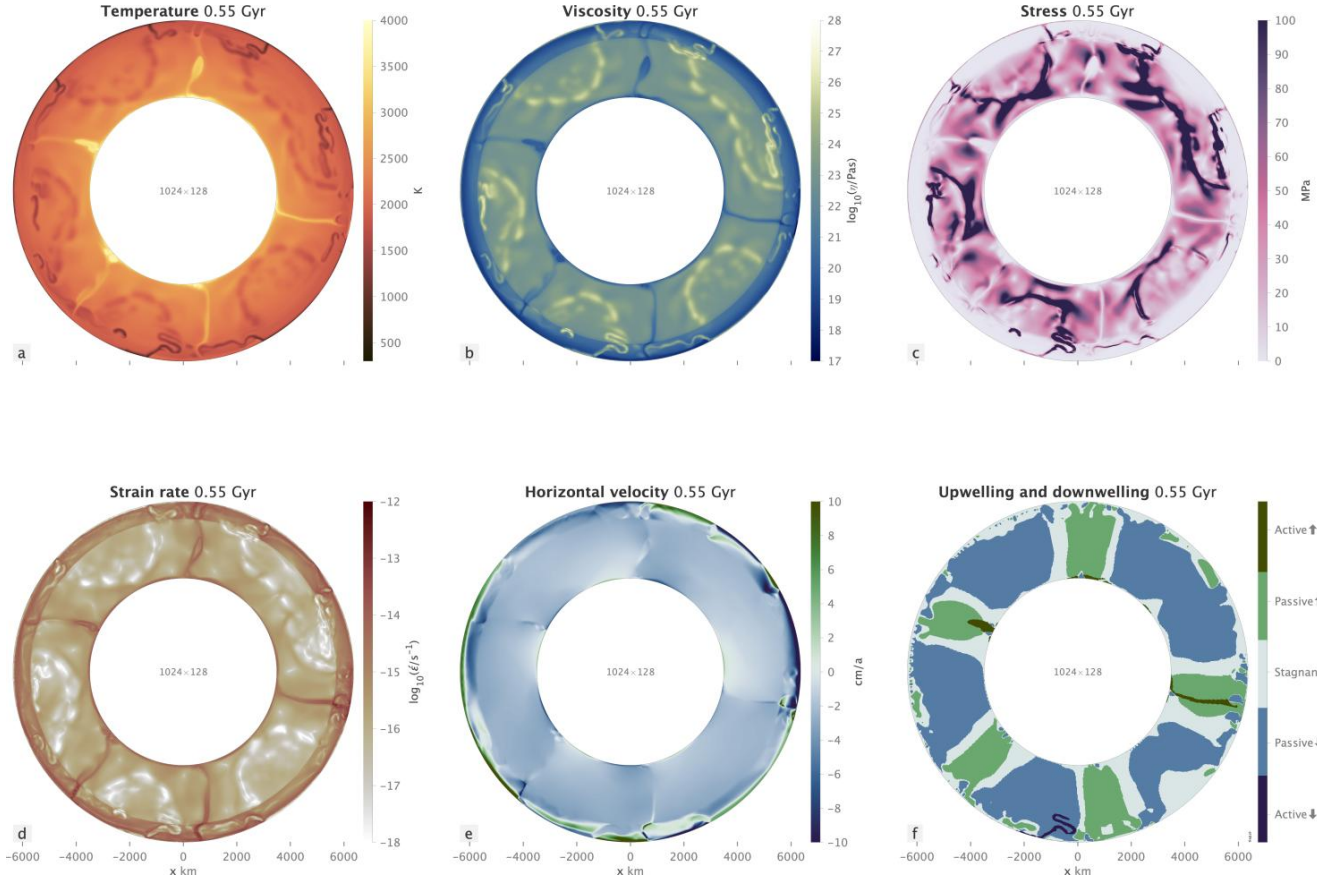

Figure 3.13. Examples of StagYY output plotted with StagLab (*Crameri, 2018*) and making use of scientific colour maps (*Crameri et al., 2020*). Employed geometry is the 2D spherical annulus (i.e. equatorial slice). Each panel shows the same time frame (i.e. 0.55 $Gyrs$) by taking into consideration a specific parameter field: (a) temperature field (*lajolla*); (b) viscosity field (*devon*); (c) stress field (*acton*); (d) strain rate field (*bilbao*); (e) horizontal velocity (*cork*) (f) mantle motion (*cork*) . In this example it is possible to notice 5 rising plumes and several subducting slabs.

3.6.12. Additional Features

StagYY is quite robust in performing global-scale mantle convection simulations, and furthermore includes Earth-like features such as: large viscosity variations (8– 10 orders of magnitude *Rolf et al., 2018*; *Guerrero et al., 2019*), *P-T* dependent phase transitions (*Nakagawa et al., 2009*; *Nakagawa & Tackley, 2011*; *Tackley et al., 2013*; *Li et al., 2016*; *Li et al., 2018*), chemical heterogeneities (*Nakagawa et al., 2010*; *Tackley, 2011*; *Nakagawa & Tackley, 2014*; *Ballmer et al., 2015*; *Khan et al., 2018*; *Gülcher et al., 2020*), partial melting (*Nakagawa & Tackley, 2012*; *Lourenço et al., 2016, 2018*), basaltic crust production (*Keller & Tackley, 2009*), continental crust production and drifting (*Sim et al., 2016*; *Rozel et al., 2017*; *Rolf & Pesonen, 2018* ; *Rolf et al., 2018*; *Jain et al., 2019a, 2019b*), plate tectonics (*Rolf & Tackley, 2011*; *Van Heck & Tackley, 2011*; *Morishige & Honda, 2013*; *Bello et al., 2014*; *Crameri & Tackley, 2015*; *Nakagawa & Tackley, 2015*; *Bocher et al., 2016*; *Honda, 2016*; *Mallard et al., 2016*; *Bocher et al., 2018*; *Coltice & Shephard, 2018*; *Arnould et al., 2019*), different tectonic regimes (*Armann & Tackley, 2012*; *Rozel et al., 2015*), free surface (*Duretz et al., 2011*) and sticky air (*Crameri et al., 2012a, 2012b*; *Crameri & Tackley, 2014, 2016*; *Crameri et al., 2017*; *Patočka et al., 2019*), dynamic topography (*Guerri et al., 2016*; *Arnould et al., 2018*), atmosphere (*Gillmann & Tackley, 2014*; *Gillmann et al., 2016, 2020*), Earth's core evolution (*Samuel & Tackley, 2008*; *Nakagawa & Tackley, 2013*; *Langemeyer et al., 2018*; *O'Rourke et al., 2018*) different core/mantle ratio (*Guerrero et al., 2018*), grain-size evolution (*Schierjott et al., 2020*), complex rheologies (*Bello et al., 2015*; *Patočka et al., 2017*), tidal heating (*Rozel et al., 2014*), meteorite impacts (*Golabek et al., 2011*; *Ruedas & Breuer, 2019*), and deep water cycle (*Nakagawa et al., 2015*; *Nakagawa, 2017*; *Nakagawa & Iwamori, 2017*; *Nakagawa & Spiegelman, 2017*; *Nakagawa & Iwamori 2019*).

3.6.13. Code Comparisons

StagYY is capable of successfully reproducing the 2D (*Blankenbach et al., 1989*) and 3D code comparisons (*Busse et al., 1994*) for thermal convection with constant and *T*-dependent viscosity as reported for Stag3D (*Tackley et al., 1994*; *Tackley, 1996*). Convergence tests for self-consistent plate tectonics with large viscosity contrast are reported in the appendix of *Tackley (2000)*. Tracer-based thermo-chemical convection (*van Keken et al., 1997*) was also tested (*Tackley & King, 2003*) and the results were in agreement with the ones obtained with the finite-element code ConMan (*King et al., 1990*). The results for steady-state basal-heated Boussinesq convection reproduced by StagYY are in agreement with the code comparison, featuring eight different codes as reported by *Stemmer et al. (2006)*. Finally, the resolution tests for thermal convection with a pseudo-plastic rheology featuring eleven codes (*Tosi et al., 2015*), show that the StagYY solutions for the code comparison is quite robust even for low grid resolutions.

CHAPTER 4 – Experimental Methods

4.1. The Multi-Anvil Technique

To synthesize the minerals that characterize the Earth's interior, it is necessary to achieve the high-P and high-T conditions typical of the mantle (*Ita & Stixrude, 1992*). This environment can be reproduced in the laboratory by employing the multi-anvil technique (*Keppler & Frost, 2015*). The multi-anvil apparatus is a type of press that employs several anvils to apply a quasi-hydrostatic load to the sample (*Huppertz, 2004*). The most commonly utilized presses are the so called 6/8 multi-anvil apparatuses or Kawai-type (*Kawai & Endo, 1970*) which are designed to apply the pressure load in 2 stages:

1) The first stage anvils are designed to split the uniaxial load into 6 orthogonal components (coupled in the three directions x,y,z), and transmit the press load uniformly to the second stage. The geometry of the first stage either presents an outer spherical/cylindrical pressure chamber with a cubic cavity in the centre (i.e. split sphere and split cylinder types) or consists of 6 independent anvils (i.e. DIA type).

2) The second stage is composed by 8 mobile tungsten-carbide (WC) anvils, in the shape of cubes with triangular truncation at the corners. These anvils are arranged in a cubic geometry so that the corner truncations isolate an octahedral cavity where the assembly sits. The purpose of the second stage anvils is to maintain the hydrostatic conditions, while increasing the pressure. The high-pressure conditions are achieved by transmitting the load applied on the faces of the cubes to the much smaller triangular truncations, which then squeeze the sample.

To seal the octahedral cavity, maintain homogeneous pressure conditions and prevent the WC anvils from touching and thus exploding, it is important to apply a pyrophyllite gasket on the truncated edges (**Figure 4.1**). The pressure load is ultimately delivered to a sample vessel which occupies the octahedral cavity.

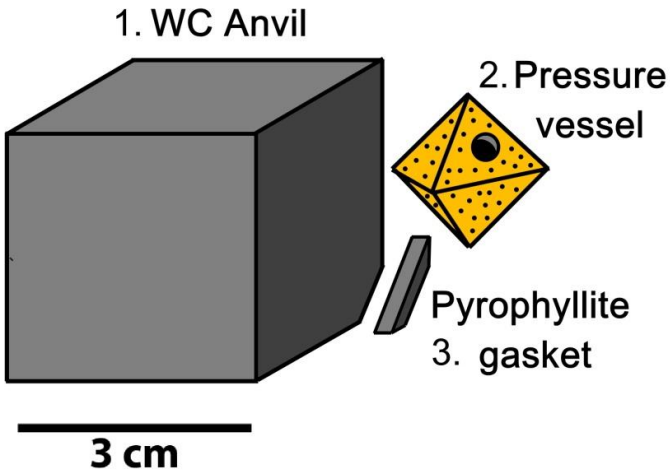

Figure 4.1. Schematics of the multi-anvil 2^{nd} stage components: (1) tungsten carbide WC anvil, (2) octahedral Cr_2O_3-doped MgO pressure vessel and (3) pyrophyllite gasket (modified from *Buchen, 2018*).

The pressure vessel hosts the sample capsule and the electric furnace. Typically, the vessel is an octahedron of $5wt\%$ Cr_2O_3-doped MgO with a cylindrical cavity running through its volume. Several concentric sleeves, along with the sample capsule, are slid inside the cavity (**Figure 4.2**):

- The ZrO_2 sleeve thermally insulates the furnace to prevent heat loss, and the consequent plastic deformation of the assembly.
- Two lids composed of molybdenum Mo electrodes close the cavity from both sides. The electrodes are necessary to transmit the current from two of the WC cubes to the furnace inside the assembly.
- The furnace is a sleeve composed of a resistive material. Typical materials are graphite, lanthanum chromite ($LaCrO_3$) or metal foils.
- The MgO sleeve to provide electrical insulation between the furnace and the capsule.
- The sample capsule.

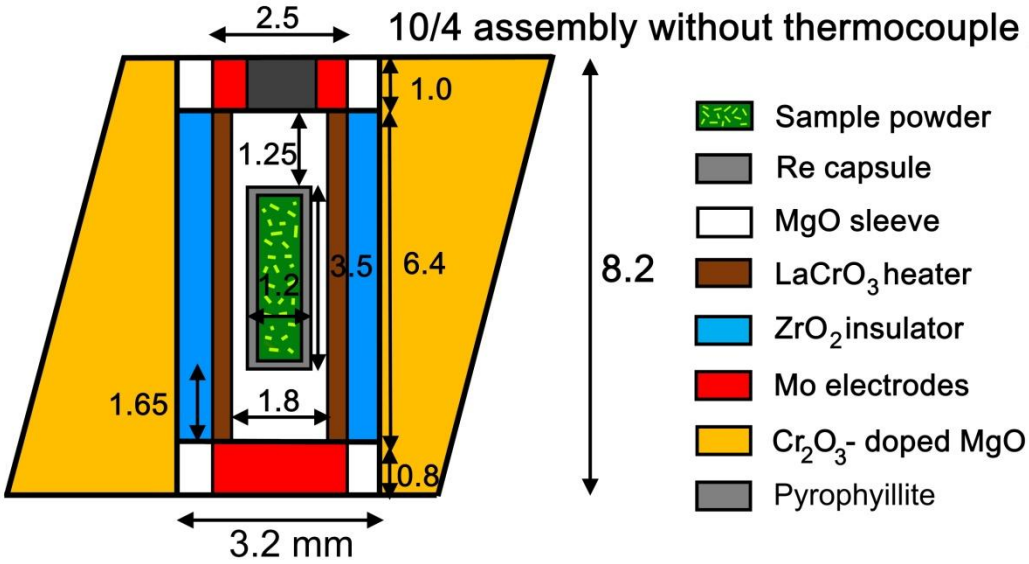

Figure 4.2. Schematics of a $10/4$ multi-anvil assembly used in high-pressure synthesis experiments. All dimensions are reported in mm.

The dimension of the sample capsule and the pressure vessel determines the maximum pressure achievable during the experiments. The experimental assembly is described by the OEL/TEL notation, indicating the Octahedral Edge Length and the Truncation Edge Length respectively. For example, a $14/8$ assembly presents 14 mm OEL and 8 mm TEL. The smaller the size of TEL and OEL, the higher is the achievable pressure range. However, this comes at the cost of studying lower sample volumes, since the capsule dimensions decrease together with the rest of the cell assembly.

In multi-anvil experiments, a non-negligible portion of the applied load is lost through friction among the various components of the assembly (i.e. gaskets, WC cubes, steel anvils). Therefore, each machine must be carefully calibrated in order to estimate the effective pressure acting on the sample. Calibration curves are useful tools to relate the oil pressure in the press with the pressure reached during the experiment. Duct tape and paper are often applied on the inner sides of the cubic anvils to facilitate gliding and protect the surface from abrasion. Moreover, the duct tape is also employed to provide electrical insulation between the anvils, thus ensuring that the electrical current flows through the assembly.

The high temperature conditions produced by the furnace are monitored by thermocouples (typically two alloys of W– Re, or Rh– Pt). The installation requires the drilling of the MgO pressure vessel, and the thermocouples have to be carefully placed in contact with the capsule. As all cell assemblies of a given size (e.g. 14/8) are supposedly identical to one another, temperature of the experiments can be also roughly estimated through power-temperature calibration curves obtained in separate runs. This method is often adopted in the experiments that do not require high accuracy in the T estimates ($\pm$ 50 K), to avoid the time-consuming procedure of installing the thermocouples.

The high-pressure cell is assembled as follows:

1. The capsule is filled with the starting material and sealed, while the pressure vessel is drilled for installing the thermocouples
2. The ceramic parts of the pressure vessel are heated for several hours at 1273 K to anneal defects and remove water impurities.
3. The pressure vessel is assembled by inserting each component, then, closed by the lids.
4. After cleaning the WC cubes with ethanol, the pyrophyllite gaskets are glued on 4 of the 8 truncated edges in contact with the sample, and the duct tape or paper are applied on the cube surfaces.
5. The sealed pressure vessel is positioned in the octahedral cavity formed by the 8 anvils. Extra care should be taken when the thermocouple is installed, since the wires might break. Normally, the gaskets are previously indented for this purpose. The two WC cubes directly in contact with the Mo electrodes are marked for recognition.
6. A square piece of epoxy is glued on the outer faces of the cubic assembly. This has the function of keeping the assembly together, provide electrical insulation, and facilitating gliding between the first and the second anvil stage. On the marked cubes, the epoxy has a slit where a piece a copper foil has been inserted. The copper foil allows the transmission of the electrical current from the first stage to the second stage anvils and thus to the resistive heater within the vessel.
7. The whole assembly is positioned inside the cubic cavity in the first anvil stage.

After loading, the sample is pre-compressed (in about 20 min) to a starting pressure value, in order to allow the experimental assembly to settle. Once this operation is complete, the press load is increased linearly to reach the target pressure. This typically takes a few hours, so that the whole assembly can gradually adjust to the increasing pressure conditions, and thus avoid rupture of its components.

4.2. Single-Crystal X-Ray Diffraction

X-Ray Diffraction (XRD) is a non-destructive experimental technique developed by William Lawrence Bragg (*Bragg, 1914*), and his father William Henry Bragg, which is particularly useful to study crystalline materials (*Giacovazzo et al., 2013*). This technique is based on the principle of diffraction, which describes the interaction between a wave front and an obstacle, whose spacing is comparable with the wavelength of the incident wave front. The interaction can be constructive or destructive interference, depending on the direction in which each wave is scattered. Only the waves resulting from the constructive interference are able to propagate beyond the obstacle, whereas the intensity of the scattered waves is zero when destructive interference occurs. In crystalline materials, constructive interference results from the interaction of electromagnetic radiation (i.e. X-rays), with a wavelengths λ of $10^{-2}-10$ Ångstrom ($1\ \text{Å} = 10^{-10}\ m$) with the periodic configuration of the atoms in the crystal structures.

In crystalline materials, diffraction phenomena can be seen as selective refractions, since the scattered wavefront is observed only for specific angles. The diffraction angle θ that describes such refraction relates to the wavelength λ of the wave front, and the spacing of the crystallographic planes d_{hkl}, through Bragg's law (*Bragg, 1914*):

$$n\lambda = 2d_{hkl}\,sin\,\theta \tag{4.2.1}$$

Where λ is the wavelength $[m]$, and n is a positive integer which indicates the diffraction order. Normally, n is assumed to be 1, i.e. first order reflections. The parameter d_{hkl} represents the spacing of the atomic planes in the three crystallographic directions h, k, l. In a typical X-ray diffraction experiment, the wavelength λ of the incident wave front is known and the diffraction angle θ is measured using a detector, thus enabling to calculate the inter-atomic spacing d_{hkl} for a given hkl plane by using equation **(4.2.1)**.

XRD techniques are routinely employed to identify and characterize the structure of both polycrystalline samples and single crystals from the analysis of their diffraction pattern. Powder XRD is typically used for phase identification. Single-crystal XRD on the other hand, is mainly used for structural characterization of a known sample, and allows to determine the unit cell parameters (edge lengths a, b, c and angles α, β, γ), the Bravais lattice and the space group of the sample. This operation requires the definition of a Cartesian coordinate system (*Busing & Levy, 1967*) and the experimental acquisition of the UB orientation matrix of the sample (*Busing & Levy, 1967*; *Angel et al., 2000*; *Haussühl, 2008*).

The equipment that performs XRD analysis is called a diffractometer. A diffractometer consists of four main components:

1. The X-ray source (cathode tube, rotating anode, synchrotron) produces bremsstrahlung (i.e. polychromatic). In the bremsstrahlung spectrum, the most intense peak is called $K\alpha$, which is produced by the replacement of an electron e^-, coming from the L shell, into the vacancy left in the K shell during the target bombardment. The wavelength of the $K\alpha$ line is characteristic of the anticathode material: molybdenum Mo ($\lambda = 0.7107$ Å), copper Cu ($\lambda = 1.5418$ Å), and cobalt Co ($\lambda = 1.7902$ Å). Mo sources are commonly used in single-crystal XRD, whereas Cu and Co sources are often employed in powder crystal diffraction.
2. A sample holder to contain the crystal sample (either single or powdered) and control its orientation throughout the XRD analysis. In single-crystal diffraction the sample is glued on

the top of a glass capillary, while in powder diffraction the sample is inside a glass container or on a metal plate (e.g. a single crystal of Si).

3. A system of goniometric circles to orient the crystal in as many directions as possible, and thus investigate diffracted beams originating from many different crystallographic directions within a sample (**Figure 4.3**). For single-crystal diffraction the most commonly used setup employs 4 circles with Eulerian or kappa geometries: the $\varphi-circle$ (i.e. goniometric head) which rotates the sample holder around its own axis, the $\chi-circle$ or $\kappa-circle$ which rotate the goniometric head in the vertical plane, the $\omega-circle$ which moves the entire instrument in the horizontal plane, and the $\theta-circle$ which is co-axial with ω and controls the detector. The aim of this component is to measure the diffraction angle θ. Powder diffraction employs several acquisition geometries (*Bish & Reynolds, 2018*), e.g. Bragg-Brentano, Debye-Scherrer, Seemann-Bohlin, and Guinier.
4. The X-ray detector measures the intensity of the diffracted X-ray beam (i.e. the number of diffracted photons). Two main options are available: area detectors (CCD cameras) with fast acquisition but typically lower precision in the measurements (i.e. larger uncertainties), and point detectors (proportional gas chambers, or scintillators) with slow acquisition time, but high precision and accuracy in determining the lattice cell parameters.

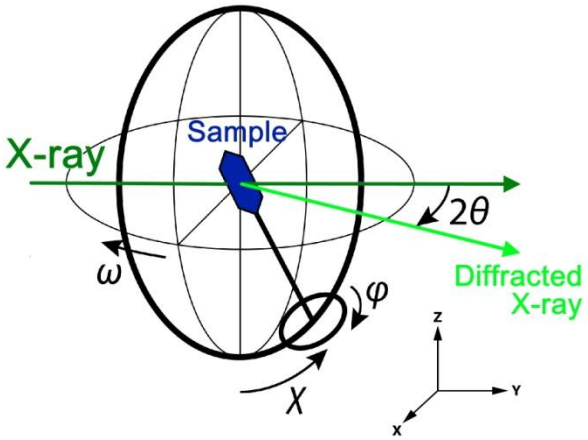

Figure 4.3. Schematics of a Eulerian four-circle cradle for X-ray diffraction analysis: (1) $\varphi-circle$, i.e. goniometric head; (2) $\chi-circle$ which rotates φ in the vertical plane; (3) $\omega-circle$ moves the diffractometer in the horizontal plane; (4) $\theta-circle$ which is co-axial with ω and controls the detector. The sample is indicated by the blue polygon, whereas the X-rays are indicated in green. The image is modified from *Buchen (2018)*.

The XRD technique can be combined with high-pressure and high-temperature experiments to investigate the physical properties of deep Earth crystals, and map their phase transitions *(Angel et al., 2000; Miletich et al., 2000; Boffa Ballaran et al., 2013*).

4.3. Electron Microprobe Analysis

Electron microscopy employs a beam of accelerated electrons to characterize the sample. The high momentum of the electrons in the beam causes them to dislodge the electrons from the inner shells of the target atoms. This produces an imbalance of charge in the target atoms, thus causing ionization of the sample surface. This atomic configuration, however, is transient and the original gap left by the knocked–out electron is promptly filled by another electron coming from the outer shells (i.e. atomic electron transition). This process involves energy loss by the electron (inelastic collision) upon jumping to an inner, lower energy orbital and the consequent emission of an X-ray photon (X-ray fluorescence). The energy of the emitted X-ray photon depends on the 'jump' necessary to move from the high-energy outer shells to the low-energy inner shells (i.e. the electron configuration of the target atom). Photon energy is calculated as:

$$E = \frac{hc}{\lambda} \tag{4.3.2}$$

Where E is the photon energy $[J]$, h is Planck constant $6.62607015 \times 10^{-34}\ J\ s$, c is the speed of light in vacuum $2.99792458 \times 10^{8}\ m\ s^{-1}$, and λ is the X-ray photon wavelength. Since both h and c are universal constants, the only variable parameter is the photon wavelength λ, which is characteristic of the emitting atom. The speed of light relates the wavelength $\lambda\ [m]$ and the linear frequency $\upsilon\ [Hz]$ through the equation:

$$c = \upsilon\lambda \tag{4.3.3}$$

Therefore equation **(4.3.2)** can be also expressed as a function of the wave frequency, and the reduced Planck constant $\hbar = h/2\pi$.

$$E = \hbar\upsilon \tag{4.3.4}$$

The emitted X-ray photons are focused toward a crystal analyzer with a known interplanar space d_{hkl}. By rotating the analyzer crystal, the diffraction angle changes, and the characteristic λ is calculated by employing Bragg's law equation **(4.2.1)** (*Bragg, 1914*), with known d_{hkl} and θ. The diffracted X-rays are collected and counted by a point detector (scintillator). The higher the count from a given diffracted direction, the higher the concentration of the element emitting that characteristic λ. Several analyzers, with different d_{hkl}, are employed in order to collect the entire wavelength range. The concentration of a given element is estimated by comparing the measurements on the sample with the analysis performed on a known, well characterized, standard.

This method of analysis is called wavelength dispersive spectrometry (WDS), since the constituting wavelengths of the characteristic X-ray spectrum 'disperse' over a certain angular range θ. This technique is employed to detect elements with an atomic number $Z \geq 6$, i.e. elements heavier than Boron. The high beam focusing (a few μm^2) allows punctual analysis of the samples, hence the name microprobe. EMPA is an excellent method to quantify the abundances of major elements in the samples ($\approx 1\%$ accuracy) while also obtaining good quality backscattered electron images. These features combined are optimal for mapping the local element distribution within the samples and producing compositional maps. This technique, however, is less indicated to quantify minor elements ($\approx 3-5\%$ accuracy) and trace elements ($\approx 10-20\%$ accuracy). Detailed description of the EMPA technique and its applications can be found in *Reed (2005)* and *Goldstein et al, (2018)*.

4.4. Absorption Spectroscopy

One of the most common techniques to investigate the concentration of impurities in minerals, is optical spectroscopy. The term optical spectroscopy includes all experimental methods that investigate the sample with an incident electromagnetic radiation extending from near ultra-violet ($\lambda = 250\ nm$) to mid infrared ($\lambda = 3000\ nm$) (*Rossman, 2014*). Each technique takes the name of the employed light spectrum, e.g. 'ultra-violet spectroscopy' or 'infrared spectroscopy'. The interactions between the sample and the light are of multiple kind: absorption, emission, reflection, scattering, and fluorescence. Most spectroscopic methods study light absorption, since it is the most sensitive to sample structure and composition.

After the light passes through an optically transparent media, its intensity is dimmed by the interactions with the object. The 'transparency' of an object is measured by its transmittance T [%]:

$$T = \frac{I}{I_0} \times 100 \tag{4.4.5}$$

Where I_0 is the intensity of the incident light before interacting with the crystal, and I is the intensity of the light after passing through the crystal. Intensities are measured by a detector which counts the number of incident photons. The reciprocal of transmittance is the absorbance A [/], i.e. the percentage of light which is absorbed by the object.

$$A = log_{10}\left(\frac{I_0}{I}\right) \tag{4.4.6}$$

Absorbance is expressed in log units, therefore: $A = 0$ means no absorption, $A = 1$ means 10% transmission (i.e. 90% absorption), and $A = 2$ means 1% transmission (i.e. 99% absorption). Normally, absorption spectra plot the absorbance as a function of the wavelength $\lambda\ [cm]$ or its reciprocal, the wavenumber $\tilde{v}\ [cm^{-1}]$. These plots are useful to determine which energy bands of the electromagnetic spectrum are absorbed by the sample.

4.4.1. Absorption Spectroscopy: Orbital Interactions

Light absorption occurs at the atomic scale, where the interactions between photons and matter are quantized (i.e. discrete energy states). The absorption of light (i.e. photon energy) in optical spectroscopy is described by the crystal field theory (*Burns, 1993*), and the ligand field theory (*Figgs & Hitchman, 1999*). The crystal field theory describes the ionic bonding, and the interaction of the atomic orbitals of the cation and the anion. Ligand field theory, on the other hand, includes the covalent bonding in its description of the orbital interaction. There are several processes that can cause light absorption:

1. Electronic transition involving d-orbitals, i.e. the first row of transition elements (Cr^{3+}, Mn^{3+}, Fe^{2+}, Fe^{3+}). When incoming radiation interacts with these elements by photon collision, it triggers a re-arrangement of their valence electrons, which are located in the outer shells. The energy requirement to promote the electrons within the d-orbitals corresponds to frequencies of the near-IR spectrum, which is thus absorbed from the electromagnetic spectrum.

2. Charge-transfer process (i.e. electron e^- transfer) between two ions. This can occur in two ways:
    - Ligand-to-metal charge transfer, which involves the exchange of electrons between an anion and a cation (e.g. $O^{2-}\ Fe^{3+} \rightarrow O^{-}\ Fe^{2+}$)
    - Intervalence charge transfer (IVCT), which involves two metal ions with different oxidation states (e.g. $Fe^{2+}\ Fe^{3+} \rightarrow Fe^{3+}\ Fe^{2+}$). This is the cause of the brown colours of oxidized minerals.
3. Band gap absorption. Materials can be classified as insulators, semiconductors (i.e. semimetals) and conductors (i.e. metals) depending on the energy gap that separates the valence band from the conduction band. Insulating material presents a considerable gap ($> 4\ eV$) between the valence and conduction bands, therefore no spontaneous conduction is possible. In semiconductors the band gap is close enough to present a thermally populated conduction band (i.e. electrons are promoted by their thermal energy). In metals the valence and the conduction band overlap, allowing the spontaneous flow of electrons. Band gap absorption occurs typically in semimetals (e.g. S), when photon collisions transfer enough energy to promote valence electrons to the conduction band. Only photons with energy greater than the band gap will be absorbed (i.e. high ω, low λ), therefore transmitting characteristic red-coloured light ($\lambda > 600\ nm$).
4. Electronic transition involving f-orbitals. These orbitals are located in the inner portion of the atoms, and they are not involved in inter-atomic bonding. Therefore, f-orbitals are shielded from the environment, and they are weakly perturbed by the vibration of the neighbouring atoms. This causes sharp absorption bands, since the energy range involved is quite narrow. Typically, this phenomenon is characteristic of uranium U ($\lambda = 400-500\ nm$ absorption, i.e. yellow colours) and rare earth elements REE in the X^{3+} oxidation state. The energy levels of the f-orbitals are typically measured by inelastic neutron scattering.
5. Electron-holes and ion defects (i.e. Farber centres or colour centres). The presence of crystallographic defects (e.g. electronic vacancies or unpaired electrons) is the source of colour in normally transparent minerals, thanks to the absorption of certain frequencies of the optical spectrum.

4.4.2. Infrared Spectroscopy: Lattice Vibration

Infrared spectroscopy is by definition a vibrational spectroscopy, since it only deals with the EM absorption caused by lattice vibrations. When bombarded by photons, molecules and lattice-bond atoms oscillate around their position with a certain vibration frequency. The number of independent vibrations depends on the geometry of the molecule (i.e. linear, non-linear, or lattice cell), and on the number of atoms in the primitive unit molecule N. During a vibration, a molecule may experience an absolute variation of its dipole moment P_Q.

$$\left|P_Q\right| = r\delta^{\pm} \tag{4.4.7}$$

Where $\delta\ [C]$ is the local concentration of positive δ^+ or negative δ^- charge, and r [Å] is the distance between two charges. A given vibration can be detected by infrared-absorption spectroscopy (i.e. IR-active) only if it causes a variation of the dipole moment.

One of the most common causes of vibrational absorption is the presence of water in minerals, either in the form of molecular H_2O or as a hydroxyl group $R-OH^-$ (see **Chapter 1.6.1-1.6.2**). Molecular water can be found in fluid/vapour inclusions or in the channel structure of some minerals (e.g. cyclosilicates, tectosilicates). Water molecules present three vibrations: symmetric stretching ($\approx 3600\ cm^{-1}$), asymmetric stretching ($\approx 3700\ cm^{-1}$), and bending ($\approx 1600\ cm^{-1}$).

The hydroxyl group is found in those minerals that present unbound oxygen atoms, which can be easily protonated (e.g. NAMs see **Chapter 1.6.2**). The hydroxyl molecule has three possible vibrations: stretching ($3000-3600\ cm^{-1}$), in-plane bending ($\approx 1000\ cm^{-1}$), and out of plane bending ($\approx 1000\ cm^{-1}$). The high vibrational frequency of H_2O and $R-OH^-$ groups is caused by their small mass.

Additional absorption is caused by the presence of overtones of the main vibration frequency, and the combined effect of two simultaneous vibrations (i.e. combined band). Typically, these absorption bands occur at high wavenumbers and they show weak intensity. The combination band of the H_2O molecule is located at $5200\ cm^{-1}$ (i.e. $3600\ cm^{-1} + 1600\ cm^{-1}$), whereas the first overtone is located at $7200\ cm^{-1}$ (i.e. $3600 \times 2\ cm^{-1}$). These two absorption bands are of key importance for the greenhouse effect on our planet (*Pfeilsticker et al., 2003*).

IR-spectroscopy is very sensitive to even the smallest amount of water in the sample (a few ppm - *Bolfan-Casanova et al., 2000*). Furthermore, vibrational absorption has sharper peaks than electronic absorption, making it easier to recognize the different absorbing species.

4.4.3. IR Spectroscopy: Lambert-Beer Law

The intensity of the absorption is related to the concentration of the impurity and/or defect that is absorbing the light. The concentration C_x of the absorbing species x is given by the Lambert-Beer law (*Libowitzky & Rossman, 1997*; *Rossman, 2014*):

$$A = \varepsilon\ d\ C_x \tag{4.4.8}$$

Where ε is the molar absorption coefficient $[mol\ L^{-1}]$, and d is the thickness of the object in $[cm]$. The parameter ε is a constant for a given material, and it has to be measured experimentally with an independent technique to quantify the concentration of the absorbing species (e.g. EMPA, or secondary-ion mass spectroscopy SIMS).

4.4.4. IR Spectroscopy: FT Spectrometer

Light absorption in the samples is normally measured by means of Fourier transform (FT) spectrometers (*Kuzmany, 2009* ; *McMillan & Hofmeister, 2019*). An FT-spectrometer (**Figure 4.4**) is schematically illustrated below:

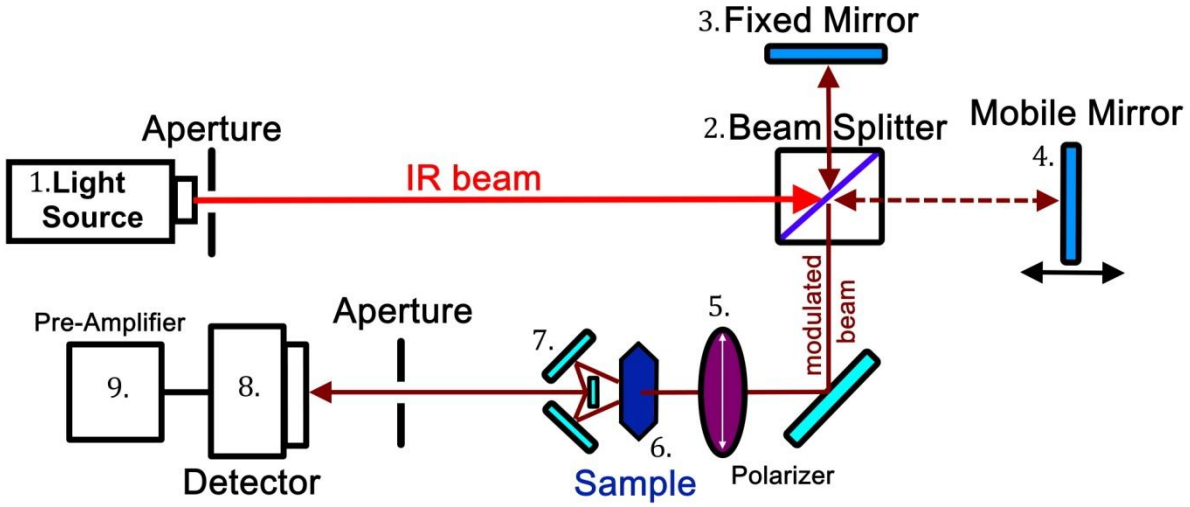

Figure 4.4. Schematics of the Bruker IFS 120 HR Fourier-transform infrared spectrometer employed at Bayerisches Geoinstitut (modified from *Buchen, 2018*). (1) Light source (e.g. tungsten lamp), (2) Si-coated CaF_2 beam splitter, (3) fixed mirror, (4) mobile scanning mirror, (5) beam polarizer, (6) sample, (7) Cassegranian reflecting optics, (8) MCT (Mercury-Cadmium-Telluride) detector cooled with liquid nitrogen (9) pre-amplifier.

1. Radiation source. The source beam is produced by thermal emission (i.e. black-body radiation). The peak of emission depends on the temperature of the source: the higher the T, the lower the wavelength λ of the peak (high energy, high-υ). Typical examples are:
   - Xenon-arc source ($\approx 5000\ °C$): near-UV ($\tilde{\upsilon} = 25000-50000\ cm^{-1}$), visible light ($\tilde{\upsilon} = 12500-23000\ cm^{-1}$).
   - Tungsten lamp ($\approx 3500\ °C$): visible, and near infrared ($\tilde{\upsilon} = 4000-12500\ cm^{-1}$).
   - SiC rod ($\approx 800\ °C$): middle infrared ($\tilde{\upsilon} = 400-4000\ cm^{-1}$).
   - Mercury-arc lamp (cold discharge): far Infrared ($\tilde{\upsilon} = 10-400\ cm^{-1}$).
2. Michelson interferometer (*Michelson & Morley, 1887*), the core element of the FT spectrometer. This is further composed of:
   - Beam splitter. This component is constituted of a semi-transparent mirror that separates the source beam in two: 50% of the radiation is reflected, 50% is transmitted. This optical property can be achieved by using a transparent object coated with a reflecting material. Different beam splitters are used for different spectral ranges:
     - Quartz coated with Al (UV)
     - Quartz with dielectric coating (Visible)
     - CaF_2 coated with Si (Near IR)
     - KBr coated with Ge (Middle IR)
     - Organic polymers or Sb_2S_3 (Far IR)
   - Fixed mirror. It is positioned at a given distance D_F from the beam splitter.

- Mobile mirror. It is positioned beyond the beam splitter at a variable distance D_M. The mirror moves back and forth with a fixed velocity v $[m\ s^{-1}]$.

Once the source beam is split, 50% of the radiation is reflected toward the fixed mirror, and 50% is transmitted through the splitter, toward the mobile mirror. Both mirrors reflect back the radiation, which recombines at the beam splitter, and the recombined beam continues its travel towards the sample and the detector. The amplitude of the recombined beam $\tilde{A}_R$ is given by the sum of the reflected beams amplitudes $\tilde{A}_F$ and $\tilde{A}_D$. The result of this sum depends on the wave interference upon recombination. If both mirrors are at the same distance (i.e. $D_F = D_M$), or if the retardation δ' (i.e. the misfit $D_F - D_M$) is equal to an integer number of wavelengths (i.e. $\delta' = n\lambda$), then the reflected beams are in-phase, and they show fully constructive interference, i.e. $\tilde{A}_R = 2\tilde{A}_F = 2\tilde{A}_M$. However, if the retardation is an integer number of half-wavelengths (i.e. $\delta' = 1/2n\lambda$), then the reflected beams are out-of-phase and they show fully destructive interference, i.e. $\tilde{A}_R = \tilde{A}_F + \tilde{A}_M = 0$. For any intermediate retardation between $n\lambda$ and $1/2n\lambda$, the recombined wave amplitude $\tilde{A}_R$ oscillates between $2\tilde{A}_{F-M}$ and 0. Therefore, through the motion of the mobile mirror, some wavelengths of the source spectrum (e.g. IR, UV, Visible) are cancelled and others show maximum intensity ($I = 0 \rightarrow max$). By measuring the intensity of the probing light with a detector, it is possible to determine which wavelengths characterize the probing spectrum and their intensity (i.e. interferogram). The aim of the interferometer is to convert the source light, with a given λ content, into a probe light, with a different λ content. This signal modulation is achieved by changing the retardation δ' over time t, i.e. through the mirror velocity $v = \delta'/(2t)$. Note that δ' indicates the beam path length difference (i.e. back and forth), whereas the mirror moves only in one direction (i.e. $\delta'/2$). The modulation frequency of the signal ω $[Hz]$ depends on the wavelength λ $[cm]$, and wavenumber $\tilde{v}$ $[cm^{-1}]$, of the source light.

$$\omega = \frac{2v}{\lambda} = 2v\tilde{v} \tag{4.4.9}$$

In this way, each sampled frequency represents a unique wavelength. A given ω is converted into the corresponding λ through a mathematical function called Fourier Transform. By convention, the acquired FT spectra are always expressed as a function of the wavenumber $\tilde{v}$. For a monochromatic light source the Fourier Transform reads

$$I(\delta') = I_0 \cdot cos(2\pi\omega t) \tag{4.4.10}$$

$$I(\delta') = I_0 \cdot cos(2\pi 2v\tilde{v}t)$$

$$I(\delta') = I_0 \cdot cos(2\pi\delta'\tilde{v})$$

Whereas for a polychromatic light source the Fourier Transform has to be integrated over an infinite retardation.

$$I(\tilde{v}) = \int_{-\infty}^{+\infty} I(\tilde{v}) \cdot cos(2\pi\delta'\tilde{v}) \cdot \delta\tilde{v} \tag{4.4.11}$$

$$I(\delta') = \int_{-\infty}^{+\infty} I(\delta') \cdot cos(2\pi\delta'\tilde{v}) \cdot \delta\delta'$$

The spectral resolution of an interferometer, i.e. its ability to distinguish among closely spaced wavenumbers, is given by the maximum retardation achievable by the machine.

$$\Delta\tilde{v} = {\delta'_{max}}^{-1} \tag{4.4.12}$$

A spectrometer with a maximum mirror displacement of $1\ m$, i.e. $\delta'_{max} = 200\ cm$, has a spectral resolution of $\Delta\tilde{v} = 5 \times 10^{-3}\ cm^{-1}$. The measured signal has to be corrected for several errors originating from the physical limits of the machine, in particular the finite δ'_{max} which prevents the Fourier Transform integration towards infinity. This may alter the acquired spectra and distort the band shape. To limit this problem apodization filters are used, i.e. the removal of the tails of the signal at large retardation. This reduces the unwanted effect at the cost of reducing the spectral resolution.

3. Sample. The preparation requires a double polished specimen to improve the probing beam transmission and exactly determine the sample thickness d. A key aspect of FT spectroscopy is that the sample must be thin enough to allow for the transmission of a detectable portion of the probing beam. The polished thickness depends on the optical qualities of the sample. The surface of the sample has to be thoroughly cleaned of any impurities (e.g. glue, dust or epoxy resin), otherwise they will cause light absorption.
4. Detector. Necessary to measure the intensities I_0 and I of the probing beam. Three types of detectors are available:
    - Pyroelectric detectors. Composed of materials that produce electrical charge upon heating (i.e. pyroelectric effect), in this case triggered by the photon absorption. An example of such a material is deuterated triglycinesulfate (DTSG).
    - Semiconducting detectors (i.e. photo diode). This detector is composed of a semiconductor material, which becomes electrically conductive once photon absorption triggers the band gap reduction.
    - Bolometers. These detectors are composed of crystals kept at extremely cold conditions (4 K, liquid He coolers). In a such cold environment, the heat capacity of the crystal is almost 0, therefore the impulse of a few photons it is sufficient to cause a significant rise in temperature.

    The physical limits of detectors may produce errors in the recorded interferogram. In particular, slow electronic response of the detector can cause phase shifts which require phase corrections.

4.4.5. IR Spectroscopy: FTIR Measurements

Fourier-Transform-spectrometers allow to the measurement of the concentrations of light-absorbing species in 4 steps:

1. Background measurements, to determine the intensity of the probing spectrum $I_0(\tilde{v})$ without the interference of the absorbing sample. This is done over a given wavenumber range which depends on the nature of the absorbing phenomenon and on the spectrum of the source light.
2. Sample measurements, to measure the dimmed intensity of the probing spectrum $I(\tilde{v})$ after it interacts with the sample. The acquisition is performed over the same wavenumber range.
3. Calculate the absorption spectra $A(\tilde{v})$ from the two measured intensities $I_0(\tilde{v})$ and $I(\tilde{v})$, see equation **(4.4.6)**. The absorption spectra have to be corrected for the background, and integrated for a meaningful wave-number range.

4. Use of the Lambert-Beer law **(4.4.8)** to calculate the concentration of the absorbing species, provided that the sample thickness d and its absorption coefficient ε is known.

4.4.6. IR Spectroscopy: Polarized Measurements

Further constraints on the source of absorptions can be obtained by performing FT measurements with a polarized light source on oriented samples. Light propagation and light absorption are both vector quantities, which can be described by a second rank tensor (*Nye, 1985*). To describe the full spectrum of the sample, it is necessary to acquire several polarized spectra, the number of which depends on the optical properties of the crystal.

- Cubic crystals are optically isotropic, i.e. their second rank tensor of light propagation/absorption is defined by only one component. Therefore, it is sufficient only one acquisition to characterize cubic minerals. Moreover, the sample can be oriented in any direction.
- Uniaxial crystals have one with optical anisotropy, i.e. their second rank tensor of light propagation/absorption is defined by two components. These crystals require the acquisition of two spectra: one with the polarized beam oriented parallel to the c-axis of the crystal (i.e. optical axis), and the other one oriented perpendicularly to the c-axis.
- Biaxial crystals have two optical anisotropies, and their second rank tensor of light propagation/absorption is defined by three components. These crystals require the acquisition of three spectra, each one polarized along a crystallographic direction: α−spectrum, β−spectrum, and γ−spectrum.

FT measurements with polarized light are extremely useful to determine the atomic environment of a given absorbing species in the crystal lattice. Polarized spectroscopy is often employed to study the orientation (*Libowitzky & Rossman 1997*; *Jacobsen et al., 2005*; *Libowitzky & Beran, 2018*) of the OH^-group hosted in minerals, and to measure the length the $OH \cdots O$ bonds (*Nakamoto et al., 1955*; *Libowitzky, 1999*). These analyses can distinguish the structurally bonded OH^- from that present in grain boundaries and/or mineral inclusions, and to quantify the strength of the OH^- bonding with the crystal lattice.

4.5. Diamond Anvil Cell

In-situ high-pressure investigations can be made by means of the Diamond Anvil Cell (DAC). This tool combines the hardness and the transparency of diamonds to establish high pressure conditions, while simultaneously probing the sample with an electromagnetic radiation (e.g. X-ray, infrared and visible laser light).

The operating principle of a DAC is simple (**Figure 4.5**): two diamonds with a flat top (culet) are aligned along the same vertical axis; the sample is located in the narrow region bounded by the culets, and the high pressure is achieved by squeezing the sample between the two diamond anvils. Contrary to the multi-anvil technique, where the high-pressure is mostly produced by the heavy loads of the press ($10^6\ kg$), the DAC takes advantage of the narrow surface of the culet (typically $\emptyset = 50\text{–}500\ \mu m$). With such small area of application, the force necessary to reach high-pressure conditions is easily produced by mechanically tightening screws.

To maintain quasi-hydrostatic conditions on the sample it is necessary to laterally confine the pressure chamber, and to fill it with a pressure-transmitting medium. Lateral confinement is provided by the use of a metallic gasket (Re), while gas (Ne), liquids (Si-oil, methanol) or solids (NaCl) can be used as pressure-transmitting media. Each pressure-transmitting medium performs differently in maintaining hydrostatic conditions (*Angel et al., 2007*). The use of a given medium is a compromise between avoiding pressure gradients, and minimizing its interaction with the sample or the probing radiation.

The pressure inside the sample chamber is determined by the use of pressure gauges. Some materials show strong pressure-dependency of their physical properties. The most commonly used pressure gauge is the P-induced frequency shift of the ruby $[Al_2O_3{:}Cr]$ R1 fluorescence line (*Forman et al., 1972*). Pressure estimates inside the DAC follows from the pressure-frequency relation reported by (*Mao et al., 1986*):

$$P(\lambda) = \frac{A}{B}\left[\left(1 + \frac{\lambda}{\lambda_0}\right)^B - 1\right] \tag{4.5.13}$$

Where $\lambda\ [nm]$ is the wavelength of the R1 fluorescence line. The parameter λ_0 is the wavelength of the R1 fluorescence at ambient conditions, whereas A and B are pressure-dependent coefficients (e.g. $A = 1920$ and $B = 9.61$, *Dewaele et al., 2008*). During a high-pressure experiment, the collection of the ruby fluorescence spectra is done before each measurement to estimate the current pressure.

The metallic cell that hosts the diamond anvils consists of a piston and a cylinder which slide into each other. Both components are characterized by the presence of a tungsten-carbide (WC) seat where the diamond is glued. Seats allow some manoeuvrability of the diamonds in order to favour the alignment of the culets. The assembly of the DAC is done as follows:

1. Diamonds are glued on the WC seats. In order to maximize pressure generation and reduce the risk of breaking the diamond anvils, it is crucial that the two diamond culets are perfectly parallel to one another. This alignment is achieved when the Newton fringes between the two culets completely disappear.
2. The metal foil that serves as gasket material is pre-indented by squeezing it between the diamonds. In general, the higher the target pressure of the experiment the thinner the gasket. The sample chamber is then obtained by piercing the indentation using a laser or a spark erosion device.

3. The sample is positioned inside the chamber along with the pressure gauge for in-situ pressure determination during the experiment.
4. Loading of the pressure-transmitting medium. Solid and liquid pressure media are easily loaded into the sample chamber using metal needles and syringes respectively. Gas-loading requires particular apparatus and safety measurements (*Kurnosov et al., 2008*). An alternative method for loading gases is cryogenic loading, where gases are first cooled below their condensation temperature and then loaded as liquids into the sample chamber.
5. The chamber is pressurized up to a certain confinement pressure ($\approx 1\ GPa$) to avoid leaks of the pressure-transmitting medium. The DAC is maintained at this pressurized condition, and unloaded only when the experiment is finished.

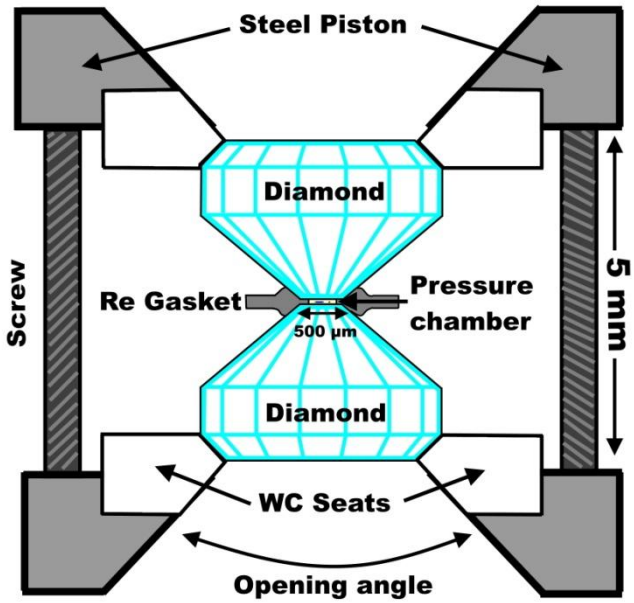

Figure 4.5. Schematics of a diamond anvil cell (modified from *Buchen, 2018* and *Satta, 2020*).

4.6. Time-Domain Thermo-Reflectance

The Time-Domain Thermo-Reflectance (TDTR) is a pump-probe optical metrology to precisely measure the thermal conductivity Λ of materials (*Young et al., 1986*; *Paddock & Eesley, 1986*; *Capinski & Maris, 1996*; *Bonello et al., 1998*; *Taketoshi et al., 2003*). To perform TDTR measurements, the samples have to be coated with $\approx 90\text{-}nm$-thick Al film as a thermal transducer (*Wang et al., 2010*; *Hsieh & Cahill, 2011*).

4.6.1. Instrument

The TDTR technique employs a linearly polarized laser emitted by a mode-locked Ti:sapphire source ($\lambda = 785\ nm$). The laser is split into a pump and a probe component by a polarized beam splitter (see PBS in **Figure 4.6**), with a typical power ratio of $P_{pump}{:}\,P_{probe} = 2{:}\,1$. A mobile retroreflector controls the path of the pump beam, thus generating a time delay t between the two components. The pump beam passes through a long pass filter (785 LP), whereas the probe beam passes through a short pass filter (785 SP). This operation separates the frequencies of the two beams in order to avoid scattering and beam interferences. Two additional beam splitters are positioned at the end of each path in order to reflect the beams toward the sample, and to prevent them from returning to the source on their way back. Once the probe beam hits the Al film, it is back-reflected towards an Si photodiode detector, while the back-reflected pump beam is stopped by an additional 785 SP filter from reaching the detector. The probe beam intensity signal is enhanced by a preamplifier, and recorded by a radio-frequency lock-in amplifier.

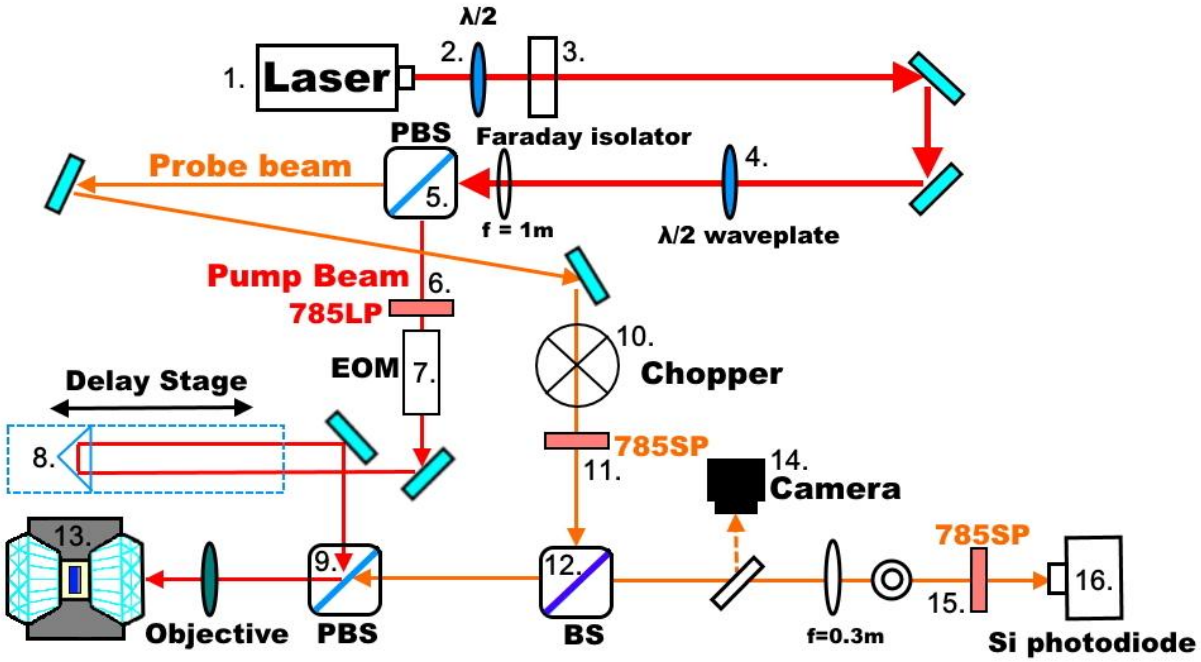

Figure 4.6. A schematic drawing of the TDTR system (modified from *Chao et al., 2018*). (1) Ti:sapphire laser source, (2) $\lambda/2$ waveplate to adjust the power of laser, (3) Faraday isolator to block the reflected beam from returning to the source, (4) $\lambda/2$ waveplate to adjust the polarized plane of light, (5) polarized beam splitter (PBS) to split the beam into pump (PP) and probe (PB) components. Pump beam (PP) path: (6) 785 long pass filter, (7) electro-optical modulator EOM to trigger the beam with 8.7 MHz sampling frequency, (8) delay stage, (9) polarized beam splitter (PBS) to reflect the beam toward the DAC containing the sample (13). Probe beam (PB) path: (10) 200 Hz chopper for double modulation of the PB (*Kang et al., 2008*), (11) 785 short pass filter, (12) beam splitter (BS) to reflect the beam toward the DAC containing the sample (13). Reflected beams path: PBS and BS stop the beams from returning to the source, (14) digital camera to monitor the laser position on the sample, (15) 785 SP short pass to prevent the PP from reaching the photodiode (16).

4.6.2. Thermo-Reflectance

In TDTR measurements, the sample is oriented with the Al coating facing the incoming laser beams, while the target sample is underneath. Typical spot size $\emptyset$ of the laser beam is $\approx 7.5–15\ \mu m$ (*Chao & Hsieh, 2019*; *Marzotto et al., 2020*). An electro-optical modulator EOM chops the pump beam with a frequency of 8.7 MHz. When the pump beam reaches the sample, it starts heating the Al coating which, in turn, converts the incoming thermal energy into changes in its optical reflectivity r_Z. Optical reflectivity describes the amount of energy that is reflected at an interface (media $1 \rightarrow 2$).

$$r_Z = \frac{z_2 - z_1}{z_2 + z_1} \tag{4.6.14}$$

With z_n representing the impedance of the corresponding propagation media, which is given by:

$$z_n = \sqrt{\frac{j\omega\mu}{\sigma + j\omega\varepsilon}} \tag{4.6.15}$$

Where j is the imaginary unity, and $\omega\ [Hz]$ is the angular frequency of the incident wave. The remaining parameters are specific to a given medium: $\sigma\ [S\ m^{-1}]$ is the electrical conductivity, $\mu\ [H\ m^{-1}]$ is the magnetic permeability, and $\varepsilon\ [F\ m^{-1}]$ is the electric permeability.

The temperature variation on the thermal transducer (Al film), causes a perturbation in its electromagnetic parameters (e.g. electrical conductivity *Starrett et al., 2020*), thus generating a change in the reflectivity. This process is called thermo-reflectance (dR_Z/dT).

The reflectivity of the Al film is a critical parameter in the TDTR measurements, since it controls the power absorbed by the metal P_A $[W]$ from the pump beam (*Wang et al., 2010*).

$$P_A = (1 - R_Z)P_{pump} \tag{4.6.16}$$

Typically, in TDTR measurements, the absorbed power is $P_A \approx 1\,mW$ which leads to a temperature increase of $\Delta T < 1\,K$ (*Cahill, 2004*), or up to $\Delta T \approx 10\,K$ (*Chang et al., 2017*). Theoretically, for a perfectly specular surface, it would be possible to measure the reflectivity by directly sampling the reflected pump beam. In practice, however, the rough morphology of the Al surface disperses part of the incident beam power P_{pump}. Therefore, in TDTR measurements, it is of fundamental importance to perform data acquisition on a surface as flat as possible. This is achieved by double polishing the samples to obtain a smooth platelet, and by removing impurities (e.g. glue residues) before coating. The quality of the surface can be monitored by checking the shape of the laser beams recorded by the optical camera.

After the Al layer is warmed by the pump beam, the excess heat is diffused to the underlying sample and to the surroundings. The thermal conductivity of the sample controls the cooling rate of the Al film. This heating-cooling cycle determines variations in the Al reflectivity (dR_Z/dT), which are monitored by the intensity variations of the reflected probe beam. These intensity fluctuations are recorded as a voltage signal $V(t)$ measured by the RF-lock-in amplifier. The voltage signal $V(t)$ and the thermo-reflectance (dR_Z/dT) are related to each other by the equation reported in *Wang et al. (2010)*:

$$\frac{dR_Z}{dT} = \left(\frac{\sqrt{2}}{GQ}\right)\left(\frac{V(t)}{V_0}\right)\left(\frac{R_Z}{\Delta T(t)}\right) \tag{4.6.17}$$

Where G is the gain of the preamplifier, Q is the quality factor of the resonant circuit, and V_0 is the average voltage measured by the photodiode detector. R_Z is the optical reflectivity on the thermal transducer, and $\Delta T(t)$ is the theoretical temperature excursion calculated according to the thermal model described by *Cahill (2004)*. The recorded signal $V(t)$ is converted by the RF-lock-in amplifier into its in-phase $V_{in}(t)$ and out-of phase $V_{out}(t)$ components:

$$V(t) = V_{in}(t) + iV_{out}(t) \tag{4.6.18}$$

4.6.3. Thermal Model

To determine the thermal conductivity of the sample, the ratio $-V_{in}/V_{out}$ is plotted as a function of the delay time t and then fitted with the bidirectional thermal model (*Cahill & Watanabe, 2004*; *Zheng et al., 2007*; *Schmidt et al., 2008*). This model takes into account the heat flow from the Al film into the sample and its surroundings, thus requiring the input of several material parameters: the thermal conductivity Λ_x $[W\,m^{-1}\,K^{-1}]$ and the volumetric heat capacity Cp_x^{vol} $[J\,m^{-3}\,K^{-1}]$ of each layer (i.e., the surroundings, the Al film, the sample), and the thickness of the Al coating h_{Al} $[m]$. Moreover, each layer's thermal effusivity e_x $[J\,m^{-2}\,K^{-1}s^{-1/2}]$ has to be calculated (*Chao & Hsieh, 2019*):

$$e_x = \sqrt{\Lambda_x Cp_x^{vol}} \tag{4.6.19}$$

The thermal effusivity quantifies the rate of heat transfer between two objects that are in contact with each other, but which have different temperatures. The higher the thermal effusivity of the sample, the faster the Al film cools down. The only relevant unknown to be determined from the theoretical model is the thermal conductivity of the sample (i.e. the intercept on the $-V_{in}/V_{out}$ axis).

The TDTR technique can be coupled with DAC experiments to perform high-pressure thermal conductivity measurements on samples (see **Figure 4.7** and *Hsieh et al, 2009*; *Chang et al., 2017*; *Hsieh et al., 2018*; *Chao & Hsieh, 2019*). In the TDTR experiments, the employed pressure-transmitting medium inside the DAC is the Silicone Oil (CAS No. 63148-62-9 from Acros Organics). The Si-oil is not an optimal media for maintaining hydrostatic condition at low pressure (i.e. $P < 50\ GPa$). However, this choice is justified by the exceptionally low thermal conductivity of the Si-oil, even at high pressures, which considerably reduces the measurement uncertainties (*Hsieh, 2015*).

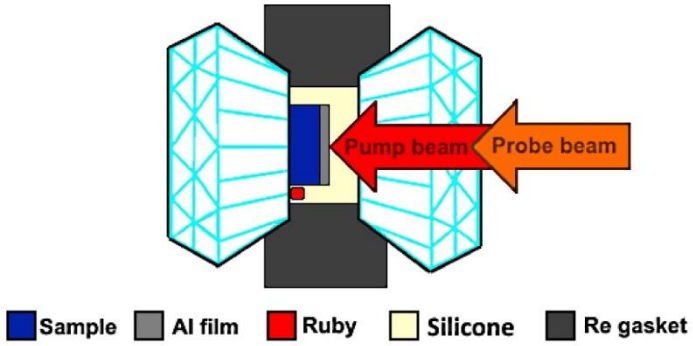

Figure 4.7. A schematic drawing of the DAC assembly for the TDTR measurements (modified from *Hsieh et al., 2009*). The Al coating (grey) serves as a transducer to absorb energy from the pump beam (red) and conduct heat to the sample (blue). Silicone oil (yellow) is the pressure transmitting medium, and the pressure in the DAC is measured by ruby fluorescence (red). The cooling rate is measured through changes in optical reflectivity of the probe beam (orange).

Inside the DAC, the configuration of the thermal model consists of five layers (**Figure 4.8**), each one characterized by a set of material properties:

1. Si-oil ($\Lambda_{Si\ oil}$, $Cp^{vol}_{Si\ oil}$, $e_{Si\ oil}$)
2. Si-oil - Al film interface (interface thermal conductance G_1)
3. Al film (Λ_{Al}, Cp^{vol}_{Al}, e_{Al}, h_{Al})
4. Al film – sample interface (interface thermal conductance G_2)
5. Sample (Λ_X, Cp^{vol}_X, e_X)

The thermal properties of each layer contribute to the total temperature distribution of the model.

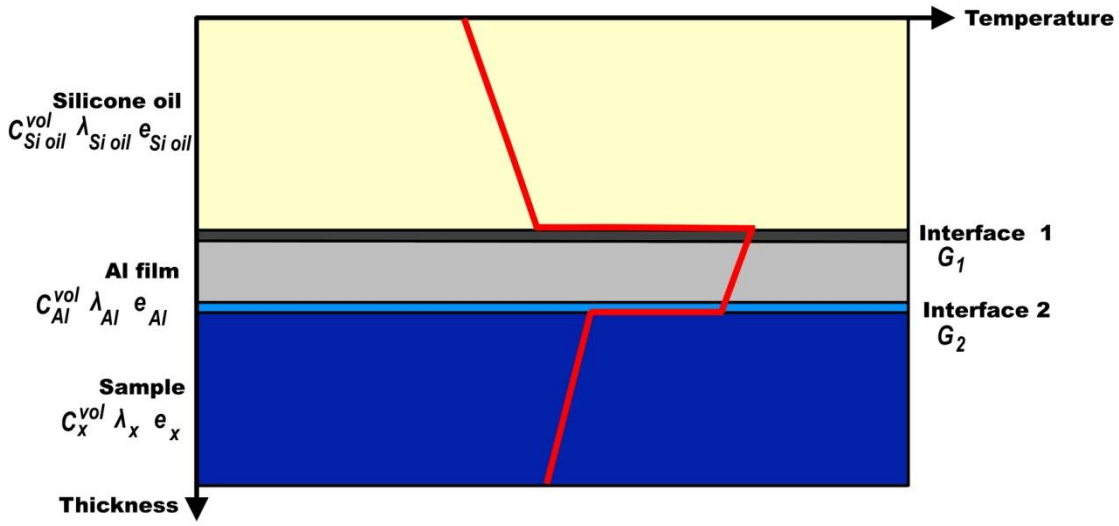

Figure 4.8. Schematics of the five-layers thermal model (modified from *Chao et al., 2018*). The red curve represents the temperature profile inside the DAC after the heating pulse of the pump beam.

4.6.4. Material Properties of the Silicone Oil

The thermal conductivity of Si-oil $\Lambda_{Si\ oil}$ as a function of pressure $[GPa]$ follows the polynomial interpolation from the *Hsieh (2015)* TDTR dataset.

$$\Lambda_{Si\ oil} = (3.39 \times 10^{-13})P^7 - (1.64 \times 10^{-10})P^6 + (3.20 \times 10^{-8})P^5 - (3.21 \times 10^{-6})P^4 + (1.78 \times 10^{-4})P^3 - (5.58 \times 10^{-3})P^2 + 0.12P + 0.18 \quad (4.6.20)$$

In the present study, the volumetric heat capacity of the silicone oil was assumed to be constant over the investigated pressure range $Cp^{vol}_{Si\ oil} = 1.4\ J\ cm^{-3}\ K^{-1}$. This assumption was dictated by the lack of experimental constraints for $Cp^{vol}_{Si\ oil}$ at high pressure.

4.6.5. Material Properties of the Aluminium Layer

The thermal conductivity of aluminium is assumed to be constant $\Lambda_{Al} = 200\ W\ m^{-1}\ K^{-1}$ based on the study performed by *Hsieh et al. (2011)*. Further investigation is necessary to derive a pressure-dependency of Al thermal conductivity. However, this limitation does not affect the TDTR measurements on the sample since the bidirectional thermal model is not significantly influenced by the Al thermal conductivity (*Chang et al., 2017*; *Chao & Hsieh, 2019*; *Marzotto et al., 2020*).

The heat capacity of the aluminium Cp^{vol}_{Al}, however, has a major impact on the calculations, and it requires a thorough constraint. The volumetric heat capacity of Al was estimated by *Hsieh et al. (2009, 2011)* by considering the Debye temperature variations T_{Debye} of Al (*Binnie, 1956*). Above the Debye temperature the heat capacity of most materials follows the Dulong-Petit law, i.e. its value is approximately constant at $Cp^{vol}_{x} = 3R$, where R is the ideal gas constant. Below the Debye temperature, however, the heat capacity is extremely sensitive to temperature variations (*Saxena, 1996*), and it decreases as the temperature decreases. The Debye temperature changes with changing pressure since it depends on the elastic and material properties (i.e. density ρ and volume V) of the object (*Binnie, 1956*). The method used by *Hsieh et al. (2009)* consists of measuring T_{Debye} for Al at high pressures, measuring its specific heat capacity Cp^{sp}_{Al} for the different T_{Debye},

and then calculating the volumetric heat capacity Cp_{Al}^{vol} from the measured Cp_{Al}^{sp}. The pressure-dependence $[GPa]$ of Cp_{Al}^{vol} estimated in (*Hsieh et al., 2009, 2011*) follows the polynomial:

$$Cp_{Al}^{vol} = -\left(3.23 \times 10^{-8}\right)P^4 + \left(5.99 \times 10^{-6}\right)P^3 - \left(4.47 \times 10^{-4}\right)P^2 + \left(1.63 \times 10^{-2}\right)P + 2.44 \quad (4.6.21)$$

The thickness of the aluminium layer h_{Al} at ambient pressure is measured with the picoseconds acoustics method described by *O'Hara et al. (2001)*. This method requires the identification of the echo peak in the time axis t, i.e. the signal produced when the beam is reflected at the interface between the Al foil and the sample. This reflection is caused by the different acoustic impedance ($z_n^A = Vp_n \cdot \rho_n$) between the Al ($\rho_{Al} = 2.7 \times 10^3\ kg\ m^{-3}$) and the sample (typically $\rho_{Silicates} > 2.7 \times 10^3\ kg\ m^{-3}$). Through Brillouin spectroscopy (*Speziale et al., 2014*) it is possible to measure the P-wave velocity of Al, i.e. $Vp_{Al} = 6420\ m\ s^{-1}$. The thickness of the aluminium foil is simply calculated by $h_{Al} = 2t \cdot Vp_{Al}$, where the integer 2 considers the back-and-forth reflection inside the layer. At high pressure, however, the acoustic signal of the aluminium layer becomes too weak to clearly identify the echo peak, and the picoseconds acoustic method cannot be used to estimate h_{Al} anymore. A possible way to measure h_{Al} at high pressure $[GPa]$ is provided by *Chen et al. (2011)* where it was assumed that the Al film adheres well to the sample substrate, and that it deforms plastically to the hydrostatic compression. Under these assumptions, h_{Al} decreases as follows: -3.1% at 5 GPa, -5.5% at 10 GPa, and -7.5% at 20 GPa.

$$h_{Al}\,[\%] = \left[1 + \left(2.87 \times 10^{-6}\right)P^3 - \left(2.11 \times 10^{-4}\right)P^2 + \left(7.84 \times 10^{-3}\right)P - 0.99\right] \cdot 100 \quad (4.6.22)$$

A more accurate estimation requires the measurement of the unit cell volume variations at high pressure through EoS (*Chao & Hsieh, 2019*). This method compares the shortening of the three crystallographic axes of the sample ($a-$, $b-$, $c-$), obtained from the correspondent EoS, with the volume shrinkage of aluminium at high pressure (*Bercegeay & Bernard, 2005*).

$$\rho_{Al} = 2700[(P + 17.77)/17.77]^{0.2222} \quad (4.6.23)$$

Here, P is expressed in $[GPa]$. To apply this method it is necessary to know the crystallographic orientation of the sample with respect to the Al coating.

4.6.6. Thermal Penetration Depth

The thermal penetration depth, i.e. skin depth d_x, is defined as the depth to which the incoming heat wave can penetrate through a certain material, and it depends on the frequency of the thermal perturbation ω.

$$d_x = \sqrt{\frac{2\Lambda_x}{Cp_x^{sp}\rho_x\omega}} \quad (4.6.24)$$

At the modulation frequency of the pump beam (8.7 MHz), the skin depths of the sample d_x and the Si-oil layer $d_{Si\ oil}$, are on the order of a few hundred nanometers (*Hsieh et al., 2009*), therefore the thermal model is insensitive to both parameters (*Chang et al., 2017*; *Chao & Hsieh, 2019*; *Marzotto et al., 2020*).

4.6.7. Thermal Conductance of the Interfaces

The thermal conductance of the interfaces G_1 (Si-oil → Al film) and G_2(Al film → sample) quantify the efficiency of heat flow across the layers (i.e. phonon-phonon transferring). Therefore the higher the G_x the lower the temperature drop at the interface. Typically, G_x increases with rising pressure, given the increasing stiffness of materials. Both parameters are an unknown in the bidirectional thermal model, and they represent the slope of the fitting curve in the $-V_{in}/V_{out}$ versus time plot. Typically, $G_1$and G_2 are estimated by trial and error during data fitting, under the assumption that $G_1 = G_2$. The uncertainties of the thermal conductance estimates have a minor impact on the bidirectional thermal model (*Chang et al., 2017*; *Chao & Hsieh, 2019*; *Marzotto et al., 2020*).

4.6.8. Material Properties of the Sample

The heat capacity of the sample Cp_x^{vol} is essential for determining the target thermal conductivity Λ_x, since it is a relevant parameter for the thermal effusivity calculations, see equation **(4.6.19)**. Typically, the heat capacity has a negligible pressure dependency, and it can be assumed to be constant over the experimental pressure range (*Saxena, 1996*). This assumption is justified by the presence of two competing effects upon compression. When the pressure rises, the number of atoms per unit cell volume increases, causing an increase of the volumetric heat capacity since every atom in the cell contributes to the total Cp_x^{vol}. Concurrently, the pressure rise increases the Debye temperature T_{Debye}, which causes a reduction of the heat capacity carried by each individual atom. These effects cancel out, and the dependency of pressure of Cp_x^{vol} is minor (*Hsieh et al., 2009*; *Chao & Hsieh, 2019*). Nevertheless, for a given sample, it would be more accurate to employ the literature data regarding the pressure evolution of Cp_x^{vol} (*Marzotto et al., 2020*). Moreover, extra care should be taken when TDTR measurements are performed in samples containing impurities (e.g. FeO or H_2O), since in this case the pressure dependency on Cp_x^{vol} can increase significantly (*Bouhifd et al., 2006*). However, the effect of impurities on $Cp_x^{vol}$of a material is typically very small if the concentration of impurities is less than 10% of the atoms in the unit cell (*Fukui et al., 2012*; *Chang et al., 2017*).

4.6.9. Computation of the Thermal Conductivity of the Sample

Once all parameters are defined, it is possible to apply the bidirectional thermal model to calculate the thermal conductivity of the sample Λ_{samp}. The $-V_{in}/V_{out}$ ratio as a function of the delay time t $(90 - 4000\ ps)$, is proportional to the thermal properties of the different layers as can be seen in the equation reported by *Cahill (2004)*.

$$-\frac{V_{in}}{V_{out}} \propto \frac{\sqrt{\Lambda_{Si\ oil} Cp_{Si\ oil}^{vol}} + \sqrt{\Lambda_{samp} Cp_{samp}^{vol}}}{h_{Al} Cp_{Al}^{vol}} \tag{4.6.25}$$

The aforementioned constraints on the parameters ($\Lambda_{Si\ oil}$, $Cp_{Si\ oil}^{vol}$, Cp_{samp}^{vol} , Cp_{Al}^{vol}, h_{Al}) allow for a trial and error procedure to fit the experimental $-V_{in}/V_{out}$ measurements with the interpolation curve (i.e. theoretical thermal model **Figure 4.9**). The variable parameters are represented by the thermal conductance G_1, as well as G_2 (i.e. the slope of the best fit curve), and the sample thermal conductivity Λ_{samp} (i.e. the intercept on the y-axis).

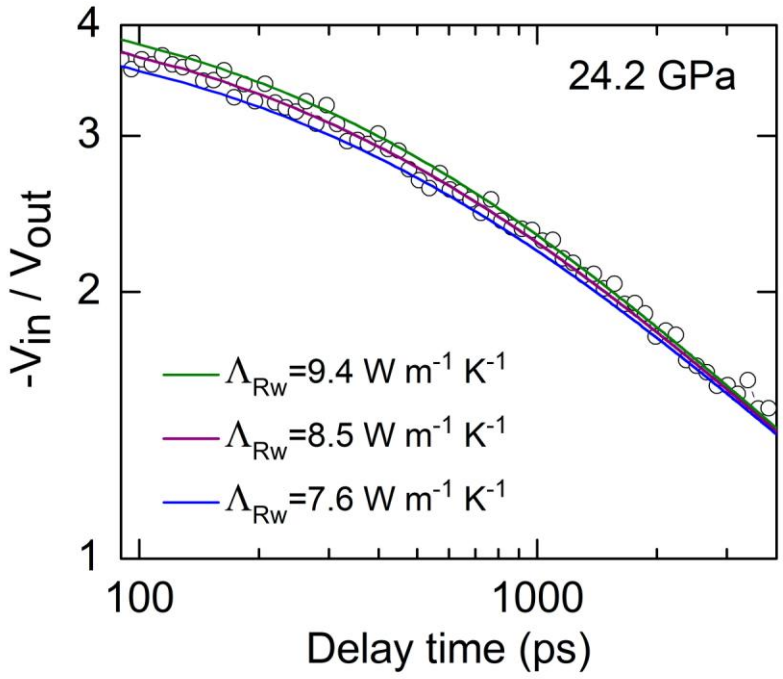

Figure 4.9. An example of TDTR data processing from (*Marzotto et al., 2020*). The measured sample is hydrous ringwoodite with $C_{\mathrm{H2O}} = 1.73\ wt\%$ at $P = 24.2\ GPa$. Open circles indicate $-V_{in}/V_{out}$ ratio, whereas the coloured lines indicate the best fitting curves produced by the thermal model calculations using three different thermal conductivities Λ_{Rw}. The best-fit gives $\Lambda_{Rw} = 8.5\ W\ m^{-1}\ \mathrm{K}^{-1}$. With a 10% variation of Λ_{Rw} (e.g. blue curve, $\Lambda_{Rw} = 7.6\ W\ m^{-1}\ \mathrm{K}^{-1}$ and green curve, $\Lambda_{Rw} = 9.4\ W\ m^{-1}\ \mathrm{K}^{-1}$), the fit curves clearly deviate from the data. This shows the reliability of the bidirectional thermal model to fit the TDTR data collection (*Cahill & Watanabe, 2004*; *Zheng et al., 2007*).

P	Cp_{Rw}^{vol}	Cp_{Al}^{vol}	h_{Al}	$e_{Si\ oil}$	r	$h_{Rw}/h_{Si\ oil}$	Λ_{Al}	$G_1 = G_2$
$[GPa]$	$[J\ cm^{-3}\ \mathrm{K}^{-1}]$	$[J\ cm^{-3}\ \mathrm{K}^{-1}]$	$[nm]^*$	$[\mathrm{J}\ m^{-2}\ K^{-1}s^{-1/2}]$	$[\mu m]$	$[\mu m]$	$[W\ m^{-1}\ \mathrm{K}^{-1}]$	$[MW\ m^{-2}\ \mathrm{K}^{-1}]$
24.2	2.62	2.64	83.6	1478	7.6	25/25	200	400

Table 4.1. Input parameters used to calculate Λ_{Rw} in **Figure 4.9** (*Marzotto et al., 2020*). Ringwoodite volumetric heat capacity Cp_{Rw}^{vol} (*Dorogokupets et al., 2015*), Aluminium volumetric heat capacity Cp_{Al}^{vol} (*Hsieh et al., 2009*), Al layer thickness h_{Al} * (calculated with the method reported in *Chen et al. (2011)* with a thickness at ambient pressure of 92.5 nm), thermal effusivity of Si-oil $e_{Si\ oil}$ (*Hsieh, 2015*), laser spot size r (measured experimentally), thickness of the ringwoodite sample h_{Rw} and of the Si-oil $\mathrm{h_{Si\ oil}}$ (measured experimentally), thermal conductivity of the Al layer Λ_{Al} (*Hsieh et al., 2009*) and thermal conductance of the interfaces $\mathrm{G_1}$ and $\mathrm{G_2}$ (measured experimentally).

4.6.10. Sensitivity Test and Experimental Error

The errors of the TDTR measurements are given by the uncertainty contributions of each parameter of the model. To assess the experimental error, it is necessary to perform sensitivity tests on each parameter of the model (*Chang et al., 2017*; *Chao & Hsieh, 2019*; *Marzotto et al., 2020*). The sensitivity S_α, of a given thermal parameter α is defined as:

$$S_\alpha = \frac{\partial ln\left(-\frac{V_{in}}{V_{out}}\right)}{\partial ln(\alpha)} = \frac{\frac{\Delta\left(-V_{in}/V_{out}\right)}{\left(-V_{in}/V_{out}\right)}}{\frac{\Delta\alpha}{\alpha}} \tag{4.6.26}$$

The purpose of a sensitivity test is to quantify the effect of the variations of α on the thermal model. By imposing $\Delta\alpha$ on the parameter α (e.g. $\Delta\alpha/\alpha = +10\%$), allows to determine the variation of the theoretical voltage in/out ratio (e.g. $\Delta\left(-V_{in}/V_{out}\right)/\left(-V_{in}/V_{out}\right) = +5\%$), which quantifies its sensitivity (e.g. $S_\alpha = 5/10 = 0.5$). This way it is possible to identify the parameter that has the most significant impact on the thermal model. Using $\Delta\left(-V_{in}/V_{out}\right)$ it is possible to calculate the sensitivity of the sample thermal conductivity $S_{\Lambda samp}$, i.e. how much a given parameter contributes to the error on Λ_{samp} estimates.

$$S_{\Lambda samp} = \frac{\partial ln\left(-\frac{V_{in}}{V_{out}}\right)}{\partial ln\left(\Lambda_{samp}\right)} = \frac{\frac{\Delta\left(-V_{in}/V_{out}\right)}{\left(-V_{in}/V_{out}\right)}}{\frac{\Delta\Lambda_{samp}}{\Lambda_{samp}}} \tag{4.6.27}$$

Error propagation is performed by calculating, for each parameter α, the ratio

$$\frac{S_{\Lambda samp}}{S_\alpha} = \frac{\Delta\alpha/\alpha}{\Delta\Lambda_{samp}/\Lambda_{samp}} \tag{4.6.28}$$

Which leads to the equation

$$\frac{\Delta\Lambda_{samp}}{\Lambda_{samp}} = \frac{S_\alpha}{S_{\Lambda samp}}\left(\frac{\Delta\alpha}{\alpha}\right) \tag{4.6.29}$$

Based on this equation, it is possible to calculate the contribution of a given parameter α to the total measurement error $\Delta\Lambda_{samp}$. The total error is given by the root mean square of all parameter contributions:

$$E_\Lambda = \sqrt{\sum\left[\frac{S_\alpha}{S_{\Lambda samp}}\left(\frac{\Delta\alpha}{\alpha}\right)\right]^2} \tag{4.6.30}$$

CHAPTER 5 – Effect of Water on Lattice Thermal Conductivity of Ringwoodite

5.1. Introduction

Ringwoodite is the high-pressure polymorph of olivine which is stable in the lowermost part of the mantle transition zone (MTZ) between approximately $520-660\ km$ depth (*Suzuki et al., 2000*). Ringwoodite is considered to be a Nominally Anhydrous Mineral (NAM) (*Kohlstedt et al., 1996*; *Ohtani et al., 2000*; *Keppler & Smyth, 2006*; *Inoue et al., 2010*), where the water molecules are incorporated into the crystal structure as hydroxyl (*Grüninger et al., 2017, 2018, 2020*). For further details on NAMs see **Chapter 1.6.2**. It is thought that ringwoodite constitutes $\approx 60\ vol\%$ of the ambient MTZ (*Frost, 2008*), and $\approx 80\ vol\%$ of the harzburgitic slab (*Irifune & Ringwood, 1987*). Its abundance, combined with its water solubility of up to $1.5-2\ wt\%$ (*Kohlstedt et al., 1996*; *Ohtani et al., 2000*; *Inoue et al., 2010*), makes ringwoodite a potential water reservoir in the MTZ.

The presence of water in the Earth's interior affects physical and chemical properties of minerals (see **Chapter 1.7**) as well as the solid-state rheology of the convecting mantle (*Karato & Jung, 1998*; *Mei & Kohlstedt, 2000*). Natural samples (*Pearson et al., 2014*; *Tschauner et al., 2018*) and geophysical observations (*Khan & Shankland, 2012*; *Utada et al., 2009*) both suggest that water is probably heterogeneously distributed within the MTZ (see **Chapter 1.8**)

Water can be transported into the Earth's interior through subduction of hydrated oceanic lithosphere (*Faccenda, 2014*). During subduction, the increase of pressure and temperature with depth results in the breakdown of hydrous phases (*Schmidt & Poli, 1998*) and the dehydration melting of the mantle wedge (*Rüpke et al., 2004*). Despite the major dehydration, significant amounts of water may be retained inside the subducted slab and reach the MTZ (*Ohtani et al., 2004*). Once the slab reaches the MTZ, two types of behaviour can be observed (*Goes et al., 2017*): (i) direct slab penetration into the lower mantle (LM), and (ii) slab stagnation within the MTZ. Whichever the case, continuous slab heating could progressively decompose water-bearing phases hosted in the subducted lithosphere, causing local hydration of the MTZ (*Richard et al., 2006*). The amount of water released by the sinking slab into the MTZ depends on its residence time in this region, and on how fast heat transfers through the lithosphere. Typically, the warmer the slab is after its residence in the MTZ, the more water is released. In reverse, with lower slab temperatures, the amount of water retained in its interior will be larger.

The lattice thermal conductivity of minerals Λ_{lat}, is a key parameter that controls the heat transfer in planets interior, and determines their geodynamics evolution (*Zhang et al., 2019*). In particular, to study the thermal evolution of water-bearing slabs, is fundamental to quantify the effects of pressure P, temperature T, and water content C_{H2O} on the Λ_{lat} of hydrous minerals. Recently, *Chang et al. (2017)* reported that the presence of $0.7\ wt\%$ of H_2O causes a 50% reduction of the Λ_{lat} of San Carlos olivine when compared to its anhydrous counterpart.

Despite their importance, the effect of water on the Λ_{lat} of most hydrous minerals remains largely unexplored. The thermal conductivity of ringwoodite, for example, has been investigated experimentally only by few authors (*Hofmeister, 1999*; *Xu et al., 2004*), without particular emphasis on the effect of water on this parameter.

In this chapter, diamond-anvil cell (DAC) experiments have been coupled with ultrafast time-domain thermo-reflectance (TDTR) to determine the P and C_{H2O} dependencies of ringwoodite thermal conductivity, Λ_{Rw}, at MTZ pressures and room temperature. Combining these measurements with finite difference (FD) numerical modelling, shows that the hydration-reduced Λ_{Rw} prolongs the time required to reach thermal equilibrium within a subducting slab, thus enabling temperature-sensitive hydrous minerals to be transported to greater depth. These results demonstrate the importance of hydration on the thermal evolution and fate of descending slabs.

5.2. Sample Synthesis

To synthesize ringwoodite for the thermal conductivity measurements, it is necessary to achieve the high-P and high-T conditions of the lower MTZ (i.e. $\approx 17-24$ GPa; *Ita & Stixrude, 1992*). This environment can be reproduced in the laboratory by means of a multi-anvil apparatus (see **Chapter 4.1**). Ringwoodite with increasing C_{H2O} was synthesized using 1000– and 1200–ton multi-anvil presses at the Bayerisches Geoinstitut (BGI), University of Bayreuth, Germany.

5.2.1. Starting Material and Capsule Preparation

Water-bearing ringwoodite crystals were synthesized starting from San Carlos olivine powder (*Lausen, 1927*; *Ross et al., 1954*; *Kuno & Aoki, 1970*; *Duba, 1972*; *Buening & Buseck, 1973*) and distilled water (*Schulze et al., 2018*). San Carlos olivine is believed to have an $Fe/(Mg+Fe)$ composition closest to the one estimated for the Earth's MTZ (*Irifune & Isshiki, 1998*; *Frost, 2003*; *Frost, 2008*), therefore it is the ideal starting material for this study. Large San Carlos olivine grains ($0.5\ cm$) were selected by considering the homogenous colour and the lack of inclusions. These grains were later crushed and pulverized using an agate mortar and pestle. The grinding process continued for half an hour, until a homogeneous powder was obtained.

The olivine powder was dried overnight at 140 °C, and packed into a 3.5 mm tall capsule with a diameter of 1.2 mm. Capsule material depended on the experimental set up: for dry synthesis the capsule was fashioned from a Re foil, whereas for the wet synthesis a $Pt_{95}Rh_{15}$ capsule was employed. To produce hydrous ringwoodite, $3-10\ wt\%$ of distilled water was added into the capsule. The Re capsule was closed by foil folding and then kept in a vacuum oven at 100 °C to avoid hygroscopic absorption. In the $Pt_{95}Rh_{15}$ capsule, the water was added few hours before the synthesis experiment, and the capsule was sealed by impulse welding to avoid water loss.

5.2.2. Multi-Anvil Synthesis Experiments

Each capsule was slid into an MgO sleeve which was surrounded by a $LaCrO_3$ heater, and a ZrO_2 thermal insulator. The whole assembly was loaded into a $5\ wt\%$ Cr_2O_3–doped MgO octahedron with $10\ mm$ edge length. Mo electrodes were located at both ends of the heater. The ceramic parts of the pressure vessel were heated for more than 3 hours at 1273 K before assembly. Finally, the pressure vessel was positioned in the second-stage of the press, composed of tungsten carbide anvils with 4 mm truncation (ha– $7\%Co$, Hawedia cubes described in *Ishii et al., 2019*).

Dry ringwoodite was synthesized at 22 GPa and 1900 K for 1.25 hours, whereas the hydrous samples were obtained after 3–8 hours at 20–22 GPa and 1600–1700 K (**Table 5.1**). For hydrous synthesis experiments a prolonged heating time was necessary to achieve homogeneity in composition, hydration and grain size due to the lower temperature conditions.

The sample was first compressed to the desired press load and then heated to the target temperature. After maintaining a constant temperature for several hours, the sample was quenched by turning off the electrical power. Temperature was estimated based on empirical power-temperature relations obtained in separate runs.

The resulting hydrous batches contained single crystals of ringwoodite ($> 100\ \mu m$), whereas the dry batch contained a polycrystalline aggregate composed by crystals with a size of a few tens of μm.

Run No.	**[H4850]**	**[S7151]**	**[S7279]**
Capsule material	Re	$Pt_{95}Re_5$	$Pt_{95}Re_5$
Starting material	SCO	SCO + Liq. H_2O	SCO + Liq. H_2O
Pressure [GPa]	22	20	22
Temperature [$°C$]	1600	1300	1400
Heating duration [h]	1.25	8	3

Table 5.1. Synthesis conditions for high-pressure and high-temperature experiments. [H4850] was conducted using the 1000–ton multi-anvil press. [S7151] and [S7279] were conducted using the 1200–ton multi-anvil press. The procedure followed in the synthesis experiments is described in *Schulze et al. (2018)*. All the experiments were performed at BGI. SCO = San Carlos olivine powder.

5.3. Sample Characterization

After the multi-anvil synthesis experiments, the ringwoodite samples were analyzed through: XRD to confirm the quality of the samples; FTIR to measure the water content of each synthesis batch; and EMPA to determine the average chemical composition of the samples. All sample characterization analysis were performed with the instrumentation installed at BGI.

5.3.1. XRD Samples Quality Check

Preliminary selection of ringwoodite crystals from the capsule was based on the clear crystal morphology under an optical microscope. The XRD analyses were performed by employing the Huber four-circle diffractometer installed at BGI (see **Figure 4.3**). This diffractometer is driven by the SINGLE software (*Angel & Finger, 2011*), and equipped with a point detector. The X-ray beam was produced by a Mo-K_α source, operated at 50 kV and 40 mA. Only ringwoodite crystals with a full width at half maximum (FWHM) of $\omega < 0.1\ °$, upon ω-scan rotation, were selected for the thermal conductivity measurements.

5.3.2. FTIR Water Content Estimation

The water content in synthesized ringwoodite samples was estimated by employing the Bruker IFS 120 HR FTIR spectrometer, installed at BGI (see **Figure 4.4**). This instrument is equipped with: a tungsten lamp source ($\tilde{v}$: 4000 – 12500 cm^{-1} peak emission), a Si–coated CaF_2 beam splitter, a Cassegranian reflecting optics, and a liquid nitrogen cooled MCT (Mercury-Cadmium-Telluride) detector (see **Chapter 4.4.3** for details).

From each batch, one representative crystal was selected, and double-side polished to a thickness of $d \approx 15-30\ \mu m$ for the FTIR measurements. The integrated absorbance A_{Int} of the $2500-4000\ cm^{-1}$ spectral range was converted into water concentration C_{H2O} by employing the Lambert-Beer law **(4.4.8)**, with the molar absorption coefficient reported in *Thomas et al. (2015)* $\varepsilon_{Rw} = 106002\ L\ mol^{-1}\ cm^{-2}$, and the density reported by *Ye et al. (2012)* $\rho_{Rw} = 3.563\ g\ cm^{-3}$. For cubic minerals, the integrated absorbance area A_{Int} measured in one crystallographic direction has to be multiplied by three (*Thomas et al., 2015*). The background absorption was corrected by subtracting a spline function, and its interpolation was kept as simple as possible to avoid peak distortion of the absorption bands. Each absorption band was modelled with Gaussian interpolation functions (**Figure 5.1**).

The C_{H2O} of the synthesized batches are: 0.11 $wt\%$ [H4850], 0.47 $wt\%$ [S7151], and 1.73 $wt\%$ [S7279] (see **Table 5.2**, **Figure 5.1**). These measurements typically have $\approx 30\%$ uncertainty (*Thomas et al., 2015*). The interference fringes that characterise the nominally dry spectrum (0.11 $wt\%$ red curve in **Table 5.2**, **Figure 5.1**), cause a 30% uncertainty in the FTIR measurements on the H4850 batch. These interferences are most likely due to the non-ideal sample thickness.

$\varepsilon_{Rw}\ (L\ mol^{-1}\ cm^{-2})$	106002		
$\rho_{Rw}\ (g\ cm^{-3})$	3.563		
Run No.	**[H4850]**	**[S7151]**	**[S7279]**
$A_{Int}\ (cm^{-2})$	71.55	148.05	1088.58
$d\ (cm)$	0.0031	0.0015	0.0030
$C_{H2O}\ (mol\ L^{-1})$	0.218	0.931	3.423
$C_{H2O}\ (wt\%)$	0.11	0.47	1.73
$C_{H2O}\ (wt\ ppm)$	1100(330)	4700(1410)	17300(5190)

Table 5.2. Water content estimates by FTIR analysis. ε_{Rw}: absorption coefficient (*Thomas et al., 2015*); ρ_{Rw}: *r*ingwoodite density (*Ye et al., 2012*); Run No.: synthesis batch; A_{Int} : integrated absorbance area within $2500-4000\ cm^{-1}$ range; d: sample thickness; C_{H2O}: water content. Typically, these measurements have a 30% error (*Thomas et al., 2015*).

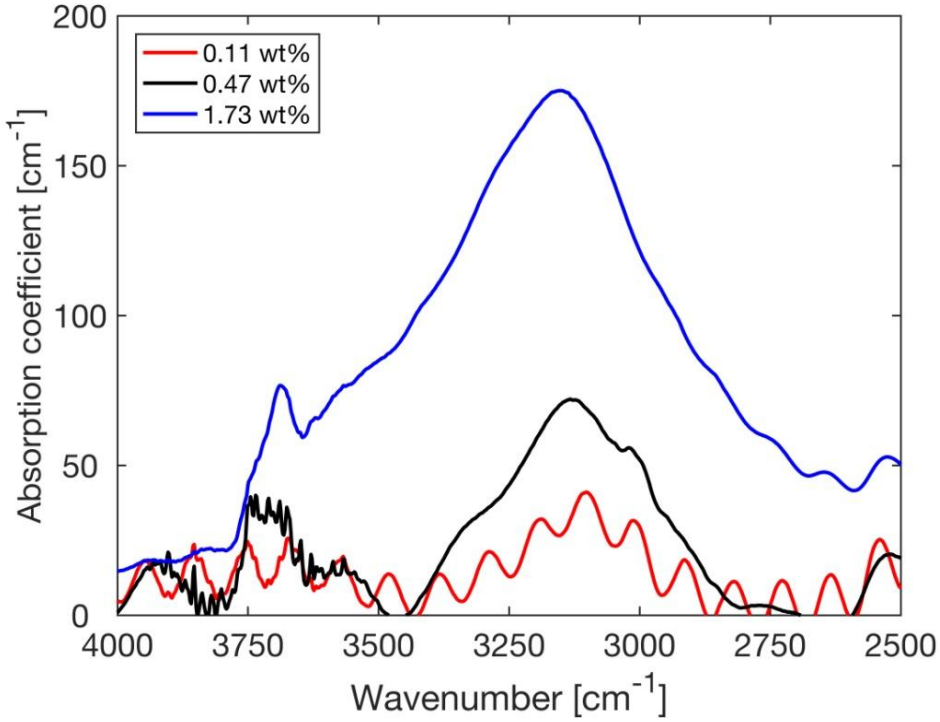

Figure 5.1. Unpolarized FTIR absorption spectra of three representative ringwoodite samples: batch [S7279] (blue line), batch [S7151] (black line) , batch [H4850] (red line). The background absorption was corrected by subtracting a spline function, and the absorption band was modelled with Gaussian interpolation. The peak of absorption at $\approx 3100\ cm^{-1}$ represent the symmetric stretching vibrations of the hydroxyl molecules, whereas the peak at $\approx 3700\ cm^{-1}$ indicates asymmetric stretching vibrations. The integrated absorbance A_{Int} was computed in the $2500-4000\ cm^{-1}$ spectral range. The Lambert-Beer law was applied by considering $\varepsilon_{Rw} = 106002\ L\ mol^{-1}\ cm^{-2}$ (*Thomas et al. 2015*), $\rho_{Rw} = 3.563\ g\ cm^{-3}$ (*Ye et al. 2012*), and the data reported in **Table 5.2**. Ringwoodite is a cubic mineral, therefore A_{Int} was measured in one crystallographic direction and then multiplied by three. The water content estimated with FTIR measurements is representative of the entire batch: $1.73\ wt\%$ [S7279], $0.47\ wt\%$ [S7151], $0.11 wt\%$ [H4850].

5.3.3. EMPA Chemical Analysis

The iron content ($wt\%$ FeO) of ringwoodite samples $(Mg, Fe)_2SiO_4$ was determined by means of EMPA analyses (see **Chapter 4.3**), performed on a JEOL JXA 8200 electron microprobe in BGI. The chemical analyses were performed using a focused ion beam ($1-2\ \mu m\ \emptyset$), with 15 kV of acceleration voltage and a beam current of 15 nA. Prior to measurement, the samples were polished and coated with a $\approx 12\ nm$ carbon film to allow charge dispersion on the surface.

For each sample, the acquisition points were collected along two perpendicular directions in order to establish the chemical homogeneity of the crystals. A minimum of 20 acquisition points were collected for each direction, and the whole sample composition was determined by averaging all the measured points (**Figure 5.2**). The analysis calibration was performed using an olivine standard (Mg, Fe, Si). A summary of the EMPA measurements is reported in **Table 5.3**. The EMPA analysis, shows that the synthesized ringwoodite contains $\approx 8.5\ wt\%$ FeO on average, with a $100MgO/(MgO + FeO)$ value of 91.7. The chemical formula calculated from EPMA data is $[Mg_{1.79}Fe_{0.17}Si_{1.02}O_4]$.

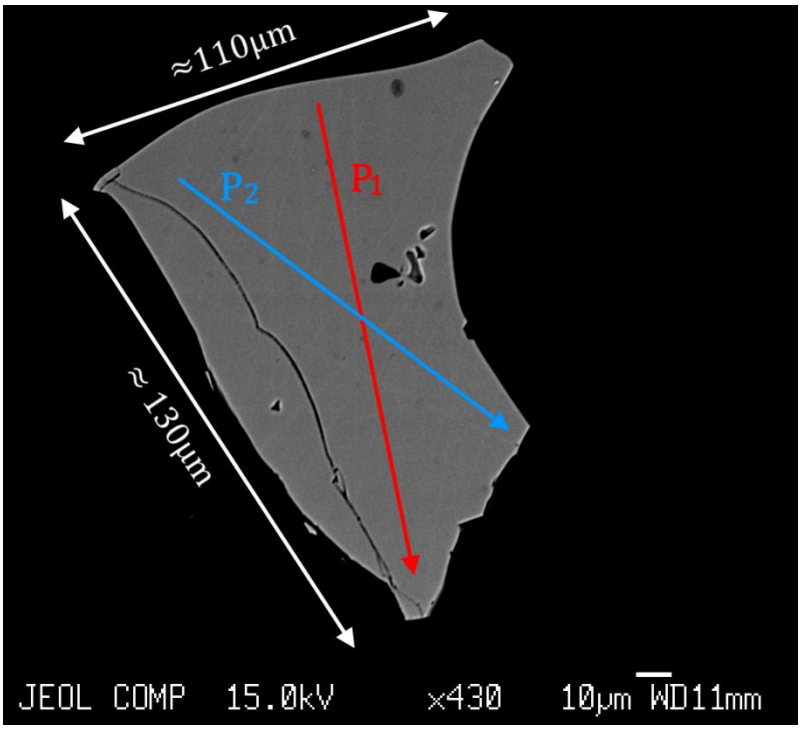

Figure 5.2. Backscattered electron image of the ringwoodite sample S_1, batch [S7151] (0.47 $wt\%$ H_2O). The sample in characterized by grey colours, while the black features inside the crystal represents voids and cracks. The red arrow indicates the acquisition profile $no.1$ (20 acquisition points and 6.33 μm step size), whereas the blue arrow indicates the acquisition profile $no.2$ (20 acquisition points and 6.30 μm step size).

The position of H^+ in the hydrous ringwoodite structure, depends on the $(Mg + Fe)/Si$ ratio. With increasing $(Mg + Fe)/Si$, and increasing water content, hydrogen H^+ is almost exclusively hosted in Mg sites (*Fei & Katsura, 2020*). This is also confirmed by the EMPA measurements for our samples that shows a ratio of ≈ 1.9 (**Table 5.3**).

As reported in *McCammon et al. (2004)*, the $Fe^{3+}/\Sigma Fe$ ratio in ringwoodite is relatively low and stabilizes around ≈ 0.15, even in oxidizing conditions. Moreover, *Schulze et al. (2018)* found almost no correlation between the hydration state of the samples and the measured $Fe^{3+}/\Sigma Fe$ ratio $(0.1-0.18\%)$, even for different capsule materials (Re and Pt). Therefore, the Fe^{3+} content in the synthesized samples was assumed to be homogeneous.

Run No.	**[H4850]**	**[S7151]**			**[S7279]**
Sample	S_1	S_1	S_2	S_3	S_1
Analyzed pt.	83	97	106	40	16
SiO_2 ($wt\%$)	40.99 (0.19)	41.71 (0.46)	42.12 (0.33)	41.79 (0.35)	37.92 (4.73)
MgO ($wt\%$)	49.24 (0.33)	48.54 (0.33)	49.41 (0.47)	49.33 (0.33)	44.54 (5.58)
FeO ($wt\%$)	9.31 (0.39)	8.65 (0.39)	7.44 (0.24)	7.83 (0.20)	5.97 (1.81)
Total	99.54	98.89	98.96	98.94	88.56
$Fe/(Mg + Fe)$	0.096 (0.008)	0.091 (0.008)	0.078 (0.006)	0.082 (0.006)	0.069 (0.004)
$(Mg + Fe)/Si$	1.981 (0.018)	1.908 (0.017)	1.896 (0.015)	1.916 (0.016)	1.882 (0.049)

Table 5.3. Chemical characterization of ringwoodite samples by EPMA. For run [S7151], samples named S_1-S_3 indicate the three crystals used for the thermal conductivity measurements. The standard deviation is reported in brackets for each measurement.

5.4. High-Pressure Lattice Thermal Conductivity Measurements

To perform thermal conductivity measurements, ringwoodite samples were first polished down to $\approx 25\ \mu m$ thickness, and then coated with $\approx 90-nm-$thick Al film as a thermal transducer (see **Chapter 4.6** for details).

5.4.1. Sample Loading in the DAC

In these experiments, the employed DACs follow the BX90 design (*Kantor et al., 2012*), with a piston-cylinder cell characterized by a 90° opening. The DAC were equipped with Ia-type Boheler-Almax diamonds (*Boehler & De Hantsetters, 2004*) with $400\ \mu m$ culet size (Almax easyLab Inc., Massachusetts, USA). The diamonds were glued on the WC seats with an UHU instant-glue (UHU GmbH & Co. KG, Germany).

A $250\ \mu m\ \emptyset$ sample chamber was obtained by drilling the pre-indented Re gasket. Ringwoodite samples ($\approx 100\ \mu m$ across), along with several ruby spheres ($\approx 20\ \mu m\ \emptyset$), were loaded into the sample chamber. Silicone-oil was employed as pressure-transmitting medium (CAS No. 63148-62-9 from Acros Organics). The Si-oil is not an optimal choice for maintaining hydrostatic condition for $P < 50\ GPa$. However, the choice of this media was dictated by its extremely low thermal conductivity, which is a fundamental characteristic for TDTR measurements (*Hsieh, 2015*).

Pressure inside the DAC was estimated by ruby fluorescence (*Mao et al., 1986*), which gives an uncertainty of typically $< 5\%$. The use of several ruby crystals, scattered around the sample chamber, ensured the monitoring of the pressure gradient during the experiment.

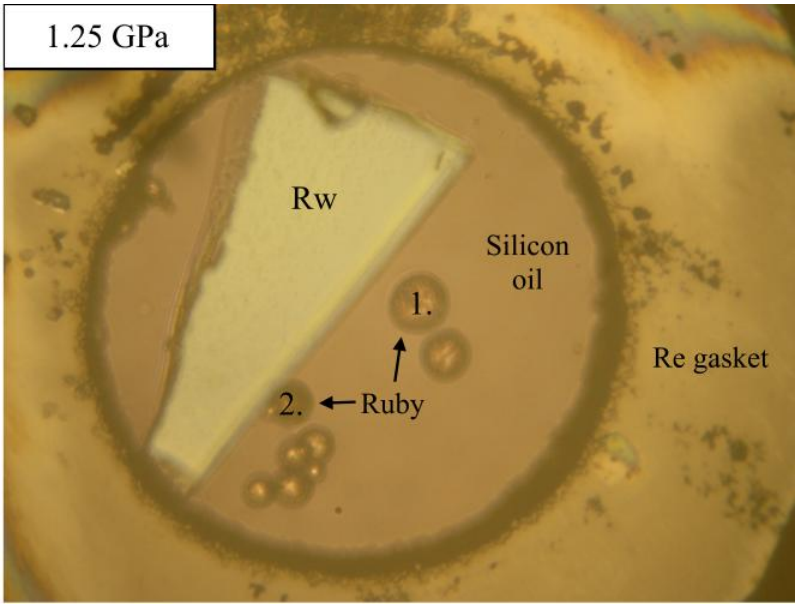

Figure 5.3. Photographic image of the inside of the DAC for the TDTR experiments. The outer annulus indicates the Re gasket, while the inner circle represents the sample chamber filled with silicone-oil as pressure pressure-transmitting medium. The polygonal feature (Rw) represents the ringwoodite sample S_2, batch [S7279] ($1.73\ wt\%\ H_2O$). The round elements on the right side of the sample are the ruby crystals. The pressure estimates were performed on ruby crystals 1 and 2 to monitor the pressure gradient inside the DAC during the experiment. The current pressure inside the DAC is indicated on the upper left corner (i.e. $1.25\ GPa$).

5.4.2. TDTR Measurements

Thermal conductivity measurements were performed by employing the Time-Domain-Thermo-Reflectance method described in **Chapter 4.6**.

To determine the Λ_{Rw}, the ratio output $-V_{in}/V_{out}$, has to be compared with the numerical calculations obtained from a bi-directional thermal model described in **Chapter 4.6.3** (*Schmidt et al., 2008*). This model requires the input of several parameters, i.e. the thermal conductivity Λ_{lat}, the volumetric heat capacity Cp^{vol}, and the thickness h for each layer (silicone oil, Al film, and ringwoodite), while Λ_{Rw} is the only significant unknown and free parameter to be determined.

At ambient pressure, the thermal conductivity of the Al film Λ_{Al} is high ($\approx 200\ W\ m^{-1}K^{-1}$), and its increase at high pressures has a negligible effect on the thermal model calculations. Therefore, Λ_{Al} is assumed to be a constant at high pressures. Pressure dependencies of the thermal conductivity of silicone oil $\Lambda_{Si\ oil}$, and its volumetric heat capacity $Cp_{Si\ oil}$, as well as the volumetric heat capacity of the Al coating Cp_{Al}, were taken from *Hsieh et al. (2009)* and *Hsieh (2015)*.

The ringwoodite volumetric heat capacity Cp_{Rw} was obtained from *Dorogokupets et al. (2015)*. Prior studies have indicated that the effect of impurities on the volumetric heat capacity of a material is typically very small if the impurity concentration is $\leq 10\ at\%$, e.g., *Fukui et al. (2012)* and *Chang et al. (2017)*. Given the relatively small amount of water in ringwoodite (only up to $\approx 9.5\ at\%$ per formula unit), the hydrous Cp_{Rw} was assumed to be equal to the anhydrous one.

The thickness of the Al film h_{Al} at ambient pressure was measured by picosecond acoustics (*O'Hara et al., 2001*). However, the acoustic signal becomes too weak to be used to derive h_{Al} during compression. Thus, the h_{Al} squeezing was estimated by employing the method developed by *Chen et al. (2011)*. Under these experimental conditions, the thermal penetration depths of ringwoodite and silicone oil are both on the order of only few hundreds of nanometers (*Hsieh et al., 2009*). Therefore, the thermal model calculation is insensitive to the thicknesses h_{Rw} and $h_{Si\ oil}$ ($\approx 25\ \mu m$).

Sensitivity tests were performed to determine the error propagation in Λ_{Rw} measurements (see **Chapter 4.6.10**). The heat diffusion thermal model was tested by varying each input parameter (**Figure 5.13**), showing an estimated error of $\approx 10\%$ at $P \leq 15\ GPa$, and $\approx 15\%$ at $15\ GPa < P < 25\ GPa$.

5.5. Experimental Results and Discussion

TDTR measurements were performed at room temperature and high pressures for three different C_{H2O} values: low ($0.11\ wt\%$), medium ($0.47\ wt\%$) and high ($1.73\ wt\%$) (**Figure 5.4**, **Table** 5.6). The ringwoodite stability field ranges between $17-24\ GPa$ (*Ishii et al., 2011*; *Litasov et al., 2006*), and therefore pressure points are closely spaced within this range. For clarity, the Λ_{Rw} for different C_{H2O} are indicated with the symbols $\Lambda_{0.11}$, $\Lambda_{0.47}$, and $\Lambda_{1.73}$.

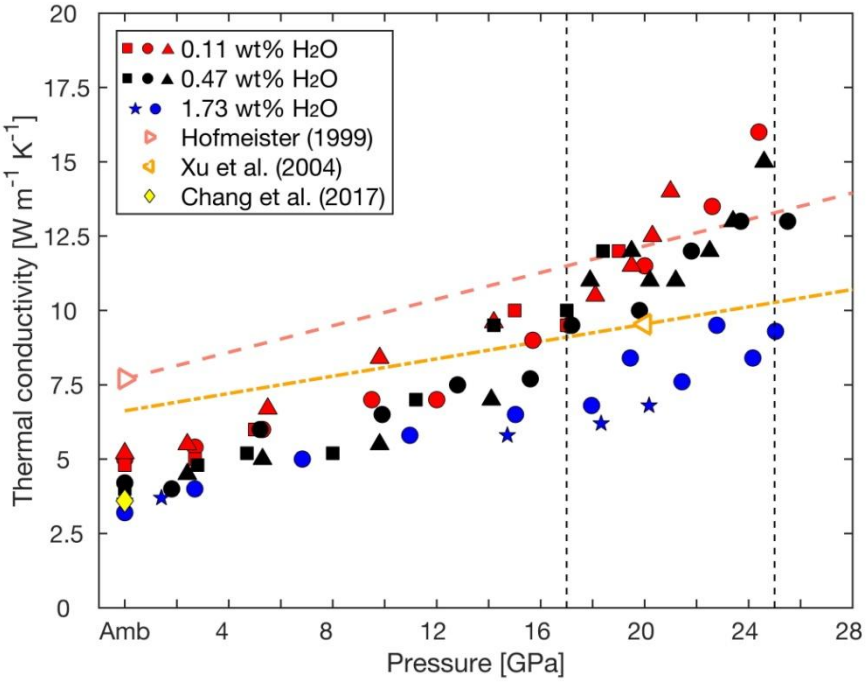

Figure 5.4. Pressure evolution of $\Lambda_{Rw}(P)$ for different C_{H2O} at room temperature ($T = 298\ K$). Each experimental run is identified by a distinct symbol (**Table 5.6**), whereas C_{H2O} is marked by colour: $0.11\ wt\%$ (red), $0.47\ wt\%$ (black), and $1.73\ wt\%$ (blue). Within the pressure range relevant to the lower MTZ (vertical dashed lines), $\Lambda_{1.73}$ is $\approx 40\%$ lower than $\Lambda_{0.11}$. Amb stands for ambient pressure. Literature data for nominally dry Λ_{Rw} are identified by open markers, together with their relative extrapolation (dashed lines). Data by *Chang et al. (2017)* for nominally dry Λ_{Ol} is also plotted for comparison.

5.5.1. Thermal Conductivity of Ringwoodite

At ambient pressure, $\Lambda_{0.47}$ is $\approx 10-15\%$ smaller than $\Lambda_{0.11}$, whereas $\Lambda_{1.73}$ shows a 30% reduction compared to $\Lambda_{0.11}$. Note that the $10-15\%$ reduction observed in $\Lambda_{0.47}$ is comparable to our measurement uncertainty. The incorporation of $1.73\ wt\%$ water, however, clearly shows a detectable difference in Λ_{Rw}, indicating a strong reduction of thermal conductivity due to the hydration effect at ambient conditions. Upon compression, the ratio of $\Lambda_{0.47}$ to $\Lambda_{0.11}$ remains approximately a constant (black curve in **Figure 5.5**). However, the hydration-induced reduction of Λ_{Rw} with $1.73\ wt\%$ water enhances with pressure, reaching $> 40\%$ reduction at the MTZ pressures.

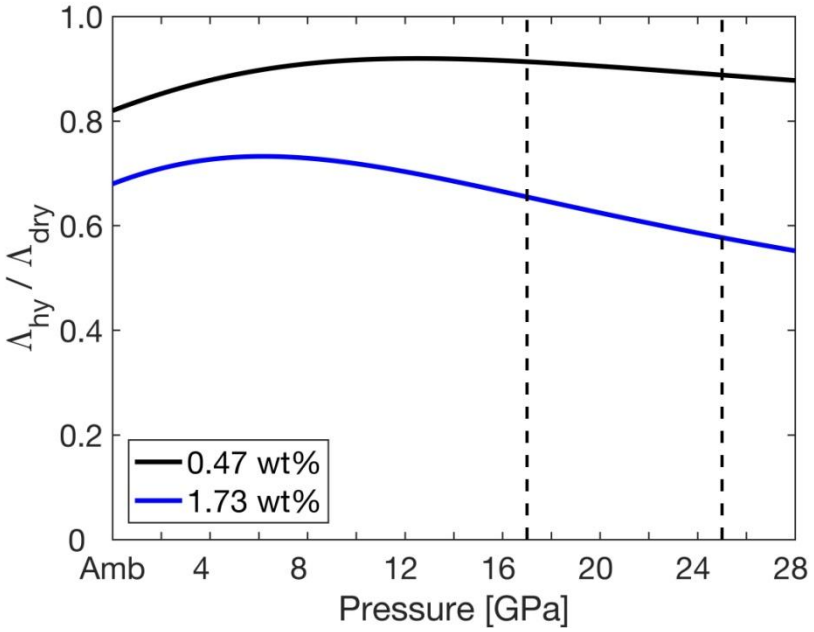

Figure 5.5. The ratio of the $\Lambda_{hy}/\Lambda_{0.11}$ as a function of pressure. The black (blue) curve represents the 0.47 (1.73) $wt\%$ case. Here, $\Lambda_{\mathrm{hy}}/\Lambda_{dry}$ was obtained by taking the ratio of the parameterized curves derived from the TDTR measurements (**Table 5.7**, **Table 5.8**, **Table 5.9**). This plot shows the effect of hydration on Λ_{lat}: with $C_{H2O} = 1.73$ wt% hydrous ringwoodite shows 40% reduction at MTZ pressures. The vertical dashed lines mark the lower mantle transition zone (*Litasov et al., 2006*; *Ishii et al., 2011*).

Note that for the polycrystalline dry samples (batch [H4850], **Table 5.7**), the measured Λ_{Rw} are obtained by averaging several measurements at different locations on the sample probed by the laser with a spot size of 15 μm in diameter. The effect of grain boundaries on Λ_{lat} in our samples should be minor, since the grain size is larger than 10 μm (*Liang, 2017*).

5.5.2. Water-Induced Reduction of Λ_{lat}

In a crystal lattice, heat is transferred by phonons, i.e. quantized vibration waves. These waves represents the elastic re-arrangements of the atoms in a crystal lattice. The lattice heat flux Q_{lat} is proportional to: (i) the number of atoms in the crystal n_a; (ii) the heat capacity of each atoms Cp_a; and (iii) the velocity of the vibration wave v_{ph} (*Chen, 2005*).

$$Q_{lat} \propto n_a Cp_a v_{ph} \tag{5.5.1}$$

Moreover, according to Fourier's Law **(2.5.47)**, the heat flow Q is directly proportional to the temperature difference ΔT between two boundaries, and the lattice thermal conductivity Λ_{lat}, and is while is inversely proportional to the distance between the boundaries Δx.

On a nano-scale level, the inverse proportionality of the heat flux can be explained by considering vibrational velocity of the phonons (*Chen, 2005*), which is given by:

$$v_{ph} = \frac{l_{fp}}{\tau_{fp}} \tag{5.5.2}$$

Where l_{fp} is the phonon's '*mean free path*', and τ_{fp} is the relaxation time, i.e. the length and time in which the phonon can travel without encountering any obstacle (i.e. defects in the crystal lattice).

When a heat carrier phonon interacts with an obstacle its vibrational direction is changed, thus increasing the chances to meet another travelling phonon, and potentially annihilating their respective vibrations. This phenomenon is called thermal resistance, since it hinders heat propagation through a crystal lattice (**Figure 5.6**). From equation **(5.5.2)** it follows that the lattice thermal conductivity Λ_{lat} is proportional to the mean free path l_{fp}:

$$\Lambda_{lat}\frac{\Delta T}{\Delta x} \propto Cp_{vol} v_{ph} l_{fp} \tag{5.5.3}$$

Where Cp_{vol} represent the volumetric heat capacity for the entire crystal lattice (i.e. $n_a Cp_a$). Therefore, the presence of ionic defects results in the pressure-induced suppression of Λ_{lat}.

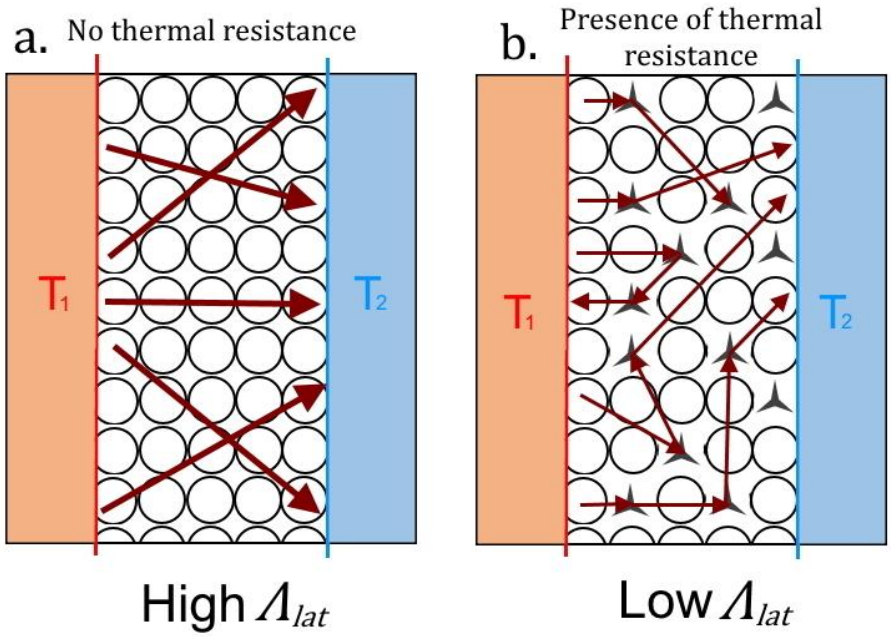

Figure 5.6. Schematics of the nano-scale heat transport. In both images, the left side (a) represents the warm boundary (labelled as T_1 in red), whereas the right (b) represents the cold boundary side (labelled as T_2 in blue). The open white circles indicate the atoms of the crystal lattice, while the grey caltrops indicate the defects in the crystal lattice. The red arrows indicate the phonon mean free paths. The left drawing (a) represents an ideal crystal without defects, with high Λ_{lat}. The right drawing (b) represents a defective crystal, hence with low Λ_{lat}.

Furthermore, from equation **(5.5.3)** it follows that Λ_{lat} increases with pressure P, since it increases the number of atoms per unit volume (i.e. higher Cp_{vol}, see **Chapter 4.6.5**), while it decreases with temperature T, since it increases the vibrational energy of the crystal and, therefore, the chances of phonon collisions (*Xu et al., 2004*).

In ringwoodite, water is incorporated in the form of hydroxyl groups (OH^-) or protons (H^+) which create defects sites by replacing the lattice cations (Si^{4+}, Mg^{2+}, and Fe^{2+}) (*Grüninger et al., 2017*; *Panero et al., 2013*). As pressure increases, the interatomic distance shortens, and these ionic defects may form an interconnected network that acts as an additional phonon-defect scattering mechanism (*Chang et al., 2017*). This effect promotes scattering of thermal energy carriers and further reduces the phonon mean-free-path, thus hindering the thermal energy transport.

A similar effect has been reported for water-bearing olivine (*Chang et al., 2017*). Compared to its effect on sound velocity, where V_P and V_S of ringwoodite decrease only by $\approx 0.25\%$ at $C_{\mathrm{H2O}} = 0.5\ wt\%$ (*Schulze et al., 2018*), the proton weakening has a significant effect on Λ_{Rw}.

5.5.3. Parameterization of Λ_{Rw}

To parameterize the effect of pressure on Λ_{Rw} with different C_{H2O}, the TDTR data (**Table** 5.6-**5.9**) were fitted with a 2^{nd} order polynomial: $\Lambda_{Rw}(P) = qP^2 + lP^2 + \Lambda_0$, where $\Lambda_{Rw}(P)$ is the thermal conductivity at a given pressure, Λ_0 the thermal conductivity at ambient pressure, q and l the quadratic and linear coefficient, respectively. The coefficients for each fit are reported in **Table 5.10**.

A linear interpolation between the parameterized curves (i.e. $\Lambda_{0.11}(P)$, $\Lambda_{0.47}(P)$, and $\Lambda_{1.73}(P)$) was employed to quantify the combined effects of hydration and pressure (**Table 5.10**, **Figure 5.14**). The thermal conductivity of ringwoodite Λ_{Rw}, as function of C_{H2O} and P, can be expressed with the linear equation:

$$\Lambda_{Rw}(C_{\mathrm{H2O}}, P) = a(P)C_{\mathrm{H2O}} + \Lambda_{Dry}(P) \qquad (5.5.4)$$

Where C_{H2O} is the water content in ppm, $a(P)$ the pressure-dependent linear parameter (**Table 5.10**, **Figure 5.15**), and $\Lambda_{Dry}(P)$ the intercept for 0 ppm (**Table 5.10**, **Figure 5.16**).

The pressure dependence of the coefficient a can be described by a 2^{nd} order polynomial: $a(P) = bP^2 + cP + a_0$, as well as $\Lambda_{Dry}(P) = dP^2 + eP + \Lambda_0$. A total of six different coefficients has to be established in order to calculate Λ_{Rw} as a function of C_{H2O} (in ppm) and P (in GPa), see equation **(5.5.5)**, and **Table 5.4**.

$$\Lambda_{Rw}(C_{H2O}, P) = (bP^2 + cP - a_0)C_{H2O} + dP^2 + eP + \Lambda_0 \qquad (5.5.5)$$

a_0	b	c	d	e	Λ_0
9×10^{-5}	-7×10^{-7}	4×10^{-6}	1.37×10^{-2}	1.055×10^{-1}	4.8403

Table 5.4. Coefficients for the water and pressure dependency equation.

This equation describes Λ_{Rw} well within the tested experimental range ($C_{\mathrm{H2O}} = 0\text{–}1.73\ wt\%$; $P = 0\text{–}25\ GPa$), showing $< 7\%$ discrepancy from the TDTR measurements (within experimental errors) (**Figure 5.17-5.20**). Note that equation **(5.5.5)** works on the assumption that C_{H2O} has a progressive effect on Λ_{Rw}, without including any sharp threshold above which the presence of water causes major reduction in Λ_{Rw}. Based on the equation **(5.5.5)**, Λ_{Rw} is 4.84 $W\ m^{-1}K^{-1}$, at $P = 10^{-4}\ GPa$ (1 atm) and $C_{\mathrm{H2O}} = 0$ wt%, whereas it is 12.4 $W\ m^{-1}K^{-1}$ at 20 GPa and 0 $wt\%$ H_2O (**Table 5.4**).

The TDTR estimates reported here are about 40% lower compared to the result obtained by infrared reflectivity measurements of *Hofmeister (1999)* for dry Mg_2SiO_4 ringwoodite. The difference may be due to the difference in FeO content of the ringwoodite, which lowers thermal conductivity of minerals (*Hsieh et al., 2018, 2020*). *Xu et al. (2004)* reported $\Lambda_{Rw} = 9.54\ W\ m^{-1}K^{-1}$ ($C_{\mathrm{H2O}} = 0$ wt%, $P = 20\ GPa$) measured using the in-situ Ångström method. The Λ_{Rw} estimated with equation **(5.5.5)** at the same conditions is 25% higher. *Xu et al. (2004)* report that the olivine thermal conductivity Λ_{Ol} is 30% lower than Λ_{Rw}. This result is coherent with the $\Lambda_{Ol}/\Lambda_{Rw}$ ratio obtained here, when the previous Λ_{Ol} from *Chang et al. (2017)* is used. Note that both measurements were acquired with the same TDTR technique. The discrepancy

between the results of this study and those by *Xu et al. (2004)* might be explained by their experimental techniques, the Ångström method, which relies on proper contacts between thermocouples and sample. In contrast, the TDTR method is based on a non-contact optical technique, avoiding this potential problem and possibly resulting in different Λ_{Rw} values.

5.6. Potential Impact on the Thermal Structure of Subducting Slabs

5.6.1. Hydration of Mantle Transition Zone

In recent years, the amount and spatial distribution of water in the mantle has been under debate (see **Chapter 1** and recent review chapters by *Ohtani, 2020*; *Bekaert et al., 2021*). Understanding the deep Earth water cycle, along with physical properties of hydrous minerals, is essential to understand the long-term evolution of the Earth's mantle. Thermo-petrological simulations performed by *van Keken et al. (2011)* estimated that $1/3$ of the initial slab water content is able to reach MTZ depths. In these models, the preserved water is mainly hosted in the cold inner regions of the slab (e.g., lower crust and upper lithospheric mantle). Following these considerations, it becomes clear that the thermal evolution of the slab determines where and how much water is released during subduction.

Variations in thermal properties of slab minerals might be responsible for the heterogeneous hydration state of different mantle regions. *Chang et al. (2017)* reported that the hydration-reduced thermal conductivity of the crustal materials can induce a low-temperature anomaly in the slab interior. Potentially, this effect might preserve hydrous minerals to be transported to greater depth by maintaining a colder slab core.

The water-bearing phase in a slab located in the MTZ are expected to consist of nominally anhydrous minerals (see **Chapter 1.4.1**) and dense hydrous magnesium silicates (DHMS, see **Chapter 1.4.2**) (*Ohtani et al., 2004*). Once ringwoodite reaches the base of the MTZ, it decomposes into LM assemblage (e.g. *Litasov et al., 2005; Ishii et al., 2018, 2019b, 2019c*), which is expected to host only $\approx 1000\ ppm$ of water (*Litasov et al., 2003*; *Fu et al., 2019*). Due to the release of water around $660\ km$ depth, this decomposition most likely causes major slab dehydration (*Schmandt et al., 2014*). A possible way to deliver water down to the LM is via subduction of DHMS. These phases are stable at high pressure (up to $40\ GPa$), but are extremely sensitive to high temperatures since they decompose at $\approx 1500\ K$ (*Ohtani et al., 2004*); however, so far it remains unclear whether DHMS can reach the LM.

5.6.2. Design of the Numerical Model

A self-written Matlab code was employed to assess the impact of a reduced Λ_{Rw} on a slab's thermal evolution (**Figure 5.7**). The modelled slab stagnates at $660\ km$ of depth, and is progressively heated by the warmer ambient mantle from the upper and lower boundaries. The oceanic lithosphere was assumed to be chemically homogeneous, i.e. monomineralic.

Slab heating was computed by solving the heat diffusion equation **(2.5.47)**, by employing the finite difference (FD) method described in **Chapter 3.3**. For simplicity the model slab was assumed to be one dimensional (i.e. 1D transect), and the domain was discretized using 1169 nodal points, corresponding to a grid spacing of 100 meters.

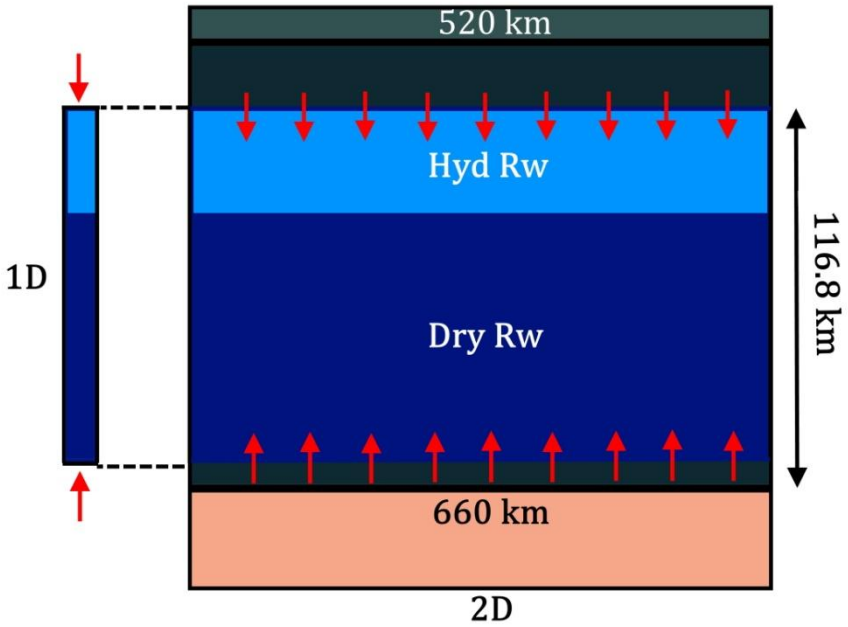

Figure 5.7. Setup for slab heating models. The left column represents a 1D transect of the slab stagnating in the lowermost MTZ (i.e. between 520–660 km depth). The slab is entirely composed of ringwoodite, with a prescribed hydrous layer in the upper part of the slab. Dry ringwoodite (0 $wt\%$ H_2O) is indicated in navy blue colour, while hydrous ringwoodite is indicated in light blue colour. The ambient MTZ is indicated in light grey (410–520 km) and in dark grey (520–660 km). The pink area represents the ambient lower mantle (> 660 km). Red arrows indicate the direction of the heat flux, i.e. from the warm ambient mantle toward the cold slab.

5.6.3. Computation of the Initial Temperature Profile

The initial temperature profile of the stagnating slab was established by performing a three stage calculation: (1) computation of the slab temperature field at the trench; (2) computation of the of the thermal evolution of the subducting slab from the trench down to the MTZ. Stage (3) features the heating of a stagnating slab.

In stage (1), the slab thickness L_{slab} along with its initial temperature profile at the trench, was computed by solving the analytical solution for the half-space cooling (*Turcotte & Schubert, 2014*).

$$L_{slab} = 2.32\sqrt{\kappa_{ol} t} \tag{5.6.6}$$

$$T_x = T_0 + erf\left(\frac{x}{2\sqrt{\kappa_{ol} t}}\right) * (T_{man} - T_0)$$

Where T_0 is the surface temperature (assumed 300 K), T_{man} is ambient mantle temperature (assumed 1600 K; *Katsura et al., 2010*), x is the spatial coordinate, κ_{ol} is olivine thermal diffusivity and t is the slab age (assumed 80 $Myrs$). The average thermal diffusivity κ_{Ol} during this stage was calculated based on literature data for thermal conductivity Λ_{Ol} (*Chang et al., 2017*), density ρ_{Ol} (*Zhang & Bass, 2016*) and specific heat capacity Cp_{Ol} (*Su et al., 2018*) of olivine (**Table 5.12**).

Slab thickness is calculated self-consistently from equation **(5.6.6)**, which gives $L_{slab} = 116.8\ km$. The value of 80 $Myrs$ is considered as the upper limit for the slab thickening by *Stein & Stein, (1992)*. This study reports a major discrepancy between the geophysical measurements of the sea floor depth and heat flux for old slabs ($\geq 80\ Myrs$), and the values predicted by the half-space cooling calculation. Above this critical age and thickness, the deepest and warmest portion of the oceanic lithosphere are characterized by a visco-plastic rheology, potentially dripping off from the rest of the plate. Therefore, 80 $Myrs$ age can be considered as a proxy for a cold old slab.

In stage (2), the slab sinks with a dipping angle of $\theta_{dip} = 60°$ toward the MTZ, assuming a sinking time $t_{\text{sink}} = 10\ Myrs$ (i.e. $v_{\text{sink}} \approx 6\ cm\ yr^{-1}$). This sinking time is comparable to those of several subduction zones, such as North and South Kurile (*Syracuse et al., 2010*). During the descent, the cold slab is progressively heated by the warm ambient mantle, as described by the heat diffusion equation **(2.5.47)**.

$$\rho Cp\left(\frac{\partial T}{\partial t}\right) = \frac{\partial}{\partial x}\left(\Lambda \frac{\partial \mathrm{T}}{\partial x}\right) \tag{5.6.7}$$

Where $\partial T/\partial t$ is the temperature evolution over time, $\partial T/\partial x$ is the local temperature gradient, ρ is the density, and Cp is the specific heat capacity.

Equation **(5.6.7)** was discretized using a central difference with a conservative discretization formulation, see equation **(3.3.12)**. The spatiotemporal discretization employed $\Delta x = 100\ m$ and $\Delta x = 1000\ yrs$ (see **Table 5.12**). The system of equations was solved by employing the implicit discretization scheme and a direct solver, see equation **(3.3.19)**. The boundary conditions at the edges of the domain were imposed as isothermal ($T_{left} = T_{right} = 1600\ K$), see equation **(3.3.21)**. Detailed description of the discretization of the heat diffusion equation is provided in **Chapter 3.3**. Code benchmark is described in section **5.8.5**.

During the descent, adiabatic compression and frictional heating were neglected for simplicity. Therefore, the ambient mantle temperature was set to be at the constant value of $T_{man} = 1600\ K$ at any depth. Complex interactions between the slab and overriding plate at the trench are also neglected. During its descent, the slab crosses two different mantle regions (**Figure 5.8**): the upper mantle ($< 410\ km$), and the upper MTZ ($410-520\ km$). The contribution to the total heat flux given by the latent heat at the phase transition was ignored. The mineralogy of the slab remains constant during the descent (i.e. Λ_{Ol}, ρ_{Ol} and Cp_{Ol}), and it is simply transformed into ringwoodite once it reaches the lower MTZ ($520-660\ km$).

In stage (2), any hydration reduction of Λ was ignored in order to focus on the effect of hydrous ringwoodite in slab thermal evolution in stage (3). The temperature structure of the slab at the end of the descent to the MTZ is shown in **Figure 5.9**, and was used as initial temperature condition for all simulations described below.

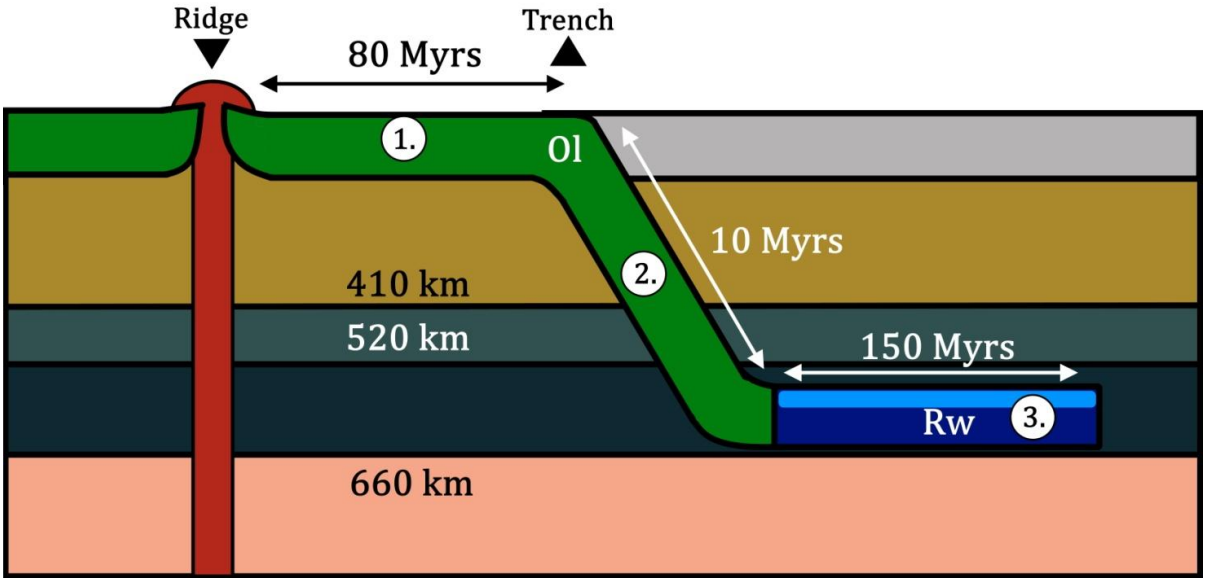

Figure 5.8. Sketch of the basic situation used for the three stage model: (1) half-space cooling of an 80 $Myrs$ old slab (*Turcotte & Schubert, 2014*); (2) slab sinking with sinking time of $t_{sink} = 10$ Myrs (*Syracuse et al., 2010*); (3) slab stagnation with stagnating time of $t_{\mathrm{stag}} = 150\ Myrs$ (*Fukao et al., 2009*). The ambient mantle in (a) and (c) is subdivided into four regions: the upper mantle ($< 410\ km$) in olive green, the upper MTZ in light grey ($410-520\ km$), the lower MTZ in dark grey ($520-660\ km$), and the lower mantle ($> 660\ km$) in pink. At the surface, the oceanic crust is coloured in green, whereas the continental crust is indicated in grey. The upwelling mantle is indicated in maroon, and the location of the mid-ocean ridge is marked by the down pointing triangle. The downwelling slab sinks at the trench (up pointing triangle) after 80 $Myrs$ of cooling. The slab is assumed to be composed of olivine ($0-520$ km of depth), and ringwoodite ($520-660\ km$ of depths). Dry ringwoodite ($0\ wt\%\ H_2O$) is indicated in navy blue colour, while hydrous ringwoodite is indicated in light blue colour.

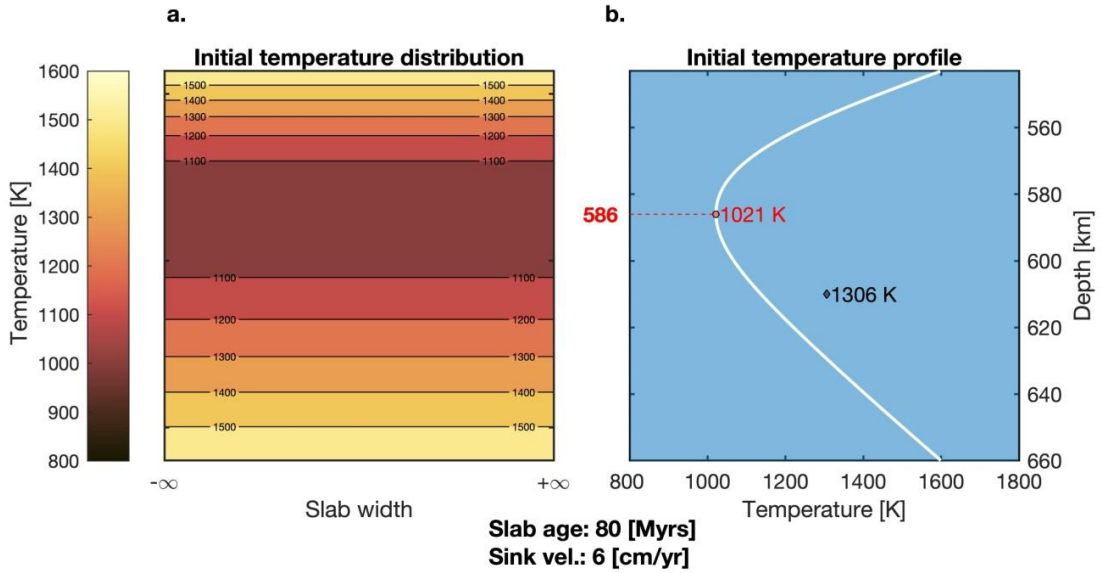

Figure 5.9. (a) Initial temperature distribution of a slab stagnating in the MTZ. Upper and lower boundaries are thermally equilibrated with the ambient mantle. The colour bar employs the scientific colour map '*lajolla*' (*Crameri et al., 2020*) (b) Initial temperature profile (white line) of a 1D transect of the slab. The modelled slab is 80 $Myrs$ old at the trench (116.8 km thick) and has a sinking velocity of 6 $cm\ yr^{-1}$ (10 $Myrs$ to reach 660 km depth). A black diamond indicates the average slab temperature, whereas in red the lowest temperature and its depth are marked.

5.6.4. Thermal Evolution of the Stagnating Slab

In stage (3), the focus is the thermal evolution of a slab stagnating in the lower MTZ ($520-660\ km$). Previous works estimated stagnation times t_{stag} to range from 50 to 140 $Myrs$ (*Zhao et al., 2004*; *Richard et al., 2006*; *Fukao et al., 2009*). Each model was run for 150 $Myrs$ of simulated time, in order to include all the estimates of stagnation age. Such long stagnation time is chosen without considering any slab avalanche phenomena in the models.

At this stage, the slab is assumed to be entirely composed of ringwoodite. Pressure- and water-dependence of Λ_{Rw} were based on the empirical equation derived in section **5.5.3**. In order to properly study thermal evolution of the slab crossing the MTZ it is fundamental to use a P-T-dependent Λ_{Rw} (*Xu et al., 2004*), ρ_{Rw} (*Ye et al., 2012*) and Cp_{Rw} (*Dorogokupets et al., 2015*) to calculate thermal diffusivity κ_{Rw} (see section **5.8.3**). As an approximation, two end-member parameters settings were used in our simulations: one given by the lowest temperature in the slab core ($1021\ K$), and the other given by highest temperature achievable by the slab, i.e. the ambient mantle temperature ($1600\ K$).

The effect of hydrous Λ_{Rw} on the slab's thermal evolution, was reproduced by prescribing a hydrous layer in the uppermost part of the slab. Following the TDTR measurements, this hydrous layer acts as a heat propagation buffer. To simulate the hydrous region, two parameters has been defined: hydrous layer thickness D_{hyd} $[km]$, and its water content C_{H2O} $[wt\%]$. The rest of the slab was considered to be dry.

The oceanic lithosphere reacts with seawater at the mid-ocean ridge (hydrothermal circulation) and in trench-rise systems (*Ranero et al., 2003*). Thus, lithosphere hydration may reach $20\ km$ of depth within the slab (*Green et al., 2010*), and it might extend further down to $40\ km$ depth due to the pressure gradient caused by slab unbending (*Faccenda et al., 2012*). Therefore, the chosen values for D_{hyd} range from 5 up to $40\ km$.

Despite the high-water solubility of ringwoodite of $1.5-2\ wt\%$ (*Inoue et al., 2010*), it is unlikely that such a large amount of water is hosted pervasively in the slab (*Koyama et al., 2006*; *Yoshino et al., 2008*; *Suetsugu et al., 2010*; *Karato, 2011*). Thus, an upper limit of $C_{\mathrm{H2O}} = 1.5\ wt\%$ was applied, which is consistent with the natural ringwoodite sample reported by *Pearson et al. (2014)*.

In this study, a total of 120 simulations has been performed, covering 150 $Myrs$ of slab stagnation in the MTZ. A completely dry slab (i.e. $D_{\mathrm{hyd}} = 0\ km$, $C_{\mathrm{H2O}} = 0\ wt\%$) was employed as the reference case (**Figure 5.10**). Based on these models, it takes $\approx 80-110\ Myrs$ to reach 99% of mantle temperature for a completely dry slab. Complete thermal equilibration is not achieved within the 150 $Myrs$ time span, and the presence of a hydrous layer significantly delays heat propagation.

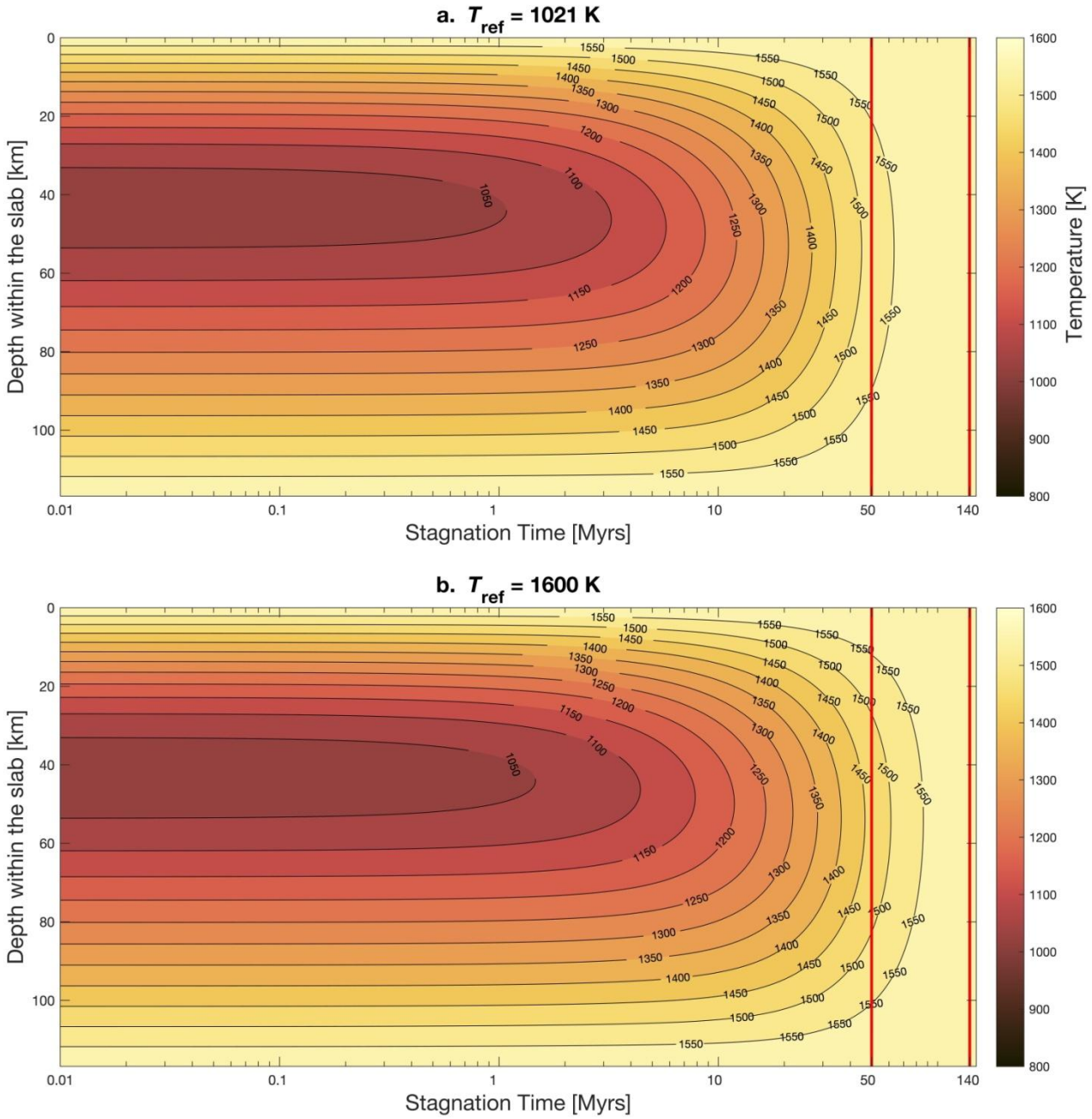

Figure 5.10. Temperature evolution of the reference case assuming a completely dry stagnating slab. Stagnation time is expressed in log units. Each isotherm is labelled with the corresponding temperature in $[K]$. Red lines indicate typical slab stagnation times from literature: 50 $Myrs$ (*Richard et al., 2006*) and 140 $Myrs$ (*Zhao et al., 2004*). Each subplot is based on separate calculations, where thermal diffusivity κ_{Rw} was calculated using end-member reference temperatures: (a) $T_{ref} = 1021\ K$ and (b) $T_{ref} = 1600\ K$. The colour bar employs the scientific colour map '*lajolla*' described in *Crameri et al. (2020)*.

5.6.5. Applications of the Model

The effects of the delayed heat propagation, can be quantified by computing the critical time t_{crit}. This parameter is defined as the time that it takes to reach the critical temperature $T_{crit} = 1500\ K$ at the base of the hydrous layer, assuming that this will mark the complete decomposition of DHMS (*Ohtani et al., 2004*). Moreover, in each simulation the delay time t_{delay} was computed as: $t_{\text{delay}} = t_{crit}^{hy} - t_{crit}^{dry}$. Where t_{crit}^{hy} is the critical time for hydrated slabs, and t_{crit}^{dry} is the time it takes to reach T_{crit} at the relevant depth inside a completely dry slab (**Figure 5.11**, **Table 5.13–5.14**).

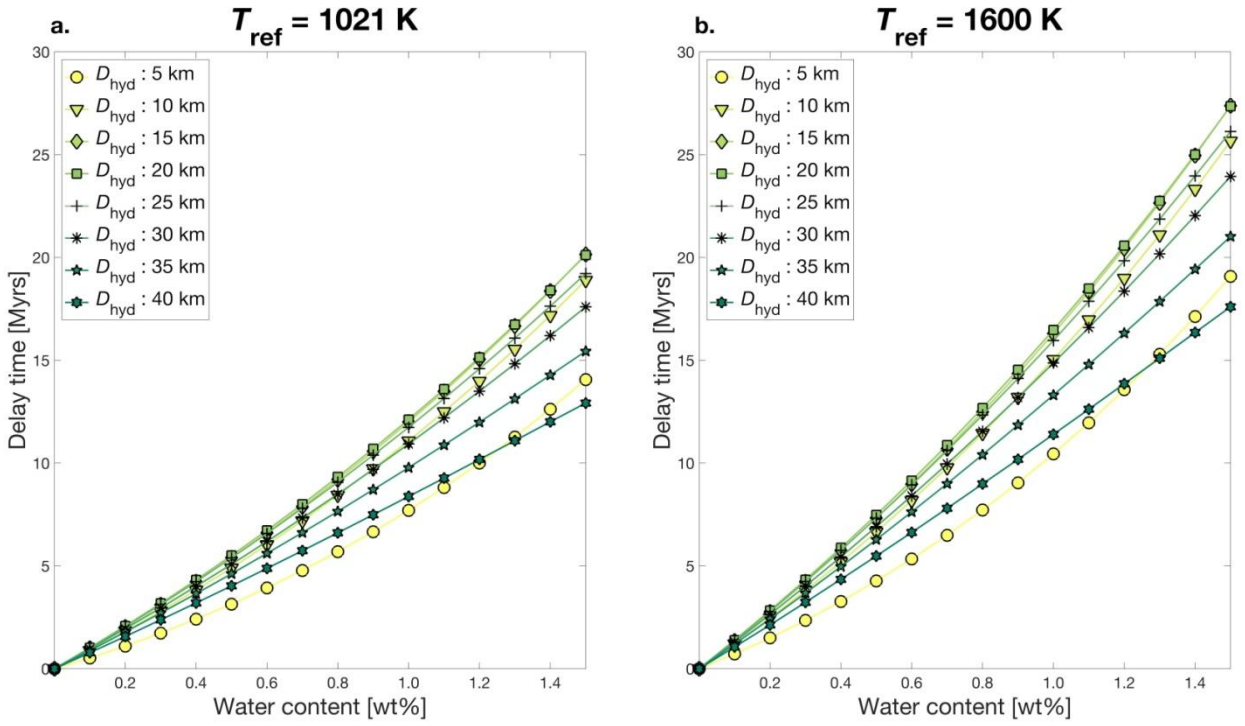

Figure 5.11. Comparison of delay time for different D_{hyd} and C_{H2O} combinations assuming $T_{crit} = 1500\ K$. Each subplot is based on a separate set of models where thermal diffusivity κ_{Rw} was calculated using end-member reference temperatures: (a) $T_{ref} = 1021\ K$ and (b) $T_{ref} = 1600\ K$.

The most pronounced delay can be observed for $15\ km < D_{hyd} < 20\ km$, reaching its maximum at $C_{\text{H2O}} = 1.5\ wt\%$ ($t_{delay} = 20–27\ Myrs$). *Fei and Katsura (2020)* reported that ringwoodite water solubility at MTZ temperatures ($1950–2000\ K$) is $\approx 0.8–1.2\ wt\%$. For a hydrous layer of $15–20\ km$ thickness containing $0.8–1.2\ wt\%$ water, t_{delay} ranges from 9 to $20\ Myrs$ (**Figure 5.11**). This delay might be crucial to hinder slab heating and DHMS breakdown, allowing them to be transported to greater depth in the LM as even a slowly descending slab with $v_{\text{sink}} = 1\ cm\ yr^{-1}$ (*Van Der Meer et al., 2010*) will sink through the MTZ within $\approx 25\ Myrs$. For a dry slab, the $1500\ K$ isotherm will penetrate to $10–15\ km$ depth within this time frame (**Table 5.13-5.14**). The effect of $1\ wt\%$ water within this layer results in a $12–15\ Myrs$ delay of DHMS breakdown (**Figure 5.11**). The numerical modelling results indicate that the hydrated ringwoodite can have a significant impact on the thermal evolution of descending slabs, and it needs to be taken into account when modelling their thermal structures.

5.6.6. Limitations of the Numerical Models

In the employed 1D geometry, the slab can only be heated from top and bottom, thus the resulting thermal structure is expected to be colder than in 3D geometry. Also, the 1D model considers only an infinitesimally thin transect, whereas a stagnating slab can be thousands of km long. As a consequence, the slab front tip would be warmer than its tail.

Additionally, the contribution of radiative Λ was ignored. For non-opaque materials the total thermal conductivity Λ_{tot} is the combination of the contribution of lattice Λ_{lat} and radiative thermal conductivity Λ_{rad}. The radiative contribution is expected to become important at high temperatures, since it increases with T^3. *Thomas et al. (2012)* measured Λ_{rad} for both dry and hydrous ringwoodite at ambient MTZ conditions (1800 K and at up to 26 GPa) and found that 1 $wt\%$ water content reduces Λ_{rad} of ringwoodite by 40%. This might additionally delay heat transport through hydrous ringwoodite.

Another limitation is that the breakdown of hydrous phases is not considered in the models. When the slab starts to heat up, hydrous ringwoodite should dehydrate, and its Λ_{Rw} should increase. This might lead to a positive feedback mechanism, where the more the slab dehydrates the faster it will lose its water. However, following *Fei and Katsura (2020)*, ringwoodite might retain a significant water content even at ambient MTZ temperatures.

Finally, the presence of oceanic crust at the top of the slab was not considered in the models. Oceanic crust might be significantly dehydrated before MTZ stagnation (*van Keken et al., 2011*), and will be mostly composed of majoritic garnet (*Irifune & Ringwood, 1993*). Due to the lower thermal conductivity of majoritic garnet ($\approx$ 53% lower than Λ_{Rw}) (*Giesting et al., 2004*), the oceanic crust might act as an additional effective heat propagation buffer.

5.7. Conclusions

The effect of water on Λ_{Rw} found in the experiments offers novel insights into the thermal evolution of subducting slabs and the fate of hydrous minerals. A Λ_{Rw} reduction of up to 40% at pressures relevant for the MTZ was determined from the TDTR analysis. The lattice thermal conductivity of ringwoodite Λ_{Rw} was parameterized as a function of water content and pressure. The empirical equation derived in this study, combined with finite difference numerical modelling, shows that a homogenously hydrated layer on top of a slab results in a slower heat propagation through its interior. The delay time caused by the reduced Λ_{Rw} provides a potential water-preserving mechanism that prolongs the lifetime of DHMS, enabling them to be transported into the lower mantle. The hydration-reduced thermal conductivity of ringwoodite and olivine (*Chang et al., 2017*) is expected to be relevant for other water-bearing minerals (e.g., DHMS and wadsleyite). Importantly, the temperature influences not only the stability field of minerals, but also key physical properties, such as density and viscosity. Therefore, including the findings of this study into a more detailed thermo-chemical model would substantially advance the understanding of the thermal evolution of subduction zones.

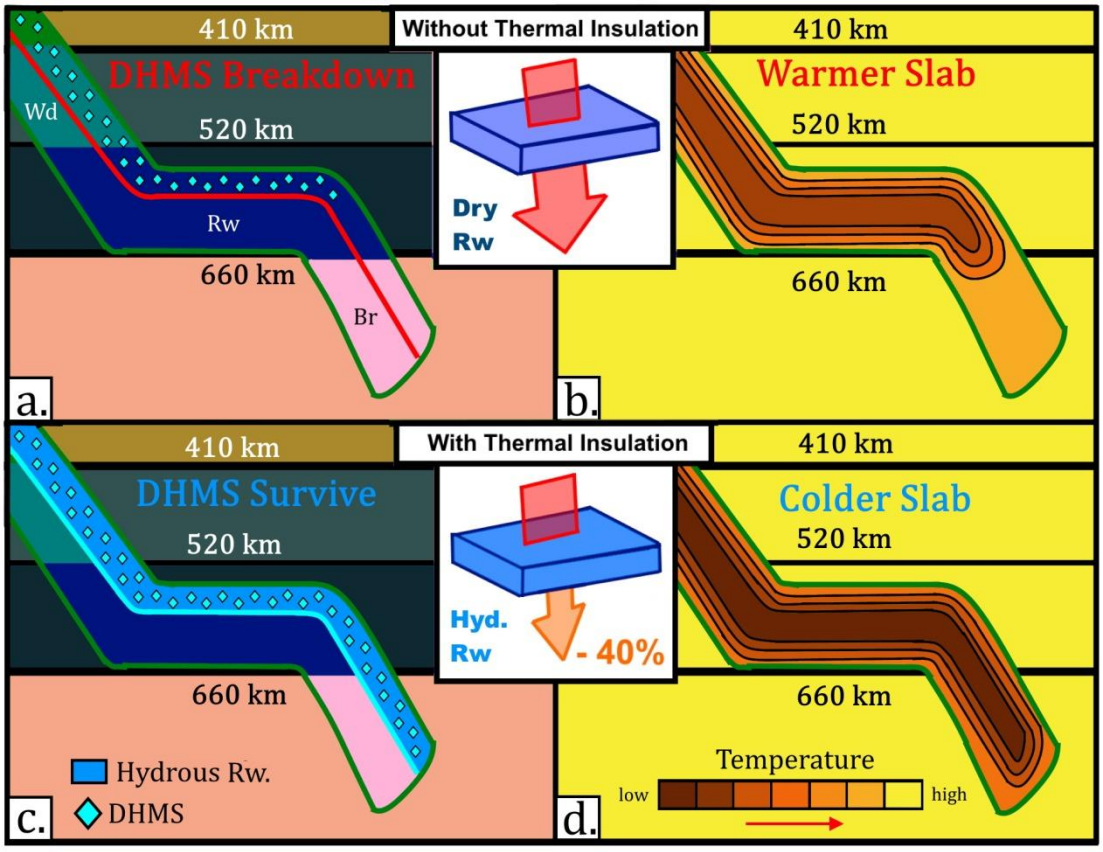

Figure 5.12. The sketch shows the thermal state of a descending slab (outlined in green), crossing the MTZ ($410-660\ km$): left panels (a. and c.) represent the composition field, whereas the right panels (b. and d.) represent the temperature field. The upper panels (a. and b.) show the thermo-chemical state of the slab without the insulation provided by hydrous ringwoodite, while the lower two panels (c. and d.) show the thermo-chemical state of the slab with the insulation provided by hydrous ringwoodite. The ambient mantle in (a) and (c) is subdivided into four regions: the upper mantle ($< 410\ km$) in olive green, the upper MTZ in light grey ($410-520\ km$), the lower MTZ in dark grey ($520-660\ km$), and the lower mantle ($> 660\ km$) in pink. In each region the dominant phase in the slab ($> 80\ vol\%$) is a different polymorph of olivine: olivine (UM, olive green), wadsleyite (U– MTZ, teal), ringwoodite (L– MTZ navy blue), bridgmanite (LM, bright pink). In panel (c) the slab is characterized by the presence of a layer of hydrous ringwoodite (light blue), whereas this layer is absent in panel (a). The red line in panel (a) is drawn to compare the two layers of dry and wet ringwoodite. The cyan diamonds indicate the presence of DHMS in the upper layer of the slab. The colour scale in the right panels (b. and d.) shows the temperature field (T) of the slab and the ambient mantle: bright colours for high T, and dim colours for low T (see '*lajolla*' scientific colour map *Crameri et al., 2020*).

5.8. Appendix

5.8.1. Sensitivity Test

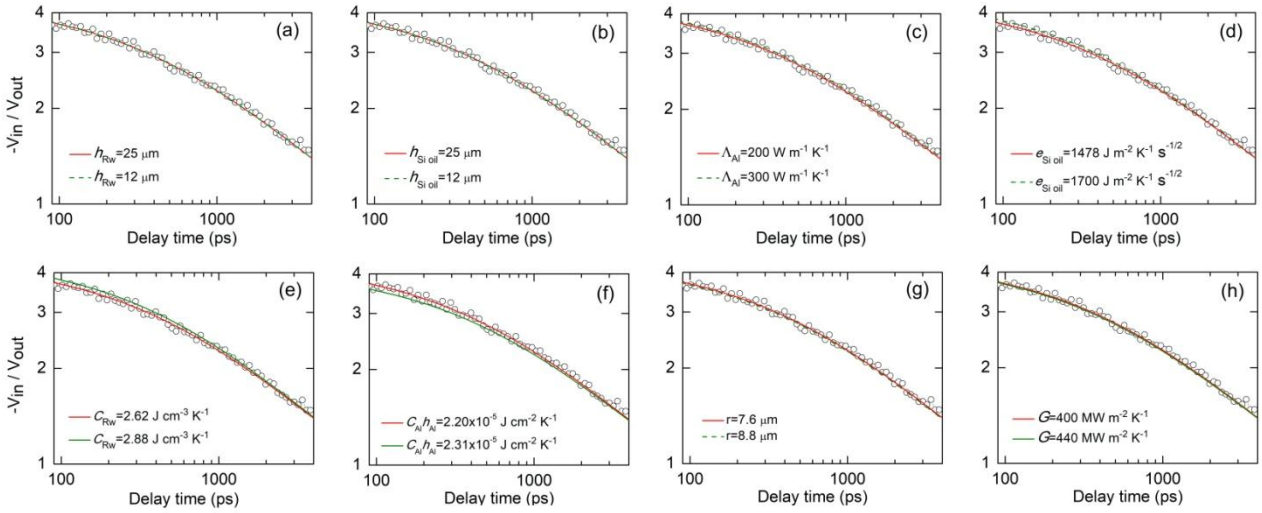

Figure 5.13. Sensitivity test of the heat diffusion model. Here the thermal conductivity is assumed to be constant $\Lambda_{Rw} = 8.5\ W\ m^{-1}\ K^{-1}$. Each subplot shows the influence of a given parameter on the bi-directional thermal model. (a) 50% reduction of the thickness of ringwoodite sample h_{Rw}; (b) 50% reduction of the thickness of the silicone oil layer $h_{Si\ oil}$; (c) 50% higher thermal conductivity of the Al film Λ_{Al}; (d) 15% increase of the thermal effusivity of silicone oil, $e_{Si\ oil}$; (e) 10% increase of the volumetric heat capacity of ringwoodite Cp_{Rw}^{vol}; (f) 5% increase of Al heat capacity per unit area ($Cp_{Al}^{sur} = Cp_{\mathrm{Al}}^{vol} \cdot h_{Al}$); (g) 15% larger laser spot size r; (h) 10% increase in uncertainty of the thermal conductance G_1 and G_2. The model calculations for the tested variations still show almost identical results, indicating that uncertainties of input parameters do not influence the derived thermal conductivity. The parameter that influences the calculated Λ_{Rw} the most is reported in subplot (f), since the ratio $-V_{in}/V_{out}$ shows an inverse proportional relationship with Cp_{Al}^{sur} (*Zheng et al., 2007*).

P	Cp_{Rw}	Cp_{Al}	h_{Al}	$e_{Si\ oil}$	r	$h_{Rw}/h_{Si\ oil}$	Λ_{Al}	G
GPa	$J\ cm^{-3}\ K^{-1}$	$J\ cm^{-3}K^{-1}$	$nm*$	$J\ m^{-2}\ K^{-1}\ s^{-1/2}$	μm	μm	$W\ m^{-1}\ K^{-1}$	$MW\ m^{-2}K^{-1}$
24.2	2.62	2.64	83.6	1478	7.6	25/25	200	400

Table 5.5. Input parameters used to calculate Λ_{Rw} in **Figure 5.13**. Cp_{Rw}: ringwoodite heat capacity (*Dorogokupets et al., 2015*), Cp_{Al}: Al heat capacity (*Hsieh et al., 2009*), h_{Al}: Al thickness (calculated from *Chen et al., 2011*) *In this experimental run, the Al thickness at ambient pressure is 92.5 nm as measured by in situ picosecond acoustics, $e_{Si\ oil}$: silicone oil thermal effusivity (*Hsieh, 2015*), r: laser spot size (measured in this study), h_{Rw}: ringwoodite thickness (measured in this study), $h_{Si\ oil}$: silicone oil thickness (measured in this study), Λ_{Al}: Al thermal conductivity (*Hsieh et al., 2009*), G: thermal conductance of Al/ringwoodite and Al/silicone oil interfaces (measured in this study).

5.8.2. Thermal Conductivity Dataset

0.11 wt% Rw [H4850] – red						0.47 wt% Rw [S7151] - black						1.73 wt% Rw [S7279] - blue			
Sample 1 (square)		Sample 2 (circle)		Sample 3 (triangle)		Sample 1 (square)		Sample 2 (circle)		Sample 3 (triangle)		Sample 1 (circle)		Sample 2 (star)	
P (GPa)	Λ_{Rw} $(W\ m^{-1}\ K^{-1})$	P (GPa)	Λ_{Rw} $(W\ m^{-1}\ K^{-1})$	P (GPa)	Λ_{Rw} $(W\ m^{-1}\ K^{-1})$	P (GPa)	Λ_{Rw} $(W\ m^{-1}\ K^{-1})$	P (GPa)	Λ_{Rw} $(W\ m^{-1}\ K^{-1})$	P (GPa)	Λ_{Rw} $(W\ m^{-1}\ K^{-1})$	P (GPa)	Λ_{Rw} $(W\ m^{-1}\ K^{-1})$	P (GPa)	Λ_{Rw} $(W\ m^{-1}\ K^{-1})$
10^{-4}	4.8	10^{-4}	5.0	10^{-4}	5.2	10^{-4}	4.0	10^{-4}	4.2	2.4	4.5	10^{-4}	3.2	10^{-4}	3.6
2.7	5.0	2.7	5.4	2.4	5.5	2.8	4.8	1.8	4.0	5.3	5.0	2.69	4.0	1.41	3.7
5.0	6.0	5.3	6.0	5.5	6.7	4.7	5.2	5.2	6.0	9.8	5.5	6.83	5.0	14.72	5.8
15.0	10.0	9.5	7.0	9.8	8.4	8.0	5.2	9.9	6.5	14.1	7.0	10.97	5.8	18.33	6.2
17.0	9.5	12.0	7.0	14.2	9.6	11.2	7.0	12.8	7.5	17.9	11.0	15.03	6.5	20.17	6.8
19.0	12.0	15.7	9.0	18.1	10.5	14.2	9.5	15.6	7.7	19.5	12.0	17.96	6.8	–	–
–	–	17.1	9.5	19.5	11.5	17.0	10.0	17.2	9.5	20.2	11.0	19.45	8.4	–	–
–	–	20.0	11.5	20.3	12.5	18.4	12.0	19.8	10.0	21.2	11.0	21.44	7.6	–	–
–	–	22.6	13.5	21.0	14.0	–	–	21.8	12.0	22.5	12.0	22.78	9.5	–	–
–	–	24.4	16.0	–	–	–	–	23.7	13.0	23.4	13.0	24.16	8.4	–	–
–	–	–	–	–	–	–	–	25.5	13.0	24.6	15.0	25.04	9.3	–	–

Table 5.6. TDTR results for each measured sample. 3 batches with 3 different water content were analyzed: $\approx 0.11\ wt\%$ [H4850], $\approx 0.47\ wt\%$ [S7151], and $\approx 1.73\ wt\%$ [S7279]. For each batch 2– 3 crystals were selected for the analysis. Thermal conductivity has been measured for ≥15 pressure points for each batch: [H4850] (25), [S7151] (31), [S7279] (15). In total, 71 measurements have been performed for this study. Uncertainty is ≈ 5% (*Mao et al., 1986*) whereas TDTR measurements have ≈ 10% error ($P < 15\ GPa$) and ≈ 15% ($P \approx 25\ GPa$). Each experimental run is identified by a specific symbol consistently used for every plot presented in this work (**Figure 5.4**, **Figure 5.17-5.18**, **Table 5.7-5.9**).

0.11 wt% ringwoodite [H4850]

P (GPa)	Λ_{Rw} $(W\ m^{-1}\ K^{-1})$
$1 * 10^{-4}$	5.0 ± 0.5
2.4 ± 0.1	5.5 ± 0.6
2.7 ± 0.1	5.0 ± 0.5
2.7 ± 0.1	5.4 ± 0.5
5.0 ± 0.3	6.0 ± 0.6
5.3 ± 0.3	6.0 ± 0.6
5.5 ± 0.3	6.7 ± 0.7
9.5 ± 0.5	7.0 ± 0.7
9.8 ± 0.5	8.4 ± 0.8
12.0 ± 0.6	7.0 ± 0.7
14.2 ± 0.7	10 ± 1
15 ± 1	10 ± 2
16 ± 1	9 ± 1
17 ± 1	10 ± 1
17 ± 1	10 ± 1
18 ± 1	11 ± 2
19 ± 1	12 ± 2
20 ± 1	12 ± 2
20 ± 1	12 ± 2
20 ± 1	13 ± 2
21 ± 1	14 ± 2
23 ± 1	14 ± 2
24 ± 1	16 ± 2

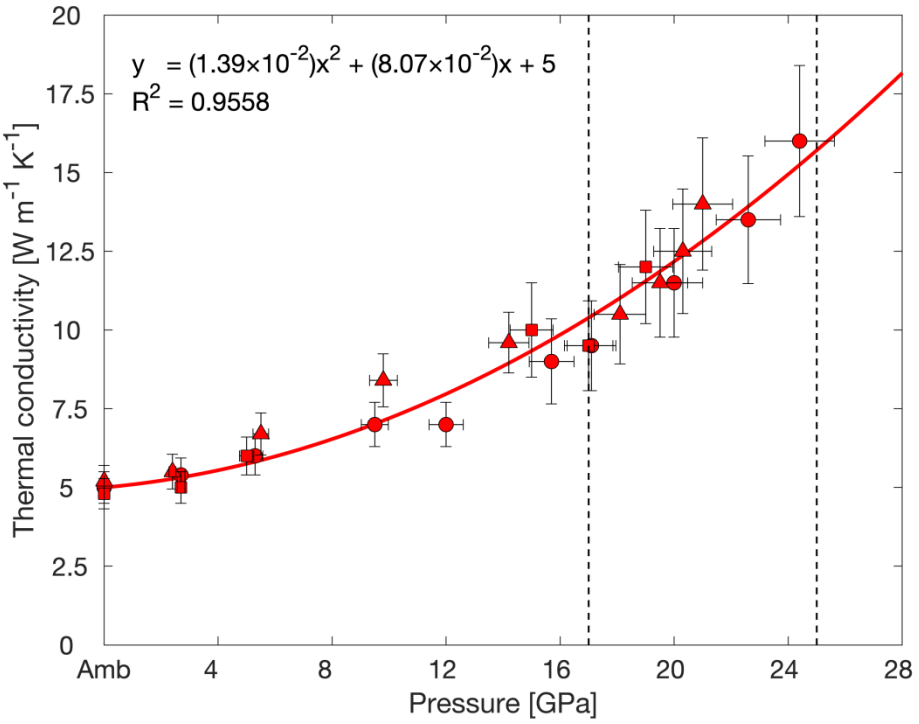

Table 5.7. Pressure dependency of thermal conductivity for $C_{H2O} =$ 0.11 wt%. For this function, all measurements performed for the [H4850] batch have been considered (23 P points). At ambient pressure ($10^{-4}GPa$), Λ_{Rw} is averaged between the ambient pressure contribution of three samples. P-dependency of Λ_{Rw} is well fitted ($R^2 =$ 0.9558) by a 2^{nd} order polynomial: $\Lambda_{Rw}(P) = qP^2 + lP^2 + \Lambda_0$. The red markers represent the actual measurements, the solid line shows the interpolation curve. Different symbols identify a given experiment run (**Table 5.6**). Error bars for each measurement show: 10/15% uncertainties Λ_{Rw}, 5% on the pressure inside the DAC.

0.47 wt% ringwoodite [S7151]	
P (GPa)	Λ_{Rw} $(W\ m^{-1}\ K^{-1})$
$1 * 10^{-4}$	4.1 ± 0.4
1.8 ± 0.1	4.0 ± 0.4
2.4 ± 0.1	4.5 ± 0.5
2.8 ± 0.1	4.8 ± 0.5
4.7 ± 0.2	5.2 ± 0.5
5.2 ± 0.3	6.0 ± 0.6
5.3 ± 0.3	5.0 ± 0.5
8.0 ± 0.4	5.2 ± 0.5
9.8 ± 0.5	5.5 ± 0.6
9.9 ± 0.5	6.5 ± 0.7
11.2 ± 0.6	7.0 ± 0.7
12.8 ± 0.6	7.5 ± 0.8
14.1 ± 0.7	7.0 ± 0.7
14.2 ± 0.7	10 ± 1
15.6 ± 0.8	8 ± 2
17.0 ± 0.9	10 ± 2
17.2 ± 0.9	10 ± 2
17.9 ± 0.9	11 ± 2
18.4 ± 0.9	12 ± 2
20 ± 1	12 ± 2
20 ± 1	10 ± 2
20 ± 1	11 ± 2
21 ± 1	11 ± 2
22 ± 1	12 ± 2
23 ± 1	12 ± 2
24 ± 1	13 ± 2
24 ± 1	13 ± 2
25 ± 1	15 ± 3
26 ± 1	13 ± 2

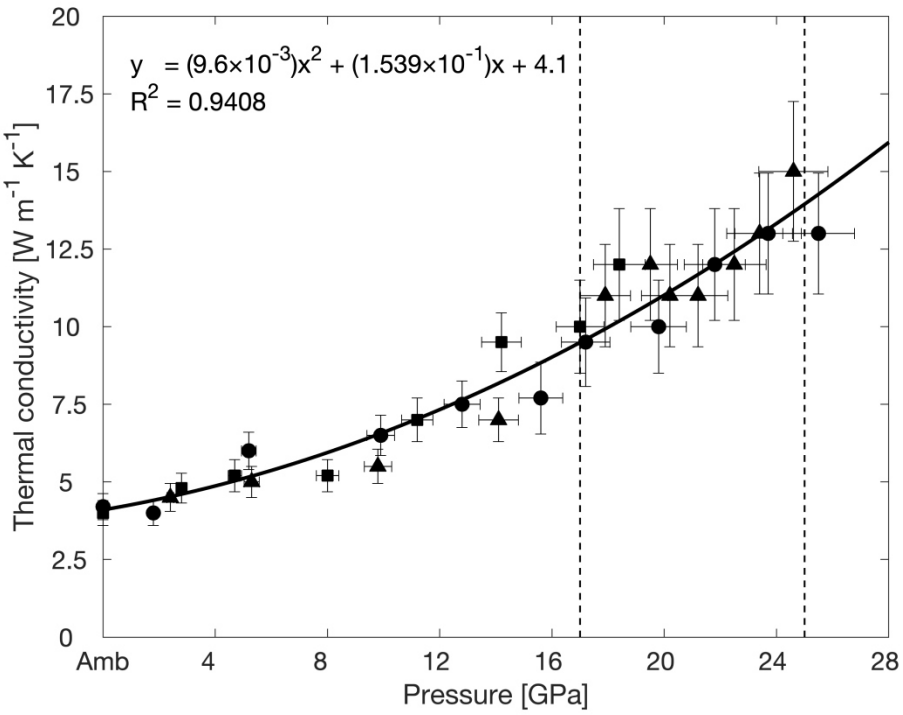

Table 5.8. Pressure dependency of thermal conductivity for $C_{H2O} = 0.47\ wt\%$. For this function, all measurements performed for the [S7151] batch have been considered (29 P points). At ambient pressure ($10^{-4} GPa$), Λ_{Rw} is averaged between the ambient pressure contribution of three samples. P-dependency of Λ_{Rw} is well fitted ($R^2 = 0.9408$) by a 2^{nd} order polynomial: $\Lambda_{Rw}(P) = qP^2 + lP^2 + \Lambda_0$. The black markers represent the actual measurements, the solid line shows the interpolation. Different symbols identify a given experiment run (**Table 5.6**). Error bars for each measurement show: $10/15\%$ uncertainties for Λ_{Rw}, 5% on the pressure inside the DAC.

1.73 wt% ringwoodite [S7279]	
P (GPa)	Λ_{Rw} $(W\ m^{-1}\ K^{-1})$
$1 * 10^{-4}$	3.4 ± 0.3
1.4 ± 0.1	3.7 ± 0.4
2.7 ± 0.1	4.0 ± 0.4
6.8 ± 0.3	5.0 ± 0.5
11.0 ± 0.6	5.8 ± 0.6
15 ± 1	5.8 ± 0.6
15 ± 1	7 ± 1
18 ± 1	7 ± 1
18 ± 1	6 ± 1
20 ± 1	8 ± 1
20 ± 1	7 ± 1
21 ± 1	8 ± 1
23 ± 1	10 ± 2
24 ± 1	8 ± 2
25 ± 1	9 ± 2
-	-
-	-

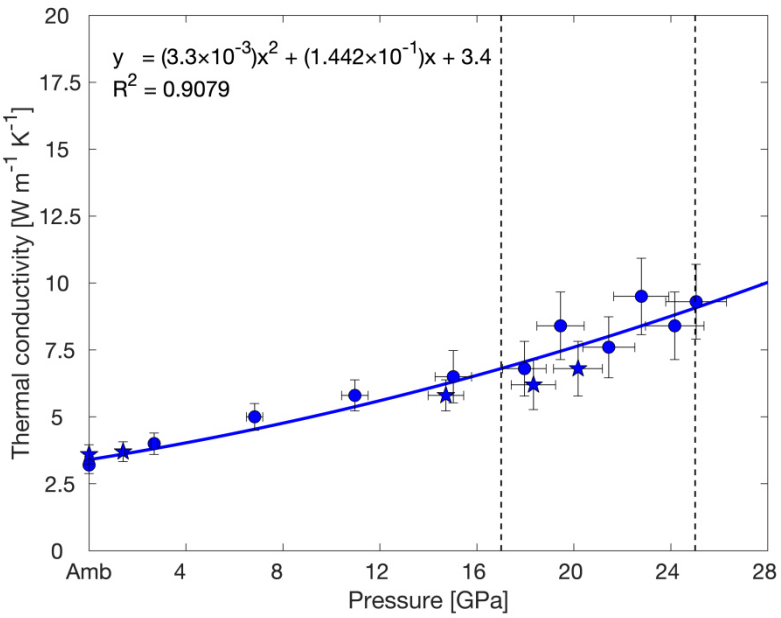

Table 5.9. Pressure dependency of thermal conductivity for $C_{H2O} =$ 1.73 wt%. For this function, all measurements performed for the [S7279] batch have been considered (15 P points). At ambient pressure ($10^{-4}GPa$), Λ_{Rw} is averaged between the ambient pressure contribution of two samples. P-dependency of Λ_{Rw} is well fitted ($R^2 =$ 0.9079) by a 2^{nd} order polynomial: $\Lambda_{Rw}(P) = qP^2 + lP^2 + \Lambda_0$. The blue markers represent the actual measurements, the solid line shows the interpolation. Different symbols identify a given experimental run (**Table 5.6**).Error bars for each measurement show: $10/15\%$ uncertainties for Λ_{Rw}, 5% on the pressure inside the DAC.

5.8.3. Calculation of Water-Dependent Thermal Conductivity

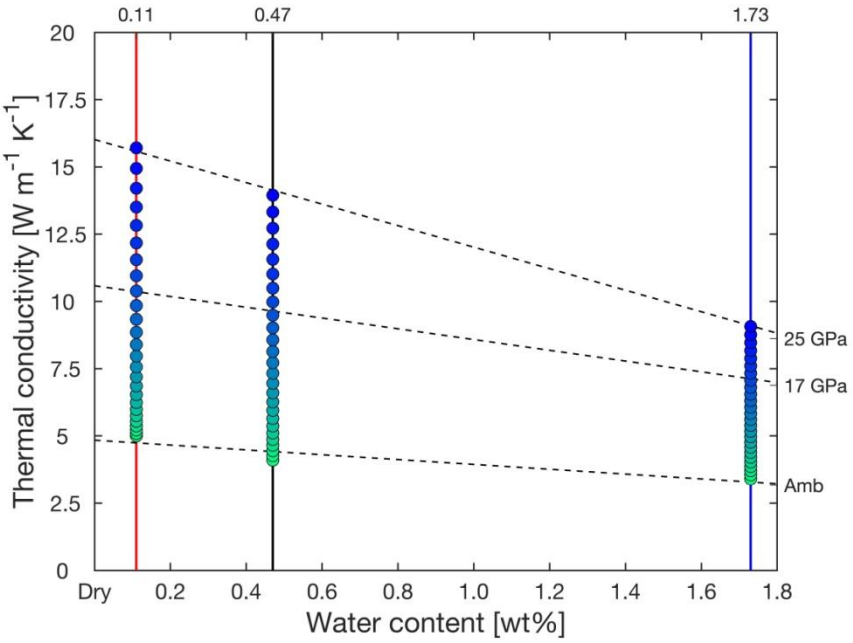

Figure 5.14. Λ_{Rw} for different C_{H2O} (0.11 $wt\%$, 0.47 $wt\%$ and 1.73 $wt\%$) at different pressures (from 0 to 25 GPa). At a given pressure, the relation between Λ_{Rw} and C_{H2O} is described by the equation $\Lambda_{Rw}(C_{H2O}) = aC_{H2O} + \Lambda_{Dry}$. The linear coefficients a and intercept Λ_{Dry} are reported in **Table 5.10**.

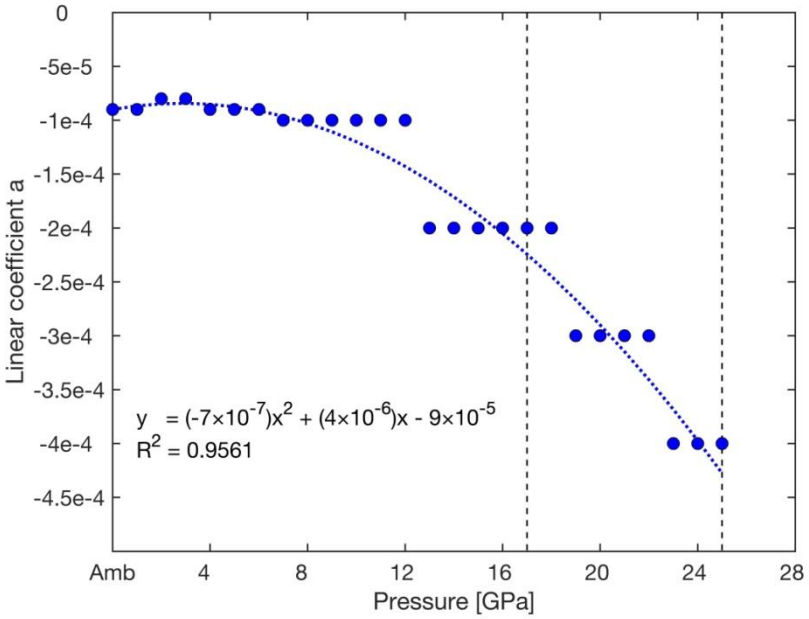

Figure 5.15. Linear coefficients a as a function of pressure. This dependency is described by a 2^{nd} order interpolation curve: $a(P) = bP^2 + cP + a_0$. The linear coefficients a are reported in **Table 5.10**.

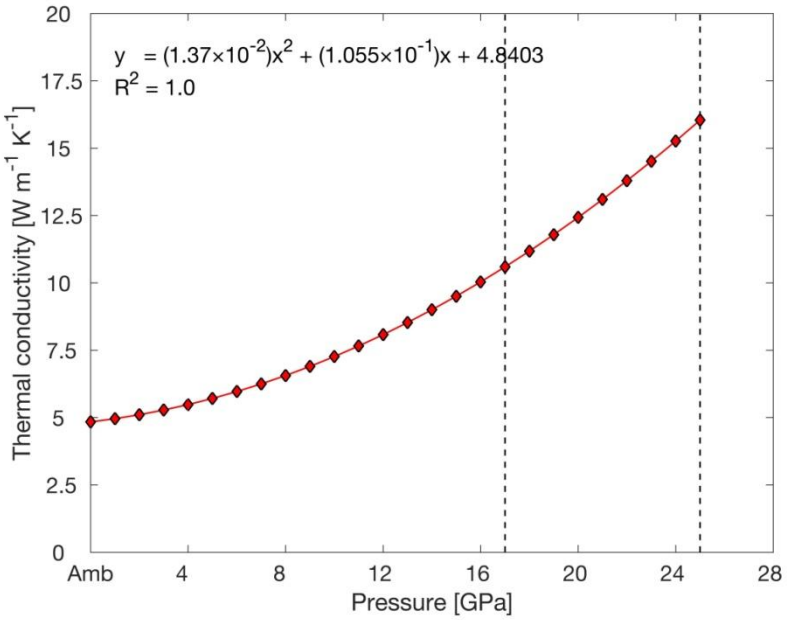

Figure 5.16. Pressure dependency of Λ_{dry} (0 $wt\%$ case, empirically derived). This dependency is described by a 2^{nd} order interpolation curve: $\Lambda_{Dry}(P) = dP^2 + eP + \Lambda_0$. Where Λ_0 is the thermal conductivity of the $C_{H2O} = 0\ wt\%$ case at ambient pressure. The intercept Λ_{Dry} values are reported in **Table 5.10**.

	0.11 *wt*% Rw [H4850]	**0.47 *wt*% Rw [S7151]**	**1.73 *wt*% Rw [S7279]**		**Linear Coefficient**	**Dry Intercept**
$\boldsymbol{P}$ $(\boldsymbol{GPa})$	$\boldsymbol{\Lambda_{Rw}}$ $(\boldsymbol{W\,m^{-1}\,K^{-1}})$	$\boldsymbol{\Lambda_{Rw}}$ $(\boldsymbol{W\,m^{-1}\,K^{-1}})$	$\boldsymbol{\Lambda_{Rw}}$ $(\boldsymbol{W\,m^{-1}\,K^{-1}})$		$\boldsymbol{a}$	$\boldsymbol{\Lambda_{dry}}$ $(\boldsymbol{W\,m^{-1}\,K^{-1}})$
0	5	4.1	3.4		-9×10^{-5}	4.8
1	5.1	4.3	3.5		-9×10^{-5}	4.9
2	5.2	4.4	3.7		-8×10^{-5}	5.1
3	5.4	4.6	3.9		-8×10^{-5}	5.3
4	5.5	4.9	4		-9×10^{-5}	5.5
5	5.8	5.1	4.2		-9×10^{-5}	5.7
6	6	5.4	4.4		-9×10^{-5}	5.9
7	6.2	5.6	4.6		-1×10^{-4}	6.2
8	6.5	5.9	4.8		-1×10^{-4}	6.6
9	6.9	6.3	5		-1×10^{-4}	6.9
10	7.2	6.6	5.2		-1×10^{-4}	7.3
11	7.6	7	5.4		-1×10^{-4}	7.7
12	8	7.3	5.6		-1×10^{-4}	8.1
13	8.4	7.7	5.8		-2×10^{-4}	8.5
14	8.9	8.1	6.1		-2×10^{-4}	8.9
15	9.3	8.6	6.3		-2×10^{-4}	9.5
16	9.8	9.0	6.6		-2×10^{-4}	10.1
17	10.4	9.5	6.8		-2×10^{-4}	10.6
18	11	10	7.1		-2×10^{-4}	11.2
19	11.6	10.5	7.3		-3×10^{-4}	11.8
20	12.2	11	7.6		-3×10^{-4}	12.4
21	12.8	11.6	7.9		-3×10^{-4}	13.1
22	13.5	12.1	8.2		-3×10^{-4}	13.8
23	14.2	12.7	8.5		-4×10^{-4}	14.5
24	15	13.3	8.8		-4×10^{-4}	15.2
25	15.7	13.9	9.1		-4×10^{-4}	16.1

Table 5.10. Columns on the left represent the data retrieved from the 0.11, 0.47 and 1.73 wt% interpolation curves (**Table 5.7-5.9**). The thermal conductivities resulting from the interpolation equations have been used to directly compare each water content dataset at the same pressure (**Figure 5.14**). Columns on the right represent the linear coefficients a and intercept Λ_{dry} for each pressure. The linear coefficient a shows a clear pressure-dependency (**Figure 5.15**). From the Λ_{dry} intercepts, it is possible to derive a pressure-dependent equation for the thermal conductivity (**Figure 5.16**).

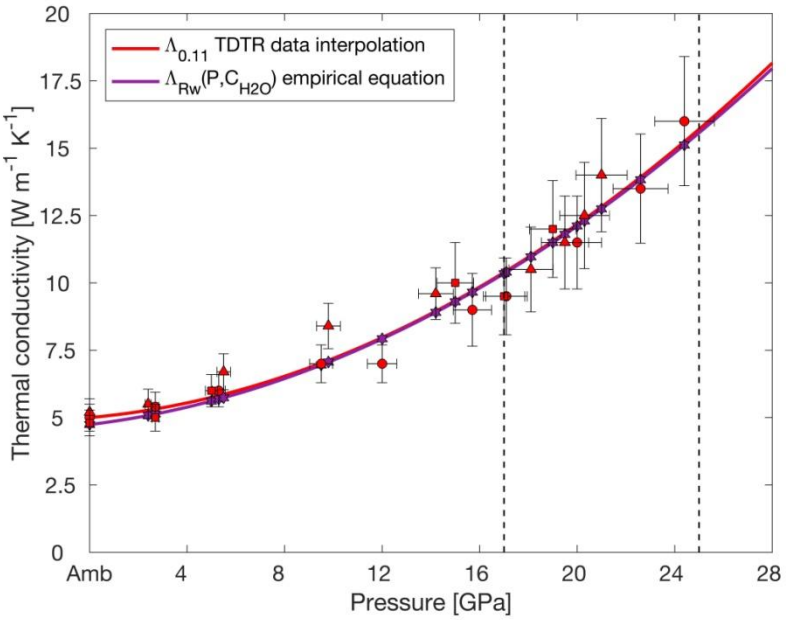

Figure 5.17. Comparison between the $\Lambda_{\mathrm{Rw}}(\mathrm{C_{H2O}}, \mathrm{P})$ equation (purple line) and the $\Lambda_{0.11}$ interpolation curve (red line) (**Table 5.7**). Red symbols indicate measured data (**Table 5.7**) and their respective error bars (10% of the value). Purple symbols indicate values of the water dependency equation at the same pressure as the measured data. Different symbols identify distinct experimental runs (**Table 5.6**).

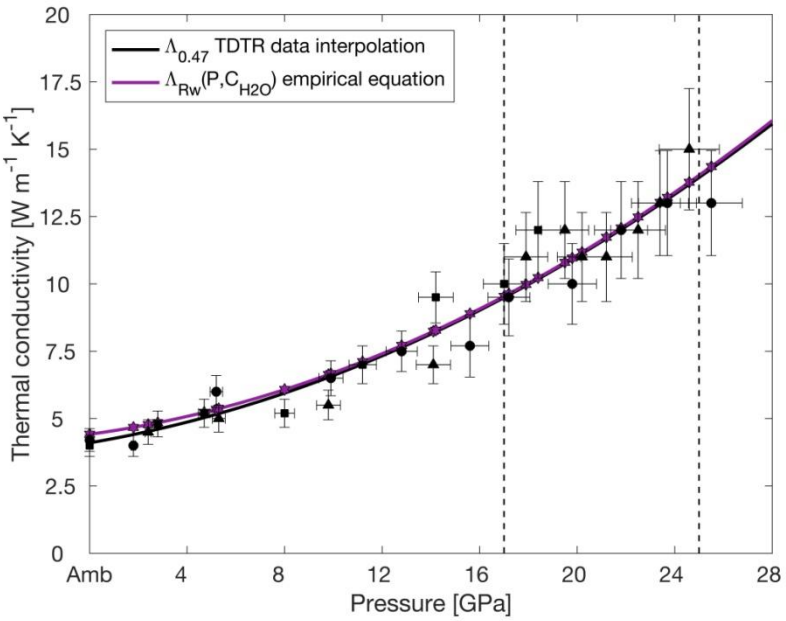

Figure 5.18. Comparison between the $\Lambda_{Rw}(C_{H2O}, P)$ equation (purple line) and the $\Lambda_{0.47}$ interpolation curve (black line) (**Table 5.8**). Black symbols indicate measured data (**Table 5.8**) and their respective error bars (10% of the value). Purple symbols indicate values of the water dependency equation at the same pressure as the measured data. Different symbols identify distinct experimental runs (**Table 5.6**).

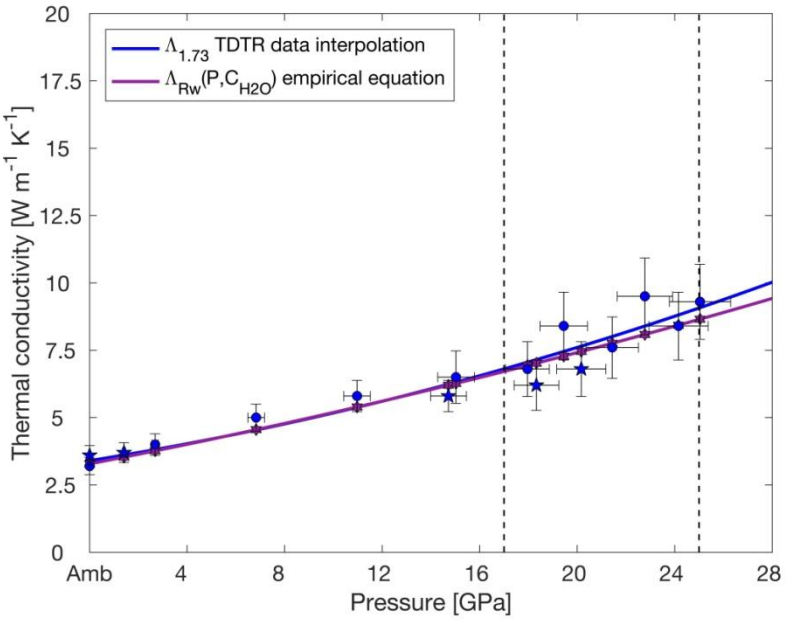

Figure 5.19. Comparison between the $\Lambda_{Rw}(C_{H2O}, P)$ equation (purple line) and the $\Lambda_{1.73}$ interpolation curve (blue line) (**Table 5.9**). Blue symbols indicate measured data (**Table 5.9**) and their respective error bars (10% of the value). Purple symbols indicate values of the water dependency equation at the same pressure as the measured data. Different symbols identify distinct experimental runs (**Table 5.6**).

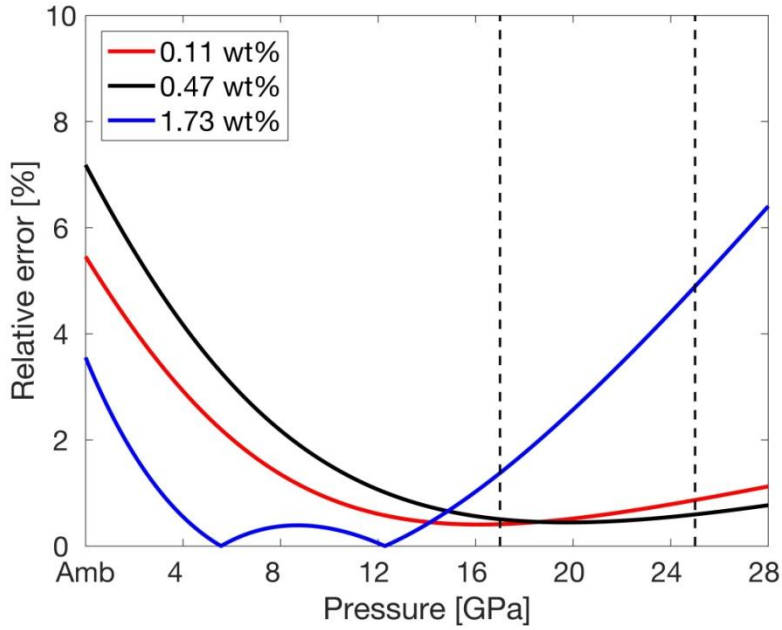

Figure 5.20. Relative error between the $\Lambda_{Rw}(C_{H2O}, P)$ equation and the experimental interpolation curves for the different C_{H2O} : 0.11 wt% (red line); 0.47 wt% (black line) and 1.73 wt% (blue line). Relative error is calculated as $100\{1 - [\Lambda_{interp}/\Lambda_{Rw}(C_{H2O}, P)]\}$.

5.8.4. Calculation of Temperature-Dependent Thermal Diffusivity

The calculations of the pressure- and temperature-dependent thermal diffusivity $\kappa_{Rw}(P,T)$ is described here. Thermal diffusivity is defined as $\kappa = \Lambda/(\rho Cp)$, where Λ is thermal conductivity, ρ density and Cp the specific heat capacity, see equation **(2.7.93)**.

In order to derive $\kappa_{Rw}\,(P,T)$ it is necessary to retrieve the $P-T$–dependency of the other parameters as well. In the following equations $a_i - h_i$ indicate the coefficients for the given equation. Values for each coefficient are summarized in **Table 5.11**.

Coefficient	Value	Coefficient	Value	Coefficient	Value
Thermal expansivity $\alpha_{Rw}\,(P,T)$		Heat capacity $Cp_{Rw}\,(P,T)$		Heat capacity $Cp_{Rw}\,(T)$	
Dorogokupets et al. (2015)		*Dorogokupets et al. (2015)*		*Saxena (1996)*	
a_{ex}	2.04×10^{-7}	a_{C}	1.05×10^{-10}	a_{S}	1.5856×10^{2}
b_{ex}	3.09×10^{-7}	b_{C}	1.55×10^{-7}	b_{S}	1.22×10^{-1}
c_{ex}	4.58×10^{-12}	c_{C}	1.38×10^{-4}	c_{S}	0.00
d_{ex}	1.99×10^{-8}	d_{C}	8.91×10^{-9}	d_{S}	-1.2297×10^{7}
$\alpha_{Rw}^{1atm\,298\,K}$	1.44×10^{-5}	e_{C}	1.87×10^{-5}	e_{S}	1.4844×10^{9}
–	–	f_{C}	1.71×10^{-2}	f_{S}	0.00
–	–	g_{C}	8.20×10^{-7}	g_{S}	7.9719×10^{3}
–	–	h_{C}	2.80×10^{-3}	–	–
–	–	$Cp_{Rw}^{1atm\,298\,K}$	2.29	–	–

Table 5.11. Coefficients used for equations **(5.8.8)-(5.8.13)** extrapolated from dataset by *Dorogokupets et al. (2015)*. Parameterization calculated by *Saxena (1996)* is also reported.

$P-T$–dependent $\Lambda_{Rw}(P,T)$ was taken from *Xu et al., (2004)*:

$$\Lambda_{lat}(P,T) = \Lambda_{lat}^{298}(P) * \left(\frac{298}{T}\right)^{0.5} \tag{5.8.8}$$

$P-T$–dependent thermal expansivity $\alpha_{Rw}(P,T)$ used to calculate $\rho_{Rw}(P,T)$ was derived from the dataset reported in *Dorogokupets et al. (2015)*.

$$\alpha_{Rw}\,(P,T) = -(a_{ex}T + b_{ex})P - c_{ex}T^2 + d_{ex}T + \alpha_{Rw}^{1atm\,298\,K} \tag{5.8.9}$$

$$\rho_{Rw}\,(P,T) = \frac{\rho_{Rw}^{298\,K}(P)}{1 + \alpha_{Rw}\,(P,T) * \Delta T}$$

$\alpha_{Rw}^{1atm\,298\,K}$ is the thermal expansivity at ambient pressure and temperature, and $\rho_{Rw}^{298\,K}(P)$ is the is P-dependent density at room temperature taken from *Ye et al. (2012)*. P-T-dependent volumetric heat capacity $Cp_{Rw}^{vol}\,(P,T)$ was derived from *Dorogokupets et al. (2015)*.

$$Cp_{Rw}^{vol}\,(P,T) = qP^2 - lP + Cp_{Rw}^{1atm}(T) \tag{5.8.10}$$

with:

$$q = a_C T^2 - b_C T + c_C \tag{5.8.11}$$

$$l = d_C T^2 - e_C T + f_C$$

$$Cp_{Rw}^{1atm}(T) = -g_C T^2 + h_C T + Cp_{Rw}^{1atm\,298\,K}$$

Specific heat capacity is given by the relation:

$$Cp_{Rw}\,(P,T) = \frac{Cp_{Rw}^{vol}(P,T)}{\rho_{Rw}\,(P,T)} \tag{5.8.12}$$

The heat capacity formulation used in this study is different from the one used in *Xu et al. (2004)*, derived from the parameterization by *Saxena (1996)*, where they assumed a P-independent Cp:

$$Cp_{Rw}\,(T) = a_S + b_S T + c_S T^2 + d_S T^{-2} + e_S T^{-3} + f_S T^{-0.5} + \frac{g_S}{T} \tag{5.8.13}$$

The results of our $\kappa_{Rw}\,(P,T)$ calculations are reported in **Figure 5.21** and **Figure 5.22**.

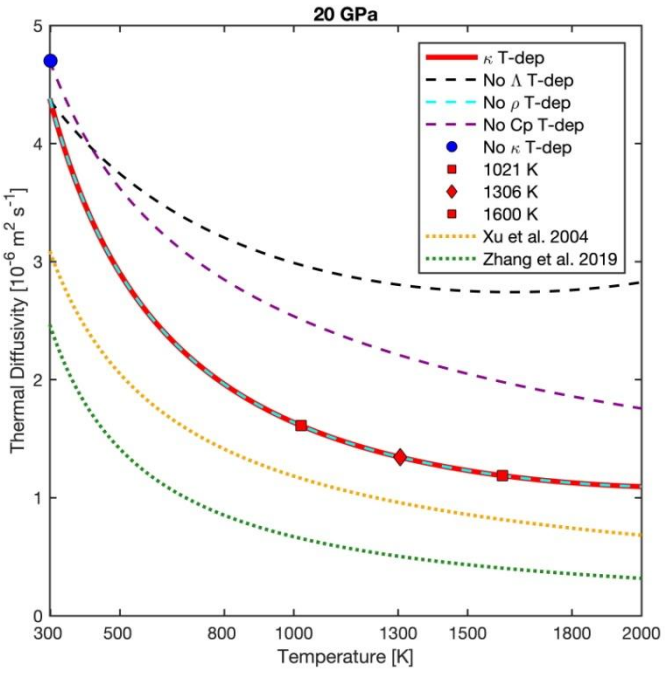

Figure 5.21. Effect of temperature on ringwoodite thermal diffusivity $\kappa_{Rw}(T)$ at constant $P = 20\ GPa$. Blue marker indicates temperature-independent κ_{Rw}. Solid red line indicates temperature-dependent $\kappa_{Rw}(T)$ calculated by using temperature-dependent parameters: $\Lambda_{\mathrm{Rw}}(P,T)$, $\rho_{\mathrm{Rw}}(P,T)$, $Cp_{\mathrm{Rw}}(P,T)$. At a given depth, $\kappa_{Rw}(T)$ decreases with increasing temperature, progressively hindering heat transport during warm-up. Red square markers represent κ_{Rw} at the two end-member temperatures experienced by the modelled slab: $1021\ K$ is the lowest temperature (T_{min}) in the cold slab core at $t = 0$, and $1600\ K$ is the final temperature (T_{max}) after thermal equilibration with the ambient mantle. Slab thermal diffusivity will evolve from T_{min} to T_{max} following the red curve. A red diamond marker represents $\kappa_{Rw}(T)$ at initial average slab temperature. Coloured dashed lines indicate T-dependencies of $\kappa_{Rw}(T)$, each one calculated by omitting one parameter: without T-dependent Λ_{Rw} (black), ρ_{Rw} (light blue), and Cp_{Rw}(purple). It appears that omitting T-dependent ρ_{Rw} does not change the result, probably due to our diffusivity formulation, where volumetric heat capacity Cp_{Rw}^{vol} is divided by ρ_{Rw} in order to obtain the specific heat capacity Cp_{Rw}. On the other hand, T-dependent $\Lambda_{\mathrm{Rw}}(T)$ and $Cp_{\mathrm{Rw}}(T)$, have a major role on $\kappa_{Rw}(T)$. For comparison dotted lines represent, T-dependent $\kappa_{Rw}(T)$ reported in literature: ringwoodite (*Xu et al., 2004*) and olivine (Fo_{90}) (*Zhang et al., 2019*). Both curves follow the equation: $\kappa(P,T) = \kappa^{300}(300/T)^n(1+aP)$, although with different values for parameters n and a. The difference between our calculations and *Xu et al. (2004)* might be due to the use of two different heat capacity formulations, and the 25% higher $\Lambda_{\mathrm{Rw}}(P)$ measured with the TDTR method.

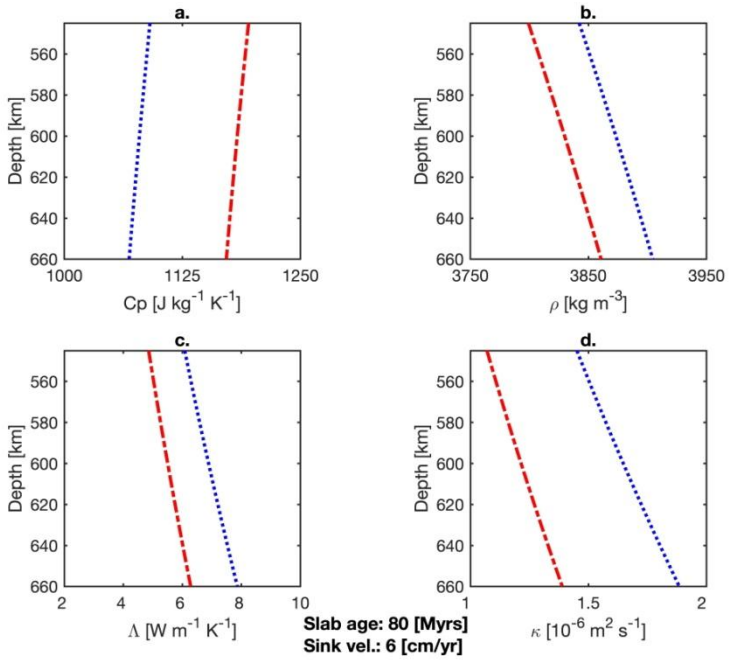

Figure 5.22. Vertical profiles of different P-dependent parameters across the modelled slab. (a) specific heat capacity $Cp_{Rw}\ (P)$, (b) density $\rho_{Rw}(P)$, (c) thermal conductivity $\Lambda_{Rw}(P)$ and (d) thermal diffusivity $\kappa_{Rw}(P)$. Equations used to calculate these profiles are **(5.8.8)-(5.8.13)**. The temperature used in each equation is neither space- nor time-dependent. This means that a fixed reference T has been used to calculate a slab parameter profile. Two end-members have been tested: T_{min} (blue) and T_{max} (red) (see **Figure 5.21** caption). All parameters are expected to evolve with depth and time between the two profiles defined by end member values T_{min} and T_{max}.

5.8.5. Code Benchmark

The self-written 1D Matlab code was benchmarked against the analytical solution for 1D heat diffusion with an initial Gaussian temperature profile:

$$T(x,t) = \frac{T_{max}}{\sqrt{1+\frac{4\kappa t}{\sigma^2}}} exp\left(\frac{-x^2}{\sigma^2+4\kappa t}\right) \quad (5.8.14)$$

Where T is temperature, x the position, t is time, T_{max} is the maximum temperature in the Gaussian profile, κ is the thermal diffusivity and σ the amplitude of the Gaussian distribution. We computed the L^2 norm given as:

$$L^2 = \frac{\sqrt{\sum(Misfit * \Delta x)^2}}{X} \quad (5.8.15)$$

Where X is the total length of the domain and Δx the grid spacing. For this we computed the misfit between analytical and numerical solution, at a given node position. We ran this simulation for 1 Myr of thermal evolution (**Figure 5.23**) and employed 1001 nodes, and 1000 years long time steps. The benchmark proves the stability of our 1D code, and that the chosen resolution is sufficient to solve numerically the heat diffusion equation (**Figure 5.23**). The L^2 norm is $\ll 1$, indicating a negligible difference between analytical and numerical solution (**Figure 5.23**).

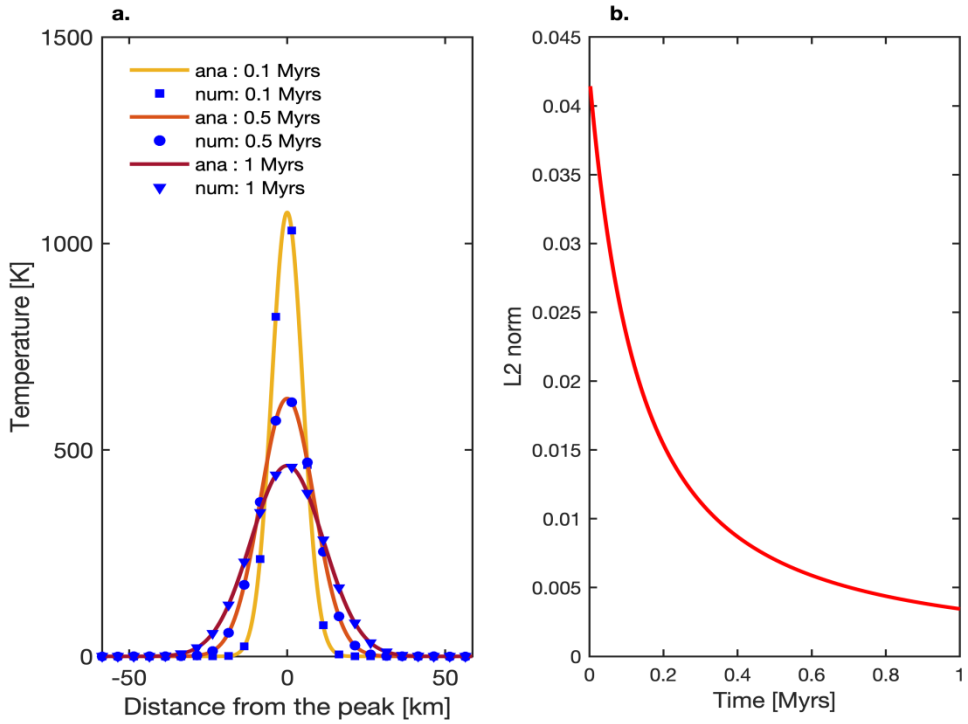

Figure 5.23. (a) Comparison between analytical and numerical solutions. Solid lines represent the analytical solutions for 3 different times, namely 0.1, 0.5 and 1 $Myrs$. Blue symbols indicate the numerical solution at selected nodes (every 50^{th} nodal point is plotted here). (b) L^2 norm over 1 $Myrs$ of thermal evolution ($L^2 \ll 1$).

Parameter	Description	Value	Reference
Stage 1: half-space cooling (*Turcotte & Schubert, 2014*)			
Λ^*_{ol}	Olivine thermal conductivity	$3.6\ W\ m^{-1}K^{-1}$	*Chang et al. (2017)*
ρ^*_{ol}	Olivine density	$3341\ kg\ m^{-3}$	*Zhang & Bass (2016)*
Cp^*_{ol}	Olivine specific heat capacity	$1073\ J\ kg^{-1}K^{-1}$	*Su et al. (2018)*
κ^*_{ol}	Olivine thermal diffusivity	$1.005 \times 10^{-6}\ m^2\ s^{-1}$	calculated
T_0	surface temperature	$300\ K$	assumed
T_{m}	mantle temperature	$1600\ K$	assumed
L_{slab}	slab thickness	$116.8\ km$	calculated
t	slab age	$80\ Myrs$	assumed
Stage 2: slab descent (*Syracuse et al., 2010*)			
Λ^*_{ol}	olivine thermal conductivity	$3.6\ W\ m^{-1}K^{-1}$	*Chang et al. (2017)*
ρ^*_{ol}	olivine density	$3341\ kg\ m^{-3}$	*Zhang & Bass (2016)*
Cp^*_{ol}	olivine specific heat capacity	$1073\ J\ kg^{-1}K^{-1}$	*Su et al. (2018)*
κ^*_{ol}	olivine thermal diffusivity	$1.005 \times 10^{-6}\ m^2\ s^{-1}$	calculated
t_{sink}	sinking time	$10\ Myrs$	assumed
v_{sink}	sinking velocity	$6\ cm\ yr^{-1}$	assumed
θ_{dip}	dipping angle	$60°$	assumed
Stage 3: slab stagnation (*Fukao et al., 2009*)			
Λ^*_{rw}	Ringwoodite thermal conductivity	$4.840\ W\ m^{-1}\ K^{-1}$	this study
ρ^*_{rw}	Ringwoodite density	$3563\ kg\ m^{-3}$	*Ye et al. (2012)*
Cp^*_{rw}	Ringwoodite specific heat capacity	$827\ J\ kg^{-1}K^{-1}$	*Dorogokupets et al. (2015)*
t_{stag}	stagnation time	$150\ Myrs$	assumed
D_{hyd}	hydrous layer thickness	$5–40\ km$	free parameter
C_{H2O}	water content	$0.1–1.5\ wt\%$	free parameter
t_{stag}	stagnation time	$150\ Myrs$	assumed
Code Benchmark			
T_{max}	peak temperature	$1500\ K$	assumed
σ	Gaussian amplitude	$5000\ m$	assumed
T_{left}	left boundary condition	$300\ K$	assumed
T_{right}	right boundary condition	$300\ K$	assumed
ρ	density	$3300\ kg\ m^{-3}$	assumed
Cp	specific heat capacity	$1200\ J\ kg^{-1}\ K^{-1}$	assumed
Λ	thermal conductivity	$3\ W\ m^{-1}\ K^{-1}$	assumed
κ	Thermal diffusivity	$7.57 \times 10^{-7}\ m^2\ s^{-1}$	calculated
X	domain length	$116.9\ km$	assumed
n	grid nodes	1000	assumed
Δx	grid spacing	$100\ m$	assumed
Δt	time step	$1000\ yrs$	assumed

Table 5.12. List of parameters used. *Room temperature conditions, dry sample

D_{hyd} [km]	C_{H2O} [wt%]	t_{crit} [Myrs]	t_{delay} [Myrs]	D_{hyd} [km]	C_{H2O} [wt%]	t_{crit} [Myrs]	t_{delay} [Myrs]	D_{hyd} [km]	C_{H2O} [wt%]	t_{crit} [Myrs]	t_{delay} [Myrs]	D_{hyd} [km]	C_{H2O} [wt%]	t_{crit} [Myrs]	t_{delay} [Myrs]
5	*dry*	2.19	0.0	**15**	*dry*	24.1	0.0	**25**	*dry*	35.19	0.0	**35**	*dry*	41.23	0.0
5	0.1	2.71	0.52	**15**	0.1	25.1	1	**25**	0.1	36.2	1.01	**35**	0.1	42.11	0.88
5	0.2	3.29	1.1	**15**	0.2	26.13	2.03	**25**	0.2	37.24	2.05	**35**	0.2	43.02	1.79
5	0.3	3.92	1.73	**15**	0.3	27.21	3.11	**25**	0.3	38.32	3.13	**35**	0.3	43.94	2.71
5	0.4	4.6	2.41	**15**	0.4	28.33	4.23	**25**	0.4	39.43	4.24	**35**	0.4	44.88	3.65
5	0.5	5.33	3.14	**15**	0.5	29.5	5.4	**25**	0.5	40.58	5.39	**35**	0.5	45.85	4.62
5	0.6	6.12	3.93	**15**	0.6	30.71	6.61	**25**	0.6	41.77	6.58	**35**	0.6	46.84	5.61
5	0.7	6.97	4.78	**15**	0.7	31.98	7.88	**25**	0.7	43	7.81	**35**	0.7	47.85	6.62
5	0.8	7.88	5.69	**15**	0.8	33.3	9.2	**25**	0.8	44.26	9.07	**35**	0.8	48.88	7.65
5	0.9	8.85	6.66	**15**	0.9	34.67	10.57	**25**	0.9	45.58	10.39	**35**	0.9	49.94	8.71
5	1	9.89	7.7	**15**	1	36.1	12	**25**	1	46.93	11.74	**35**	1	51.01	9.78
5	1.1	11	8.81	**15**	1.1	37.59	13.49	**25**	1.1	48.33	13.14	**35**	1.1	52.11	10.88
5	1.2	12.19	10	**15**	1.2	39.15	15.05	**25**	1.2	49.78	14.59	**35**	1.2	53.22	11.99
5	1.3	13.46	11.27	**15**	1.3	40.77	16.67	**25**	1.3	51.27	16.08	**35**	1.3	54.36	13.13
5	1.4	14.81	12.62	**15**	1.4	42.47	18.37	**25**	1.4	52.82	17.63	**35**	1.4	55.51	14.28
5	1.5	16.25	14.06	**15**	1.5	44.25	20.15	**25**	1.5	54.41	19.22	**35**	1.5	56.67	15.44
10	*dry*	15.06	0.0	**20**	*dry*	30.51	0.0	**30**	*dry*	38.67	0.0	**40**	*dry*	43.06	0.0
10	0.1	15.95	0.89	**20**	0.1	31.53	1.02	**30**	0.1	39.63	0.96	**40**	0.1	43.84	0.78
10	0.2	16.88	1.82	**20**	0.2	32.59	2.08	**30**	0.2	40.62	1.95	**40**	0.2	44.63	1.57
10	0.3	17.86	2.8	**20**	0.3	33.69	3.18	**30**	0.3	41.63	2.96	**40**	0.3	45.44	2.38
10	0.4	18.89	3.83	**20**	0.4	34.83	4.32	**30**	0.4	42.68	4.01	**40**	0.4	46.26	3.2
10	0.5	19.96	4.9	**20**	0.5	36.02	5.51	**30**	0.5	43.75	5.08	**40**	0.5	47.09	4.03
10	0.6	21.09	6.03	**20**	0.6	37.24	6.73	**30**	0.6	44.86	6.19	**40**	0.6	47.94	4.88
10	0.7	22.26	7.2	**20**	0.7	38.51	8	**30**	0.7	46	7.33	**40**	0.7	48.8	5.74
10	0.8	23.5	8.44	**20**	0.8	39.84	9.33	**30**	0.8	47.16	8.49	**40**	0.8	49.67	6.61
10	0.9	24.79	9.73	**20**	0.9	41.21	10.7	**30**	0.9	48.37	9.7	**40**	0.9	50.55	7.49
10	1	26.14	11.08	**20**	1	42.63	12.12	**30**	1	49.6	10.93	**40**	1	51.44	8.38
10	1.1	27.56	12.5	**20**	1.1	44.11	13.6	**30**	1.1	50.87	12.2	**40**	1.1	52.33	9.27
10	1.2	29.04	13.98	**20**	1.2	45.65	15.14	**30**	1.2	52.17	13.5	**40**	1.2	53.24	10.18
10	1.3	30.6	15.54	**20**	1.3	47.25	16.74	**30**	1.3	53.5	14.83	**40**	1.3	54.15	11.09
10	1.4	32.24	17.18	**20**	1.4	48.91	18.4	**30**	1.4	54.87	16.2	**40**	1.4	55.07	12.01
10	1.5	33.95	18.89	**20**	1.5	50.63	20.12	**30**	1.5	56.27	17.6	**40**	1.5	55.98	12.92

Table 5.13. $T_{ref} = 1021\ K$. D_{hyd}: hydrous layer thickness; C_{H2O}: water content; t_{crit}: breakdown age; t_{delay}: delay time

D_{hyd} [km]	C_{H2O} [wt%]	t_{crit} [Myrs]	t_{delay} [Myrs]	D_{hyd} [km]	C_{H2O} [wt%]	t_{crit} [Myrs]	t_{delay} [Myrs]	D_{hyd} [km]	C_{H2O} [wt%]	t_{crit} [Myrs]	t_{delay} [Myrs]	D_{hyd} [km]	C_{H2O} [wt%]	t_{crit} [Myrs]	t_{delay} [Myrs]
5	*dry*	2.96	0.0	**15**	*dry*	32.7	0.0	**25**	*dry*	47.76	0.0	**35**	*dry*	55.97	0.0
5	0.1	3.68	0.72	**15**	0.1	34.05	1.35	**25**	0.1	49.13	1.37	**35**	0.1	57.17	1.2
5	0.2	4.46	1.5	**15**	0.2	35.46	2.76	**25**	0.2	50.55	2.79	**35**	0.2	58.39	2.42
5	0.3	5.31	2.35	**15**	0.3	36.93	4.23	**25**	0.3	52.01	4.25	**35**	0.3	59.65	3.68
5	0.4	6.23	3.27	**15**	0.4	38.45	5.75	**25**	0.4	53.52	5.76	**35**	0.4	60.94	4.97
5	0.5	7.23	4.27	**15**	0.5	40.03	7.33	**25**	0.5	55.09	7.33	**35**	0.5	62.25	6.28
5	0.6	8.3	5.34	**15**	0.6	41.68	8.98	**25**	0.6	56.7	8.94	**35**	0.6	63.6	7.63
5	0.7	9.45	6.49	**15**	0.7	43.4	10.7	**25**	0.7	58.37	10.61	**35**	0.7	64.97	9
5	0.8	10.68	7.72	**15**	0.8	45.19	12.49	**25**	0.8	60.1	12.34	**35**	0.8	66.38	10.41
5	0.9	12	9.04	**15**	0.9	47.05	14.35	**25**	0.9	61.88	14.12	**35**	0.9	67.82	11.85
5	1	13.41	10.45	**15**	1	49	16.3	**25**	1	63.72	15.96	**35**	1	69.28	13.31
5	1.1	14.92	11.96	**15**	1.1	51.03	18.33	**25**	1.1	65.63	17.87	**35**	1.1	70.77	14.8
5	1.2	16.53	13.57	**15**	1.2	53.14	20.44	**25**	1.2	67.6	19.84	**35**	1.2	72.29	16.32
5	1.3	18.25	15.29	**15**	1.3	55.35	22.65	**25**	1.3	69.63	21.87	**35**	1.3	73.83	17.86
5	1.4	20.09	17.13	**15**	1.4	57.66	24.96	**25**	1.4	71.73	23.97	**35**	1.4	75.4	19.43
5	1.5	22.04	19.08	**15**	1.5	60.08	27.38	**25**	1.5	73.89	26.13	**35**	1.5	76.99	21.02
10	*dry*	20.43	0.0	**20**	*dry*	41.4	0.0	**30**	*dry*	52.49	0.0	**40**	*dry*	58.46	0.0
10	0.1	21.64	1.21	**20**	0.1	42.79	1.39	**30**	0.1	53.79	1.3	**40**	0.1	59.52	1.06
10	0.2	22.9	2.47	**20**	0.2	44.23	2.83	**30**	0.2	55.13	2.64	**40**	0.2	60.59	2.13
10	0.3	24.23	3.8	**20**	0.3	45.73	4.33	**30**	0.3	56.51	4.02	**40**	0.3	61.69	3.23
10	0.4	25.62	5.19	**20**	0.4	47.28	5.88	**30**	0.4	57.93	5.44	**40**	0.4	62.81	4.35
10	0.5	27.08	6.65	**20**	0.5	48.88	7.48	**30**	0.5	59.4	6.91	**40**	0.5	63.94	5.48
10	0.6	28.61	8.18	**20**	0.6	50.55	9.15	**30**	0.6	60.9	8.41	**40**	0.6	65.09	6.63
10	0.7	30.21	9.78	**20**	0.7	52.28	10.88	**30**	0.7	62.45	9.96	**40**	0.7	66.26	7.8
10	0.8	31.88	11.45	**20**	0.8	54.08	12.68	**30**	0.8	64.04	11.55	**40**	0.8	67.45	8.99
10	0.9	33.63	13.2	**20**	0.9	55.94	14.54	**30**	0.9	65.68	13.19	**40**	0.9	68.64	10.18
10	1	35.47	15.04	**20**	1	57.88	16.48	**30**	1	67.36	14.87	**40**	1	69.86	11.4
10	1.1	37.4	16.97	**20**	1.1	59.89	18.49	**30**	1.1	69.08	16.59	**40**	1.1	71.08	12.62
10	1.2	39.42	18.99	**20**	1.2	61.98	20.58	**30**	1.2	70.85	18.36	**40**	1.2	72.32	13.86
10	1.3	41.53	21.1	**20**	1.3	64.15	22.75	**30**	1.3	72.67	20.18	**40**	1.3	73.56	15.1
10	1.4	43.75	23.32	**20**	1.4	66.41	25.01	**30**	1.4	74.53	22.04	**40**	1.4	74.81	16.35
10	1.5	46.09	25.66	**20**	1.5	68.76	27.36	**30**	1.5	76.43	23.94	**40**	1.5	76.06	17.6

Table 5.14. $T_{ref} =$ 1600 K. D_{hyd}: hydrous layer thickness; C_{H2O}: water content; t_{crit}: breakdown age; t_{delay}: delay time

CHAPTER 6 – Effect of Grid Resolution on Tectonic Regimes in Global-Scale Convection Models

6.1. Introduction

As described in **Chapter 1.2.3**, the rheology of the lithosphere, i.e. its resistance to rupture, control the tectonic regime of terrestrial planets (*O'Neill et al., 2007*; *Stern & Gerya, 2018*). In the following sections, a few examples of tectonic regimes are described.

6.1.1. Plate Tectonics Regime

Plate tectonics regime has been described in **Chapter 1.2**, here is reported a brief summary. In plate tectonics, the lithosphere is fragmented into a mosaic of plates which float and drift on top of the asthenosphere (*Turcotte & Schubert, 2002*). Each plate is rigid at its centre, and most of the deformation occurs at its boundaries. There are three types of plate margins: (1) divergent plate margins (i.e. mid ocean ridges and continental rifts); (2) convergent plate margins (i.e. subduction zones and continental collision); (3) transform margins (e.g. San Andreas fault). The subduction of the oceanic lithosphere represent the key characteristic feature of plate tectonics (*Crameri et al., 2019*), and its major driving force (*Forsyth & Uyeda, 1975*; *Conrad & Lithgow-Bertelloni, 2002, 2004*). So far, Earth is the only known terrestrial planet that exhibit this tectonic regime (*Korenaga, 2013*).

6.1.2. Stagnant Lid

Most terrestrial planets and moons display an immobile surface, characterized by the lack of active spreading centres and subduction zones (*Tosi & Padovan, 2019*). However, these bodies are not necessarily tectonically inactive, since they feature faulting and folding, active volcanism, and impact craters that might trigger surface melting (*Stern et al., 2018*). This means that mantle convection still occurs, although it is confined by a strong immobile lithosphere (*Ogawa et al., 1991*).

This convective style is a consequence of the large viscosity contrast ($\Delta\eta > 10^4$) between the warm mantle and the cold lid, which arises from the strong T-dependent formulation of the Newtonian and non-Newtonian viscosity (*Solomatov, 1995*). In the stagnant lid regime, the lithosphere is too viscous to be entrained by the mantle flow, and its yield strength is too high to achieve brittle failure and form plate boundaries (*Moresi & Solomatov, 1995*; *Solomatov & Moresi, 1997, 2000*). Convective cooling in the stagnant lid regime can still occur by sub-lithospheric sinking of cold thermal instabilities, and the intermittent rise of warm tail-less plumes (*Manga et al., 2001*; *Jellinek, 2002*; *Solomatov & Moresi, 2000*). Classic paradigms of stagnant-lid bodies are: Mercury and the Moon and present-day Mars (*Tosi & Padovan, 2019*). However, for Mercury and the moon, some models predict that mantle convection has already ceased.

6.1.3. Episodic Resurfacing

Venus, on the other hand, displays a complex and poorly understood tectonic regime, called episodic lid regime (*Turcotte, 1995*). From the distribution of impact craters, it appears that Venus' surface has the same age uniformly, and that a major change in the geological activity has occurred no more than 800 $Myrs$ ago (*Herrick, 1994*; *Hauck et al., 1998*). Moreover, Venus does not show any feature of Earth-like plate tectonics, given the absence of spreading ridges and subduction zones (*Nimmo & McKenzie, 1998*). Potential sites of lithosphere subduction are represented by the volcano-tectonic structure called *coronae* (*Schubert & Sandwell, 1995*). Coronae are produced by the interaction of mantle plumes with the lithosphere, and they represent a unique feature of Venus' surface (*Davaille et al., 2017*; *Gülcher et al., 2020*).

A possible explanation for this odd juxtaposition of young lithosphere and absence of resurfacing mechanism, can be found in the episodic overturn hypothesis (*Turcotte, 1993*; *Fowler & O'Brien, 1996*; *Moresi & Solomatov, 1998*). This model implies the complete collapse of the lithosphere as a catastrophic event, after the progressive localization of the strain during a stagnant lid stage (*Turcotte et al., 1999*). The evolution of an episodic overturn regime occurs in five stages (*Crameri & Tackley, 2016*): (1) plume-induced localization of the deformation, and formation of weak zones in the lithosphere (i.e. coronae); (2) subduction initiation and propagation of horse-shoe trenches throughout the lid; (3) formation of a global-scale subduction belt from the progressive merging of all the trenches; (4) the complete resurfacing of the lid, which is faster than the life-cycle of the newly formed lithosphere, and finally (5) a new stagnant lid stage.

So far, the episodic resurfacing hypothesis is the one that best explains the geophysical observations on Venus's surface (*Rolf et. al., 2018*). Numerical modelling predicts 5–8 overturns event in Venus' history, with a duration of each event being 150–200 Myrs (*Armann & Tackley, 2012*; *Rolf et al., 2018*).

6.1.4. Micro-Plate Dripping

This tectonic style is characterized by short-term subduction episodes, interrupted by slab break-off due to the low strength of the lithosphere (*van Hunen & van den Berg, 2008*). The dripping regime may have been important during the Archean Eon on Earth (4–2.5 $Gyrs$).

The presence of active subduction zones in early stages of Earth's history has been inferred from thermobarometry constraints on $> 4\,Gyrs$–old zircons, which record a low–T, high–P environment (*Hopkins et al., 2008*). This is also confirmed by the $Re-Os$ isotopic signature on eclogitic diamond inclusions, which implies an oceanic crustal recycling in the mid Archean (3.2–2.9 $Gyrs$) (*Richardson et al., 2001*; *Shirey & Richardson, 2011*). These subduction zones were much hotter than their present-day counterparts, as indicated by 2.8–2.5 $Gyrs$ old outcrops of ultra-high-temperature granulites (*Brown, 2006*).

Both geochemical data and numerical models seem to agree on the existence of an Archean tectonic regime, which could have been a non-matured stage of modern plate tectonics (*Moyen & van Hunen, 2012*). The combined effect of a weak lithosphere and a low viscosity mantle during the hot Archean Eon, was probably the principle limitation for the onset of a present-day style of plate tectonics (*van Hunen & Moyen, 2012*).

This hot subduction regime might have played a crucial role in the sequestration of the organic carbon from the surface, thus favouring the rise of atmospheric oxygen levels in the Archean (*Duncan & Dasgupta, 2017*).

6.1.5. Exotic Regimes

These regimes are represented by the plutonic-squishy lid (*Lourenço et al., 2020*), which might be applicable to the Archean Earth and the present-day Venus, and the ridge only regime (*Rozel et al., 2015*) which may occur on icy satellites. Furthermore, Archean Earth might have been characterized by the heat-pipe regime (*Moore & Webb, 2013*), where a thick, strong lithosphere was the result of prolonged eruptions, and the internal heat was lost through the sustained surface volcanism (*Moore et al., 2017*). It is likely that the heat-pipe regime is active in preset-day Jupiter's moon Io (*Lourenço et al., 2018*; *O'Reilly & Davies, 1981*) where the excess tidal heat is dissipated by over 300 volcanoes present on its surface (*Lopes et al., 2004*; *Lopes, 2014*).

6.1.6. Tectonic Regimes in Numerical Models

In numerical models, the implementation of a strong T-dependent viscosity (*Weertman, 1970*) produces a stiff lid in the cold upper boundary of the model (*Tackley, 2000b*). Plate boundaries are formed self-consistently by imposing a pseudoplastic behaviour, i.e. the lithosphere yields once the stresses associated with mantle convection reaches a prescribed value (i.e. yield stress *O'Neill et al., 2007*; *Tackley, 2000b*). For a given model setting, the progressive increase of the lithosphere strength, generates a sequence of the aforementioned tectonic regimes that align as follows: micro-plate dripping, plate tectonics, episodic resurfacing, and stagnant lid (*Tackley, 2000b*). However, it has been shown that the critical value of the yield stress at which a tectonic regime transition occurs, depends heavily on the grid resolution of the numerical model (*Tosi et al., 2015*).

In this chapter, the effect of numerical resolution on the resulting tectonic regimes for an Earth-like model setup will be discussed. The aim is to constrain the best resolution that can be used to study plate tectonics of Earth-like planets in the future.

6.2. Physical Model

To answer the question posed above, a global-scale mantle convection model has been designed to reproduce the tectonic regimes on an Earth-like planet in a self-consistent manner. In this section, the model setup, material parameters, and the governing equations are described.

6.2.1. Assumptions and Geometry

The governing equations of mass, momentum and energy conservation are solved for a compressible fluid (truncated anelastic approximation - *Tackley, 2008*), and by employing the infinite Prandtl number approximation to simulate solid state mantle convection (see **Chapter 2.8.5**).

The employed geometry is the 2D spherical annulus (*Hernlund & Tackley, 2008*), where the conservation equations are computed along two polar coordinates: the radial distance from the centre r, and the azimuthal angle φ (see **Chapter 2.9.2**). The modelled domain consists of an equatorial slice of a $r^{surf} = 2890\ km$ thick mantle, which overlays a core with radius $r^{CMB} = 3480\ km$ (not computed). Gravity only acts in the radial direction r, and is assumed to have a constant value of $g = 9.81\ m\ s^{-2}$ throughout the mantle.

6.2.2. Boundary Conditions and Heating Modes

The prescribed boundary conditions at the top (i.e. surface), and the bottom (i.e. CMB), of the domain are: $free-slip$ conditions for the velocity field (see **Chapter 3.3.3**), and $isothermal$ conditions for the temperature field, with $T_{\text{top}} = 300\ K$ and $T_{\text{bot}} = 4000\ K$. Moreover, the mantle is heated internally by prescribing a constant radiogenic heating source $R_{\text{H}} = 5.2 \times 10^{-12}\ W\ kg^{-1}$ with an extended half-life time $t_{1/2} = 1.0 \times 10^{30}\ yr$ to maintain a quasi steady-state internal heating rate. The value used for R_{H} is based on measurements for carbonaceous chondrites, which are assumed to be representative of Earth's mantle material (*Tackley, 1998*; *Jaupart & Mareschal, 2015*; *Palme & O'Neill, 2007*).

6.2.3. Chemical Composition and Phase Transitions

The bulk chemical composition of the mantle is simplified as a two phase system: Mg-Si olivine (ol) and Al-Mg-Si pyroxene-garnet ($pxgt$). The mantle is assumed to have a pyrolitic mineral assemblage made of $X_{ol} = 60\%$ and $X_{pxgt} = 40\%$. This translates into a rock fraction of 80% harzburgite (75% ol + 25% $pxgt$), and 20% basalt (100% $pxgt$). The chemical composition of the mantle remains homogeneous over time given the absence of melting processes and chemical fractionation. Therefore, convective instabilities (i.e. slabs and plumes) are thermo-mechanical (i.e. cold-dense vs. warm-buoyant).

Each chemical system is characterized by several mineral phases Γ. The phase boundaries within each system are handled using a parameterized approach (*Faccenda & Dal Zilio, 2017*), where the number of phases is controlled by the parameter n. For the ol–system $n_{ol} = 4$, i.e. for CMB to the surface: post-perovskite (PPV) → lower mantle (LM) → mantle transition zone (MTZ) → upper mantle (UM); whereas for the $pxgt$–system $n_{pxgt} = 5$, i.e. PPV → LM → MTZ → UM → lithosphere (LT). The reference temperatures T_X^Γ and depths D_X^Γ of each phase transition along with their relative Clapeyron slopes Υ_X^Γ, density jumps $\Delta\rho_X^\Gamma$, and viscosity ratios $\Delta\eta_X^\Gamma$ are reported in **Table 6.2**.

6.2.4. Compressibility and Depth-Dependent Parameters

In the anelastic approximation, density ρ, thermal expansivity α, specific heat capacity Cp, and thermal conductivity Λ are a function of depth (see **Chapter 3.6.5**). The depth-dependent profile of the thermodynamic parameters is computed for each mineral phase of the given system using the 3^{rd}–order Birch-Murnaghan Equation of State for density $\rho(r)_X^\Gamma$ **(2.7.89)**, equation **(3.6.58)** for the thermal expansivity $\alpha(r)_X^\Gamma$, and equation **(3.6.60)** for the thermal conductivity $\Lambda(r)_X^\Gamma$. The specific heat capacity is assumed to be constant for all mineral phases $Cp(r)_X^\Gamma = 1200\ J\ kg^{-1}\ K^{-1}$.

The surface reference density $\rho_{0_X}^\Gamma$, the surface bulk modulus $K_{0_X}^\Gamma$, its pressure derivative K'^Γ_X, the Grüneisen parameter γ_X^Γ, and the thermal conductivity exponent k_X^Γ, necessary for the depth-dependent parameter calculations are reported in **Table 6.2**. The cumulative radial profile of each parameter is computed by considering: (i) the stable mineral assemblage at the respective depth, and (ii) the prescribed mineral fraction of the pyrolitic mantle **Chapter 3.6.8**.

The latent heat L_H **(2.6.82)** at each phase transition is calculated by using the effective heat capacity $\acute{C}p$ and thermal expansivity $\acute{\alpha}$ approach (*Schubert et al., 1975*; *Christensen & Yuen, 1985*) as described in **Chapter 2.6.3**. The adiabatic temperature profile of the pyrolitic mantle T_S **(2.6.87)** is computed from the radial profile of the thermodynamic parameters $(\rho, \alpha, Cp, \Lambda, K, \gamma)$, and the contribution of the released/absorbed L_H caused by convection. The initial potential temperature is prescribed as $T_P^{init} = 1600\ K$, corresponding to present-day estimates for Earth (*Katsura et al., 2010*).

6.2.5. Visco-Plastic Rheology

In this model, the rheology of the Earth's mantle is assumed to be governed by diffusion creep only (*Yamazaki & Karato, 2001*), which is strongly temperature dependent (*Weertman, 1970*):

$$\eta_{diff}(P,T) = \eta_0 exp\left[\left(\frac{E_X^\Gamma + PV_X^\Gamma}{RT}\right) - \left(\frac{E_X^\Gamma}{RT_0}\right)\right] \tag{6.2.1}$$

Here, $\eta_0 = 10^{20}\ Pa\ s$ is the reference viscosity for the reference state T_0, P_0 (here assumed as $T_0 = 1600$ K, $P_0 = 0\ Pa$), $E_X^\Gamma [J\ mol^{-1}]$ is the activation energy, $V_X^\Gamma [m^3\ mol^{-1}]$ is the activation volume, and $R = 8.314\ J\ mol^{-1}$ K^{-1} is the universal gas constant. The phase-dependent activation energies and volumes used in equation **(6.2.1)** are reported in **Table 6.2**. These values are based on mineral physics constraints (e.g. *Stixrude & Lithgow-Bertelloni, 2005*).

The Arrhenius law **(6.2.1)** causes the formation of an high viscosity lid ($\eta_{lid} \approx 10^{60}\ Pa\ s$) at the upper cold boundary of the model (*Tackley, 2000b*). Given the extreme viscosity contrast between hot and cold material ($\Delta\eta \approx 10^{40}\ Pa\ s$) it is necessary to introduce both upper and lower viscosity cut-offs: $\eta_{min} = 10^{17}\ Pa\ s$ and $\eta_{max} = 10^{28}\ Pa\ s$.

Breaking of the lithosphere is modelled using a pseudoplastic rheology (*Tackley, 2000b*), where the effective viscosity η_{eff} is computed by choosing the minimum value between the diffusion creep viscosity η_{diff} and the apparent viscosity η_{app} (see **Chapter 3.6.10**). The apparent viscosity is computed as $\eta_{app} = \tau_y/(2\dot{\varepsilon}_{II})$ where $\dot{\varepsilon}_{II}$ is the second invariant of strain-rate tensor **(2.4.34)**, and τ_y is the yield stress. This means that the higher the deformation in a given portion, the lower the apparent viscosity.

Since η_{diff} of the cold lithosphere is extremely high, the effective viscosity η_{eff} of the highly deformed regions is controlled by the yield stress τ_y. When the stress reaches τ_y, the material is significantly weakened, thus favouring the formation of weak zones, i.e. plate boundaries. The higher τ_y, the harder it is to "break" the lithosphere, which consequently results in a stronger lithosphere.

Generally, the strength envelope of the lithosphere is computed by minimizing the contribution from two parameterizations **(6.2.2)**: pressure-dependent yield stress (brittle criterion) and depth-dependent yield stress (ductile criterion) (*Tackley, 2000b*; *Crameri & Tackley, 2016*).

$$\tau_y = \min\left[\tau_y^{brittle}(P), \tau_y^{ductile}(D)\right] \tag{6.2.2}$$

$$\tau_y^{brittle}(P) = c_y + f_\phi P$$

$$\tau_y^{ductile}(D) = \sigma_y + f_\sigma D$$

Where c_y is the cohesion coefficient, f_ϕ is the frictional coefficient, σ_y the ductile yield stress, and f_σ the depth gradient.

In this model, the lithosphere strength envelope is simplified by considering only a constant ductile yield criterion $\tau_y^{ductile}(D)$. This is achieved by prescribing a large value for c_y (i.e. '*huge*' Fortran90 function - *Adams et al., 1992*), and $f_\sigma = 0.01\ Pa\ m^{-1}$. The negligible depth gradient f_σ is prescribed to avoid the plastic yielding to occur in the deep mantle (i.e. the formation of shear zones). This eventuality is prevented by prescribing a switch that activates when the gradient is $f_\sigma \neq 0$. Therefore, the lithosphere strength envelope is solely controlled by the input parameter σ_y, i.e. $\tau_y = \sigma_y$. The simple yield stress parameterization is chosen in order to reduce the number of target variables, and to focus solely on the effect of grid resolution on tectonic regimes.

Nevertheless, the target parameter τ_y is crucial for this study, since it controls the strength of the lithosphere, eventually leading to a characteristic tectonic regime. In this study, simulations are performed for nine different τ_y ranging from 10 to 90 MPa.

6.3. Numerical Model

For the calculations, the finite-difference code StagYY (*Tackley, 2008*) has been employed. The formulation of the mass, momentum and energy conservation is reported in **Chapter 2.9.2**, equations **(2.9.102)-(2.9.107)**. The energy conservation equation is advanced in time using the explicit FD discretization scheme (*Tackley, 2008*) described in **Chapter 3.6.2**. All simulations were run on the high performance computer clusters btrzx2 and btrzx1 at the University of Bayreuth.

6.3.1. Grid Resolution

Spatial discretization makes use of a staggered grid, where the Stokes' velocities are defined at the edges of the cell, while the scalar parameters are defined at the centre of the cell (**Chapter 3.6.1**).

The 2D spherical annulus (*Hernlund & Tackley, 2008*) is discretized by setting the number of cells in the azimuthal direction (i.e. longitude) R_{azi}, and in the radial direction R_{rad}. In the 2D spherical annulus geometry, the zenithal resolution (i.e. colatitude) is set to $R_{zen} = 1$. The model resolution is expressed as $R_{azi} \times R_{rad}$, with typical values of 512×64 (e.g. *Rozel et al., 2015*) or 1024×128 (e.g. *Nakagawa et al., 2015*). In the azimuthal direction, the number of nodes and cells is equal (the last and the first node/cell are the same for periodicity reasons), whereas in the radial direction the number of nodes is 1 more than the number of cells (e.g. 65 or 129).

Given the nature of this study, R_{azi}, and R_{rad} are the main variable parameters: simulations were performed with four azimuthal resolutions (1024, 512, 256, 128) and three radial resolutions (128, 64, 32). A total of 12 different resolution combinations were tested, so the number of grid cells ranges from 4096 to 131072.

To accurately resolve the upper and lower boundaries of the domain, the grid was refined in radial direction (e.g. *Foley & Becker, 2009*). The fraction of nodes located at the boundaries was kept constant for all resolutions (**Figure 6.1**): 12.5% of the nodes were placed in the top 10% of the domain ($wresl\ surf$), and 6.25% of the nodes were placed in the bottom 5% of the domain ($wresl\ cmb$). The minimum cell thickness ranges from 13 km ($R_{rad} = 128$ cells) to 54 km ($R_{rad} = 32$ cells) (**Table 6.3**), whereas the cell width at the top boundary ranges from 39 km ($R_{azi} = 1024$ cells) to 312 km ($R_{azi} = 128$ cells) (**Table 6.4**).

Given the circular nature of the model, controlling the cell aspect ratio a is not as straightforward as it is for the case of a Cartesian box. The cell aspect ratio is defined as $a = \Delta\varphi_d / \Delta r$, where $\Delta\varphi_d$ is the azimuthal distance in $[m]$ (i.e. cell width) at a given height, and Δr is the cell thickness. The aspect ratio reported in **Figure 6.1** is calculated by considering Δr, and the azimuthal distance $\Delta\varphi_d$ of the top part of the cell. Since the azimuthal distance decreases from the top to bottom boundary (arc of a circle), and given the grid refinement at the boundaries, it is hard to maintain a constant aspect ratio along the radial direction (**Figure 6.1**). However, with the exception of two resolutions (i.e. 128×128 and 1024×32), the resolutions that share the same R_{azi}: R_{rad} ratio (2: 1, 4: 1, 8: 1, 16: 1) have similar cell aspect ratios a as reported in **Table 6.5**.

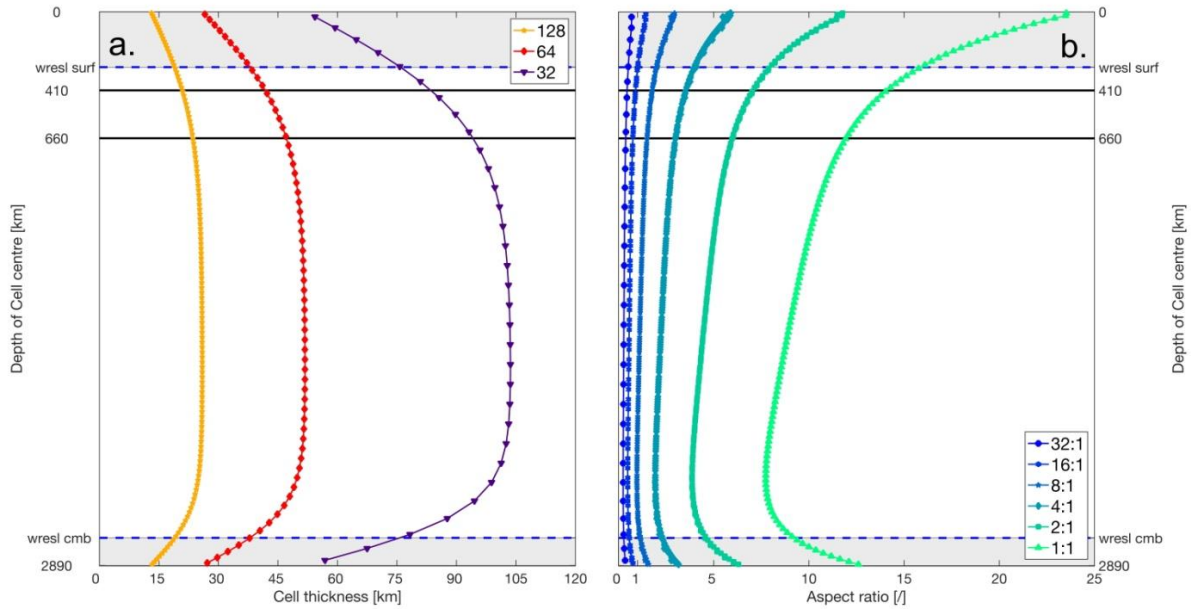

Figure 6.1. (a) radial profile of cell thickness Δr for different radial resolutions: 128 (yellow stars), 64 (red diamonds), and 32 (purple triangles); (b) radial profile of cell aspect ratio a. Each point reports the position of the centre of the corresponding cell.

6.3.2. Advection and Tracers

In StagYY, mantle advection is performed through the marker-in-cell technique (**Chapter 3.5.2**) (*Harlow & Welch, 1965*), where the Lagrangian tracers are moved following an 4^{th}-order (in space) Runge-Kutta scheme (*Gerya, 2019*). The total number of tracers varies between 8.2×10^4 and 2.6×10^6, depending on the cell resolution, i.e. 20 tracers per cell. The temperature field is advected at the Eulerian nodes with the MPDATA acvection scheme (*Smolarkiewicz, 1984*), and a correction routine to compensate for the numerical diffusion of the upwind donor (*Tackley, 2008*).

6.3.3. Initial Conditions

The initial reference state conditions (i.e. temperature T_S, pressure P, density distribution) are identical for all simulations. The initial lithosphere thickness is prescribed to be $L_{init}^{LT} = 100\ km$, with an initial potential temperature of $T_P^{init} = 1600\ K$. Moreover, 8 thermal instabilities (4 upwelling and 4 downwelling) were prescribed in order to initiate mantle convection (**Figure 6.2**).

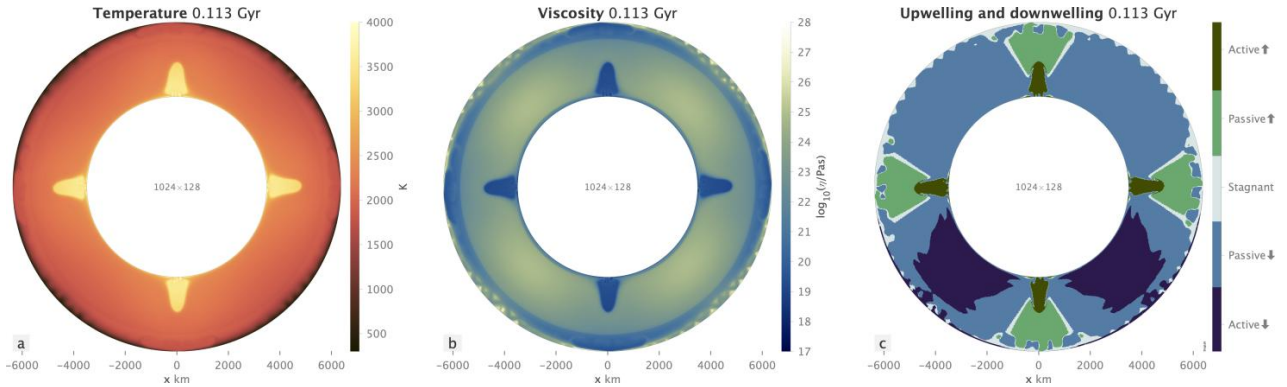

Figure 6.2. Initial mantle conditions, here plotted with StagLab (*Crameri, 2018*) and making use of a scientific colour map (*Crameri et al., 2020*): (a) temperature field (*lajolla*); (b) viscosity field (*devon*); (c) mantle motion (*cork*).

Each simulation is run for 15 $Gyrs$ to achieve a statistical steady-state tectonic regime, and to avoid the influence of the prescribed initial conditions on the outcome of the model.

The validity of this assumption was tested by running a set of simulations with five different initial potential temperatures T_P^{init} $(1200,\ 1400,\ 1600,\ 1800,\ 2000\ K)$ and four representative values for the yield stress τ_y $(10,\ 40,\ 60,\ 90,\ MPa)$. The grid resolution was kept constant at 512×64 cells. As reported in **Figure 6.3**, the root-mean-square (rms) temperature of the whole mantle tends to converge around an equilibrium value which is different for each τ_y: ≈ 2900 K for 90 MPa; ≈ 2500 K for 60 MPa; ≈ 1950 K for 40 MPa; ≈ 1800 K for 10 MPa. These results are coherent with the simulations reported in Chapter 14 of *Schubert et al. (2001)*, and show that the chosen simulation time span is sufficiently long for the model to forget the initial conditions and stabilize into a tectonic regime.

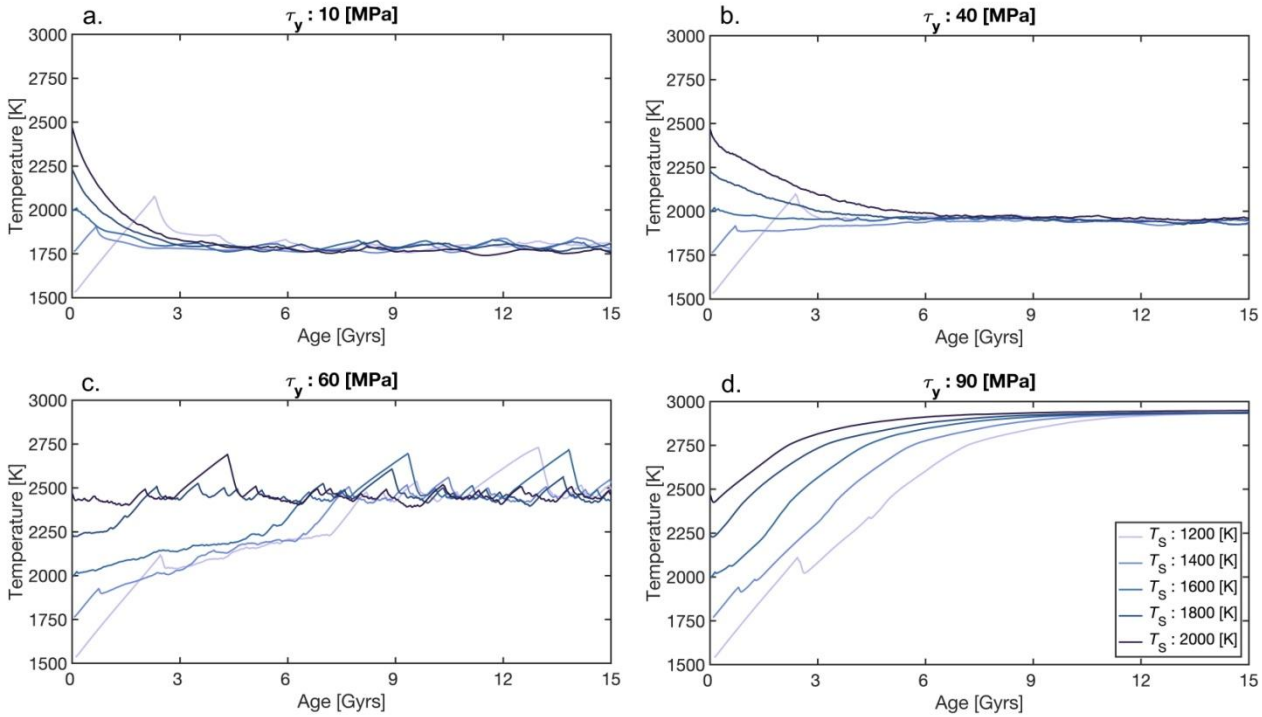

Figure 6.3. Comparison of the evolution of the mean mantle temperature for different initial potential temperatures T_P^{init} $[K]$ (see colours in the legend). Each simulation was run with a resolution of 512×64 grid. The steady state temperature depends on the yield stress, which was chosen to be: (a) $\tau_y = 10\ MPa$; (b) $\tau_y = 40\ MPa$; (c) $\tau_y = 60\ MPa$; (d) $\tau_y = 90\ MPa$.

6.3.4. Variable Parameters

A total of 108 simulation was performed in this study. These simulations vary by different yield stress τ_y, and 12 different resolutions $R_{azi} \times R_{rad}$. The key parameters changed between the simulations are summarized in **Table 6.1**.

Parameter	Symbol	Value	Unit
Yield stress	τ_y	10/20/30/40/50/60/70/80/90	$[MPa]$
Azimuthal resolution	R_{azi}	128/256/512/1024	[/]
Radial resolution	R_{rad}	32/64/128	[/]

Table 6.1. Free parameters

6.4. Target Parameters and Post-Processing

To distinguish the different tectonic regimes a set of target parameters was defined. These parameters requires the re-elaboration and re-computation the outputs produced by StagYY.

6.4.1. Mantle Regions

For a given time frame t_{frame} (**Chapter 3.6.11**), the mantle is subdivided into four regions (LT, UM, MTZ, LM) in order to better analyse the model (**Figure 6.4**). Starting from the bottom, the lower mantle is defined by considering all the cells located between 2890 km (i.e. CMB) and 660 km depth. The mantle transition zone is defined by considering all the cells located between 410 km and 660 km depth. Since it is not possible to position a cell node at these specific depths, the boundaries of the MTZ are represented by the closest cell-centre. The upper mantle starts above 410 km depth, and its top is given by the bottom of the lithosphere.

The lithosphere thickness L^{LT} , for the given t_{frame}, is computed by mapping the 2D ($R_{azi} \times R_{rad}$) topography of the 1600 K isotherm, as reported by *Crameri, (2018)*. An arbitrary threshold of 200 km is prescribed in order to truncate the contribution of subducting slabs. Each cell along the azimuthal direction φ contains a local L_{φ}^{LT}, and the global value for a given time frame is calculated from the median of all L_{φ}^{LT}. The median is used to reduce the contribution of subducting slabs and upwelling plumes. Among all regions, only the LT and the UM change their thickness over time.

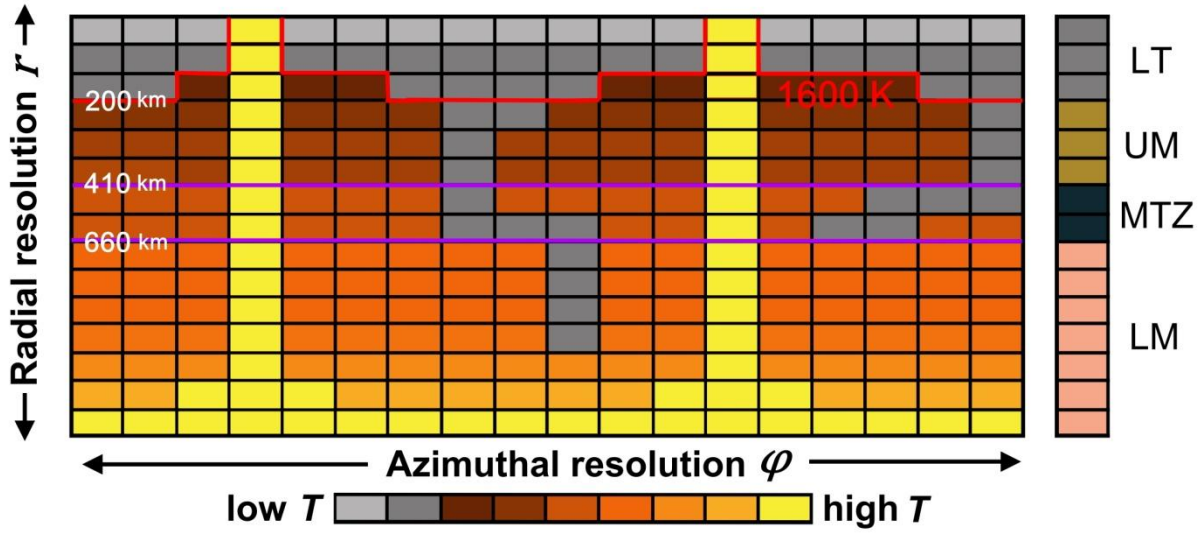

Figure 6.4. Schematics of a 2D $R_{azi} \times R_{rad}$ temperature field. Each cell is defined by one $T_{r,\varphi}$ value computed from the interpolation of the numerical solution at the 4 nodal points. The row index r indicates the radial position, whereas the column index φ indicates the azimuthal position. The pillar on the right represent a 1D radial profile of the domain subdivided into the four regions described in section **6.4.1**. The 1600 K isotherm (combined with the 200 km threshold) is used to defined the lithosphere (LT, grey) and the upper mantle (UM, olive green). The remaining mantle regions are defined by the conventional depth limits: 410 – 600 km mantle transition zone (MTZ, blue), and lower mantle (LM, pink) 660 – 2890 km. The employed colour scheme is the *lajolla* scientific colour map (*Crameri et al., 2020*).

6.4.2. Volume Ratio

When computing a given regional parameter (e.g. lithosphere stress), it is necessary to weight the contribution of the values contained in each cell by considering the ratio $w_r^{region} = V_{r,\varphi}/V^{region}$. Where $V_{r,\varphi}$ is the volume of a cell identified by the row index (r, radial) and the column index (φ, azimuthal), while V^{region} is the total volume of the region. Given the nature of the spherical annulus, $V_{r,\varphi}$ is not constant throughout the domain, but changes in the radial direction r, showing at maximum a 50 % difference between the thin cells at the boundaries and the thick cells in the middle of the model domain (**Figure 6.1**). The volume weight w_r^{region} for the lithosphere and upper mantle is recomputed at each t_{frame}.

6.4.3. Temperature

The first target parameter is the evolution of the rms temperature of the whole mantle (**Chapter 3.6.11**). As shown in **Figure 6.3**, the models described in sections **6.2-6.3** tend to stabilize into a tectonic regime, which is characterized by a distinct temperature evolution profile, as has also been described by *Schubert et al. (2001)* in chapter 14.

For mobile lid behaviour (dripping and plate-like) the convective mantle is constantly able to transport heat to the surface through the plate boundaries, while heat transport in the rest of the lithosphere occurs via conduction. The characteristic temperature profile shows a general cooling of the mantle temperature until the system reaches a low equilibrium temperature ($1800 - 1950\ K$, as in **Figure 6.3-a-b**).

Episodic behaviour is characterized by a saw-tooth temperature profile featuring two stages: stagnant lid stage (raising temperature), and mantle overturn (temperature drop) (**Figure 6.3-c**). During the global resurfacing events the convective mantle is able to transport the heat to the surface and a large amount of heat is released.

For stagnant lid regimes the convective mantle is covered by a strong purely conductive lithosphere. The slow heat diffusion at the top boundary leads to a general increase of the inner mantle temperature, until it reaches an equilibrium plateau (**Figure 6.3-d**).

6.4.4. Viscosity & Rayleigh Number

The weighted median viscosity is computed for: specific mantle depths (surface, mid mantle and CMB), mantle regions (LM, MTZ, UM, LT), and the whole mantle. The calculation is performed in two steps (**Figure 6.5**):

1. Computation of the azimuthal median for all rows of the matrix (i.e. the heights of the domain) to obtain 1D radial profile of the mantle. The median is used instead of the mean to reduce the contribution of high viscosity slabs and low viscosity plumes. In this step it is not necessary to weight the contribution of each cell, since for a given depth the cell volume is constant.
2. Computation of the weighted average by multiplying each cell of the 1D radial profile for w_r^{region} and by summing up the cells of a specific region.

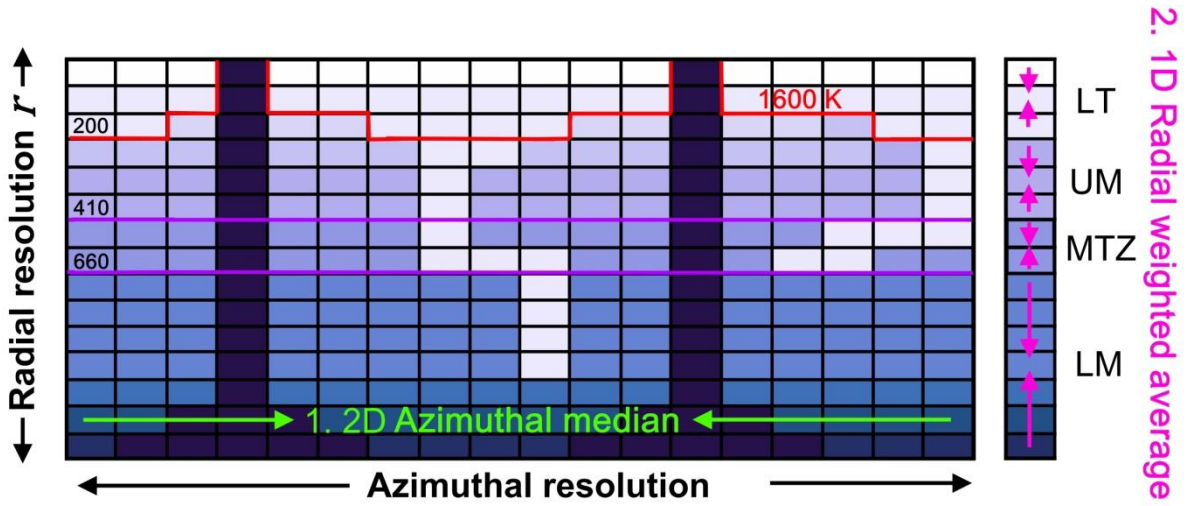

Figure 6.5. Schematics of a 2D $R_{azi} \times R_{rad}$ viscosity field. Each cell is defined by one η value computed from the interpolation of the numerical solution at the 4 nodal points. The green arrows in the 2D field represent the computation of the azimuthal median for each row (step 1), while the pink arrows in the 1D radial profile indicate the radial weighted average for each region (step 2). The employed colour scheme is the *devon* scientific colour map (*Crameri et al., 2020*).

The viscosity at specific mantle depths is computed as the azimuthal median of the cell array at a given height, i.e. surface η considers the first cell row, mid mantle η employs the closest cells to 1445 km depth, and CMB η compute only the last row. Regional viscosity is computed from the 1D azimuthal median profile by performing the weighted mean (w_r^{LM}, w_r^{MTZ}, w_r^{UM}, w_r^{LT}).

The whole mantle viscosity is computed following the procedure mentioned above, while removing the lithospheric contribution from the computation (w_r^{tot-LT}). Without the lithospheric correction, the presence of a $\approx 100\ km$ thick high viscosity layer would significantly alter the computation of the total viscosity which may result in misinterpretation of the data.

Mobile lid behaviours are expected to maintain high mantle viscosity due to the low internal temperatures.

For episodic regimes, the characteristic periodicity should result in a low internal viscosity during the stagnation stage, and a sudden increase in viscosity during a mantle overturn event. This peak correspond to the temperature drop caused by resurfacing event, and the presence of high viscosity lithosphere at depth.

For stagnant lid regimes, a low internal viscosity can be expected due to the high internal temperatures (see section **6.4.3**, and **Figure 6.3-d**), and the absence of high viscosity materials in the mantle.

Given the exponential temperature dependency of viscosity **(6.2.1)**, limited changes of T can cause variations in viscosity spanning several orders of magnitude. This strongly affects the vigour of convection, which is quantified by the effective Rayleigh number Ra_{eff} (see **Chapter 2.8.1**). The parameter Ra_{eff} is calculated as:

$$Ra_{eff} = \frac{\rho(r)\, g\, \alpha(r)\, \Delta T\, D^3}{\kappa(r)\, \eta^{Tot-LM}(t)} \tag{6.4.3}$$

With the gravity acceleration $g = 9.81\ m\ s^{-2}$, the temperature jump $\Delta T = 2400\ K$ which is computed as the difference between the temperatures at the CMB ($4000\ K$) and the base of the lithosphere ($1600\ K$), and the mantle thickness $D = 2890\ km$. The density $\rho(r)$, thermal expansivity $\alpha(r)$, and thermal diffusivity κ(r) are depth-dependent (see section **6.2.4**) and calculated as the arithmetic mean over the 1D radial profile of the mantle. Thermal diffusivity is calculated from thermal conductivity $\Lambda(r)$, density $\rho(r)$ and specific heat capacity $Cp = 1200\ J\ kg^{-1}\ K^{-1}$. The whole mantle viscosity η^{Tot-LM} is computed for each time step (t), and employed for the calculation of the effective Rayleigh number.

It can be expected that the effective Rayleigh number should show an opposite trend compared to the one of viscosity: low Ra_{eff} when the viscosity of the mantle is high (i.e. mobile regimes), whereas high Ra_{eff} when the viscosity of the mantle is low (i.e. stagnant and episodic).

6.4.5. Nusselt Number

As heat transport in the Earth's mantle is strongly affected by the tectonic regime, the Nusselt number Nu (**Chapter 2.8.3**) is a useful tool to compare different tectonic regimes (*Tosi et al., 2015*). To determine the relative contribution of convective and conductive heat transport in the different simulations, the Nusselt number at the surface (Nu_{top}) and at the core mantle boundary (Nu_{bot}) are computed:

$$Nu_{top} = \frac{Q_{top}}{Q_{cond}} \qquad Nu_{bot} = \frac{Q_{bot}}{Q_{cond}} \tag{6.4.4}$$

Where Q_{top}, and Q_{bot} are the heat fluxes at the top and bottom boundary respectively, whereas Q_{cond} is the heat flux delivered by mere conduction (**Figure 6.6**) and is computed as:

$$Q_{cond} = R_H \rho_{ave} D \tag{6.4.5}$$

Where R_H is the internal heating rate, ρ_{ave} is the average mantle density, and D is the domain thickness. Both top and bottom heat flux for each timestep are computed as the summation of all local heat fluxes, times the length of the outer and inner circumference (i.e. $2\pi r^{surf}$ and $2\pi r^{CMB}$).

(6.4.6)

$$Q_{top} = \sum_{\varphi=1}^{R_{azi}} Q_{top}\,(\varphi) * (2\pi r^{surf})$$

$$Q_{bot} = \sum_{\varphi=1}^{R_{azi}} Q_{bot}\,(\varphi) * (2\pi r^{CMB})$$

Where $Q_{top}(\varphi)$ and $Q_{bot}(\varphi)$ are the local heat fluxes in the cells $[1, \varphi]$ and $[R_{rad}, \varphi]$ respectively, and φ is the cell index in the azimuthal direction. The local heat flux is calculated considering the isothermal boundaries (i.e. $T_{top} = 300\ K$ and $T_{bot} = 4000\ K$), the temperature at the base of the first cell (bounded by the nodes $[1, \varphi]$ and $[2, \varphi]$), and the temperature at the top of the last cell (bounded by the nodes $[R_{rad}, \varphi]$ and $[R_{rad} + 1, \varphi]$) as reported in equation **(3.3.25)**.

(6.4.7)

$$Q_{top}(\varphi) = \left(\Lambda_1 \frac{T_{2,\varphi} - 300}{\Delta r}\right)$$

$$Q_{bot}(\varphi) = \left(\Lambda_{R_{rad}} \frac{4000 - T_{R_{rad},\varphi}}{\Delta r}\right)$$

Where Λ_1 and $\Lambda_{R_{rad}}$ are the thermal conductivities at the centre of the first and last cell in the radial direction, and Δr is the cell thickness.

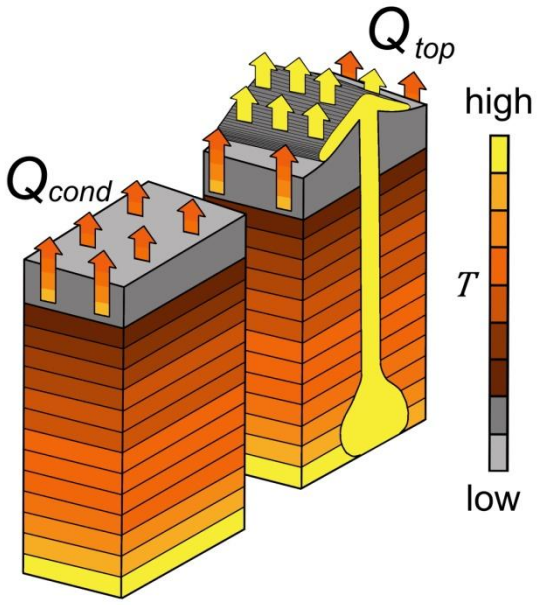

Figure 6.6. Schematics of the heat fluxes: Q_{cond} pure conduction, and Q_{top} includes convection (due to the rising plume in yellow) and conduction. The employed colour scheme for the temperature T is the *lajolla* scientific colour map (*Crameri et al., 2020*).

The higher the Nusselt number, the more effective is the convective heat transport. Nu_{top} should be high for mobile lid regimes given the presence of numerous spreading margins where the mantle cools directly at the surface. For stagnant lid regimes Nu_{top} should be much lower, since the strong lithosphere prevents the heat exchange between the mantle and the surface. The episodic regime is expected to present strong variations of Nu_{top}, given the sudden burst of heat flux Q_{top} caused by the mantle overturn events (*Moresi & Solomatov, 1998*; *Tosi et al., 2015*).

6.4.6. Mobility, Plateness & Surface Velocity

The two parameters to analyze the lithosphere, namely mobility M_o and plateness P_{80} are defined in *Tackley (2000b)*. Mobility is defined as:

$$M_o = \frac{u_{rms}^{surf}}{\boldsymbol{u}_{rms}^{whole}} \tag{6.4.8}$$

Where u_{rms}^{surf} is the root mean square value of the azimuthal velocity (i.e. computed from the first cell), and $\boldsymbol{u}_{rms}^{whole}$ is the root mean square value of the whole mantle velocity (radial and azimuthal).

The mobility for mobile lid regimes would be characterized by high M_o due to the presence of moving plates. Episodic behaviour should present $M_o \approx 0$ during the stagnant lid stages, followed by bursts of mobility caused by the sudden lithosphere collapse. In the stagnant lid regimes, instead, the mobility should be $M_o \approx 0$ all the time given the negligible azimuthal surface velocity and the internal high velocity of the convective mantle.

Plateness is defined as:

$$P_{80} = 1 - \frac{f_{80}}{0.6} \tag{6.4.9}$$

Where f_{80} is the fraction of the surface area where $> 80\%$ of the deformation occurs. Ideally, for perfect plates, all of the deformation would be concentrated in an infinite small portion of the plate, i.e. $f_{80} \to 0$. For the opposite case, where all deformation is uniformly distributed, $f_{80} = 0.8$. In the reference model presented in *Tackley (2000b)* (i.e. internally heated with $Ra = 10^6$), 80% of the deformation is distributed in 60% of the area, resulting in a value of $f_{80} = 0.6$. This value is taken as a reference for the computation of plateness. For a perfect plate $P_{80} = 1$ ($f_{80} \to 0$), whereas uniformly deformed lithosphere shows a plateness, $P_{80} < 0$ ($f_{80} > 0.6$). A plateness value of $0 < P_{80} < 1$ means that 80% of the deformation is concentrated in less than 60% of the surface area ($f_{80} < 0.6$).

From these considerations it follows that mobile lid regimes would have a high plateness given the presence of localized plate margins. Episodic behaviour should be characterized by high plateness during the stagnant lid regimes and a sudden drop of P_{80} when the lithosphere collapses and deformation is diffuse. Stagnant lid regimes should exhibit a low plateness due to the absence of plate boundaries as a consequence of the diffuse deformation.

From the surface azimuthal velocity u^{surf} it is possible to detect the plate boundaries by locating the reversing polarities (converging →← and diverging ←→) and by applying a threshold to remove minor fluctuations. The polarity reversal can be detected by multiplying the values for each cell with those for the consecutive one, and then locate the cells where the computation shows negative values. The rms velocity at the plate boundary u_{plbn}^{surf}, is computed by considering the velocities of the cell where the polarity reversal is located $[1, \varphi]$, and the two neighbouring cells $[1, \varphi - 1]$ and $[1, \varphi + 1]$.

$$u_{plbn}^{surf} = \sqrt{\left(u_{1,\varphi-1}^{surf}\right)^2 + \left(u_{1,\varphi}^{surf}\right)^2 + \left(u_{1,\varphi+1}^{surf}\right)^2} \tag{6.4.10}$$

A given location is considered to be a plate boundary if $u_{plbn}^{surf} > 1\ cm\ yr^{-1}$ (*Syracuse et al., 2010*). The average number of plate boundaries over time should progressively decrease as τ_y increases, reaching ≈ 0 for the stagnant lid regime.

6.4.7. Lithosphere Stress

For a given azimuthal position φ, a lithosphere sector is defined by all the cells composing the lithosphere in the radial direction, i.e. $[1 \rightarrow R_{rad}^{LT}, \varphi]$ (see section **6.4.1**). For each sector, the volume weight is computed as $w_{r,\varphi}^{sec} = V_{r,\varphi}/V_{\varphi}^{sec}$, where $V_{r,\varphi}$ is the cell volume, and V_{φ}^{sec} is the sector volume. From the 2D lithosphere thickness field, it is possible to compute the weighted average stress σ_{φ}^{sec} of each sector (**Figure 6.7**).

$$\sigma_{\varphi}^{sec} = \sum_{r=1}^{R_{rad}^{LT}} \sigma_{r,\varphi} * w_{r,\varphi}^{sec} \tag{6.4.11}$$

The fraction of yielded lithosphere f_y is calculated as the number of sectors with $\sigma_{\varphi}^{sec} = \tau_y$, divided the total number of sectors in the azimuthal direction R_{azi}.

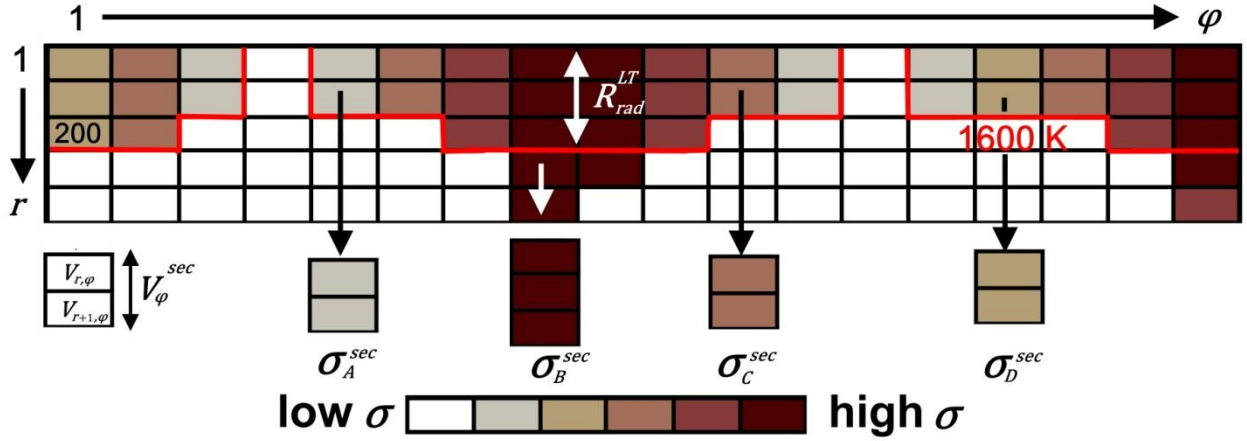

Figure 6.7. Schematics of a 2D $R_{azi} \times R_{rad}$ stress field. Each cell is defined by one σ value computed from the interpolation of the numerical solution at the 4 nodal points. Lithosphere is bounded by the 1600 K isotherm (red line), and the 200 km threshold. The row index r indicate the radial position, whereas the column index φ indicates the azimuthal position. The parameter R_{rad}^{LT} indicates the number of cells that compose the lithosphere at a given azimuthal position, and it defines a sector. The volume of each sector is indicated as V_{φ}^{sec}, while the volume of each cell is given by $V_{r,\varphi}$. The stress of each sector σ_{φ}^{sec} is computed as described in the main text. The employed colour scheme is the *bilbao* scientific colour map (*Crameri et al., 2020*).

From the $2D$ stress field, it is possible to calculate the cumulative maximum stress of the lithosphere σ_{max}^{LT}, similar to what was done by *Dal Zilio et al. (2018)*.

$$\sigma_{max}^{LT} = \sum_{r=1}^{R_{rad}^{LT}} \sigma_r^{max} * \frac{\Delta r_r}{L_{ave}^{LT}} \tag{6.4.12}$$

Where σ_r^{max} is the maximum stress at each depth interval, Δr_r is the thickness of the depth interval, and L_{ave}^{LT} is the average thickness of the lithosphere at a given time frame.

Moreover, the 2D weighted stress $\sigma_{r,\varphi}^{w}$ field of the lithosphere is computed by considering $w_{r,\varphi}^{LT} = V_{r,\varphi}/V^{LT}$ where V^{LT} is the total lithosphere volume for a given time frame. From the weighted stress it is possible to compute the average stress per cell σ_{ave}^{LT}, and the cumulative lithosphere stress σ_{tot}^{LT}. The parameter σ_{ave}^{LT} is then used to calculate the ratio $r_y = \sigma_{ave}^{LT}/\tau_y$ to quantify whether a cell in the lithosphere is close to reaching the yield stress τ_y.

In general, mobile lid behaviour is expected to result in a highly stressed lithosphere where the fraction f_y and the ratio r_y decrease from dripping (diffuse subduction) to plate-like behaviour (plate margins subduction). Episodic behaviour should display alternate periods of accumulating stress (stagnant lid period) and sudden stress-release events (mantle overturns), whereas the stagnant lid regime should be characterized by a low-σ lithosphere with f_y and r_y tending towards 0.

6.5. Numerical Results

After reaching its statistical steady-state, each simulation stabilizes into one of the four tectonic regimes, i.e. micro-plate dripping, plate-like subduction, episodic overturn, and stagnant lid (**Figure 6.8**).

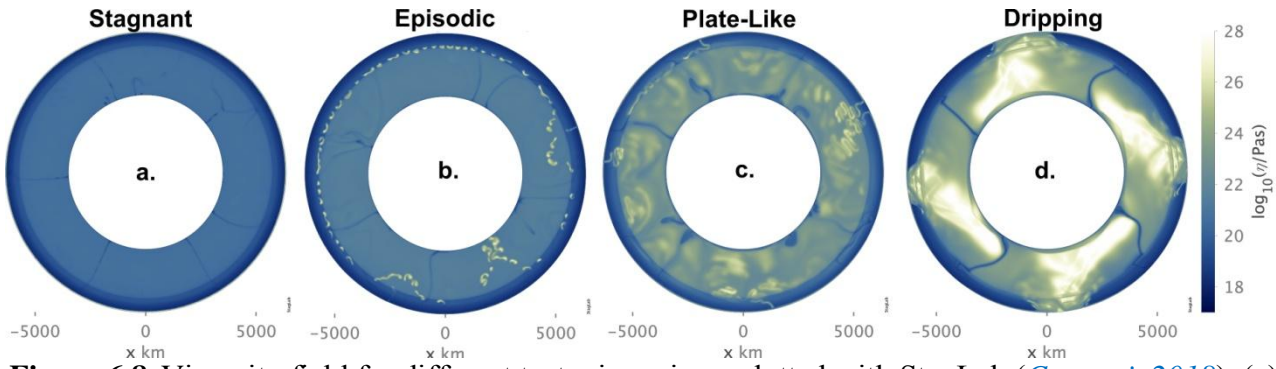

Figure 6.8. Viscosity field for different tectonic regimes plotted with StagLab (*Crameri, 2018*): (a) stagnant-lid mode characterized by the absence of high-η lid in the mantle; (b) episodic resurfacing where the entire lithosphere collapses in one event; (c) plate-like regime characterized by the presence of long and continuous subducting slabs in the mantle; (d) micro-plates dripping where subduction occurs similar to a snowfall. The viscosity fields use the *devon* scientific colour map (*Crameri et al., 2020*).

Each regime has been identified by analyzing the parameters described in section **6.4**: temperature, viscosity (and Ra), surface Nusselt number (and Nu_{bot}), mobility, plateness and lithosphere stress (in particular the ratio r_y and fraction f_y).

The examples reported here are taken from the set of simulations with a resolution of 512×64 and a yield stress τ_y of: $10\ MPa$ (dripping); $40\ MPa$ (plate-like); $60\ MPa$ (episodic); $90\ MPa$ (stagnant). Additional parameters are reported in black (e.g. Ra, Nu_{bot}, f_y).

6.5.1. Lithosphere Thickness Analysis

Some diagnostic information regarding the tectonic regimes can be drawn from the study of the time evolution of lithosphere thickness (**Figure 6.9**, **Table 6.6**), as reported in Chapter 14 of *Schubert et al. (2001)*.

In this study, the mobile lid regime models tend to maintain an approximately constant lithosphere thickness over time ($\pm 25\ km$) (**Figure 6.9-a-b**, **Table 6.6**). This is in contrast with the models reported by *Schubert et al. (2001)*. However, this can be explained by the different model parameters, since their initial lithosphere thickness L_{init}^{LT} is set to $0\ km$, whereas in the present study $L_{init}^{LT} = 100\ km$. The thick lithosphere observed in the dripping mode is caused by the broad subduction areas **Figure 6.8-d**, and the vast input of cold lithospheric material, which pushes the $1600\ K$ isotherm downwards.

The stagnant lid regime is characterized by a general thinning of the lithosphere over time (**Figure 6.9-d**), which stabilizes around $50-60\ km$ (**Table 6.6**) once the system reaches a statistical steady-state equilibrium between the internal heat production and the heat dissipation. The thin lithosphere is a result of the high mantle temperatures, and the vigorous convection that erodes the deepest portion of the lid (*Crameri & Tackley, 2016*).

In the episodic overturn regime, the lithosphere shows a thinning trend similar to the one of the stagnant lid (*Armann & Tackley, 2012*; *Rolf et al., 2018*). However, the lithosphere is far from being at steady-state at it shows abrupt oscillations which are characteristic for this regime (**Figure 6.9-c**): collapses of the lithosphere thickness (i.e. $L^{LT} \rightarrow 0$), followed by fast lithosphere thickening caused by the sudden cooling of the surface.

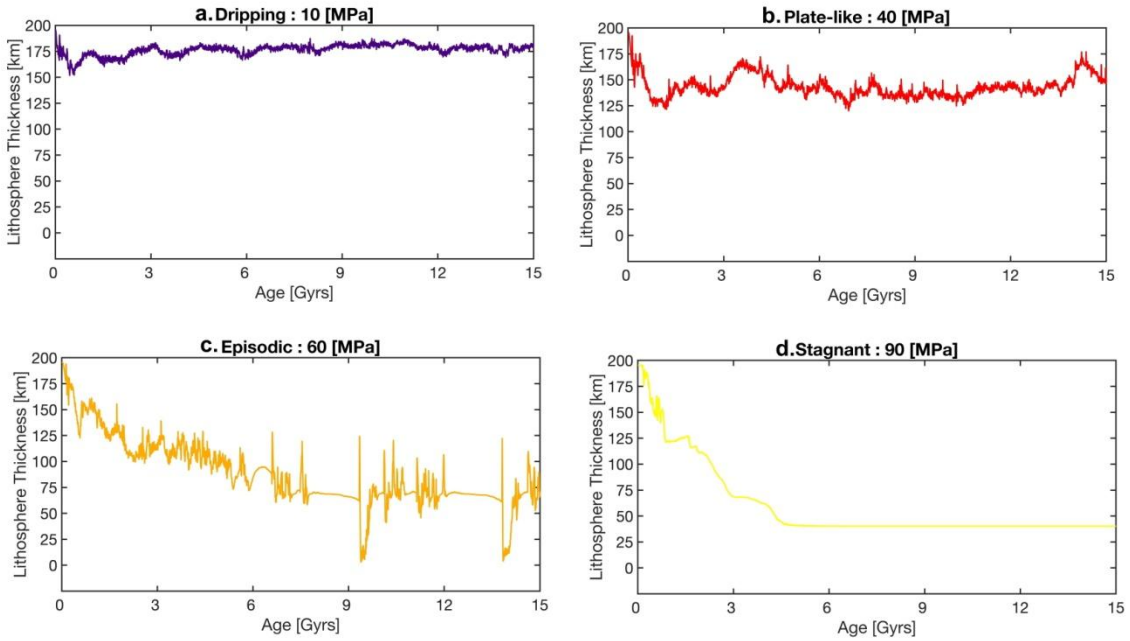

Figure 6.9. Time evolution of the lithosphere thickness L^{LT} $[km]$ for different tectonic regimes: (a) dripping (purple); (b) plate-like (red); (c) episodic (orange); (d) stagnant lid (yellow). These examples are taken from simulations with 512×64 grid points.

6.5.2. Dripping Mode

Snowfall-like subduction (see **Figure 6.10**) occurs in simulations where a low yield stress ($10 \leq \tau_y \leq 30\ MPa$, for the 512×64 resolution) is employed and is characterized by:

- Root mean square temperature (**Figure 6.10-a**): the heat loss at the surface is higher than the internal heat production, thus leading to a general cooling of the system. The low yield stress offered by the lithosphere allow for an effective heat exchange between the warm rising plumes and the surface, while the cold sinking plates cool the mantle (**Figure 6.8-d**).
- Mantle viscosity and Ra_{eff} (**Figure 6.10-b**): the low T_{rms}, combined with the large quantity of stiff lithospheric material at depth, result in a high median mantle viscosity ($\eta^{Tot-LM} \approx O(10^{25}\ Pa\ s)$), and a low effective Rayleigh number ($Ra_{eff} \approx O(10^4)$).
- Surface Nusselt number Nu_{top} (**Figure 6.10-c**): the efficient convective heat transport established in this regime is reflected by the high fluctuating values of Nu_{top} (i.e. $Q_{top} \approx 40 Q_{cond}$). The contribution of the CMB heat flux to the total heat balance is quantified by $N_{bot} \approx 0.5 Nu_{top}$.
- Mobility M_o (**Figure 6.10-d**): dripping tends to stabilize a configuration characterized by 4 spreading margins and 4 convergent margins, where a continuous subduction of micro-plates occurs (**Figure 6.8-d**). Most of the mantle motion occurs at the edges of the

convective cells, since this configuration is neither destabilized by the onset of new plumes, nor by stirring due to strong subducting plates. The cores of the convective cells remain relatively motionless. Therefore, the fast lateral migration of the lid u_{rms}^{surf} is larger than the whole mantle velocity $\boldsymbol{u}_{rms}^{whole}$, leading to a high mobility $M_o \approx 3$.

- Plateness P_{80} (**Figure 6.10-e**): despite the low yield stress τ_y, the dripping behaviour results in broad convergent margins where most of the deformation is concentrated (**Figure 6.8-d**). The remaining plates are relatively undeformed and migrate laterally from the spreading margins, which is also reflected by the high plateness $P_{80} > 0.8$.
- Yield ratio r_y and yield fraction f_y (**Figure 6.10-f**): the low τ_y that characterizes the dripping behaviour produces an overly stressed lithosphere with $\sigma_{ave}^{LT} > \tau_y$, thus leading to a high yield ratio $r_y > 1$. However, the yield fraction is $f_y < 0.5$, which indicates that the yield stress is reached in less than 50% of the lithospheric volume. This is in agreement with the high plateness P_{80}. The high r_y is determined by the 1600 K isotherm criteria defining the lithosphere thickness, and the broad subduction zone areas that characterize the dripping mode (**Figure 6.8-d**). In these locations, the large volume of cold lithospheric material extends the 1600 K isotherm down to the prescribed thickness limit ($200\ km$), and the computation of σ_{ave}^{LT} considers everything within this depth to be lithosphere. In this way, the contribution of already subducted micro-plates is included in the computation of r_y.

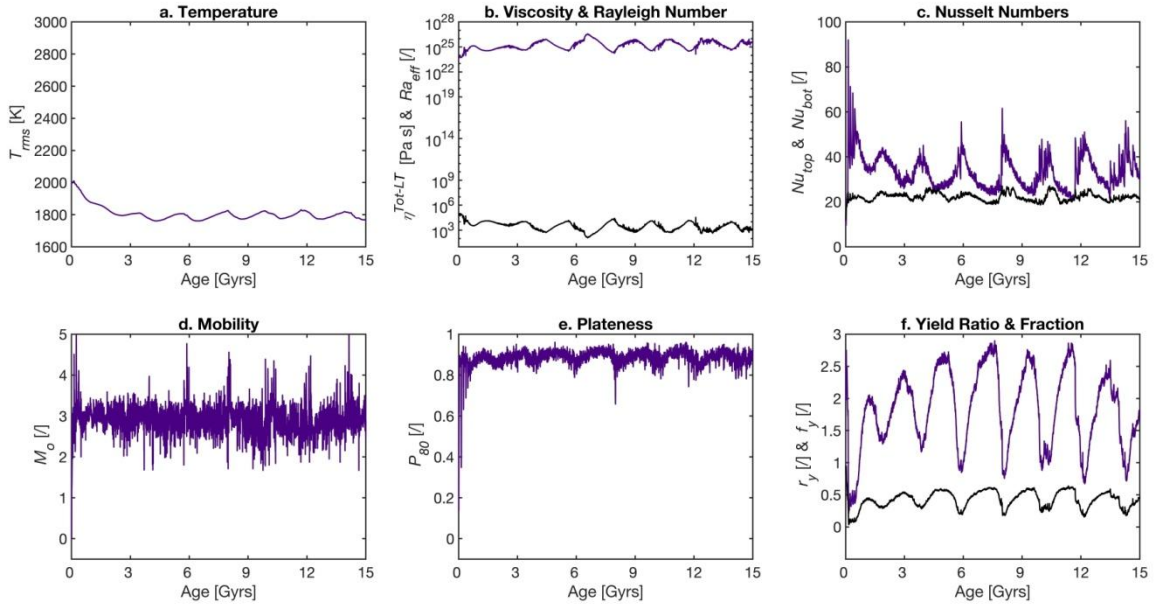

Figure 6.10. Dripping mode evolution profiles (purple lines): (a) rms temperature; (b) median mantle viscosity η^{Tot-LM} and Ra_{eff} (black); (c) surface and CMB Nusselt number Nu_{top} and Nu_{bot} (black); (d) mobility M_o; (e) plateness P_{80}; (f) yield ratio r_y and yield fraction f_y (black).

6.5.3. Plate-Like Regime

The plate tectonic regime (see **Figure 6.11**) occurs for intermediate yield stress ($40 \leq \tau_y \leq 50\ MPa$, for the 512×64 resolution), and is characterized by:

- Root mean square temperature (**Figure 6.11-a**): similar to the dripping mode, the yielding of the lithosphere establishes an efficient heat transport that maintains a relatively cold mantle.
- Mantle viscosity and Ra_{eff} (**Figure 6.11-b**): given the low T_{rms}, and the presence of cold and stiff lithospheric material, the median mantle viscosity η^{Tot-LM} tends to be quite high ($\approx O(10^{25}\ Pa\ s)$), which leads to a low $Ra_{eff} \approx O(10^4)$.
- Surface Nusselt number Nu_{top} (**Figure 6.11-c**): the efficiency of convective heat transport is indicated by a high $Nu_{top} \approx 40$. The contribution of the CMB heat flux to the total heat balance is quantified by $N_{bot} \approx 0.5 Nu_{top}$.
- Mobility M_o (**Figure 6.11-d**): the subduction of strong lithosphere allows for the propagation of slab pull to the rest of the plate, thus causing sustained lateral migration of the lid. The azimuthal velocity u_{rms}^{surf} is also enhanced by the ridge push at the spreading margins, and leads to a high mobility $M_o \approx 2$.
- Plateness P_{80} (**Figure 6.11-e**): in plate-like behaviour, most of the deformation is concentrated at the plate margins (spreading ridges and converging trenches), hence the plateness is very high $P_{80} \approx 0.9$.
- Yield ratio r_y and yield fraction f_y (**Figure 6.11-f**): stress localization is also evident from $r_y \approx 0.5$ (50% of the cells are at the yield), and $f_y < 0.2$ (the stress is focussed in less than 20% of the lithosphere).

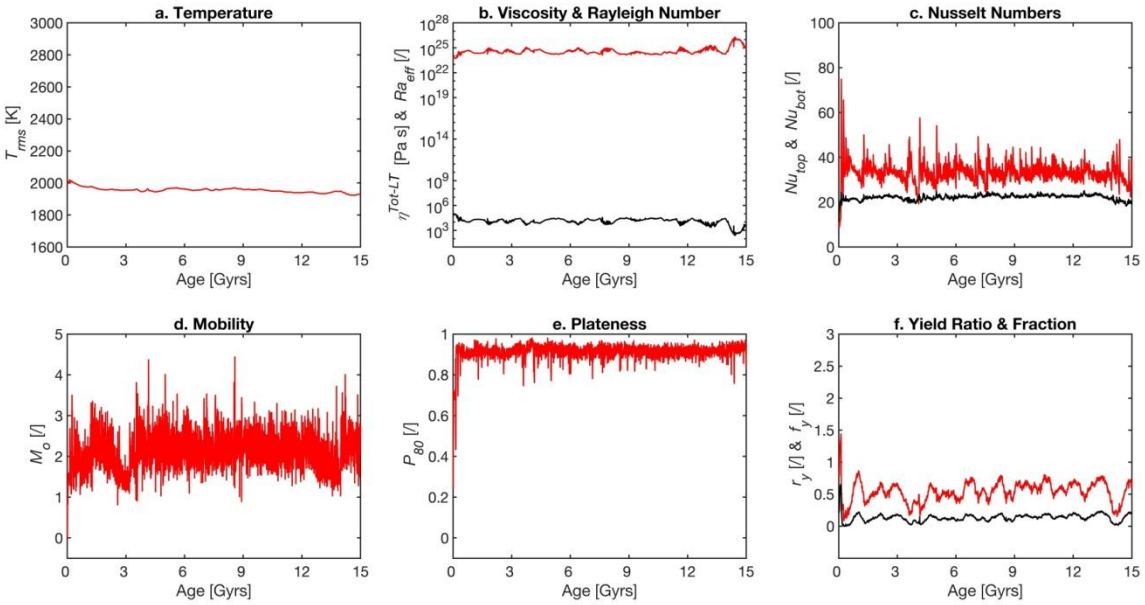

Figure 6.11. Plate-like regime evolution profiles (red lines): (a) rms temperature; (b) median mantle viscosity η^{Tot-LT} and Ra_{eff} (black); (c) surface and CMB Nusselt number Nu_{top} and Nu_{bot} (black); (d) mobility M_o; (e) plateness P_{80}; (f) yield ratio r_y and yield fraction f_y (black).

6.5.4. Episodic Lid Regime

The episodic lid regime (see **Figure 6.12**) occurs at intermediate to high yield stresses ($\tau_y = 60\ MPa$, for the 512×64 resolution), and is characterized by:

- Root mean square temperature (**Figure 6.12-a**): the T_{rms} evolution shows the typical saw-tooth profile with peaks (stagnant lid stage) and drops (resurfacing events). The overall trend shows an increase of internal temperatures.
- Mantle viscosity and Ra_{eff} (**Figure 6.12-b**): the temperature oscillations affect the median mantle viscosity which is lower than in previous regimes ($\approx O(10^{22}\ Pa\ s)$), leading to a higher effective Rayleigh number ($\approx O(10^7)$). Viscosity decreases during the stagnant lid stages, while it increases during the mobile phase due to the sudden cooling of the mantle.
- Surface Nusselt number Nu_{top} (**Figure 6.12-c**): the strongest evidence for an episodic lid behaviour are the extreme oscillations of Nu_{top}, which range between 20 and 100, as consequence of heat flux bursts during resurfacing (*Moresi & Solomatov, 1998*). The sudden cooling during a mantle overturn increases the temperature difference at the lower boundary, and consequently enhances the bottom heat flux Q_{bot}.
- Mobility M_o (**Figure 6.12-d**): mantle overturns causes large variations of mobility, with $M_o = 0$ during the stagnant lid phases and $M_o = 3$ during resurfacing events.
- Plateness P_{80} (**Figure 6.12-e**): the sudden collapse of the lithosphere starts from few trenches, and propagates quickly throughout the rest of the plate (*Crameri & Tackley, 2016*). During the stagnant lid phase, deformation is localized in incipient plate boundaries, while the rest of the plate remains relatively undeformed. This explains the overall high $P_{80} \approx 0.8$, which suddenly drops to ≈ 0.3 when the entire lithosphere deforms.
- Yield ratio r_y and yield fraction f_y (**Figure 6.12-f**): the episodic lid regime exhibits a non-negligible yield ratio $r_y < 0.5$, where most of the time the yielding fraction is ≈ 0, while it is extremely high during resurfacing.

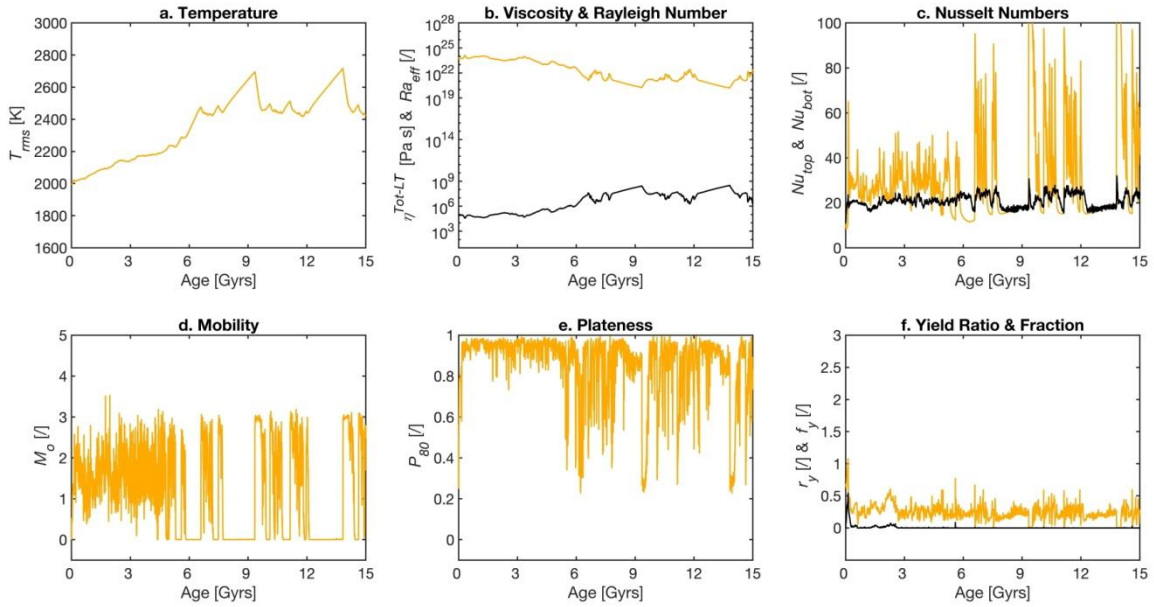

Figure 6.12. Episodic lid evolution profiles (orange lines): (a) rms temperature; (b) median mantle viscosity η^{Tot-LT} and Ra_{eff} (black); (c) surface and CMB Nusselt number Nu_{top} and Nu_{bot} (black); (d) mobility M_o; (e) plateness P_{80}; (f) yield ratio r_y and yield fraction f_y (black).

6.5.5. Stagnant Lid Mode

The stagnant lid mode (see **Figure 6.13**) occurs at high yield stress ($\tau_y > 60\ MPa$ for the 512×64 resolution), and is characterized by:

- Root mean square temperature (**Figure 6.13-a**): the presence of a strong unbreakable lid reduces the heat transport towards the surface, and the balance between internal heat production and heat dissipation leads to an overall T_{rms} increase.
- Mantle viscosity and Ra_{eff} (**Figure 6.13-b**): the very high T_{rms} ($> 2800\ K$) determines a low median mantle viscosity ($\eta^{Tot-LM} < O(10^{20}\ Pa\ s)$), and an extremely vigorous mantle convection ($Ra_{eff} \approx O(10^9)$).
- Surface Nusselt number Nu_{top} (**Figure 6.13-c**): the strong lid prevents convective heat transport to the surface, thus leading to a low Nu_{top} (≈ 20). This value is $\neq 1$ due to the onset of convective instabilities at the base of the lithosphere, which are still capable of removing more heat than through mere conduction (*Manga et al., 2001*; *Jellinek, 2002*; *Solomatov & Moresi, 2000*). The contribution of the CMB heat flux to the total heat balance is quantified by $N_{bot} \approx 0.5 Nu_{top}$.
- Mobility M_o (**Figure 6.13-d**): due to the absence of plate boundaries and lateral plate motion $M_o = 0$.
- Plateness P_{80} (**Figure 6.13-e**): the value of $P_{80} < 0.6$ and not $P_{80} \leq 0$ indicates that deformation is not uniformly distributed, but is apparently concentrated in a few locations of the lid. Most likely this happens where the rising plumes interact with the base of the lithosphere, thus causing mild tensile deformation (*Manga et al., 2001*).
- Yield ratio r_y and yield fraction f_y (**Figure 6.13-f**): in every portion of the lithosphere, the accumulated stress is well below the yield stress, which results in $r_y \approx 0$ and $f_y \approx 0$.

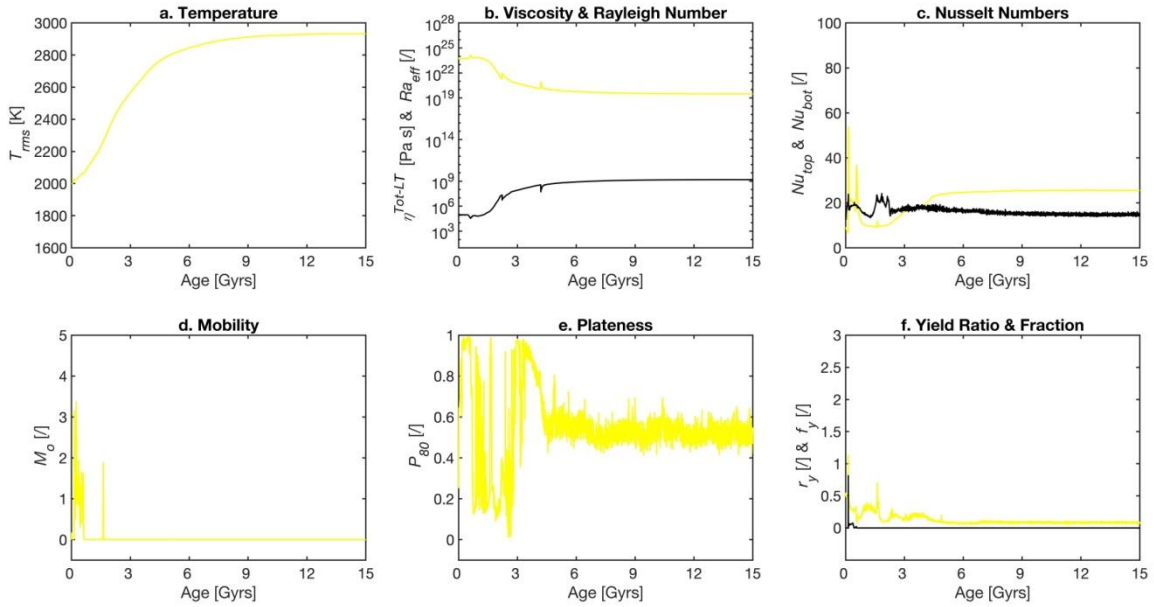

Figure 6.13. Stagnant lid evolution profiles (yellow lines): (a) rms temperature; (b) median mantle viscosity η^{Tot-LT} and Ra_{eff} (black); (c) surface and CMB Nusselt number Nu_{top} and Nu_{bot} (black); (d) mobility M_o; (e) plateness P_{80}; (f) yield ratio r_y and yield fraction f_y (black).

6.5.6. Tectonic Regime Map

In this study, a set of 108 simulations has been run by varying the yield stress τ_y, the azimuthal resolution R_{azi}, and the radial resolution R_{rad}. Each simulation stabilizes one tectonic regime, which was distinguished by employing the aforementioned target parameters: (1) rms temperature T_{rms}, (2) mantle viscosity η^{Tot-LM} and effective Rayleigh number Ra_{eff}, (3) top and bottom Nusselt number Nu_{top} and Nu_{top}, (4) mobility M_o, (5) plateness P_{80}, (6) yield ratio r_y and yield fraction f_y. Based on the tectonic regime distribution map (see **Figure 6.14**), it is possible to draw few conclusions regarding the effect of yield stress, azimuthal resolution, and radial resolution on the statistical steady-state behaviour.

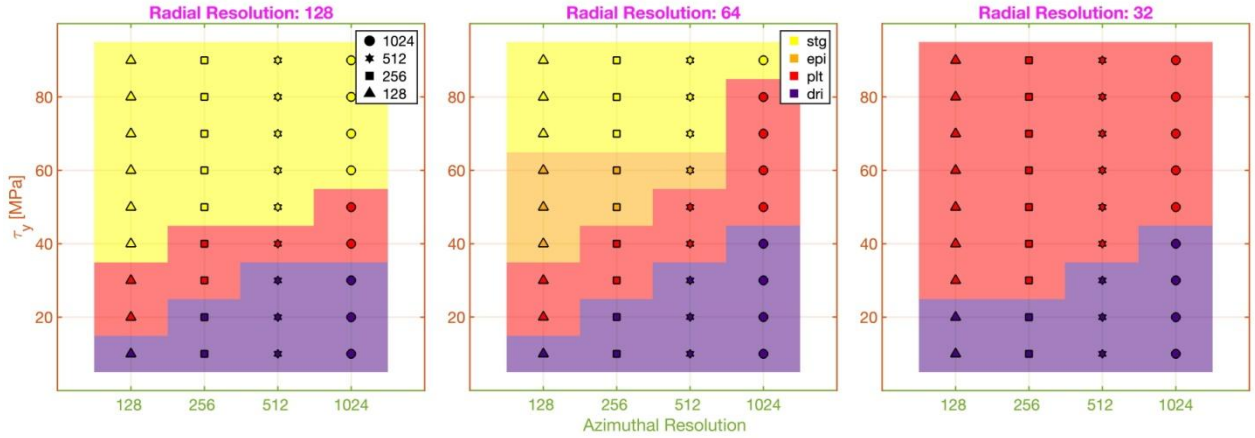

Figure 6.14. Tectonic regimes obtained for various τ_y, R_{azi}, and R_{rad}. Each point represents a simulation. In each box R_{rad} is kept constant: 128 cells (left column), 64 cells (mid column), and 32 cells (right column). Each marker represent R_{azi}: 128 cells (triangles), 256 cells (squares), 512 cells (stars), 1024 cells (circles). Each colour indicates a specific tectonic regime: micro-plate dripping (purple), plate-like regime (red), episodic lid mode (orange), stagnant lid regime (yellow).

By increasing the yield stress τ_y, the strength of the lithosphere is increased, thus resulting in a shift from mobile lid to stagnant lid regime. However, as can be seen in **Figure 6.14**, the tectonic regime does not only depend on the employed yield stress, but also on the numerical parameters R_{azi}, and R_{rad}. Increasing R_{azi} leads to weaker lids and the models display the mobile lid regime (purple and red), whereas increasing R_{rad} leads to stronger lids and the models evolve into the stagnant lid regime (yellow). For the employed model settings, the episodic behaviour appears only for $R_{rad} = 64$.

6.5.7. The Effect of the Yield Stress

Increasing the yield stress increases the strength of the lithosphere, thus favouring stagnant lid regime (**Figure 6.15**). By increasing τ_y it increases the rms mantle temperature T_{rms} (**Figure 6.15-b.1-3**, **Table 6.7**), while decreasing all the other parameters: the thickness of the lithosphere L^{LT} (**Figure 6.15-a.1-3**, **Table 6.6**), the median mantle viscosity η^{tot-LT} (**Figure 6.15-c.1-3**, **Table 6.8**), the surface Nusselt number Nu_{top} (**Figure 6.15-d.1-3**, **Table 6.10**), the mobility M_o (**Figure 6.15-e.1-3**, **Table 6.12**), and the yield ratio r_y (**Figure 6.15-g.1-3**, **Table 6.14**). Plateness P_{80} (**Figure 6.15-f.1-3**, **Table 6.13**) drops below 0.6 for stagnant lid regimes, while remaining > 0.8 for mobile lid regimes. The episodic regime is characterized by anomalous values of the surface Nusselt number (**Figure 6.15-d.2**), which appear only for $R_{rad} = 64$. **Table 6.11** and **Table 6.9** report the

bottom Nusselt number Nu_{bot} and the effective Rayleigh number Ra_{eff}. For each simulation it can be noticed that Nu_{bot} is approximately $0.5Nu_{tot}$, and Ra_{eff} shows an opposite trend to η^{tot-LT} (i.e. it increases with τ_y).

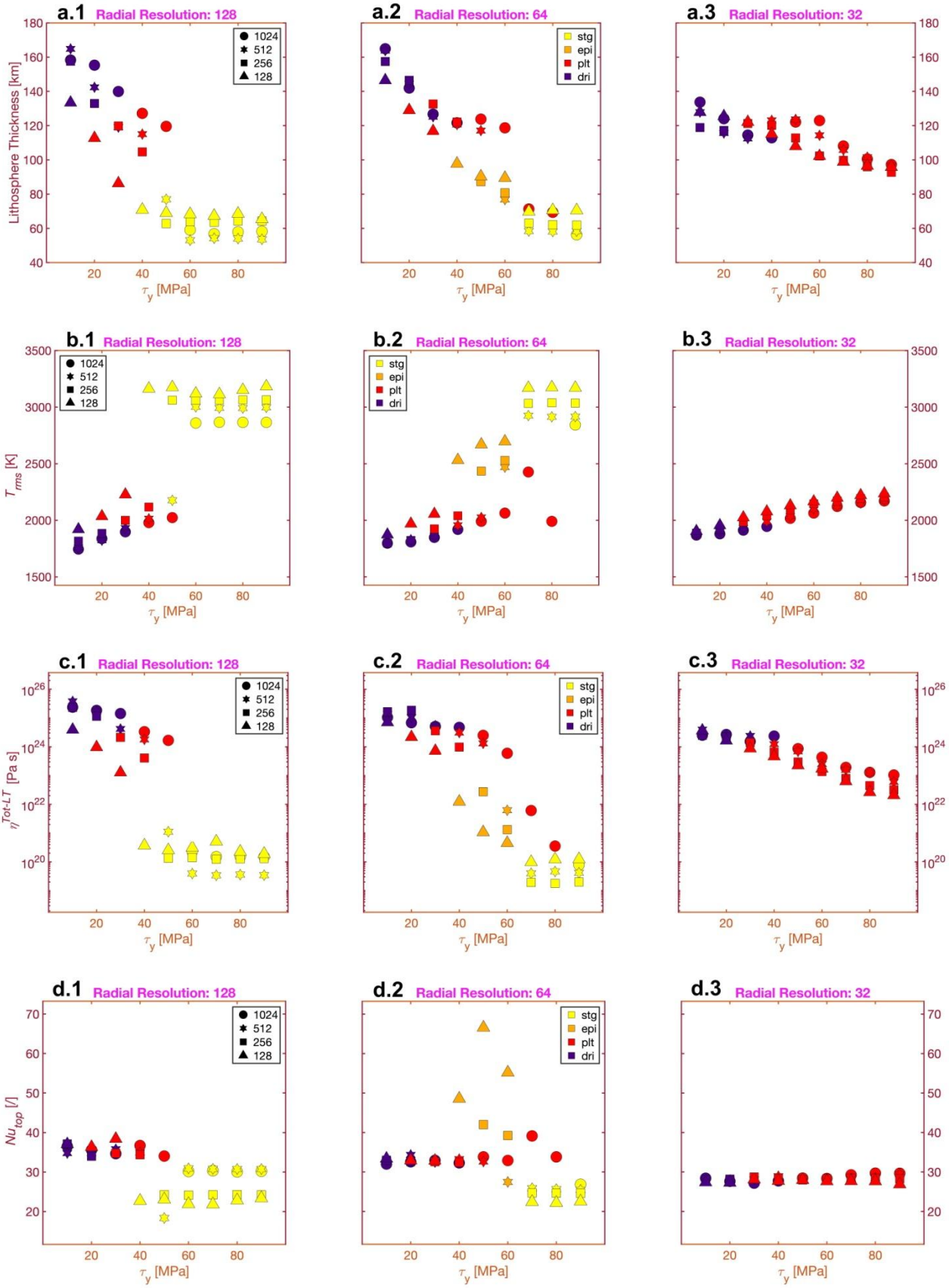

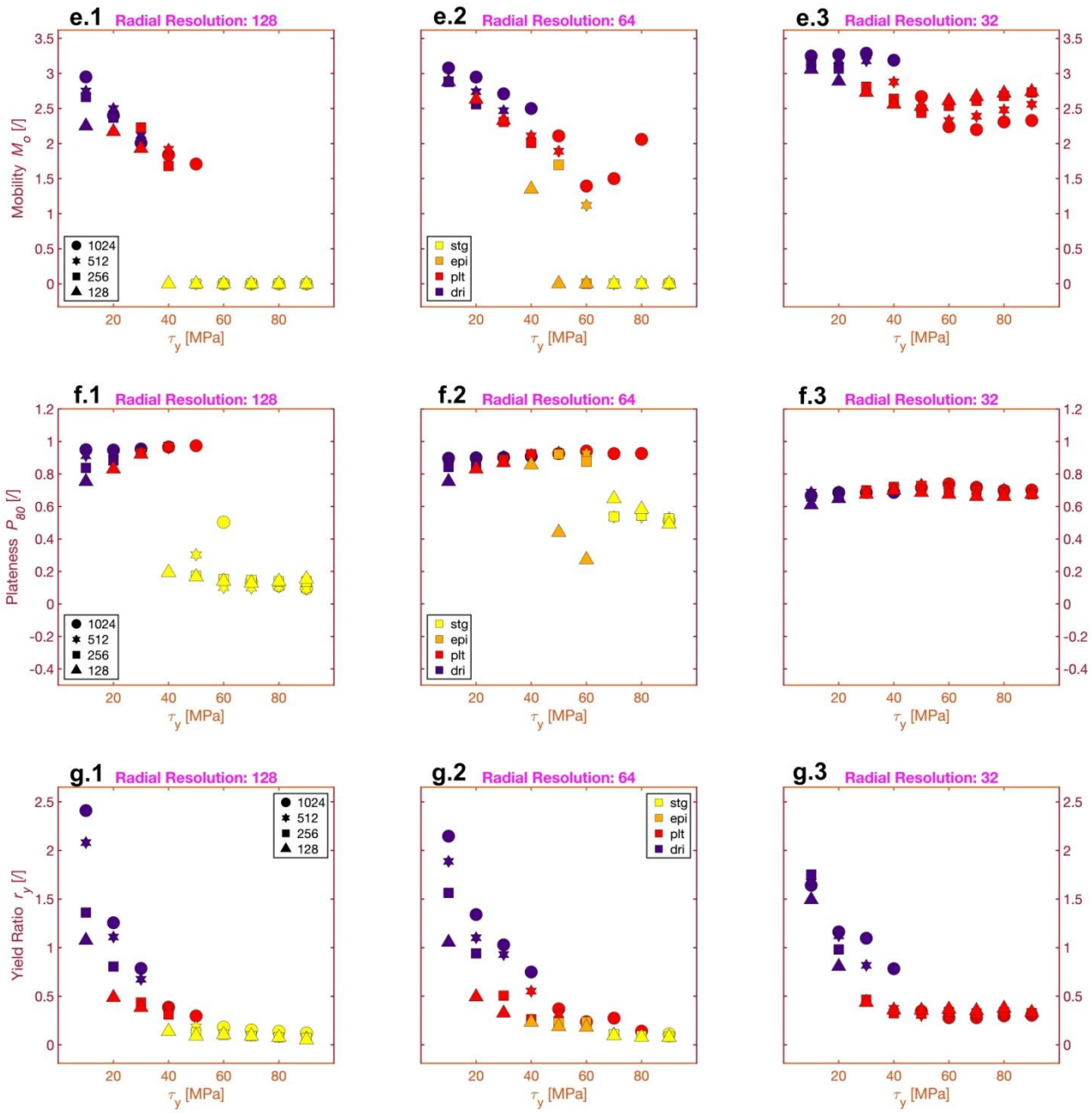

Figure 6.15. Different parameters as a function of the yield stress τ_y. The parameters are: (a.1-3) lithosphere thickness L^{LT} (**Table 6.6**), (b.1-3) rms temperature T_{rms} (**Table 6.7**), (c.1-3) median mantle viscosity η^{tot-LT} (**Table 6.8**), (d.1-3) surface Nusselt number Nu_{tot} (**Table 6.10**), (e.1-3) mobility M_o (**Table 6.12**), (f.1-3) plateness P_{80} (**Table 6.13**), (g.1-3) yield ratio r_y (**Table 6.14**). Each point represents a given simulation (i.e. $R_{azi} \times R_{rad}$, τ_y) where the plotted value is the median time evolution ($0 \rightarrow 15$ $Gyrs$) of that specific parameter. In each box R_{rad} is kept constant: 128 cells (left column), 64 cells (mid column), and 32 cells (right column). Markers and colours are the same as the ones employed in **Figure 6.14**.

6.5.8. The Effect of the Azimuthal Resolution

From **Figure 6.14**, it can be noticed that increasing R_{azi} promotes mobile lid regimes. The azimuthal resolution affects the stress state of the lithosphere, as reported by the analysis of the stress-related parameters r_y, f_y, σ_{max}^{LT} and σ_{tot}^{LT} (**Figure 6.16**). The yield ratio r_y (**Figure 6.16-a.1-3**, **Table 6.14**), and the yield fraction f_y (**Figure 6.16-b.1-3**, **Table 6.15**), increase linearly with the increasing azimuthal resolution. This is caused by the higher average stress-per-cell σ_{ave}^{LT} which reflects a diffuse yielding of more sectors of the lithosphere ($\sigma_{\varphi}^{sec} = \tau_y$). The cumulative maximum stress of the lithosphere σ_{max}^{LT} (**Figure 6.16-c.1-3**, **Table 6.16**) show a similar linear increase, indicating that the enhanced stress field is prominent throughout the whole lithosphere. The total stress of the lithosphere (**Figure 6.16-d.1-3**, **Table 6.17**), on the other hand, grows exponentially with R_{azi}, thus promoting the rupture of the lid.

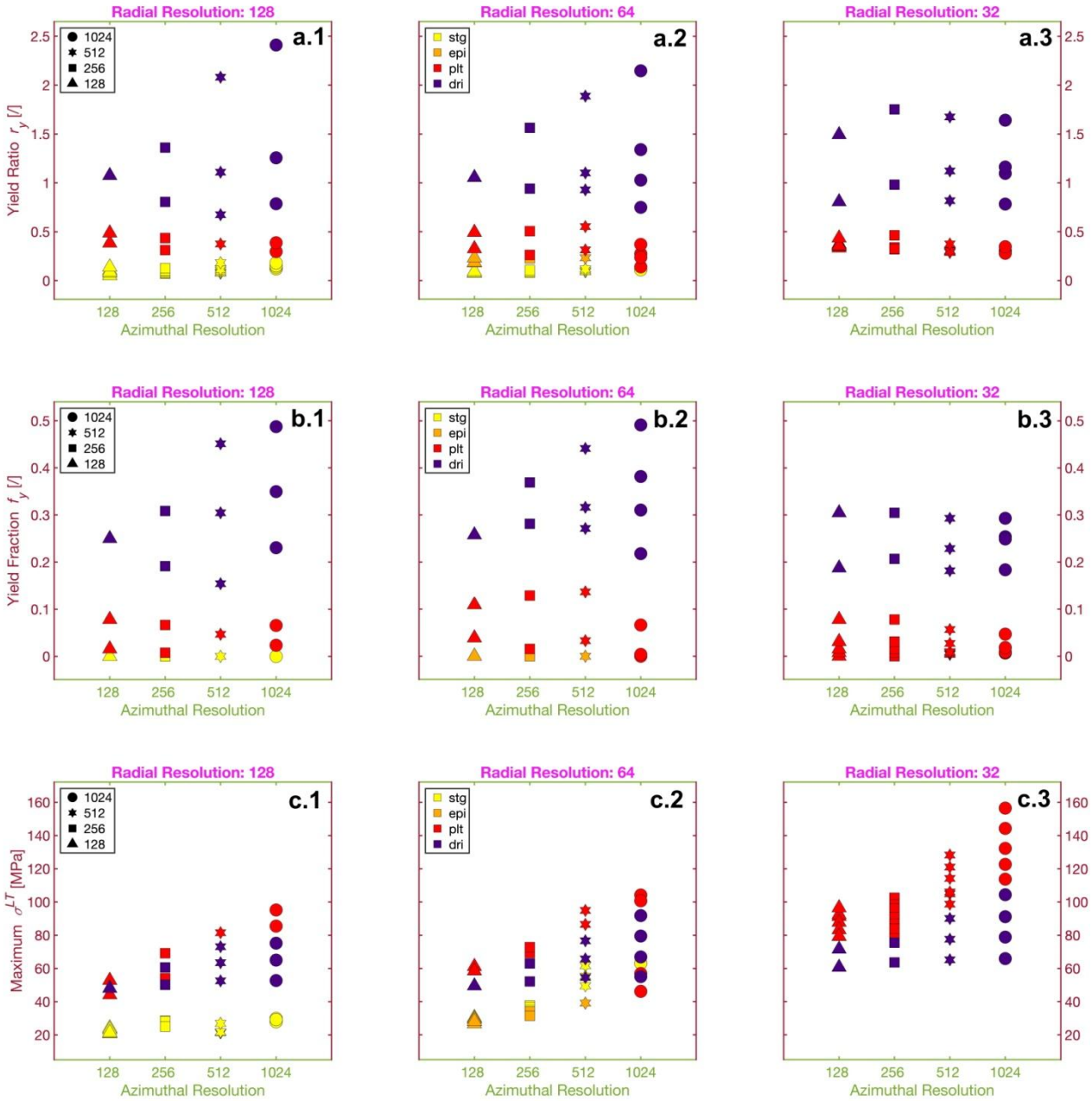

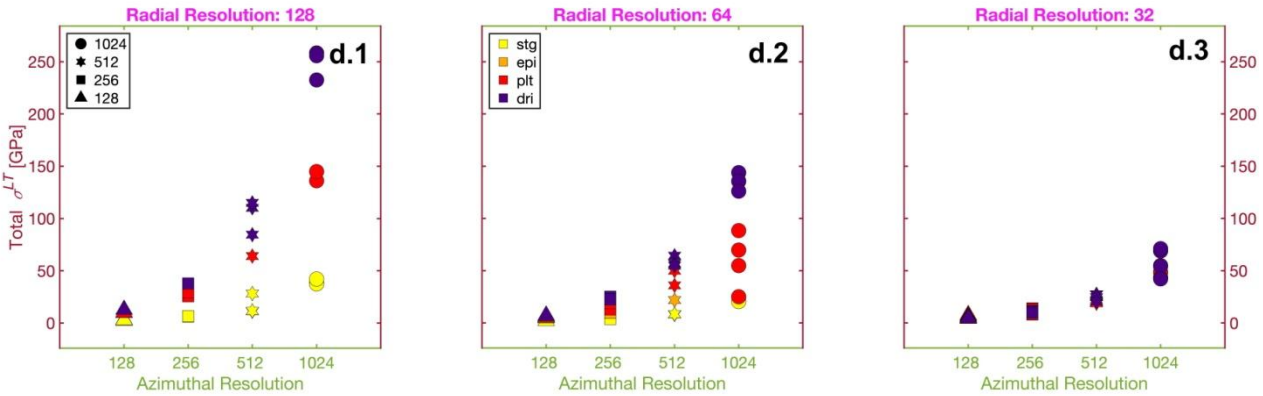

Figure 6.16. Different parameters as a function of the azimuthal resolution R_{azi}. The parameters are: (a.1-3) yield ratio r_y (**Table 6.14**), (b.1-3) yield fraction f_y (**Table 6.15**), (c.1-3) cumulative maximum stress in the lithosphere σ_{max}^{LT} (**Table 6.16**), and (d.1-3) cumulative stress in the lithosphere σ_{tot}^{LT} (**Table 6.17**). Each point represents a given simulation (i.e. $R_{azi} \times R_{rad}$, τ_y) where the plotted value is the median of time evolution ($0 \rightarrow 15\ Gyrs$) of that specific parameter. In each box R_{rad} is kept constant: 128 cells (left column), 64 cells (mid column), and 32 cells (right column). Markers and colours are the same as the ones employed in **Figure 6.14**.

6.5.9. The Effect of the Radial Resolution

From **Figure 6.14**, it can be seen that increasing R_{rad} promotes stagnant lid regimes, by producing a lithosphere that is progressively colder (T^{LT}decrease **Figure 6.17-a.1-4**, **Table 6.18**), and stiffer (η^{LT} increase **Figure 6.17-b.1-4**, **Table 6.19**). Moreover, the parameter σ_{max}^{LT} (**Figure 6.17-c.1-4**, **Table 6.16**) reveals that, for increasing R_{rad}, the lithosphere is less stressed throughout its entire thickness.

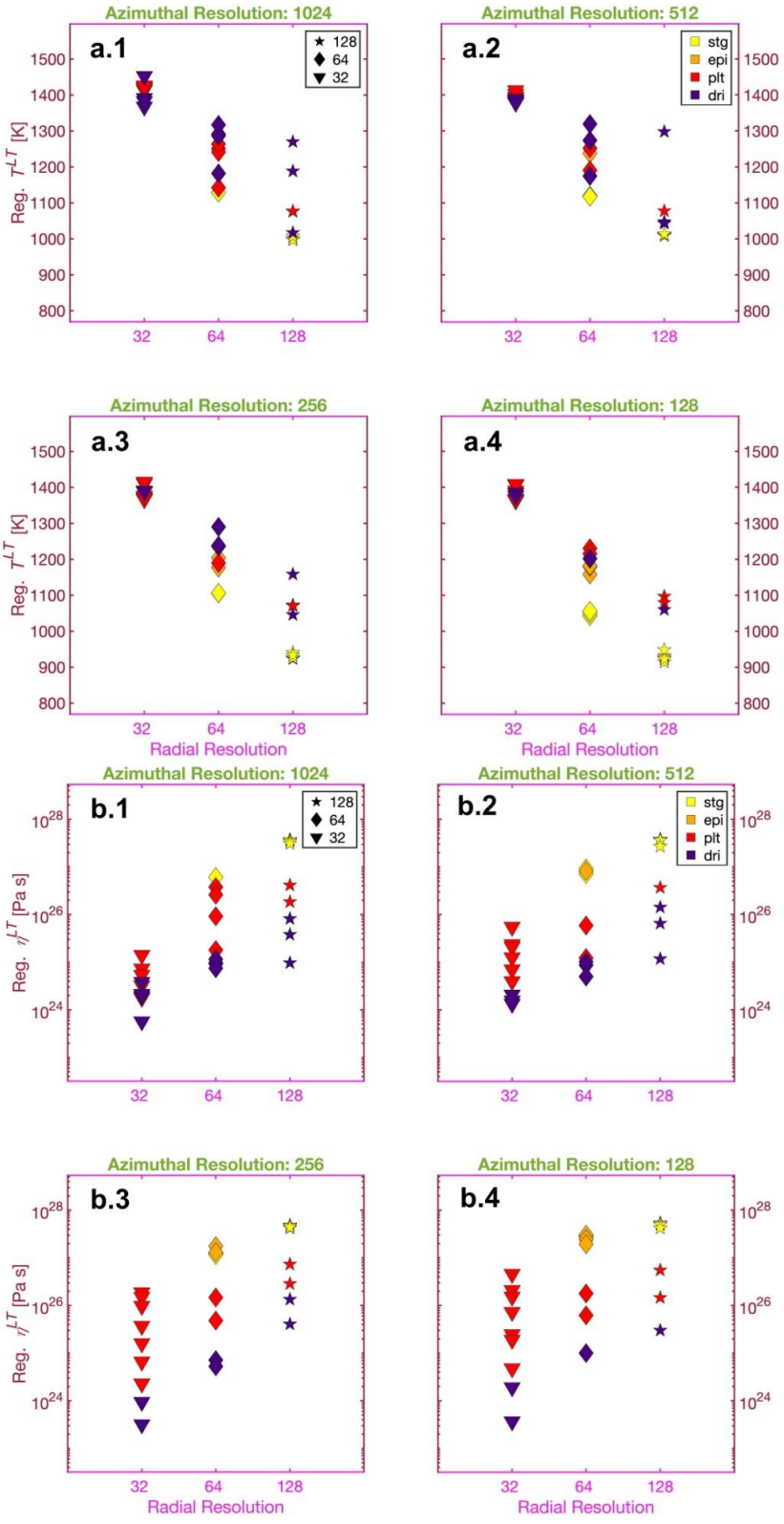

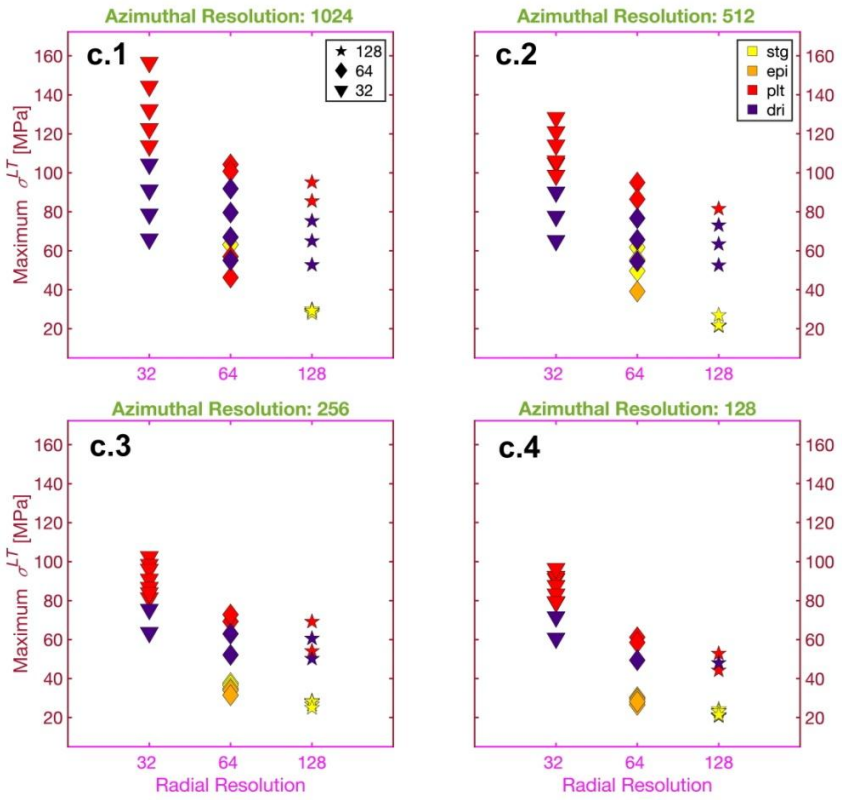

Figure 6.17. Different parameters as a function of the azimuthal resolution R_{rad}. The parameters are: (a.1-4) mean lithosphere temperature T^{LT} (**Table 6.18**), (b.1-4) mean lithosphere viscosity η^{LT} (**Table 6.19**), and (c.1-4) cumulative maximum stress in the lithosphere σ_{max}^{LT} (**Table 6.16**). Each point represents a given simulation (i.e. $R_{azi} \times R_{rad}$, τ_y) where the plotted value is the median of time evolution ($0 \rightarrow 15\ Gyrs$) of that specific parameter. In each box R_{azi} is kept constant: 1024 cells (top left), 512 cells (top right), 256 cells (bottom left), and 128 cells (bottom right). In this case, each marker represent R_{rad}: 32 cells (triangles), 64 cells (diamonds), 128 cells (stars). Colours are the same as the ones employed in **Figure 6.14**.

6.6. Discussion

The results reported in sections **6.5.6-6.5.9** show that grid resolution has a significant effect on the resulting tectonic regime. This influence is not as intuitive as the effect of the yield stress, where its increase simply leads to stronger lids, and results in the stagnant lid regime. Increasing the azimuthal and radial resolutions in isolation has two opposite effects: a high azimuthal resolution producing a weak lid, whereas a high radial resolution causes a strong lid.

Despite these competing effects, the most accurate solution for the current model setup is always given by the highest grid resolution, i.e. 1024×128 grid points for this study (131072 cells). The 1024×128 grid point simulation set provides a unique tectonic regime sequence that is not reproduced by any other resolution (**Figure 6.14**): dripping ($10 \leq \tau_y \leq 30\ MPa$), plate-like ($40 \leq \tau_y \leq 50\ MPa$) and stagnant ($\tau_y \geq 60\ MPa$) (**Figure 6.18**, right column). The second highest resolution (65536 cells), leads to significantly different results compared to those with halved R_{azi} (i.e. 512×128). In this case the stagnant lid regime occurs from $\tau_y \geq 50\ MPa$ (**Figure 6.18**, mid column). A reduction of R_{rad} (i.e. 1024×64) causes the plate-like behaviour regime to expand to the range $40 \leq \tau_y \leq 80\ MPa$ (**Figure 6.18**, left column). For the current model setup, the episodic regime appears only for $R_{rad} = 64$ and $R_{azi} < 1024$ (**Figure 6.14**, mid column).

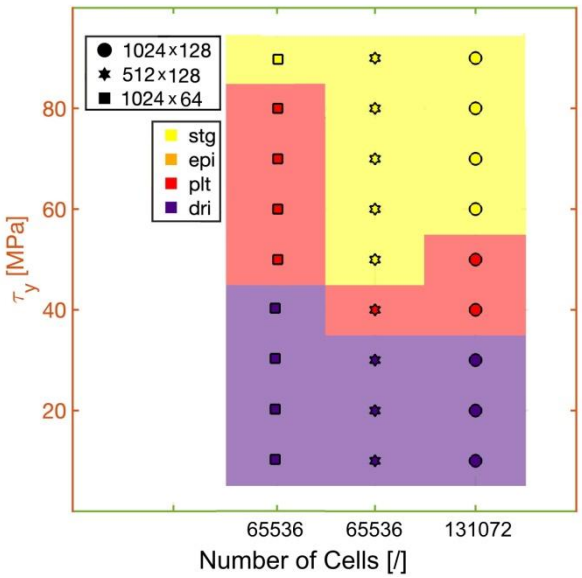

Figure 6.18. Tectonic regimes obtained for various τ_y, for the three highest grid resolutions, i.e. 1024×128 (right column, circles), 512×128 (mid columns, stars), and 1024×64 (left column, squares). Each point represents a simulation. Colours are the same as the ones employed in **Figure 6.14**.

Based on these considerations, R_{rad} has a much larger impact on the tectonic regime map, most likely due to its crucial role in defining the properties of the boundary layers. In the following section, the effect of both R_{azi}, and R_{rad} will be discussed in more detail to provide an explanation for the grid resolution dependency of the tectonic regimes.

6.6.1. Azimuthal Resolution

From the plots in **Figure 6.16**, it can be seen that R_{azi} influences heavily the computation of the stress field $\sigma_{r,\varphi}$. As reported in equation **(2.9.104)**, in the 2D spherical annulus geometry, the normal stresses $\sigma_{\theta\theta}$, $\sigma_{\varphi\varphi}$, and σ_{rr} are a function of the derivative $\partial u_\varphi/\partial\varphi$, while the shear stress $\tau_{\varphi r}$ is a function of $\partial u_r/\partial\varphi$, where u_φ and u_r are the azimuthal and radial velocities respectively, while $\partial\varphi$ is the angular distance between two points. In the finite difference method, these two derivatives are approximated as the quotients (i.e. $\Delta u_\varphi/\Delta\varphi$ and $\Delta u_r/\Delta\varphi$), and $\Delta\varphi$ indicates the angular distance between two grid nodes. For the tested resolutions, the azimuthal distance $\Delta\varphi_d$ at the surface ranges from $39\ km$ to $312\ km$. Each cell features one value at its centre ($\Delta\varphi_d/2$), which results from the interpolation of the stress from the edge nodes.

For low azimuthal resolutions, the stress field in the lithosphere is insufficiently resolved, as the length scales of the modelled structures are on the order of the grid spacing. **Figure 6.19-a** shows the initial stress field of the entire lithosphere, while **Figure 6.19-b.1-4** represent a detail of a low stress region of the lithosphere, for increasing R_{azi} (**b.1**:128, **b.2**:256, **b.3**:512, **b.4**:1024). As the number of nodes in the azimuthal direction increases, the contour lines of the σ field becomes narrower, thus showing a more complex stress distribution (**Figure 6.19-b.1-4**). Moreover, the high stress regions (bordeaux colour) expands laterally at the expenses of lower stress regions.

For low R_{azi}, the interpolation of the stress from the edges is computed considering grid nodes which are considerably far apart from each other (up to $312\ km$ for R_{azi}: 128). Between the nodes, large variations of the stress field might occur, which are smothered by the interpolation function. This lead to a misrepresentation of the local stress at the edges, and prevents the cell from reaching the yield stress τ_y.

A large value for R_{azi}, on the other hand, provides a much more accurate description of the local stress, since the local variations of σ are computed on relatively closely spaced nodes (up to $39\ km$ for R_{azi}: 1014). In this way, the interpolation function does not smooth the stress over vast blocks of the lithosphere, and the yield stress τ_y is more easily reached. Due to this effects, a large R_{azi} value causes the formation of more plate boundaries (**Figure 6.20**, and **Table 6.20**) which, in turn, results in a weaker lid compared to low R_{azi} simulations.

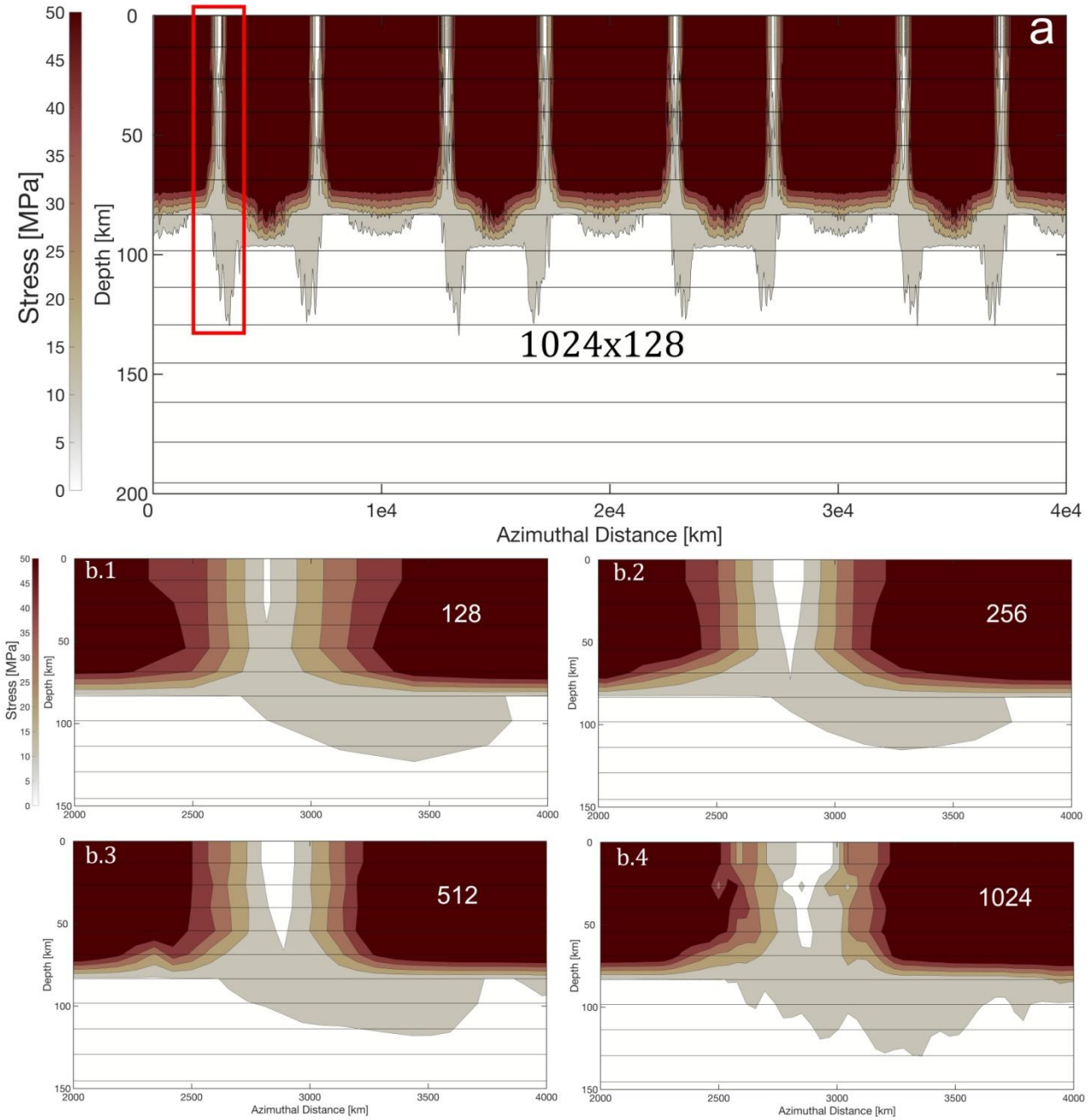

Figure 6.19. (a) $2D$ stress field of the lithosphere representing the 8 convection cell configuration at $t_{frame} = 0$ (see **Chapter 3.6**). The chosen simulation is 1024×128 and $\tau_y = 50\ MPa$. (b.1-4) $2000\ km$–wide section of the lithosphere for different resolutions, representing the red area in (a), for different R_{azi}: 128 (b.1), 256 (b.2), 512 (b.3), 1024 (b.4). Radial resolution is kept constant at 128 cells, and the solid horizontal black lines represent a stencil of nodes at a given depth. The yielded area ($\tau_y = 50\ MPa$, deep red) becomes progressively broader with increasing R_{azi}. The employed colour scheme is the *bilbao* scientific colour map (*Crameri et al., 2020*).

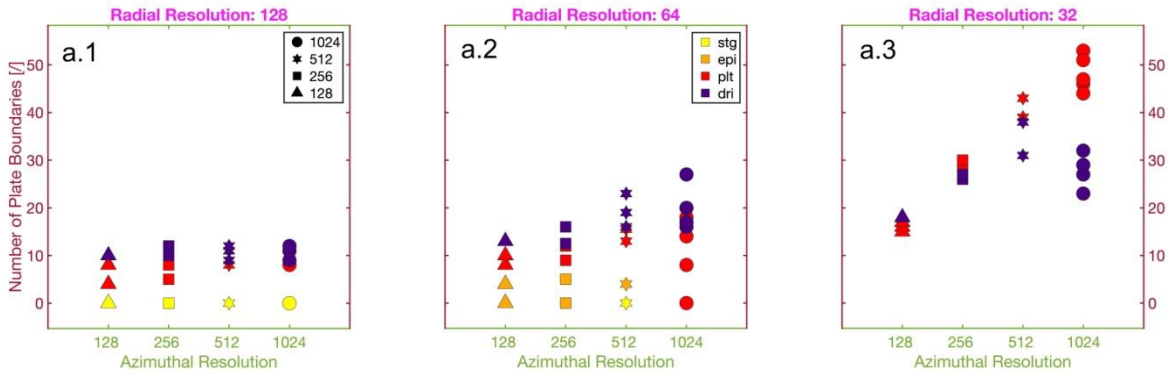

Figure 6.20. Number of plate boundaries (**Table 6.20**) as a function of the azimuthal resolution R_{azi}. Plate boundaries are detected using the method described in section **6.4.6**. Each point represents a given simulation (i.e. $R_{azi} \times R_{rad}$ τ_y), where the plotted value is the median of time evolution ($0 \rightarrow 15$ $Gyrs$) of that specific parameter. In each box R_{rad} is kept constant: 128 cells (left column), 64 cells (mid column), and 32 cells (right column). Markers and colours are the same as the ones employed in **Figure 6.14**.

The effect of the azimuthal resolution R_{azi} on the model is not only limited to the computation of the lithospheric stress field, but impacts every parameter displaying spatial variations. For example, small-scale variations of T and η are insufficiently resolved in the case of low azimuthal resolutions. This is particularly true in the case of a large number of convection cells (see example in **Figure 6.21**), is employed as initial condition (see section **6.3.3**).

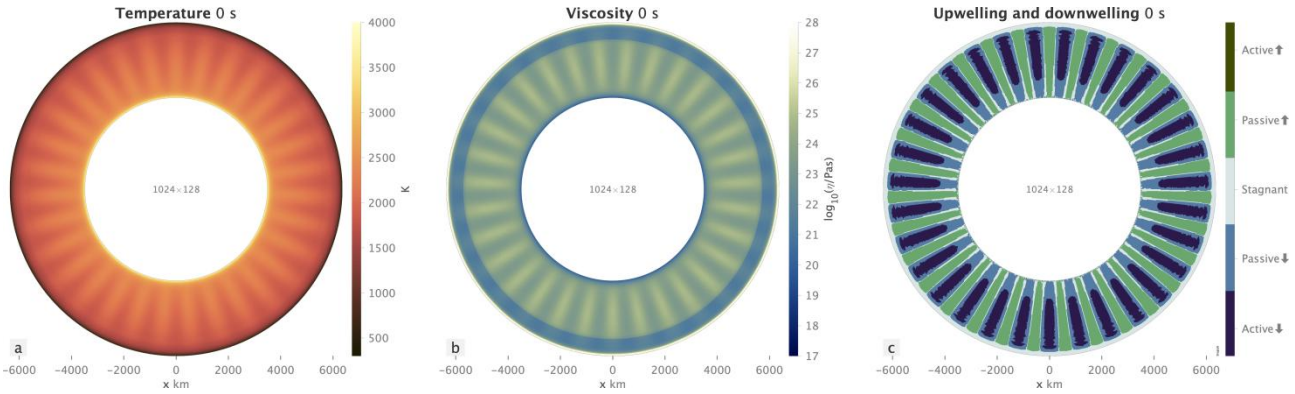

Figure 6.21. Initial mantle conditions (64 cell configuration), here plotted with StagLab (*Crameri, 2018*) and making use of a scientific colour map (*Crameri et al., 2020*): a) temperature field (*lajolla*) b) viscosity field (*devon*) c) mantle motion (*cork*).

The 1D radial profiles of the azimuthal average viscosity (**Figure 6.22**), display an artificial kink, however only for a low azimuthal resolution (i.e. < 1024).

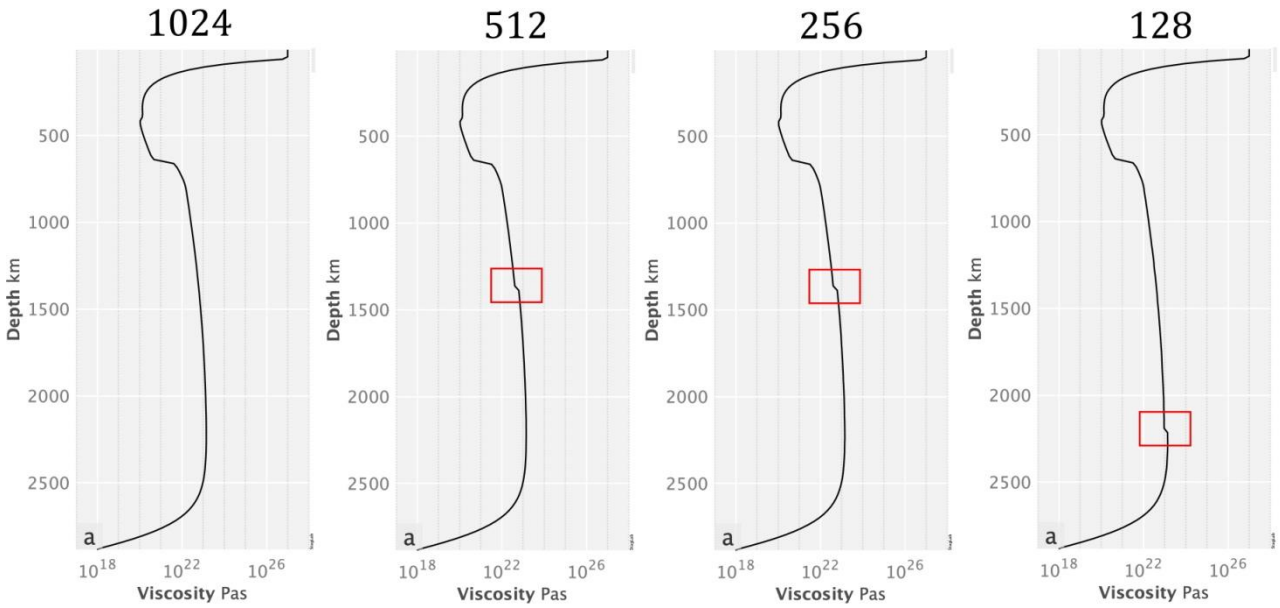

Figure 6.22. 1D radial viscosity profiles of the mantle (StagLab, *Crameri, 2018*), for different R_{azi} (decreasing from left to right). The artificial kinks are marked in red.

These kinks are the result of the interpolation of the viscosity field over large distances and might build up over time causing major changes in the convective style. It is important to notice that these features are far from the boundaries. Therefore, it is important to maintain a high R_{azi} in order to minimize the presence of any numerical anomaly.

6.6.2. Radial Resolution

The results shown in **Figure 6.17**, indicate that with increasing R_{rad} the lithosphere becomes progressively colder (**Figure 6.17-a.1-4**), stiffer (**Figure 6.17-b.1-4**), and stronger (**Figure 6.17-c.1-4**). This effect is again related to insufficiently resolved structures in the case of low radial resolutions. In this case, the problems arise from the computation of the temperature T and viscosity η fields, since the values saved at the centre of a cell are given by the contributions of the nodes $n_{r,\varphi}$ and $n_{r+1,\varphi}$. At the surface (i.e. 1^{st}cell), the distance between the two nodes is 13, 27 and 54 km, for R_{rad} values of 128, 64 and 32, respectively (see **Table 6.3**). Since both temperature and viscosity increase with depth due to compressibility (see section **6.2.4**), the first cell would present a progressively higher T (therefore lower η) as the radial resolution decreases. The same reasoning applies for every cell of the domain, where for large grid spacing Δr, it increases the temperature (and viscosity) difference computed at the bounding nodes.

As stated in section **6.3.1**, the cell thickness Δr is particularly crucial near the top and bottom of the domain to properly resolve the thermal boundaries. These two regions of the domain are fundamental because they generate the convective instabilities that drive mantle convection. The interpolation of the temperature over thick cells, generates a low viscosity upper boundary layer (i.e. weak lithosphere), and a high viscosity lower boundary layer (i.e. stiff CMB). As reported in **Figure 6.23**, by reducing Δr (i.e. increasing R_{rad}) the interpolated viscosity at the surface is $\approx 10^2 - 10^5$ higher (**Figure 6.23-a.1-4**, **Table 6.21**), while is $\approx 10^2$ lower at the CMB (**Figure 6.23-b.1-4**, **Table 6.22**). It follows that high a high radial resolution R_{rad}, promotes a stiffer lithosphere and a weaker CMB where plume rise is favoured.

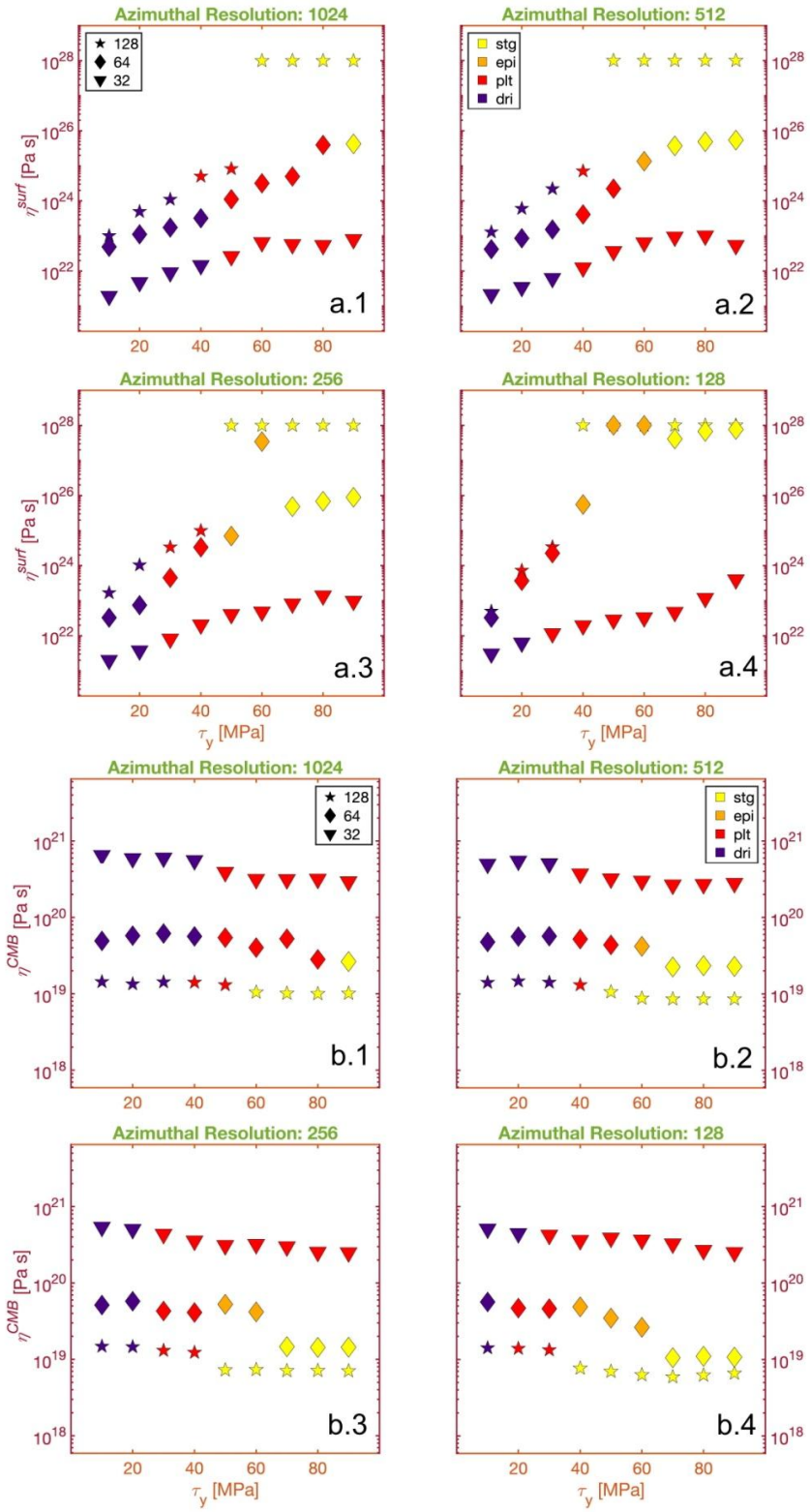

Figure 6.23. Viscosity at the boundaries as a function of the yield stress τ_y. (a.1-4) mean surface viscosity η^{surf} (**Table 6.21**), (b.1-4) mean core mantle boundary viscosity η^{CMB} (**Table 6.22**). Each point represents a given simulation ($R_{azi} \times R_{rad}$ τ_y) where the plotted value is the median of time evolution ($0 \rightarrow 15$ $Gyrs$) of viscosity. In each box R_{azi} is kept constant: 1024 cells (top left), 512 cells (top right), 256 cells (bottom left), and 128 cells (bottom right). The markers represent R_{rad}: 32 cells (triangles), 64 cells (diamonds), 128 cells (stars). Colours are the same as the ones employed in **Figure 6.14**.

The stress exerted by mantle convection at the base of the lithosphere is computed at the nodes, and then interpolated to the centre of the basal cells. If the radial spacing Δr is too coarse, the stress interpolation reaches the shallow portion of the lithosphere, and the shear zones are able to cut through the entire lid.

Figure 6.25 displays how the computed physical parameters of the lid change with increasing R_{rad}. With increasing radial resolution, the lithosphere is characterized by a progressively colder isotherms (i.e., brown colours $T < 400$ K **Figure 6.25-a.1-3**), with higher viscosities (i.e., lilac to white colours $\eta > 10^{26}$ $Pa\ s$ **Figure 6.25-b.1-3**). For $R_{rad} = 32$ (**Figure 6.25-c.1**), the yield stress is reached over 150 km of depths (deep red colours), thus cutting through the initial lithosphere thickness of $L_{init}^{LT} = 100$ km. For $R_{rad} = 64$ (**Figure 6.25-c.2**), the yield stress is barely reached at 100 km of depth, while it remains above 100 km for $R_{rad} = 128$ (**Figure 6.25-c.3**). In these models the lithosphere starts to yield from the bottom because of the employed lithosphere strength envelope, i.e. constant τ_y. If a depth dependent formulation is used **(6.2.2)** the lithosphere would yield from the top, where is weaker **Figure 3.12**. The progressively stronger lid is also reflected in the decreasing number of plate boundaries (**Figure 6.24**, and **Table 6.20**).

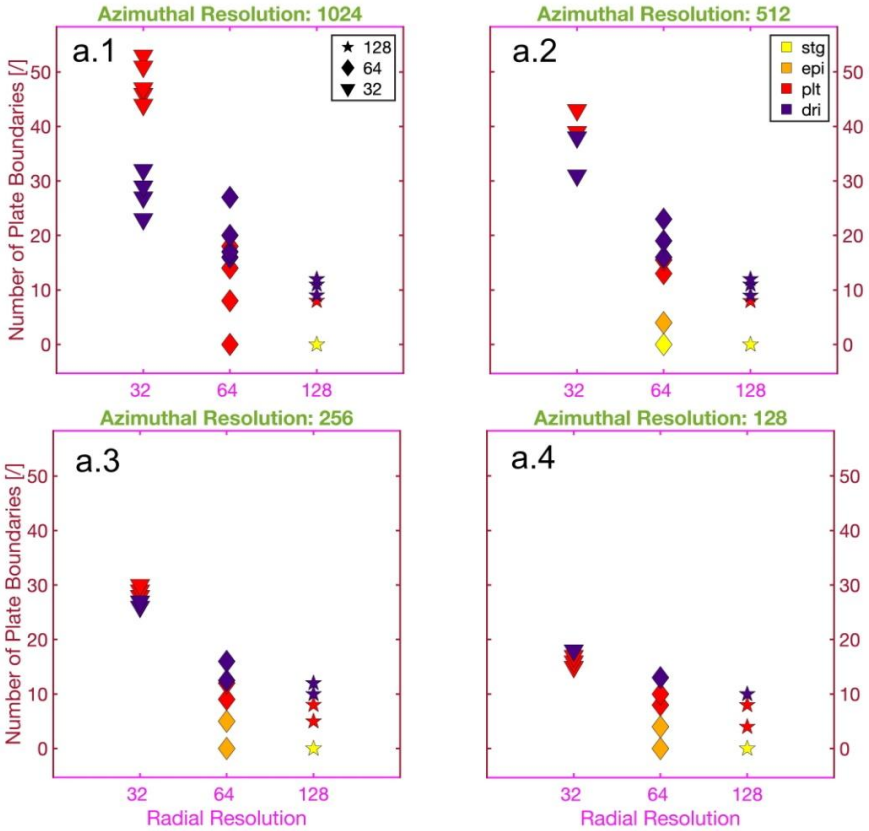

Figure 6.24. Number of plate boundaries (**Table 6.20**) as a function of the radial resolution R_{rad}. Plate boundaries are detected using the method described in section **6.4.6**. Each point represents a given simulation (i.e. $R_{azi} \times R_{rad}$ τ_y) where the plotted value is the median of time evolution ($0 \rightarrow 15$ $Gyrs$) of that specific parameter. In each box R_{azi} is kept constant: 1024 cells (top left), 512 cells (top right), 256 cells (bottom left), and 128 cells (bottom right). The markers represent R_{rad}: 32 cells (triangles), 64 cells (diamonds), 128 cells (stars). Colours are the same as the ones employed in **Figure 6.14**.

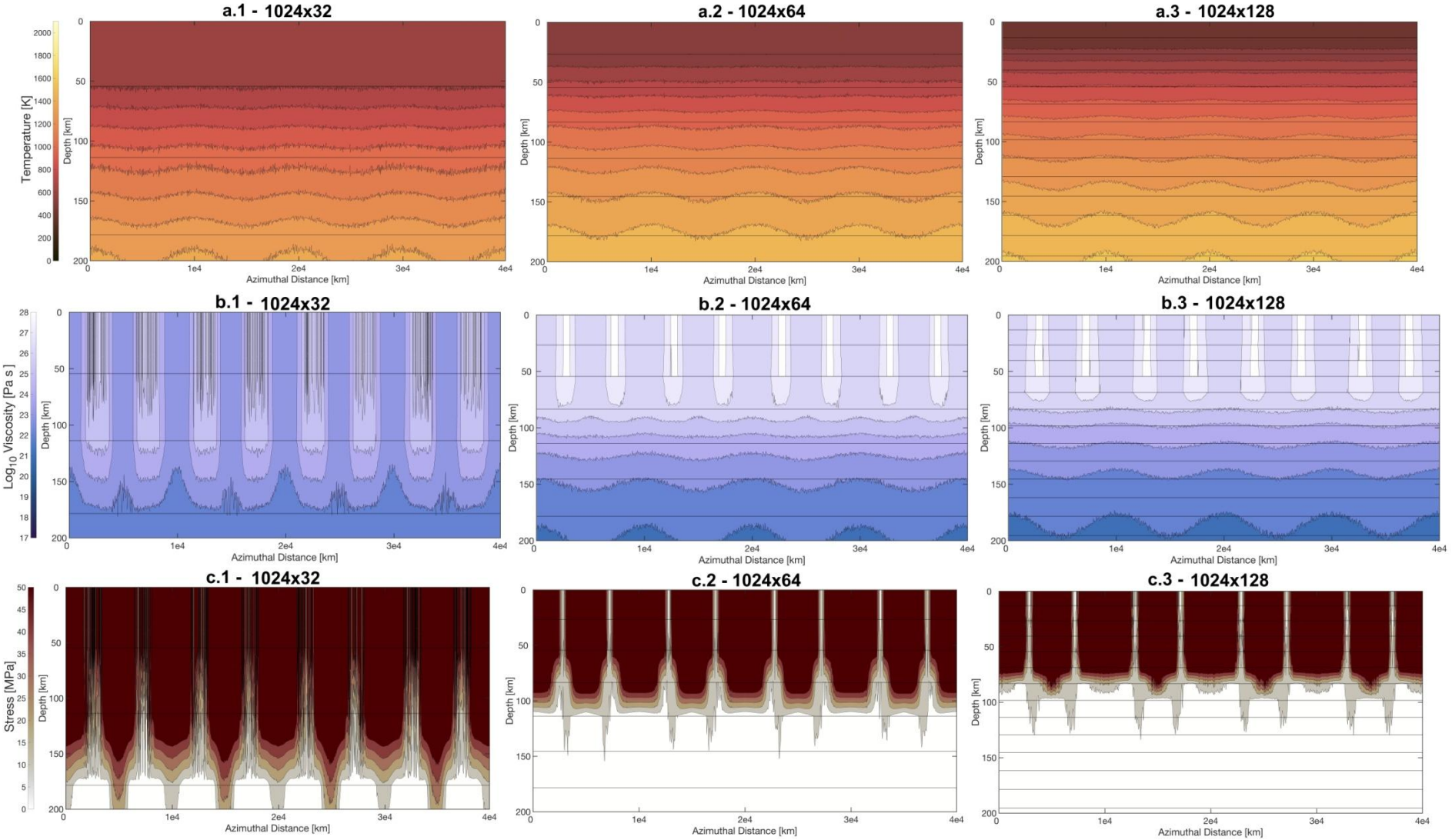

Figure 6.25. $2D$ parameter field of the lithosphere representing the 8 convection cell configuration at $t_{frame} = 0$ (see **Chapter 3.6**): (a.1-3, top row) 2D temperature field T, (b.1-3, mid row) 2D viscosity field η, and (c.1-3, bottom row) 2D stress field σ. Colour field is based on scientific colour map (*Crameri et al., 2020*): *lajolla* (T), *devon* (η), *bilbao* (σ). The chosen simulations have constant azimuthal resolution ($R_{azi} = 1024$), and $\tau_y = 50\ MPa$. Radial resolution increases from left to right. The horizontal black lines represent a stencil of nodes at a given depth.

6.7. Study Limitations

The aim of this study is to show the effect of grid resolution on the tectonic style of mantle convection simulations. To do so, it is necessary to design a model setup where most parameters remain constant overtime, thus statistical steady-state can be achieved. The resulting model, however, is far from being realistic and several assumptions have to be made.

One of the most important assumptions regards the heating mode of the mantle, here it was assumed isothermal boundaries and a constant concentration of heat producing elements in the mantle (see section **6.2.2**). In a more realistic model, the heating mode of the mantle should take into account both the cooling of the core (*Nakagawa & Tackley, 2014*), and the decline of radiogenic heating (*Palme & O'Neill, 2007*). To illustrate the effect of the heating modes on the resulting tectonic regime, two additional sets of simulations have been run (**Figure 6.26**). Both sets share the same resolution (512×64) and four representative yield stress ($10-40-60-90\ MPa$)**.** Model set (1) represent the '*steady-state heating*' mantle described in section **6.2.2**; while model set (2) represent the '*radioactive decay'* mantle with $R_H = 18.77 \times 10^{-12}\ W\ kg^{-1}$ and $t_{1/2} = 2.43 \times 10^9\ yr$; finally model set (3) represent the '*combined cooling*' considering both core cooling (employing the analytical model for core growth described by *Buffett et al., 1992*) and radioactive decay (same parameters as in model set 2). These model sets show that the heating mode significantly influences the resulting tectonic regime at a given time. The tectonic regimes obtained with heating mode 1 (solid lines) are the same as the ones reported in **Figure 6.3**: dripping ($10\ MPa$), plate-like regime ($40\ MPa$), episodic lid behaviour ($60\ MPa$), stagnant lid mode ($90\ MPa$). For heating mode 2 (dotted lines), the regime distribution becomes: episodic lid behaviour ($10\ MPa$), dripping regime ($40\ MPa$), stagnant lid ($60-90\ MPa$). Whereas for heating mode 3 (dashed lines), the regime distribution becomes: dripping behaviour ($10-40\ MPa$), and plate-like regime ($60-90\ MPa$).

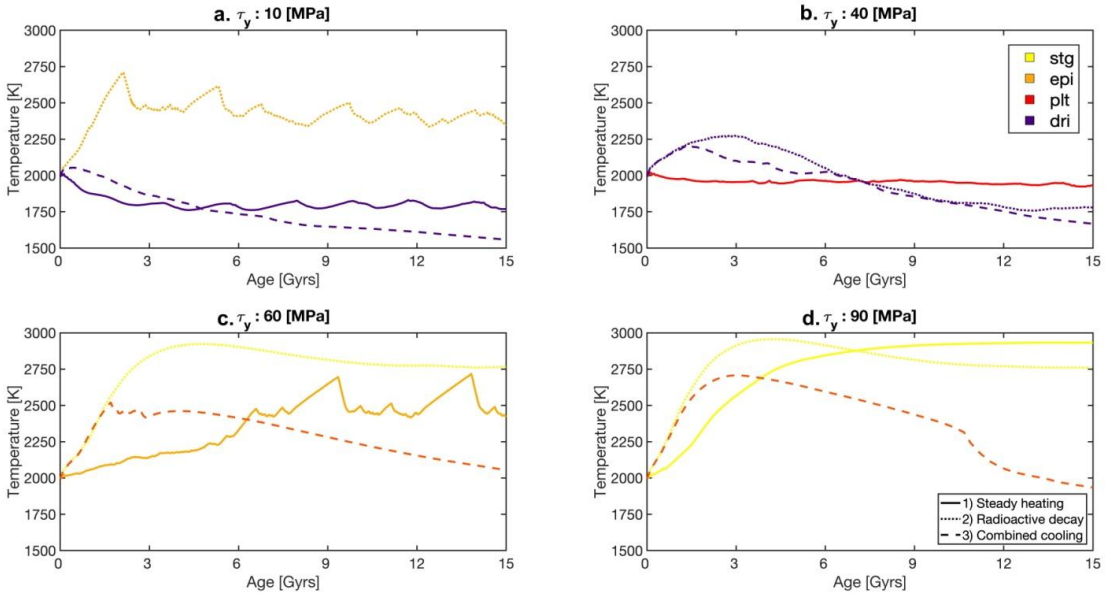

Figure 6.26. Comparison of temperature evolution for different heating modes: (1) steady-state heating (solid line), (2) radioactive decay (dotted line), and (3) core cooling (dashed line). Each simulation was run with a grid resolution of 512×64 cells, and a given yield stress τ_y: $10\ MPa$ (a.), $40\ MPa$ (b.), $60\ MPa$ (c.), and $90\ MPa$ (d.). Colours are the same as the ones employed in **Figure 6.9**.

Another limitation is the absence of mantle melting in the computation of the energy equation. The presence of melting, coupled with surface magmatism, is one of the main heat loss mechanism in celestial bodies, and it can strongly buffer the mantle temperatures over time (*Xie & Tackley, 2004*; *Keller & Tackley, 2009*; *Ogawa & Yanagisawa, 2011*; *Nakagawa & Tackley, 2012*; *Armann & Tackley, 2012*). Therefore, it is unlikely that the internal temperature reaches values as high as the one shown for the stagnant lid regimes (i.e. $2800-3000$ K) as in a realistic model the mantle would melt (*Solomatov & Moresi, 2000*).

Another main limitation of the current models is the simplified treatment of the strength envelope of the lithosphere **(6.2.2)**. It is important to note that the yield stress values employed in the designed models ($\tau_y = 10-90\ MPa$) are much lower than those predicted from the strength envelope at mid-lithosphere depths ($\approx 800\ MPa$) (*Kohlstedt et al., 1995*). This gap between numerical simulations and laboratory experiments is still one of the biggest issues of geodynamical models, and the use of realistic τ_y would inevitably create a stagnant lid. This conundrum will not be investigated here, since it is beyond the aims of this study. Nonetheless, this issue can be partially solved by employing strain focussing mechanisms such as: lithospheric shear heating (*Thielmann & Kaus, 2012*), free surface (*Duretz et al., 2011*; *Thielmann et al., 2015*), sticky air (*Crameri et al., 2012*), continental crust (*Nikolaeva et al., 2010*; *Rolf & Tackley, 2011*), 3D geometry (*Tackley, 2000a*), strain weakening and asthenosphere (*Tackley, 2000b*). The lack of these features in the models hinders a realistic localization of the stress, and causes a stagnant lid regime already at $60\ MPa$.

Finally, in a more realistic model the yield stress should present a composite envelope including both a brittle (i.e. depth-dependent) and a ductile (i.e. depth-constant) yielding (*Kohlstedt et al., 1995*; *Crameri & Tackley, 2016*), which makes the lithosphere weaker at the surface and progressively stronger at depth. In order to keep the current model settings as simple as possible, the yield stress was assumed to be a constant value (see section **6.2.5**).

Despite all the aforementioned limitations, the designed model is still effective in producing different tectonic regimes within a τ_y range coherent with what is reported in recent literature (e.g. *Crameri & Tackley, 2016*; *Gülcher et al., 2020*; *Schierjott et al., 2020*). Moreover, the simplicity of the model setup was intended to reduce the number of variables, and determine the influence of both R_{azi} and R_{rad} on the model outcome. As reported in section **6.5.6**, the numerical resolution influences the computation of every parameter field (i.e. T, η, σ, u). Therefore, even if the current model is not realistic, our results can provide a useful guideline for future studies when choosing the model resolution.

6.8. Conclusions

In this chapter, I have shown that the tectonic regime for an Earth-like model setup is mostly controlled by strength of the lithosphere, which is controlled by the yield stress τ_y in our model. Mantle convection and plate motion concentrate the stress in the lithosphere, which yields when τ_y is reached and plate boundaries form. With increasing τ_y, less plate boundaries are formed. In the current model setup, different tectonic regimes can be observed depending on the value of τ_y: micro-plate dripping (low τ_y), plate-like subduction (intermediate-low τ_y), episodic behaviour (intermediate-high τ_y) and stagnant lid (high τ_y). This is consistent with previous studies in 3D Cartesian geometry by *Tackley, (2000a)*.

Each regime can be identified based on the analysis of several target parameters: rms temperature evolution T_{rms}, mantle viscosity η^{Tot-LT}(and effective Rayleigh number Ra_{eff}), surface Nusselt number Nu_{top}, mobility of the plates M_o, strain distribution (i.e. plateness P_{80}), and the ratio between the average stress of the lithosphere σ_{ave}^{LT} and the yield stress τ_y (i.e. ratio r_y).

The mobile lid regime (dripping and plate-like) is characterized by an highly stressed lithosphere ($r_y \geq 0.5$), where most of the deformation occurs at the plate boundaries ($P_{80} \geq 0.5$). The rupture of the lithosphere, followed by the movement of the plates and their final subduction, account for the high mobility observed for this regime ($M_o \geq 1.0$). The effective heat exchange established by mantle convection determines a high heat flux at the surface ($Nu_{top} \approx 30$) that prevents internal heating ($T_{rms} \approx 1800-2000\,K$), and leads to a high viscosity of the mantle ($\eta^{Tot-LT} \approx 10^{24}-10^{25}\,Pa\,s$, and $Ra_{eff} \approx 10^3-10^4$). Based on the aforementioned parameters, the differences between micro-plate dripping and plate-like subduction appear to be minimal. However, some useful tools to distinguish the two behaviours are the yield ratio r_y, and the yield fraction f_y. The dripping behaviour displays $r_y > 1.0$ with broad subduction zones ($f_y \geq 0.2$), whereas the plate-like regime features a yielding lithosphere ($r_y \approx 0.5$), and narrow plate boundaries ($f_y \leq 0.2$).

The stagnant lid regime is characterized by the absence of plate boundaries, where the stress is much lower than the yield stress ($r_y \leq 0.2$). The single plate is immobile and stagnant ($M_o \approx 0.0$). Since the convective mantle is unable to reach the surface, the heat exchange at the top boundary is controlled by the thermal conduction across the lid, and sub-lithospheric convection ($Nu_{top} \leq 30$). This lead to an increase of the internal temperatures ($T_{rms} \approx 2800-3000$ K), and a low viscosity of the mantle ($\eta^{Tot-LT} \approx 10^{19}-10^{21}\,Pa\,s$, and $Ra_{eff} \approx 10^7-10^9$).

The episodic lid regime represents an intermediate behaviour, where stagnant lid epochs are followed by sudden collapses of the entire lithosphere. The target parameters reflect the current tectonic stage of the lithosphere: e.g. $M_o \approx 0.0$ during lid stagnation and $M_o \approx 3.0$ when a lid resurfacing events occurs. The most reliable parameters to identify the episodic regime is the surface Nusselt number, which quantifies the sudden burst of heat flux released during the mantle overturn ($Nu_{top} \approx 100$). The rms temperature evolution show a characteristic saw-tooth profile.

By examining both Nu_{top} and Nu_{bot}, the efficiency of the convective heat transport is higher at the surface than at the CMB. The reason for this asymmetry between the two boundaries is due to the spherical shell geometry of the model (i.e. the areas $A_{top} > A_{bot}$), and the internal heat production. For an Earth-like model setup, the upper boundary layer controls the internal

temperature of the domain (*Sotin & Labrosse, 1999*; *Deschamps et al., 2010*), as different tectonic regimes result in different temperature evolution paths (**Figure 6.3**). Therefore, a proper grid size should be chosen in order to properly resolve the lithosphere, and thus minimize the effect of numerical parameters on the model evolution.

In this study I show that resolution-dependent tectonic regimes are a non-negligible issue in mantle convection simulations. In particular, the azimuthal (horizontal) and radial (vertical) grid resolutions can influence the outcome of the model.

For low R_{azi}, the long-distance horizontal interpolation of the stress smears out the contribution of highly stressed nodes over a broad area, leading to a low average stress σ_{ave}^{LT}. By doubling R_{azi}, the average stress per cell σ_{ave}^{LT} increases by $\approx 30\%$, while the total stress of the lithosphere σ_{tot}^{LT} can even double. By increasing R_{azi}, the stress in the lithosphere is higher, hence weaker, and mobile regimes are promoted.

For low R_{rad}, the interpolation of the stress fields over thicker cells, determines the propagation of the stress across the lithosphere thickness. It also facilitates the formation of plate boundaries. By doubling R_{rad}, the model produces an $\approx 15\%$ colder lithosphere, with a $O(10^1 - 10^2)$ higher viscosity η^{LT}, and $\approx 20-40\%$ lower cumulative maximum stress σ_{max}^{LT}. This determines the formation of a cold stiff lithosphere, where the stress hardly propagates throughout the entire thickness of the lid, thus promoting the stagnant lid regime.

The tectonic regime map in **Figure 6.14** shows that the radial resolution R_{rad} has a dominant impact on the tectonic regimes, since the regime distribution shifts from mobile only regimes ($R_{rad} = 32$), to stagnant-lid dominated distribution ($R_{rad} = 128$). The lack of stagnant lid regimes for $R_{rad} = 32$ is a major consequence of the insufficient number of grid nodes to compute the stress in the lithosphere, i.e. only 4 nodes for the dripping regimes and 3 for the plate-like subduction. The radial grid spacing in this case ranges from $\Delta r = 54-64\ km$. The average number of nodes that defines the lithosphere for $R_{rad} = 128$ is 15 (dripping), 9 (plate-like), and 6 (stagnant), with a radial grid spacing $\Delta r = 13-17\ km$. The minor differences between $R_{rad} = 128$ and $R_{rad} = 64$ are probably due to the similar number of nodes employed 8 (dripping), 6 (plate-like), and 4 (stagnant), with $\Delta r = 26-34\ km$.

Theoretically, the effect of R_{rad} on the tectonic regime can be mitigated by grid refinement of the upper boundary, however this method has not been tested in this study and it requires further analysis. The effect of R_{azi}, should not be underestimated since it causes a two times higher σ_{tot}^{LT}, and it reproduces more faithfully the narrow structures of the mantle (**Figure 6.22**).

Therefore, the most reliable tectonic regime distribution in this study is provided by the highest tested resolution tested (1024×128) featuring micro-plate dripping ($10 \leq \tau_y \leq 30\ MPa$), plate-like subduction ($40 \leq \tau_y \leq 50\ MPa$) and stagnant lid regime ($\tau_y \geq 60\ MPa$). The dense mapping of the tectonic regimes provides a useful reference for future simulations, that can be expanded by adding more complexities to the simple setting model setup described here (e.g. free surface, continents, melting). Grid resolution has a non-negligible influence on the computation of numerous physical parameters. For example, the absence of episodic behaviour for $R_{rad} > 64$ can be problematic for modelling mantle convection on Venus. Although this result might be due to the physical model designed for this study, caution is recommended when a simulation feature the episodic regime. To exclude the possibility that a tectonic regime is simply caused by the employed grid spacing, it is advised to perform resolution tests.

6.9. Appendix

Parameter	Symbol	Value	Units
Domain size			
Mantle thickness	r^{surf}	2890×10^3	$[m]$
Outer core thickness	r^{CMB}	3480×10^3	$[m]$
Boundaries conditions			
Surface cooling mode	T_{top}^{mode}	$isothermal$	$[/]$
Surface temperature	T_{top}	300	$[K]$
Surface velocity mode	V_{top}^{mode}	$free-slip$	$[/]$
CMB cooling mode	T_{bot}^{mode}	$isothermal$	$[/]$
CMB temperature	T_{bot}	4000	$[K]$
Surface velocity mode	V_{bot}^{mode}	$free-slip$	$[/]$
Internal heating parameters			
Heat production per unit mass	R_H	5.2×10^{-12}	$[W\ kg^{-1}]$
Half-life of heat producing elements	$t_{1/2}$	1.0×10^{30}	$[yr]$
Initial potential temperature	T_P	1600	$[K]$
Mineral phase fraction in the pyrolitic mantle			
Olivine fraction	X_{ol}	60	[%]
Pyroxene-Garnet	X_{pxgt}	40	[%]
Rock fraction in the pyrolitic mantle			
Basalt fraction (100% $pxgt$ system)	X_{basalt}	20	[%]
Harzburgite fraction (75% ol-25% $pxgt$)	X_{harz}	80	[%]
Phase system 1: olivine			
Phase transitions			
Number of mineral phases	n_{ol}	4	$[/]$
Phase transition depths	D_{ol}^{Γ}	$2740/660/410$	$[km]$
Phase transition temperature	T_{ol}^{Γ}	$2300/1900/1600$	[K]
Phase transition density jump	ρ_{ol}^{Γ}	$61.6/400/180$	$[kg\ m^{-3}]$
Phase transition Clapeyron slope	Υ_{ol}^{Γ}	$10/-2.5/2.5$	$[MPa\ \mathrm{K}^{-1}]$
Phase transition viscosity ratio	η/η_{ol}^{Γ}	$0.1/10/1.0$	$[/]$
Birch-Murnaghan compressibility $PPV/LM/MTZ/UM$			
Surface reference density	$\rho_{0_{ol}}$	3240	$[kg\ m^{-3}]$
Surface bulk modulus	$K_{0_{ol}}^{\Gamma}$	$210/210/85/163/163$	$[GPa]$
Pressure derivative of the bulk modulus	K'^{Γ}_{ol}	$3.9/3.9/4.0/4.0/4.0$	$[Pa\ m^{-1}]$
Grüneisen parameter	γ_{ol}^{Γ}	$1.3/1.3/0.85/1.3/1.3$	$[/]$
Exponent for thermal conductivity	k_{ol}^{Γ}	$1.0/1.0/1.0/1.0/1.0$	$[/]$
Diffusion creep parameters $PPV/LM/MTZ/UM$			
Activation energy	E_{ol}^{Γ}	$162/370/300/300$	$[kJ\ mol^{-1}]$
Activation volume	V_{ol}^{Γ}	$1.4/3.65/5.0/5.0$	$[cm^3\ mol^{-1}]$
Phase system 2: pyroxene-garnet			
Phase transitions			
Number of mineral phases	n_{pxgt}	5	$[/]$
Phase transition depths	D_{pxgt}^{Γ}	$2740/720/400/40$	$[km]$

Phase transition temperature	T^{Γ}_{pxgt}	$2300/1900/1600/1000$	$[K]$
Phase transition density jump	ρ^{Γ}_{pxgt}	$61.6/400/150/350$	$[kg\ m^{-3}]$
Phase transition Clapeyron slope	Υ^{Γ}_{pxgt}	$10/1.0/1.0/1.5$	$[MPa\ \mathrm{K}^{-1}]$
Viscosity ratio	$\eta/\eta^{\Gamma}_{pxgt}$	$0.1/10/1.0/1.0/1.0$	$[/]$
Birch-Murnaghan compressibility $PPV/LM/MTZ/UM/LT$			
Surface reference density	$\rho_{0_{pxgt}}$	3080	$[kg\ m^{-3}]$
Surface bulk modulus	$K_{0}{}^{\Gamma}_{pxgt}$	$210/210/85/163/163$	$[GPa]$
Pressure derivative of the bulk modulus	K'^{Γ}_{pxgt}	$3.9/3.9/4.0/4.0/4.0$	$[Pa\ m^{-1}]$
Grüneisen parameter	γ^{Γ}_{pxgt}	$1.3/1.3/0.85/1.3/1.3$	$[/]$
Exponent for thermal conductivity	k^{Γ}_{pxgt}	$1.0/1.0/1.0/1.0/1.0$	$[/]$
Diffusion creep parameters $PPV/LM/MTZ/UM/LT$			
Activation energy	E^{Γ}_{pxgt}	$162/370/300/300/300$	$[kJ\ mol^{-1}]$
Activation volume	V^{Γ}_{pxgt}	$1.4/3.65/5.0/5.0/5.0$	$[cm^3\ mol^{-1}]$
Viscous rheology			
Reference viscosity	η_0	1.0×10^{20}	$[Pa\ s]$
Reference temperature for η_0	T_0^{η}	1600	$[K]$
Reference pressure for η_0	P_0^{η}	0.0	$[Pa]$
Reference stress for η_0	σ_0^{η}	0.0	$[Pa]$
Upper viscosity cutoff	η_{max}	1.0×10^{28}	$[Pa\ s]$
Lower viscosity cutoff	η_{min}	1.0×10^{17}	$[Pa\ s]$
Plastic rheology			
Initial lithosphere thickness	d_{init}	100	$[km]$
Cohesion coefficient	c_y	∞	$[Pa]$
Frictional coefficient	f_{ϕ}	0	$[/]$
Depth gradient	f_{σ}	0.01	$[Pa\ m^{-1}]$

Table 6.2. StagYY parameters.

R_{rad}	$\Delta r_{min}[km]$	$\Delta r_{max}[km]$	$\Delta r_{mean}[km]$	n^{top}	$\Delta r_{mean}^{top}[km]$	n^{bot}	$\Delta r_{mean}^{top}[km]$
128	13	26	19	19	16	9	16
64	27	52	40	10	32	4	31
32	54	104	81	5	65	2	62

Table 6.3. Grid refinement at the surface (top) and CMB (bot) for each radial resolution R_{rad}. Δr $[km]$ indicates the thickness of the cells, whereas n indicates the number of cells in the refined portion of the domain.

R_{azi}	$\Delta\varphi_{d\,min}$ $[km]$	$\Delta\varphi_{d\,max}$ $[km]$
1024	21	39
512	42	78
256	85	156
128	171	312

Table 6.4. Azimuthal widths $\Delta\varphi$ $[km]$ for each azimuthal resolutions R_{azi}.

$R_{azi\times rad}$	a_{min}	a_{max}	a_{mean}	a_{mean}^{top}	a_{mean}^{bot}
128 × 128	7.78	23.79	15.3	19.33	11.08
256 × 128	3.88	11.90	7.95	9.67	5.54
128 × 64	3.88	11.75	7.43	9.56	5.63
512 × 128	1.94	5.95	3.83	4.83	2.77
256 × 64	1.94	5.87	3.71	4.78	2.82
128 × 32	1.94	5.73	3.64	4.78	2.81
1024 × 128	0.97	2.97	1.91	2.42	1.39
512 × 64	0.97	2.94	1.86	2.39	1.41
256 × 32	0.97	2.87	1.82	2.39	1.41
1024 × 64	0.49	1.47	0.93	1.20	0.70
512 × 32	0.49	1.43	0.91	1.19	0.70
1024 × 32	0.24	0.72	0.46	0.60	0.35

Table 6.5. Aspect ratio $a = \Delta\varphi/\Delta r$ for each tested resolution $R_{azi\times rad}$.
The resolutions in the left most column are arrange for increasing R_{azi}: R_{rad} ratio.

Lithosphere Thickness L^{LT} $[km]$												
	1024×128	**512×128**	**256×128**	**128×128**	**1024×64**	**512×64**	**256×64**	**128×64**	**1024×32**	**512×32**	**256×32**	**128×32**
90 $[MPa]$	58	54	64	65	56	58	62	71	97	72	93	96
80 $[MPa]$	58	54	64	69	69	58	62	72	100	102	96	97
70 $[MPa]$	57	54	64	67	71	58	63	70	108	106	100	99
60 $[MPa]$	59	53	64	68	119	77	81	89	123	114	102	102
50 $[MPa]$	120	77	63	69	124	117	87	90	122	124	113	108
40 $[MPa]$	127	115	105	71	122	121	122	98	113	123	120	115
30 $[MPa]$	140	119	120	86	127	125	133	117	114	112	121	122
20 $[MPa]$	155	142	133	113	142	144	147	129	124	116	117	125
10 $[MPa]$	158	165	158	133	165	164	157	146	134	128	119	128

Table 6.6. Median of time evolution $(0 \rightarrow 15\ Gyrs)$ of the lithosphere thickness L^{LT} $[km]$

rms temperature T^{rms} $[K]$												
	1024×128	**512×128**	**256×128**	**128×128**	**1024×64**	**512×64**	**256×64**	**128×64**	**1024×32**	**512×32**	**256×32**	**128×32**
90 $[MPa]$	2865	2997	3064	3183	2843	2917	3037	3171	2170	2176	2205	2237
80 $[MPa]$	2866	2992	3064	3152	1990	2915	3039	3175	2156	2151	2192	2221
70 $[MPa]$	2866	2993	3063	3114	2426	2926	3033	3170	2122	2127	2170	2197
60 $[MPa]$	2860	3002	3061	3119	2063	2469	2529	2696	2064	2099	2146	2166
50 $[MPa]$	2024	2176	3062	3177	1990	2026	2435	2670	2017	2036	2094	2130
40 $[MPa]$	1979	2014	2117	3163	1918	1957	2040	2532	1945	1991	2039	2076
30 $[MPa]$	1897	1931	2000	2227	1848	1862	1924	2055	1912	1932	1986	2025
20 $[MPa]$	1838	1822	1885	2035	1808	1829	1822	1968	1880	1902	1922	1955
10 $[MPa]$	1745	1758	1817	1920	1797	1800	1799	1873	1868	1879	1887	1904

Table 6.7. Median of time evolution $(0 \rightarrow 15\ Gyrs)$ of the rms temperature $T^{rms}[K]$

Whole mantle viscosity η^{Tot-LT} $[Pa\ s]$												
	1024×128	**512×128**	**256×128**	**128×128**	**1024×64**	**512×64**	**256×64**	**128×64**	**1024×32**	**512×32**	**256×32**	**128×32**
90 $[MPa]$	1.49×10^{20}	3.45×10^{19}	1.32×10^{20}	1.91×10^{20}	7.82×10^{19}	4.18×10^{19}	2.00×10^{19}	1.23×10^{20}	1.05×10^{23}	5.99×10^{22}	3.19×10^{22}	2.06×10^{22}
80 $[MPa]$	1.54×10^{20}	3.59×10^{19}	1.27×10^{20}	2.25×10^{20}	3.55×10^{20}	4.65×10^{19}	1.76×10^{19}	1.22×10^{20}	1.29×10^{23}	1.26×10^{23}	4.47×10^{22}	2.63×10^{22}
70 $[MPa]$	1.52×10^{20}	3.40×10^{19}	1.24×10^{20}	5.08×10^{20}	6.06×10^{21}	4.00×10^{19}	1.92×10^{19}	9.78×10^{19}	1.92×10^{23}	1.58×10^{23}	7.94×10^{22}	6.30×10^{22}
60 $[MPa]$	2.31×10^{20}	3.93×10^{19}	1.42×10^{20}	3.11×10^{20}	5.98×10^{23}	6.21×10^{21}	1.32×10^{21}	4.49×10^{20}	4.34×10^{23}	2.53×10^{23}	1.38×10^{23}	1.73×10^{23}
50 $[MPa]$	1.66×10^{24}	1.11×10^{21}	1.34×10^{20}	2.52×10^{20}	2.48×10^{24}	1.31×10^{24}	2.74×10^{22}	1.06×10^{21}	8.59×10^{23}	6.89×10^{23}	2.98×10^{23}	2.25×10^{23}
40 $[MPa]$	3.33×10^{24}	1.79×10^{24}	4.07×10^{23}	3.70×10^{20}	4.76×10^{24}	3.11×10^{24}	9.72×10^{23}	1.23×10^{22}	2.37×10^{24}	1.23×10^{24}	6.56×10^{23}	4.62×10^{23}
30 $[MPa]$	1.43×10^{25}	4.17×10^{24}	2.13×10^{24}	1.28×10^{23}	5.12×10^{24}	5.50×10^{24}	3.60×10^{24}	7.18×10^{23}	1.54×10^{24}	2.39×10^{24}	1.39×10^{24}	8.65×10^{23}
20 $[MPa]$	1.84×10^{25}	1.67×10^{25}	1.14×10^{25}	9.69×10^{23}	6.88×10^{24}	1.06×10^{25}	1.86×10^{25}	2.19×10^{24}	2.68×10^{24}	2.47×10^{24}	2.17×10^{24}	1.64×10^{24}
10 $[MPa]$	2.37×10^{25}	3.80×10^{25}	2.32×10^{25}	3.90×10^{24}	1.06×10^{25}	1.37×10^{25}	1.67×10^{25}	7.06×10^{24}	2.52×10^{24}	3.97×10^{24}	2.49×10^{24}	3.70×10^{24}

Table 6.8. Median of time evolution $(0 \rightarrow 15\ Gyrs)$ of the whole mantle viscosity $\eta^{Tot-LT}[Pa\ s]$

Effective Rayleigh number Ra_{eff} [/]												
	1024 × 128	**512 × 128**	**256 × 128**	**128 × 128**	**1024 × 64**	**512 × 64**	**256 × 64**	**128 × 64**	**1024 × 32**	**512 × 32**	**256 × 32**	**128 × 32**
90 [MPa]	3.19×10^8	1.38×10^9	3.62×10^8	2.50×10^8	6.03×10^8	1.13×10^9	2.36×10^9	3.82×10^8	4.41×10^5	7.71×10^5	1.45×10^6	2.24×10^6
80 [MPa]	3.09×10^8	1.33×10^9	3.74×10^8	2.11×10^8	1.33×10^8	1.01×10^9	2.67×10^9	3.87×10^8	3.58×10^5	3.68×10^5	1.04×10^6	1.76×10^6
70 [MPa]	3.14×10^8	1.40×10^9	3.86×10^8	9.37×10^7	7.77×10^6	1.18×10^9	2.45×10^9	4.82×10^8	2.41×10^5	2.92×10^5	5.82×10^5	7.31×10^5
60 [MPa]	2.07×10^8	1.21×10^9	3.36×10^8	1.53×10^8	7.85×10^4	7.57×10^6	3.55×10^7	1.05×10^8	1.06×10^5	1.83×10^5	3.36×10^5	2.68×10^5
50 [MPa]	2.86×10^4	4.25×10^7	3.55×10^8	1.89×10^8	1.89×10^4	3.58×10^4	1.72×10^6	4.40×10^7	5.37×10^4	6.71×10^4	1.55×10^5	2.05×10^5
40 [MPa]	1.43×10^4	2.66×10^4	1.17×10^5	1.29×10^8	9.86×10^3	1.51×10^4	4.84×10^4	3.81×10^6	1.95×10^4	3.76×10^4	7.04×10^4	9.99×10^4
30 [MPa]	3.34×10^3	1.14×10^4	2.22×10^4	3.72×10^5	9.12×10^3	8.53×10^3	1.31×10^4	6.54×10^4	2.99×10^4	1.93×10^4	3.31×10^4	5.33×10^4
20 [MPa]	2.57×10^3	2.85×10^3	4.16×10^3	4.91×10^4	6.76×10^3	4.39×10^3	2.52×10^3	2.15×10^4	1.72×10^4	1.87×10^4	2.13×10^4	2.81×10^4
10 [MPa]	1.98×10^3	1.23×10^3	2.04×10^3	1.22×10^4	4.38×10^3	3.36×10^3	2.79×10^3	6.66×10^3	1.81×10^4	1.17×10^4	1.86×10^4	1.25×10^4

Table 6.9. Median of time evolution ($0 \rightarrow 15\ Gyrs$) of the effective Rayleigh number Ra_{eff} [/]

Surface Nusselt number Nu_{top}[/]												
	1024 × 128	**512 × 128**	**256 × 128**	**128 × 128**	**1024 × 64**	**512 × 64**	**256 × 64**	**128 × 64**	**1024 × 32**	**512 × 32**	**256 × 32**	**128 × 32**
90 [MPa]	29.51	30.02	24.17	23.16	26.81	25.44	24.59	21.80	28.73	28.34	27.29	26.34
80 [MPa]	29.48	29.73	24.22	22.45	33.43	25.58	24.64	22.07	28.90	27.64	27.09	26.72
70 [MPa]	29.43	29.79	24.19	21.59	35.06	25.78	24.68	21.91	28.75	27.61	26.90	27.11
60 [MPa]	29.74	30.42	24.13	21.73	32.29	27.84	33.04	46.79	28.08	27.74	27.45	27.15
50 [MPa]	34.55	25.37	24.17	22.95	33.43	32.40	36.65	50.67	28.76	28.01	27.50	27.29
40 [MPa]	35.96	35.07	33.67	22.74	33.16	33.47	32.78	40.18	28.19	28.93	28.18	27.47
30 [MPa]	35.63	36.18	35.03	37.05	33.48	33.30	33.02	32.86	27.92	28.39	28.85	27.79
20 [MPa]	37.20	35.96	35.01	36.51	33.73	35.18	33.83	33.63	28.57	28.72	28.58	27.56
10 [MPa]	37.10	36.54	37.74	37.81	34.18	34.68	34.08	34.69	29.15	28.86	28.49	27.78

Table 6.10. Median of time evolution ($0 \rightarrow 15\ Gyrs$) of the surface Nusselt number Nu_{top}[/]

Bottom Nusselt number Nu_{bot}[/]												
	1024 × 128	**512 × 128**	**256 × 128**	**128 × 128**	**1024 × 64**	**512 × 64**	**256 × 64**	**128 × 64**	**1024 × 32**	**512 × 32**	**256 × 32**	**128 × 32**
90 [MPa]	18.94	15.78	12.45	10.60	16.54	15.26	11.73	7.81	15.98	15.80	15.35	15.21
80 [MPa]	18.98	15.87	12.53	10.56	22.52	15.29	11.72	7.68	16.14	15.70	15.45	15.40
70 [MPa]	18.93	15.88	12.56	9.95	23.15	15.08	11.87	7.53	16.10	15.72	15.88	15.92
60 [MPa]	19.17	15.80	12.60	10.67	20.59	20.54	22.78	19.82	16.08	15.94	16.18	16.30
50 [MPa]	23.23	21.85	12.60	11.01	22.52	21.10	22.79	20.29	16.77	16.16	16.08	16.43
40 [MPa]	24.82	23.45	22.26	11.50	22.78	22.46	20.73	22.72	17.56	16.63	16.37	16.32
30 [MPa]	24.91	25.43	23.31	23.18	23.84	23.02	21.07	21.26	17.90	17.36	16.97	16.72
20 [MPa]	24.24	25.63	25.06	23.97	23.27	23.10	22.75	21.65	17.65	17.45	17.45	16.90
10 [MPa]	26.07	24.81	25.23	24.34	22.50	22.41	22.24	22.62	17.92	17.39	17.53	17.26

Table 6.11. Median of time evolution ($0 \rightarrow 15\ Gyrs$) of the bottom Nusselt number Nu_{bot}[/]

Mobility $M_o[/]$												
	1024×128	**512×128**	**256×128**	**128×128**	**1024×64**	**512×64**	**256×64**	**128×64**	**1024×32**	**512×32**	**256×32**	**128×32**
90 $[MPa]$	8.08×10^{-7}	2.40×10^{-7}	1.47×10^{-7}	3.00×10^{-8}	1.69×10^{-4}	6.20×10^{-5}	1.82×10^{-5}	9.54×10^{-7}	2.33	2.56	2.73	2.74
80 $[MPa]$	8.55×10^{-7}	2.38×10^{-7}	1.48×10^{-7}	8.37×10^{-8}	2.06	7.10×10^{-5}	2.60×10^{-5}	6.26×10^{-7}	2.31	2.48	2.68	2.72
70 $[MPa]$	9.53×10^{-7}	2.53×10^{-7}	1.51×10^{-7}	8.46×10^{-8}	1.50	1.00×10^{-4}	3.73×10^{-5}	1.30×10^{-6}	2.20	2.39	2.61	2.67
60 $[MPa]$	3.35×10^{-6}	2.50×10^{-7}	1.58×10^{-7}	8.50×10^{-8}	1.40	1.12	9.51×10^{-4}	3.25×10^{-6}	2.24	2.33	2.54	2.61
50 $[MPa]$	1.71	3.93×10^{-6}	1.87×10^{-7}	3.24×10^{-8}	2.11	1.89	1.70	6.50×10^{-5}	2.67	2.51	2.44	2.53
40 $[MPa]$	1.84	1.92	1.68	8.29×10^{-8}	2.50	2.11	2.01	1.35	3.19	2.88	2.64	2.56
30 $[MPa]$	2.01	2.12	2.23	1.93	2.71	2.47	2.31	2.33	3.29	3.18	2.81	2.73
20 $[MPa]$	2.40	2.50	2.37	2.17	2.95	2.74	2.56	2.63	3.27	3.19	3.07	2.89
10 $[MPa]$	2.95	2.75	2.67	2.25	3.08	2.91	2.88	2.88	3.25	3.16	3.12	3.06

Table 6.12. Median of time evolution ($0 \rightarrow 15\ Gyrs$) of the Mobility $M_o[/]$

Plateness $P_{80}[/]$												
	1024×128	**512×128**	**256×128**	**128×128**	**1024×64**	**512×64**	**256×64**	**128×64**	**1024×32**	**512×32**	**256×32**	**128×32**
90 $[MPa]$	0.10	0.09	0.14	0.15	0.51	0.53	0.52	0.49	0.70	0.69	0.68	0.68
80 $[MPa]$	0.11	0.11	0.14	0.14	0.93	0.54	0.55	0.58	0.70	0.71	0.69	0.66
70 $[MPa]$	0.14	0.10	0.15	0.13	0.93	0.54	0.54	0.65	0.72	0.72	0.70	0.66
60 $[MPa]$	0.50	0.10	0.15	0.14	0.94	0.93	0.88	0.27	0.74	0.73	0.71	0.68
50 $[MPa]$	0.97	0.30	0.17	0.17	0.93	0.93	0.92	0.44	0.72	0.74	0.73	0.69
40 $[MPa]$	0.97	0.96	0.97	0.19	0.91	0.92	0.92	0.86	0.69	0.71	0.72	0.70
30 $[MPa]$	0.95	0.94	0.93	0.92	0.90	0.91	0.89	0.87	0.69	0.69	0.70	0.68
20 $[MPa]$	0.95	0.93	0.88	0.83	0.90	0.90	0.86	0.83	0.69	0.69	0.68	0.65
10 $[MPa]$	0.95	0.91	0.84	0.75	0.89	0.89	0.84	0.75	0.67	0.69	0.66	0.61

Table 6.13. Median of time evolution ($0 \rightarrow 15\ Gyrs$) of the plateness $P_{80}[/]$

Yield ratio $r_y[/]$												
	1024×128	**512×128**	**256×128**	**128×128**	**1024×64**	**512×64**	**256×64**	**128×128**	**1024×32**	**512×32**	**256×32**	**128×32**
90 $[MPa]$	0.12	0.08	0.07	0.05	0.11	0.09	0.08	0.07	0.30	0.31	0.33	0.33
80 $[MPa]$	0.14	0.08	0.08	0.07	0.14	0.10	0.09	0.08	0.30	0.30	0.34	0.37
70 $[MPa]$	0.15	0.10	0.09	0.09	0.27	0.12	0.11	0.09	0.28	0.29	0.32	0.35
60 $[MPa]$	0.18	0.12	0.10	0.11	0.24	0.23	0.24	0.18	0.28	0.29	0.34	0.37
50 $[MPa]$	0.30	0.18	0.13	0.09	0.37	0.31	0.23	0.19	0.35	0.30	0.32	0.35
40 $[MPa]$	0.39	0.37	0.31	0.14	0.75	0.55	0.26	0.23	0.78	0.37	0.32	0.36
30 $[MPa]$	0.79	0.67	0.44	0.38	1.03	0.93	0.50	0.33	1.10	0.82	0.46	0.43
20 $[MPa]$	1.26	1.11	0.80	0.49	1.34	1.10	0.94	0.49	1.16	1.12	0.98	0.81
10 $[MPa]$	2.41	2.08	1.36	1.08	2.15	1.89	1.56	1.05	1.64	1.67	1.75	1.50

Table 6.14. Median of time evolution ($0 \rightarrow 15\ Gyrs$) of the yield ratio $r_y[/]$

Yield fraction $f_y[/]$												
	1024 × 128	**512 × 128**	**256 × 128**	**128 × 128**	**1024 × 64**	**512 × 64**	**256 × 64**	**128 × 128**	**1024 × 32**	**512 × 32**	**256 × 32**	**128 × 32**
90 $[MPa]$	0.00	0.00	0.00	0.00	0.00	0.00	0.00	0.00	0.01	0.00	0.00	0.00
80 $[MPa]$	0.00	0.00	0.00	0.00	0.00	0.00	0.00	0.00	0.01	0.01	0.00	0.00
70 $[MPa]$	0.00	0.00	0.00	0.01	0.00	0.00	0.00	0.00	0.01	0.01	0.00	0.01
60 $[MPa]$	0.00	0.00	0.00	0.01	0.00	0.00	0.00	0.00	0.02	0.01	0.00	0.02
50 $[MPa]$	0.02	0.00	0.00	0.02	0.07	0.03	0.00	0.00	0.05	0.03	0.00	0.02
40 $[MPa]$	0.07	0.05	0.01	0.03	0.22	0.14	0.02	0.00	0.18	0.06	0.00	0.03
30 $[MPa]$	0.23	0.15	0.07	0.08	0.31	0.27	0.13	0.02	0.25	0.18	0.04	0.08
20 $[MPa]$	0.35	0.30	0.19	0.21	0.38	0.32	0.28	0.08	0.25	0.23	0.11	0.19
10 $[MPa]$	0.49	0.45	0.31	0.30	0.49	0.44	0.37	0.25	0.29	0.29	0.26	0.30

Table 6.15. Median of time evolution ($0 \rightarrow 15\ Gyrs$) of the yield fraction $f_y[/]$

Cumulative maximum stress of the lithosphere $\sigma_{max}^{LT}\ [MPa]$												
	1024 × 128	**512 × 128**	**256 × 128**	**128 × 128**	**1024 × 64**	**512 × 64**	**256 × 64**	**128 × 128**	**1024 × 32**	**512 × 32**	**256 × 32**	**128 × 32**
90 $[MPa]$	28.84	21.42	26.66	20.71	63.09	61.73	37.64	30.37	156.59	128.28	102.54	79.19
80 $[MPa]$	29.91	21.32	28.36	23.32	56.92	55.37	36.60	28.05	144.33	121.03	98.47	91.23
70 $[MPa]$	27.92	21.70	28.51	24.22	46.22	49.62	34.93	29.66	132.31	114.21	96.06	92.45
60 $[MPa]$	29.19	21.77	28.11	23.20	104.24	39.12	34.01	29.52	122.64	104.91	90.93	96.47
50 $[MPa]$	95.17	26.96	24.98	20.99	100.72	94.95	31.50	26.64	113.74	106.01	86.76	87.75
40 $[MPa]$	85.48	81.54	54.12	21.39	91.83	86.46	69.31	28.15	104.39	98.66	81.31	83.31
30 $[MPa]$	75.24	73.08	69.16	44.21	79.55	76.65	72.78	61.17	91.16	90.01	84.03	79.37
20 $[MPa]$	65.01	63.47	60.60	52.82	66.89	65.69	62.94	58.52	78.84	77.60	75.45	71.65
10 $[MPa]$	52.71	52.51	50.18	48.08	55.05	54.58	52.16	49.44	65.96	65.23	63.60	60.73

Table 6.16. Median of time evolution ($0 \rightarrow 15\ Gyrs$) of the cumulative maximum stress of the lithosphere $\sigma_{max}^{LT}[MPa]$

Total stress of the lithosphere $\sigma_{tot}^{LT}\ [GPa]$												
	1024 × 128	**512 × 128**	**256 × 128**	**128 × 128**	**1024 × 64**	**512 × 64**	**256 × 64**	**128 × 64**	**1024 × 32**	**512 × 32**	**256 × 32**	**128 × 32**
90 $[MPa]$	37.46	11.32	6.22	2.32	20.50	8.31	3.97	1.91	53.84	26.56	13.71	7.23
80 $[MPa]$	38.06	11.21	6.23	3.19	25.16	8.25	3.90	1.87	47.71	24.08	12.90	7.48
70 $[MPa]$	37.20	11.48	6.22	3.30	53.93	8.47	3.97	1.96	42.43	21.78	11.43	6.23
60 $[MPa]$	41.52	11.60	6.40	3.33	66.20	21.48	12.02	5.38	41.35	19.87	10.51	5.71
50 $[MPa]$	129.05	27.35	6.40	2.40	86.58	34.63	9.33	4.53	42.57	18.94	9.30	4.91
40 $[MPa]$	140.95	61.90	24.28	2.98	137.30	50.00	12.40	4.76	69.88	18.58	8.07	4.18
30 $[MPa]$	235.21	85.23	28.47	9.38	147.08	65.45	18.93	5.55	72.65	27.94	8.61	4.03
20 $[MPa]$	264.57	112.73	38.22	9.99	139.26	57.93	25.55	6.08	55.51	25.20	11.46	5.08
10 $[MPa]$	264.86	118.94	38.59	12.97	130.00	56.36	23.09	7.15	43.19	21.02	10.12	4.73

Table 6.17. Median of time evolution ($0 \rightarrow 15\ Gyrs$) of the total stress of the lithosphere $\sigma_{tot}^{LT}[GPa]$

Temperature of the lithosphere $T^{LT}[K]$												
	1024×128	**512×128**	**256×128**	**128×128**	**1024×64**	**512×64**	**256×64**	**128×64**	**1024×32**	**512×32**	**256×32**	**128×32**
90 [MPa]	997	1009	924	914	1128	1119	1106	1043	1414	1382	1372	1367
80 [MPa]	1000	1009	925	926	1142	1117	1106	1050	1422	1381	1369	1363
70 [MPa]	997	1009	926	932	1251	1117	1106	1056	1426	1385	1367	1368
60 [MPa]	1007	1011	940	927	1241	1238	1177	1158	1418	1394	1377	1377
50 [MPa]	1076	1013	933	923	1263	1252	1204	1180	1426	1403	1391	1390
40 [MPa]	1077	1077	1072	948	1182	1190	1236	1182	1391	1413	1412	1407
30 [MPa]	1017	1048	1071	1097	1287	1175	1189	1230	1367	1389	1415	1409
20 [MPa]	1188	1043	1046	1080	1291	1274	1238	1215	1382	1388	1390	1384
10 [MPa]	1270	1298	1158	1060	1317	1319	1290	1202	1452	1378	1388	1377

Table 6.18. Median of time evolution ($0 \rightarrow 15\ Gyrs$) of the temperature of the lithosphere $T^{LT}[K]$

Viscosity of the lithosphere $\eta^{LT}\ [Pa\ s]$												
	1024×128	**512×128**	**256×128**	**128×128**	**1024×64**	**512×64**	**256×64**	**128×64**	**1024×32**	**512×32**	**256×32**	**128×32**
90 [MPa]	3.75×10^{27}	3.80×10^{27}	4.89×10^{27}	5.39×10^{27}	6.08×10^{26}	9.22×10^{26}	1.29×10^{27}	2.86×10^{27}	1.42×10^{25}	5.51×10^{25}	1.89×10^{26}	4.57×10^{26}
80 [MPa]	3.58×10^{27}	3.82×10^{27}	4.81×10^{27}	5.35×10^{27}	3.77×10^{26}	8.09×10^{26}	1.23×10^{27}	2.78×10^{27}	7.31×10^{24}	2.37×10^{25}	1.51×10^{26}	2.10×10^{26}
70 [MPa]	3.48×10^{27}	3.72×10^{27}	4.69×10^{27}	5.31×10^{27}	2.61×10^{26}	7.09×10^{26}	1.16×10^{27}	2.43×10^{27}	5.40×10^{24}	2.12×10^{25}	9.77×10^{25}	1.52×10^{26}
60 [MPa]	3.09×10^{27}	3.60×10^{27}	4.26×10^{27}	5.30×10^{27}	9.20×10^{25}	8.15×10^{26}	1.76×10^{27}	3.03×10^{27}	3.23×10^{24}	1.25×10^{25}	3.70×10^{25}	7.28×10^{25}
50 [MPa]	4.16×10^{26}	2.70×10^{27}	4.33×10^{27}	4.97×10^{27}	1.80×10^{25}	5.91×10^{25}	1.31×10^{27}	2.45×10^{27}	1.78×10^{24}	7.06×10^{24}	1.61×10^{25}	2.48×10^{25}
40 [MPa]	1.86×10^{26}	3.68×10^{26}	7.33×10^{26}	4.21×10^{27}	9.23×10^{24}	1.23×10^{25}	1.47×10^{26}	1.94×10^{27}	1.94×10^{24}	3.96×10^{24}	6.64×10^{24}	1.89×10^{25}
30 [MPa]	8.17×10^{25}	1.42×10^{26}	2.86×10^{26}	5.49×10^{26}	9.74×10^{24}	8.71×10^{24}	4.83×10^{25}	1.79×10^{26}	3.83×10^{24}	2.09×10^{24}	2.31×10^{24}	4.80×10^{24}
20 [MPa]	3.80×10^{25}	6.51×10^{25}	1.34×10^{26}	1.46×10^{26}	1.16×10^{25}	1.02×10^{25}	7.13×10^{24}	6.22×10^{25}	2.15×10^{24}	1.56×10^{24}	9.46×10^{23}	1.92×10^{24}
10 [MPa]	9.70×10^{24}	1.17×10^{25}	4.07×10^{25}	3.01×10^{25}	7.48×10^{24}	5.00×10^{24}	5.29×10^{24}	1.00×10^{25}	5.68×10^{23}	1.34×10^{24}	3.19×10^{23}	3.69×10^{23}

Table 6.19. Median of time evolution ($0 \rightarrow 15\ Gyrs$) of the viscosity of the lithosphere $\eta^{LT}[Pa\ s]$

Number of plate boundaries [/]												
	1024×128	**512×128**	**256×128**	**128×128**	**1024×64**	**512×64**	**256×64**	**128×64**	**1024×32**	**512×32**	**256×32**	**128×32**
90 [MPa]	0	0	0	0	0	0	0	0	46	39	26	15
80 [MPa]	0	0	0	0	0	0	0	0	47	39	26	16
70 [MPa]	0	0	0	0	8	0	0	0	53	38	28	16
60 [MPa]	0	0	0	0	14	4	0	0	51	43	26	16
50 [MPa]	8	0	0	0	18	13	5	0	44	43	28	17
40 [MPa]	9	8	5	0	16	16	9	4	27	39	29	18
30 [MPa]	9	9	8	4	17	16	12	8	23	31	30	18
20 [MPa]	11	11	10	8	20	19	13	10	29	31	26	18
10 [MPa]	12	12	12	10	27	23	16	13	32	38	27	18

Table 6.20. Median of time evolution ($0 \rightarrow 15\ Gyrs$) of the number of plate boundaries [/]

Viscosity of the surface η^{surf} $[Pa\ s]$ $(1^{st}$ cell)												
	1024 × 128	**512 × 128**	**256 × 128**	**128 × 128**	**1024 × 64**	**512 × 64**	**256 × 64**	**128 × 64**	**1024 × 32**	**512 × 32**	**256 × 32**	**128 × 32**
90 $[MPa]$	1.00×10^{28}	1.00×10^{28}	1.00×10^{28}	1.00×10^{28}	4.24×10^{25}	5.44×10^{25}	8.85×10^{25}	7.69×10^{27}	8.04×10^{22}	5.41×10^{22}	9.82×10^{22}	4.02×10^{23}
80 $[MPa]$	1.00×10^{28}	1.00×10^{28}	1.00×10^{28}	1.00×10^{28}	3.97×10^{25}	4.85×10^{25}	6.88×10^{25}	6.69×10^{27}	5.40×10^{22}	1.02×10^{23}	1.39×10^{23}	1.18×10^{23}
70 $[MPa]$	1.00×10^{28}	1.00×10^{28}	1.00×10^{28}	1.00×10^{28}	4.95×10^{24}	3.71×10^{25}	4.81×10^{25}	4.11×10^{27}	5.73×10^{22}	9.49×10^{22}	8.21×10^{22}	4.71×10^{22}
60 $[MPa]$	1.00×10^{28}	1.00×10^{28}	1.00×10^{28}	1.00×10^{28}	3.18×10^{24}	1.36×10^{25}	3.44×10^{27}	1.00×10^{28}	6.59×10^{22}	6.46×10^{22}	4.82×10^{22}	3.33×10^{22}
50 $[MPa]$	8.26×10^{24}	1.00×10^{28}	1.00×10^{28}	1.00×10^{28}	1.12×10^{24}	2.25×10^{24}	7.00×10^{24}	1.00×10^{28}	2.62×10^{22}	3.66×10^{22}	4.11×10^{22}	2.85×10^{22}
40 $[MPa]$	5.05×10^{24}	7.06×10^{24}	9.94×10^{24}	1.00×10^{28}	3.21×10^{23}	4.10×10^{23}	3.33×10^{24}	5.52×10^{25}	1.46×10^{22}	1.25×10^{22}	2.07×10^{22}	1.95×10^{22}
30 $[MPa]$	1.11×10^{24}	2.21×10^{24}	3.38×10^{24}	3.43×10^{24}	1.74×10^{23}	1.54×10^{23}	4.50×10^{23}	2.26×10^{24}	9.08×10^{21}	6.25×10^{21}	8.13×10^{21}	1.17×10^{22}
20 $[MPa]$	4.97×10^{23}	6.08×10^{23}	1.04×10^{24}	7.28×10^{23}	1.11×10^{23}	8.60×10^{22}	7.43×10^{22}	3.72×10^{23}	4.75×10^{21}	3.45×10^{21}	3.73×10^{21}	6.35×10^{21}
10 $[MPa]$	1.01×10^{23}	1.30×10^{23}	1.68×10^{23}	4.98×10^{22}	4.87×10^{22}	4.19×10^{22}	3.27×10^{22}	3.27×10^{22}	1.91×10^{21}	2.17×10^{21}	2.00×10^{21}	3.09×10^{21}

Table 6.21. Median of time evolution $(0 \rightarrow 15\ Gyrs)$ of the viscosity of the lithosphere η^{surf} $[Pa\ s]$

Viscosity of the CMB η^{CMB} $[Pa\ s]$ (last cell)												
	1024 × 128	**512 × 128**	**256 × 128**	**128 × 128**	**1024 × 64**	**512 × 64**	**256 × 64**	**128 × 64**	**1024 × 32**	**512 × 32**	**256 × 32**	**128 × 32**
90 $[MPa]$	1.01×10^{19}	8.56×10^{18}	7.06×10^{18}	6.59×10^{18}	2.64×10^{19}	2.28×10^{19}	1.45×10^{19}	1.07×10^{19}	2.95×10^{20}	2.80×10^{20}	2.50×10^{20}	2.52×10^{20}
80 $[MPa]$	1.00×10^{19}	8.56×10^{18}	7.14×10^{18}	6.22×10^{18}	2.83×10^{19}	2.34×10^{19}	1.43×10^{19}	1.10×10^{19}	3.19×10^{20}	2.72×10^{20}	2.55×10^{20}	2.68×10^{20}
70 $[MPa]$	1.01×10^{19}	8.54×10^{18}	7.11×10^{18}	5.90×10^{18}	5.27×10^{19}	2.24×10^{19}	1.47×10^{19}	1.05×10^{19}	3.15×10^{20}	2.67×10^{20}	2.99×10^{20}	3.27×10^{20}
60 $[MPa]$	1.04×10^{19}	8.76×10^{18}	7.33×10^{18}	6.26×10^{18}	4.03×10^{19}	4.19×10^{19}	4.19×10^{19}	2.63×10^{19}	3.17×10^{20}	2.99×10^{20}	3.22×10^{20}	3.66×10^{20}
50 $[MPa]$	1.31×10^{19}	1.06×10^{19}	7.27×10^{18}	6.97×10^{18}	5.43×10^{19}	4.38×10^{19}	5.27×10^{19}	3.47×10^{19}	3.91×10^{20}	3.22×10^{20}	3.12×10^{20}	3.89×10^{20}
40 $[MPa]$	1.41×10^{19}	1.31×10^{19}	1.24×10^{19}	7.69×10^{18}	5.64×10^{19}	5.19×10^{19}	4.10×10^{19}	4.86×10^{19}	5.57×10^{20}	3.73×10^{20}	3.57×10^{20}	3.63×10^{20}
30 $[MPa]$	1.43×10^{19}	1.41×10^{19}	1.31×10^{19}	1.33×10^{19}	6.17×10^{19}	5.67×10^{19}	4.29×10^{19}	4.62×10^{19}	6.03×10^{20}	5.08×10^{20}	4.37×10^{20}	4.25×10^{20}
20 $[MPa]$	1.34×10^{19}	1.47×10^{19}	1.46×10^{19}	1.39×10^{19}	5.77×10^{19}	5.62×10^{19}	5.77×10^{19}	4.70×10^{19}	5.95×10^{20}	5.50×10^{20}	5.06×10^{20}	4.45×10^{20}
10 $[MPa]$	1.44×10^{19}	1.40×10^{19}	1.48×10^{19}	1.41×10^{19}	4.92×10^{19}	4.78×10^{19}	5.15×10^{19}	5.65×10^{19}	6.51×10^{20}	5.00×10^{20}	5.40×10^{20}	5.11×10^{20}

Table 6.22. Median of time evolution $(0 \rightarrow 15\ Gyrs)$ of the viscosity of the CMB η^{CMB} $[Pa\ s]$

CHAPTER 7 – Slab Stagnation in the Mantle Transition Zone

7.1. Introduction

The mantle transition zone (MTZ) is bounded by two seismic discontinuities, at 410 km and 660 km of depth. The reason why seismologists were able to detect these discontinuities, is given by the sudden acceleration of seismic body waves caused by the phase transformations.

At $\approx 410\ km$ olivine Ol transforms through an exothermic phase reaction into wadsleyite Wd, thus involving a positive Clapeyron slope $\Upsilon^{410} > 0\ MPa\ K^{-1}$ (*Bina & Wood, 1987*; *Frost, 2008*). At $\approx 660\ km$ ringwoodite Rw breaks down into bridgmanite Br and ferropericlase Fp through an endothermic phase reaction, i.e. negative Clapeyron slope $\Upsilon^{660} < 0\ MPa\ K^{-1}$ (*Frost, 2008*; *Ishii et al., 2018, 2019*). The 660 km phase transition is also known as post-spinel phase reaction, since ringwoodite has a cubic symmetry and belongs to the spinel group (*Kubo et al., 2002*; *Katsura et al., 2003*). In Earth's mantle, the phase transitions encountered by the sinking slab always produce a denser mineral assemblage. The lithological definition of the MTZ is given in **Chapter 1.5.3**, while the explanation of the Clapeyron slope is given in **Chapter 2.6.3**.

The seismic tomographies of the Earth's mantle, reveal that subducting slabs display a wide variety of morphologies (*Goes et al., 2017*). Two main behaviours can be observed: (i) the direct slab penetration into the lower mantle (LM) (e.g. Marianas, Nazca plate, Cocos plate), and (ii) the slab stagnation within the MTZ (e.g. Izu-Bonin, and Pacific plate beneath Japan and southern Kuril Islands).

The focal mechanisms in Wadati-Benioff zones provide evidence that the slabs encounter resistance between $500-700\ km$ of depth. This resistance is inferred from the switch in the brittle failure mechanism, i.e. extension for the intermediate-deep earthquakes ($300-350\ km$) and compression for the deep earthquakes ($\approx 600-700\ km$). It appears that the 660 km discontinuity can act as a barrier to prevent the further descend of the slab into the LM. In the last years the parameters controlling the interaction between slab and the MTZ have been studied extensively.

7.1.1. Trench Rollback

It appears that the main controlling factor that leads to slab stagnation is the retrograde motion of the trench, i.e. trench rollback (*Christensen, 2001*). The trench rollback distributes the slab over a larger surface and reduces the dip angle of subduction θ. This migration promotes slab flattening and stagnation. A static trench, on the other hand, aligns the slab pull with the trench push, thus providing sufficient force to overcome the 660 km barrier. However, once trench retreat condition is satisfied, mantle resistance plays a decisive role.

7.1.2. Density Jump at the 660 km Phase Transition

The density profile of the Earth's mantle can be extrapolated from seismic data (e.g. *Dziewonski & Anderson, 1981*). The density jumps $\Delta\rho$ associated with the 660 km seismic discontinuity is predicted to range between $290-400\ kg\ m^{-3}$ (**Table 7.1**). Experimental constraints and thermodynamic calculations, on the other hand, predict a lower density jump of

$\approx 220\ kg\ m^{-3}$ for the ambient pyrolitic mantle ($\approx 60\ vol\%$ olivine), and $\approx 350\ kg\ m^{-3}$ for pure olivine (*Stixrude & Lithgow-Bertelloni, 2011*).

Model	$\Delta\rho\ [kg\ m^{-3}]$ at 660 km	Reference
PREM	+389	*Dziewonski & Anderson (1981)*
ak135-f	+319	*Kennett et al. (1995)*
PEM	+300	*Dziewonski et al. (1975)*
STW105	+292	*Kustowski et al. (2008)*

Table 7.1. Density jumps at 660 km for different 1D seismic radial models of the Earth.

7.1.3. Negative Clapeyron Slope of the 660 *km* Phase Transition

The negative Clapeyron slope of the post-spinel phase reaction implies a resistance to slab sinking. When cold material (i.e. a slab) approaches the 660 km discontinuity, the phase boundary moves to larger depths, thus preventing the transition to a denser mineral assemblage (*Schubert et al., 1975*). Therefore, the negative Clapeyron slope favours the stagnation of the slab.

The most recent experimental estimates for the Clapeyron slope of the post-spinel reaction range between -0.5 to $-3.0\ MPa\ K^{-1}$ (*Hirose, 2002*; *Fei et al., 2004*; *Katsura et al., 2004*; *Litasov et al., 2005*; *Stixrude and Lithgow-Bertelloni, 2011*). The steeper the Clapeyron slope, the deeper the post-spinel transition will be. For $\Upsilon^{660} < -4.0\ MPa\ K^{-1}$, the sinking of the slab is prevented completely, and the mantle assumes a two layer convection configuration (*Christensen and Yuen, 1984*; *Fukao et al., 2009*).

Moreover, experimental evidence shows that the presence of water in the crystal lattice of ringwoodite decreases the Clapeyron slope. *Litasov and Ohtani (2007)* report $\Upsilon^{660} = -0.5\ MPa\ K^{-1}$ for dry Rw, and $\Upsilon^{660} = -3.0\ MPa\ K^{-1}$ for $2wt\%$ water-bearing Rw. Therefore, the presence of water in the slab favours its stagnation in the MTZ. However, Υ^{660} should increase over stagnation time, due to the dehydration processes caused by slab heating. The resulting slab dehydration enables slab sinking into the LM (*Agrusta et al., 2017*).

7.1.4. Viscosity Jump at the 660 *km* Phase Transition

The geophysical inversion models report a substantial increase of the mantle viscosity between the MTZ and the lower mantle (*Lambeck et al., 1996, 1998*; *Chen & King, 1998*; *Panasyuk & Hager, 2000*). The magnitude of the proposed viscosity jump ranges between a factor of 0.5 and 200, as reported in **Table 7.2** (*Forte & Mitrovica, 1996*; *Peltier, 1999*; *Mitrovica & Forte, 2004*; *Steinberger & Calderwood, 2006*; *Steinberger & Holme, 2008*; *Steinberger et al., 2010*; *Steinberger, 2016*; *Lau et al., 2016*). The viscosity increase related to the 660 km discontinuity, has been attributed to the dominance of bridgmanite Br in the LM ($\approx 80\ vol\%$ - *Marquardt & Thomson, 2020*). Rheologically speaking, Br represents a relatively strong phase when compared to the other minerals of the LM (*Yamazaki and Karato, 2001*). This sudden increase in viscosity hinders the further sinking of the slab by reducing its descent velocity.

Reference	Model	$\eta^{650}[Pa\ s]$	$\eta^{670}[Pa\ s]$	η^{670}/η^{650}
Forte & Mitrovica (1996)	(A) joint inversion of convection observables and post-glacial decay time data	1.50×10^{20}	1.80×10^{21}	12.0
Peltier (1999)	(VM2) viscosity-model 2 Bayesian inversion on glacial isostatic adjustment observations	6.31×10^{20}	1.59×10^{21}	2.5
Mitrovica & Forte (2004)	(A) Occam-style inversion of long-wavelength free-air gravity anomalies and post-glacial decay time data	6.31×10^{18}	1.26×10^{21}	200.0
Steinberger & Calderwood (2006)	(red) density model from $s-$ wave anomalies	1.12×10^{21}	7.94×10^{21}	7.1
Steinberger & Holme (2008)	(A) density model from $p-$ $s-$ wave anomalies	2.22×10^{20}	4.90×10^{21}	22.1
	(B) density model from $s-$ wave anomalies	2.84×10^{20}	4.19×10^{21}	14.8
	(C) density model from $s-$ wave anomalies below 1%	2.47×10^{20}	5.75×10^{21}	23.3
Steinberger et al.(2010)	Inversion of gravity anomalies in the geoid assuming a stress-free surface	6.51×10^{20}	6.24×10^{21}	9.6
Steinberger (2016)	tomography model GyPSuM	1.26×10^{21}	4.01×10^{21}	3.2
	tomography model S40RTS	1.29×10^{21}	3.60×10^{21}	2.8
	tomography model SAVANI	7.22×10^{20}	5.69×10^{21}	7.9
	tomography model SL + Gra	2.28×10^{21}	4.41×10^{21}	1.9
Lau et al. (2016)	$(\widehat{\mathrm{X}}_{\mathrm{PO}})$ Bayesian inversion of glacial isostatic adjustment (GIA) data	6.14×10^{21}	3.14×10^{21}	0.5

Table 7.2. Viscosity jumps at the 660 km discontinuity reported by different authors. The symbol η^{650} indicates the viscosity at 650 km, η^{670} indicates the viscosity at 670 km, and η^{670}/η^{650} indicates the viscosity ratio between LM and MTZ.
The viscosity profiles from *Steinberger et al., (2016)* are produced by employing different mantle tomographies: GyPSuM (*Simmons et al., 2010*); S40RTS (*Ritsema et al., 2011*); SAVANI (*Auer et al., 2014*); SL (*Schaeffer & Lebedev, 2013*) + Gra (*Grand, 2002*).

7.1.5. The Role of Phase Transitions in Mantle Convection

An exhaustive description on the effect of different phase transitions in mantle convection models was provided by *Schubert et al. (1975)* (**Figure 7.1**). Each phase transition is influenced by the presence of three mechanisms which affect the phase transition itself, as well as the convection of the mantle. These mechanisms are: (1) the advection of warm/cold material (**Figure 7.1-A**), (2) the latent heat L_H $[W\ kg^{-1}]$ absorbed/produced by the reacting material (**Figure 7.1-B**), (3) the combined action of latent heat and thermal expansivity (**Figure 7.1-C**).

The positive Υ^{410} of the 410 km discontinuity, causes an upward deflection of the phase boundary for cold materials (**Figure 7.1-1.a**), and a downward deflection for warm materials (**Figure 7.1-1.b**). This pressure shift results in the production of high-ρ minerals at shallower depths in the case of the cold sinking slabs, and low-ρ minerals at higher depths in the case of warm rising plumes.

The effect of the negative Υ^{660} of the 660 km discontinuity on the advecting material is opposite: downward deflection for cold materials (**Figure 7.1-2.c**), and upward deflection for warm materials (**Figure 7.1-2.d**). This results in the retention of low-ρ minerals at larger depths for the cold slab, and high-ρ minerals at shallower depths for the warm plumes.

The 410 km phase transition is exothermic for the descending slabs, while is endothermic for ascending plumes. The latent heat provided by the Ol → Wd reaction increases the temperature of the slab, thus causing a downward deflection of the discontinuity due to the positive Υ^{410} (**Figure 7.1-3.e**). On the other hand, the latent heat absorbed by the Ol ← Wd reaction reduces the temperature of the plume, and causes an upward deflection of the discontinuity (**Figure 7.1-3.f**).

The 660 km phase transition is endothermic for the descending slabs, while is exothermic for ascending plumes. The latent heat absorbed by the Rw → Br + Fp reaction reduces the temperature of the slab, and causes a downward deflection of the discontinuity due to the negative Υ^{660} (**Figure 7.1-4.g**). The latent heat produced by the Rw ← Br + Fp reaction increase the temperature of the plume, and causes an upward deflection of the discontinuity (**Figure 7.1-4.h**).

The combined action of latent heat and thermal expansivity determines: (i) a density reduction following the exothermic phase transitions (slabs at 410 km **Figure 7.1-5.i**; plumes at 660 km **Figure 7.1-6.l**), and (ii) a density increase following the endothermic phase transitions (plumes at 410 km **Figure 7.1-5.j**; slabs at 660 km **Figure 7.1-6.k**).

The three mechanisms described in this section operate simultaneously, and their combined effects influence the stability of the convecting material in the MTZ. For the 410 km discontinuity, mechanisms (2) and (3) provide a stabilizing effect (**Figure 7.1-B-C**), whereas the destabilizing effect is given by mechanism (1) (**Figure 7.1-A**). For the 660 km discontinuity, on the other hand, only mechanism (3) destabilizes the convecting material (**Figure 7.1-C**), while the other two (**Figure 7.1-A-B**) promote stagnation.

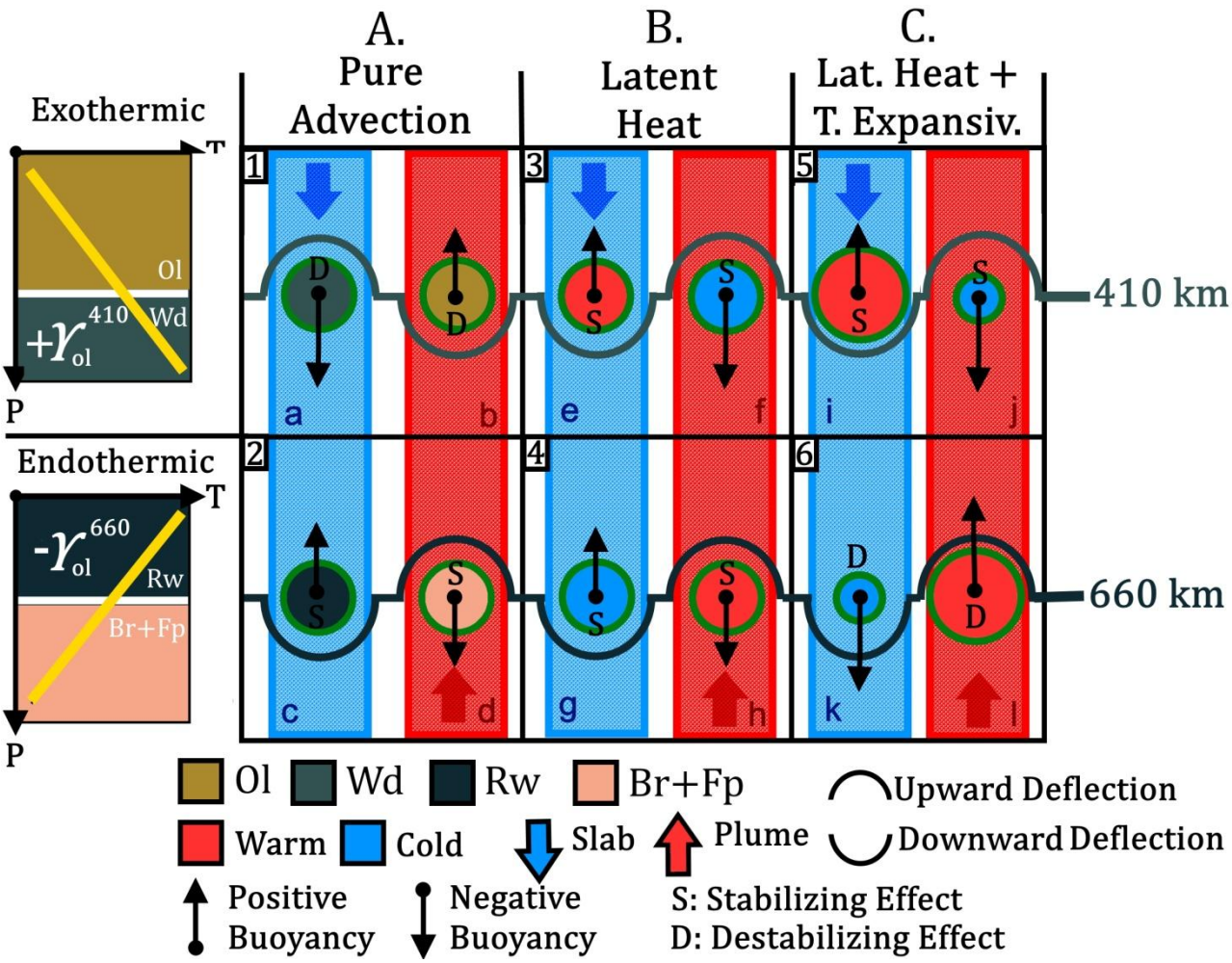

Figure 7.1. Schematics of the different mechanisms active at the exothermic (410 km) and endothermic (660 km) phase transitions. The exothermic phase transition (light grey) has a positive Clapeyron slope $\Upsilon^{410}\ MPa\ K^{-1}$ (yellow line) and it features Ol → Wd, whereas the endothermic phase transition (dark grey) has a negative Υ^{660} (yellow line) and it features Rw → Br + Fp. Each phase is indicated with a different colour: olivine (olive green), wadsleyite (light grey), ringwoodite (dark grey), lower mantle assemblage (pink). The three mechanisms active at the phase transitions are: pure advection of material (A. - left column); only latent heat (B. - mid column); latent heat and consequent thermal expansion of the material (C. - right column). Depending on the temperature of the advecting material, each mechanism causes a deflection of the discontinuities (concave and convex curves), and a variation in the buoyancy of the material (black arrows). The red colour indicates warm material, while blue indicates cold material. The advected material is represented with coloured arrows: upward pointing red arrows for the rising plumes, and downward pointing blue arrows for the descending slabs. The overall effect of a given mechanism on the stability of the material crossing a discontinuity is marked with letters 'S' (stabilizing) and 'D' (destabilizing). The subpanels 1– 6 are discussed in the main text. This figure has been modified from (*Schubert et al., 1975*).

All the three mechanisms are heavily dependent on the Clapeyron slope Υ of the phase transition: (1) for pure advection, Υ influences the pressure shift of the discontinuity; (2) the amount of latent heat absorbed/released is proportional to Υ, see eq. **(2.6.82)**; and (3) the density changes produced by thermal expansivity depend on the temperature variations caused by mechanism (2).

Apart from being influenced by Υ, each mechanism also depends on other independent parameters, which may not be relevant for the other mechanisms. For example, mechanism (1) is heavily dependent on the intrinsic temperature of the advecting material, which is inherited from its thermal evolution path. In the case of the lithosphere subduction, the temperature of the slab is proportional to $T^{slab} \propto \log(t^{-a} v^{-b})$, where $t\,[s]$ is the age of the slab, $v\,[m\,s^{-1}]$ its sinking velocity, and a, b are position-dependent parameters (*Maunder et al., 2019*). The colder is the slab geotherm, the larger is the deflection of the 410 km and 660 km phase transitions.

For mechanism (2), instead, the absorbed/released latent heat is proportional to the density jump $\Delta\rho\,[kg\,m^{-3}]$ of the phase transition, along with the densities of the reactants ρ_A and the products ρ_B, see eq. **(2.6.82)**. Moreover, the temperature variations $\Delta T_H[K]$ caused by the latent heat $L_H\,[W\,kg^{-1}]$, depend on the heat capacity of the material $Cp\,[J\,kg^{-1}\,K^{-1}]$, and on the rate of the phase transformation $\dot{t}\,[s^{-1}]$. Finally, the density variations caused by mechanism (3), depends on ΔT_H and on the thermal expansivity of the material $\alpha\,[K^{-1}]$.

7.1.6. Which Parameters Controls Slab Stagnation in the MTZ?

Given the large variety of parameters, it is difficult to establish the dominant factor controlling the slab stagnation in the MTZ. Parameters like Cp and α should have little influence on the slab stagnation, since they do not vary by more than one order of magnitude over the P-T range of the mantle (*Katsura et al., 2010*). Therefore, four key physical properties can be identified as the dominant parameters: (1) the temperature of the slab T^{slab}, (2) the Clapeyron slopes of the phase transitions $\Upsilon^{410}$and Υ^{660}, (3) the density jumps at each phase transition $\Delta\rho^{410}$ and $\Delta\rho^{660}$, and (4) the viscosity increase between the MTZ and the LM.

The numerical simulations performed by *Agrusta et al. (2017)* show the dominant effect of the Υ^{410} and Υ^{660} Clapeyron slopes in determining the stagnation of the slab in the MTZ. In this work, the mantle was assumed to be entirely composed of olivine, with a fixed density jump of 250 $kg\,m^{-3}$ at the 410 km discontinuity, and 350 $kg\,m^{-3}$ at the 660 km discontinuity. The tested Clapeyron slopes were $\Upsilon^{410} \in [2.5, 5.0]\ MPa\,K^{-1}$ and $\Upsilon^{660} \in [-0.5, -3.0]\ MPa\,K^{-1}$. The tested range of the viscosity increase η^{LM}/η^{MTZ} related to the post-spinel phase transition ranged from a factor 5 up to factor 30. Another input parameter was the age of the slab $t \in [25, 150]\ Myrs$ which controls its temperature evolution T^{slab}.

The work strategy of this chapter is to expand the investigation of *Agrusta et al. (2017)* by considering: (i) a global-scale domain, (ii) a composite mantle lithology (i.e. including pyroxene-garnet components), (iii) self-consistent slab subduction and thermal evolution, (iv) an extended range of viscosity increase inferred from geophysical constraints (i.e. η^{LM}/η^{MTZ} = 1-100).

This study focuses on the interactions between the slabs and the 660 km discontinuity (i.e. **Figure 7.1 -2.c –4.g –6.k**), therefore all the parameters related to the 410 km discontinuity were kept constant. The aim of this study is to constrain the parameters which cause the stagnation of the slab in the MTZ, while also providing a description of the physical phenomena occurring at the 660 km discontinuity.

7.2. Physical Model

A global-scale mantle convection model has been designed to reproduce self-consistently the plate tectonic regime on an Earth-like planet. The overall structure of the physical model used in this study is very similar to the one described in **Chapter 6.2**. Therefore, in this section, a description of the differences between the two model setups is reported.

7.2.1. Geometry and Domain Size

The employed geometry is the 2D spherical annulus (*Hernlund & Tackley, 2008*) (**Chapter 2.9.2**) with a mantle thickness of $r^{surf} = 2890\ km$ and a core radius of $r^{CMB} = 3480\ km$ (not part of the numerical domain). Gravity is assumed to be constant throughout the mantle with $g = 9.81\ m\ s^{-2}$.

7.2.2. Chemical Composition and Phase Transitions

The mantle is assumed to have a pyrolitic mineral assemblage made of Mg-Si olivine ($X_{ol} = 60\%$), and Al-Mg-Si pyroxene-garnet ($X_{pxgt} = 40\%$), i.e. a rock fraction of 80% harzburgite, and 20% basalt. Given the absence of melting processes, the chemical composition of the mantle remains homogeneous over time.

The phase boundaries within each phase system are handled using a parameterized approach (*Faccenda & Dal Zilio, 2017*) (**Chapters 3.6.8** and **6.2.3**). For the ol–system the number of phases is 4 (PPV → LM → MTZ → UM); whereas for the $pxgt$–system the number of phases is 5 (PPV → LM → MTZ → UM → LT). The reference parameters of each phase transition ($D_X^\Gamma, T_X^\Gamma, \Upsilon_X^\Gamma, \Delta\rho_X^\Gamma, \eta/\eta_X^\Gamma$) are reported in **Table 7.3**.

The depths of the MTZ discontinuities for both systems are respectively: $410\ km$ - $660\ km$ for the olivine system (D_{ol}^{410}, D_{ol}^{660}) (*Dziewonski & Anderson, 1981*), and $400\ km$ - $720\ km$ for the pyroxene-garnet system (D_{ol}^{400}, D_{ol}^{720}) (*Gasparik, 1989*; *Simmons & Gurrola, 2000*; *Irifune et al., 2008*). The reference temperatures of the MTZ discontinuities are: $T_{ol}^{410} = T_{pxgt}^{400} = 1600\ K$ and $T_{ol}^{660} = T_{pxgt}^{720} = 1900\ K$ (*Katsura et al., 2004, 2010*). The Clapeyron slopes of MTZ phase transitions are: $\Upsilon_{ol}^{410} = 2.5\ MPa\ K^{-1}$ (*Katsura & Ito, 1989*; *Litasov, 2006*) and $\Upsilon_{pxgt}^{400} = \Upsilon_{pxgt}^{720} = 1.0\ MPa\ K^{-1}$ (the latter is assumed). The Clapeyron slope of the post-ringwoodite phase transition Υ_{ol}^{660} is one of the variable parameters of this study (**Table 7.5**).

In this model setup, the density jumps $\Delta\rho_X^\Gamma$ at the $410-600\ km$ and $400-720\ km$ phase transitions are taken from *Faccenda & Dal Zilio (2017)*. These values have been estimated with the software EosFit7 (*Angel et al., 2014*), by employing the Thermocalc database (*Powell et al., 1998*), with a modified EoS for the Mg-end member phases (*Holland et al., 2013*). For the olivine system the prescribed $\Delta\rho_{ol}^\Gamma$ are: $+200\ kg\ m^{-3}$ at the $410\ km$ discontinuity (i.e. $+120\ kg\ m^{-3}$ for $60\ wt\%\ ol$), and $+320\ kg\ m^{-3}$ at the $660\ km$ discontinuity (i.e. $+192\ kg\ m^{-3}$ for $60\ wt\%\ ol$). For the pyroxene-garnet system the prescribed ρ_{pxgt}^Γ are: $+150\ kg\ m^{-3}$ at the $400\ km$ discontinuity (i.e. $+60\ kg\ m^{-3}$ for $40\ wt\%\ pxgt$), $+480\ kg\ m^{-3}$ at the $720\ km$ discontinuity (i.e. $+192\ kg\ m^{-3}$ for $40\ wt\%\ pxgt$). This leads to a density jump of $+180\ kg\ m^{-3}$ at the $400/410\ km$, and $+384\ kg\ m^{-3}$ at the $660/720\ km$. These values are comparable to the density jumps in the Preliminary Reference Earth Model (i.e. PREM - *Dziewonski & Anderson, 1981*): $+180\ kg\ m^{-3}$ for the $410\ km$ discontinuity, and $+389\ kg\ m^{-3}$ for the $660\ km$ discontinuity.

The viscosity ratio between the upper mantle and the MTZ ($\eta/\eta_X^\Gamma = \eta_X^{MTZ}/\eta_X^{UM}$) is set to be $\eta/\eta_{ol}^{410} = \eta/\eta_{ol}^{400} = 1.0$, i.e. no sudden increase in viscosity between the two regions (*Forte & Mitrovica, 1996*; *Peltier, 1999*; *Mitrovica & Forte, 2004*; *Steinberger & Calderwood, 2006*). The viscosity ratio between MTZ and lower mantle ($\eta/\eta_X^\Gamma = \eta_X^{LM}/\eta_X^{MTZ}$), on the other hand, represents one of the target parameters of this study (**Table 7.5**). A summary of the MTZ phase transition parameters is reported in **Table 7.3**.

Note that, in this model, there is no distinction between wadsleyite and ringwoodite in the olivine system: the UM olivine simply transforms into its MTZ polymorph which is here referred as '*spinel*'. Therefore, the breakdown of ringwoodite into LM assemblage is labelled as '*post-spinel*' reaction.

Parameter	Symbol	Value	Symbol	Value	Unit
Phase transition depths	D_{ol}^{410}	410	D_{ol}^{660}	660	$[km]$
	D_{pxgt}^{400}	400	D_{pxgt}^{720}	720	
Phase transition temperature	T_{ol}^{410}	1600	T_{ol}^{660}	1900	$[K]$
	T_{pxgt}^{400}	1600	T_{pxgt}^{720}	1900	
Phase transition Clapeyron slope	Υ_{ol}^{410}	2.5	Υ_{ol}^{660}	$Free$	$[MPa\ K^{-1}]$
	Υ_{pxgt}^{400}	1.0	Υ_{pxgt}^{720}	1.0	
Phase transition density jump	$\Delta\rho_{ol}^{410}$	320	$\Delta\rho_{ol}^{660}$	200	$[kg\ m^{-3}]$
	$\Delta\rho_{pxgt}^{400}$	480	$\Delta\rho_{pxgt}^{720}$	150	
Phase transition viscosity ratio	η/η_{ol}^{410}	1.0	η/η_{ol}^{660}	$Free$	$[/]$
	η/η_{pxgt}^{400}	1.0	η/η_{pxgt}^{720}	$Free$	

Table 7.3. MTZ phase transition parameters: depth D, temperature T, Clapeyron slope Υ, density ρ and viscosity η. The superscript indicates the phase transition ($400-410-660-720\ km$), while the subscription indicates the phase system (ol: olivine, $pxgt$: pyroxene-garnet).

7.2.3. Compressibility and Depth-Dependent Parameters

The computation of the depth-dependent thermodynamic parameters is reported in **Chapters 3.6.5**, **3.6.8**, **6.2.4**. Density $\rho(r)_X^\Gamma$ is calculated from eq. **(2.7.89)**, thermal expansivity $\alpha(r)_X^\Gamma$ with eq. **(3.6.58)**, and thermal conductivity $\Lambda(r)_X^\Gamma$ with eq. **(3.6.60)**. The specific heat capacity is assumed to be constant for all mineral phases $Cp(r)_X^\Gamma = 1200\ J\ kg^{-1}\ K^{-1}$. The surface reference density $\rho_{0_X}^\Gamma$, the surface bulk modulus $K_{0_X}^\Gamma$, its pressure derivative K'^Γ_X, the Grüneisen parameter γ_X^Γ, and the thermal conductivity exponent k_X^Γ, are reported in **Table 7.6**. The reference pressure profile $P(r)$ is computed at the beginning of the simulation (**Chapters 3.6.5**, **3.6.8**).

The latent heat L_H **(2.6.82)** at each phase transition is computed by employing the effective heat capacity $\acute{C}p$ and thermal expansivity $\acute{\alpha}$ approach (*Schubert et al., 1975*; *Christensen & Yuen, 1985*) as described in **Chapter 2.6.3**. The adiabatic temperature profile T_S **(2.6.87)** is calculated from the radial profile of the thermodynamic parameters ($\rho, \alpha, Cp, \Lambda, K, \gamma$), and by including the contribution of the released/absorbed L_H caused by convection. The initial potential temperature of the mantle is prescribed as $T_P^{init} = 1600\ K$ (*Katsura et al., 2010*).

7.2.4. Visco-Plastic Rheology

The rheology of the Earth's mantle is approximated as temperature-dependent diffusion creep, see eq. **(6.2.1)** (*Weertman, 1970*; *Yamazaki & Karato, 2001*). The reference viscosity of the mantle is set to be $\eta_0 = 10^{20}\ Pa\ s$, at $T_0 = 1600$ K, $P_0 = 0\ Pa$. The breaking of the lithosphere is achieved by employing a pseudoplastic rheology (*Tackley, 2000*) (**Chapters 3.6.3**, **6.2.5**) with a constant yield stress $\tau_y = 25\ MPa$, see eq. **(6.2.2)**. The low value of the yield stress was chosen to ensure the onset of the plate-like regime for a grid resolution of 1024×128 nodes (see **Chapter 6**). The lower and upper viscosity cut-offs are $\eta_{min} = 10^{17}\ Pa\ s$ and $\eta_{max} = 10^{28}\ Pa\ s$.

The values of the phase-dependent activation energy $E_X^\Gamma\ [J\ mol^{-1}]$ are based on mineral physics constraints (e.g. *Stixrude & Lithgow-Bertelloni, 2005*), and they were kept identical to those employed in the previous study (**Table 7.6**). The values chosen for the phase-dependent activation volume $V_X^\Gamma\ [cm^3\ mol^{-1}]$, reproduce a radial viscosity profile consistent with the geophysical constraints reported by *Forte & Mitrovica, (1996)*; *Peltier (1999)*; *Mitrovica & Forte (2004)*; *Steinberger & Calderwood, (2006)* , see **Table 7.4**, **Figure 7.3**.

Parameter	Symbol	Value					Unit
		PPV	LM	MTZ	UM	LT	
Activation volume olivine system	V_{ol}^Γ	1.65	2.5	3.0	6.0	–	$[cm^3\ mol^{-1}]$
Activation volume pyroxene garnet	V_{pxgt}^Γ	1.65	2.5	3.0	6.0	6.0	$[cm^3\ mol^{-1}]$

Table 7.4. Phase-dependent activation volume $V_X^\Gamma\ [cm^3\ mol^{-1}]$ for different mantle regions: post-perovskite (PPV), lower mantle (LM), mantle transition zone (MTZ), upper mantle (UM), and lithosphere (LT). In StagYY, the model is defined starting from the CMB up to the surface (**Chapter 3.6.7**), hence the values of V_X^Γ are reported in this order. The subscript indicates the phase system (ol: olivine, $pxgt$: pyroxene-garnet).

7.2.5. Variable Parameters

Two variable parameters have been selected for this study: the Clapeyron slopes of the Rw → Br + Fp phase transition $\Upsilon_{ol}^{660}\ [MPa\ K^{-1}]$, and the viscosity ratio between the MTZ and the lower mantle $\eta/\eta_{ol}^{660} = \eta_{ol}^{LM}/\eta_{ol}^{MTZ}$. A total of 77 simulation was performed for this study. Seven values for Υ_{ol}^{660} were tested, ranging from 0.0 to $-3.0\ MPa\ K^{-1}$, while eleven ratios for η/η_{ol}^{660} were employed, spanning from 1 to 100 (see **Table 7.5**). In order to produce a sudden viscosity increase in the lower mantle pyrolite, it is also necessary to control the viscosity ratio of the pyroxene-garnet system η/η_{pxgt}^{720}. The parameters η/η_{ol}^{660} and η/η_{pxgt}^{720} were adjusted accordingly.

Parameter	Symbol	Value	Unit
Clapeyron Slope	Υ_{ol}^{660}	$-0.0/-0.5/-1.0/-1.5/-2.0/-2.5/-3.0$	$[MPa\ K^{-1}]$
Viscosity ratio (ol)	η/η_{ol}^{660}	$1/10/20/30/40/50/60/70/80/90/100$	[/]
Viscosity ratio $(pxgt)$	η/η_{pxgt}^{720}	$1/10/20/30/40/50/60/70/80/90/100$	[/]

Table 7.5. Variable parameters: the 660 phase transition Clapeyron slope Υ_{ol}^{660}, and the associated viscosity ratio η/η_{ol}^{660}. The viscosity ratio of the pyroxene-garnet system η/η_{pxgt}^{720}, correspond to those of the olivine system for every simulation.

7.2.6. Adiabatic Temperature Profile of the Mantle

The reference adiabatic temperature profile of the mantle T_s is taken from equation **(2.6.87)**.

$$T_S = T_P \left(\frac{\rho(r)}{\rho_0}\right)\gamma \tag{7.2.1}$$

Where γ is the Grüneisen parameter (*Brugger & Fritz, 1967*), ρ_0 $[kg\ m^{-3}]$ is the reference density of pyrolite at the surface, T_P^{init} is the potential temperature, $\rho(r)$ $[kg\ m^{-3}]$ is the depth-dependent density. Given the presence of the latent heat of the phase transition L_H $[W\ kg^{-1}]$ **(2.6.82)**, the adiabatic temperature profile T_S depends on the Clapeyron slope Υ_X^{Γ}. The temperature of the ambient mantle is increased by the exothermic phase transition ($410\ km$), whereas is reduced by the endothermic phase transition ($660\ km$) (**Chapter 2.6.3**, and section **7.1.5**).

Since the Clapeyron slope of the post-spinel reaction is one of the target parameters, each Υ_{ol}^{660} produces a different adiabatic temperature profile (**Figure 7.2**). For $\Upsilon_{ol}^{660} = 0\ MPa\ K^{-1}$ (**Figure 7.2-a**) the adiabatic temperature profile does not show any sudden variation caused by the phase transition, and the temperature simply increases due to mantle compressibility **(7.2.1)**, i.e. $\Delta T_s^{660} \approx 2$ K. For decreasing Υ_{ol}^{660}(**Figure 7.2-b-g**), it decreases the negative temperature jump at the endothermic discontinuity, reaching $\Delta T_s^{660} \approx -50$ K for $\Upsilon_{ol}^{660} = -3.0\ MPa\ K^{-1}$.

Moreover, the adiabatic temperature profile depends also on the density jumps at the phase transitions. In **Figure 7.2-h** it is reported the reference case with no density jump caused by the post-spinel reaction, i.e. $\Delta\rho_{ol}^{660} = 0$ and $\Upsilon_{ol}^{660} = 0$. In this case the adiabatic temperature profile of the LM is sensibly lower than the one of **Figure 7.2-a**, which has $\Delta\rho_{ol}^{660} = 320\ kg\ m^{-3}$, $\Upsilon_{ol}^{660} = 0\ MPa\ K^{-1}$. This is due to the overall lower density of the **Figure 7.2-h** model. Such different T_S profiles lead to a different computation of the temperature-dependent viscosity **(6.2.1)**, thus affecting the mantle rheology and the vigour of the convection (see Rayleigh number, **Chapter 2.8.1**). The initial adiabatic temperature profile is not affected by the viscosity ratio at the $660\ km$ discontinuity η/η_{ol}^{660}.

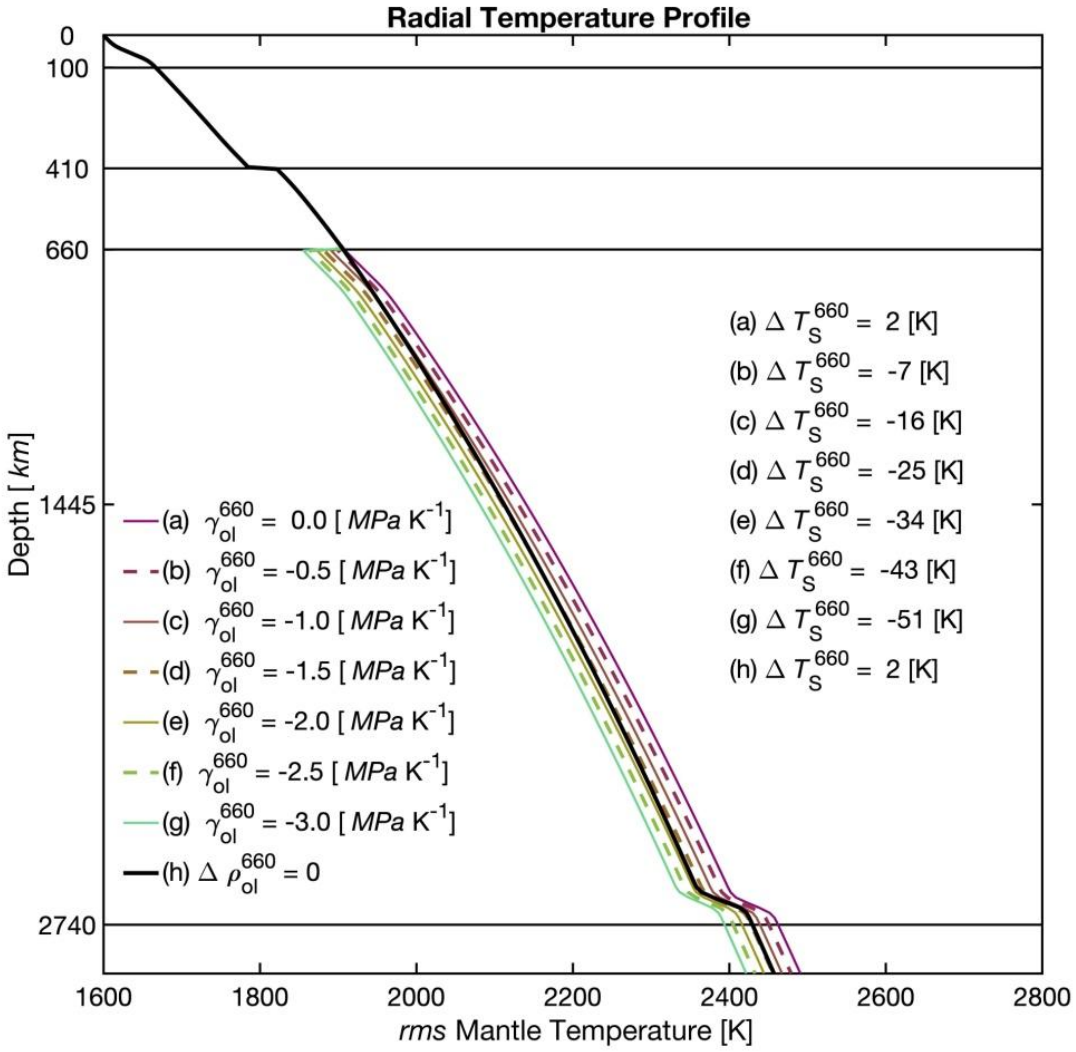

Figure 7.2. Adiabatic temperature profile of the mantle. Each line represents the rms radial temperature profile of a given model. The root mean square has been calculated considering the temperature of the mantle at each depth interval (i.e. azimuthal rms, see **Figure 6.5**). Shown are 7 Clapeyron slopes of the 660 km discontinuity Υ_{ol}^{660}, ranging from 0 to $-3.0\ MPa\ K^{-1}$, see the lines (a)-(g). The viscosity ratio at the 660 km discontinuity is set constant at $\eta/\eta_{ol}^{660} = 1$. The black line (h) represents the adiabatic temperature profile of a model with $\Delta\rho_{ol}^{660} = 0$, and $\Upsilon_{ol}^{660} = 0$. The employed colour scheme is the *hawaii* scientific colour map (*Crameri et al., 2020*).

7.2.7. Radial Viscosity Profile of the Mantle

The initial viscosity profile of the mantle is reported in **Figure 7.3**: the light blue area represents the geophysical constraints on mantle viscosity (*Forte & Mitrovica, 1996*; *Peltier, 1999*; *Mitrovica & Forte, 2004*; *Steinberger & Calderwood, 2006*; *Steinberger & Holme, 2008*; *Steinberger et al., 2010*; *Steinberger, 2016*; *Lau et al., 2016*), while the black lines represent the 11 viscosity ratios η/η_{ol}^{660} chosen as target parameters. Each profile is identical in the UM and in the MTZ, while they diverge in the LM.

The initial viscosity profiles fall within the geophysical constraints in the UM-MTZ region ($\approx 150-660\ km$). However, they show major discrepancies in the lower mantle. For most values of η/η_{ol}^{660} (i.e. $20-100$), the computed viscosity for the depth range $660-1800\ km$ is $1-4$ orders of magnitude higher than the geophysical constraints. The viscosity profiles are coherent with the geophysical constraints in the $1800-2800\ km$ region, while diverging in proximity of the CMB. This discrepancy is due to the higher temperatures at the bottom of the mantle, and the prescribed viscosity ratio at the post-perovskite transition **Table 7.6**. The $\eta/\eta_{ol}^{660} = 1$ viscosity profile shows an opposite trend, falling within the constraints in the upper half of the LM, and diverging in the lower half. The best match for the initial viscosity profile is given for $\eta/\eta_{ol}^{660} = 10$.

As stated before, for decreasing Υ_{ol}^{660}, it increases the viscosity contrast at the $660\ km$ discontinuity, since the endothermic reaction subtracts more heat from the advecting material. Therefore, the reference viscosity profile depends also on the endothermic Clapeyron slope Υ_{ol}^{660}. However, the general trend shown in **Figure 7.3** is maintained for every Υ_{ol}^{660}, and each profile is simply shifted toward higher η for decreasing Clapeyron slope.

Moreover, is should be noticed that the viscosity jump does not occur entirely at the $660\ km$ phase transition (**Figure 7.3**). The two parameters η/η_{ol}^{660} and η/η_{ol}^{720} spread the viscosity increase over a $\approx 200\ km$ thick region. The viscosity ratio reaches its nominal value at about $\approx 800\ km$ of depth. The effective viscosity ratio at the 660 discontinuity is only $\approx 0-30$, depending on η/η_{ol}^{660}. The remaining viscosity increase occurs within the $660-800\ km$ region.

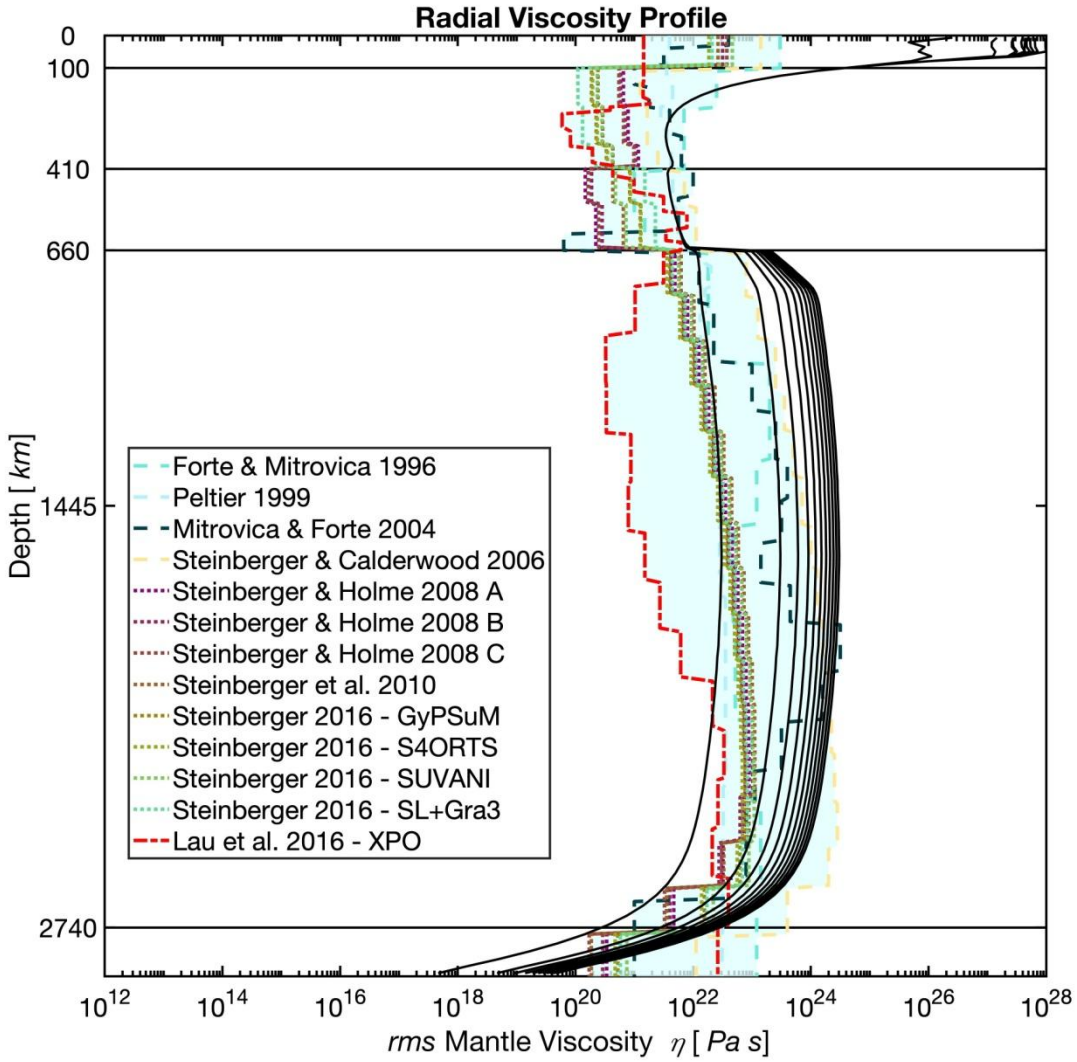

Figure 7.3. Radial viscosity profile of the mantle. The black lines spreading from left to right represent the 11 viscosity ratios used for the 660 km discontinuity $\Delta\eta_{ol}^{660}$. The viscosity ratio progressively increases from the left most ($\eta/\eta_{ol}^{660} = 1$) to the right most black line ($\eta/\eta_{ol}^{660} = 100$). The Clapeyron slope of the 660 km discontinuity Υ_{ol}^{660} is constant at $-1.5\ MPa\ K^{-1}$. Each black line represents the rms radial viscosity profile of a given model. The root mean square has been calculated considering the viscosity of the mantle at each depth interval (i.e. azimuthal rms, see **Figure 6.5**). The light blue area represents the geophysical constraints, where each coloured line represents a reference study (colours are reported in the legend). The dashed lines represents the geophysical constraints used to build the model (*Forte & Mitrovica, 1996*; *Peltier, 1999*; *Mitrovica & Forte, 2004*; *Steinberger & Calderwood, 2006*), the dotted lines represents the constraints provided by *Steinberger & Holme, (2008)*; *Steinberger et al., (2010)*; *Steinberger, (2016)*, while the red dashed-dotted line represent the constraints provided by (*Lau et al., 2016*). Each viscosity profile was derived from a geophysical model of the mantle, as summarized in **Table 7.2**.

7.3. Numerical Model

The solid-state mantle convection is reproduced by solving the mass, momentum and energy conservation reported in **Chapter 2**, see equations **(2.9.102)-(2.9.107)**. The governing equations are solved by employing the finite-difference code StagYY (**Chapter 3.6**) with the truncated anelastic approximation (*Tackley, 2008*), and the infinite Prandtl number approximation (see **Chapter 2.8.5**). StagYY employs the explicit FD discretization scheme to compute the energy conservation equation (*Tackley, 2008*) (**Chapter 3.6.2**). All models were run on the high performance computer clusters btrzx2 and btrzx1 at the University of Bayreuth.

7.3.1. Boundary Conditions and Heating Modes

For both the top and at the bottom of the domain $free-slip$ boundary conditions are prescribed for the velocity field (see **Chapter 3.3.3**), and $isothermal$ boundary conditions for the temperature field ($T_{\mathrm{top}} = 300\ K$ and $T_{\mathrm{bot}} = 4000\ K$). Quasi steady-state internal heating is achieved by prescribing a constant radiogenic heating source $R_{\mathrm{H}} = 5.2 \times 10^{-12}\ W\ kg^{-1}$ (*Tackley, 1998*; *Jaupart & Mareschal, 2015*; *Palme & O'Neill, 2007*) with an extended half-life time $t_{1/2} = 1.0 \times 10^{30}\ yr$.

7.3.2. Grid Resolution

The grid resolution employs $R_{azi} = 1024$ cell in the azimuthal direction φ, and $R_{rad} = 128$ cells in the radial direction r (see **Chapter 6**). The grid has been refined in the proximity of the upper and lower boundaries of the domain to ensure that the thermal boundary layers are properly resolved. The radial grid nodes distribution features: 44% of the nodes in the top 26% of the domain (0–750 km, and 5% of the nodes in the bottom 5% of the domain (**Figure 7.4**). The average cell thickness in the UM–MTZ region is 13 km.

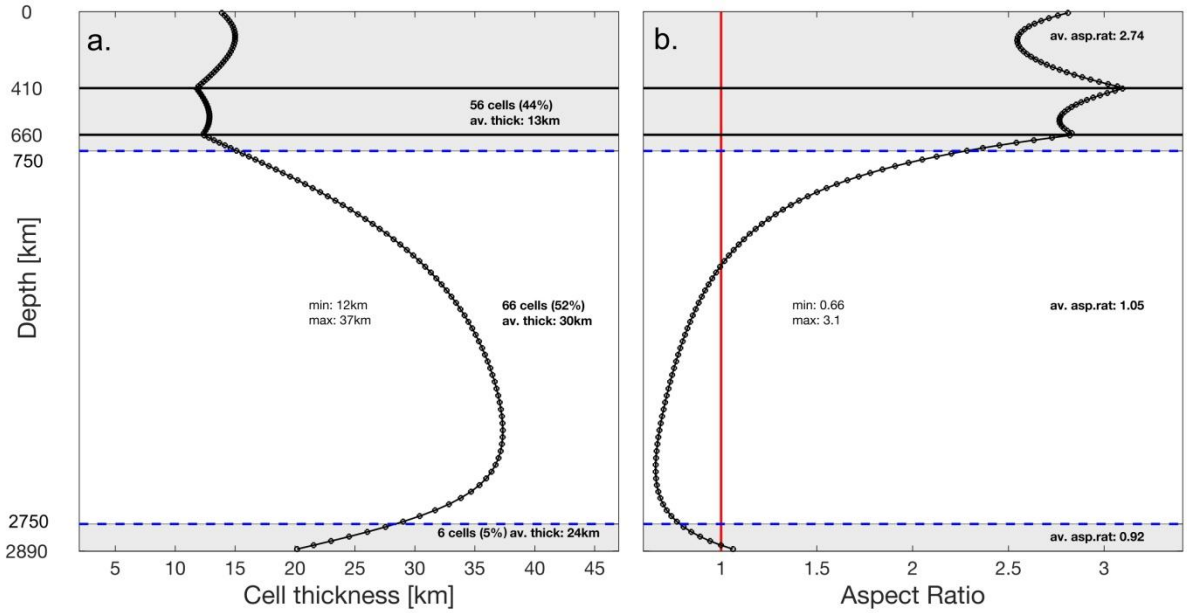

Figure 7.4. (a) radial profile of cell thickness Δr, and (b) radial profile of cell aspect ratio a. Each point reports the position of the centre of the corresponding cell. The aspect ratio a is calculated by considering the cell thickness Δr, and the azimuthal distance $\Delta\varphi_d$ of the top part of the cell. The grey areas indicate the refined regions, which are bounded by the dashed blue lines (750 km and 2750 km). The red line indicates the aspect ratio $a = 1$.

7.3.3. Advection and Tracers

The advection of the mantle material is performed through the marker-in-cell technique (**Chapter 3.5.2**) (*Harlow & Welch, 1965*). An 4^{th}-order (in space) Runge-Kutta scheme was employed to move the Lagrangian tracers (*Gerya, 2019*). Initially, each cell contains 60 tracers which are randomly distributed throughout the cell volume. The total number of tracers prescribed in each simulation is $\approx 7.9 \times 10^6$. In StagYY, the temperature field is advected at the Eulerian nodes with the MPDATA advection scheme (*Smolarkiewicz, 1984*). A correction routine is employed to compensate for the numerical diffusion arising from the computation of the advection (*Tackley, 2008*).

7.3.4. Initial Conditions

The initial mantle conditions features a 64 cell configuration (32 upwelling and 32 downwelling) to promote the onset of mantle convection (**Figure 7.5**).

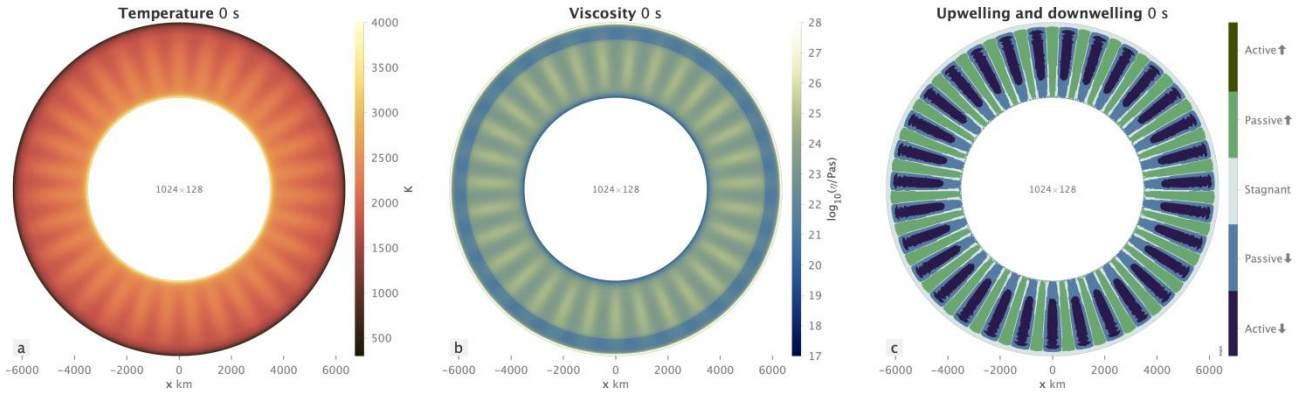

Figure 7.5. Initial mantle conditions (64 cell configuration), here plotted with StagLab (*Crameri, 2018*) and using a scientific colour map (*Crameri et al., 2020*): a) temperature field, (*lajolla*) b) viscosity field, (*devon*) c) mantle motion (*cork*).

The initial lithosphere thickness is set as $L_{init}^{LT} = 100\ km$, with an initial potential temperature of $T_P^{init} = 1600\ K$. Each simulation is run for $5\ Gyrs$ to achieve a stable tectonic regime, while avoiding the influence of the prescribed initial conditions on the outcome of the model.

7.4. Target Parameters and Post-Processing

When a slab undergoes through the post-spinel phase transition, it increases it density while acquiring additional gravitational pull. The thermal contraction caused by the endothermic reaction further contributes to the total pull (**Figure 7.1–6.k**). However, for cold materials, the transition is deflected to higher pressure due to the negative Clapeyron slope of the reaction, and the endothermic temperature reduction (**Figure 7.1-2.c** and **Figure 7.1–4.g**). Because of this, a slab gains buoyancy potentially stagnating in the MTZ. Moreover, the high viscosity of the LM produces a strong resistance against slab sinking. All these interactions were quantified by defining a set of target parameters.

7.4.1. Discontinuity Mechanism (1): Cold Advection

The cold temperatures of the slab causes the downward deflection of the 660 km discontinuity, i.e. mechanism (1) (section **7.1.5**, **Figure 7.1–2.c**). The inherited thermal state of the slab depends on several parameters which are independent from Υ_{ol}^{660} and η/η_{ol}^{660} (*Syracuse et al., 2010*; *Maunder et al., 2019*). In this study, the thermal evolution of the slab is computed self-consistently by solving the governing equations described in section **7.2**.

The temperature of the slab in the mantle can be estimated by computing the residual temperature T_R $[K]$. This parameter is a 2D field defined as:

$$T_R(t) = T_{r,\varphi}(t) - T_S(\Upsilon_{ol}^{660}, \eta/\eta_{ol}^{660}) \tag{7.4.2}$$

Where $T_{r,\varphi}[K]$ is the temperature of a given cell, and $T_S(\Upsilon_{ol}^{660}, \eta/\eta_{ol}^{660})$ $[K]$ is the reference adiabatic temperature profile calculated at the beginning of the simulation. The field T_R is computed by comparing the temperatures at the same depths. From the 2D residual temperature field, is easy to identify the positive and negative temperature anomalies in the mantle (**Figure 7.6**).

The residual temperature for each region of the mantle T_R^r, was computed following the procedure described for the viscosity in **Chapter 6.4.4**. The MTZ residual temperature T_R^{MTZ} should reveal the presence of cold material stagnating in the region.

Moreover, the residual temperature at 660 km of depth T_R^{660} $[K]$ was calculated to quantify the downward deflection of the phase transition. The temperature of the slab at base of the MTZ, was approximated as:

$$T_{adv}^{660} = T_{R\,min}^{660} - T_{pyr}^{660} \tag{7.4.3}$$

Where $T_{R\,min}^{660}$ is temperature of the coldest advective material crossing the 660 km discontinuity, and T_{pyr}^{660} is the temperature reduction caused by the latent heat, i.e. mechanism (2) (section **7.1.5**). The parameter, T_{pyr}^{660} will be defined in the following section. The pressure shift, ΔP_{adv}^{660} $[MPa]$ caused by the cold advection was computed as:

$$\Delta P_{adv}^{660} = T_{adv}^{660} \cdot \Upsilon_{ol}^{660} \tag{7.4.4}$$

$$P_{adv}^{660} = P_{ol}^{660} + \Delta P_{adv}^{660}$$

Where P_{ol}^{660} is the pressure corresponding to the input depth of the 660 km phase transition D_{ol}^{660} (**Table 7.3**). The depth of the 660 km phase transition D_{adv}^{660}, was retrieve by finding the closest node to the computed P_{adv}^{660}. The deflection of the 660 km phase transition due to mechanism (1), Δd_{adv}^{660} was computed as the difference between the shifted depth D_{adv}^{660} and the original depth D_{ol}^{660}.

$$\Delta d_{adv}^{660} = D_{adv}^{660} - D_{ol}^{660} \tag{7.4.5}$$

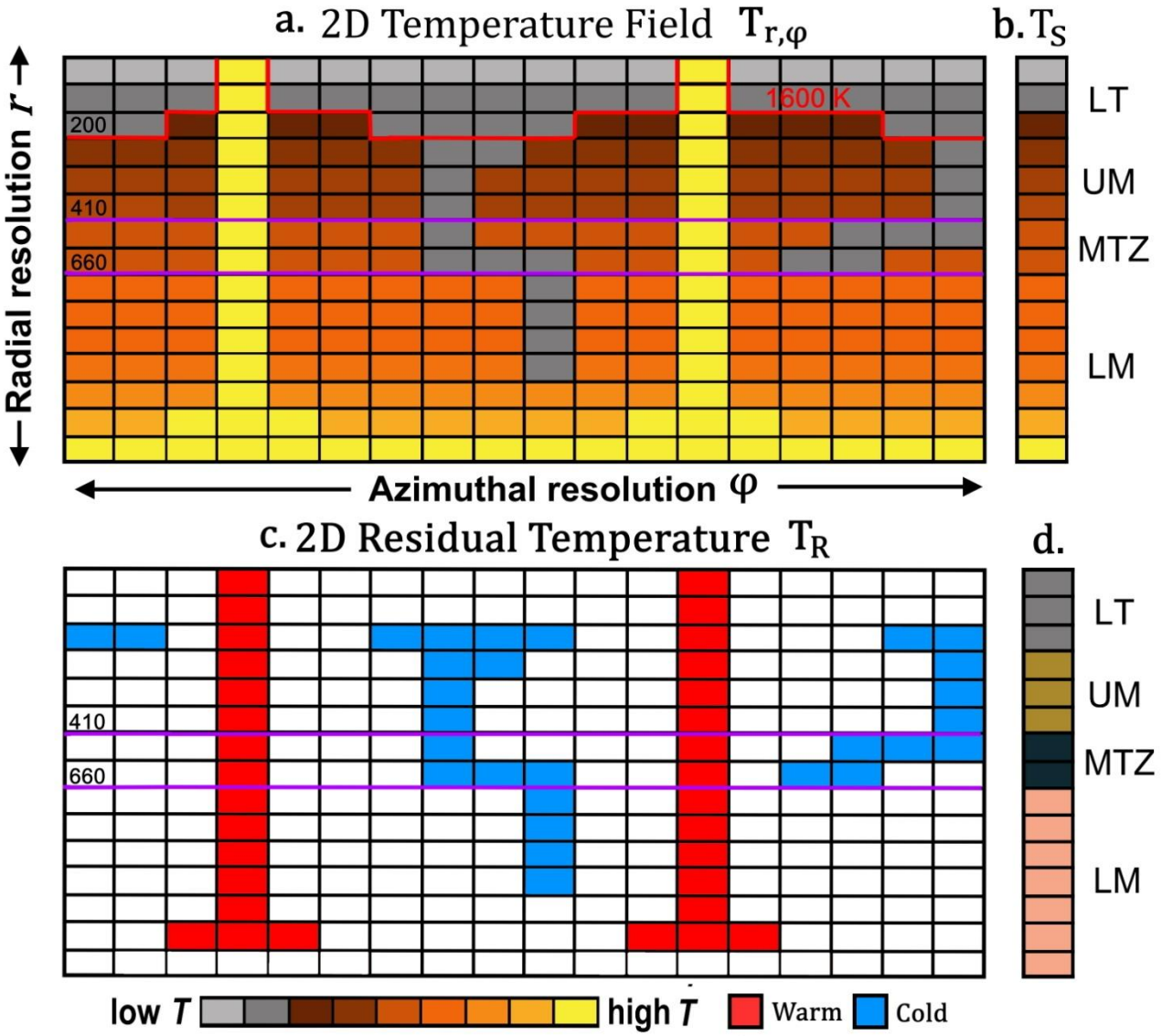

Figure 7.6. (a) Schematics of a 2D temperature field $T_{r,\varphi}$ (see **Figure 6.4**), (b) the 1D adiabatic temperature profile T_S, (c) the 2D residual temperature field T_R, (d) the different mantle regions (see **Figure 6.4**). The 1600 K isotherm defines the lithosphere (200 km limit), while the purple lines indicate the boundaries of the MTZ: 410– 600 km. The employed colour scheme for (a)-(b) is the '*lajolla*' scientific colour map (*Crameri et al., 2020*). The positive and negative temperature anomalies in (c) are indicated in red and blue respectively. The colour scheme for (d) is reported in **Figure 6.4**.

7.4.2. Discontinuity Mechanism (2): Endothermic Reaction

The endothermic phase transition causes energy absorption, temperature reduction, and downward deflection of the the 660 km discontinuity, i.e. mechanism (2) (section **7.1.5**, **Figure 7.1–4.g**). These effects were analyzed by computing: the latent energy E_{pyr}^{660} $[J\ kg^{-1}]$, the temperature reduction T_{pyr}^{660} $[K]$, and the deflection of the phase transition Δd_{pyr}^{660} $[m]$.

The latent energy E $[J\ kg^{-1}]$ quantifies the amount of energy that 1 kg of material has to absorb/release to fully complete a phase transition. In the specific case of the 660 km endothermic reaction, E_{ol}^{660} indicates the amount of energy that 1 kg of Rw has to absorb to breakdown into Br + Fp. The latent energy is calculated from equation **(2.6.82)** (*Schubert et al., 1975*).

$$E_{ol}^{660} = \frac{T_{ol}^{660}\Delta\rho_{ol}^{660}\Upsilon_{ol}^{660}}{\rho_{ol}^{659}\rho_{ol}^{661}} \tag{7.4.6}$$

Where $T_{ol}^{660}, \Delta\rho_{ol}^{660}, \Upsilon_{ol}^{660},$ are the temperature, density jump and Clapeyron slope of the 660 discontinuity (**Table 7.3**), ρ_{ol}^{659} is the density of the spinel phase at 659 km, and ρ_{ol}^{661} is the density of the post-spinel phase at 661 km (**Figure 3.11**). The latent energy obtained from equation **(7.4.6)** is referred to 1 kg of pure spinel (i.e. olivine phase system). Therefore E_{ol}^{660} has to be scaled down by considering the mass fraction of olivine in the pyrolite, i.e. $E_{pyr}^{660} = E_{ol}^{660} \cdot X_{ol}$, with $X_{ol} = 0.6$.

From E_{pyr}^{660} it is possible to calculate the temperature reduction T_{pyr}^{660} by dividing it for the specific heat capacity Cp, which has a constant value of $1200\ J\ kg^{-1}\ K^{-1}$.

$$T_{pyr}^{660} = \frac{E_{pyr}^{660}}{Cp} \tag{7.4.7}$$

The deflection of the 660 km phase transition due to mechanism (2), Δd_{pyr}^{660} was computed by substituting T_{pyr}^{660} in equation **(7.4.4)**, and by further substituting D_{pyr}^{660} in equation **(7.4.5)**.

7.4.3. Discontinuity Mechanism (3.a): Thermal Contraction

The combined action of latent heat and thermal expansivity causes the thermal contraction of the reacting material, i.e. mechanism (3) (section **7.1.5**, **Figure 7.1–6.k**). The density variations caused by the thermal expansivity, $\Delta\rho_{\alpha}^{660}$ were computed as:

$$\Delta\rho_{\alpha}^{660} = -\rho_{ol}^{660} \cdot \left(T_{pyr}^{660} \cdot \alpha_{ol}^{ave}\right) \tag{7.4.8}$$

Where $\rho_{ol}^{660}$is the density of the unreacted spinel phase at 660 km, T_{pyr}^{660} was taken from eq. **(7.4.7)**, and α_{ol}^{ave} is the average thermal expansion coefficient computed as:

$$\alpha_{ol}^{ave} = \frac{\alpha_{ol}^{659} + \alpha_{ol}^{661}}{2} \tag{7.4.9}$$

With α_{ol}^{659} as the thermal expansivity of spinel at 659 km of depth, and α_{ol}^{661} as the thermal expansivity of post-spinel at 661 km of depth (**Chapter 3.6.8**). The total density jump $\Delta\rho_{pyr}^{660}$ was given by:

$$\Delta\rho_{pyr}^{660} = (\Delta\rho_{ol}^{660} \cdot X_{ol}) + \Delta\rho_{\alpha}^{660} \tag{7.4.10}$$

Where $\Delta\rho_{ol}^{660}$ is the density jump at the phase transition (**Table 7.3**).

7.4.4. Discontinuity Mechanism (3.b): Gravitational Pull

The density increase due to thermal contraction, $\Delta\rho_{\alpha}^{660}$ enhances the gravitational pull on the reacted material, i.e. mechanism (3) (section **7.1.5**, **Figure 7.1–6.k**). This pull was computed as:

$$\Delta F_{\alpha}^{660} = g \cdot \Delta\rho_{\alpha}^{660} \tag{7.4.11}$$

Where $g\ [m\ s^{-2}]$ is the gravity acceleration, and $\Delta\rho_{\alpha}^{660}$ is taken from equation **(7.4.8)**. The pull force, $\Delta F_{\alpha}^{660}[N\ m^{-3}]$ represents the extra pull exerted per 1 m^3 of material after the 660 km phase transformation. The total extra pull gained after the 660 km phase transition, $\Delta F_{pyr}^{660}[N\ m^{-3}]$ is computed by substituting the total density jump, $\Delta\rho_{pyr}^{660}$ in equation **(7.4.11)**.

7.4.5. Discontinuity Mechanism (4.a): Resisting Force

The extra negative buoyancy produced by the post-spinel reaction competes against the resisting force induced by the viscosity jump at the 660 km discontinuity (section **7.1.4**). The viscosity jump hinders the further sinking of material down to the lower mantle. This resisting force ΔF_{R}^{660} $[N]$ was computed as:

$$\Delta F_{R}^{660} = \kappa_{ol}^{ave} \cdot \Delta\eta_{ol}^{660} \tag{7.4.12}$$

Where $\Delta\eta_{ol}^{660}$ $[Pa\ s]$ is the viscosity jump at the phase transition, calculated considering the viscosity of the MTZ at 659 km of depth η_{ol}^{659}, and the viscosity of the LM at 750 km of depth η_{ol}^{750}, i.e. $\Delta\eta_{ol}^{660} = \eta_{ol}^{LM} - \eta_{ol}^{MTZ}$. The choice of the 750 km depth reference was made to include the whole viscosity ratio η/η_{ol}^{720} prescribed in the model setting (see discussion in section **7.2.7**).

The parameter κ_{ol}^{ave} $[m^2 s^{-1}]$ indicates the average thermal diffusivity **(2.7.93)** of the phase transition. Thermal diffusivity is included in eq. **(7.4.12)** to consider the heating of the slab. Heating processes promote the stagnation of the slab by reducing its gravitational pull.

$$\kappa_{ol}^{ave} = \frac{\Lambda_{ol}^{ave}}{\rho_{ol}^{ave} Cp} \tag{7.4.13}$$

With Λ_{ol}^{ave} $[W\ m^{-1}\ K^{-1}]$ and ρ_{ol}^{ave} indicating the average thermal diffusivity and density of the phase transitions. Both values have been calculated using the same depth references employed for equation **(7.4.9)**.

In order to overcome the additional resistance offered by the 660 km discontinuity, a certain amount of material has to react to provide the required extra pull. This amount can be quantified as the 'avalanche' volume V_{ava}^{660} $[m^3]$, i.e. the volume of reacted material necessary to break the high viscosity barrier.

$$V_{ava}^{660} = \frac{\Delta F_{R}^{660}}{\Delta F_{pyr}^{660}} \tag{7.4.14}$$

7.4.6. Discontinuity Mechanism (4.b): Terminal Velocity

An additional estimate on the resisting action caused by the higher viscosity of the LM is given by the terminal velocity of the slab. Recently, it has been shown that the sinking velocity of the slab follows the scaling laws valid for a Stokes sinker (*Ribe & Xu, 2020*), i.e. a sphere falling through a viscous fluid. Therefore, it is possible to compute the terminal velocity of a 2D slab from the equation reported in *Ribe (2010)* and in *Ribe & Xu (2020)*.

$$V_{Stokes} = g\frac{h^{slab} l^{slab} \Delta\rho_{ave}^{slab}}{\eta_{ave}^{mantle}} \tag{7.4.15}$$

Where h^{slab} is the thickness of the slab assumed to be $10^5\ m$ ($100\ km$), l^{slab} is the length of the slab assumed as $5 \times 10^5\ m$ ($500\ km$), and g is the gravity acceleration $9.81\ m\ s^{-2}$. The viscosity of the ambient mantle η_{ave}^{mantle} $[Pa\ s]$ is computed as described in **Chapter 6.4.4**. The density jump between the slab and the ambient mantle ($\Delta\rho_{ave}^{slab} = \rho^{slab} - \rho_{ave}^{mantle}$) is computed with equation **(7.4.8)**.

$$\Delta\rho_{ave}^{slab} = -\rho_{ave}^{mantle} \cdot (T_{R\ slab} \cdot \alpha_{ave}^{mantle}) \tag{7.4.16}$$

Where $T_{R\ slab}$ is the residual temperature of the slab assumed to be constant at -800 K, and α_{mantle}^{ave} is the average thermal expansivity of the mantle $[K^{-1}]$.

The terminal velocity V_{Stokes} $[m\ yr^{-1}]$ indicates the maximum velocity attainable by the slab as it falls through the mantle. The terminal velocity of the UM and the LM should differ substantially, given the large viscosity increase at the 660 discontinuity. Therefore, the velocities V_{Stokes}^{UM} $(\eta_{ave}^{UM}, \rho_{ave}^{UM}, \alpha_{ave}^{UM})$ and V_{Stokes}^{LM} $(\eta_{ave}^{LM}, \rho_{ave}^{LM}, \alpha_{ave}^{LM})$ are computed for both mantle regions, from eq. **(7.4.15)**-**(7.4.16)**. If $V_{Stokes}^{UM} \gg V_{Stokes}^{LM}$ it means that the slab is forced to decelerate while descending through the mantle. This sudden stop is likely to occur at the interface between the two regions.

7.5. Numerical Results and Discussion

Within the 5 $Gyrs$ of simulated time, each simulation stabilizes into one of the following tectonic regimes: plate-like subduction, episodic overturn, or stagnant lid. Each regime has been identified based on the target parameters described in **Chapter 6.4**: (1) *root mean square* mantle temperature T_{rms}, (2) viscosity η, (3) surface and CMB Nusselt numbers Nu_{top} and Nu_{bot}, (4) mobility M_o, (5) plateness P_{80} and (6) lithosphere stress (r_y, f_y). The plate-like regime can be recognized from the high M_o (**Table 7.9**), the episodic regimes is recognized from the ramping Nu_{top} (**Table 7.8**), whereas the stagnant lid shows an increase in T_{rms} (**Table 7.7**) and decrease in η (**Table 7.10**, **Table 7.11**, **Table 7.12**).

The tectonic regime distribution map (**Figure 7.7**) shows that the influence of the viscosity ratio η/η_{ol}^{660} is predominant, and three main domains can be distinguished: (1) an upper domain dominated by the plate-like regime (red stars) at $\eta/\eta_{ol}^{660} \geq 60$, (2) an intermediate domain dominated by the episodic resurfacing (orange squares) at $20 \leq \eta/\eta_{ol}^{660} \leq 50$, and (3) a lower domain dominated by stagnant lid regime (yellow circles) at $\eta/\eta_{ol}^{660} \leq 10$. Moreover, from these results, it appears that there is no clear correlation between the Clapeyron slope Υ_{ol}^{660} and the displayed tectonic regime.

There are several outliers scattered across the plot, e.g. $\Upsilon_{ol}^{660} = -1.5\ MPa\ K^{-1}$ and $\eta/\eta_{ol}^{660} = 40$. The tectonic regime of the outliers might be the result of the hysteresis of mantle convection (*Weller & Lenardic, 2012*). Two models with identical physical parameters may display two different tectonic regimes because their evolution pathway diverged early on. This could have also happened in this study, especially when two target parameters are quite similar. The domains (1)-(3) in **Figure 7.7** can be subdivided into six sub-domains: (a.) plate-like only, (b.) plate-like dominated, (c.) episodic resurfacing dominated, (d.) episodic resurfacing only, (e.) episodic to stagnant transition, (f.) stagnant lid dominated.

The sub-domains (a.) $\eta/\eta_{ol}^{660} \geq 80$, and ($d$.) $20 \leq \eta/\eta_{ol}^{660} \leq 30$ are characterized by a single tectonic regime, i.e. plate tectonics (a.) and episodic resurfacing (d.). It is likely that within these two sub-domains, the physical parameters lead to the stabilization of one regime without much influence of the hysteresis of convection.

The sub-domains (b.)-(c.) for $40 \leq \eta/\eta_{ol}^{660} \leq 70$, appear to be a transition region between the episodic resurfacing and the plate-like regime. In this transition domain, the prescribed η/η_{ol}^{660} does not feature a distinct tectonic regime, and different results may be achieved depending on the evolution path of the model. However, in order to prove the hysteresis of the transition domain, each simulation should be repeated with the same parameter settings.

Domain (3) in **Figure 7.7** shows an internal distinction: (e.) an upper sub-domain dominated by episodic regime ($\eta/\eta_{ol}^{660} = 10$), and ($f$.) a lower sub-domain dominated by stagnant lid regime ($\eta/\eta_{ol}^{660} = 1$). As for the sub-domains (b.) and (c.), the sub-domain (e.) may represent an area characterized by hysteresis where a model can either develop episodic resurfacing or stagnant lid regime. It is unclear if the models in the sub-domain (f.) are subject to hysteresis or if the stagnant lid regime is actually established for $\Upsilon_{ol}^{660} > -3.0\ MPa\ K^{-1}$. If that is the case, this correlation requires deeper insight. For decreasing Υ_{ol}^{660}, the warm plumes should stagnate at the 660 discontinuity, hence being hindered from reaching the surface. This interaction removes a source of stress from the lithosphere and it should favour the stagnant lid regime. However, this is not the case, and stagnant lid occur for higher Υ_{ol}^{660}. It would be interesting to explore this behaviour in

further models, since it appears that the viscosity of the lower mantle is linked with the tectonic regime at the surface. However, this is beyond the scope of this study.

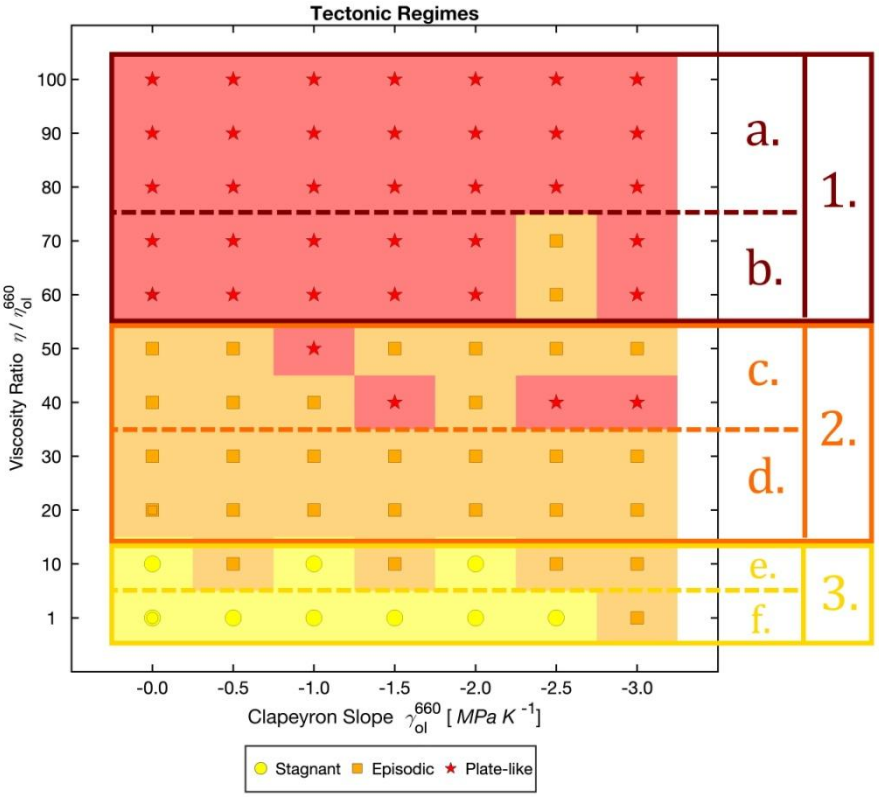

Figure 7.7. Tectonic regimes obtained for various Υ_{ol}^{660}, and η/η_{ol}^{660}. Each point represents a simulation. The tectonic regimes are distinguished by different markers and colours: stagnant lid (yellow circles), episodic behaviour (orange squares), and plate-like regime (red stars). The domains ($1.-3.$) and the sub-domains ($a.-e.$) are labelled on the right side of the figures and are explained in the main text.

7.5.1. Viscosity Structure of the Mantle

The initial viscosity profile of each simulation (**Figure 7.3**) evolves over time depending on the tectonic regime, and the mantle thermal history. **Figure 7.8** shows the median viscosities of different mantle regions: upper mantle η^{UM} (**Figure 7.8-a.1-3**, **Table 7.10**), mantle transition zone η^{MTZ} (**Figure 7.8-b.1-3**, **Table 7.11**), and lower mantle η^{LM} (**Figure 7.8-c.1-3**, **Table 7.12**).

Each point in **Figure 7.8** represents the median η of a given simulation, and is calculated as described in **Chapter 6.4.4**: (1) the regional median η_t^r is computed for each time frame t_{frame} in order to smoothen the contribution of high–η slabs and low–η plumes, (2) the cumulative η^r is computed as the median of η_t^r of all time frames ($0 \rightarrow 5$ Gyrs). The red areas in each plot represent the minimum and maximum viscosity at various depths as derived from geophysical constraints (see **Figure 7.3**). Each dashed black line in **Figure 7.3** indicates the average viscosity of a given region, and is computed considering all the geophysical constraints reported in **Table 7.2**.

The simulations displaying a stagnant lid regime (yellow symbols) are characterized by an overall η which is lower than given by geophysical constraints. This low viscosity is due to the high internal temperatures of the stagnant lid regime (**Chapter 6.5.5**).

For the episodic resurfacing regime (orange symbols), the periodic mantle overturns cause sudden cooling of the mantle leading to an overall higher η (**Chapter 6.5.4**). Although the upper mantle η remains below the geophysical constraints, for other regions, the η tends to approach the constraints.

For the plate-like regime (red symbols), the low temperatures of the mantle (**Chapter 6.5.3**) produces higher η values which fall within the geophysical constraints, for both the MTZ and the LM. In this two regions, the viscosity of the model is $O(1-3)$ higher than the average estimated viscosity (dashed black line, **Figure 7.8-b.c**). In the UM, however η remains $\approx O(1)$ lower than the average (**Figure 7.8-a**). This be attributed to the accumulation of low–η material in the UM, which was delivered by the warm rising plumes.

From **Figure 7.8**, it is clear that by increasing the viscosity ratio η/η_{ol}^{660} (different marker shapes) the overall mantle viscosity increases as well.

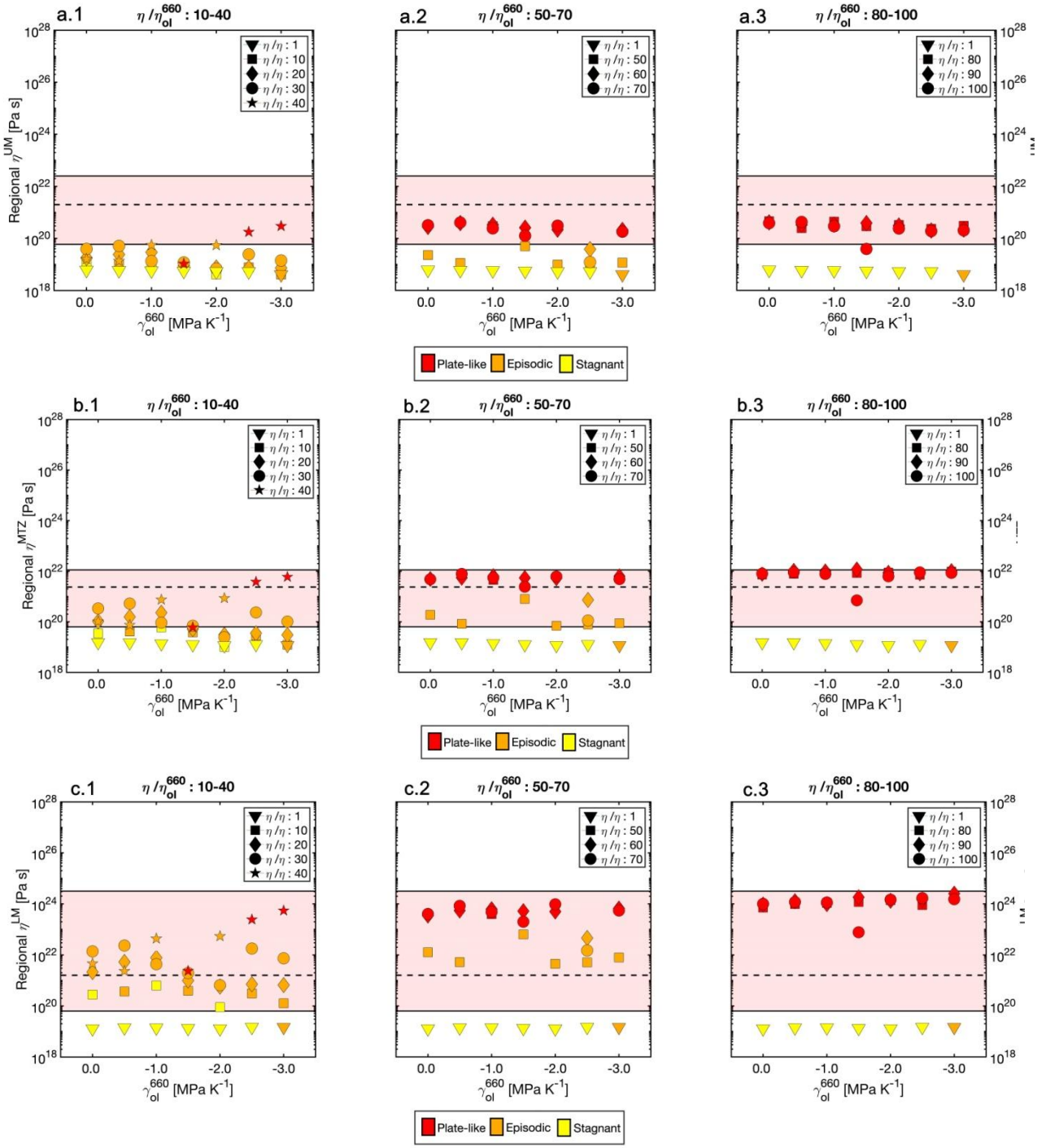

Figure 7.8. Viscosity η^r $[Pa\ s]$ of different mantle regions: (a-top row) upper mantle η^{UM} (**Table 7.10**); (b-mid row) mantle transition zone η^{MTZ} (**Table 7.11**); (c-bottom row) lower mantle η^{LM} (**Table 7.12**). Each symbol represents a given simulation (i.e. Υ_{ol}^{660}, η/η_{ol}^{660}) where the plotted viscosity is the median of its evolution over time ($0 \rightarrow 5$ Gyrs). The symbols indicate the viscosity ratio η/η_{ol}^{660}: triangles (1), squares (10– 50– 80), diamonds (20– 60– 90), circles (30– 70– 100), and stars (40). Each box regroups sets of simulations: $\eta/\eta_{ol}^{660} = 10-40$ (1-left column), $\eta/\eta_{ol}^{660} = 50-70$ (2-mid column), and $\eta/\eta_{ol}^{660} = 80-100$ (3-right column). The set with $\eta/\eta_{ol}^{660} = 1$ is reported in each box as a reference. The red areas are bounded by the min and max regional viscosity obtained from the reference reported in **Table 7.2**, whereas the dashed black line is average viscosity. The symbol colours indicate the tectonic regime as **Figure 7.7**.

7.5.2. Presence of Slabs in the MTZ

The subducting slabs deliver cold and stiff material into the deeper mantle. The presence of slabs in the MTZ can be verified by analyzing the average regional viscosity η_{ave}^{MTZ} (**Figure 7.9-a.1-3**, **Table 7.13**), stress σ_{ave}^{MTZ} (**Figure 7.9-b.1-3**, **Table 7.14**) and temperature T_{ave}^{MTZ} (**Figure 7.9-c.1-3**, **Table 7.15**) of the region.

The stagnant lid regime (yellow symbols) is characterized by the absence of subducted lithosphere at any depth. This is clear from the high-T ($\approx 2400\ K$), and low-η ($\approx 10^{19}\ Pa\ s$) of the MTZ, and the lack of stress build-up in the region ($\approx 0\ MPa$).

In the episodic resurfacing regime (orange symbols), the sudden collapse of the lithosphere is related to an average stress $\sigma_{ave}^{MTZ} > 0\ MPa$. The periodicity of these events limits the accumulation of slabs in the MTZ, thus reducing their contributions to the total time average of this region. The overall lower T_{ave}^{MTZ} and higher η_{ave}^{MTZ} are mostly a consequence of the massive heat release of the resurfacing event, rather than a solid indicator of stagnating slabs.

In the plate-like regime (red symbols), the presence of slabs in the MTZ is quite evident: (1) the average η_{ave}^{MTZ} is $> O(2)$ higher than the mean estimated viscosity of the region (dashed line **Figure 7.9-a.1-3**); (2) the average σ_{ave}^{MTZ} of the region is close to the prescribed yield stress $\tau_y = 25\ MPa$, thus indicating heavily stressed material. The average temperature T_{ave}^{MTZ}, does not register any cold anomaly in the MTZ. However, this can be explained by the equal contribution of cold slabs and warm plumes which cancel out when computing the average value.

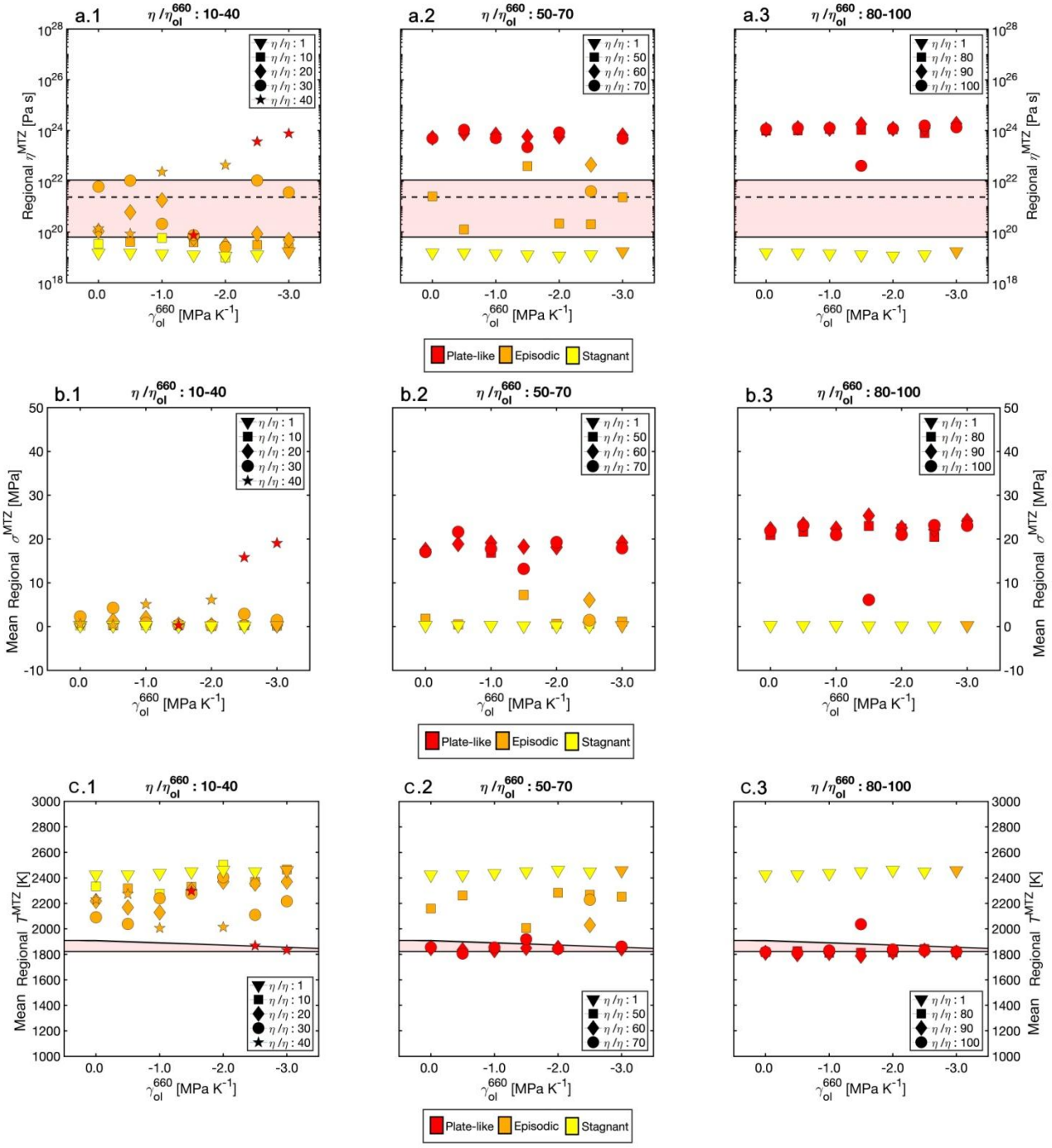

Figure 7.9. Different parameters of the MTZ: (a-top row) mean viscosity η_{ave}^{MTZ} (**Table 7.13**); (b-mid row) mean stress σ_{ave}^{MTZ} (**Table 7.14**); (c-bottom row) mean temperature T_{ave}^{MTZ} (**Table 7.15**). Each symbol represents a given simulation (i.e. Υ_{ol}^{660}, η/η_{ol}^{660}) where the plotted parameter is the median of its evolution over time ($0 \rightarrow 5\ Gyrs$). The red areas in (a.1-3) are bounded by the min and max regional viscosity obtained from the reference reported in **Table 7.2**, whereas the dashed black line is average viscosity. The red area in (c.1-3) represents the reference temperature profile of the MTZ, which is bounded by the adiabatic temperatures at 410 and 660 km (**Figure 7.2**). The symbols and their colour are the same as described in **Figure 7.8**.

7.5.3. Residual Temperature of the 660 Discontinuity

To provide a deeper insight into the processes occurring at the base of the MTZ, it is fundamental to analyze the residual temperature at the 660 km discontinuity. The mean residual temperature T_R^{660} is reported in **Figure 7.10-a.1-3** and **Table 7.16**.

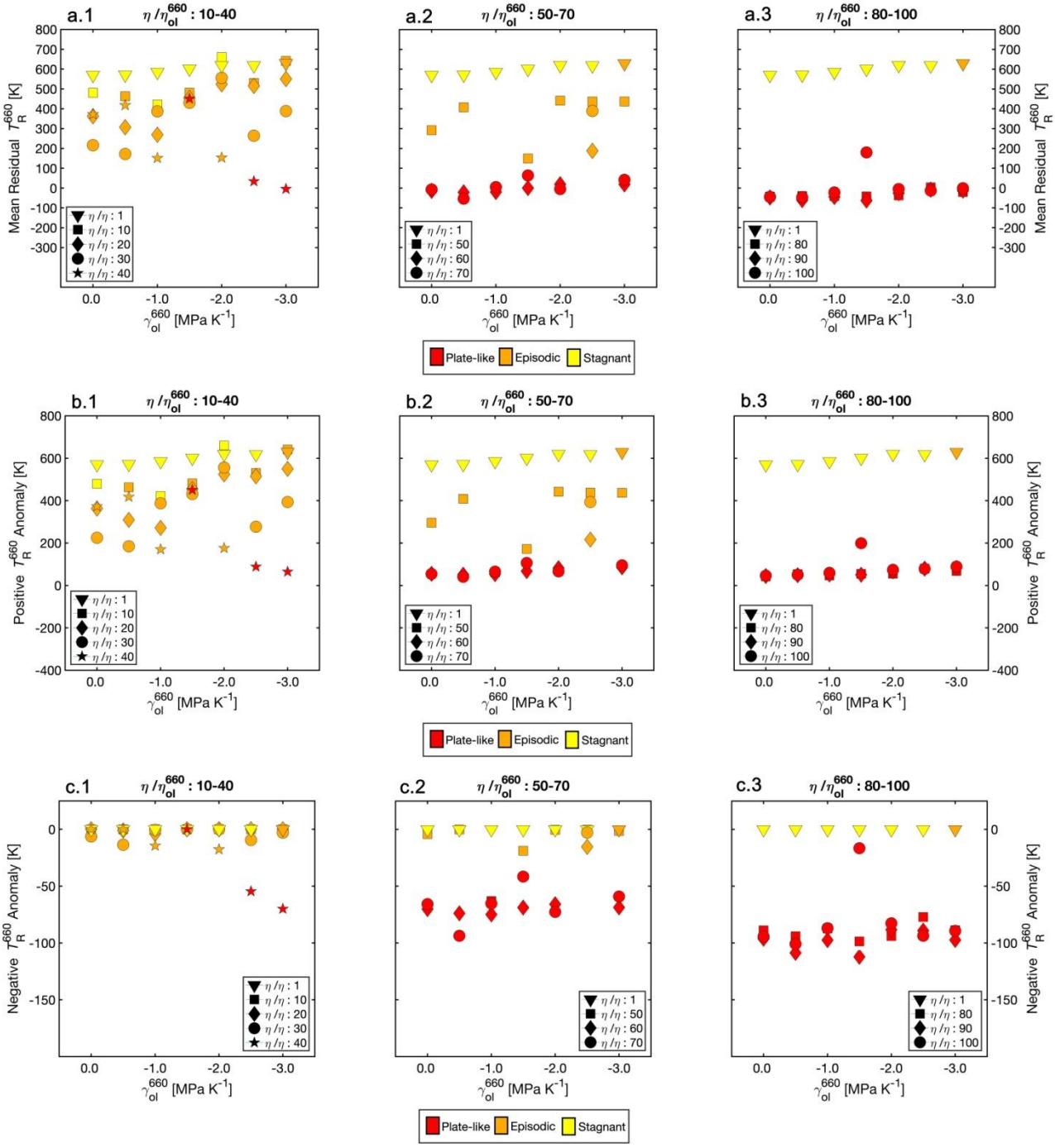

Figure 7.10. Average residual temperature T_R^{660} at the 660 km discontinuity: (a-top row) mean temperature (**Table 7.16**); (b-mid row) mean temperature of the positive anomalies (**Table 7.17**); (c-bottom row) mean temperature of the negative anomalies (**Table 7.18**). Each symbol represents a given simulation (i.e. Υ_{ol}^{660}, η/η_{ol}^{660}) where the plotted parameter is the median of its evolution over time (0 → 5 Gyrs). The symbols and their colour are the same described as in **Figure 7.8**.

For stagnant lid regime (yellow symbols) $T_R^{660} \approx 600\ K$; for episodic regime (orange symbols) $200\ K < T_R^{660} < 600\ K$; for the plate-like regime (red markers) $-50\ K < T_R^{660} < 50\ K$. The overall mantle heating in stagnant lid regime and episodic resurfacing is evident from the high positive temperature anomalies (see **Figure 7.10-b.1-3** and **Table 7.17**) with $+T_R^{660} > 200\ K$, and the absence of negative temperature anomalies (see **Figure 7.10-c.1-3** and **Table 7.18**) with $-T_R^{660} \approx 0\ K$.

The plate-like regime, on the other hand, is characterized by the presence of both anomalies which, on average, show the same value range, $0 < |T_r^{660}| < 100\ K$ (**Figure 7.10-b/c.1-3**). As stated above, both plumes and slabs are present in this region and their contributions compensate each other. This becomes evident by observing the maximum $T_{R\,max}^{660}$ and the minimum $T_{R\,min}^{660}$ residual temperatures at the 660 km discontinuity (**Figure 7.11**).

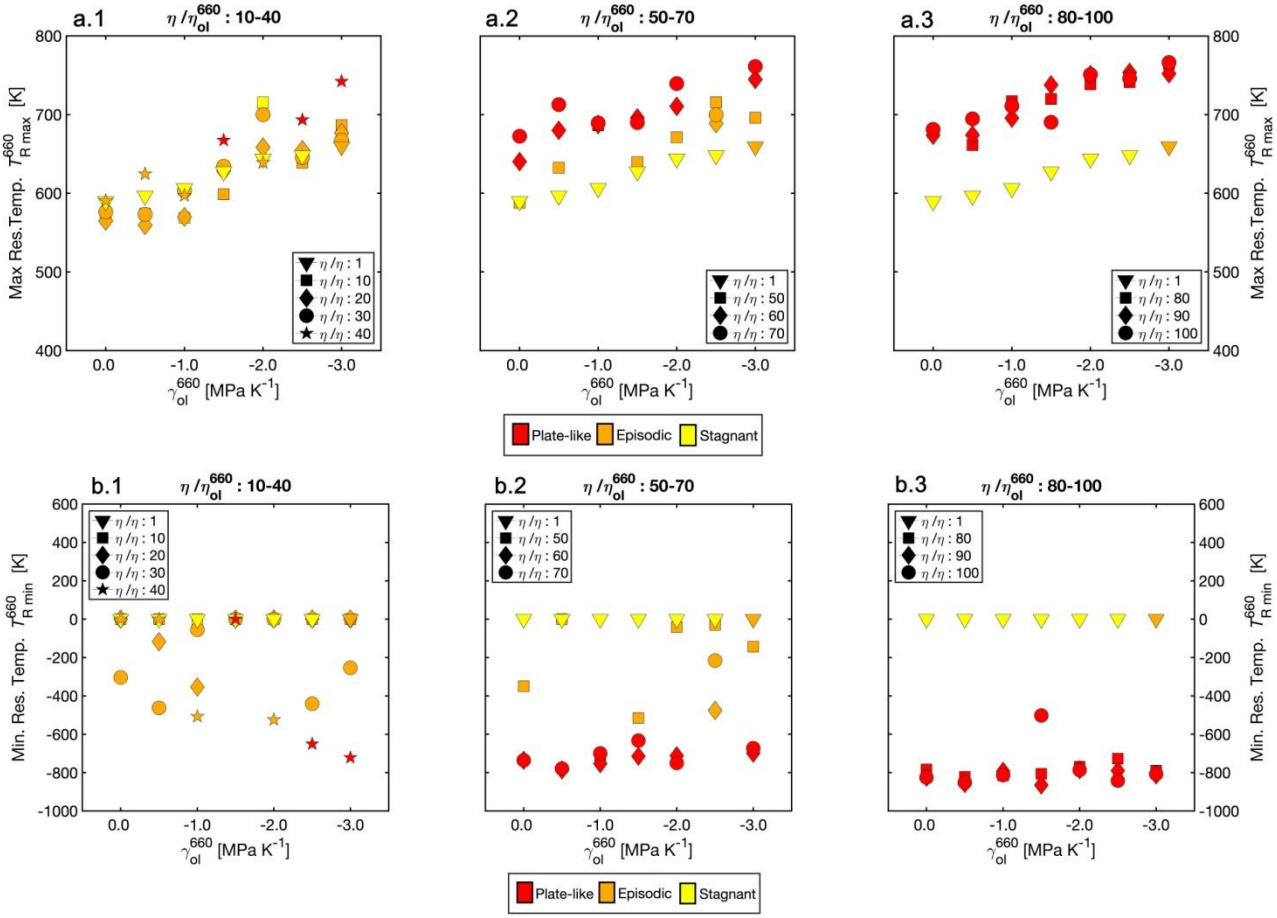

Figure 7.11. Residual temperature T_R^{660} at the 660 km discontinuity: (a-top row) maximum residual temperature $T_{R\,max}^{660}$; (b-bottom row) minimum residual temperature $T_{R\,min}^{660}$. Each symbol represents a given simulation (i.e. Υ_{ol}^{660}, η/η_{ol}^{660}) where the plotted parameter is the median of its evolution over time (0 → 5 Gyrs). The symbols and their colours are the same as described in **Figure 7.8**.

In the plate-like regime, $T_{R\,max}^{660} > +700\ K$ (**Figure 7.11-a.1-3**, **Table 7.19**), while $T_{R\,min}^{660} \approx -800\ K$ (**Figure 7.11-b.1-3**, **Table 7.20**). Interestingly, plate-like regime displays an higher maximum thermal anomaly compared to the other two regimes (**Figure 7.11-a.1-3**). The reason for this, can be attributed to the higher mantle temperatures that characterize the stagnant lid and the episodic resurfacing. Under these conditions, the temperature difference between the rising plumes

and the ambient mantle is much lower, hence the buoyancy of the plumes is dampened. Plumes rise more slowly in the stagnant-lid regime, thus progressively losing their initial excess temperature through heat diffusion.

Moreover, $T_{R\ max}^{660}$ increases linearly with the decreasing Clapeyron slope Υ_{ol}^{660} (**Figure 7.11-a.1-3**). Quite likely, this is due to the stabilizing effect of the negative Υ_{ol}^{660} of the endothermic phase transition (**Figure 7.1-2.d**). The rising plumes are stopped in their ascent, thus accumulating at the base of the 660 km discontinuity, thus increasing its temperature. This effect is not evident for subducting slabs (**Figure 7.11-b.1-3**).

7.5.4. Pure Advection of Cold Material

The residual temperature given by the solely intrinsic temperature of the slab T_{adv}^{660} (i.e. without the latent temperature reduction) is reported in **Figure 7.12-a.1-3**. The average temperature anomaly of the cold advective material is $\approx -765\ K$ (**Table 7.21**). The low temperature of the slab causes a major downward deflection of the post-spinel discontinuity reaching a depth of $\approx 720\ km$ (**Figure 7.12-b.1-3**, **Table 7.22**). This deflection is inversely proportional to the Clapeyron slope of the reaction Υ_{ol}^{660}, as reported in eq. **(7.4.4)**.

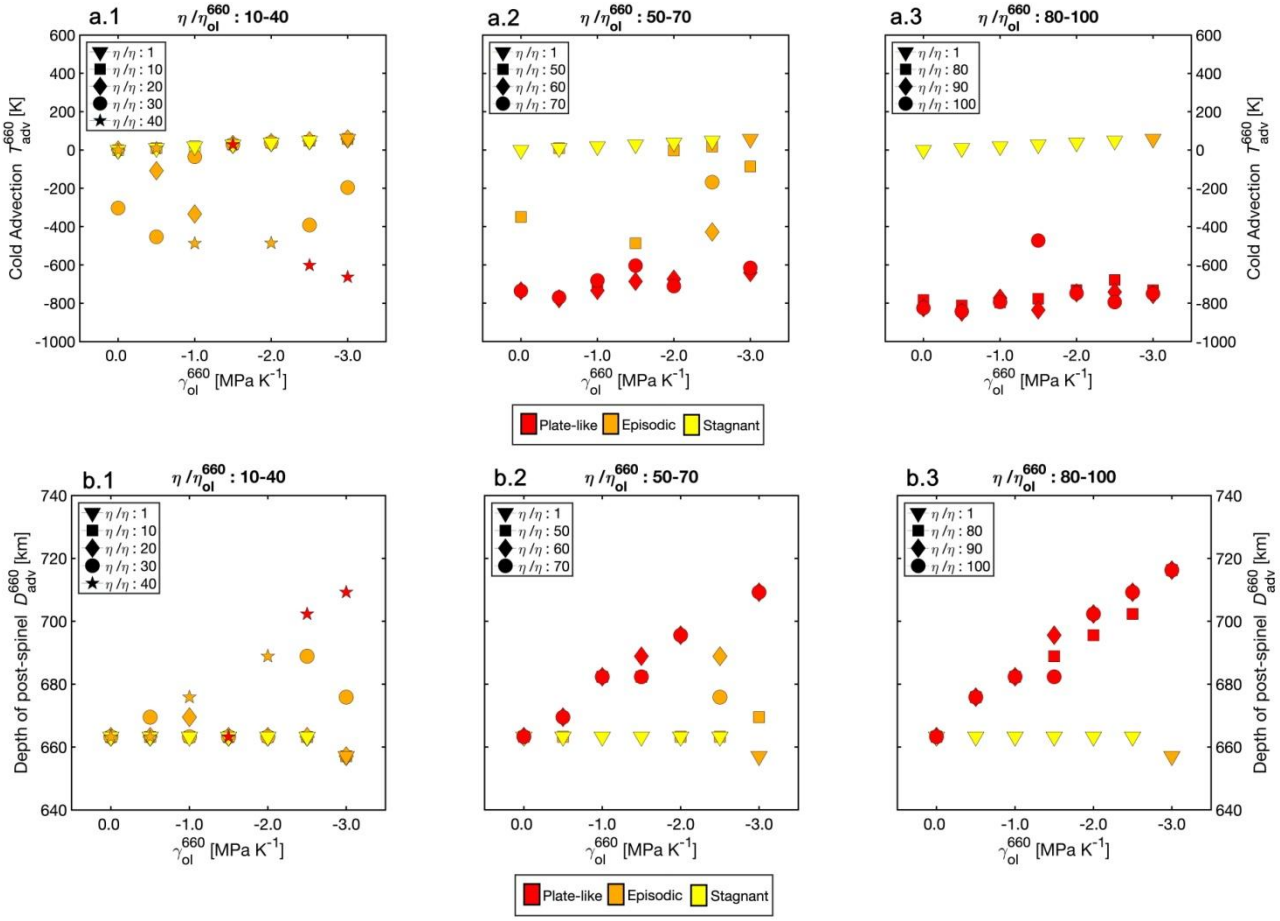

Figure 7.12. Different parameters relevant for the advection of cold material crossing the post-spinel phase transition (**Figure 7.1-2.c**): (a- top row) temperature of the cold advecting material T_{adv}^{660} (**Table 7.21**); (b-bottom row) depth of the post-spinel phase transition D_{adv}^{660} (**Table 7.22**). Each symbol represents a given simulation (i.e. Υ_{ol}^{660}, η/η_{ol}^{660}) where the value is the median of the parameter over time (0 → 5 Gyrs). The symbols and their colours are the same as described in **Figure 7.8**.

7.5.5. Latent Heat and Temperature Reduction

The latent energy E_{pyr}^{660} absorbed by the system during the post-spinel phase transition is linearly proportional to the Clapeyron slope of the reaction Υ_{ol}^{660}(**Figure 7.13-a**). The energy absorption ranges between 0 to $-70\ kJ\ kg^{-1}$ (**Table 7.23**), which leads to a temperature reduction between 0 and 58 K(**Figure 7.13-b**, **Table 7.24**). The latent temperature reduction T_{pyr}^{660} (**Table 7.24**) is $< 10\%$ of the advecting material temperature, T_{adv}^{660} for the simulations featuring the plate-like regime (**Table 7.21**).

Following equation **(7.4.4)**, the pressure of the phase boundary after heat extraction increases by $0.3\ GPa$ (**Figure 7.13-c**, **Table 7.25**), causing a downward deflection of the 660 discontinuity by $\Delta d_{lat}^{660} < 6\ km$. These estimates are comparable with that reported by *Steinberger (2007)*. The calculations show that the advection mechanism (**Figure 7.1-2.c**) has a much higher impact on the deflection of the phase transition compared to the solely latent heat contribution (**Figure 7.13-c**), i.e., $\Delta d_{lat}^{660} < 6\ km$ while $\Delta d_{adv}^{660} \approx 12\text{–}60\ km$.

The data reported in **Figure 7.13** and in **Table 7.23**-**Table 7.25** are valid for the case of a cold slab sinking through the post-spinel phase transition (**Figure 7.1-4.g**). The parameters E_{pyr}^{660}, $T_{pyr}^{660}, P_{pyr}^{660}$ are independent of the viscosity ratio η/η_{ol}^{660}. Therefore, for clarity reasons, only the simulations with $\eta/\eta_{ol}^{660} \geq 80$ are shown in **Figure 7.13**, i.e., the ones within a plate-like regime in **Figure 7.7-a**.

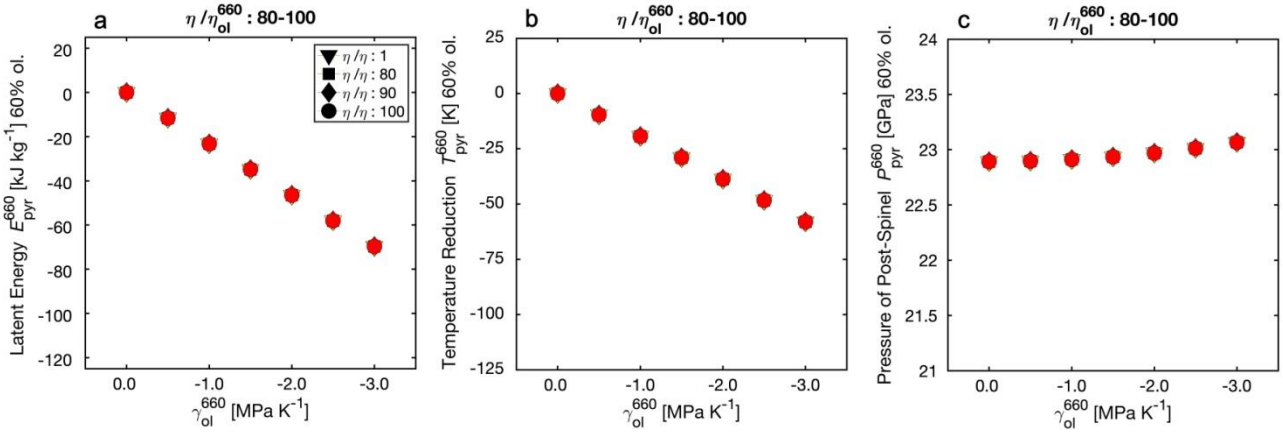

Figure 7.13. Different parameters for a cold sinking object undergoing the post-spinel phase reaction (**Figure 7.1-4.g**): (a-left column) latent energy E_{pyr}^{660} (**Table 7.23**); (b-mid column) temperature reduction T_{pyr}^{660} (**Table 7.24**); (c-right column) pressure of the phase transition P_{pyr}^{660} (**Table 7.25**). Each symbol represents a given simulation (i.e. Υ_{ol}^{660}, η/η_{ol}^{660}) where the plotted symbol represents the median of the value over its time evolution ($0 \rightarrow 5$ Gyrs). The symbols and their colours are the same as described in **Figure 7.8**.

7.5.6. Thermal Expansivity and Negative Buoyancy

The temperature reduction following the post-spinel phase transition causes a density increase of $0 \leq \Delta\rho_{\alpha}^{660} \leq 4.4\, kg\ m^{-3}$ (**Figure 7.14-a**, **Table 7.26**). This value has to be added to the prescribed post-spinel density jump $\Delta\rho_{ol}^{660}$, hence $202\, kg\ m^{-3} \leq \Delta\rho_{pyr}^{660} \leq 206\, kg\ m^{-3}$ with $60\ wt\%$ olivine in the pyrolitic mantle (**Figure 7.14-b**, **Table 7.27**). The additional pull gained by the slab after the phase transition ranges between $1980\ N\ m^{-3} \leq \Delta F_{pyr}^{660} \leq 2020\ N\ m^{-3}$ (**Figure 7.14-c**, **Table 7.28**). The density increase due to thermal expansivity, $\Delta\rho_{\alpha}^{660}$ is $< 2\%$ compared to the density jump, $\Delta\rho_{ol}^{660}$ caused by the Rw → Br + Fp transformation. Therefore, the contribution of mechanism (3) (see section **7.1.5** and **Figure 7.1-6.k**) to the total slab pull is negligible.

The density increase $\Delta\rho_{\alpha}^{660}$, and the additional pull ΔF_{pyr}^{660}, are inversely proportional to the Clapeyron slope of the reaction Υ_{ol}^{660}, and independent of the viscosity ratio η/η_{ol}^{660} (**Figure 7.14**).

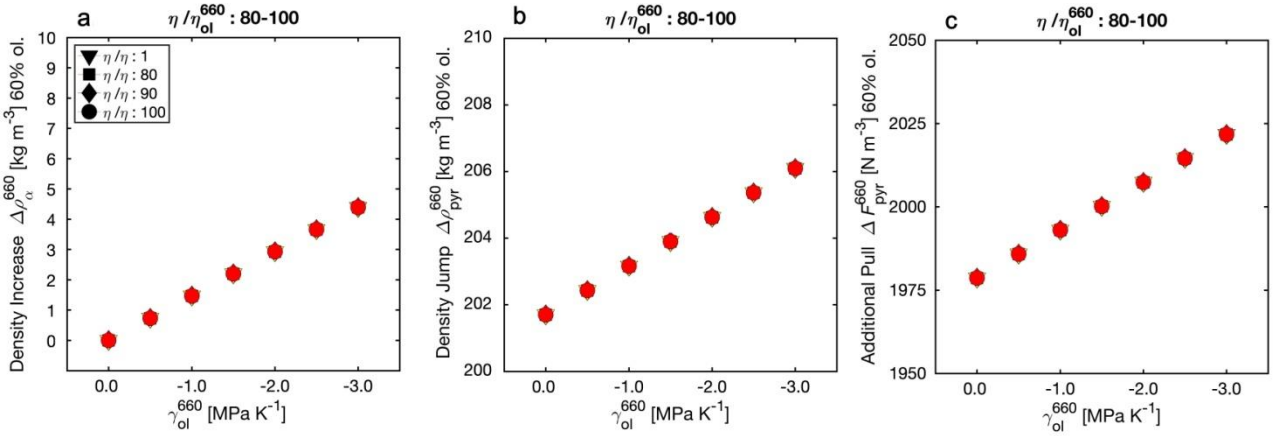

Figure 7.14. Different parameters related to the thermal contraction after the endothermic reaction (**Figure 7.1-6.k**): (a-left column) density increase $\Delta\rho_{\alpha}^{660}$(**Table 7.26**); (b-mid column) density jump $\Delta\rho_{pyr}^{660}$ (**Table 7.27**); (c-right column) additional pull ΔF_{pyr}^{660} (**Table 7.28**). Each symbol represents a given simulation (i.e. Υ_{ol}^{660}, η/η_{ol}^{660}) where the plotted symbol represents the median of the value over its time evolution ($0 \rightarrow 5\ Gyrs$). The symbols and their colours are the same as described in **Figure 7.8**.

7.5.7. Resisting Force of the 660 *km* Discontinuity

The additional resistance provided by the viscosity jump in the shallow-most LM (659 – 750 km) is shown in **Figure 7.15-a1-3**. The maximum resistance is obtained for the upper half of the tested viscosity ratios $\eta/\eta_{ol}^{660} \geq 50$, and it reaches $\Delta F_R^{660} \approx 4.0 \times 10^{17} N$ (**Table 7.29**).

This translates into an avalanche volume which ranges between $0 < V_{ava}^{660} < 2.0 \times 10^5\ km^3$ (**Figure 7.15-b1-3**, **Table 7.30**). An estimate of the surface area occupied by such a volume can be inferred by assuming a flat slab stagnation at the 660 km discontinuity. If only the bottom 1 km of the slab reacts to provide the additional pull ΔF_{pyr}^{660}, the maximum surface will be $\approx 2.0 \times 10^5\ km^2$ (approximately the surface area of Great Britain). This corresponds to a slab keel of $1000 \times 200 \times 1\ km$. Both ΔF_R^{660} and V_{ava}^{660} depend on the viscosity ratio η/η_{ol}^{660}, while they do not show a clear correlation with the Clapeyron slope of the reaction Υ_{ol}^{660} (**Figure 7.15**).

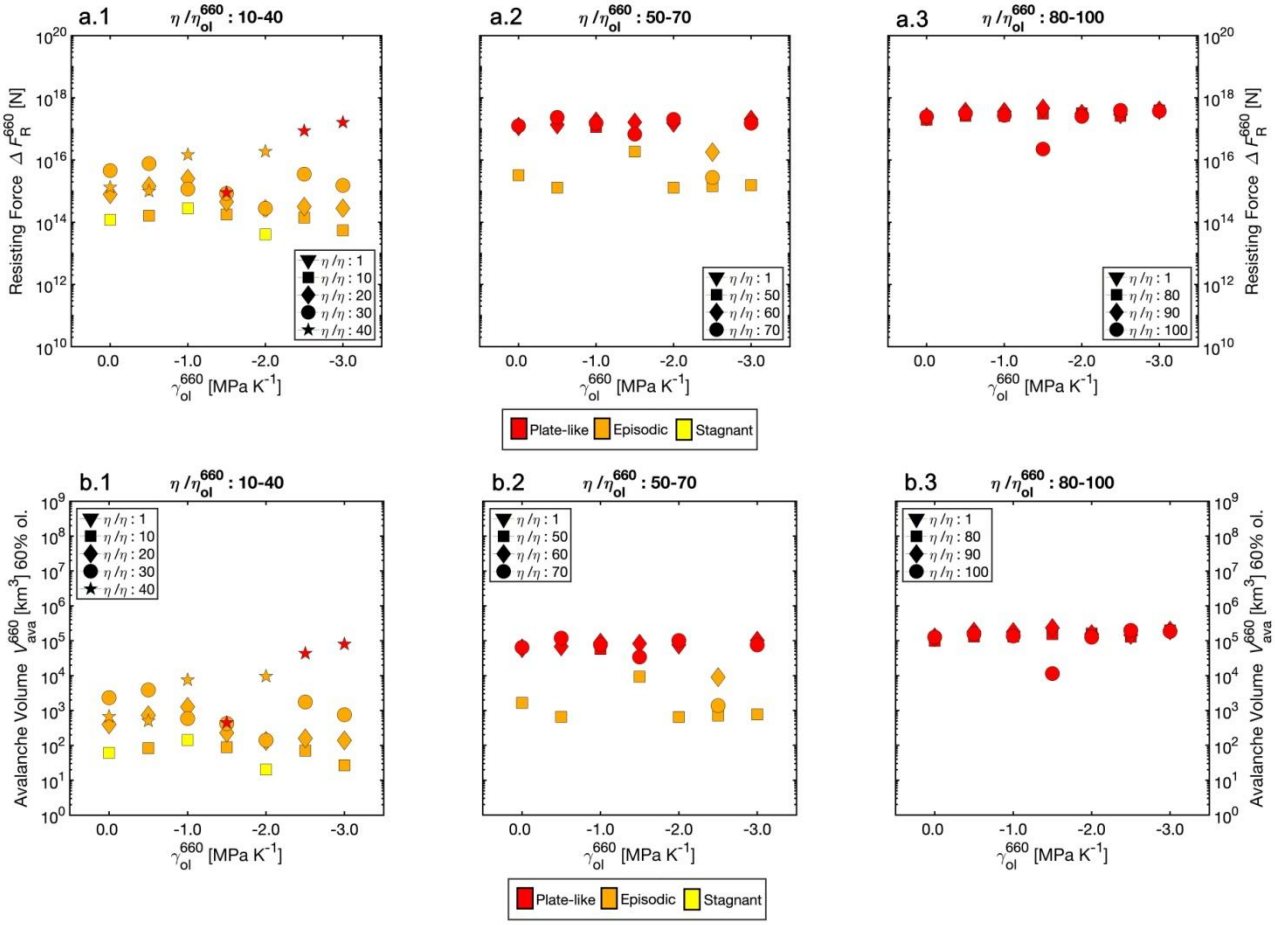

Figure 7.15. (a-top row) Resisting force of at 660 km discontinuity ΔF_R^{660} (**Table 7.29**); (b-bottom row) avalanche volume V_{ava}^{660} (**Table 7.30**). Each symbol represents a given simulation (i.e. Υ_{ol}^{660}, η/η_{ol}^{660}) where the symbol represent the median of the parameter over time evolution ($0 \rightarrow 5$ Gyrs). The symbols and their colours are the same as described in **Figure 7.8**.

7.5.8. Terminal Velocity

The terminal velocities computed for a 2D slab (assuming dimensions of $100 \times 500\ km$) are reported in **Figure 7.16**.

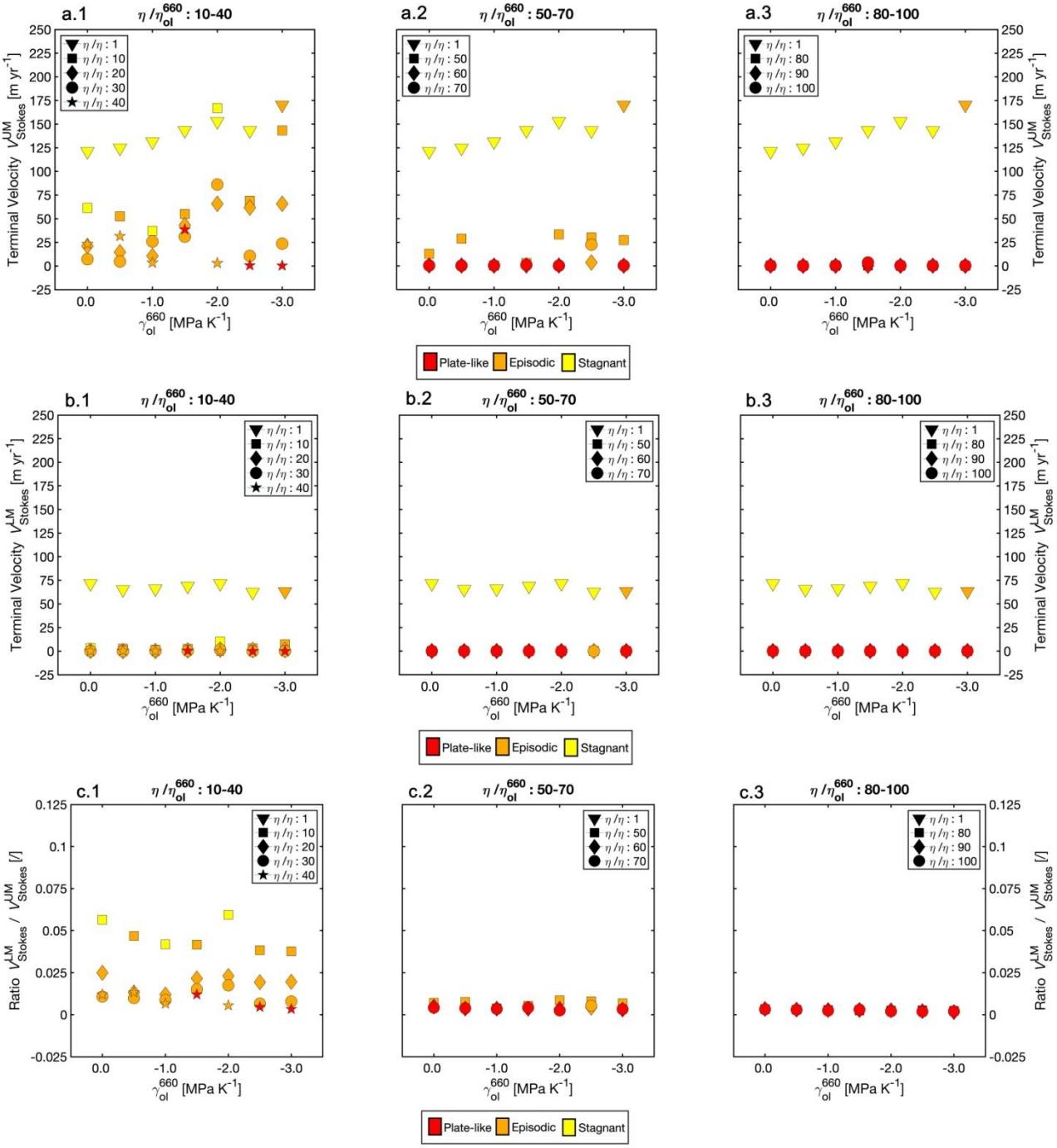

Figure 7.16. Terminal velocities of a slab: (a- top row) terminal velocity in the upper mantle V_{Stokes}^{UM} (**Table 7.31**); (b-mid row) terminal velocity in the lower mantle V_{Stokes}^{LM} (**Table 7.32**); (c-bottom row) ratio between $V_{Stokes}^{LM}/V_{Stokes}^{UM}$ (**Table 7.33**) Each symbol represents a given simulation (i.e. Υ_{ol}^{660}, η/η_{ol}^{660}) where the plotted value is the median of the parameter evolution over time ($0 \rightarrow 5$ Gyrs). The symbols and their colours are the same as described in **Figure 7.8**.

For the stagnant lid regime the terminal velocity in the upper mantle V_{Stokes}^{UM} (**Figure 7.16-a.1-3**, **Table 7.31**) is extremely high ($> 10^2\ m\ yr^{-1}$), and also high for the episodic resurfacing regime ($10^{-1}-10^2\ m\ yr^{-1}$), and low for the plate-like regime ($\approx 10^{-1}\ m\ yr^{-1}$). The high V_{Stokes}^{UM} values obtained for the stagnant lid regime are due to the low viscosity of the upper mantle $\eta^{UM} \approx 10^{18}\ Pa\ s$ (**Figure 7.8-a.1-3**, **Table 7.10**). This viscosity is three orders of magnitude lower than the geophysical constraints average (dashed line in **Figure 7.8-a.1-3**), thus leading to an unrealistically high terminal velocity. The upper mantle viscosity in the plate-like regime is two orders of magnitude higher than in the stagnant lid, $\eta^{UM} \approx 10^{20}\ Pa\ s$ (**Figure 7.8-a.1-3**, **Table 7.10**), hence V_{Stokes}^{UM} is much smaller.

The terminal velocity in the lower mantle V_{Stokes}^{LM} (**Figure 7.16-b.1-3**; **Table 7.32**) is: $60-75\ m\ yr^{-1}$ for $\eta/\eta_{ol}^{660} = 1$; $\approx 10^1\ m\ yr^{-1}$ for $\eta/\eta_{ol}^{660} = 10$; $\approx 10^{-1}\ m\ yr^{-1}$ for $\eta/\eta_{ol}^{660} = 20-50$; and $\approx 10^{-3}-10^{-4}\ m\ yr^{-1}$ for $\eta/\eta_{ol}^{660} \geq 60$. For $\eta/\eta_{ol}^{660} = 1$ the lower mantle viscosity is $\eta^{LM} \approx 10^{19}\ Pa\ s$, whereas for $\eta/\eta_{ol}^{660} > 1$ it ranges between $\eta^{LM} \approx 10^{20}-10^{24}\ Pa\ s$ (**Figure 7.8-a.1-3**, **Table 7.10**). The higher viscosity of the lower mantle drastically reduces the terminal velocity V_{Stokes}^{LM}, which becomes negligible for $\eta/\eta_{ol}^{660} \geq 60$.

Such a low value of V_{Stokes}^{LM} is unrealistic for the case of the Earth, since it would prevent any slab to sink through the lower mantle and reach the CMB (*Kaneshima & Helffrich, 1998*; *Niu et al., 2003*; *Hutko et al. 2006*). The low V_{Stokes}^{LM} is justified by the relatively small slab considered in the computation (only $500\ km$ in length), and by the absence of a third dimension, i.e. the width of the slab.

Nevertheless the ratio of velocities $V_{Stokes}^{LM}/V_{Stokes}^{UM}$ (**Figure 7.16-c.1-3**; **Table 7.33**) provides an important insight: for $\eta/\eta_{ol}^{660} \geq 60$, the slab experiences an abrupt deceleration once it enters into the LM ($V_{Stokes}^{UM} \approx 1000\ V_{Stokes}^{LM}$). As shown in **Figure 7.3**, the viscosity jump in the models occurs between $660-800\ km$ depth, hence the slab stagnates within this region of the mantle.

7.6. Conclusions

In this chapter, two parameters that influence the stagnation of a slab at 660 km have been tested: the negative Clapeyron slope at the post-spinel transition Υ_{ol}^{660}(0 to $-3.0\ MPa\ K^{-1}$), and the viscosity ratio between the MTZ and the LM η/η_{ol}^{660} (1 to 100). The stable tectonic regime of each simulation was achieved self-consistently. The data reveal that η/η_{ol}^{660} controls the tectonic regime of the model and the plate-like regime is obtained for models with $\eta/\eta_{ol}^{660} \geq 80$ (**Figure 7.7**). The Clapeyron slope does not show any clear correlation with the stable tectonic regime.

The MTZ and LM viscosities are compatible with the geophysical constraints, while UM viscosity is $O(10^1 - 10^2)$ lower (**Figure 7.8**). Higher values of activation volume V_{ol}^{UM} and V_{pxgt}^{UM} should be employed in order to obtained more realistic viscosities in the upper mantle.

For an active plate-like regime the presence of a slab in the MTZ is mostly inferred from the average viscosity and stress state of the region (**Figure 7.9**). The average residual temperature at 660 km of depth (**Figure 7.10**) is controlled by both the strong positive and the strong negative thermal anomalies that populate the discontinuity (**Figure 7.11**). The plumes appear to be more affected by Υ_{ol}^{660}, while the slabs are not influenced by this parameter.

The Clapeyron slope controls three mechanisms occurring at the 660 km phase transition (**Figure 7.1**). By decreasing Υ_{ol}^{660}: (1) it increases the downward deflection of the discontinuity for the cold descending material, (2) it increases the latent heat absorbed by the endothermic reaction, and (3) it increases the density jump due to thermal contraction. These effects have been quantified for each model.

The maximum deflection of the post-spinel phase transition caused by mechanism (1) is achieved for $\Upsilon_{ol}^{660} = -3.0\ MPa\ K^{-1}$, where it reaches 720 km of depth (**Figure 7.12**). The downward deflection of the 660 km discontinuity heavily depends on the temperature of the slab at the base of the MTZ. Therefore, it is fundamental to constrain experimentally the thermal parameters of the slab, and compute its thermal evolution with numerical models as previously reported in **Chapter 6**.

The temperature drop caused by the endothermic reaction (mechanism 2) produces $< 6\ km$ downward shift of the phase transition, and has a stabilizing effect on the slab (**Figure 7.13**). The downward deflection produced by mechanism (2) is 2 – 10 times smaller than the one caused by mechanism (1).

The thermal contraction (mechanism 3) following the temperature drop, causes a maximum density increase of $\approx 4\ kg\ m^{-3}$ which destabilizes the slab by producing an additional pull of $\approx 40\ N\ m^{-3}$ (**Figure 7.14**). This additional pull is $< 2\%$ than the one provided by the breakdown of ringwoodite into lower mantle assemblage, i.e. $\Delta\rho_{ol}^{660} = 200\ kg\ m^{-3}$ and $F_{ol}^{660} \approx 2000\ N\ m^{-3}$.

From the analysis, it appears that mechanisms (2) and (3) are also controlled by the density jump at the phase transition, $\Delta\rho_{ol}^{660}$. Theoretically, by increasing $\Delta\rho_{ol}^{660}$, it should increase the temperature drop at the endothermic phase transition as well as the additional slab pull. The geophysical and thermodynamic constraints for $\Delta\rho_{ol}^{660}$ have uncertainties of 100 $kg\ m^{-3}$ (**Table 7.1**). Given the potential effects of $\Delta\rho_{ol}^{660}$ on mechanisms (2) and (3), it would be of a great importance to investigate this parameter further.

The viscosity jump between MTZ and LM represents a stronger obstacle that opposes the slab descent, by providing $O(10^{12} - 10^{17})N$ of resisting force (**Figure 7.15**). This resistance to sinking

determines a significant deceleration of the slab descent in the $660-800\ km$ region, as shown by the computation of the slab terminal velocity (**Figure 7.16**).

From this study, it can be concluded that the viscosity ratio η/η_{ol}^{660} have a much larger impact than the Clapeyron slope Υ_{ol}^{660} in promoting slab stagnation. This is in contrast with the results reported by *Agrusta et al. (2017)*. The reasons of this discrepancy may be: (i) the larger viscosity ratio explored in this study, (ii) the mixed composition of the mantle which reduces the contribution of olivine's Clapeyron slope in the interactions between the slab and the $660\ km$ discontinuity.

It is still not clear why the plate-like regime occurs only for large η/η_{ol}^{660}. A possible explanation was provided by *Yuen et al. (1998)* who reported progressively stronger plumes for increasing η/η_{ol}^{660}. This explanation, however, requires further analysis.

To conclude, from this study it can be inferred that three parameters controls different aspects of the slab stagnation in the MTZ: (1) the Clapeyron slope Υ_{ol}^{660} controls the depth of the phase transition; (2) the density jump $\Delta\rho_{ol}^{660}$ controls the slab pull and the temperature reduction due to the latent heat; (3) the η/η_{ol}^{660} decelerates the descent of a slab by providing an obstacle. Key parameter contributing to the stagnation is the temperature of the slab once it reaches the base of the MTZ.

If the slab is sufficiently cold, the post-spinel reaction will be deflected to larger depths, the deflection depending on Υ_{ol}^{660}. The resisting force at the phase transition reduces the sinking velocity of a slab and prevents its further descent. The outer portions of the slab undergo the phase transformation when they reach the appropriate P-T conditions. Each m^3 of reacted material increases its density and increases the slab pull. Once the reacted material matches the avalanche volume, the slab can overcome the viscosity barrier and continue its descent into the lower mantle. The key question now is: how fast can this process be? To answer the posed question it is fundamental to constrain the rate of the post-spinel reaction, as well as to model the heating of the relevant areas of a slab.

7.7. Appendix

Parameter	Symbol	Value	Units
Domain size			
Mantle thickness	r^{surf}	2890×10^3	$[m]$
Outer core thickness	r^{CMB}	3480×10^3	$[m]$
Boundaries conditions			
Surface cooling mode	T_{top}^{mode}	$isothermal$	[/]
Surface temperature	T_{top}	300	[K]
Surface velocity mode	V_{top}^{mode}	$free-slip$	[/]
CMB cooling mode	T_{bot}^{mode}	$isothermal$	[/]
CMB temperature	T_{bot}	4000	[K]
Surface velocity mode	V_{bot}^{mode}	$free-slip$	[/]
Internal heating parameters			
Heat production per unit mass	R_H	5.2×10^{-12}	$[W\ kg^{-1}]$
Half-life of heat producing elements	$t_{1/2}$	1.0×10^{30}	$[yr]$
Initial potential temperature	T_P	1600	[K]
Mineral phase fraction in the pyrolitic mantle			
Olivine fraction	X_{ol}	60	[%]
Pyroxene-Garnet	X_{pxgt}	40	[%]
Rock fraction in the pyrolitic mantle			
Basalt fraction (100% $pxgt$ system)	X_{basalt}	20	[%]
Harzburgite fraction (75% ol-25% $pxgt$)	X_{harz}	80	[%]
Phase system 1: olivine			
Phase transitions			
Number of mineral phases	n_{ol}	4	[/]
Phase transition depths	D_{ol}^{Γ}	$2740/660/410$	$[km]$
Phase transition temperature	T_{ol}^{Γ}	$2300/1900/1600$	[K]
Phase transition density jump	ρ_{ol}^{Γ}	$61.6/320/120$	$[kg\ m^{-3}]$
Phase transition Clapeyron slope	Υ_{ol}^{Γ}	$10/Free/2.5$	$[MPa\ \mathrm{K}^{-1}]$
Phase transition viscosity ratio	$\Delta\eta_{ol}^{\Gamma}$	$0.1/Free/1.0$	[/]
Birch-Murnaghan compressibility $PPV/LM/MTZ/UM$			
Surface reference density	${\rho_0}_{ol}$	3240	$[kg\ m^{-3}]$
Surface bulk modulus	${K_0}_{ol}^{\Gamma}$	$210/210/85/163/163$	$[GPa]$
Pressure derivative of the bulk modulus	${K'}_{ol}^{\Gamma}$	$3.9/3.9/4.0/4.0/4.0$	$[Pa\ m^{-1}]$
Grüneisen parameter	γ_{ol}^{Γ}	$1.3/1.3/0.85/1.3/1.3$	[/]
Exponent for thermal conductivity	k_{ol}^{Γ}	$1.0/1.0/1.0/1.0/1.0$	[/]
Diffusion creep parameters $PPV/LM/MTZ/UM$			
Activation energy	E_{ol}^{Γ}	$162/370/300/300$	$[kJ\ mol^{-1}]$
Activation volume	V_{ol}^{Γ}	$1.65/2.5/3.0/6.0$	$[cm^3\ mol^{-1}]$
Phase system 2: pyroxene-garnet			
Phase transitions			
Number of mineral phases	n_{pxgt}	5	[/]
Phase transition depths	D_{pxgt}^{Γ}	$2740/720/400/40$	$[km]$

Phase transition temperature	T^{Γ}_{pxgt}	$2300/1900/1600/1000$	[K]
Phase transition density jump	ρ^{Γ}_{pxgt}	$61.6/480/150\ /350$	$[kg\ m^{-3}]$
Phase transition Clapeyron slope	Υ^{Γ}_{pxgt}	$10/1.0/1.0\ /1.5$	$[MPa\ \mathrm{K}^{-1}]$
Viscosity ratio	$\Delta\eta^{\Gamma}_{pxgt}$	$0.1/Free/1.0/1.0/1.0$	[/]
Birch-Murnaghan compressibility $PPV/LM/MTZ/UM/LT$			
Surface reference density	$\rho_{0_{pxgt}}$	3080	$[kg\ m^{-3}]$
Surface bulk modulus	$K_{0}{}^{\Gamma}_{pxgt}$	$210/210/85/163/163$	$[GPa]$
Pressure derivative of the bulk modulus	K'^{Γ}_{pxgt}	$3.9/3.9/4.0/4.0/4.0$	$[Pa\ m^{-1}]$
Grüneisen parameter	γ^{Γ}_{pxgt}	$1.3/1.3/0.85/1.3/1.3$	[/]
Exponent for thermal conductivity	k^{Γ}_{pxgt}	$1.0/1.0/1.0/1.0/1.0$	[/]
Diffusion creep parameters $PPV/LM/MTZ/UM/LT$			
Activation energy	E^{Γ}_{pxgt}	$162/370/300/300/300$	$[kJ\ mol^{-1}]$
Activation volume	V^{Γ}_{pxgt}	$1.65/2.5/3.0/6.0/6.0$	$[cm^3\ mol^{-1}]$
Viscous rheology			
Reference viscosity	η_0	1.0×10^{20}	$[Pa\ s]$
Reference temperature for η_0	T_0^{η}	1600	[K]
Reference pressure for η_0	P_0^{η}	0.0	$[Pa]$
Reference stress for η_0	σ_0^{η}	0.0	$[Pa]$
Upper viscosity cutoff	η_{max}	1.0×10^{28}	$[Pa\ s]$
Lower viscosity cutoff	η_{min}	1.0×10^{17}	$[Pa\ s]$
Plastic rheology			
Initial lithosphere thickness	d_{init}	100	$[km]$
Yield stress	τ_y	25	$[Pa]$
Cohesion coefficient	c_y	∞	$[Pa]$
Frictional coefficient	f_{ϕ}	0	[/]
Depth gradient	f_{σ}	0.01	$[Pa\ m^{-1}]$

Table 7.6. StagYY parameters

rms Mantle Temperature T^{rms} $[K]$								
		660 Clapeyron Slope $\Upsilon_{ol}^{660}[MPa\ K^{-1}]$						
		0.0	**−0.5**	**−1.0**	**−1.5**	**−2.0**	**−2.5**	**−3.0**
Viscosity ratio η/η_{ol}^{660}	**1**	2705	3015	2919	2894	2867	2843	2704
	10	2705	2673	2619	2712	2848	2705	2697
	20	2650	2520	2427	2700	2734	2647	2693
	30	2423	2314	2504	2669	2724	2332	2483
	40	2546	2607	2235	2600	2213	2094	2037
	50	2360	2532	2060	2200	2648	2557	2585
	60	2047	2009	2017	2018	2003	2676	1993
	70	2080	2044	2083	2155	2040	2411	2104
	80	2039	2041	2022	2031	2018	2066	2004
	90	2041	2038	2038	1997	2036	2016	1999
	100	2003	1987	1996	2543	1999	1980	1974

Table 7.7. rms Mantle Temperature T^{rms}

Surface Nusselt Number Nu_{top} [/]								
		660 Clapeyron Slope $\Upsilon_{ol}^{660}[MPa\ K^{-1}]$						
		0.0	**−0.5**	**−1.0**	**−1.5**	**−2.0**	**−2.5**	**−3.0**
Viscosity ratio η/η_{ol}^{660}	**1**	22	227	217	25	24	24	132
	10	22	22	22	104	24	47	111
	20	49	43	40	81	23	69	54
	30	39	45	39	52	23	42	42
	40	30	23	46	22	47	43	39
	50	42	35	39	46	61	22	59
	60	38	35	37	37	37	77	36
	70	39	36	40	43	37	43	41
	80	37	37	36	36	36	39	36
	90	37	36	37	34	37	37	36
	100	34	33	33	49	34	33	34

Table 7.8. Surface Nusselt Number Nu^{top}

Mobility M_o [/]								
		660 Clapeyron Slope $\Upsilon_{ol}^{660}[MPa\ K^{-1}]$						
		0.0	**−0.5**	**−1.0**	**−1.5**	**−2.0**	**−2.5**	**−3.0**
Viscosity ratio η/η_{ol}^{660}	**1**	4.87×10^{-4}	5.86×10^{-4}	1.87×10^{-3}	2.56×10^{-4}	1.66×10^{-4}	3.07×10^{-4}	2.04
	10	2.59×10^{-3}	3.76×10^{-3}	7.10×10^{-3}	2.39	4.93×10^{-4}	2.02×10^{-2}	2.14
	20	2.20	2.26	2.23	2.42	4.28×10^{-3}	2.47	1.84
	30	2.09	2.45	2.06	2.2	2.06×10^{-3}	2.23	2.10
	40	1.34	2.80×10^{-2}	2.57	1.19×10^{-2}	2.59	2.63	2.74
	50	2.36	1.30	2.69	2.48	2.25	7.50×10^{-2}	2.40
	60	2.64	2.74	2.65	2.63	2.66	2.51	2.56
	70	2.79	2.59	2.62	2.65	2.73	1.89	2.66
	80	2.78	2.57	2.65	2.67	2.64	2.66	2.62
	90	2.64	2.51	2.61	2.66	2.62	2.52	2.48
	100	2.60	2.56	2.64	2.35	2.61	2.49	2.53

Table 7.9. Mobility M_o

Median Viscosity of the Upper Mantle η^{UM} $[Pa\ s]$								
		660 Clapeyron Slope $\Upsilon_{ol}^{660}[MPa\ K^{-1}]$						
		0.0	**−0.5**	**−1.0**	**−1.5**	**−2.0**	**−2.5**	**−3.0**
Viscosity ratio η/η_{ol}^{660}	**1**	6.07×10^{18}	5.91×10^{18}	5.76×10^{18}	5.57×10^{18}	5.31×10^{18}	5.31×10^{18}	4.08×10^{18}
	10	1.02×10^{19}	9.29×10^{18}	1.14×10^{19}	9.21×10^{18}	4.20×10^{18}	7.74×10^{18}	4.10×10^{18}
	20	1.76×10^{19}	2.39×10^{19}	2.92×10^{19}	8.82×10^{18}	7.46×10^{18}	7.21×10^{18}	7.36×10^{18}
	30	3.95×10^{19}	5.16×10^{19}	1.34×10^{19}	1.18×10^{19}	6.88×10^{18}	2.44×10^{19}	1.40×10^{19}
	40	1.61×10^{19}	1.36×10^{19}	5.53×10^{19}	1.06×10^{19}	5.48×10^{19}	1.77×10^{20}	2.99×10^{20}
	50	2.27×10^{19}	1.13×10^{19}	2.95×10^{20}	5.00×10^{19}	9.73×10^{18}	1.14×10^{19}	1.17×10^{19}
	60	2.74×10^{20}	3.88×10^{20}	3.33×10^{20}	2.56×10^{20}	2.15×10^{20}	3.82×10^{19}	2.12×10^{20}
	70	3.21×10^{20}	4.04×10^{20}	2.41×10^{20}	1.25×10^{20}	3.08×10^{20}	1.23×10^{19}	1.81×10^{20}
	80	4.57×10^{20}	2.47×10^{20}	4.35×10^{20}	2.94×10^{20}	3.26×10^{20}	2.32×10^{20}	3.05×10^{20}
	90	4.10×10^{20}	3.33×10^{20}	3.36×10^{20}	3.86×10^{20}	3.11×10^{20}	2.00×10^{20}	2.18×10^{20}
	100	3.86×10^{20}	4.25×10^{20}	2.93×10^{20}	3.92×10^{19}	2.38×10^{20}	1.90×10^{20}	2.02×10^{20}

Table 7.10. Median viscosity of the upper mantle η^{UM}

Median Viscosity of the Mantle Transition Zone η^{MTZ} $[Pa\ s]$								
		660 Clapeyron Slope $\Upsilon_{ol}^{660}[MPa\ K^{-1}]$						
		0.0	**−0.5**	**−1.0**	**−1.5**	**−2.0**	**−2.5**	**−3.0**
Viscosity ratio η/η_{ol}^{660}	**1**	1.52×10^{19}	1.51×10^{19}	1.39×10^{19}	1.26×10^{19}	1.16×10^{19}	1.28×10^{19}	1.16×10^{19}
	10	3.48×10^{19}	4.07×10^{19}	5.93×10^{19}	3.76×10^{19}	1.00×10^{19}	2.79×10^{19}	1.23×10^{19}
	20	1.04×10^{20}	1.57×10^{20}	2.28×10^{20}	5.15×10^{19}	3.07×10^{19}	3.50×10^{19}	3.00×10^{19}
	30	3.39×10^{20}	5.23×10^{20}	9.13×10^{19}	6.93×10^{19}	2.42×10^{19}	2.34×10^{20}	1.02×10^{20}
	40	1.02×10^{20}	7.40×10^{19}	7.43×10^{20}	5.99×10^{19}	8.54×10^{20}	3.80×10^{21}	$5.91E+21$
	50	1.89×10^{20}	8.30×10^{19}	4.51×10^{21}	7.98×10^{20}	6.95×10^{19}	7.74×10^{19}	8.67×10^{19}
	60	4.91×10^{21}	5.48×10^{21}	6.40×10^{21}	5.44×10^{21}	5.23×10^{21}	7.27×10^{20}	6.29×10^{21}
	70	4.75×10^{21}	7.79×10^{21}	5.48×10^{21}	2.41×10^{21}	6.16×10^{21}	1.11×10^{20}	4.85×10^{21}
	80	7.30×10^{21}	7.78×10^{21}	8.22×10^{21}	8.45×10^{21}	8.93×10^{21}	7.20×10^{21}	9.72×10^{21}
	90	7.86×10^{21}	1.04×10^{21}	9.77×10^{21}	1.17×10^{22}	8.61×10^{21}	8.15×10^{21}	1.00×10^{22}
	100	8.04×10^{21}	9.09×10^{21}	7.69×10^{21}	7.03×10^{20}	6.27×10^{21}	8.96×10^{21}	8.57×10^{21}

Table 7.11. Median viscosity of the mantle transition zone η^{MTZ}

Median Viscosity of the Lower Mantle η^{LM} $[Pa\ s]$								
		660 Clapeyron Slope $\Upsilon_{ol}^{660}[MPa\ K^{-1}]$						
		0.0	**−0.5**	**−1.0**	**−1.5**	**−2.0**	**−2.5**	**−3.0**
Viscosity ratio η/η_{ol}^{660}	**1**	1.29×10^{19}	1.41×10^{19}	1.40×10^{19}	1.34×10^{19}	1.29×10^{19}	1.48×10^{19}	1.46×10^{19}
	10	2.78×10^{20}	3.70×10^{20}	6.37×10^{20}	3.93×10^{20}	8.97×10^{19}	3.09×10^{20}	1.27×10^{20}
	20	2.13×10^{21}	5.33×10^{21}	7.76×10^{21}	9.91×10^{20}	5.73×10^{20}	7.06×10^{20}	6.57×10^{20}
	30	1.38×10^{22}	2.32×10^{22}	4.35×10^{21}	1.96×10^{21}	6.52×10^{20}	1.79×10^{22}	7.33×10^{21}
	40	4.63×10^{21}	2.32×10^{21}	4.38×10^{22}	2.35×10^{21}	5.45×10^{22}	2.45×10^{23}	5.48×10^{21}
	50	1.27×10^{22}	5.19×10^{21}	3.93×10^{23}	6.39×10^{22}	4.51×10^{21}	5.07×10^{21}	7.97×10^{21}
	60	3.49×10^{23}	5.48×10^{23}	6.25×10^{23}	5.19×10^{23}	5.00×10^{23}	4.57×10^{22}	6.58×10^{23}
	70	4.02×10^{23}	8.43×10^{23}	4.85×10^{23}	1.98×10^{23}	9.67×10^{23}	1.50×10^{22}	5.50×10^{23}
	80	7.16×10^{23}	9.81×10^{23}	1.08×10^{24}	1.18×10^{24}	1.40×10^{24}	8.96×10^{23}	2.20×10^{24}
	90	9.46×10^{23}	1.28×10^{24}	9.79×10^{23}	1.82×10^{24}	1.32×10^{24}	1.47×10^{24}	2.52×10^{24}
	100	9.99×10^{23}	1.18×10^{24}	1.15×10^{24}	7.71×10^{22}	1.47×10^{24}	1.69×10^{24}	1.53×10^{24}

Table 7.12. Median viscosity of the lower mantle η^{LM}

Average Viscosity of the Mantle Transition Zone η_{ave}^{MTZ} $[Pa\ s]$								
		660 Clapeyron Slope $\Upsilon_{ol}^{660}[MPa\ K^{-1}]$						
		0.0	**−0.5**	**−1.0**	**−1.5**	**−2.0**	**−2.5**	**−3.0**
Viscosity ratio η/η_{ol}^{660}	**1**	1.52×10^{19}	1.51×10^{19}	1.38×10^{19}	1.26×10^{19}	1.16×10^{19}	1.27×10^{19}	1.69×10^{19}
	10	3.47×10^{19}	4.10×10^{19}	5.85×10^{19}	3.94×10^{19}	1.00×10^{19}	3.11×10^{19}	2.42×10^{19}
	20	1.07×10^{20}	6.03×10^{20}	1.79×10^{21}	5.70×10^{19}	3.03×10^{19}	8.56×10^{19}	4.88×10^{19}
	30	6.13×10^{21}	1.07×10^{22}	2.09×10^{20}	7.51×10^{19}	2.55×10^{19}	1.08×10^{22}	3.66×10^{21}
	40	1.38×10^{20}	8.55×10^{19}	2.36×10^{22}	7.54×10^{19}	4.40×10^{22}	3.67×10^{23}	7.62×10^{23}
	50	2.53×10^{21}	1.26×10^{20}	5.12×10^{23}	3.98×10^{22}	2.16×10^{20}	2.03×10^{20}	2.34×10^{21}
	60	5.17×10^{23}	7.63×10^{23}	6.99×10^{23}	5.77×10^{23}	5.72×10^{23}	4.49×10^{22}	6.60×10^{23}
	70	4.90×10^{23}	1.07×10^{24}	4.98×10^{23}	2.22×10^{23}	8.43×10^{23}	4.01×10^{21}	4.76×10^{23}
	80	9.68×10^{23}	9.99×10^{23}	1.13×10^{24}	1.04×10^{24}	1.10×10^{24}	7.88×10^{23}	1.46×10^{24}
	90	1.10×10^{24}	1.27×10^{24}	1.16×10^{24}	1.79×10^{24}	1.18×10^{24}	1.24×10^{24}	1.85×10^{24}
	100	1.15×10^{24}	1.27×10^{24}	1.27×10^{24}	4.07×10^{22}	1.18×10^{24}	1.58×10^{24}	1.39×10^{24}

Table 7.13. Average viscosity of the mantle transition zone η_{ave}^{MTZ}

Average Stress in the Mantle Transition Zone σ_{ave}^{MTZ} $[MPa]$								
		660 Clapeyron Slope $\Upsilon_{ol}^{660}[MPa\ K^{-1}]$						
		0.0	**−0.5**	**−1.0**	**−1.5**	**−2.0**	**−2.5**	**−3.0**
Viscosity ratio η/η_{ol}^{660}	**1**	0.29	0.27	0.31	0.21	0.18	0.16	0.28
	10	0.28	0.29	0.34	0.32	0.16	0.30	0.26
	20	0.54	1.28	1.89	0.37	0.26	0.35	0.33
	30	2.27	4.26	0.82	0.36	0.23	2.86	1.45
	40	0.55	0.34	5.10	0.31	6.15	15.81	19.05
	50	1.79	0.51	16.84	7.21	0.59	0.61	1.13
	60	17.48	18.86	19.14	18.26	18.11	6.06	19.18
	70	17.03	21.60	17.76	13.17	19.26	1.46	17.88
	80	20.90	21.63	21.46	22.95	22.42	20.45	23.66
	90	22.24	23.29	22.36	25.34	22.54	22.16	24.13
	100	21.87	23.10	20.94	6.10	20.94	23.17	23.02

Table 7.14. Average stress in the mantle transition zone σ_{ave}^{MTZ}

Average Temperature in the Mantle Transition Zone T_{ave}^{MTZ} $[K]$								
		660 Clapeyron Slope $\Upsilon_{ol}^{660}[MPa\ K^{-1}]$						
		0.0	**−0.5**	**−1.0**	**−1.5**	**−2.0**	**−2.5**	**−3.0**
Viscosity ratio η/η_{ol}^{660}	**1**	2424	2425	2436	2449	2461	2448	2459
	10	2334	2318	2275	2330	2502	2369	2466
	20	2219	2168	2128	2303	2369	2355	2370
	30	2091	2038	2240	2277	2405	2110	2216
	40	2230	2274	2007	2298	2014	1868	1833
	50	2160	2262	1854	2007	2283	2268	2252
	60	1848	1834	1832	1849	1852	2030	1845
	70	1855	1806	1854	1918	1843	2228	1862
	80	1817	1826	1811	1814	1815	1843	1814
	90	1813	1800	1810	1788	1816	1830	1815
	100	1819	1812	1831	2036	1838	1829	1822

Table 7.15. Average temperature in the mantle transition zone T_{ave}^{MTZ}

Average residual temperature T_R^{660} $[K]$								
		660 Clapeyron Slope $\Upsilon_{ol}^{660}[MPa\ K^{-1}]$						
		0.0	**−0.5**	**−1.0**	**−1.5**	**−2.0**	**−2.5**	**−3.0**
Viscosity ratio η/η_{ol}^{660}	**1**	571	572	585	601	620	618	629
	10	480	463	422	481	661	530	642
	20	362	307	269	454	524	515	550
	30	216	172	387	430	556	264	389
	40	372	418	151	451	153	35	−4
	50	292	408	−1	149	442	437	437
	60	−14	−21	−20	0	20	188	18
	70	−7	−53	5	64	−5	389	41
	80	−43	−40	−40	−42	−37	4	−20
	90	−48	−60	−45	−63	−25	−8	−12
	100	−44	−47	−22	180	−5	−13	−1

Table 7.16. Average residual temperature at the 660 km discontinuity T_R^{660}

Positive residual temperature T_R^{660} $[K]$ anomaly								
		660 Clapeyron Slope $\Upsilon_{ol}^{660}[MPa\ K^{-1}]$						
		0.0	**−0.5**	**−1.0**	**−1.5**	**−2.0**	**−2.5**	**−3.0**
Viscosity ratio η/η_{ol}^{660}	**1**	571	572	585	601	620	618	629
	10	480	463	422	481	661	530	642
	20	362	309	272	454	524	515	550
	30	225	185	388	431	556	277	393
	40	373	418	170	451	176	89	65
	50	296	409	61	172	442	438	437
	60	55	51	53	68	82	216	86
	70	54	40	65	106	66	394	96
	80	42	54	47	55	55	80	68
	90	44	48	52	50	66	79	82
	100	46	50	60	199	74	79	89

Table 7.17. Positive residual temperature anomaly at the 660 km discontinuity T_R^{660}

Negative residual temperature T_R^{660} $[K]$ anomaly								
		660 Clapeyron Slope $\Upsilon_{ol}^{660}[MPa\ K^{-1}]$						
		0.0	**−0.5**	**−1.0**	**−1.5**	**−2.0**	**−2.5**	**−3.0**
Viscosity ratio η/η_{ol}^{660}	**1**	0	0	0	0	0	0	0
	10	0	0	0	0	0	0	0
	20	0	−1	−4	0	0	0	0
	30	−6	−13	0	0	0	−9	−3
	40	0	0	−14	0	−18	−55	−70
	50	−4	0	−63	−19	0	0	−1
	60	−70	−74	−75	−69	−66	−15	−69
	70	−66	−94	−65	−42	−73	−23	−59
	80	−89	−94	−87	−99	−94	−77	−89
	90	−96	−109	−98	−112	−88	−89	−97
	100	−94	−101	−87	−17	−83	−94	−89

Table 7.18. Negative residual temperature anomaly at the 660 km discontinuity T_R^{660}

Maximum residual temperature $T_{R\,max}^{660}$ $[K]$								
		660 Clapeyron Slope $\Upsilon_{ol}^{660}[MPa\,K^{-1}]$						
		0.0	**−0.5**	**−1.0**	**−1.5**	**−2.0**	**−2.5**	**−3.0**
Viscosity ratio η/η_{ol}^{660}	**1**	590	597	606	627	644	648	659
	10	569	574	569	599	715	639	686
	20	565	559	570	628	658	655	677
	30	576	573	603	634	700	645	667
	40	591	625	597	668	639	693	742
	50	588	633	686	639	671	716	696
	60	640	680	687	696	711	689	745
	70	673	713	689	690	739	700	761
	80	677	661	717	720	739	741	764
	90	674	674	695	738	751	753	752
	100	681	695	711	690	751	746	766

Table 7.19. Maximum residual temperature at the 660 km discontinuity $T_{R\,max}^{660}$

Minimum residual temperature $T_{R\,min}^{660}$ $[K]$								
		660 Clapeyron Slope $\Upsilon_{ol}^{660}[MPa\,K^{-1}]$						
		0.0	**−0.5**	**−1.0**	**−1.5**	**−2.0**	**−2.5**	**−3.0**
Viscosity ratio η/η_{ol}^{660}	**1**	0	0	0	0	0	0	0
	10	0	0	0	0	0	0	0
	20	0	−118	−353	0	0	0	0
	30	−303	−463	−55	0	0	−440	−254
	40	0	0	−507	0	−524	−651	−721
	50	−349	0	−729	−516	−41	−30	−144
	60	−736	−786	−753	−715	−713	−476	−699
	70	−736	−779	−700	−633	−750	−216	−673
	80	−783	−822	−815	−806	−769	−727	−790
	90	−825	−857	−793	−865	−785	−790	−813
	100	−825	−852	−813	−502	−787	−843	−807

Table 7.20. Minimum residual temperature at the 660 km discontinuity $T_{R\,min}^{660}$

Temperature Difference of the Cold Advecting Material T_{adv}^{660} $[K]$								
		660 Clapeyron Slope $\Upsilon_{ol}^{660}[MPa\,K^{-1}]$						
		0.0	**−0.5**	**−1.0**	**−1.5**	**−2.0**	**−2.5**	**−3.0**
Viscosity ratio η/η_{ol}^{660}	**1**	0	10	20	29	39	48	58
	10	0	10	20	29	39	48	58
	20	0	−108	−334	29	39	48	58
	30	−303	−453	−35	29	39	−392	−196
	40	0	10	−488	29	−485	−602	−663
	50	−349	10	−710	−487	−2	19	−86
	60	−736	−777	−734	−686	−674	−428	−641
	70	−736	−770	−681	−604	−711	−168	−615
	80	−783	−812	−796	−777	−731	−679	−732
	90	−825	−847	−773	−836	−746	−742	−754
	100	−826	−842	−794	−473	−748	−794	−749

Table 7.21. Temperature difference of the cold advecting material T_{adv}^{660}

Depth of the Post-Spinel Discontinuity D_{adv}^{660} [km]								
		660 Clapeyron Slope $\Upsilon_{ol}^{660}[MPa\ K^{-1}]$						
		0.0	**−0.5**	**−1.0**	**−1.5**	**−2.0**	**−2.5**	**−3.0**
Viscosity ratio η/η_{ol}^{660}	**1**	663	663	663	663	663	663	663
	10	663	663	663	663	663	663	663
	20	663	663	670	663	663	663	663
	30	663	670	663	663	663	689	682
	40	663	663	676	663	689	702	716
	50	663	663	682	682	663	663	676
	60	663	676	682	689	670	689	716
	70	663	676	682	689	702	676	709
	80	663	676	682	670	702	709	723
	90	663	676	682	670	702	709	723
	100	663	676	682	682	702	716	723

Table 7.22. Depth of the post-spinel discontinuity D_{adv}^{660}

Latent Energy E_{pyr}^{660} [$kJ\ kg^{-1}$]								
		660 Clapeyron Slope $\Upsilon_{ol}^{660}[MPa\ K^{-1}]$						
		0.0	**−0.5**	**−1.0**	**−1.5**	**−2.0**	**−2.5**	**−3.0**
Viscosity ratio η/η_{ol}^{660}	**1**	0	−11.6	−23.2	−34.8	−46.5	−58.1	−69.7
	10	0	−11.6	−23.2	−34.8	−46.5	−58.1	−69.7
	20	0	−11.6	−23.2	−34.8	−46.5	−58.1	−69.7
	30	0	−11.6	−23.2	−34.8	−46.5	−58.1	−69.7
	40	0	−11.6	−23.2	−34.8	−46.5	−58.1	−69.7
	50	0	−11.6	−23.2	−34.8	−46.5	−58.1	−69.7
	60	0	−11.6	−23.2	−34.8	−46.5	−58.1	−69.7
	70	0	−11.6	−23.2	−34.8	−46.5	−58.1	−69.7
	80	0	−11.6	−23.2	−34.8	−46.5	−58.1	−69.7
	90	0	−11.6	−23.2	−34.8	−46.5	−58.1	−69.7
	100	0	−11.6	−23.2	−34.8	−46.5	−58.1	−69.7

Table 7.23. Latent energy of the endothermic phase transition E_{pyr}^{660}

Temperature Reduction T_{pyr}^{660} [K]								
		660 Clapeyron Slope $\Upsilon_{ol}^{660}[MPa\ K^{-1}]$						
		0.0	**−0.5**	**−1.0**	**−1.5**	**−2.0**	**−2.5**	**−3.0**
Viscosity ratio η/η_{ol}^{660}	**1**	0	−10	−20	−29	−39	−48	−58
	10	0	−10	−20	−29	−39	−48	−58
	20	0	−10	−20	−29	−39	−48	−58
	30	0	−10	−20	−29	−39	−48	−58
	40	0	−10	−20	−29	−39	−48	−58
	50	0	−10	−20	−29	−39	−48	−58
	60	0	−10	−20	−29	−39	−48	−58
	70	0	−10	−20	−29	−39	−48	−58
	80	0	−10	−20	−29	−39	−48	−58
	90	0	−10	−20	−29	−39	−48	−58
	100	0	−10	−20	−29	−39	−48	−58

Table 7.24. Temperature reduction due to the endothermic phase transition T_{pyr}^{660}

Pressure of Phase Transition P_{pyr}^{660} $[GPa]$								
		660 Clapeyron Slope $\Upsilon_{ol}^{660}[MPa\ K^{-1}]$						
		0.0	**−0.5**	**−1.0**	**−1.5**	**−2.0**	**−2.5**	**−3.0**
Viscosity ratio η/η_{ol}^{660}	**1**	22.89	22.90	22.92	22.96	23.02	23.09	23.18
	10	22.89	22.90	22.92	22.96	23.02	23.09	23.18
	20	22.89	22.90	22.92	22.96	23.02	23.09	23.18
	30	22.89	22.90	22.92	22.96	23.02	23.09	23.18
	40	22.89	22.90	22.92	22.96	23.02	23.09	23.18
	50	22.89	22.90	22.92	22.96	23.02	23.09	23.18
	60	22.89	22.90	22.92	22.96	23.02	23.09	23.18
	70	22.89	22.90	22.92	22.96	23.02	23.09	23.18
	80	22.89	22.90	22.92	22.96	23.02	23.09	23.18
	90	22.89	22.90	22.92	22.96	23.02	23.09	23.18
	100	22.89	22.90	22.92	22.96	23.02	23.09	23.18

Table 7.25. Pressure of the endothermic phase transition P_{pyr}^{660}

Density Increase due to Thermal Expansion $\Delta\rho_{\alpha}^{660}$ $[kg\ m^{-3}]$								
		660 Clapeyron Slope $\Upsilon_{ol}^{660}[MPa\ K^{-1}]$						
		0.0	**−0.5**	**−1.0**	**−1.5**	**−2.0**	**−2.5**	**−3.0**
Viscosity ratio η/η_{ol}^{660}	**1**	0	0.73	1.46	2.20	2.93	3.66	4.39
	10	0	0.73	1.46	2.20	2.93	3.66	4.39
	20	0	0.73	1.46	2.20	2.93	3.66	4.39
	30	0	0.73	1.46	2.20	2.93	3.66	4.39
	40	0	0.73	1.46	2.20	2.93	3.66	4.39
	50	0	0.73	1.46	2.20	2.93	3.66	4.39
	60	0	0.73	1.46	2.20	2.93	3.66	4.39
	70	0	0.73	1.46	2.20	2.93	3.66	4.39
	80	0	0.73	1.46	2.20	2.93	3.66	4.39
	90	0	0.73	1.46	2.20	2.93	3.66	4.39
	100	0	0.73	1.46	2.20	2.93	3.66	4.39

Table 7.26. Density increase due to thermal expansion $\Delta\rho_{\alpha}^{660}$

Density Jump at the Phase Transition $\Delta\rho_{pyr}^{660}$ $[kg\ m^{-3}]$								
		660 Clapeyron Slope $\Upsilon_{ol}^{660}[MPa\ K^{-1}]$						
		0.0	**−0.5**	**−1.0**	**−1.5**	**−2.0**	**−2.5**	**−3.0**
Viscosity ratio η/η_{ol}^{660}	**1**	201.70	202.43	203.16	203.90	204.63	205.36	206.09
	10	201.70	202.43	203.16	203.90	204.63	205.36	206.09
	20	201.70	202.43	203.16	203.90	204.63	205.36	206.09
	30	201.70	202.43	203.16	203.90	204.63	205.36	206.09
	40	201.70	202.43	203.16	203.90	204.63	205.36	206.09
	50	201.70	202.43	203.16	203.90	204.63	205.36	206.09
	60	201.70	202.43	203.16	203.90	204.63	205.36	206.09
	70	201.70	202.43	203.16	203.90	204.63	205.36	206.09
	80	201.70	202.43	203.16	203.90	204.63	205.36	206.09
	90	201.70	202.43	203.16	203.90	204.63	205.36	206.09
	100	201.70	202.43	203.16	203.90	204.63	205.36	206.09

Table 7.27. Density jump at the phase transition $\Delta\rho_{pyr}^{660}$

Additional Pull after the Phase Transition ΔF_{pyr}^{660} $[N\,m^{-3}]$								
		660 Clapeyron Slope $\Upsilon_{ol}^{660}[MPa\,K^{-1}]$						
		0.0	**−0.5**	**−1.0**	**−1.5**	**−2.0**	**−2.5**	**−3.0**
Viscosity ratio η/η_{ol}^{660}	**1**	1979	1986	1993	2000	2007	2015	2022
	10	1979	1986	1993	2000	2007	2015	2022
	20	1979	1986	1993	2000	2007	2015	2022
	30	1979	1986	1993	2000	2007	2015	2022
	40	1979	1986	1993	2000	2007	2015	2022
	50	1979	1986	1993	2000	2007	2015	2022
	60	1979	1986	1993	2000	2007	2015	2022
	70	1979	1986	1993	2000	2007	2015	2022
	80	1979	1986	1993	2000	2007	2015	2022
	90	1979	1986	1993	2000	2007	2015	2022
	100	1979	1986	1993	2000	2007	2015	2022

Table 7.28. Additional pull after the phase transition ΔF_{pyr}^{660}

Resisting Force at the Phase Transition ΔF_{R}^{660} $[N]$								
		660 Clapeyron Slope $\Upsilon_{ol}^{660}[MPa\,K^{-1}]$						
		0.0	**−0.5**	**−1.0**	**−1.5**	**−2.0**	**−2.5**	**−3.0**
Viscosity ratio η/η_{ol}^{660}	**1**	-6.14×10^{12}	-5.08×10^{12}	-3.73×10^{12}	-2.72×10^{12}	-2.37×10^{12}	-2.19×10^{12}	-3.91×10^{12}
	10	1.21×10^{14}	1.64×10^{14}	2.81×10^{14}	1.78×10^{14}	4.06×10^{13}	1.42×10^{14}	5.47×10^{13}
	20	7.89×10^{14}	1.44×10^{15}	2.54×10^{15}	4.57×10^{14}	2.69×10^{14}	3.20×10^{14}	2.79×10^{14}
	30	4.61×10^{15}	7.68×10^{15}	1.17×10^{15}	8.45×10^{14}	2.81×10^{14}	3.53×10^{15}	1.53×10^{15}
	40	1.33×10^{15}	9.94×10^{14}	1.50×10^{16}	8.93×10^{14}	1.90×10^{16}	8.72×10^{16}	1.62×10^{17}
	50	3.25×10^{15}	1.30×10^{15}	1.15×10^{17}	1.86×10^{16}	1.30×10^{15}	1.46×10^{15}	1.55×10^{15}
	60	1.20×10^{17}	1.36×10^{17}	1.77×10^{17}	1.65×10^{17}	1.54×10^{17}	1.81×10^{16}	2.04×10^{17}
	70	1.27×10^{17}	2.37×10^{17}	1.54×10^{17}	6.80×10^{16}	2.04×10^{17}	2.78×10^{15}	1.53×10^{17}
	80	1.96×10^{17}	2.63×10^{17}	2.63×10^{17}	3.08×10^{17}	3.24×10^{17}	2.61×10^{17}	4.00×10^{17}
	90	2.48×10^{17}	3.66×10^{17}	3.59×10^{17}	4.67×10^{17}	3.13×10^{17}	2.94×10^{17}	3.99×10^{17}
	100	2.51×10^{17}	3.16×10^{17}	2.72×10^{17}	2.27×10^{17}	2.52×10^{17}	3.98×10^{17}	3.77×10^{17}

Table 7.29. Resisting Force at the Phase Transition ΔF_{R}^{660}

Avalanche Volume V_{ava}^{660} $[km^3]$								
		660 Clapeyron Slope $\Upsilon_{ol}^{660}[MPa\,K^{-1}]$						
		0.0	**−0.5**	**−1.0**	**−1.5**	**−2.0**	**−2.5**	**−3.0**
Viscosity ratio η/η_{ol}^{660}	**1**	−3.10	−2.56	−1.87	−1.36	−1.18	−1.09	−1.93
	10	61	83	141	89	20	70	27
	20	399	727	1274	228	134	159	138
	30	2329	3868	585	423	140	1752	756
	40	673	501	7505	446	9473	43264	80141
	50	1643	653	57848	9295	649	723	768
	60	60555	68247	88782	82452	76703	8980	101044
	70	64094	119528	77435	34004	101518	1379	75655
	80	99128	132281	132190	154079	161245	129761	197758
	90	125472	184408	179977	233398	155795	146127	197255
	100	126900	159113	136492	11366	125621	197722	186235

Table 7.30. Avalanche volume V_{ava}^{660}

Terminal Velocity of the Upper Mantle V_{Stokes}^{UM} $[m\ yr^{-1}]$								
		660 Clapeyron Slope $\Upsilon_{ol}^{660}[MPa\ K^{-1}]$						
		0.0	**−0.5**	**−1.0**	**−1.5**	**−2.0**	**−2.5**	**−3.0**
Viscosity ratio η/η_{ol}^{660}	**1**	121.19	124.87	131.41	143.38	152.86	143.14	170.22
	10	61.43	52.53	37.08	55.08	166.86	69.03	143.35
	20	21.11	14.68	10.68	43.16	65.83	61.74	65.81
	30	7.22	4.83	25.93	31.10	86.21	10.70	23.62
	40	23.39	31.65	3.46	38.69	3.09	0.68	0.43
	50	12.97	28.93	0.57	3.25	33.45	30.30	27.41
	60	0.53	0.46	0.40	0.48	0.50	3.67	0.42
	70	0.54	0.31	0.48	1.09	0.42	22.57	0.54
	80	0.34	0.33	0.30	0.30	0.29	0.37	0.25
	90	0.31	0.23	0.26	0.21	0.29	0.32	0.24
	100	0.30	0.25	0.33	3.74	0.42	0.29	0.31

Table 7.31. Terminal velocity of the upper mantle V_{Stokes}^{UM}

Terminal Velocity of the Lower Mantle V_{Stokes}^{LM} $[m\ yr^{-1}]$								
		660 Clapeyron Slope $\Upsilon_{ol}^{660}[MPa\ K^{-1}]$						
		0.0	**−0.5**	**−1.0**	**−1.5**	**−2.0**	**−2.5**	**−3.0**
Viscosity ratio η/η_{ol}^{660}	**1**	71.72	65.40	66.11	68.97	71.77	62.53	63.27
	10	3.32	2.50	1.45	2.35	10.31	2.99	7.30
	20	0.43	0.17	0.12	0.93	1.61	1.31	1.41
	30	0.07	0.04	0.21	0.47	1.42	0.05	0.13
	40	0.20	0.40	0.02	0.39	0.02	3.77×10^{-3}	1.69×10^{-3}
	50	0.07	0.18	2.35×10^{-3}	0.01	0.21	0.18	0.12
	60	2.65×10^{-3}	1.69×10^{-3}	1.48×10^{-3}	1.78×10^{-3}	1.85×10^{-3}	0.02	1.40×10^{-3}
	70	2.30×10^{-3}	1.01×10^{-3}	1.90×10^{-3}	4.66×10^{-3}	9.57×10^{-4}	7.83×10^{-4}	1.68×10^{-3}
	80	1.29×10^{-3}	9.42×10^{-4}	8.58×10^{-4}	7.83×10^{-4}	6.61×10^{-4}	1.03×10^{-3}	4.79×10^{-4}
	90	9.77×10^{-4}	7.25×10^{-4}	9.44×10^{-4}	5.07×10^{-4}	6.98×10^{-4}	6.28×10^{-4}	3.68×10^{-4}
	100	9.25×10^{-4}	7.84×10^{-4}	8.07×10^{-4}	0.01	6.28×10^{-4}	5.47×10^{-4}	6.06×10^{-4}

Table 7.32. Terminal velocity of the lower mantle V_{Stokes}^{LM}

Thermal Velocity Ratio $V_{Stokes}^{LM}/V_{Stokes}^{UM}$[/]								
		660 Clapeyron Slope $\Upsilon_{ol}^{660}[MPa\ K^{-1}]$						
		0.0	**−0.5**	**−1.0**	**−1.5**	**−2.0**	**−2.5**	**−3.0**
Viscosity ratio η/η_{ol}^{660}	**1**	5.55×10^{-1}	5.02×10^{-1}	4.56×10^{-1}	4.31×10^{-1}	4.23×10^{-1}	3.88×10^{-1}	3.16×10^{-1}
	10	5.64×10^{-2}	4.69×10^{-2}	4.18×10^{-2}	4.17×10^{-2}	5.94×10^{-2}	3.83×10^{-2}	3.77×10^{-2}
	20	2.49×10^{-2}	1.33×10^{-2}	1.20×10^{-2}	2.15×10^{-2}	2.31×10^{-2}	1.93×10^{-2}	1.96×10^{-2}
	30	1.08×10^{-2}	9.87×10^{-3}	8.76×10^{-3}	1.51×10^{-2}	1.75×10^{-2}	6.67×10^{-3}	7.95×10^{-3}
	40	1.21×10^{-2}	1.33×10^{-2}	6.58×10^{-3}	1.20×10^{-2}	5.53×10^{-3}	4.62×10^{-3}	3.38×10^{-3}
	50	7.10×10^{-3}	7.66×10^{-3}	3.73×10^{-3}	5.38×10^{-3}	8.59×10^{-3}	8.01×10^{-3}	6.79×10^{-3}
	60	4.82×10^{-2}	3.55×10^{-3}	3.60×10^{-3}	3.52×10^{-3}	3.52×10^{-3}	4.16×10^{-3}	2.99×10^{-3}
	70	4.15×10^{-3}	3.80×10^{-3}	3.39×10^{-3}	4.14×10^{-3}	2.49×10^{-3}	5.27×10^{-3}	3.23×10^{-3}
	80	3.37×10^{-2}	3.03×10^{-3}	2.81×10^{-3}	2.42×10^{-3}	2.53×10^{-3}	2.69×10^{-3}	2.36×10^{-3}
	90	3.43×10^{-2}	2.98×10^{-3}	2.79×10^{-3}	2.74×10^{-3}	2.61×10^{-3}	2.09×10^{-3}	1.51×10^{-3}
	100	3.19×10^{-2}	2.89×10^{-3}	2.41×10^{-3}	3.03×10^{-3}	2.01×10^{-3}	1.89×10^{-3}	2.05×10^{-3}

Table 7.33. Thermal velocity ratio $V_{Stokes}^{LM}/V_{Stokes}^{UM}$

CHAPTER 8 – Final Considerations and Future Research

8.1. Final Considerations

The studies reported in this thesis provide some useful tools for future investigations of the deep Earth water cycle: (1) a parameterized equation to model the thermal evolution of a slab in the MTZ, (2) a combined methodology to distinguish different tectonic regime, (3) a map of the tectonic regime distribution as a function of the yield stress, (4) empirical constraints on the relevant parameters of the 660 km discontinuity. Combining these tools will help future studies simulating the stagnation of slabs at the 660 km discontinuity and the related hydration of the MTZ.

8.1.1. Thermal Conductivity of Ringwoodite

Ringwoodite is the key mineral of the lower mantle transition zone MTZ (520–660 km). Until recently, the lattice thermal conductivity of ringwoodite Λ_{Rw} has been barely investigated. The measurements performed in this thesis provide sound data on Λ_{Rw} for both dry and hydrous conditions. The most important finding from this study is the fact that the presence of 1.73 $wt\%$ of water in ringwoodite significantly reduces its thermal conductivity by up to $\approx 40\%$.

The analyses were performed using an advanced technique (TDTR), which can be compared in the future with other measuring methods. Such a cross-comparison is fundamental for achieving a complementary constraint on the value range of a given parameter.

Moreover, the study provides a parameterized equation that describes the dependency of Λ_{Rw} on pressure P and water content C_{H2O}. The equation reproduces the dataset within the range $P = 0–25\ GPa$ and $C_{H2O} = 0.11–1.73\ wt\%$ H_2O. This equation is a valid tool for the computation of the thermal evolution of a slab in the lower MTZ. This of importance since the temperature inside a slab is a crucial parameter for deep Earth water cycle studies, since it controls the stability of the nominally hydrous phases, e.g. DHMS.

The parameterized equation, $\Lambda_{\mathrm{Rw}}(P, C_{\mathrm{H2O}})$ can be easily implemented in a numerical model to simulate the temperature evolution of a slab. The 1D models reveal that the DHMS breakdown critical temperature is reached with a delay of a few million years in the case of a water-bearing slab. The models show that the water-induced reduction of Λ_{Rw} remains relevant on the large scale. The 1D analysis shows promising results, thus it would be important to include more complexities in the future.

8.1.2. The Effect of Grid Resolution on Tectonic Regimes

The deep Earth water cycle is not possible without slab subduction and plate tectonics. In numerical modelling, a given tectonic regime is obtained by adjusting the yield stress of the lithosphere τ_y. With increasing τ_y, the following tectonic regimes can be obtained: micro-plate dripping, plate-like behaviour, episodic resurfacing and stagnant lid. Therefore, plate-like behaviour can be achieved using an intermediate yield stress.

However, it has been shown that the style of convection heavily depends on the number of grid nodes used to solve the governing equations. To minimize the influence of the numerical parameters, it is fundamental to choose an appropriate grid resolution. Chapter 6 discusses the

effect of the grid resolution on the resulting tectonic regime. For this purpose a 2D global-scale simulation of an Earth-like planet was employed. In this analysis the target parameters were the yield stress τ_y, the azimuthal (horizontal) resolution R_{azi}, and the radial (vertical) resolution R_{rad}.

Five diagnostic parameters, proposed by different authors, have been employed to distinguish each tectonic regime: (1) rms mantle temperature and (2) mantle viscosity (*Schubert et al., 2001*); (3) surface Nusselt number (*Tosi et al., 2015*); (4) mobility and (5) plateness (*Tackley, 2000a*). Furthermore, this study introduces an additional parameter: (6) the ratio between the average lithospheric stress and the yield stress. This parameter has proved to be useful to distinguish between the micro-plate dripping and the plate-like tectonic regime.

This analysis reveals that the lithosphere becomes weaker for higher azimuthal resolution, whereas it becomes stronger for higher radial resolution. This behaviour is caused by long-range interpolation of the temperature, viscosity and stress fields of the lithosphere. Therefore, a larger number of grid nodes is recommended for the boundary layers. A fine grid spacing in the lithosphere would be also advantageous to constrain the water influx in subduction zones.

8.1.3. Slab Stagnation in the Mantle Transition Zone

The overview of the interactions between slabs and the 660 km discontinuity is reported in chapter 7. One possible mechanism that can cause hydration of the MTZ is the stagnation of a slab at 660 km. The stagnation is controlled by three parameters: (1) the Clapeyron slope of the post spinel reaction; (2) the density jump between ringwoodite and lower mantle assemblage; (3) the viscosity jump between the MTZ and the LM.

The Clapeyron slope controls the depth of the phase transition which is deflected downwards for cold materials; the density jump controls the negative pull experienced by a slab and the latent heat absorbed by the reaction; and the viscosity jump reduces the sinking velocity of a slab.

The effect of the Clapeyron slope depends on the temperature of a slab at the base of the MTZ. The absence of additional slab pull due to the deflected phase transition also depends on a slab's temperature state. Once warm enough to react, a slab will experience extra pull of the denser LM mineral assemblage.

The viscosity jump, on the other hand, is active regardless of the slab temperature. Moreover, the 10 – 100 higher viscosity of the LM causes a sinking velocity reduction of factor 10 – 100. Other parameters like thermal expansivity and heat capacity have a minor effect on the stagnation of a slab. Based on these results, it can be concluded that the two main factors responsible for the stagnation are the viscosity jump and the slab temperature field.

8.2. Future Research

The studies performed in this thesis will help to build a self-consistent global-scale model of the deep Earth water cycle. Three key aspects in particular will be fundamental for future studies: (1) constraining the temperature field of the water bearing slab, (2) the importance of employing high resolution in the models and necessity of reducing the grid spacing further, (3) quantifying the effect of each parameter on a given physical phenomena in order to establish a hierarchy of effects. To reach the ultimate goal of this thesis, i.e. a deep Earth water cycle model, a large number of future models, analyses, and experiments are still necessary. Future studies should focus on:

- Measuring the thermal conductivity of garnet and pyroxenes in the upper mantle and MTZ.
- Measuring the effect of water on the thermal conductivity of wadsleyite.
- Modelling the thermal evolution of a slab considering the aggregate thermal conductivity of each lithology (Al-rich sediments, meta-basaltic crust, harzburgite).
- Implementation of the $520\ km$ discontinuity in StagYY to distinguish wadsleyite from ringwoodite.
- Analyzing the interactions between rising plumes and the $660\ km$ discontinuity.
- Employing a free surface/sticky air layer at the top of the model to reproduce a more accurate stress localization in the lithosphere.
- Constraining the optimal resolution for computing the topography of the lithosphere and reduce the numerical instabilities.
- Implementing a routine to hydrate the lithosphere, and to carry water into the mantle via the subduction of slabs.
- Implementing a phase-dependent water solubility for mantle material. At this stage, water will not have any effect on the physical properties of the mantle, and will be carried passively. This water-redistribution routine should be benchmarked carefully to avoid violations of the mass conservation law.
- Implementing water-dependency for different rheological parameters and studying the effect of water on mantle convection.
- Implementing a dehydration melting routine to reproduce the water-filter mechanism proposed by *Bercovici & Karato (2003)* and the asthenosphere formation model proposed by *Mierdel et al. (2007)*.

These studies have been left for the future, but they are nevertheless important for unravelling the effect of water on Earth's plate tectonics.

REFERENCES - A

Abe, R., Shibazaki, Y., Ozawa, S., Ohira, I., Tobe, H., & Suzuki, A. (2018). In situ X-ray diffraction studies of hydrous aluminosilicate at high pressure and temperature. *J. Miner. Petrol. Sci.*, 170714. https://doi.org/10.2465/jmps.170714

Abe, Y. (1997). Thermal and chemical evolution of the terrestrial magma ocean. *Phys. Earth Planet. In.*, 100(1–4), 27–39. https://doi.org/10.1016/S0031-9201(96)03229-3

Adams, J. C., Brainerd, W. S., Martin, J. T., Smith, B. T., & Wagener, J. L. (1992). Fortran 90 Handbook Complete ANSI / ISO Reference.

Agrusta, R., Goes, S., & van Hunen, J. (2017). Subducting-slab transition-zone interaction: stagnation, penetration and mode switches. *Earth Plan. Sci. Lett.*, *464*, 10–23. https://doi.org/10.1016/j.epsl.2017.02.005

Akaogi, M., Ito, E., & Navrotsky, A. (1989). Olivine-modified spinel-spinel transitions in the system Mg_2SiO_4-Fe_2SiO_4: calorimetric measurements, thermochemical calculation, and geophysical application. *J. Geophys. Res.*, *94*(B11), 671–686. https://doi.org/10.1029/jb094ib11p15671

Akaogi, M., Yano, M., Tejima, Y., Iijima, M., & Kojitani, H. (2004). High-pressure transitions of diopside and wollastonite: Phase equilibria and thermochemistry of $CaMgSi_2O_6$, $CaSiO_3$ and $CaSi_2O_5$-$CaTiSiO_5$ system. *Phys. Earth Planet. In.*, *143*(1–2), 145–156. https://doi.org/10.1016/j.pepi.2003.08.008

Aki K., Richards P. G. (1980). Quantitative Seismology: Theory and Methods (2nd Ed.). *University Science Books*, 704 pages, ISBN 0-935702-96-2

Alejano, L. R., & Bobet, A. (2012). Drucker–Prager Criterion. In The ISRM Suggested Methods for Rock Characterization, Testing and Monitoring: 2007-2014 (pp. 247–252). *Springer International Publishing*. https://doi.org/10.1007/978-3-319-07713-0_22

Alexander, C. M. O. D., Bowden, R., Fogel, M. L., Howard, K. T., Herd, C. D. K., & Nittler, L. R. (2012). The provenances of asteroids, and their contributions to the volatile inventories of the terrestrial planets. *Science*, *337*(6095), 721–723. https://doi.org/10.1126/science.1223474

Alt, J. C. (1995). Subseafloor processes in mid-ocean ridge hydrothermal systems. *Geoph. Monog. Series*, *91*, 85-114. https://doi.org/10.1029/GM091p0085

Alt, J. C., Honnorez, J., Laverne, C., & Emmermann, R. (1986). Hydrothermal alteration of a 1 km section through the upper oceanic crust, Deep Sea Drilling Project Hole 504B: Mineralogy, chemistry and evolution of seawater-basalt interactions. *J. Geophys. Res.*, *91*(B10), 10309. https://doi.org/10.1029/jb091ib10p10309

Altwegg, K., Balsiger, H., Bar-Nun, A., Berthelier, J. J., Bieler, A., Bochsler, P., … Wurz, P. (2015). 67P/Churyumov-Gerasimenko, a Jupiter family comet with a high D/H ratio. *Science*, *347*(6220). https://doi.org/10.1126/science.1261952

Ammann, M. W., Brodholt, J. P., & Dobson, D. P. (2009). DFT study of migration enthalpies in $MgSiO_3$ perovskite. *Phys. Chem. Min., 36*(3), 151–158. https://doi.org/10.1007/s00269-008-0265-z

Ammann, M. W., Brodholt, J. P., Wookey, J., & Dobson, & D. P. (2010). First-principles constraints on diffusion in lower-mantle minerals and a weak D99 layer. *Nature, 465* (7297), 462-465. https://doi.org/10.1038/nature09052

Anderson, D. L., & Bass, J. D. (1984). Mineralogy and composition of the upper mantle. *Geophys. Res. Lett.*, *11*(7), 637–640. https://doi.org/10.1029/GL011i007p00637

Anderson, D. L. (1987). A seismic equation of state II. Shear properties and thermodynamics of the lower mantle. *Phys. Earth Planet, 45*(4), 307-323. In. https://doi.org/10.1016/0031-9201(87)90039-2

Anderson, D. L. (1995). Lithosphere, asthenosphere, and perisphere. *Rev. Geophys.*, *33*(1), 125. https://doi.org/10.1029/94RG02785

Anderson, D. L. (2007). New Theory of the Earth. *Cambridge University Press*, 405 pages. https://doi.org/10.1017/CBO9781139167291

Angel, R. J., Downs, R. T., & Finger, L. W. (2000). High-temperature-high-pressure diffractometry. *Rev. Min. Geochem., 41*(1), 559-597. https://doi.org/10.2138/rmg.2000.41.16

Angel, R. J., Bujak, M., Zhao, J., Gatta, G. D., & Jacobsen, S. D. (2007). Effective hydrostatic limits of pressure media for high-pressure crystallographic studies. *J. App. Cryst., 40*(1), 26-32. https://doi.org/10.1107/S0021889806045523

Angel, R. J., & Finger, L. W. (2011). SINGLE: A program to control single-crystal diffractometers. *J. Appl. Cryst., 44*(1), 247-251. https://doi.org/10.1107/S0021889810042305

Angel, R. J., Gonzalez-Platas, J., & Alvaro, M. (2014). EosFit7c and a Fortran module (library) for equation of state calculations. *Cryst. Mat., 229*(5), 405–419. https://doi.org/10.1515/zkri-2013-1711

Aramberri, H., Rurali, R., & Íñiguez, J. (2017). Thermal conductivity changes across a structural phase transition: The case of high-pressure silica. *Phys. Rev. B*, 96(19). https://doi.org/10.1103/PhysRevB.96.19520

Armann, M., & Tackley, P. J. (2012). Simulating the thermochemical magmatic and tectonic evolution of Venus's mantle and lithosphere: Two-dimensional models. *J. Geophys. Res. E - Plan., 117*(E12). https://doi.org/10.1029/2012JE004231

Arnould, M., Coltice, N., Flament, N., Seigneur, V., & Müller, R. D. (2018). On the scales of dynamic topography in whole-mantle convection models. *Geochem. Geophys. Geosys.*, *19*(9), 3140-3163. https://doi.org/10.1029/2018GC007516

Arnould, M., Ganne, J., Coltice, N., & Feng, X. (2019). Northward drift of the Azores plume in the Earth's mantle. *Nat. Comm., 10*(1), 1-8. https://doi.org/10.1038/s41467-019-11127-7

Asahara, Y., Frost, D. J., & Rubie, D. C. (2007). Partitioning of FeO between magnesiowüstite and liquid iron at high pressures and temperatures: Implications for the composition of the Earth's outer core. *Earth Planet Sc. Lett., 257*(3-4), 435-449. https://doi.org/10.1016/j.epsl.2007.03.006

Asimow, P. D., Hirschmann, M. M., Ghiorso, M. S., O'Hara, M. J., & Stolper, E. M. (1995). The effect of pressure-induced solid-solid phase transitions on decompression melting of the mantle. *Geochim. Cosmochim. Ac.*, 59(21), 4489–4506.https://doi.org/10.1016/0016-7037(95)00252-U

Asimow, P. D., Hirschmann, M. M., & Stolper, E. M. (2001). Calculation of peridotite partial melting from thermodynamic models of minerals and melts, IV. Adiabatic decompression and the composition and mean properties of mid-ocean ridge basalts. *J. Petrol.*, *42*(5), 963-998. https://doi.org/10.1093/petrology/42.5.963

Auer, L., Boschi, L., Becker, T. W., Nissen-Meyer, T., & Giardini, D. (2014). SAVANI: A variable resolution whole-mantle model of anisotropic shear velocity variations based on multiple data sets. *J. Geophys. Res. - Sol. Ea.*, 119(4), 3006–3034. https://doi.org/10.1002/2013JB010773

REFERENCES - B

Bagley, B., & Revenaugh, J. (2008). Upper mantle seismic shear discontinuities of the Pacific. *J. Geophys. Res.- Sol. Ea.*, *113*(B12). https://doi.org/10.1029/2008JB005692

Balay, S., Abhyankar, S., Adams, M. F., Brown, J., Brune, P., Buschelman, K., … Zhang, H. (2015). PETSc Users Manual. ANL-95/11 - Revision 3.6.

Ballaran, T. B. (2010). Equations of state and their applications in geosciences. In *High-Pressure Crystallography* (pp. 135-145). Springer, Dordrecht. https://doi.org/10.1007/978-90-481-9258-8-12

Ballaran, T. B., Kurnosov, A., & Trots, D. (2013). Single-crystal X-ray diffraction at extreme conditions: A review. *High Press. Res., 33*(3), 453-465. https://doi.org/10.1080/08957959.2013.834052

Ballmer, M. D., Schmerr, N. C., Nakagawa, T., & Ritsema, J. (2015). Compositional mantle layering revealed by slab stagnation at ~1000-km depth. *Sci. Adv. 1*(11), e1500815. https://doi.org/10.1126/sciadv.1500815

Barnes, J. D., & Straub, S. M. (2010). Chorine stable isotope variations in Izu Bonin tephra: implications for serpentinite subduction. *Chem. Geol.*, *272*(1–4), 62–74. https://doi.org/10.1016/j.chemgeo.2010.02.005

Barrell, J. (1914). The strength of the Earth's crust. *J. Geol.*, *22*(7), 655–683. https://doi.org/10.1086/622181

Becker, T. W. (2006). On the effect of temperature and strain-rate dependent viscosity on global mantle flow, net rotation, and plate-driving forces. *Geophys. J. Int., 167*(2), 943–957. https://doi.org/10.1111/j.1365-246X.2006.03172.x

Becker, T. W., & Faccenna, C. (2009). A review of the role of subduction dynamics for regional and global plate motions. *Subduction zone geodynamics*, 3-34. https://doi.org/10.1007/978-3-540-87974-9_1

Bekaert, D. V., Turner, S. J., Broadley, M. W., Barnes, J. D., Halldórsson, S. A., Labidi, J., … Barry, P. H. (2021). Subduction-driven volatile recycling: a global mass balance. *Annu. Rev. Earth Pl. Sc.*, *49*(1), 37–70. https://doi.org/10.1146/annurev-earth-071620-055024

Bell, D. R., & Rossman, G. R. (1992). Water in Earth's mantle: the role of nominally anhydrous minerals. *Science* , *255*(5050), 1391-1397. https://doi.org/10.1126/science.255.5050.1391

Bell, D. R., Rossman, G. R., & Moore, R. O. (2004). Abundance and partitioning of OH in a high-pressure magmatic system: Megacrysts from the monastery kimberlite, South Africa. *J. Petrol., 45*(8), 1539-1564.

Bello, L., Coltice, N., Tackley, P. J., Dietmar Müller, R., & Cannon, J. (2015). Assessing the role of slab rheology in coupled plate-mantle convection models. *Earth Plan. Sci. Lett., 430*, 191-201. https://doi.org/10.1016/j.epsl.2015.08.010

Bercegeay, C., & Bernard, S. (2005). First-principles equations of state and elastic properties of seven metals. *Phys. Rev. B - Cond. Matt. Mat. Phys., 72*(21), 214101. https://doi.org/10.1103/PhysRevB.72.214101

Bercovici, D. (2003). The generation of plate tectonics from mantle convection. *Earth Planet Sc. Lett.*, *205*(3–4), 107–121. https://doi.org/10.1016/S0012-821X(02)01009-9

Bercovici, D., & Karato, S.-I. (2003). Whole-mantle convection and the transition-zone water filter. *Nature*, *425*(6953), 39-44. https://doi.org/10.1038/nature01918

Bergin, E. A., Blake, G. A., Ciesla, F., Hirschmann, M. M., Li, J., & Designed, J. L. (2015). Tracing the ingredients for a habitable earth from interstellar space through planet formation. *P. Natl. Acad. Sci.*, *112*, 2021. https://doi.org/10.1073/P. Natl. Acad. Sci..1500954112

Beuthe, M. (2015). Tides on Europa: The membrane paradigm. *Icarus, 248*, 109–134. https://doi.org/10.1016/j.icarus.2014.10.027

Bina, C. R., & Wood, B. J. (1987). Olivine-spinel transitions: Experimental and thermodynamic constraints and implications for the nature of the 400-km seismic discontinuity. *J. Geophys. Res.*, *92*(B6), 4853. https://doi.org/10.1029/jb092ib06p04853

Binnie, W. P. (1956). Calculation of the mean Debye temperature of cubic crystals. *Phys. Rev., 103*(3), 579. https://doi.org/10.1103/PhysRev.103.579

Birch, F. (1947). Finite elastic strain of cubic crystals. *Phys. Rev., 71*(11), 809. https://doi.org/10.1103/PhysRev.71.809

Birch, F. (1952). Elasticity and constitution of the Earth's interior. *J. Geophys. Res., 57*(2), 227-286. https://doi.org/10.1029/jz057i002p00227

Birch, F. (1965). Speculations on the Earth's thermal history. *Bull. Geol. Soc. Am.*, *76*(2), 133-154. https://doi.org/10.1130/00167606(1965)76[133:SOTETH]2.0.CO;2

Bish, D. L., & Reynolds, R. C. (2018). Sample preparation for X-ray diffraction. *Mod. Pwd. Diff.*, *73*-100. https://doi.org/10.1515/9781501509018-007

Blankenbach, B., Busse, F., Christensen, U., Cserepes, L., Gunkel, D., Hansen, U., … Schnaubelt, T. (1989). A benchmark comparison for mantle convection codes. *Geophys. J. Int., 98*(1), 23–38. https://doi.org/10.1111/j.1365-246X.1989.tb05511.x

Bocher, M., Coltice, N., Fournier, A., & Tackley, P. J. (2016). A sequential data assimilation approach for the joint reconstruction of mantle convection and surface tectonics. *Geophys. J. Int. 204*(1), 200-214. https://doi.org/10.1093/gji/ggv427

Bocher, M., Fournier, A., & Coltice, N. (2018). Ensemble Kalman filter for the reconstruction of the Earth's mantle circulation. *Non-Li. Proc. Geophys., 25*(1), 99-123.. https://doi.org/10.5194/npg-25-99-2018

Bock, G. (1994). Synthetic seismogram images of upper mantle structure: no evidence for a 520-km discontinuity. *J. Geophys. Res.*, *99*(B8), 843–858. https://doi.org/10.1029/94jb00992

Bockelée-Morvan, D., Crovisier, J., Mumma, M. J., & Weaver, H. A. (2004). The Composition of Cometary Volatiles. *Comets Ii*, *1*, 391-423.

Boehler, R. (2000). High-pressure experiments and the phase diagram of lower mantle and core materials. *Rev. Geophys., 38*(2), 221-245.. https://doi.org/10.1029/1998RG000053

Boehler, R., & De Hantsetters, K. (2004). New anvil designs in diamond-cells. *High Pres. Res., 24*(3), 391-396. https://doi.org/10.1080/08957950412331323924

Boenigk, J., Wodniok, S., & Glücksman, E. (2015). Biodiversity and earth history. *Springer*, 401 pages.

Bolfan-Casanova, N., Keppler, H., & Rubie, D. C. (2000). Water partitioning between nominally anhydrous minerals in the MgO-SiO_2-H_2O system up to 24 GPa: Implications for the distribution of water in the Earth's mantle. *Earth Planet Sc. Lett.*, *182*(3-4), 209-221. https://doi.org/10.1016/S0012-821X(00)00244-2

Bolfan-Casanova, N., Mackwell, S., Keppler, H., McCammon, C., & Rubie, D. C. (2002). Pressure dependence of H solubility in magnesiowüstite up to 25 GPa: Implications for the storage of water in the Earth's lower mantle. *Geophys. Res. Lett.*, *29*(10), 89-1-89–4. https://doi.org/10.1029/2001gl014457

Bolfan-Casanova, N., Keppler, H., & Rubie, D. C. (2003). Water partitioning at 660 km depth and evidence for very low water solubility in magnesium silicate perovskite. *Geophys. Res. Lett.*, *30*(17). https://doi.org/10.1029/2003GL017182

Bolfan-Casanova N. (2005). Water in the Earth's mantle. *Mineral. Mag.*, *69*(13), 229–257. https://doi.org/10.1180/0026461056930248

Bonello, B., Perrin, B., & Rossignol, C. (1998). Photothermal properties of bulk and layered materials by the picosecond acoustics technique. *J. App. Phys., 83*(6), 3081-3088. https://doi.org/10.1063/1.367064

Borch, R. S., & Green, H. W. (1987). Dependence of creep in olivine on homologous temperature and its implications for flow in the mantle. *Nature, 330*(6146), 345–348. https://doi.org/10.1038/330345a0

Boudier, F., & Nicolas, A. (1985). Harzburgite and lherzolite subtypes in ophiolitic and oceanic environments. *Earth Planet Sc. Lett.*, *76*(1–2), 84–92. https://doi.org/10.1016/0012-821X(85)90150-5

Bouffard, M., Choblet, G., Labrosse, S., & Wicht, J. (2019). Chemical convection and stratification in the earth's outer core. *Front Earth Sci.*, 7, 99.. https://doi.org/10.3389/feart.2019.00099

Bouhifd, M. A., Whittington, A., Roux, J., & Richet, P. (2006). Effect of water on the heat capacity of polymerized aluminosilicate glasses and melts. *Geochim. Cosmochim. Acta , 70*(3), 711-722. https://doi.org/10.1016/j.gca.2005.09.012

Boussinesq, J. (1903). Théorie analytique de la chaleur mise en harmonic avec la thermodynamique et avec la théorie mécanique de la lumière: Tome I-[II].. (Vol. 2). *Gauthier-Villars*.

Brace, W. F., & Byerlee, J. D. (1966). Stick-slip as a mechanism for earthquakes. *Science*, *153*(3739), 990–992. https://doi.org/10.1126/science.153.3739.990

Brace, W. F., & Kohlstedt, D. L. (1980). Limits on lithospheric stress imposed by laboratory experiments. *J. Geophys. Res.- Sol. Ea.*, *85*(B11), 6248–6252. https://doi.org/10.1029/jb085ib11p06248

Brace, W. F., & Kohlstedt, D. L. (1980). Limits on lithospheric stress imposed by laboratory experiments. *J. Geophys. Res. - Sol. Ea., 85*(B11), 6248–6252. https://doi.org/10.1029/jb085ib11p06248

Bragg, W. L. (1914). The analysis of crystals by the X-ray spectrometer. *P. R. London - Series A Mat. Phys. Char., 89*(613), 468-489. https://doi.org/10.1098/rspa.1914.0015

Braginsky, S. I., & Roberts, P. H. (1995). Equations governing convection in earth's core and the geodynamo. *Geophys Astro. Fluid Dyn., 79*(1-4), 1-97.. https://doi.org/10.1080/03091929508228992

Brändli, S., & Tackley, P. (2016). The influence of water on mantle convection and plate tectonics. *AGU, Fall Meeting 2016*, Abstract #DI41C-2648

Brennen, C. (1974). Isostatic recovery and the strain rate dependent viscosity of the Earth's mantle. *J. Geophys. Res., 79*(26), 3993–4001. https://doi.org/10.1029/JB079i026p03993

Brewster, M. Q. (1992). Thermal radiative transfer and properties. *John Wiley & Sons*, 568 pages. ISBN: 978-0-471-53982-7

Broadley, M. W., Barry, P. H., Bekaert, D. V., Byrne, D. J., Caracausi, A., Ballentine, C. J., & Marty, B. (2020). Identification of chondritic krypton and xenon in Yellowstone gases and the timing of terrestrial volatile accretion. *P. Natl. Acad. Sci. USA*, *117*(25), 13997–14004. https://doi.org/10.1073/pnas.2003907117

Brown, M. (2006). Duality of thermal regimes is the distinctive characteristics of plate tectonics since the Neoarchean. *Geology, 34*(11), 961–964. https://doi.org/10.1130/G22853A.1

Brugger, K., & Fritz, T. C. (1967). Grüneisen gamma from elastic data. *Phys. Rev., 157*(3), 524–531. https://doi.org/10.1103/PhysRev.157.524

Brune, S., Williams, S. E., & Müller, R. D. (2017). Potential links between continental rifting, CO_2 degassing and climate change through time. *Nat. Geosci.*, *10*(12), 941–946. https://doi.org/10.1038/s41561-017-0003-6

Bryson, K. L., Chevrier, V., Sears, D. W. G., & Ulrich, R. (2008). Stability of ice on Mars and the water vapor diurnal cycle: Experimental study of the sublimation of ice through a fine-grained basaltic regolith. *Icarus*, *196*(2), 446–458. https://doi.org/10.1016/j.icarus.2008.02.011

Buchen, J. (2018). The Elastic Properties of Wadsleyite and Stishovite at High Pressures. *Ph.D. Thesis*. Retrieved from https://epub.uni-bayreuth.de/4410/

Buchen, J., Marquardt, H., Speziale, S., Kawazoe, T., Boffa Ballaran, T., & Kurnosov, A. (2018). High-pressure single-crystal elasticity of wadsleyite and the seismic signature of water in the shallow transition zone. *Earth Planet Sc. Lett.*, *498*, 77–87. https://doi.org/10.1016/j.epsl.2018.06.027

Budyko M. I. Ronov A. B. Yanshin A. L. (1987). History of the Earth's atmosphere.*Springer*, 389 pages. ISBN 978-3-540-17235-2

Buening, D. K., & Buseck, P. R. (1973). Fe-Mg lattice diffusion in olivine. *J. Geophys. Res., 78*(29), 6852-6862. https://doi.org/10.1029/jb078i029p06852

Buffett, B. A., Huppert, H. E., Lister, J. R., & Woods, A. W. (1992). Analytical model for solidification of the Earth's core. *Nature, 356*(6367), 329–331. https://doi.org/10.1038/356329a0

Bull, A. J. (1921). A Hypothesis of Mountain Building. *Geol. Mag.*, *58*(8), 364–367. https://doi.org/10.1017/S0016756800104686

Bull, A. J. (1927). Some aspects of the mountain building problem: Presidential address. *P. Geologist. Assoc.*, *38*(2), 145–156. https://doi.org/10.1016/S0016-7878(27)80002-7

Bull, A. J. (1931). The Convection Current Hypothesis of Mountain Building. *Geol. Mag.*, *68*(11), 495–498. https://doi.org/10.1017/S001675680009840X

Bullard, E. C., & Griggs, D. T. (1961). The Nature of the Mohorovičić Discontinuity. *Geophys. J. Int.*, *6*(1), 118–123. https://doi.org/10.1111/j.1365-246X.1961.tb02966.x

Bunge, H. P., Richards, M. A., & Baumgardner, J. R. (1996). Effect of depth-dependent viscosity on the planform of mantle convection. *Nature*, *379*(6564), 436–438. https://doi.org/10.1038/379436a0

Bürgmann, R., & Dresen, G. (2008). Rheology of the lower crust and upper mantle: evidence from rock mechanics, geodesy, and field observations. *Annu. Rev. Earth Pl. Sc.*, *36*, 531–567.https://doi.org/10.1146/annurev.earth.36.031207.124326

Burns, R. G. (1993). Mineralogical applications of crystal field theory (2^{nd} Ed.). *Cambridge University Press*, 576 pages. ISBN-10: 0521430771

Burstedde, C., Stadler, G., Alisic, L., Wilcox, L. C., Tan, E., Gurnis, M., & Ghattas, O. (2013). Large-scale adaptive mantle convection simulation. *Geophys. J. Int., 192*(3), 889–906. https://doi.org/10.1093/gji/ggs070

Busing, W. R., & Levy, H. A. (1967). Angle calculations for 3- and 4-circle X-ray and neutron diffractometers. *Acta Cryst., 22*(4), 457-464. https://doi.org/10.1107/s0365110x67000970

Busse, F. H., Christensen, U., Clever, R., Cserepes, L., Gable, C., Giannandrea, E., … Travis, B. (1994). 3D Convection At Infinite Prandtl Number In Cartesian Geometry a Benchmark Comparison. *Geophys. Astrophys. Fluid Dyn., 75*(1), 39–59. https://doi.org/10.1080/03091929408203646

Byerlee, J. D. (1970). Static and kinetic friction of granite at high normal stress. *Int. J. Rock Mech. Min.*, *7*(6), 577–582. https://doi.org/10.1016/0148-9062(70)90018-5

Byerlee, J. (1978). Friction of Rocks. In Rock Friction and Earthquake Prediction (pp. 615–626). *Birkhäuser Basel*. https://doi.org/10.1007/978-3-0348-7182-2_4

Byrne, P. K. (2021). Unveiling Earth's Wayward Twin: Venus, the closest planet, seems like a hellish version of our own; studying how it got that way will tell us a lot about the prospects for life among the stars. *Am. Sci.*, *109*(1), 30–38.

REFERENCES - C

Cahill, D. G. (2004). Analysis of heat flow in layered structures for time-domain thermoreflectance. *Rev. Sci. Instr., 75*(12), 5119-5122. https://doi.org/10.1063/1.1819431

Cahill, D. G., & Watanabe, F. (2004). Thermal conductivity of isotopically pure and Ge-doped Si epitaxial layers from 300 to 550 K. *Phys. Rev. B - Cond. Matt. Mat. Phys., 70*(23), 235322. https://doi.org/10.1103/PhysRevB.70.235322

Cammarano, F., Tackley, P., & Boschi, L. (2011). Seismic, petrological and geodynamical constraints on thermal and compositional structure of the upper mantle: Global thermochemical models. *Geophys. J. Int., 187*(3), 1301-1318.. https://doi.org/10.1111/j.1365-246X.2011.05223.x

Campione, M., & Capitani, G. C. (2013). Subduction-zone earthquake complexity related to frictional anisotropy in antigorite. *Nat. Geosci.*, *6*(10), 847–851. https://doi.org/10.1038/ngeo1905

Caner, B., Cannon, W. H., & Livingstone, C. E. (1967). Geomagnetic depth sounding and upper mantle structure in the Cordillera region of western North America. *J. Geophys. Res.*, *72*(24), 6335–6351. https://doi.org/10.1029/JZ072i024p06335

Capinski, W. S., & Maris, H. J. (1996). Improved apparatus for picosecond pump-and-probe optical measurements. *Rev. Sci. Instr., 67*(8), 2720-2726. https://doi.org/10.1063/1.1147100

Carlson, R. L., & Raskin, G. S. (1984). Density of the ocean crust. *Nature*, *311*(5986), 555–558. https://doi.org/10.1038/311555a0

Carlson, R. L., & Miller, D. J. (2003). Mantle wedge water contents estimated from seismic velocities in partially serpentinized peridotites. *Geophys. Res. Lett.*, *30*(5), 1250. https://doi.org/10.1029/2002gl016600

Catling D. C., J. F. K. (2017). Atmospheric evolution inhabited and lifeless worlds (1st ed.). *Cambridge University Press*, 592 pages. 9780521844123

Chambers, J. E. (2004). Planetary accretion in the inner Solar System. *Earth Planet Sc. Lett., 223*(3–4), 241–252. https://doi.org/10.1016/j.epsl.2004.04.031

Chambers, K., Woodhouse, J. H., & Deuss, A. (2005). Topography of the 410-km discontinuity from PP and SS precursors. *Earth Planet Sc. Lett.*, *235*(3–4), 610–622. https://doi.org/10.1016/j.epsl.2005.05.014

Chang, Y. Y., Hsieh, W. P., Tan, E., & Chen, J. (2017). Hydration-reduced lattice thermal conductivity of olivine in Earth's upper mantle. *P. Natl. A. Sci. - USA, 114*(16), 4078-4081. https://doi.org/10.1073/pnas.1616216114

Chao, K. H., & Hsieh, W. P. (2019). Thermal Conductivity Anomaly in $(Fe_{0.78}Mg_{0.22})CO_3$ Siderite Across Spin Transition of Iron. *J. Geophys. Res. - Sol. Ea., 124*(2), 1388-1396. https://doi.org/10.1029/2018JB017003

Chao, K.-H., Huang, W.-J., & Hsieh, W.-P. 生：趙耕賢研 究 (2018). Spin Transition and Thermal Conductivity of ($Fe_{0.78}Mg_{0.22}CO_3$) Siderite under High Pressure. Master Thesis, National Central University, Taiwan.

Chen, B., Hsieh, W. P., Cahill, D. G., Trinkle, D. R., & Li, J. (2011). Thermal conductivity of compressed H_2O to 22 GPa: A test of the Leibfried-Schlömann equation. *Phys. Rev. B - Cond. Matt. Mat. Phys., 83*(13), 132301.. https://doi.org/10.1103/PhysRevB.83.132301

Chen, G. (2005). Nanoscale energy transport and conversion: a parallel treatment of electrons, molecules, phonons, and photons. *Oxford University Press*, 560 pages. ISBN-10: 019515942X

Chen, J., & King, S. D. (1998). The influence of temperature and depth dependent viscosity on geoid and topography profiles from models of mantle convection. *Phys. Earth Plan. Int., 106*(1-2), 75-92.

Chen, S., Hiraga, T., & Kohlstedt, D. L. (2006). Water weakening of clinopyroxene in the dislocation creep regime. *J. Geophys. Res. - Sol. Ea.*, *111*(8), 8203. https://doi.org/10.1029/2005JB003885.

Chepurov, A. I., Tomilenko, A. A., Zhimulev, E. I., Sonin, V. M., Chepurov, A. A., Kovyazin, S. V., … Surkov, N. V. (2012). The conservation of an aqueous fluid in inclusions in minerals and their interstices at high pressures and temperatures during the decomposition of antigorite. *Russ. Geol. Geophys.*, *53*(3), 234–246. https://doi.org/10.1016/j.rgg.2012.02.002

Christensen, N. I., & Mooney, W. D. (1995). Seismic velocity structure and composition of the continental crust: a global view. *J. Geophys. Res.*, *100*(B6), 9761–9788. https://doi.org/10.1029/95JB00259

Christensen, U. R., & Yuen, D. A. (1984). The interaction of a subducting lithospheric slab with a chemical or phase boundary. *J. Geophys. Res. - Sol. Ea., 89*(B6), 4389–4402. https://doi.org/10.1029/JB089iB06p04389

Christensen, U. R., & Yuen, D. A. (1985). Layered convection induced by phase transitions. *J. Geophys. Res., 90*(B12), 10291-10300.. https://doi.org/10.1029/jb090ib12p10291

Christensen, U. R. (2001). Geodynamic models of deep subduction. *Phys. Earth Plan. Int., 127*(1-4), 25-34. https://doi.org/10.1016/S0031-9201(01)00219-9

Chung, J. I., & Kagi, H. (2002). High concentration of water in stishovite in the MORB system. *Geophys. Res. Lett.*, *29*(21), 16-1-16–4. https://doi.org/10.1029/2002GL015579

Chyba, C. F. (1991). Terrestrial mantle siderophiles and the lunar impact record. *Icarus*, *92*(2), 217–233. https://doi.org/10.1016/0019-1035(91)90047-W

Chyba, C. F., Thomas, P. J., Brookshaw, L., & Sagan, C. (1990). Cometary delivery of organic molecules to the early earth. *Science*, *249*(4967), 366–373. https://doi.org/10.1126/science.11538074

Clayton, R. N., Mayeda, T. K., & Rubin, A. E. (1984). Oxygen isotopic compositions of enstatite chondrites and aubrites. *J. Geophys. Res.*, *89*(S01), C245. https://doi.org/10.1029/jb089is01p0c245

Coble, R. L. (1963). A model for boundary diffusion controlled creep in polycrystalline. *Mat. J. App. Phys., 34*(6), 1679–1682. https://doi.org/10.1063/1.1702656

Cockell, C. S. (1999). Life on Venus. *Plan. Space Sci.*, *47*(12), 1487–1501. https://doi.org/10.1016/S0032-0633(99)00036-7

Colli, L., Stotz, I., Bunge, H. P., Smethurst, M., Clark, S., Iaffaldano, G., … Bianchi, M. C. (2014). Rapid South Atlantic spreading changes and coeval vertical motion in surrounding continents: Evidence for temporal changes of pressure-driven upper mantle flow. *Tectonics, 33*(7), 1304–1321. https://doi.org/10.1002/2014TC003612

Coltice, N., & Shephard, G. E. (2018). Tectonic predictions with mantle convection models. *Geophys. J. Int., 213*(1), 16-29.. https://doi.org/10.1093/gji/ggx531

Coltice, N., Husson, L., Faccenna, C., & Arnould, M. (2019). What drives tectonic plates? *Sci. Adv.*, *5*(10), eaax4295. https://doi.org/10.1126/sciadv.aax4295

Connolly, J. A. D. (2005). Computation of phase equilibria by linear programming: A tool for geodynamic modeling and its application to subduction zone decarbonation. *Earth. Plan. Sci. Lett., 236*(1–2), 524–541. https://doi.org/10.1016/j.epsl.2005.04.033

Conrad, C. P., & Molnar, P. (1999). Convective instability of a boundary layer with temperature- and strain-rate-dependent viscosity in terms of "available buoyancy." *Geophys. J. Int., 139*(1), 51–68. https://doi.org/10.1046/j.1365-246X.1999.00896.x

Conrad, C. P., & Lithgow-Bertelloni, C. (2002). How mantle slabs drive plate tectonics. *Science*, *298*(5591), 207–209. https://doi.org/10.1126/science.1074161

Conrad, C. P., & Lithgow-Bertelloni, C. (2004). The temporal evolution of plate driving forces: Importance of "slab suction" versus "slab pull" during the Cenozoic. *J. Geophys. Res.- Sol. Ea.*, *109*(B10). https://doi.org/10.1029/2004JB002991

Cottaar, S., & Romanowicz, B. (2012). An unsually large ULVZ at the base of the mantle near Hawaii. *Earth Planet Sc. Lett.*, *355*, 213–222. https://doi.org/10.1016/j.epsl.2012.09.005

Coumou, D., Driesner, T., & Heinrich, C. A. (2008). The structure and dynamics of mid-ocean ridge hydrothermal systems. *Science*, *321*(5897), 1825–1828. https://doi.org/10.1126/science.1159582

Crameri, F, Schmeling, H., Golabek, G. J., Duretz, T., Orendt, R., H Buiter, S. J., … Tackley, P. J. (2012). A comparison of numerical surface topography calculations in geodynamic modelling: an evaluation of the 'sticky air' method. *Geophys. J. Int., 189*(1), 38-54. https://doi.org/10.1111/j.1365-246X.2012.05388.x

Crameri, F., Tackley, P. J., Meilick, I., Gerya, T. V., & Kaus, B. J. P. (2012). A free plate surface and weak oceanic crust produce single-sided subduction on Earth. *Geophys. Res. Lett., 39*(3), 1–7. https://doi.org/10.1029/2011GL050046

Crameri, F., & Tackley, P. J. (2014). Spontaneous development of arcuate single-sided subduction in global 3-D mantle convection models with a free surface. *J. Geophys. Res. - Sol. Ea., 119*(7), 5921–5942. https://doi.org/10.1002/2014JB010939

Crameri, F., & Tackley, P. J. (2015). Parameters controlling dynamically self-consistent plate tectonics and single-sided subduction in global models of mantle convection. *J. Geophys. Res. - Sol. Ea., 120*(5), 3680-3706. https://doi.org/10.1002/2014JB011664

Crameri, F., & Tackley, P. J. (2016). Subduction initiation from a stagnant lid and global overturn: new insights from numerical models with a free surface. *Prog. Earth Planet. Sci.*, 3(1), 1-19. https://doi.org/10.1186/s40645-016-0103-8

Crameri, F., Lithgow-Bertelloni, C. R., & Tackley, P. J. (2017). The dynamical control of subduction parameters on surface topography. *Geochem. Geophys. Geosys., 18*(4), 1661-1687. https://doi.org/10.1002/2017GC006821

Crameri, F. (2018). Geodynamic diagnostics, scientific visualisation and StagLab 3.0. *Geosci. Mod. Dev., 11*(6), 2541–2562. https://doi.org/10.5194/gmd-11-2541-2018

Crameri, F., Conrad, C. P., Montési, L., & Lithgow-Bertelloni, C. R. (2019). The dynamic life of an oceanic plate. *Tectonophysics*, 760, 107–135. https://doi.org/10.1016/j.tecto.2018.03.016

Crameri, F., Shephard, G. E., & Heron, P. J. (2020). The misuse of colour in science communication. *Nat. Comm., 11*(1), 1–10. https://doi.org/10.1038/s41467-020-19160-7

Cummins, P. R., Kennett, B. L. N., Bowman, J. R., & Bostock, M. G. (1992). The 520 km Discontinuity? *B. Seismol. Soc. Am.*, *82*(1), 323-336.

REFERENCES - D

Dal Zilio, L., Faccenda, M., & Capitanio, F. (2018). The role of deep subduction in supercontinent breakup. *Tectonophysics, 746*, 312–324. https://doi.org/10.1016/j.tecto.2017.03.006

Dalton, C. A., Langmuir, C. H., & Gale, A. (2014). Geophysical and geochemical evidence for deep temperature variations beneath mid-ocean ridges. *Science, 344*(6179), 80-83. https://doi.org/10.1126/science.1249466

Dalton, D. A., Hsieh, W. P., Hohensee, G. T., Cahill, D. G., & Goncharov, A. F. (2013). Effect of mass disorder on the lattice thermal conductivity of MgO periclase under pressure. *Sci. Rep., 3*(1), 1–5. https://doi.org/10.1038/srep02400

Dartnell, L. R. (2011). Ionizing radiation and life. *Astrobiology*, *11*(6), 551-582. https://doi.org/10.1089/ast.2010.0528

Dauphas, N., & Marty, B. (2002). Inference on the nature and the mass of Earth's late veneer from noble metals and gases. *J. Geophys. Res. E: Planets*, *107*(12), 5129. https://doi.org/10.1029/2001je001617

Dauphas, N., Marty, B., & Reisberg, L. (2002). Inference on terrestrial genesis from molybdenum isotope systematics. *Geophys. Res. Lett.*, *29*(6). https://doi.org/10.1029/2001GL014237

Dauphas, N. (2017). The isotopic nature of the Earth's accreting material through time. *Nature*, *541*(7638), 521–524. https://doi.org/10.1038/nature20830

Davaille, A., Smrekar, S. E., & Tomlinson, S. (2017). Experimental and observational evidence for plume-induced subduction on Venus. *Nat. Geosci., 10*(5), 349–355. https://doi.org/10.1038/ngeo2928

Davies, J. H., & Davies, D. R. (2010). Earth's surface heat flux. *Solid Earth, 1*(1), 5-24. https://doi.org/10.5194/se-1-5-2010

Davis, E. E., & Elderfield, H. (2004). Hydrogeology of the oceanic lithosphere. *Cambridge University Press*, 728 pages. 978110741423-5

Davis, T. A. (2004). Algorithm 832: UMFPACK V4.3-An Unsymmetric-Pattern Multifrontal Method. *ACM T. Mathem. Soft.* (TOMS), *30*(2), 196-199.

De Bremaecker, J. C. (1977). Convection in the earth's mantle. *Tectonophysics, 41*(1-3), 195-208.. https://doi.org/10.1016/0040-1951(77)90190-1

De Wijs, G. A., Kresse, G., Vočadlo, L., Dobson, D., Alfè, D., Gillan, M. J., & Price, G. D. (1998). The viscosity of liquid iron at the physical conditions of the Earth's core. *Nature, 392*(6678), 805-807. https://doi.org/10.1038/33905

Deschamps, F., Tackley, P. J., & Nakagawa, T. (2010). Temperature and heat flux scalings for isoviscous thermal convection in spherical geometry. *Geophys. J. Int., 182*(1), 137–154. https://doi.org/10.1111/j.1365-246X.2010.04637.x

Deschamps, F., & Hsieh, W.-P. (2019). Lowermost mantle thermal conductivity constrained from experimental data and tomographic models. *Geophys. J. Int., 219*(1), S115–S136. https://doi.org/10.1093/gji/ggz231

Descombes, P., Gaboriau, T., Albouy, C., Heine, C., Leprieur, F., & Pellissier, L. (2018). Linking species diversification to palaeo-environmental changes: A process-based modelling approach. *Global Ecol. Biogeogr.*, 27(2), 233–244. https://doi.org/10.1111/geb.12683

Dewaele, A., Torrent, M., Loubeyre, P., & Mezouar, M. (2008). Compression curves of transition metals in the Mbar range: Experiments and projector augmented-wave calculations. *Phys. Rev. B - Cond. Matt. Mat. Phys., 78*(10), 104102. https://doi.org/10.1103/PhysRevB.78.104102

Diao, Y., & Espinosa-Marzal, R. M. (2018). The role of water in fault lubrication. *Nat. Comm.*, 9(1), 1–10. https://doi.org/10.1038/s41467-018-04782-9

Diehl, R., Halloin, H., Kretschmer, K., Lichti, G. G., Schönfelder, V., Strong, A. W., … Wunderer, C. (2006). Radioactive 26Al from massive stars in the Galaxy. *Nature, 439*(7072), 45-47. https://doi.org/10.1038/nature04364

Dietz, R. S. (1961). Continent and ocean basin evolution by spreading of the sea floor. *Nature*, *190*(4779), 854–857. https://doi.org/10.1038/190854a0

Dilek, Y., & Furnes, H. (2014). Ophiolites and their origins. *Elements*, *10*(2), 93–100. https://doi.org/10.2113/gselements.10.2.93

Directorate Of Scientific Information Services Ottawa (Ontario).

Dorogokupets, P. I., Dymshits, A. M., Sokolova, T. S., Danilov, B. S., & Litasov, K. D. (2015). The equations of state of forsterite, wadsleyite, ringwoodite, akimotoite, $MgSiO_3$-perovskite, and postperovskite and phase diagram for the Mg_2SiO_4 system at pressures of up to 130GPa. *Russ. Geo. Geophys., 56*(1-2), 172-189. https://doi.org/10.1016/j.rgg.2015.01.011

Drake, M. J., & Righter, K. (2002). Determining the composition of the Earth. *Nature*, *416*(6876), 39-44. https://doi.org/10.1038/416039a

Duan, Y., Sun, N., Wang, S., Li, X., Guo, X., Ni, H., … Mao, Z. (2018). Phase stability and thermal equation of state of δ-AlOOH: Implication for water transportation to the Deep Lower Mantle. *Earth Planet Sc. Lett.*, *494*, 92–98. https://doi.org/10.1016/j.epsl.2018.05.003

Duarte, J. C., Schellart, W. P., & Cruden, A. R. (2015). How weak is the subduction zone interface? *Geophys. Res. Lett., 42*(8), 2664–2673. https://doi.org/10.1002/2014GL062876

Duba, A. (1972). Electrical conductivity of olivine. *J. Geophys. Res., 77*(14), 2483-2495. https://doi.org/10.1029/jb077i014p02483

Duncan, M. S., & Dasgupta, R. (2017). Rise of Earth's atmospheric oxygen controlled by efficient subduction of organic carbon. *Nat. Geosci., 10*(5), 387–392. https://doi.org/10.1038/ngeo2939

Duretz, T., May, D. A., Gerya, T. V., & Tackley, P. J. (2011). Discretization errors and free surface stabilization in the finite difference and marker-in-cell method for applied geodynamics: A numerical study. *Geochem. Geophys. Geosys., 12*(7).. https://doi.org/10.1029/2011GC003567

Duxbury, A. C., Duxbury, A. B., & Sverdrup, K. A. (1997). Introduction to the World's Oceans (6th Ed.). *McGraw-Hill College*

Dye, S. T. (2012). Geoneutrinos and the radioactive power of the Earth. *Rev. Geophys., 50*(3).. https://doi.org/10.1029/2012RG000400

Dziewonski, A. M., Hales, A. L., & Lapwood, E. R. (1975). Parametrically simple Earth models consistent with geophysical data. *Phys. Earth Planet. In.*, *10*(1), 12-48. https://doi.org/10.1016/0031-9201(75)90017-5

Dziewonski, A. M., & Anderson, D. L. (1981). Preliminary reference Earth model. *Phys. Earth Plan. Int., 25*(4), 297-356. https://doi.org/10.1016/0031-9201(81)90046-7

REFERENCES - E

Eakins, B.W., & Sharman, G.F. (2010). Volumes of the World's Oceans from ETOPO1, NOAA National Geophysical Data Center, Boulder, CO, 2010. *Earth Planet Sc. Lett., 211*(1–2), 189–203. https://doi.org/10.1016/S0012-821X(03)00200-0

Eggleton, R. A., Boland, J. N., & Ringwood, A. E. (1978). High pressure synthesis of a new aluminium silicate: $Al_5Si_5O_{17}(OH)$. *Geochem. J., 12*(3), 191–194. https://doi.org/10.2343/geochemj.12.191

Eichheimer, P., Thielmann, M., Fujita, W., Golabek, G. J., Nakamura, M., Okumura, S., … Kottwitz, M. O. (2020). Combined numerical and experimental study of microstructure and permeability in porous granular media. *Solid Earth, 11*(3), 1079–1095. https://doi.org/10.5194/se-11-1079-2020

El-Kadi, A. I., & Ling, G. (1993). The Courant and Peclet Number criteria for the numerical solution of the Richards Equation. *Water Resour. Res., 29*(10), 3485–3494. https://doi.org/10.1029/93WR00929

Enomoto, S., Ohtani, E., Inoue, K., & Suzuki, A. (2007). Neutrino geophysics with KamLAND and future prospects. *Earth Planet Sc. Lett., 258*(1-2), 147-159. https://doi.org/10.1016/j.epsl.2007.03.038

Ernst, W. G. (2017). Earth's thermal evolution, mantle convection, and Hadean onset of plate tectonics. *J. Asian. Earth Sci., 145*, 334–348. https://doi.org/10.1016/j.jseaes.2017.05.037

Erwin, D. H., Laflamme, M., Tweedt, S. M., Sperling, E. A., Pisani, D., & Peterson, K. J. (2011). The Cambrian conundrum: Early divergence and later ecological success in the early history of animals. *Science, 334*(6059), 1091–1097. https://doi.org/10.1126/science.1206375

Ewing, J., & Ewing, M. (1967). Sediment distribution on the mid-ocean ridges with respect to spreading of the sea floor. *Science, 156*(3782), 1590–1592. https://doi.org/10.1126/science.156.3782.1590

REFERENCES - F

Faccenda, M., Burlini, L., Gerya, T. V., & Mainprice, D. (2008). Fault-induced seismic anisotropy by hydration in subducting oceanic plates. *Nature, 455*(7216), 1097–1100. https://doi.org/10.1038/nature07376

Faccenda, M., Gerya, T. V, & Burlini, L. (2009). Deep slab hydration induced by bending-related variations in tectonic pressure. *Nat. Geosc., 2*(11), 790-793. https://doi.org/10.1038/NGEO656

Faccenda, M., & Mancktelow, N. S. (2010). Fluid flow during unbending: Implications for slab hydration, intermediate-depth earthquakes and deep fluid subduction. *Tectonophysics, 494*(1–2), 149–154. https://doi.org/10.1016/j.tecto.2010.08.002

Faccenda, M., Gerya, T. V., Mancktelow, N. S., & Moresi, L. (2012). Fluid flow during slab unbending and dehydration: Implications for intermediate-depth seismicity, slab weakening and deep water recycling. *Geochem. Geophys. Geosyst., 13*(1). https://doi.org/10.1029/2011GC003860

Faccenda, M. (2014). Water in the slab: A trilogy. *Tectonophysics, 614*, 1-30. https://doi.org/10.1016/j.tecto.2013.12.020

Faccenda, M., & Dal Zilio, L. (2017). The role of solid–solid phase transitions in mantle convection. *Lithos*, 268–271, 198–224. https://doi.org/10.1016/j.lithos.2016.11.007

Fefferman, C. L. (2006). Existence and smoothness of the Navier-Stokes equation. *The millennium prize problems*, 57(67), 22.

Fegley, B. . J., Treiman, A., Fegley, B. . J., & Treiman, A. (1992). Chemistry of the surface and lower atmosphere of Venus. *Astronomicheskii Vestnik, 26*(2), 3–65.

Fei, H., Wiedenbeck, M., Yamazaki, D., & Katsura, T. (2013). Small effect of water on upper-mantle rheology based on silicon self-diffusion coefficients. *Nature, 498*(7453), 213–215. https://doi.org/10.1038/nature12193

Fei, H., Yamazaki, D., Sakurai, M., Miyajima, N., Ohfuji, H., Katsura, T., & Yamamoto, T. (2017). A nearly water-saturated mantle transition zone inferred from mineral viscosity. *Sci. Adv., 3*(6), 1–8. https://doi.org/10.1126/sciadv.1603024

Fei, H., & Katsura, T. (2020). High water solubility of ringwoodite at mantle transition zone temperature. *Earth Planet Sc. Lett., 531*, 115987. https://doi.org/10.1016/j.epsl.2019.115987

Fei, Y., Van Orman, J., Li, J., van Westrenen, W., Sanloup, C., Minarik, W., … Funakoshi, K. (2004). Experimentally determined postspinel transformation boundary in Mg_2SiO_4 using MgO as an internal pressure standard and its geophysical implications. *J. Geophys. Res. - Sol. Ea., 109*(B2). https://doi.org/10.1029/2003JB002562

Ferrand, T. P., Hilairet, N., Incel, S., Deldicque, D., Labrousse, L., Gasc, J., … Schubnel, A. (2017). Dehydration-driven stress transfer triggers intermediate-depth earthquakes. *Nat. Comm., 8*(1), 1–11. https://doi.org/10.1038/ncomms15247

Fialko, Y. (2006). Interseismic strain accumulation and the earthquake potential on the southern San Andreas fault system. *Nature, 441*(7096), 968–971. https://doi.org/10.1038/nature04797

Figgis, B. N., & Hitchman, M. A. (1999). Ligand field theory and its applications (1st Ed.). Wiley, 376 pages. ISBN-10 : 0471317764

Fischer, D. A., Howard, A. W., Laughlin, G. P., Macintosh, B., Mahadevan, S., Sahlmann, J., & Yee, J. C. (2015). Exoplanet Detection Techniques. *Protostars and Planets VI*. arXiv preprint arXiv:1505.06869. https://doi.org/10.2458/azu_uapress_9780816531240-ch031

Fitoussi, C., & Bourdon, B. (2012). Silicon isotope evidence against an enstatite chondrite earth. *Science, 335*(6075), 1477-1480. https://doi.org/10.1126/science.1219509

Flamini, E. (2014). The earth: One of the planets of the solar system. *Rendiconti Lincei, 25*(1), 13-20. https://doi.org/10.1007/s12210-013-0275-8

Foley, B. J., & Becker, T. W. (2009). Generation of plate-like behavior and mantle heterogeneity from a spherical, viscoplastic convection model. *Geochem. Geophys. Geosys*, *10*(8). https://doi.org/10.1029/2009GC002378

Ford, P. G., & Pettengill, G. H. (1992). Venus topography and kilometer-scale slopes. *J. Geophys. Res., 97*(E8), 103–116. https://doi.org/10.1029/92je01085

Forman, R. A., Piermarini, G. J., Dean Barnett, J., & Block, S. (1972). Pressure measurement made by the utilization of ruby sharp-line luminescence. *Science, 176*(4032), 284-285. https://doi.org/10.1126/science.176.4032.284

Fornberg, B. (1996). A Practical Guide to Pseudospectral Methods. *Cambridge University Press*, 244 pages. https://doi.org/10.1017/cbo9780511626357

Forsyth, D., & Uyeda, S. (1975). On the relative importance of the driving forces of plate motion. *Geophys. J. Int., 43*(1), 163–200. https://doi.org/10.1111/j.1365-246X.1975.tb00631.x

Forte, A. M., & Mitrovica, J. X. (1996). New inferences of mantle viscosity from joint inversion of long-wavelength mantle convection and post-glacial rebound data. *Geophys. Res. Lett., 23*(10), 1147–1150. https://doi.org/10.1029/96GL00964

Fowler, A. C., & O'Brien, S. B. G. (1996). A mechanism for episodic subduction on Venus. *J. Geophys. Res. - Plan., 101*(E2), 4755–4763. https://doi.org/10.1029/95JE03261

Frost, D. A., & Rost, S. (2014). The P-wave boundary of the Large-Low Shear Velocity Province beneath the Pacific. *Earth Planet Sc. Lett., 403*, 380–392. https://doi.org/10.1016/j.epsl.2014.06.046

Frost, D. J. (1999). The stability of dense hydrous magnesium silicates in Earth's transition zone and lower mantle. Mantle Petrology: Field Observations and High Pressure Experimentation: A Tribute to Francis R.(Joe) Boyd. *The Geochemical Society*, (6), 283–296.

Frost, D. J. (2003). The structure and sharpness of $(Mg,Fe)_2SiO_4$ phase transformations in the transition zone. *Earth Plan. Sci. Lett., 216*(3), 313-328. https://doi.org/10.1016/S0012-821X(03)00533-8

Frost, D. J. (2008). The Upper Mantle and Transition Zone. *Elements, 4*(3), 171–176. https://doi.org/10.2113/GSELEMENTS.4.3.171

Fu, S., Yang, J., Karato, S. I., Vasiliev, A., Presniakov, M. Y., Gavrilliuk, A. G., … Lin, J. F. (2019). Water Concentration in Single-Crystal (Al,Fe)-Bearing Bridgmanite Grown From the Hydrous Melt: Implications for Dehydration Melting at the Topmost Lower Mantle. *Geophys. Res. Lett., 46*(17–18), 10346–10357. https://doi.org/10.1029/2019GL084630

Fukai, Y. (1984). The iron-water reaction and the evolution of the Earth. *Nature, 308*(5955), 174–175. https://doi.org/10.1038/308174a0

Fukai, Y. (1992). Some Properties of the Fe-H System at High Pressures and Temperatures, and their Implications for the Earth's Core. *Geoph. Monog. Series, AGU*, 373–385. https://doi.org/10.1029/gm067p0373

Fukao, Y., Hori, S., & Ukawa, M. (1983). A seismological constraint on the depth of basalt-eclogite transition in a subducting oceanic crust. *Nature, 303*(5916), 413–415. https://doi.org/10.1038/303413a0

Fukao, Y., Obayashi, M., Nakakuki, T., Utada, H., Suetsugu, D., Irifune, T., … Hirose, K. (2009). Stagnant slab: A review. *Ann. Rev. Earth and Plan. Sci., 37*, 19-46. https://doi.org/10.1146/annurev.earth.36.031207.124224

Fukui, H., Tsuchiya, T., & Baron, A. Q. R. (2012). Lattice dynamics calculations for ferropericlase with internally consistent LDA+U method. *J. Geophys. Res. B - Sol. Ea., 117*(B12). https://doi.org/10.1029/2012JB009591

Fumagalli, P., Stixrude, L., Poli, S., & Snyder, D. (2001). The 10Å phase: A high-pressure expandable sheet silicate stable during subduction of hydrated lithosphere. *Earth Planet Sc. Lett., 186*(2), 125–141. https://doi.org/10.1016/S0012-821X(01)00238-2

REFERENCES - G

Gale, A., Dalton, C. A., Langmuir, C. H., Su, Y., & Schilling, J. G. (2013). The mean composition of ocean ridge basalts. *Geochem. Geophys. Geosyst., 14*(3), 489–518. https://doi.org/10.1029/2012GC004334

Galer, S. J. G., & O'Nions, R. K. (1985). Residence time of thorium, uranium and lead in the mantle with implications for mantle convection. *Nature , 316*(6031), 778-782. https://doi.org/10.1038/316778a0

Galer, S. J. G. (1991). Interrelationships between continental freeboard, tectonics and mantle temperature. *Earth Planet Sc. Lett., 105*(1–3), 214–228. https://doi.org/10.1016/0012-821X(91)90132-2

Garnero, E. J., & Helmberger, D. V. (1996). Seismic detection of a thin laterally varying boundary layer at the base of the mantle beneath the central-Pacific. *Geophys. Res. Lett., 23*(9), 977–980. https://doi.org/10.1029/95GL03603

Gasparik, T. (1989). Transformation of enstatite-diopside-jadeite pyroxenes to garnet. *Contrib. Min. Petr., 102*(4), 389-405. https://doi.org/10.1007/BF00371083

Gerlach, T. M. (2004). Volcanic sources of tropospheric ozone-depleting trace gases. *Geochem. Geophys. Geosyst., 5*(9), 9007. https://doi.org/10.1029/2004GC000747

Gerya, T. V., & Yuen, D. A. (2007). Robust characteristics method for modelling multiphase visco-elasto-plastic thermo-mechanical problems. *Phys. Earth Plan. In., 163*(1–4), 83–105. https://doi.org/10.1016/j.pepi.2007.04.015

Gerya, T. (2019). Introduction to Numerical Geodynamic Modelling (2nd Ed.). *Cambridge University Press*, 484 pages. https://doi.org/10.1017/9781316534243

Giacovazzo, C., Monaco, H. L., Artioli, G., Viterbo, D., Milanesio, M., Gilli, G., … Catti, M. (2013). Fundamentals of crystallography (Vol. 7). *Oxford University Press*, 842 pages https://doi.org/10.1093/acprof:oso/9780199573653.001.0001

Giesting, P. A., Hofmeister, A. M., Wopenka, B., Gwanmesia, G. D., & Jolliff, B. L. (2004). Thermal conductivity and thermodynamics of majoritic garnets: Implications for the transition zone. *Earth Plan. Sci. Lett., 218*(1–2), 45–56. https://doi.org/10.1016/S0012-821X(03)00630-7

Giggenbach, W. F. (1996). Chemical Composition of Volcanic Gases. In Monitoring and Mitigation of Volcano Hazards (pp. 221–256). Springer Berlin Heidelberg. https://doi.org/10.1007/978-3-642-80087-0_7

Gillmann, C., & Tackley, P. (2014). Atmosphere/mantle coupling and feedbacks on Venus. *J. Geophys. Res. E - Plan., 119*(6), 1189-1217. https://doi.org/10.1002/2013JE004505

Gillmann, C., Golabek, G. J., & Tackley, P. J. (2016). Effect of a single large impact on the coupled atmosphere-interior evolution of Venus. *Icarus, 268*, 295–312. https://doi.org/10.1016/j.icarus.2015.12.024

Gillmann, C., Golabek, G. J., Raymond, S. N., Schönbächler, M., Tackley, P. J., Dehant, V., & Debaille, V. (2020). Dry late accretion inferred from Venus's coupled atmosphere and internal evolution. *Nat. Geosci., 13*(4), 265–269. https://doi.org/10.1038/s41561-020-0561-x

Glassmeier, K. H., Boehnhardt, H., Koschny, D., Kührt, E., & Richter, I. (2007). The Rosetta mission: Flying towards the origin of the solar system. *Space Sci. Rev., 128*(1–4), 1–21. https://doi.org/10.1007/s11214-006-9140-8

Glatzmaier, G. A., & Roberts, P. H. (1995). A three-dimensional convective dynamo solution with rotating and finitely conducting inner core and mantle. *Phys. Earth Planet. In., 91*(1–3), 63–75. https://doi.org/10.1016/0031-9201(95)03049-3

Goes, S., Agrusta, R., van Hunen, J., & Garel, F. (2017). Subduction-transition zone interaction: A review. *Geosphere, 13*(3), 644–664. https://doi.org/10.1130/GES01476.1

Golabek, G. J., Keller, T., Gerya, T. V., Zhu, G., Tackley, P. J., & Connolly, J. A. D. (2011). Origin of the martian dichotomy and Tharsis from a giant impact causing massive magmatism. *Icarus, 215*(1), 346-357. https://doi.org/10.1016/j.icarus.2011.06.012

Goldstein, J. I., Newbury, D. E., Michael, J. R., Ritchie, N. W. M., Scott, J. H. J., Joy, D. C., … Joy, D. C. (2018). Scanning Electron Microscopy and X-Ray Microanalysis. *Springer*, 573 pages. https://doi.org/10.1007/978-1-4939-6676-9_5

Gomes, R., Levison, H. F., Tsiganis, K., & Morbidelli, A. (2005). Origin of the cataclysmic Late Heavy Bombardment period of the terrestrial planets. *Nature, 435*(7041), 466–469. https://doi.org/10.1038/nature03676

Goncharov, A. F., Haugen, B. D., Struzhkin, V. V., Beck, P., & Jacobsen, S. D. (2008). Radiative conductivity in the Earth's lower mantle. *Nature , 456*(7219), 231-234. https://doi.org/10.1038/nature07412

Goncharov, A. F., Beck, P., Struzhkin, V. V., Haugen, B. D., & Jacobsen, S. D. (2009). Thermal conductivity of lower-mantle minerals. *Phys. Earth Planet. In, 174*(1–4), 24–32. https://doi.org/10.1016/j.pepi.2008.07.033

Gough, D. O. (1969). The Anelastic Approximation for Thermal Convection. *J. Atm. Sci., 26*(3), 448-456. https://doi.org/10.1175/1520-0469(1969)026<0448:taaftc>2.0.co;2

Grand, S. P. (2002). Mantle shearwave tomography and the fate of subducted slabs. *Philos. Trans. Roy. Soc. London Ser. - A: Mat. Phys. Eng. Sci., 360*(1800), 2475–2491. https://doi.org/10.1098/RSTA.2002.1077

Green, D. H., & Ringwood, A. E. (1972). A Comparison of Recent Experimental Data on the Gabbro-Garnet Granulite-Eclogite Transition. *J. Geol., 80*(3), 277–288. https://doi.org/10.1086/627731

Green, D. H. (1973). Experimental melting studies on a model upper mantle composition at high pressure under water-saturated and water-undersaturated conditions. *Earth Planet Sc. Lett., 19*(1), 37–53. https://doi.org/10.1016/0012-821X(73)90176-3

Green, D. H., Hibberson, W. O., Kovács, I., & Rosenthal, A. (2010). Water and its influence on the lithosphere-asthenosphere boundary. *Nature, 467*(7314), 448–451. https://doi.org/10.1038/nature09369

Green, D. H., & Falloon, T. J. (2015). Mantle-derived magmas: intraplate, hot-spots and mid-ocean ridges. *Sci. Bull., 60*(22), 1873-1900. https://doi.org/10.1007/s11434-015-0920-y

Green, H. W., Chen, W. P., & Brudzinski, M. R. (2010). Seismic evidence of negligible water carried below 400-km depth in subducting lithosphere. *Nature, 467*(7317), 828–831. https://doi.org/10.1038/nature09401

Grevemeyer, I., Ranero, C. R., & Ivandic, M. (2018). Structure of oceanic crust and serpentinization at subduction trenches. *Geosphere, 14*(2), 395–418. https://doi.org/10.1130/GES01537.1

Griggs, D. T. (1939). A theory of mountain-building. *Am. J. Sci., 237*(9), 611–650. https://doi.org/10.2475/ajs.237.9.611

Griggs, D. T.(1967). Hydrolytic Weakening of Quartz and Other Silicates. *Geophys. J. Int., 14*(1–4), 19–31. https://doi.org/10.1111/j.1365-246X.1967.tb06218.x

Grinspoon, D. (2013). The surface and atmosphere of venus: Evolution and present state. In Towards Understanding the Climate of Venus: Applications of Terrestrial Models to Our Sister Planet. *Springer New York*, *11*, 17–22. https://doi.org/10.1007/978-1-4614-5064-1_3

Grüninger, H., Armstrong, K., Greim, D., Boffa-Ballaran, T., Frost, D. J., & Senker, J. (2017). Hidden Oceans? Unraveling the Structure of Hydrous Defects in the Earth's Deep Interior. *J. Am. Chem. Soc., 139*(30), 10499-10505. https://doi.org/10.1021/jacs.7b05432

Grüninger, H., Schmutzler, A., Siegel, R., Armstrong, K., Frost, D. J., & Senker, J. (2018). Quantitative description of 1H SQ and DQ coherences for the hydroxyl disorder within hydrous ringwoodite. *Phys. Chem. Chem., 20*(22), 15098-15105. Phys.. https://doi.org/10.1039/c8cp00863a

Grüninger, H., Liu, Z., Brauckmann, J. O., Fei, H., Ballaran, T. B., Martin, T., … Senker, J. (2020). Hydroxyl Defects and Oxide Vacancies within Ringwoodite - Toward Understanding the Defect Chemistry of Spinel-Type Oxides. *J. Phys. Chem. C., 124*(22), 12001-12009. https://doi.org/10.1021/acs.jpcc.0c03016

Guerrero, J. M., Lowman, J. P., Deschamps, F., & Tackley, P. J. (2018). The Influence of Curvature on Convection in a Temperature-Dependent Viscosity Fluid: Implications for the 2D and 3D Modeling of Moons. *J. Geophys. Res.: Planets, 123*(7), 1863-1880. https://doi.org/10.1029/2017JE005497

Guerrero, J. M., Lowman, J. P., & Tackley, P. J. (2019). Spurious Transitions in Convective Regime Due to Viscosity Clipping: Ramifications for Modeling Planetary Secular Cooling. *Geochem. Geophys. Geosys., 20*(7), 3450-3468. https://doi.org/10.1029/2019GC008385

Guerri, M., Cammarano, F., & Tackley, P. J. (2016). Modelling Earth's surface topography: Decomposition of the static and dynamic components. *Phys. Earth Plan. In., 261*, 172-186. https://doi.org/10.1016/j.pepi.2016.10.009

Gueydan, F., Précigout, J., & Montési, L. G. J. (2014). Strain weakening enables continental plate tectonics. *Tectonophysics, 631*(C), 189–196. https://doi.org/10.1016/j.tecto.2014.02.005

Gülcher, A. J. P., Gebhardt, D. J., Ballmer, M. D., & Tackley, P. J. (2020). Variable dynamic styles of primordial heterogeneity preservation in the Earth's lower mantle. *Earth. Plan. Sci. Lett., 536*, 116160. https://doi.org/10.1016/j.epsl.2020.116160

Gülcher, A. J. P., Gerya, T. V., Montési, L. G. J., & Munch, J. (2020). Corona structures driven by plume–lithosphere interactions and evidence for ongoing plume activity on Venus. *Nat. Geosci., 13*(8), 547–554. https://doi.org/10.1038/s41561-020-0606-1

Gutenberg, B. (1913). Uber die Konstitution des Erdinnern, erschlossen aus Erdbebenbeobachtungen. *Phys. Z*, 14, 1217–1218.

Gutenberg, B. (1925). Der Aufbau Der Erde. *Gebrüder Borntraeger*, Berlin, 168 pages, 23 figures

REFERENCES - H

Hacker, B. R., Abers, G. A., & Peacock, S. M. (2003). Subduction factory 1. Theoretical mineralogy, densities, seismic wave speeds, and H_2O contents. *J. Geophys. Res.- Sol. Ea., 108*(B1), 2029. https://doi.org/10.1029/2001jb001127

Hacker, B. R., Peacock, S. M., Abers, G. A., & Holloway, S. D. (2003). Subduction factory 2. Are intermediate-depth earthquakes in subducting slabs linked to metamorphic dehydration reactions? *J. Geophys. Res.- Sol. Ea., 108*(B1), 2030. https://doi.org/10.1029/2001jb001129

Hacker, B. R. (2008). H_2O subduction beyond arcs. *Geochem. Geophys. Geosyst., 9*(3). https://doi.org/10.1029/2007GC001707

Hall, C. E., Gurnis, M., Sdrolias, M., Lavier, L. L., & Müller, R. D. (2003). Catastrophic initiation of subduction following forced convergence across fracture zones. *Earth Planet Sc. Lett., 212*(1–2), 15–30. https://doi.org/10.1016/S0012-821X(03)00242-5

Hallis, L. J., Huss, G. R., Nagashima, K., Taylor, G. J., Halldórsson, S. A., Hilton, D. R., … Meech, K. J. (2015). Evidence for primordial water in Earth's deep mantle. *Science, 350*(6262), 795–797. https://doi.org/10.1126/science.aac4834

Hamilton, C. W., Beggan, C. D., Still, S., Beuthe, M., Lopes, R. M. C., Williams, D. A., … Wright, W. (2013). Spatial distribution of volcanoes on Io: Implications for tidal heating and magma ascent. *Earth Planet Sc. Lett., 361*, 272–286. https://doi.org/10.1016/j.epsl.2012.10.032

Handy, M. R. (1989). Deformation regimes and the rheological evolution of fault zones in the lithosphere: the effects of pressure, temperature, grainsize and time. *Tectonophysics, 163*(1–2), 119–152. https://doi.org/10.1016/0040-1951(89)90122-4

Hansen, L. N., Zimmerman, M. E., & Kohlstedt, D. L. (2011). Grain boundary sliding in San Carlos olivine: Flow law parameters and crystallographic-preferred orientation. *J. Geophys. Res., 116*(B8), B08201. https://doi.org/10.1029/2011JB008220

Harlow, F. H., & Welch, J. E. (1965). Numerical calculation of time-dependent viscous incompressible flow of fluid with free surface. *Physics of Fluids, 8*(12), 2182-2189. https://doi.org/10.1063/1.1761178

Hart, S. R., & Zindler, A. (1986). In search of a bulk-Earth composition. *Chem. Geol., 57*(3-4), 247-267. https://doi.org/10.1016/0009-2541(86)90053-7

Hartogh, P., Lis, D. C., Bockelée-Morvan, D., De Val-Borro, M., Biver, N., Küppers, M., … Blake, G. A. (2011). Ocean-like water in the Jupiter-family comet 103P/Hartley 2. *Nature, 478*(7368), 218–220. https://doi.org/10.1038/nature10519

Haskell, N. A. (1935). The motion of a viscous fluid under a surface load. *J. Appl. Phys., 6*(8), 265–269. https://doi.org/10.1063/1.1745329

Haskell, N. A. (1936). The motion of a viscous fluid under a surface load. Part II. *J. Appl. Phys., 7*(2), 56–61. https://doi.org/10.1063/1.1745362

Haskell, N. A. (1937). The viscosity of the asthenosphere. *Am. J. Sci., s5-33*(193), 22–28. https://doi.org/10.2475/ajs.s5-33.193.22

Hassan, S. R., Islam, T., Ali, M., & Islam, M. Q. (2014). Numerical study on aerodynamic drag reduction of racing cars. *Procedia Engineering, 90*, 308-313. https://doi.org/10.1016/j.proeng.2014.11.854

Hauck, S. A., Phillips, R. J., & Price, M. H. (1998). Venus: Crater distribution and plains resurfacing models. *J. Geophys. Res. - Plan., 103*(E6), 13635–13642. https://doi.org/10.1029/98JE00400

Haussühl, S. (2008). Physical Properties of Crystals: An Introduction. Physical Properties of Crystals: An Introduction. *John Wiley & Sons*, 453 pages https://doi.org/10.1002/9783527621156

Hawkesworth, C. J., Cawood, P. A., & Dhuime, B. (2016). Tectonics and crustal evolution. *GSA Today, 26*(9), 4–11. https://doi.org/10.1130/GSATG272A.1

Heezen, B. C., & Ewing, M. (2019). The Mid-Oceanic Ridge and its Extension through the Arctic Basin. In Geology of the Arctic (pp. 622–642). *University of Toronto Press*. https://doi.org/10.3138/9781487584979-055

Heinz, D. L., & Jeanloz, R. (1987). Measurement of the melting curve of Mg 0.9 Fe 0.1 SiO 3 at lower mantle conditions and its geophysical implications. *J. Geophys. Res. - Sol. Ea.*, 92(B11), 11437–11444. https://doi.org/10.1029/JB092iB11p11437

Hernlund, J. W., Thomas, C., & Tackley, P. J. (2005). A doubling of the post-perovskite phase boundary and structure of the Earth's lowermost mantle. *Nature, 434*(7035), 882–886. https://doi.org/10.1038/nature03472

Hernlund, J. W., & Tackley, P. J. (2008). Modeling mantle convection in the spherical annulus. *Phys. Earth Plan. In., 171*(1–4), 48–54. https://doi.org/10.1016/j.pepi.2008.07.037

Herrick, R. R. (1994). Resurfacing history of Venus. *Geology, 22*(8), 703–706. https://doi.org/10.1130/0091-7613(1994)022<0703:RHOV>2.3.CO;2

Herring, C. (1950). Diffusional viscosity of a polycrystalline solid. *J. App. Phys.*, *21*(5), 437–445. https://doi.org/10.1063/1.1699681

Hess, H. H., Engel, A. E. J., James, H. L., & Leonard, B. F. (1962). History of ocean basins. Petrologic Studies: A Volume to Honor A. F. Buddington, *Geo. Soc. Am.*, Boulder, 599-620.

Hewitt, J. M., McKenzie, D. P., & Weiss, N. O. (1975). Dissipative heating in convective flows. *J. Fluid Mech., 68*(4), 721–738. https://doi.org/10.1017/S002211207500119X

Higo, Y., Inoue, T., Irifune, T., & Yurimoto, H. (2001). Effect of water on the spinel-postspinel transformation in Mg_2SiO_4. *Geophys. Res. Lett., 28*(18), 3505–3508. https://doi.org/10.1029/2001GL013194

Hirose, K. (2002). Phase transitions in pyrolitic mantle around 670-km depth: Implications for upwelling of plumes from the lower mantle. *J. Geophys. Res. - Sol. Ea., 107*(B4), ECV 3-1-ECV 3-13. https://doi.org/10.1029/2001JB000597

Hirschmann, M. M. (2006). Water, melting, and the deep Earth H_2O cycle. *Annu. Rev. Earth Pl. Sc., 34*,629–653. https://doi.org/10.1146/annurev.earth.34.031405.125211

Hirth, G., & Kohlstedt, D. (2003). Rheology of the Upper Mantle and the Mantle Wedge: A View from the Experimentalists. *Geophys. Monog. AGU, 138,* 83-106. https://doi.org/10.1029/138GM06

Hoffman, J. H., Hodges, R. R., Donahue, T. M., & McElroy, M. B. (1980). Composition of the Venus lower atmosphere from the Pioneer Venus Mass Spectrometer. *J. Geophys. Res., 85*(A13), 7882. https://doi.org/10.1029/ja085ia13p07882

Hofmann, A. W. (1988). Chemical differentiation of the Earth: the relationship between mantle, continental crust, and oceanic crust. *Earth Planet Sc. Lett., 90*(3), 297–314. https://doi.org/10.1016/0012-821X(88)90132-X

Hofmeister, A. M. (1999). Mantle values of thermal conductivity and the geotherm from phonon lifetimes. *Science, 283*(5408), 1699–1706. https://doi.org/10.1126/science.283.5408.1699

Höink, T., & Lenardic, A. (2008). Three-dimensional mantle convection simulations with a low-viscosity asthenosphere and the relationship between heat flow and the horizontal length scale of convection. *Geophys. Res. Lett., 35*(10). https://doi.org/10.1029/2008GL033854

Holder, R. M., Viete, D. R., Brown, M., & Johnson, T. E. (2019). Metamorphism and the evolution of plate tectonics. *Nature, 572*(7769), 378–381. https://doi.org/10.1038/s41586-019-1462-2

Hole, M. J., & Millett, J. M. (2016). Controls of mantle potential temperature and lithospheric thickness on magmatism in the North Atlantic igneous province. *J. Petrol., 57*(2), 417-436.. https://doi.org/10.1093/petrology/egw014

Holland, T. B., Hudson, N. F. C., Powell, R., & Harte, B. (2013). Newthermodynamic models and calculated phase equilibria in NCFMAS for basic and ultrabasic compositions through thetransition zone into the uppermost lower mantle. *J. Petr., 54*(9), 1901–1920. https://doi.org/10.1093/petrology/egt035

Holmes, A. (1931). Radioactivity and earth movements. *Nature, 128*(3229), 496-496. https://doi.org/10.1038/128496e0

Holmes, A. (1933). The thermal history of the earth. *J. Washington Acad. Sci., 23*(4), 169-195.

Honda, S. (2016). Slab stagnation and detachment under northeast China. *Tectonophysics, 671*, 127-138. https://doi.org/10.1016/j.tecto.2016.01.025

Hopkins, M., Harrison, T. M., & Manning, C. E. (2008). Low heat flow inferred from >4 Gyr zircons suggests Hadean plate boundary interactions. *Nature, 456*(7221), 493–496. https://doi.org/10.1038/nature07465

Houser, C. (2016). Global seismic data reveal little water in the mantle transition zone. *Earth Planet Sc. Lett., 448*, 94–101. https://doi.org/10.1016/j.epsl.2016.04.018

Hrma, P. (2008). Arrhenius model for high-temperature glass-viscosity with a constant pre-exponential factor. *J. Non-Cryst. Sol., 354*(18), 1962–1968. https://doi.org/10.1016/j.jnoncrysol.2007.11.016

Hsieh, W. P., Chen, B., Li, J., Keblinski, P., & Cahill, D. G. (2009). Pressure tuning of the thermal conductivity of the layered muscovite crystal. *Phys. Rev. B - Cond. Matt. Mat. Phys., 80*(18), 180302. https://doi.org/10.1103/PhysRevB.80.180302

Hsieh, W. P., & Cahill, D. G. (2011). Ta and Au(Pd) alloy metal film transducers for time-domain thermoreflectance at high pressures. *J. App. Phys., 109*(11), 113520.. https://doi.org/10.1063/1.3592882

Hsieh, W. P., Losego, M. D., Braun, P. V., Shenogin, S., Keblinski, P., & Cahill, D. G. (2011). Testing the minimum thermal conductivity model for amorphous polymers using high pressure. *Phys. Rev. B - Cond. Matt. Mat. Phys., 83*(17), 174205. https://doi.org/10.1103/PhysRevB.83.174205

Hsieh, W. P. (2015). Thermal conductivity of methanol-ethanol mixture and silicone oil at high pressures. *J. App. Phys., 117*(23), 235901. https://doi.org/10.1063/1.4922632

Hsieh, W. P., Deschamps, F., Okuchi, T., & Lin, J. F. (2017). Reduced lattice thermal conductivity of Fe-bearing bridgmanite in Earth's deep mantle. *J. Geophys. Res.- Sol. Ea., 122*(7), 4900-4917. https://doi.org/10.1002/2017JB014339

Hsieh, W. P., Deschamps, F., Okuchi, T., & Lin, J. F. (2018). Effects of iron on the lattice thermal conductivity of Earth's deep mantle and implications for mantle dynamics. *P. Natl. A. Sci. - USA., 115*(16), 4099-4104. https://doi.org/10.1073/pnas.1718557115

Hsieh, W. P., Goncharov, A. F., Labrosse, S., Holtgrewe, N., Lobanov, S. S., Chuvashova, I., … Lin, J. F. (2020). Low thermal conductivity of iron-silicon alloys at Earth's core conditions with implications for the geodynamo. *Nat. Comm., 11*(1), 1–7. https://doi.org/10.1038/s41467-020-17106-7

Hu, Q., Kim, D. Y., Yang, W., Yang, L., Meng, Y., Zhang, L., & Mao, H. K. (2016). FeO_2 and FeOOH under deep lower-mantle conditions and Earth's oxygen-hydrogen cycles. *Nature, 534*(7606), 241–244. https://doi.org/10.1038/nature18018

Huang, X., Xu, Y., & Karato, S. I. (2005). Water content in the transition zone from electrical conductivity of wadsleyite and ringwoodite. *Nature, 434*(7034), 746–749. https://doi.org/10.1038/nature03426

Huang, Y., Nakatani, T., Nakamura, M., & McCammon, C. (2019). Saline aqueous fluid circulation in mantle wedge inferred from olivine wetting properties. *Nat. Comm., 10*(1), 1–10. https://doi.org/10.1038/s41467-019-13513-7

Huang, Y., Nakatani, T., Nakamura, M., & McCammon, C. (2020). Experimental constraint on grain-scale fluid connectivity in subduction zones. *Earth Planet Sc. Lett., 552*, 116610. https://doi.org/10.1016/j.epsl.2020.116610

Huppertz, H. (2004). Multianvil high-pressure/high-temperature preparation, crystal structure, and properties of the new oxoborates $Dy_4B_6O_{14}(OH)_2$ and $Ho_4B_6O_{14}(OH)_2$. *J. Sol. State Chem., 177*(10), 3700-3708.. https://doi.org/10.1016/j.jssc.2004.06.026

Hutko, A. R., Lay, T., Garnero, E. J., & Revenaugh, J. (2006). Seismic detection of folded, subducted lithosphere at the core-mantle boundary. *Nature, 441*(7091), 333–336. https://doi.org/10.1038/nature04757

Hutko, A. R., Lay, T., Revenaugh, J., & Garnero, E. J. (2008). Anticorrelated seismic velocity anomalies from post-perovskite in the lowermost mantle. *Science, 320*(5879), 1070–1074. https://doi.org/10.1126/science.1155822

Ildefonse, B., Blackman, D. K., John, B. E., Ohara, Y., Miller, D. J., MacLeod, C. J., … Zhao, X. (2007). Oceanic core complexes and crustal accretion at slow-speading ridges. *Geology, 35*(7), 623–626. https://doi.org/10.1130/G23531A.1

REFERENCES - I

Inoue, T., Wada, T., Sasaki, R., & Yurimoto, H. (2010). Water partitioning in the Earth's mantle. *Phys. Earth Planet. In., 183*(1–2), 245–251. https://doi.org/10.1016/j.pepi.2010.08.003

Irifune, T., & Ringwood, A. E. (1987). Phase transformations in a harzburgite composition to 26 GPa: implications for dynamical behaviour of the subducting slab. *Earth Planet Sc. Lett., 86*(2–4), 365–376. https://doi.org/10.1016/0012-821X(87)90233-0

Irifune, T., & Ringwood, A. E. (1993). Phase transformations in subducted oceanic crust and buoyancy relationships at depths of 600-800 km in the mantle. *Earth Plan. Sci. Lett., 117*(1–2), 101–110. https://doi.org/10.1016/0012-821X(93)90120-X

Irifune, T., & Isshiki, M. (1998). Iron partitioning in a pyrolite mantle and the nature of the 410-km seismic discontinuity. *Nature, 392*(6677), 702-705. https://doi.org/10.1038/33663

Irifune, T., Kubo, N., Isshiki, M., & Yamasaki, Y. (1998). Phase transformations in serpentine and transportation of water into the lower mantle. *Geophys. Res. Lett., 25*(2), 203–206. https://doi.org/10.1029/97GL03572

Irifune, T., Higo, Y., Inoue, T., Kono, Y., Ohfuji, H., & Funakoshi, K. (2008). Sound velocities of majorite garnet and the composition of the mantle transition region. *Nature, 451*(7180), 814–817. https://doi.org/10.1038/nature06551

Ishii, T., Kojitani, H., & Akaogi, M. (2011). Post-spinel transitions in pyrolite and Mg_2SiO_4 and akimotoite-perovskite transition in $MgSiO_3$: Precise comparison by high-pressure high-temperature experiments with multi-sample cell technique. *Earth Plan. Sci. Lett., 309*(3–4), 185–197. https://doi.org/10.1016/j.epsl.2011.06.023

Ishii, T., Huang, R., Fei, H., Koemets, I., Liu, Z., Maeda, F., … Katsura, T. (2018). Complete agreement of the post-spinel transition with the 660-km seismic discontinuity. *Sci. Rep., 8*(1), 6358. https://doi.org/10.1038/s41598-018-24832-y

Ishii, T., Huang, R., Myhill, R., Fei, H., Koemets, I., Liu, Z., … Katsura, T. (2019). Sharp 660-km discontinuity controlled by extremely narrow binary post-spinel transition. *Nat. Geosci., 12*(10), 869–872. https://doi.org/10.1038/s41561-019-0452-1

Ishii, T., Kojitani, H., & Akaogi, M. (2019). Phase Relations of Harzburgite and MORB up to the Uppermost Lower Mantle Conditions: Precise Comparison With Pyrolite by Multisample Cell High-Pressure Experiments With Implication to Dynamics of Subducted Slabs. *J. Geophys. Res.- Sol. Ea., 124*(4), 3491–3507. https://doi.org/10.1029/2018JB016749

Ishii, T., Liu, Z., & Katsura, T. (2019). A Breakthrough in Pressure Generation by a Kawai-Type Multi-Anvil Apparatus with Tungsten Carbide Anvils. *Engineering, 5*(3), 434-440. https://doi.org/10.1016/j.eng.2019.01.013

Ismail-Zadeh, A., & Tackley, P. J. (2010). Computational methods for geodynamics. Computational Methods for Geodynamics. *Cambridge University Press*, 349 pages. https://doi.org/10.1017/CBO9780511780820

Ita, J., & Stixrude, L. (1992). Petrology, elasticity, and composition of the mantle transition zone. *J. Geophys. Res., 97*(B5), 6849-6866. https://doi.org/10.1029/92JB00068

Iwamori, H. (1998). Transportation of H_2O and melting in subduction zones. *Earth Planet Sc. Lett., 160*(1–2), 65–80. https://doi.org/10.1016/S0012-821X(98)00080-6

Iwamori, H. (2006). Transportation of H_2O beneath the Japan arcs and its implications for global water circulation. *Chem. Geo., 239*(3-4), 182-198. https://doi.org/10.1016/j.chemgeo.2006.08.011

Izidoro, A., De Souza Torres, K., Winter, O. C., & Haghighipour, N. (2013). A compound model for the origin of Earth's water. *Astrophys. J., 767*(1), 54. https://doi.org/10.1088/0004-637X/767/1/54

REFERENCES - J

Jacobsen, S. D., Demouchy, S., Frost, D. J., Ballaran, T. B., & Kung, J. (2005). A systematic study of OH in hydrous wadsleyite from polarized FTIR spectroscopy and single-crystal X-ray diffraction: Oxygen sites for hydrogen storage in Earth's interior. *Am. Min., 90*(1), 61-70. https://doi.org/10.2138/am.2005.1624

Jacobsen, S. D., & Van Der Lee, S. (2013). Earth's Deep Water Cycle. *AGU Geoph. Monog. Series*, Vol.168. Wiley Blackwell. https://doi.org/10.1029/GM168

Jacobsen, S. D. (2018). Effect of water on the equation of state of nominally anhydrous minerals. *Rev. Mineral. Geochem., 62*(1), 321-342. https://doi.org/10.2138/rmg.2006.62.14

Jain, C., Rozel, A. B., & Tackley, P. J. (2019). Quantifying the Correlation Between Mobile Continents and Elevated Temperatures in the Subcontinental Mantle. *Geochem. Geophys. Geosys., 20*(3), 1358-1386. https://doi.org/10.1029/2018GC007586

Jain, C., Rozel, A. B., Tackley, P. J., Sanan, P., & Gerya, T. V. (2019). Growing primordial continental crust self-consistently in global mantle convection models. *Gondw. Res., 73*, 96-122. https://doi.org/10.1016/j.gr.2019.03.015

Jakosky, B. (1998). The Search for Life on Other Planets. *Cambridge University Press*, 326 pages.

Jakosky, B. M., Brain, D., Chaffin, M., Curry, S., Deighan, J., Grebowsky, J., … Zurek, R. (2018). Loss of the Martian atmosphere to space: Present-day loss rates determined from MAVEN observations and integrated loss through time. *Icarus*, 315, 146–157. https://doi.org/10.1016/j.icarus.2018.05.030

Jakosky, B. M. (2021). Atmospheric Loss to Space and the History of Water on Mars. *Annu. Rev. Earth Pl. Sc., 49*(1). https://doi.org/10.1146/annurev-earth-062420-052845

Janecky, D. R., & Seyfried, W. E. (1986). Hydrothermal serpentinization of peridotite within the oceanic crust: Experimental investigations of mineralogy and major element chemistry. *Geochim. Cosmochim. Ac., 50*(7), 1357–1378. https://doi.org/10.1016/0016-7037(86)90311-X

Jarchow, C. M., & Thompson, G. A. (1989). The nature of the Mohorovicic discontinuity. *Annu. Rev. Earth Pl. Sc., 17*(1), 475-506.

Jarrard, R. D. (2003). Subduction fluxes of water, carbon dioxide, chlorine, and potassium. *Geochem. Geophys. Geosyst., 4*(5), 8905. https://doi.org/10.1029/2002GC000392

Jarvis, G. T., & Mckenzie, D. P. (1980). Convection in a compressible fluid with infinite Prandtl number. *J. Fluid Mech., 96*(3), 515-583. https://doi.org/10.1017/S002211208000225X

Jarvis, G. T., Glatzmaier, G. A., & Vangelov, V. I. (1995). Effects Of Curvature, Aspect Ratio And Plan Form In Two- And Three-Dimensional Spherical Models Of Thermal Convection. *Geophys Astro. Fluid Dyn., 79*(1–4), 147–171. https://doi.org/10.1080/03091929508228995

Jaupart, C., & Mareschal, J. C. (2015). Heat Flow and Thermal Structure of the Lithosphere. *Treat. Geophys., 6*, 217-252. https://doi.org/10.1016/B978-0-444-53802-4.00114-7

Javadi, K., & Kazemi, K. (2018). Microgravity modulation effects on free convection problems LBM simulation. *Physics of Fluids, 30*(1), 017104. https://doi.org/10.1063/1.5019798

Javaux, E. J. (2019). Challenges in evidencing the earliest traces of life. *Nature, 572*(7770), 451-460. https://doi.org/10.1038/s41586-019-1436-4

Javoy, M., Kaminski, E., Guyot, F., Andrault, D., Sanloup, C., Moreira, M., … Jaupart, C. (2010). The chemical composition of the Earth: Enstatite chondrite models. *Earth Planet Sc. Lett., 293*(3-4), 259-268. https://doi.org/10.1016/j.epsl.2010.02.033

Jeffreys, H. (1926). The Rigidity of the Earth's Central Core. *Geophys. J. Int., 1*(7), 371-383.. https://doi.org/10.1111/j.1365-246X.1926.tb05385.x

Jellinek, A. M. (2002). The influence of interior mantle temperature on the structure of plumes: Heads for Venus, Tails for the Earth. *Geophys. Res. Lett.*, *29*(11), 1532. https://doi.org/10.1029/2001GL014624

Jellinek, A. M., & Manga, M. (2004). Links between long-lived hot spots, mantle plumes, D″, and plate tectonics. *Rev. Geophy , 42*(3). https://doi.org/10.1029/2003RG000144

Johansen, A., Oishi, J. S., Low, M. M. Mac, Klahr, H., Henning, T., & Youdin, A. (2007). Rapid planetesimal formation in turbulent circumstellar disks. *Nature, 448*(7157), 1022–1025. https://doi.org/10.1038/nature06086

John, T., Scambelluri, M., Frische, M., Barnes, J. D., & Bach, W. (2011). Dehydration of subducting serpentinite: Implications for halogen mobility in subduction zones and the deep halogen cycle. *Earth Planet Sc. Lett., 308*(1–2), 65–76. https://doi.org/10.1016/j.epsl.2011.05.038

Johnson, H. P., & Semyan, S. W. (1994). Age variation in the physical properties of oceanic basalts: implications for crustal formation and evolution. *J. Geophys. Res., 99*(B2), 3123–3134. https://doi.org/10.1029/93JB00717

Johnson, N. M., & Fegley, B. (2000). Water on Venus: New Insights from Tremolite Decomposition. *Icarus, 146*(1), 301–306. https://doi.org/10.1006/icar.2000.6392

Johnson, N. M., & Fegley, B. (2002). Experimental studies of atmosphere-surface interactions on Venus. *Adv. Space Res., 29*(2), 233–241. https://doi.org/10.1016/S0273-1177(01)00573-7

Jones, A. G., Fishwick, S., Evans, R. L., Muller, M. R., & Fullea, J. (2013). Velocity-conductivity relations for cratonic lithosphere and their application: Example of Southern Africa. *Geochem. Geophys. Geosyst., 14*(4), 806–827. https://doi.org/10.1002/ggge.20075

Joseph, R. G., Dass, R. S., Rizzo, V., Cantasano, N., & Bianciardi, G. (2019). Evidence of life on Mars. *J. Astrobio. Space Sci. Rev., 1*, 40-81.

Jung, H., & Karato, S. I. (2001). Water-induced fabric transitions in olivine. *Science, 293*(5534), 1460–1463. https://doi.org/10.1126/science.1062235

Jung, H., Greon, H. W., & Dobrzhinetskaya, L. F. (2004). Intermediate-depth earthquake faulting by dehydration embrittlement with negative volume change. *Nature, 428*(6982), 545–549. https://doi.org/10.1038/nature02412

REFERENCES - K

Kageyama, A., & Sato, T. (2004). "Yin-Yang grid": An overset grid in spherical geometry. *Geochem. Geophys. Geosys., 5*(9). https://doi.org/10.1029/2004GC000734

Kaneshima, S., & Helffrich, G. (1998). Detection of lower mantle scatterers northeast of the Marianna subduction zone using short-period array data. *J. Geophys. Res. - Sol. Ea., 103*(B3), 4825–4838. https://doi.org/10.1029/97jb02565

Kang, K., Koh, Y. K., Chiritescu, C., Zheng, X., & Cahill, D. G. (2008). Two-tint pump-probe measurements using a femtosecond laser oscillator and sharp-edged optical filters. *Rev. Sci., 79*(11), 114901. Instr.. https://doi.org/10.1063/1.3020759

Kantor, I., Prakapenka, V., Kantor, A., Dera, P., Kurnosov, A., Sinogeikin, S., … Dubrovinsky, L. (2012). BX90: A new diamond anvil cell design for X-ray diffraction and optical measurements. *Rev. Sci. Instr., 83*(12), 125102. https://doi.org/10.1063/1.4768541

Kanzaki, M. (1991). Stability of hydrous magnesium silicates in the mantle transition zone. *Phys. Earth Planet. In., 66*(3–4), 307–312. https://doi.org/10.1016/0031-9201(91)90085-V

Karato, S. I. (1990). The role of hydrogen in the electrical conductivity of the upper mantle. *Nature, 347*(6290), 272–273. https://doi.org/10.1038/347272a0

Karato, S. I., & Wu, P. (1993). Rheology of the upper mantle: A synthesis. *Science, 260*(5109), 771–778. https://doi.org/10.1126/science.260.5109.771

Karato, S. I. (1995). Effects of Water on Seismic Wave Velocities in the Upper Mantle. *P. Jpn. Acad. B-Phys., 71*(2), 61–66. https://doi.org/10.2183/pjab.71.61

Karato, S. I., & Murthy, V. R. (1997). Core formation and chemical equilibrium in the Earth - I. Physical considerations. *Phys. Earth Planet. In, 100*(1–4), 61–79. https://doi.org/10.1016/S0031-9201(96)03232-3

Karato, S. I., & Jung, H. (1998). Water, partial melting and the origin of the seismic low velocity and high attenuation zone in the upper mantle. *Earth Plan. Sci. Lett, 157*(3-4), 193-207, https://doi.org/10.1016/S0012-821X(98)00034-X

Karato, S. I. (2006). Remote sensing of hydrogen in Earth's mantle. *Rev. Mineral. Geochem., 62*(1), 343-375. https://doi.org/10.2138/rmg.2006.62.15

Karato, S. I. (2008). Deformation of earth materials: An introduction to the rheology of solid earth. Deformation of Earth Materials: An Introduction to the Rheology of Solid Earth. *Cambridge University Press*, 463 pages. https://doi.org/10.1017/CBO9780511804892

Karato, S. I., & Dai, L. (2009). Comments on "Electrical conductivity of wadsleyite as a function of temperature and water content" by Manthilake et al. *Phys. Earth Planet. In., 174*(1-4), 19-21. https://doi.org/10.1016/j.pepi.2009.01.012

Karato, S. I. (2010). Rheology of the Earth's mantle: A historical review. *Gondwana Res., 18*(1), 17–45. https://doi.org/10.1016/j.gr.2010.03.004

Karato, S. I. (2011). Water distribution across the mantle transition zone and its implications for global material circulation. *Earth Planet Sc. Lett., 301*(3–4), 413–423. https://doi.org/10.1016/j.epsl.2010.11.038

Karki, B. B., & Stixrude, L. P. (2010). Viscosity of $MgSiO_3$ liquid at earth's mantle conditions: Implications for an early magma ocean. *Science, 328*(5979), 740-742. https://doi.org/10.1126/science.1188327

Katayama, I., & Karato, S. I. (2008). Low-temperature, high-stress deformation of olivine under water-saturated conditions. *Phys. Earth Planet. In., 168*(3–4), 125–133. https://doi.org/10.1016/j.pepi.2008.05.019

Katsura, T., & Ito, E. (1989). The system Mg_2SiO_4-Fe_2SiO_4 at high pressures and temperatures: precise determination of stabilities of olivine, modified spinel, and spinel. *J. Geophys. Res., 94*(B11), 663–678. https://doi.org/10.1029/jb094ib11p15663

Katsura, T., Yamada, H., Shinmei, T., Kubo, A., Ono, S., Kanzaki, M., … Utsumi, W. (2003). Post-spinel transition in Mg_2SiO_4 determined by high P - T in situ X-ray diffractometry. *Phys. Earth Plan. Int., 136*(1–2), 11–24. https://doi.org/10.1016/S0031-9201(03)00019-0

Katsura, T., Yamada, H., Nishikawa, O., Song, M., Kubo, A., Shinmei, T., … Funakoshi, K. (2004). Olivine-wadsleyite transition in the system $(Mg,Fe)_2SiO_4$. *J. Geophys. Res.- Sol. Ea., 109*(B2). https://doi.org/10.1029/2003JB002438

Katsura, T., Yoneda, A., Yamazaki, D., Yoshino, T., Ito, E., Suetsugu, D., … Jellinek, M. (2010). Adiabatic temperature profile in the mantle. *Phys. Earth Planet In., 183*(1-2), 212-218. https://doi.org/10.1016/j.pepi.2010.07.001

Katsura, T., & Tange, Y. (2019). A simple derivation of the Birch–Murnaghan equations of state (EOSs) and comparison with EOSs derived from other definitions of finite strain. *Minerals, 9*(12), 745. https://doi.org/10.3390/min9120745

Kattenhorn, S. A. (2018). Commentary: The Feasibility of Subduction and Implications for Plate Tectonics on Jupiter's Moon Europa. *J. Geophys. Res.: Planets, 123*(3), 684–689. https://doi.org/10.1002/2018JE005524

Kawai, K., & Tsuchiya, T. (2009). Temperature profile in the lowermost mantle from seismological and mineral physics joint modeling. *P. Natl. A. Sci. USA., 106*(52), 22119-22123. https://doi.org/10.1073/pnas.0905920106

Kawai, N., & Endo, S. (1970). The generation of ultrahigh hydrostatic pressures by a split sphere apparatus. *Rev. Sci. Instr., 41*(8), 1178-1181. https://doi.org/10.1063/1.1684753

Kawamoto, T., & Holloway, J. R. (1997). Melting temperature and partial melt chemistry to H_2O-saturated mantle peridotite to 11 gigapascals. *Science, 276*(5310), 240–243. https://doi.org/10.1126/science.276.5310.240

Keller, T., & Tackley, P. J. (2009). Towards self-consistent modeling of the martian dichotomy: The influence of one-ridge convection on crustal thickness distribution. *Icarus*, *202*, 429–443. https://doi.org/10.1029/2005JB003905

Keller, B., & Schoene, B. (2018). Plate tectonics and continental basaltic geochemistry throughout Earth history. *Earth Planet Sc. Lett., 481*, 290–304. https://doi.org/10.1016/j.epsl.2017.10.031

Kendrick, M. A., Danyushevsky, L. V., Falloon, T. J., Woodhead, J. D., Arculus, R. J., & Ireland, T. (2020). SW Pacific arc and backarc lavas and the role of slab-bend serpentinites in the global halogen cycle. *Earth Planet Sc. Lett., 530*, 115921. https://doi.org/10.1016/j.epsl.2019.115921

Kennett, B. L. N., Engdahl, E. R., & Buland, R. (1995). Constraints on seismic velocities in the Earth from traveltimes. *Geophys. J. Int., 122*(1), 108–124. https://doi.org/10.1111/j.1365-246X.1995.tb03540.x

Keppler, H., & Bolfan-Casanova, N. (2006). Thermodynamics of water solubility and partitioning. *Rev. Mineral. Geochem.*, 62(1), 193-230. https://doi.org/10.2138/rmg.2006.62.9

Keppler, H., & Smyth, J. R. (2006). Water in nominally anhydrous minerals. *Rev. Mineral. Geochem., 62*, 486 pages.

Keppler, H., Dubrovinsky, L. S., Narygina, O., & Kantor, I. (2008). Optical absorption and radiative thermal conductivity of silicate perovskite to 125 gigapascals. *Science, 322*(5907), 1529-1532. https://doi.org/10.1126/science.1164609

Keppler, H., & Frost, D. J. (2015). Introduction to minerals under extreme conditions. https://doi.org/10.1180/emu-notes.7.1

Kern, C., Masias, P., Apaza, F., Reath, K. A., & Platt, U. (2017). Remote measurement of high preeruptive water vapor emissions at Sabancaya volcano by passive differential optical absorption spectroscopy. *J. Geophys. Res.- Sol. Ea.*, 122(5), 3540–3564. https://doi.org/10.1002/2017JB014020

Khan, A., & Shankland, T. J. (2012). A geophysical perspective on mantle water content and melting: Inverting electromagnetic sounding data using laboratory-based electrical conductivity profiles. *Earth Planet Sc. Lett., 317*, 27-43. https://doi.org/10.1016/j.epsl.2011.11.031

Khan, A., Liebske, C., Rozel, A., Rivoldini, A., Nimmo, F., Connolly, J. A. D., … Giardini, D. (2018). A geophysical perspective on the bulk composition of Mars. *J. Geophys. Res.: Planets, 123*(2), 575-611. https://doi.org/10.1002/2017JE005371

Khramov, A. N., Rodionov, V. P., & Komissarova, R. A. (1966). New Data On The Paleozoic History Of The Geomagnetic Field In The USSR; Dipole Character Of The Geomagnetic Field In The Late Cambrian And The Ordovician In The South Of The Siberian Platform.

King, E. R., Zietz, I., & Alldredge, L. R. (1966). Magnetic data on the structure of the central Arctic region. *Geol. Soc. Am. Bull., 77*(6), 619-646. https://doi.org/10.1130/0016-7606(1966)77[619:MDOTSO]2.0.CO;2

King, G. (1983). The accommodation of large strains in the upper lithosphere of the earth and other solids by self-similar fault systems: the geometrical origin of b-Value. *Pure App. Geophys., 121*(5–6), 761–815. https://doi.org/10.1007/BF02590182

King, S. D., Raefsky, A., & Hager, B. H. (1990). Conman: vectorizing a finite element code for incompressible two-dimensional convection in the Earth's mantle. *Phys. Earth Plan. In., 59*(3), 195–207. https://doi.org/10.1016/0031-9201(90)90225-M

Koglin, D. E., Ghias, S. R., King, S. D., Jarvis, G. T., & Lowman, J. P. (2005). Mantle convection with reversing mobile plates: A benchmark study. *Geochem. Geophys. Geosys., 6*(9). https://doi.org/10.1029/2005GC000924

Kohlstedt, D. L., Evans, B., & Mackwell, S. J. (1995). Strength of the lithosphere: Constraints imposed by laboratory experiments. *J. Geophys. Res.- Sol. Ea., 100*(B9), 17587–17602. https://doi.org/10.1029/95JB01460

Kohlstedt, D. L., Keppler, H., & Rubie, D. C. (1996). Solubility of water in the α, β and γ phases of $(Mg,Fe)_2SiO_4$. *Contrib. Mineral. Petr., 123*, 345–357.

Kohlstedt, D. L. (2006). The role of water in high-temperature rock deformation. *Rev. Mineral. Geochem., 62*(1), 377-396.. https://doi.org/10.2138/rmg.2006.62.16

Korenaga, J., & Karato, S. I. (2008). A new analysis of experimental data on olivine rheology. *J. Geophys. Res.- Sol. Ea., 113*(B2). https://doi.org/10.1029/2007JB005100

Korenaga, J. (2011). Thermal evolution with a hydrating mantle and the initiation of plate tectonics in the early Earth. *J. Geophys. Res.- Sol. Ea., 116*(12), 1–20. https://doi.org/10.1029/2011JB008410

Korenaga, J. (2013). Initiation and Evolution of Plate Tectonics on Earth: Theories and Observations. *Annu. Rev. Earth Pl. Sc., 41*(1), 117–151. https://doi.org/10.1146/annurev-earth-050212-124208

Korenaga, J. (2017). On the extent of mantle hydration caused by plate bending. *Earth Planet Sc. Lett., 457*, 1–9. https://doi.org/10.1016/j.epsl.2016.10.011

Korenaga, J., Planavsky, N. J., & Evans, D. A. D. (2017). Global water cycle and the coevolution of the Earth's interior and surface environment. *Philos. T. R. Soc.-A, 375*(2094). https://doi.org/10.1098/rsta.2015.0393

Koyama, T., Shimizu, H., Utada, H., Ichiki, M., Ohtani, E., & Hae, R. (2006). Water content in the mantle transition zone beneath the north pacific derived from the electrical conductivity anomaly. *Geoph. Monog. Series, 168*, 171–179. https://doi.org/10.1029/168GM13

Kretke, K. A., & Levison, H. F. (2014). Challenges in forming the solar system's giant planet cores via pebble accretion. *Astron. J., 148*(6), 109. https://doi.org/10.1088/0004-6256/148/6/109

Kronbichler, M., Heister, T., & Bangerth, W. (2012). High accuracy mantle convection simulation through modern numerical methods. *Geophys. J. Int., 191*(1), 12–29. https://doi.org/10.1111/j.1365-246X.2012.05609.x

Kubo, T., Ohtani, E., Kato, T., Urakawa, S., Suzuki, A., Kanbe, Y., … Fujino, K. (2002). Mechanism and kinetics of the post-spinel transformation in Mg_2SiO_4. *Phys. Earth Plan. Int., 129*(1–2), 153–171. https://doi.org/10.1016/S0031-9201(01)00270-9

Kulikov, Y. N., Lammer, H., Lichtenegger, H. I. M., Terada, N., Ribas, I., Kolb, C., … Biernat, H. K. (2006). Atmospheric and water loss from early Venus. *Plan. Space Sci., 54*(13–14), 1425–1444. https://doi.org/10.1016/j.pss.2006.04.021

Kuno, H., & Aoki, K. I. (1970). Chemistry of ultramafic nodules and their bearing on the origin of basaltic magmas. *Phys. Earth Plan. Int., 3*, 273-301. https://doi.org/10.1016/0031-9201(70)90065-8

Kurnosov, A., Kantor, I., Boffa-Ballaran, T., Lindhardt, S., Dubrovinsky, L., Kuznetsov, A., & Zehnder, B. H. (2008). A novel gas-loading system for mechanically closing of various types of diamond anvil cells. *Rev. Sci. Instr., 79*(4), 045110. https://doi.org/10.1063/1.2902506

Kurosawa, K. (2015). Impact-driven planetary desiccation: The origin of the dry Venus. *Earth Planet Sc. Lett., 429*, 181–190. https://doi.org/10.1016/j.epsl.2015.07.061

Kushiro, I. (1972). Effect of water on the composition of magmas formed at high pressures. *J. Petrol., 13*(2), 311–334. https://doi.org/10.1093/petrology/13.2.311

Kushiro, I., Syono, Y., & Akimoto, S.I. (1968). Melting Of Peridotite Nodule At High Pressures And High Water Pressures. *J. Geophys. Res., 73*(18), 6023–6029. https://doi.org/10.1029/jb073i018p06023

Kustowski, B., Ekström, G., & Dziewoński, A. M. (2008). Anisotropic shear-wave velocity structure of the Earth's mantle: A global model. *J. Geophys. Res., 113*(B6), B06306. https://doi.org/10.1029/2007JB005169

Kuzmany, H. (2009). Solid-state spectroscopy: an introduction. *Springer Science & Business Media*, 574 pages. https://doi.org/10.1007/978-3-642-01479-6

REFERENCES - L

Labrosse, S. (2014). Thermal evolution of the core with a high thermal conductivity. *Phys. Earth Planet., 247*, 36-55. In. https://doi.org/10.1016/j.pepi.2015.02.002

Labuz, J. F., & Zang, A. (2012). Mohr–Coulomb failure criterion. In The ISRM Suggested Methods for Rock Characterization, Testing and Monitoring: 2007-2014 (pp. 227–231). *Springer International Publishing*. https://doi.org/10.1007/978-3-319-07713-0_19

Lamadrid, H. M., Rimstidt, J. D., Schwarzenbach, E. M., Klein, F., Ulrich, S., Dolocan, A., & Bodnar, R. J. (2017). Effect of water activity on rates of serpentinization of olivine. *Nat. Comm., 8*(1), 1–9. https://doi.org/10.1038/ncomms16107

Lambeck, K. (1977). Tidal dissipation in the oceans: astronomical, geophysical and oceanographic consequences. *T. R. Soc. S.-A., 287*(1347), 545-594. https://doi.org/10.1098/rsta.1977.0159

Lambeck, K., Johnston, P., Smither, C., & Nakada, M. (1996). Glacial Rebound of the British Isles-Iii. Constraints On Mantle Viscosity. *Geophys. J. Int., 125*(2), 340–354. https://doi.org/10.1111/j.1365-246X.1996.tb00003.x

Lambeck, K., Smither, C., & Johnston, P. (1998). Sea-level change, glacial rebound and mantle viscosity fornorthern Europe. *Geophys. J. Int., 134*(1), 102–144. https://doi.org/10.1046/j.1365-246x.1998.00541.x

Lambrechts, M., & Johansen, A. (2012). Rapid growth of gas-giant cores by pebble accretion. *Astron. Astro., 544*, 32. https://doi.org/10.1051/0004-6361/201219127

Langemeyer, S. M., Lowman, J. P., & Tackley, P. J. (2018). The sensitivity of core heat flux to the modeling of plate-like surface motion. *Geochem. Geophys. Geosys., 19*(4), 1282-1308. https://doi.org/10.1002/2017GC007266

Lau, H. C. P., Mitrovica, J. X., Austermann, J., Crawford, O., Al-Attar, D., & Latychev, K. (2016). Inferences of mantle viscosity based on ice age data sets: Radial structure. *J. Geophys. Res. - Sol. Ea., 121*(10), 6991–7012. https://doi.org/10.1002/2016JB013043

Lausen, C. (1927). The occurrence of olivine bombs near Globe, Arizona. *Am. J. Sci., 5*(82), 293-306. https://doi.org/10.2475/ajs.s5-14.82.293

Lawrence, J. F., & Wysession, M. E. (2006). QLM9: A new radial quality factor (Qμ) model for the lower mantle. *Earth Planet Sc. Lett., 241*(3–4), 962–971. https://doi.org/10.1016/j.epsl.2005.10.030

Le Fort, P., Cuney, M., Deniel, C., France-Lanord, C., Sheppard, S. M. F., Upreti, B. N., & Vidal, P. (1987). Crustal generation of the Himalayan leucogranites. *Tectonophysics, 134*(1–3), 39–57. https://doi.org/10.1016/0040-1951(87)90248-4

Le Pichon, X. (1968). Sea-floor spreading and continental drift. *J. Geophys. Res., 73*(12), 3661–3697. https://doi.org/10.1029/JB073i012p03661

Le Voyer, M., Hauri, E. H., Cottrell, E., Kelley, K. A., Salters, V. J. M., Langmuir, C. H., … Füri, E. (2019). Carbon Fluxes and Primary Magma CO_2 Contents Along the Global Mid-Ocean Ridge System. *Geochem. Geophys. Geosyst., 20*(3), 1387–1424. https://doi.org/10.1029/2018GC007630

Lécuyer, C., Gillet, P., & Robert, F. (1998). The hydrogen isotope composition of seawater and the global water cycle. *Chem. Geol., 145*(3–4), 249–261. https://doi.org/10.1016/S0009-2541(97)00146-0

Lee, C.-T. A., Caves, J., Jiang, H., Cao, W., Lenardic, A., McKenzie, N. R., … Dyer, B. (2018). Deep mantle roots and continental emergence: implications for whole-Earth elemental cycling, long-term climate, and the Cambrian explosion. *Int. Geol. Rev., 60*(4), 431–448. https://doi.org/10.1080/00206814.2017.1340853

Lehmann, I. (1936). P'. *Publ. Bur. Centr. Seism. Internat, 14*, 87–115.

Levison, H. F., Kretke, K. A., & Duncan, M. J. (2015). Growing the gas-giant planets by the gradual accumulation of pebbles. *Nature, 524*(7565), 322–324. https://doi.org/10.1038/nature14675

Lewis, D. E. (2012). Early Russian Organic Chemists and Their Legacy. *Springer Science & Business Media*, 148 pages. ISBN-10: 3642282180

Li, Y., Deschamps, F., & Tackley, P. J. (2016). Small post-perovskite patches at the base of lower mantle primordial reservoirs: Insights from 2D numerical modeling and implications for ULVZs. *Geophys. Res. Lett., 43*(7), 3215-3225. https://doi.org/10.1002/2016GL067803

Li, Y., Vilella, K., Deschamps, F., Zhao, L., & J. Tackley, P. (2018). Effects of Iron Spin Transition on the Structure and Stability of Large Primordial Reservoirs in Earth's Lower Mantle. *Geophys. Res. Lett., 45*(12), 5918-5928. https://doi.org/10.1029/2018GL078125

Li, Y., Vočadlo, L., Sun, T., & Brodholt, J. P. (2020). The Earth's core as a reservoir of water. *Nat. Geosci., 13*(6), 453–458. https://doi.org/10.1038/s41561-020-0578-1

Liang, X. (2017). Impact of grain boundary characteristics on lattice thermal conductivity: A kinetic theory study on ZnO. *Phys. Rev. B, 95*(15), 155313. https://doi.org/10.1103/PhysRevB.95.155313

Libowitzky, E., & Rossman, G. R. (1997). An IR absorption calibration for water in minerals. Am. Min., 82(11-12), 1111-1115. https://doi.org/10.2138/am-1997-11-1208

Libowitzky, E. (1999). Correlation of O-H stretching frequencies and O-H···O hydrogen bond lengths in minerals. *Chemical Monthly, 130*(8), 1047-1059. https://doi.org/10.1007/BF03354882

Libowitzky, E., & Beran, A. (2018). The structure of hydrous species in nominally anhydrous minerals: Information from Polarized IR spectroscopy. *Rev. Min Geochem., 62*(1), 29-52. https://doi.org/10.2138/rmg.2006.62.2

Lichtenberg, T., Golabek, G. J., Burn, R., Meyer, M. R., Alibert, Y., Gerya, T. V., & Mordasini, C. (2019). A water budget dichotomy of rocky protoplanets from 26 Al-heating. *Nat. Astro., 3*(4), 307-313. https://doi.org/10.1038/s41550-018-0688-5

Liebske, C., Schmickler, B., Terasaki, H., Poe, B. T., Suzuki, A., Funakoshi, K. ichi, … Rubie, D. C. (2005). Viscosity of peridotite liquid up to 13 GPa: Implications for magma ocean viscosities. *Earth Planet Sc. Lett., 240*(3-4), 589-604. https://doi.org/10.1016/j.epsl.2005.10.004

Limaye, S. S., Mogul, R., Smith, D. J., Ansari, A. H., Słowik, G. P., & Vaishampayan, P. (2018). Venus' spectral signatures and the potential for life in the clouds. *Astrobiology, 18*(9), 1181–1198. https://doi.org/10.1089/ast.2017.1783

Lis, D. C., Biver, N., Bockelée-Morvan, D., Hartogh, P., Bergin, E. A., Blake, G. A., … Szutowicz, S. (2013). A herschel study of D/H in water in the jupiter-family comet 45P/honda-mrkos-pajdušáková and prospects for D/H measurements with CCAT. *Astrophys. J. Letters, 774*(1), L3. https://doi.org/10.1088/2041-8205/774/1/L3

Litasov, K. D., & Ohtani, E. (2002). Phase relations and melt compositions in CMAS-pyrolite-H_2O system up to 25 GPa. *Phys. Earth Planet. In., 134*(1–2), 105–127. https://doi.org/10.1016/S0031-9201(02)00152-8

Litasov, K. D., & Ohtani, E. (2003). Stability of various hydrous phases in CMAS pyrolite-H_2O system up to 25 GPa. *Phys. Chem. Miner., 30*(3), 147–156. https://doi.org/10.1007/s00269-003-0301-y

Litasov, K. D., Ohtani, E., Langenhorst, F., Yurimoto, H., Kubo, T., & Kondo, T. (2003). Water solubility in Mg-perovskites and water storage capacity in the lower mantle. *Earth Planet Sc. Lett., 211*(1–2), 189–203. https://doi.org/10.1016/S0012-821X(03)00200-0

Litasov, K. D., Ohtani, E., Sano, A., Suzuki, A., & Funakoshi, K. (2005). Wet subduction versus cold subduction. *Geophys. Res. Lett., 32*(13), L13312. https://doi.org/10.1029/2005GL022921

Litasov, K. D., Ohtani, E., & Sano, A. (2006). Influence of water on major phase transitions in the Earth's mantle. *Geophys. Monogr.-AGU, 168*, 95. https://doi.org/10.1029/168GM08

Litasov, K. D., & Ohtani, E. (2007). Effect of water on the phase relations in Earth's mantle and deep water cycle. *Sp. Pap. Geo. Soc. Am., 421*, 115. https://doi.org/10.1130/2007.2421(08)

Litasov, K. D., Kagi, H., Shatskiy, A., Ohtani, E., Lakshtanov, D. L., Bass, J. D., & Ito, E. (2007). High hydrogen solubility in Al-rich stishovite and water transport in the lower mantle. *Earth Planet Sc. Lett., 262*(3–4), 620–634. https://doi.org/10.1016/j.epsl.2007.08.015

Liu, J., Hu, Q., Young Kim, D., Wu, Z., Wang, W., Xiao, Y., … Mao, W. L. (2017). Hydrogen-bearing iron peroxide and the origin of ultralow-velocity zones. *Nature, 551*(7681), 494–497. https://doi.org/10.1038/nature24461

Liu, L. G. (1987). Effects of H_2O on the phase behaviour of the forsterite-enstatite system at high pressures and temperatures and implications for the Earth. *Phys. Earth Planet. In., 49*(1–2), 142–167. https://doi.org/10.1016/0031-9201(87)90138-5

Liu, L., & Hasterok, D. (2016). High-resolution lithosphere viscosity and dynamics revealed by magnetotelluric imaging. *Science, 353*(6307), 1515-1519. https://doi.org/10.1126/science.aaf6542

Lopes, R. M. C., Kamp, L. W., Smythe, W. D., Mouginis-Mark, P., Kargel, J., Radebaugh, J., … Douté, S. (2004). Lava lakes on Io: Observations of Io's volcanic activity from Galileo NIMS during the 2001 fly-bys. *Icarus, 169*(1), 140–174. https://doi.org/10.1016/j.icarus.2003.11.013

Lopes, R. M. C. (2014). Io. In Encyclopedia of the Solar System (pp. 779–792). *Elsevier*. https://doi.org/10.1016/B978-0-12-415845-0.00035-9

Lourenço, D. L., Rozel, A., & Tackley, P. J. (2016). Melting-induced crustal production helps plate tectonics on Earth-like planets. *Earth. Plan. Sci. Lett., 439*, 18-28. https://doi.org/10.1016/j.epsl.2016.01.024

Lourenço, D. L., Rozel, A. B., Gerya, T., & Tackley, P. J. (2018). Efficient cooling of rocky planets by intrusive magmatism. *Nat. Geosci., 11*(5), 322-327. https://doi.org/10.1038/s41561-018-0094-8

Lovering, J. F. (1958). The nature of the Mohorovicic discontinuity. *Eos, Transactions AGU, 39*(5), 947–955. https://doi.org/10.1029/TR039i005p00947

Lowrie, W. (2007). Fundamentals of Geophysics (2nd Ed.). *Cambridge University Press*, 391 pages. ISBN-10 : 0521675960

Łukaszewicz, G., & Kalita, P. (2016). Navier–Stokes Equations: An Introduction with Applications. *Springer Nature*, 390 pages. ISBN: 9783319277608

REFERENCES - M

Magni, V., Bouilhol, P., & Van Hunen, J. (2014). Deep water recycling through time. *Geochem. Geophys. Geosyst., 15*(11), 4203–4216. https://doi.org/10.1002/2014GC005525

Maier, W. D., Barnes, S. J., Campbell, I. H., Fiorentini, M. L., Peltonen, P., Barnes, S. J., & Smithies, R. H. (2009). Progressive mixing of meteoritic veneer into the early Earths deep mantle. *Nature, 460*(7255), 620–623. https://doi.org/10.1038/nature08205

Malcuit, R. J. (2014). The Twin Sister Planets Venus and Earth: Why are they so different? *Springer*, 401 pages.

Mallard, C., Coltice, N., Seton, M., Müller, R. D., & Tackley, P. J. (2016). Subduction controls the distribution and fragmentation of Earth's tectonic plates. *Nature, 535*(7610), 140-143.. https://doi.org/10.1038/nature17992

Mallet, R. (1846). On the Dynamics of Earthquakes; Being an Attempt to Reduce Their Observed Phenomena to the Known Laws of Wave Motion in Solids and Fluids. *The Transactions of the Royal Irish Academy, 21*, 51-105.

Manga, M., Weeraratne, D., & Morris, S. J. S. (2001). Boundary-layer thickness and instabilities in Bénard convection of a liquid with a temperature-dependent viscosity. *Phys. Fluids, 13*(3), 802–805. https://doi.org/10.1063/1.1345719

Mao, H. K., Xu, J., & Bell, P. M. (1986). Calibration of the ruby pressure gauge to 800 kbar under quasi-hydrostatic conditions. *J. Geophys. Res., 91*(B5), 4673. https://doi.org/10.1029/jb091ib05p04673

Mao, H.-K., Hu, Q., Yang, L., Liu, J., Kim, D. Y., Meng, Y., … Mao, W. L. (2017). When water meets iron at Earth's core–mantle boundary. *Natl. Sci. Rev., 4*(6), 870–878. https://doi.org/10.1093/nsr/nwx109

Margot, J. L., Campbell, D. B., Giorgini, J. D., Jao, J. S., Snedeker, L. G., Ghigo, F. D., & Bonsall, A. (2021). Spin state and moment of inertia of Venus. *Nat. Astr.*, 1–8. https://doi.org/10.1038/s41550-021-01339-7

Marlatt, W. E., Budyko, M. I., & Miller, D. H. (1975). Climate and Life. *J. Range Manag., 28*(2), 160. https://doi.org/10.2307/3897455

Marquardt, H., & Thomson, A. R. (2020). Experimental elasticity of Earth's deep mantle. *Nat. Rev. Earth Envi., 1(*9), 455–469. https://doi.org/10.1038/s43017-020-0077-3

Martin, R. G., & Livio, M. (2012). On the evolution of the snow line in protoplanetary discs. Mon *Not. R. Astron. Soc. Let., 425*(1), L6-L9. https://doi.org/10.1111/j.1745-3933.2012.01290.x

Marty, B. (2012). The origins and concentrations of water, carbon, nitrogen and noble gases on Earth. *Earth Planet Sc. Lett.*, 313–314, 56–66. https://doi.org/10.1016/j.epsl.2011.10.040

Marty, B., Avice, G., Bekaert, D. V., & Broadley, M. W. (2018). Salinity of the Archaean oceans from analysis of fluid inclusions in quartz. *C. R. - Geosci., 350*(4), 154–163. https://doi.org/10.1016/j.crte.2017.12.002

Marzoli, A., Renne, P. R., Piccirillo, E. M., Ernesto, M., Bellieni, G., & De Min, A. (1999). Extensive 200-million-year-old continental flood basalts of the Central Atlantic Magmatic Province. *Science, 284*(5414), 616–618. https://doi.org/10.1126/science.284.5414.616

Marzotto, E., Hsieh, W. P., Ishii, T., Chao, K. H., Golabek, G. J., Thielmann, M., & Ohtani, E. (2020). Effect of Water on Lattice Thermal Conductivity of Ringwoodite and Its Implications for the Thermal Evolution of Descending Slabs. *Geophys. Res. Lett., 47*(13), e2020GL087607. https://doi.org/10.1029/2020GL087607

Mashino, I., Murakami, M., & Ohtani, E. (2016). Sound velocities of δ-AlOOH up to core-mantle boundary pressures with implications for the seismic anomalies in the deep mantle. *J. Geophys. Res.- Sol. Ea., 121*(2), 595–609. https://doi.org/10.1002/2015JB012477

Matyska, C., Moser, J., & Yuen, D. A. (1994). The potential influence of radiative heat transfer on the formation of megaplumes in the lower mantle. *Earth Planet Sc. Lett., 125*(1–4), 255–266. https://doi.org/10.1016/0012-821X(94)90219-4

Matyska, C., & Yuen, D. A. (2005). The importance of radiative heat transfer on superplumes in the lower mantle with the new post-perovskite phase change. *Earth Planet Sc. Lett., 234*(1-2), 71-81. https://doi.org/10.1016/j.epsl.2004.10.040

Maunder, B., van Hunen, J., Bouilhol, P., & Magni, V. (2019). Modeling Slab Temperature: A Reevaluation of the Thermal Parameter. *Geochem. Geophys. Geosys., 20*(2), 673–687. https://doi.org/10.1029/2018GC007641

McCammon, C. A., Frost, D. J., Smyth, J. R., Laustsen, H. M. S., Kawamoto, T., Ross, N. L., & van Aken, P. A. (2004). Oxidation state of iron in hydrous mantle phases: Implications for subduction and mantle oxygen fugacity. *Phys. Earth Plan. Int., 143*(1–2), 157–169. https://doi.org/10.1016/j.pepi.2003.08.009

McDonough, W. F., & Sun, S. S. (1995). The composition of the Earth. *Chem. Geo., 120*(3-4), 223-253. https://doi.org/10.1016/0009-2541(94)00140-4

McDonough, W. F. (2003). Compositional Model for the Earth's Core. *Treatise on Geochem., 2*, 547-568. https://doi.org/10.1016/B0-08-043751-6/02015-6

McGovern, P. J., & Schubert, G. (1989). Thermal evolution of the Earth: effects of volatile exchange between atmosphere and interior. *Earth Planet Sc. Lett., 96*(1–2), 27–37. https://doi.org/10.1016/0012-821X(89)90121-0

McKenzie, D. P., & Parker, R. L. (1967). The North Pacific: An example of tectonics on a sphere. *Nature, 216*(5122), 1276–1280. https://doi.org/10.1038/2161276a0

McKenzie, D. P., & Bickle, M. J. (1988). The Volume and Composition of Melt Generated by Extension of the Lithosphere. *J. Petrol., 29*(3), 625–679. https://doi.org/10.1093/petrology/29.3.625

McMillan P. F., Akaogi, M., Sato, R. K., Poe, B., & Foley, J. (1991). Hydroxyl groups in β-Mg_2SiO_4. *Am. Mineral., 76*(3-4), 354-360.

McMillan, P. F., & Hofmeister, A. M. (2019). Infrared and Raman spectroscopy. *Spectroscopic methods in mineralogy and geology*, 99-160. https://doi.org/10.1201/b16932-10

McNamara, A. K., Garnero, E. J., & Rost, S. (2010). Tracking deep mantle reservoirs with ultra-low velocity zones. *Earth Planet Sc. Lett., 299*(1–2), 1–9. https://doi.org/10.1016/j.epsl.2010.07.042

Mei, S., & Kohlstedt, D. L. (2000a). Influence of water on plastic deformation of olivine aggregates: 1. Diffusion creep regime. *J. Geophys. Res.- Sol. Ea., 105*(B9), 21457–21469. https://doi.org/10.1029/2000JB900179

Mei, S., & Kohlstedt, D. L. (2000b). Influence of water on plastic deformation of olivine aggregates: 2. Dislocation creep regime. *J. Geophys. Res.- Sol. Ea., 105*(B9), 21471–21481. https://doi.org/10.1029/2000JB900180

Meinesz, F.A. (2012). The Earth's crust and Mantle (1st Ed.). *Elsevier*, 134 pages

Meyer, J., & Wisdom, J. (2007). Tidal heating in Enceladus. *Icarus, 188*(2), 535–539. https://doi.org/10.1016/j.icarus.2007.03.001

Mian, Z. U., & Tozer, D. C. (1990). No water, no plate tectonics: convective heat transfer and the planetary surfaces of Venus and Earth. *Terra Nova, 2*(5), 455–459. https://doi.org/10.1111/j.1365-3121.1990.tb00102.x

Michelson, A. A., & Morley, E. W. (1887). On the relative motion of the Earth and the luminiferous ether. *Sidereal Messenger*, *6*, 306-310. https://doi.org/10.2475/ajs.s3-34.203.333

Michibayashi, K., Tasaka, M., Ohara, Y., Ishii, T., Okamoto, A., & Fryer, P. (2007). Variable microstructure of peridotite samples from the southern Mariana Trench: Evidence of a complex tectonic evolution. *Tectonophysics, 444*(1–4), 111–118. https://doi.org/10.1016/j.tecto.2007.08.010

Mierdel, K., Keppler, H., Smyth, J. R., & Langenhorst, F. (2007). Water Solubility in Aluminous Orthopyroxene and the Origin of Earth's Asthenosphere. *Science, 315*(5810), 364–368. https://doi.org/10.1126/science.1135422

Milashuk, S., & Crane, W. A. (2011). Wind speed prediction accuracy and expected errors of RANS equations in low relief inland terrain for wind resource assessment purposes. *Environ. Modell. Softw., 26*(4), 429–433. https://doi.org/10.1016/j.envsoft.2010.10.004

Miletich, R., Allan, D. R., & Kuhs, W. F. (2000). High-Pressure Single-Crystal Techniques. *Rev. Min. Geochem., 41*(1), 445-519. https://doi.org/10.2138/rmg.2000.41.14

Miller, G. H., Rossman, G. R., & Harlow, G. E. (1987). The natural occurrence of hydroxide in olivine. *Phys. Chem. Miner., 14*(5), 461–472. https://doi.org/10.1007/BF00628824

Mitri, G., & Showman, A. P. (2008). Thermal convection in ice-I shells of Titan and Enceladus. *Icarus, 193*(2), 387-396. https://doi.org/10.1016/j.icarus.2007.07.016

Mitrovica, J. X., & Forte, A. M. (2004). A new inference of mantle viscosity based upon joint inversion of convection and glacial isostatic adjustment data. *Earth Planet Sc. Lett., 225*(1-2), 177-189. https://doi.org/10.1016/j.epsl.2004.06.005

Moore, W. B. (2003). Tidal heating and convection in Io. *J. Geophys. Res., 108*(E8), 5096. https://doi.org/10.1029/2002JE001943

Moore, W. B., & Webb, A. A. G. (2013). Heat-pipe earth. *Nature, 501*(7468), 501–505. https://doi.org/10.1038/nature12473

Moore, W. B., Simon, J. I., & Webb, A. A. G. (2017). Heat-pipe planets. *Earth Plan. Sci. Lett., 474*, 13–19. https://doi.org/10.1016/j.epsl.2017.06.015

Mora, C., Tittensor, D. P., Adl, S., Simpson, A. G. B., & Worm, B. (2011). How many species are there on earth and in the ocean? *PLoS Biology, 9*(8), 1001127. https://doi.org/10.1371/journal.pbio.1001127

Morbidelli, A., Chambers, J., Lunine, J. I., Petit, J. M., Robert, F., Valsecchi, G. B., & Cyr, K. E. (2000). Source regions and timescales for the delivery of water to the Earth. *Meteorit. Planet. Sci., 35*(6), 1309–1320. https://doi.org/10.1111/j.1945-5100.2000.tb01518.x

Morbidelli, A., Levison, H. F., Tsiganis, K., & Gomes, R. (2005). Chaotic capture of Jupiter's Trojan asteroids in the early Solar System. *Nature, 435(7041)*, 462–465. https://doi.org/10.1038/nature03540

Moresi, L. N., & Solomatov, V. S. (1995). Numerical investigation of 2D convection with extremely large viscosity variations. *Phys. Fluids, 7*(9), 2154–2162. https://doi.org/10.1063/1.868465

Moresi, L., & Solomatov, V. (1998). Mantle convection with a brittle lithosphere: throughts on the global tectonic styles of the Earth and Venus. *Geophys. J., 133*(3), 669-682. Int.. https://doi.org/10.1046/j.1365-246X.1998.00521.x

Morgan, W. J. (1968). Rises, trenches, great faults, and crustal blocks. *J. Geophys. Res., 73*(6), 1959–1982. https://doi.org/10.1029/JB073i006p01959

Morishige, M., & Honda, S. (2013). Mantle flow and deformation of subducting slab at a plate junction. Earth. *Plan. Sci. Lett., 365*, 132-142. https://doi.org/10.1016/j.epsl.2013.01.033

Morley, L. W., & Larochelle, A. (2020). Paleomagnetism As a Means Of Dating Geological Events. In Geochronology in Canada (pp. 39–51). *University of Toronto Press*. https://doi.org/10.3138/9781487586041-007

Moroz, V. I., Moshkin, B. E., Ekonomov, A. P., Sanko, N. F., Parfentev, N. A., & Golovin, Y. M. (1979). Venera 11 and 12 descent-probe spectrophotometry - The Venus dayside sky spectrum. *SvAL, 5*, 118–121.

Moyen, J. F., & van Hunen, J. (2012). Short-term episodicity of Archaean plate tectonics. *Geology, 40*(5), 451–454. https://doi.org/10.1130/G322894.1

Murakami, M., Hirose, K., Yurimoto, H., Nakashima, S., & Takafuji, N. (2002). Water in earth's lower mantle. *Science, 295*(5561), 1885–1887. https://doi.org/10.1126/science.1065998

Murakami, M., Hirose, K., Kawamura, K., Sata, N., & Ohishi, Y. (2004). Post-Perovskite Phase Transition in $MgSiO_3$. *Science, 304*(5672), 855–858. https://doi.org/10.1126/science.1095932

Murnaghan, F. D. (1937). A theory of elasticity. *Phys. Rev., 51*(7), 593. https://doi.org/10.1103/PhysRev.51.593

REFERENCES - N

Nabarro, F. R. N. (1948). Report of a Conference on the Strength of Solids. *The Physical Society*, London, 75.

Nakagawa, T., & Tackley, P. J. (2005). Three-dimensional numerical simulations of thermo-chemical multiphase convection in Earth's mantle. *P. 3rd MIT Conf. Comput. Fluid Sol. Mech*. https://doi.org/10.1029/2001GC000167

Nakagawa, T., Tackley, P. J., Deschamps, F., & Connolly, J. A. D. (2009). Incorporating self-consistently calculated mineral physics into thermochemical mantle convection simulations in a 3-D spherical shell and its influence on seismic anomalies in Earth's mantle. *Geochem. Geophys. Geosys., 10*(3). https://doi.org/10.1029/2008GC002280

Nakagawa, T., Tackley, P. J., Deschamps, F., & Connolly, J. A. D. (2010). The influence of MORB and harzburgite composition on thermo-chemical mantle convection in a 3D spherical shell with self-consistently calculated mineral physics. *Earth. Plan. Sci. Lett., 296*(3–4), 403–412. https://doi.org/10.1016/j.epsl.2010.05.026

Nakagawa, T., & Tackley, P. J. (2010). Influence of initial CMB temperature and other parameters on the thermal evolution of Earth's core resulting from thermochemical spherical mantle convection. *Geochem. Geophys. Geosyst., 11*(6), 6001. https://doi.org/10.1029/2010GC003031

Nakagawa, T., & Tackley, P. J. (2011). Effects of low-viscosity post-perovskite on thermo-chemical mantle convection in a 3-D spherical shell. *Geophys. Res. Lett., 38*(4). https://doi.org/10.1029/2010GL046494

Nakagawa, T., & Tackley, P. J. (2012). Influence of magmatism on mantle cooling, surface heat flow and Urey ratio. *Earth Plan. Sci. Lett., 329*, 1-10. https://doi.org/10.1016/j.epsl.2012.02.011

Nakagawa, T., & Tackley, P. J. (2013). Implications of high core thermal conductivity on Earth's coupled mantle and core evolution. *Geophys. Res. Lett., 40*(11), 2652-2656.. https://doi.org/10.1002/grl.50574

Nakagawa, T., & Tackley, P. J. (2014). Influence of combined primordial layering and recycled MORB on the coupled thermal evolution of Earth's mantle and core. *Geochem. Geophys. Geosys., 15*(3), 619-633. https://doi.org/10.1002/2013GC005128

Nakagawa, T., & Tackley, P. J. (2015). Influence of plate tectonic mode on the coupled thermochemical evolution of Earth's mantle and core. *Geochem. Geophys. Geosys.*, *16*(10), 3400-3413. https://doi.org/10.1002/2015GC005996

Nakagawa, T., Nakakuki, T., & Iwamori, H. (2015). Water circulation and global mantle dynamics: Insight from numerical modeling. *Geochem. Geophys. Geosyst , 16*(5), 1449-1464. https://doi.org/10.1002/2014GC005701

Nakagawa, T. (2017). On the numerical modeling of the deep mantle water cycle in global-scale mantle dynamics: The effects of the water solubility limit of lower mantle minerals. *J. Earth Sci., 28*(4), 563–577. https://doi.org/10.1007/s12583-017-0755-3

Nakagawa, T., & Iwamori, H. (2017). Long-Term Stability of Plate-Like Behavior Caused by Hydrous Mantle Convection and Water Absorption in the Deep Mantle. *J. Geophys. Res. - Sol. Ea., 122(10), 8431-8445*. https://doi.org/10.1002/2017JB014052

Nakagawa, T., & Spiegelman, M. W. (2017). Global-scale water circulation in the Earth's mantle: Implications for the mantle water budget in the early Earth. *Earth Planet Sc. Lett., 464*, 189-199. https://doi.org/10.1016/j.epsl.2017.02.010

Nakagawa, T., & Iwamori, H. (2019). On the implications of the coupled evolution of the deep planetary interior and the presence of surface ocean water in hydrous mantle convection. *C. R. - Geosci*. https://doi.org/10.1016/j.crte.2019.02.001

Nakamoto, K., Margoshes, M., & Rundle, R. E. (1955). Stretching Frequencies as a Function of Distances in Hydrogen Bonds. *J. Am. Chem. Soc., 77*(24), 6480-6486. https://doi.org/10.1021/ja01629a013

Namouni, F., Luciani, J. F., Pellat, R., Namouni, F., Luciani, J. F., & Pellat, R. (1996). The formation of planetary cores: a numerical approach. *Astro. Astrophy.*, *307*, 972-980
Nat. Geosci., 12(10), 869–872. https://doi.org/10.1038/s41561-019-0452-1

Natali, C., Beccaluva, L., Bianchini, G., & Siena, F. (2011). Rhyolites associated to Ethiopian CFB: Clues for initial rifting at the Afar plume axis. *Earth Planet Sc. Lett., 312*(1–2), 59–68. https://doi.org/10.1016/j.epsl.2011.09.059
Nature, 438(7070), 1004–1007. https://doi.org/10.1038/nature04345

Nestola, F., & Smyth, J. R. (2016). Diamonds and water in the deep Earth: a new scenario. *Int. Geol. Rev., 58*(3), 263–276. https://doi.org/10.1080/00206814.2015.1056758

Newton, I. (1833). Philosophiae naturalis principia mathematica (Vol. 2). *typis A. et JM Duncan*, 474 pages.

Nikolaeva, K., Gerya, T. V., & Marques, F. O. (2010). Subduction initiation at passive margins: Numerical modeling. *J. Geophys. Res., 115*(B3), B03406. https://doi.org/10.1029/2009JB006549

Nimmo, F., & McKenzie, D. (1998). Volcanism And Tectonics On Venus. *Annu. Rev. Earth Pl. Sc., 26*(1), 23–51. https://doi.org/10.1146/annurev.earth.26.1.23

Nimmo, F. (2002). Why does Venus lack a magnetic field. *Geology, 11*, 987–990. https://doi.org/10.1130/0091-7613(2002)030<0987:WDVLAM>2.0.CO;2

Nimmo, F. (2015). Thermal and compositional evolution of the core. *Treat. Geophys., 9,* 201-219. https://doi.org/10.1016/B978-0-444-53802-4.00139-1

Nishi, M., Irifune, T., Tsuchiya, J., Tange, Y., Nishihara, Y., Fujino, K., & Higo, Y. (2014). Stability of hydrous silicate at high pressures and water transport to the deep lower mantle. *Nat. Geosci., 7*(3), 224–227. https://doi.org/10.1038/ngeo2074

Nishi, M., Kuwayama, Y., Tsuchiya, J., & Tsuchiya, T. (2017). The pyrite-type high-pressure form of FeOOH. *Nature, 547*(7662), 205–208. https://doi.org/10.1038/nature22823

Niu, F., Silver, P. G., Nadeau, R. M., & McEvilly, T. V. (2003). Migration of seismic scatterers associated with the 1993 Parkfield aseismic transient event. *Nature, 426*(6966), 544–548. https://doi.org/10.1038/nature02151

Nolet, G., & Zielhuis, A. (1994). Low S velocities under the Tornquist-Teisseyre zone: evidence for water injection into the transition zone by subduction. *J. Geophys. Res., 99*(B8), 813–828. https://doi.org/10.1029/94jb00083

Nye, J. F. (1985). Physical Properties of Crystals: Their Representation by Tensors and Matrices (2nd Ed.). *Clarendon Press*, 352 pages. ISBN-10: 0198511655

REFERENCES - O

O'Brien, D. P., Morbidelli, A., & Levison, H. F. (2006). Terrestrial planet formation with strong dynamical friction. *Icarus, 184*(1), 39–58. https://doi.org/10.1016/j.icarus.2006.04.005

O'Brien, D. P., Walsh, K. J., Morbidelli, A., Raymond, S. N., & Mandell, A. M. (2014). Water delivery and giant impacts in the "Grand Tack" scenario. *Icarus, 239*, 74–84. https://doi.org/10.1016/j.icarus.2014.05.009

O'Brien, D. P., Izidoro, A., Jacobson, S. A., Raymond, S. N., & Rubie, D. C. (2018). The Delivery of Water During Terrestrial Planet Formation. *Space Sci. Rev., 214*(1), 1-24. https://doi.org/10.1007/s11214-018-0475-8

O'Hara, K. E., Hu, X., & Cahill, D. G. (2001). Characterization of nanostructured metal films by picosecond acoustics and interferometry. *J. App. Phys., 90*(9), 4852-4858. https://doi.org/10.1063/1.1406543

O'Neill, C., Jellinek, A. M., & Lenardic, A. (2007). Conditions for the onset of plate tectonics on terrestrial planets and moons. *Earth Plan. Sci. Lett., 261*(1–2), 20–32. https://doi.org/10.1016/j.epsl.2007.05.038

O'Reilly, T. C., & Davies, G. F. (1981). Magma transport of heat on Io: A mechanism allowing a thick lithosphere. *Geophys. Res. Lett., 8*(4), 313–316. https://doi.org/10.1029/GL008i004p00313

Oganov, A. R., & Ono, S. (2004). Theoretical and experimental evidence for a post-perovskite phase of $MgSiO_3$ in Earth's D″ layer. *Nature, 430*(6998), 445–448. https://doi.org/10.1038/nature02701

Ogawa, M., Schubert, G., & Zebib, A. (1991). Numerical simulations of three-dimensional thermal convection in a fluid with strongly temperature-dependent viscosity. *J. Fluid Mech., 233*(299), 299–328. https://doi.org/10.1017/S0022112091000496

Ogawa, M., & Yanagisawa, T. (2011). Numerical models of Martian mantle evolution induced by magmatism and solid-state convection beneath stagnant lithosphere. *J. Geophys. Res., 116*(E8), E08008. https://doi.org/10.1029/2010JE003777

Ogura, Y., & Phillips, N. A. (1962). Scale Analysis of Deep and Shallow Convection in the Atmosphere. *J. Atm. Sci., 19*(2), 173-179. https://doi.org/10.1175/1520-0469(1962)019<0173:saodas>2.0.co;2

Oguri, K., Funamori, N., Sakai, F., Kondo, T., Uchida, T., & Yagi, T. (1997). High-pressure and high-temperature phase relations in diopside $CaMgSi_2O_6$. *Phys. Earth Planet. In., 104*(4), 363–370. https://doi.org/10.1016/S0031-9201(97)00029-0

Ohtani, E., Shibata, T., Kubo, T., & Kato, T. (1995). Stability of hydrous phases in the transition zone and the upper most part of the lower mantle. *Geophys. Res. Lett., 22*(19), 2553–2556. https://doi.org/10.1029/95GL02338

Ohtani, E., Mizobata, H., Kudoh, Y., Nagase, T., Arashi, H., Yurimoto, H., & Miyagi, I. (1997). A new hydrous silicate, a water reservoir, in the upper part of the lower mantle. *Geophys. Res. Lett., 24*(9), 1047–1050. https://doi.org/10.1029/97GL00874

Ohtani, E., Mizobata, H., & Yurimoto, H. (2000). Stability of dense hydrous magnesium silicate phases in the systems Mg_2SiO_4-H_2O and $MgSiO_3$-H_2O at pressures up to 27 GPa. *Phys. Chem. Miner., 27*(8), 533–544. https://doi.org/10.1007/s002690000097

Ohtani, E., Toma, M., Litasov, K., Kubo, T., & Suzuki, A. (2001). Stability of dense hydrous magnesium silicate phases and water storage capacity in the transition zone and lower mantle. *Phys. Earth Planet. In., 124*(1-2), 105-117. https://doi.org/10.1016/S0031-9201(01)00192-3

Ohtani, E., Litasov, K., Hosoya, T., Kubo, T., & Kondo, T. (2004). Water transport into the deep mantle and formation of a hydrous transition zone. *Phys. Earth Planet. In*., 255–269. https://doi.org/10.1016/j.pepi.2003.09.015

Ohtani, E. (2005). Water in the Mantle. *Elements, 1*(1), 25–30. https://doi.org/10.2113/gselements.1.1.25

Ohtani, E., & Zhao, D. (2009). The role of water in the deep upper mantle and transition zone: dehydration of stagnant slabs and its effects on the big mantle wedge. *Russ. Geol. Geophys., 50*(12), 1073–1078. https://doi.org/10.1016/j.rgg.2009.11.006

Ohtani, E., Amaike, Y., Kamada, S., Sakamaki, T., & Hirao, N. (2014). Stability of hydrous phase H MgSiO4H2 under lower mantle conditions. *Geophys. Res. Lett., 41*(23), 8283–8287. https://doi.org/10.1002/2014GL061690

Ohtani, E., & Litasov, K. D. (2018). The effect of water on mantle phase transitions. *Rev. Min. Geochem., 62*(1), 397-420. https://doi.org/10.2138/rmg.2006.62.17

Ohtani, E., Yuan, L., Ohira, I., Shatskiy, A., & Litasov, K. (2018). Fate of water transported into the deep mantle by slab subduction. *J. Asian. Earth Sci., 167*, 2–10. https://doi.org/10.1016/j.jseaes.2018.04.024

Ohtani, E. (2020). The role of water in Earth's mantle. *Natl. Sci. Rev., 7*(1), 224-232. https://doi.org/10.1093/nsr/nwz071.

Ohuchi, T., Kawazoe, T., Higo, Y., Funakoshi, K. I., Suzuki, A., Kikegawa, T., & Irifune, T. (2015). Dislocation-accommodated grain boundary sliding as the major deformation mechanism of olivine in the Earth's upper mantle. *Sci. Adv., 1*(9), e1500360. https://doi.org/10.1126/sciadv.1500360

Okamoto, K., & Maruyama, S. (1999). The high-pressure synthesis of lawsonite in the MORB+H_2O system. *Am. Min., 84*(3), 362–373. https://doi.org/10.2138/am-1999-0320

Oki, T., Entekhabi, D., & Harrold, T. I. (2004). The global water cycle. *Global energy and water cycles, 10*, 27. https://doi.org/10.1029/150GM18

Oldham, R. D. (1906). The constitution of the interior of the earth, as revealed by earthquakes. *Q. J. Geo. Soc. Lond., 62*(1–4), 456–475. https://doi.org/10.1144/GSL.JGS.1906.062.01-04.21

Olson, P., Schubert, G., & Anderson, C. (1987). Plume formation in the D″-layer and the roughness of the core-mantle boundary. *Nature, 327*(6121), 409–413. https://doi.org/10.1038/327409a0

Osako, M., & Ito, E. (1991). Thermal diffusivity of $MgSiO_3$ perovskite. *Geophys. Res. Lett., 18*(2), 239-242. https://doi.org/10.1029/91GL00212

Oufi, O. (2002). Magnetic properties of variably serpentinized abyssal peridotites. *J. Geophys. Res., 107*(B5), EPM 3-1. https://doi.org/10.1029/2001jb000549

Owen, T., & Bar-Nun, A. (1995). Comets, impacts, and atmospheres. *Icarus, 116*(2), 215–226. https://doi.org/10.1006/icar.1995.1122

REFERENCES - P

Pacalo, R. E., & Parise, J. B. (1992). Crystal structure of superhydrous B, a hydrous magnesium silicate synthesized at 1400 C and 20 GPa. *Am. Min.*, *77*(5-6), 681-684.

Paddock, C. A., & Eesley, G. L. (1986). Transient thermoreflectance from thin metal films. *J. App. Phys., 60*(1), 285-290. https://doi.org/10.1063/1.337642

Palme, H., & O'Neill, H. S. C. (2007). Cosmochemical Estimates of Mantle Composition. Treatise on Geochemistry (The Mantle and Core), Vol. HD *Holland & KK Turekian*. https://doi.org/10.1016/B0-08-043751-6/02177-0

Panasyuk, S. V, & Hager, B. H. (2000). Inversion for mantle viscosity profiles constrained by dynamic topography and the geoid, and their estimated errors. *Geophys. J. Int., 143*(3), 821-836.

Panero, W. R., Pigott, J. S., Reaman, D. M., Kabbes, J. E., & Liu, Z. (2015). Dry $(Mg,Fe)SiO_3$ perovskite in the Earth's lower mantle. *J. Geophys. Res.- Sol. Ea., 120*(2), 894–908. https://doi.org/10.1002/2014JB011397

Parai, R., & Mukhopadhyay, S. (2012). How large is the subducted water flux? New constraints on mantle regassing rates. *Earth Planet Sc. Lett.*, 317–318, 396–406. https://doi.org/10.1016/j.epsl.2011.11.024

Patočka, V., Čadek, O., Tackley, P. J., & Čížková, H. (2017). Stress memory effect in viscoelastic stagnant lid convection. *Geophys. J. Int., 209*(3), 1462-1475. https://doi.org/10.1093/gji/ggx102

Patočka, V., Čížková, H., & Tackley, P. (2019). Do elasticity and a free surface affect lithospheric stresses caused by upper-mantle convection. *Geophys. J. Int. , 216*(3), 1740-1760. https://doi.org/10.1093/gji/ggy513

Pearson, D. G., Brenker, F. E., Nestola, F., Mcneill, J., Nasdala, L., Hutchison, M. T., … Vincze, & L. (2014). Hydrous mantle transition zone indicated by ringwoodite included within diamond. *Nature, 507*(7491), 221-224. https://doi.org/10.1038/nature13080

Pellissier, L., Heine, C., Rosauer, D. F., & Albouy, C. (2018). Are global hotspots of endemic richness shaped by plate tectonics? *Biol. J. Linn. Soc., 123*(1), 247–261. https://doi.org/10.1093/biolinnean/blx125

Peltier, W. R. (1996). Mantle viscosity and ice-age ice sheet topography. *Science, 273*(5280), 1359-1364. https://doi.org/10.1126/science.273.5280.1359

Peltier, W. R. (1999). Global sea level rise and glacial isostatic adjustment. *Global Plan. Change, 20*(2-3), 93-123. https://doi.org/10.1016/S0921-8181(98)00066-6

Peslier, A. H., Schönbächler, M., Busemann, H., & Karato, S. I. (2017). Water in the Earth's Interior: Distribution and Origin. *Space Sci. Rev., 212*(1–2), 1–68. https://doi.org/10.1007/s11214-017-0387-z

Pfeilsticker, K., Lotter, A., Peters, C., & Bösch, H. (2003). Atmospheric detection of water dimers via near-infrared absorption. *Science, 300*(5628), 2078-2080. https://doi.org/10.1126/science.1082282

Phillips, R. J., Kaula, W. M., McGill, G. E., & Malin, M. C. (1981). Tectonics and evolution of venus. *Science, 212*(4497), 879–887. https://doi.org/10.1126/science.212.4497.879

Philos. T. R. Soc.-A, 376(2132), 20170401. https://doi.org/10.1098/rsta.2017.0401

Phys. Earth Planet. In., 159(1–2), 118–126. https://doi.org/10.1016/j.pepi.2006.07.004

Planini, G., & Vollmer, M. (2008). The surface-to-volume ratio in thermal physics: From cheese cube physics to animal metabolism. *Europ. J. Phys., 29*(2), 369–384. https://doi.org/10.1088/0143-0807/29/2/017

Plank, T., & Langmuir, C. H. (1998). The chemical composition of subducting sediment and its consequences for the crust and mantle. *Chem. Geol., 145*(3–4), 325–394. https://doi.org/10.1016/S0009-2541(97)00150-2

Plank, T. (2013). The Chemical Composition of Subducting Sediments. In Treatise on Geochemistry: Second Edition, 4, 607–629. *Elsevier Inc*. https://doi.org/10.1016/B978-0-08-095975-7.00319-3

Poirier, J. P., & Tarantola, A. (1998). A logarithmic equation of state. *Phys. Earth Planet. In , 109*(1-2), 1-8. https://doi.org/10.1016/S0031-9201(98)00112-5

Poli, S., & Schmidt, M. W. (2002). Petrology of Subducted Slabs. *Annu. Rev. Earth Pl. Sc., 30*(1), 207–235. https://doi.org/10.1146/annurev.earth.30.091201.140550

Pollack, J. B., Toon, O. B., & Boese, R. (1980). Greenhouse models of Venus' High surface temperature, as constrained by Pioneer Venus measurements. *J. Geophys. Res., 85*(A13), 8223. https://doi.org/10.1029/ja085ia13p08223

Pommier, A. (2014). Interpretation of Magnetotelluric Results Using Laboratory Measurements. *Surveys in Geophysics, 35*(1), 41-84. https://doi.org/10.1007/s10712-013-9226-2

Popov, A., Kaus, B., & Gutenberg, J. (2013). LaMEM (Lithosphere and Mantle Evolution Model): advancing a staggered-grid finite difference version of the code. *EGU General Assembly Conference* Abstracts (pp. EGU2013-7761).

Posner, E. S., & Steinle-Neumann, G. (2019). Mass Transport and Structural Properties of Binary Liquid Iron Alloys at High Pressure. *Geochem. Geophy. Geosy., 20*(7), 3556-3568. https://doi.org/10.1029/2019GC008393

Powell, R., Holland, T., & Worley, B. (1998). Calculating phase diagrams involving solid solutions via non-linear equations, with examples using THERMOCALC. *J. Metam. Geoph., 16*(4), 577–588. https://doi.org/10.1111/j.1525-1314.1998.00157.x

Prager, W., & Hodge, P. G. (1968). Theory of perfectly plastic solids. *Dover Publications*, 497 pages. https://doi.org/10.1017/s0368393100128263

Price, D. G., Alfèd, D., Vocadlo, L., & Gillan, M. J. (2004). The earth's core: An approach from first principles. *Geophys. Monog. Series*, 1-12. https://doi.org/10.1029/150GM02

Priymak, V. G., & Miyazaki, T. (1998). Accurate Navier-Stokes Investigation of Transitional and Turbulent Flows in a Circular Pipe. *J. Comput. Phys., 142*(2), 370–411. https://doi.org/10.1006/jcph.1998.5931

REFERENCES - R

Ranalli, G. (1995). Rheology of the Earth. *Springer Science & Business Media*, 432 pages. ISBN-10: 0412546701

Ranero, C. R., Morgan, J. P., Mcintosh, K., & Reichert, C. (2003). Bending-related faulting and mantle serpentinization at the Middle America trench. *Nature, 425*(6956), 367-373. https://doi.org/10.1038/nature01961.

Raymond, S. N., O'Brien, D. P., Morbidelli, A., & Kaib, N. A. (2009). Building the terrestrial planets: Constrained accretion in the inner Solar System. *Icarus, 203*(2), 644–662. https://doi.org/10.1016/j.icarus.2009.05.016

Raymond, S. N., & Izidoro, A. (2017a). Origin of water in the inner Solar System: Planetesimals scattered inward during Jupiter and Saturn's rapid gas accretion. *Icarus, 297*, 134–148. https://doi.org/10.1016/j.icarus.2017.06.030

Raymond, S. N., & Izidoro, A. (2017b). The empty primordial asteroid belt. *Sci. Adv., 3*(9), e1701138. https://doi.org/10.1126/sciadv.1701138

Reed, S. J. B. (2005). Electron microprobe analysis and scanning electron microscopy in geology (2nd Ed.). *Cambridge University Press*, 232 pages. ISBN: 9780521848756
Rev. Mineral. Geochem., 62(1), 193-230. https://doi.org/10.2138/rmg.2006.62.9

Revenaugh, J., & Sipkin, S. A. (1994). Seismic evidence for silicate melt atop the 410-km mantle discontinuity. *Nature, 369*(6480), 474–476. https://doi.org/10.1038/369474a0

Ribe, N. M. (2010). Bending mechanics and mode selection in free subduction: A thin-sheet analysis. *Geophys. J. Int., 180*(2), 559–576. https://doi.org/10.1111/j.1365-246X.2009.04460.x

Ribe, N. M., & Xu, B. (2020). Subduction of non-Newtonian plates: Thin-sheet dynamics of slab necking and break-off. *Geophys. J. Int., 220*(2), 910–927. https://doi.org/10.1093/gji/ggz500

Richard, G., Bercovici, D., & Karato, S. I. (2006). Slab dehydration in the Earth's mantle transition zone. *Earth Planet Sc. Lett., 251*(1–2), 156–167. https://doi.org/10.1016/j.epsl.2006.09.006

Richards, M. A., Yang, W.-S., Baumgardner, J. R., & Bunge, H.-P. (2001). Role of a low-viscosity zone in stabilizing plate tectonics: Implications for comparative terrestrial planetology. *Geochem. Geophys. Geosyst., 2*(8). https://doi.org/10.1029/2000gc000115

Richardson, S. H., Shirey, S. B., Harris, J. W., & Carlson, R. W. (2001). Archean subduction recorded by Re-Os isotopes in eclogitic sulfide inclusions in Kimberley diamonds. *Earth Plan. Sci. Lett., 191*(3–4), 257–266. https://doi.org/10.1016/S0012-821X(01)00419-8

Ricolleau, A., Fei, Y., Cottrell, E., Watson, H., Deng, L., Zhang, L., … Prakapenka, V. (2009). Density profile of pyrolite under the lower mantle conditions. *Geophys. Res. Lett., 36*(6), L06302. https://doi.org/10.1029/2008GL036759

Ringwood, A. E. (1962). A model for the upper mantle. *J. Geophys. Res., 67*(2), 857–867. https://doi.org/10.1029/jz067i002p00857

Ringwood, A. E., & Major, A. (1967). High-pressure reconnaissance investigations in the system Mg_2SiO_4 - MgO - H_2O. *Earth Planet Sc. Lett., 2*(2), 130–133. https://doi.org/10.1016/0012-821X(67)90114-8

Ringwood, A. E., & Anderson, D. L. (1977). Earth and Venus: A comparative study. *Icarus, 30*(2), 243–253. https://doi.org/10.1016/0019-1035(77)90156-7

Ritsema, J., Deuss, A., van Heijst, H. J., & Woodhouse, J. H. (2011). S40RTS: a degree-40 shear-velocity model for the mantle from new Rayleigh wave dispersion, teleseismic traveltime and normal-mode splitting function measurements. *Geophys. J. Int., 184*(3), 1223–1236. https://doi.org/10.1111/J.1365-246X.2010.04884.X

Ritsema, J., & Lekić, V. (2020). Heterogeneity of Seismic Wave Velocity in Earth's Mantle. *Annu. Rev. Earth Pl. Sc , 48*, 377-401. https://doi.org/10.1146/annurev-earth-082119-065909

Rolf, T., & Tackley, P. J. (2011). Focussing of stress by continents in 3D spherical mantle convection with self-consistent plate tectonics. *Geophys. Res. Lett., 38*(18).. https://doi.org/10.1029/2011GL048677

Rolf, T., & Pesonen, L. J. (2018). Geodynamically consistent inferences on the uniform sampling of Earth's paleomagnetic inclinations. *Gondw. Res., 63*, 1-14. https://doi.org/10.1016/j.gr.2018.05.008

Rolf, T., Capitanio, F. A., & Tackley, P. J. (2018). Constraints on mantle viscosity structure from continental drift histories in spherical mantle convection models. *Tectonophysics, 746*, 339-351. https://doi.org/10.1016/j.tecto.2017.04.031

Rolf, T., Steinberger, B., Sruthi, U., & Werner, S. C. (2018). Inferences on the mantle viscosity structure and the post-overturn evolutionary state of Venus. *Icarus, 313*, 107–123. https://doi.org/10.1016/j.icarus.2018.05.014

Ross, C. S., Foster, M. D., & Myers, A. T. (1954). Origin of dunites and of olivine-rich inclusions in basaltic rocks. *Am. Min., 39*(9-10), 693-737.

Ross, M. N., & Schubert, G. (1987). Tidal heating in an internal ocean model of Europa. *Nature, 325*(6100), 133–134. https://doi.org/10.1038/325133a0

Ross, M. N., & Schubert, G. (1989). Viscoelastic models of tidal heating in Enceladus. *Icarus, 78*(1), 90–101. https://doi.org/10.1016/0019-1035(89)90071-7

Rossman, G. R. (2014). Optical spectroscopy. *Rev. Min. Geochem., 78*(1), 371-398. https://doi.org/10.2138/rmg.2014.78.9

Rost, S., Garnero, E. J., Williams, Q., & Manga, M. (2005). Seismological constraints on a possible plume root at the core-mantle boundary. *Nature, 435*(7042), 666–669. https://doi.org/10.1038/nature03620

Rozel, A., Besserer, J., Golabek, G. J., Kaplan, M., & Tackley, P. J. (2014). Self-consistent generation of single-plume state for Enceladus using non-Newtonian rheology. *J. Geophys. Res. E - Plan., 119*(3), 416-439. https://doi.org/10.1002/2013JE004473

Rozel, A., Golabek, G. J., Näf, R., & Tackley, P. J. (2015). Formation of ridges in a stable lithosphere in mantle convection models with a viscoplastic rheology. *Geophys. Res. Lett., 42*(12), 4770-4777. https://doi.org/10.1002/2015GL063483

Rozel, A., Golabek, G. J., Jain, C., Tackley, P. J., & Gerya, T. (2017). Continental crust formation on early Earth controlled by intrusive magmatism. *Nature, 545*(7654), 332-335. https://doi.org/10.1038/nature22042

Rubie, D. C., Frost, D. J., Mann, U., Asahara, Y., Nimmo, F., Tsuno, K., … Palme, H. (2011). Heterogeneous accretion, composition and core-mantle differentiation of the Earth. *Earth Planet Sc. Lett., 301*(1–2), 31–42. https://doi.org/10.1016/j.epsl.2010.11.030

Rubie, D. C., Jacobson, S. A., Morbidelli, A., O'Brien, D. P., Young, E. D., de Vries, J., … Frost, D. J. (2015). Accretion and differentiation of the terrestrial planets with implications for the compositions of early-formed Solar System bodies and accretion of water. *Icarus, 248*, 89–108. https://doi.org/10.1016/j.icarus.2014.10.015

Ruedas, T., & Breuer, D. (2019). Dynamical effects of multiple impacts: Large impacts on a Mars-like planet. *Phys. Earth Plan. In., 287*, 76-92. https://doi.org/10.1016/j.pepi.2019.01.003

Rüpke, L. H., Morgan, J. P., Hort, M., & Connolly, J. A. D. (2004). Serpentine and the subduction zone water cycle. *Earth Planet Sc. Lett., 223*(1–2), 17–34. https://doi.org/10.1016/j.epsl.2004.04.018

Russell, C. T. (1980). Planetary magnetism. *Rev. Geophys., 18*(1), 77-106. https://doi.org/10.1029/RG018i001p00077

Rustioni, G., Audétat, A., & Keppler, H. (2019). Experimental evidence for fluid-induced melting in subduction zones. *Geochem. Persp. Let, 11*, 49–54. https://doi.org/10.7185/geochemlet.1925

Rybacki, E., & Dresen, G. (2000). Dislocation and diffusion creep of synthetic anorthite aggregates. *J. Geophys. Res.- Sol. Ea., 105*(B11), 26017–26036. https://doi.org/10.1029/2000jb900223

REFERENCES - S

Saffer, D. M., & Tobin, H. J. (2011). Hydrogeology and Mechanics of Subduction Zone Forearcs: Fluid Flow and Pore Pressure. *Annu. Rev. Earth Pl. Sc., 39*(1), 157–186. https://doi.org/10.1146/annurev-earth-040610-133408

Sagan, C. (1994). Pale Blue Dot : a vision of the human future in space Sagan. *Random House Digital, Inc*., 456 pages.

Saikia, A., Frost, D. J., & Rubie, D. C. (2008). Splitting of the 520-kilometer seismic discontinuity and chemical heterogeneity in the mantle. *Science, 319*(5869), 1515–1518. https://doi.org/10.1126/science.1152818

Sakamaki, T., Ohtani, E., Urakawa, S., Suzuki, A., & Katayama, Y. (2009). Measurement of hydrous peridotite magma density at high pressure using the X-ray absorption method. *Earth Planet Sc. Lett., 287*(3–4), 293–297. https://doi.org/10.1016/j.epsl.2009.07.030

Samuel, H., & Tackley, P. J. (2008). Dynamics of core formation and equilibration by negative diapirism. *Geochem. Geophys. Geosys., 9*(6). https://doi.org/10.1029/2007GC001896

Samuel, H., & Evonuk, M. (2010). Modeling advection in geophysical flows with particle level sets. *Geochem. Geophys. Geosys., 11*(8). https://doi.org/10.1029/2010GC003081

Sanchez-Valle, C., Sinogeikin, S. V., Smyth, J. R., & Bass, J. D. (2008). Sound velocities and elasticity of DHMS phase A to high pressure and implications for seismic velocities and anisotropy in subducted slabs. *Phys. Earth Planet. In., 170*(3–4), 229–239. https://doi.org/10.1016/j.pepi.2008.07.015

Sangi, R., Amidpour, M., & Hosseinizadeh, B. (2011). Modeling and numerical simulation of solar chimney power plants. *Solar Energy, 85*(5), 829–838. https://doi.org/10.1016/j.solener.2011.01.011

Sano, A., Ohtani, E., Kubo, T., & Funakoshi, K. I. (2004). In situ X-ray observation of decomposition of hydrous aluminum silicate $AlSiO_3OH$ and aluminum oxide hydroxide d-AlOOH at high pressure and temperature. *J. Phys. and Chem. Solids, 65*(8-9), 1547-1554. https://doi.org/10.1016/j.jpcs.2003.12.015

Sano, A., Ohtani, E., Litasov, K., Kubo, T., Hosoya, T., Funakoshi, K., & Kikegawa, T. (2006). In situ X-ray diffraction study of the effect of water on the garnet-perovskite transformation in MORB and implications for the penetration of oceanic crust into the lower mantle.

Sarafian, E., Gaetani, G. A., Hauri, E. H., & Sarafian, A. R. (2017). Experimental constraints on the damp peridotite solidus and oceanic mantle potential temperature. *Science, 355*(6328), 942-945. https://doi.org/10.1126/science.aaj2165

Satta, N., Marquardt, H., Kurnosov, A., Buchen, J., Kawazoe, T., McCammon, C., & Ballaran, T. B. (2019). Single-crystal elasticity of iron-bearing phase e and seismic detection of water in Earth's upper mantle. *Am. Min., 104*(10), 1526–1529. https://doi.org/10.2138/am-2019-7084

Satta, N. (2020). High Pressure Minerals in the Earth and Moon: Understanding the Lunar Impact History and Earth's Deep Water Cycle. *Ph.D. Thesis*. Retrieved from https:// https://epub.uni-bayreuth.de/5517/

Saunders, A. D., Norry, M. J., & Tarney, J. (1988). Origin of morb and chemically-depleted mantle reservoirs: Trace element constraints. *J. Petrol.*, (1), 415-445.. https://doi.org/10.1093/petrology/Special_Volume.1.415

Saxena, S. K. (1996). Earth mineralogical model: Gibbs free energy minimization computation in the system MgO-FeO-SiO_2. *Geochim. Cosmochim. Acta., 60*(13), 2379-2395. https://doi.org/10.1016/0016-7037(96)00096-8

Saxena, S. K., Chatterjee, N., Fei, Y., & Shen, G. (2012). Thermodynamic data on oxides and silicates: An assessed data set based on thermochemistry and high pressure phase equilibrium. *Springer Science & Business Media*, 436 pages. ISBN-10: 3540568980

Schaeffer, A. J., & Lebedev, S. (2013). Global shear speed structure of the upper mantle and transition zone. *Geophys. J. Int., 194*(1), 417–449. https://doi.org/10.1093/GJI/GGT095

Schermaier, A., Haunschmid, B., & Finger, F. (1997). Distribution of Variscan I- and S-type granites in the Eastern Alps: A possible clue to unravel pre-Alpine basement structures. *Tectonophysics*, 272(2–4), 315–333. https://doi.org/10.1016/S0040-1951(96)00265-X

Scheurer, P. B., & Debrock, G. (1988). Newton's scientific and philosophical legacy (Vol. 123). *Springer Science & Business Media*, 396 pages. ISBN-10: 9401077649

Schierjott, J., Rozel, A., & Tackley, P. (2020). On the self-regulating effect of grain size evolution in mantle convection models: Application to thermochemical piles. *Sol. Earth, 11*(3), 959-982. https://doi.org/10.5194/se-11-959-2020

Schilling, J. G., Meyer, P. S., & Kingsley, R. H. (1982). Evolution of the Iceland hotspot. *Nature, 296*(5855), 313–320. https://doi.org/10.1038/296313a0

Schlichting, H. E., Sari, R., & Yalinewich, A. (2015). Atmospheric mass loss during planet formation: The importance of planetesimal impacts. *Icarus, 247*, 81–94. https://doi.org/10.1016/j.icarus.2014.09.053

Schmandt, B., Jacobsen, S. D., Becker, T. W., Liu, Z., & Dueker, K. G. (2014). Dehydration melting at the top of the lower mantle. *Science, 344*(6189), 1265–1268. https://doi.org/10.1126/science.1253358

Schmeling, H., Babeyko, A. Y., Enns, A., Faccenna, C., Funiciello, F., Gerya, T., … van Hunen, J. (2008). A benchmark comparison of spontaneous subduction models-Towards a free surface. *Phys. Earth Plan. In., 171*(1–4), 198–223. https://doi.org/10.1016/j.pepi.2008.06.028

Schmidt, A., Chiesa, M., Chen, X., & Chen, G. (2008). An optical pump-probe technique for measuring the thermal conductivity of liquids. *Rev. Sci. Instr., 79*(6), 064902. https://doi.org/10.1063/1.2937458

Schmidt, M. W. (1995). Lawsonite: upper pressure stability and formation of higher density hydrous phases. *Am. Min., 80*(11–12), 1286–1292. https://doi.org/10.2138/am-1995-11-1218

Schmidt, M. W., & Poli, S. (1998). Experimentally based water budgets for dehydrating slabs and consequences for arc magma generation. *Earth Planet Sc. Lett., 163*(1–4), 361–379. https://doi.org/10.1016/S0012-821X(98)00142-3

Schubert, G., Yuen, D. A., & Turcotte, D. L. (1975). Role of Phase Transitions in a Dynamic Mantle. *Geophys. J. Roy. Astro. Soc., 42*(2), 705-735.. https://doi.org/10.1111/j.1365-246X.1975.tb05888.x

Schubert, G., & Sandwell, D. T. (1995). A global survey of possible subduction sites on Venus. *Icarus, 117*(1), 173–196. https://doi.org/10.1006/icar.1995.1150

Schubert, G., Russell, C. T., & Moore, W. B. (2000). Timing of the Martian dynamo. *Nature, 408*(6813), 666–667. https://doi.org/10.1038/35047163

Schubert, G., Turcotte, D. L., & Olson, P. (2001). Mantle Convection in the Earth and Planets. *Cambridge University Press*, 912 pages. https://doi.org/10.1017/cbo9780511612879

Schulze, K., Marquardt, H., Kawazoe, T., Boffa Ballaran, T., McCammon, C., Koch-Müller, M., … Marquardt, K. (2018). Seismically invisible water in Earth's transition zone? *Earth Planet Sc. Lett., 498*, 9–16. https://doi.org/10.1016/j.epsl.2018.06.021

Sci. Rep., 8(1), 6358. https://doi.org/10.1038/s41598-018-24832-y

Scott, T., & Kohlstedt, D. L. (2006). The effect of large melt fraction on the deformation behavior of peridotite. *Earth Planet Sc. Lett., 246*(3–4), 177–187. https://doi.org/10.1016/j.epsl.2006.04.027

Secco, A., LeBlanc, G. E., Yang, H., & Seibel, J. N. (1997). High pressure viscosity of an Fe-S liquid: Experimentally derived estimate of the viscosity of earth's outer core. *Geophys. Mono. Ser. AGU, 101*, 495-505. https://doi.org/10.1029/GM101p0495

Seiff, A., Kirk, D. B., Sommer, S. C., Young, R. E., Blanchard, R. C., Juergens, D. W., … Derr, J. S. (1979). Structure of the atmosphere of Venus up to 110 kilometers: Preliminary results from the four Pioneer Venus entry probes. *Science, 203*(4382), 787–790. https://doi.org/10.1126/science.203.4382.787

Seiff, A., Kirk, D. B., Young, R. E., Sommer, S. C., Blanchard, R. C., Findlay, J. T., & Kelly, G. M. (1979). Thermal contrast in the atmosphere of Venus: Initial appraisal from Pioneer Venus probe data. *Science, 205*(4401), 46–49. https://doi.org/10.1126/science.205.4401.46

Shearer, P. M. (1990). Seismic imaging of upper-mantle structure with new evidence for a 520-km discontinuity. *Nature, 344*(6262), 121–126. https://doi.org/10.1038/344121a0

Shearer, P. M. (1996). Transition zone velocity gradients and the 520-km discontinuity. *J. Geophys. Res. B- Sol. Ea., 101*(2), 3053–3066. https://doi.org/10.1029/95jb02812

Shephard, G., Crameri, F., & Heron, P. J. (2020). At the end of the rainbow-Scientific Colour Maps for science and society. *ESSOAr*. https://doi.org/10.1002/essoar.10505399.1

Shirey, S. B., & Richardson, S. H. (2011). Start of the wilson cycle at 3 Ga shown by diamonds from subcontinental mantle. *Science, 333*(6041), 434–436. https://doi.org/10.1126/science.1206275

Silver, P. G., & Holtz, W. E. (2002). The mantle flow field beneath Western North America. *Science, 295*(5557), 1054–1057. https://doi.org/10.1126/science.1066878

Sim, S. J., Stegman, D. R., & Coltice, N. (2016). Influence of continental growth on mid-ocean ridge depth. *Geochem. Geophys. Geosys., 17*(11), 4425-4437.. https://doi.org/10.1002/2016GC006629

Simmons, N. A., & Gurrola, H. (2000). Multiple seismic discontinuities near the base of the transition zone in the Earth's mantle. *Nature, 405*(6786), 559–562. https://doi.org/10.1038/35014589

Simmons, Nathan A., Forte, A. M., Boschi, L., & Grand, S. P. (2010). GyPSuM: A joint tomographic model of mantle density and seismic wave speeds. *J. Geophys. Res. - Sol. Ea., 115*(B12), 12310. https://doi.org/10.1029/2010JB007631

Sinogeikin, S. V., Bass, J. D., & Katsura, T. (2003). Single-crystal elasticity of ringwoodite to high pressures and high temperatures: Implications for 520 km seismic discontinuity. *Phys. Earth Planet. In., 136*(1–2), 41–66. https://doi.org/10.1016/S0031-9201(03)00022-0

Smolarkiewicz, P. K. (1984). A fully multidimensional positive definite advection transport algorithm with small implicit diffusion. *J. Comput. Phys., 54*(2), 325-362. https://doi.org/10.1016/0021-9991(84)90121-9

Smyth, J. R. (1987). The β-Mg_2SiO_4: a potential host for water in the mantle? *Am. Min., 72*(11-12), 1051-1055.

Smyth, J. R., & Frost, D. J. (2002). The effect of water on the 410-km discontinuity: An experimental study. *Geophys. Res. Lett., 29*(10), 123-1-123–124. https://doi.org/10.1029/2001gl014418

Solheim, L. P., & Peltier, W. R. (1994). Avalanche effects in phase transition modulated thermal convection: a model of Earth's mantle. *J. Geophys. Res., 99*(B4), 6997–7018. https://doi.org/10.1029/93JB02168

Solomatov, V. S. (1995). Scaling of temperature- and stress-dependent viscosity convection. *Phys. Fluids, 7*(2), 266–274. https://doi.org/10.1063/1.868624

Solomatov, V. S., & Moresi, L.-N. (1997). Three regimes of mantle convection with non-Newtonian viscosity and stagnant lid convection on the terrestrial planets. *Geophys. Res. Lett., 24*(15), 1907–1910. https://doi.org/10.1029/97GL01682

Solomatov, V. S., & Moresi, L.-N. (2000). Scaling of time-dependent stagnant lid convection: Application to small-scale convection on Earth and other terrestrial planets. *J. Geophys. Res-Sol. Ea., 105*(B9), 21795–21817. https://doi.org/10.1029/2000JB900197

Solomatov, V. S. (2001). Grain size-dependent viscosity convection and the thermal evolution of the earth. *Earth Planet Sc. Lett., 191*(3–4), 203–212. https://doi.org/10.1016/S0012-821X(01)00426-5

Song, T. R. A., Helmberger, D. V., & Grand, S. P. (2004). Low-velocity zone atop the 410-km seismic discontinuity in the northwestern United States. *Nature, 427*(6974), 530–533. https://doi.org/10.1038/nature02231

Sotin, C., & Labrosse, S. (1999). Three-dimensional thermal convection in an iso-viscous, infinite Prandtl number fluid heated from within and from below: Applications to the transfer of heat through planetary mantles. *Phys. Earth Plan. Int., 112*(3–4), 171–190. https://doi.org/10.1016/S0031-9201(99)00004-7

Sotin, C., Head, J. W., & Tobie, G. (2002). Europa: Tidal heating of upwelling thermal plumes and the origin of lenticulae and chaos melting. *Geophys. Res. Lett., 29*(8), 74-1-74–4. https://doi.org/10.1029/2001GL013844

Spektor, K., Nylen, J., Stoyanov, E., Navrotsky, A., Hervig, R. L., Leinenweber, K., … Häussermann, U. (2011). Ultrahydrous stishovite from high-pressure hydrothermal treatment of SiO_2. *P. Natl. Acad. Sci. USA, 108*(52), 20918–20922. https://doi.org/10.1073/pnas.1117152108

Speziale, S., Marquardt, H., & Duffy, T. S. (2014). Brillouin scattering and its application in geosciences. *Rev. Min. Geochem., 78*(1), 543-603. https://doi.org/10.2138/rmg.2014.78.14

Starrett, C. E., Perriot, R., Shaffer, N. R., Nelson, T., Collins, L. A., & Ticknor, C. (2020). Tabular electrical conductivity for aluminium. *Contr. Plasma Phys., 60*(3), e201900123. https://doi.org/10.1002/ctpp.201900123

Stein, C. A., & Stein, S. (1992). A model for the global variation in oceanic depth and heat flow with lithospheric age. *Nature, 359*(6391), 123–129. https://doi.org/10.1038/359123a0

Steinberger, B. (2000). Plumes in a convecting mantle: Models and observations for individual hotspots. *J. Geophys. Res.- Sol. Ea., 105*(B5), 11127–11152. https://doi.org/10.1029/1999JB900398

Steinberger, B., & Calderwood, A. R. (2006). Models of large-scale viscous flow in the Earth's mantle with constraints from mineral physics and surface observations. *Geophys. J. Int., 167*(3), 1461-1481. https://doi.org/10.1111/j.1365-246X.2006.03131.x

Steinberger, B. (2007). Effects of latent heat release at phase boundaries on flow in the Earth's mantle, phase boundary topography and dynamic topography at the Earth's surface. *Phys. Earth Plan. Int., 164*(1–2), 2–20. https://doi.org/10.1016/J.PEPI.2007.04.021

Steinberger, B., & Holme, R. (2008). Mantle flow models with core-mantle boundary constraints and chemical heterogeneities in the lowermost mantle. *J. Geophys. Res. - Sol. Ea., 113*(B5), 5403. https://doi.org/10.1029/2007JB005080

Steinberger, B., Werner, S. C., & Torsvik, T. H. (2010). Deep versus shallow origin of gravity anomalies, topography and volcanism on Earth, Venus and Mars. *Icarus, 207*(2), 564-577. https://doi.org/10.1016/j.icarus.2009.12.025

Steinberger, B. (2016). Topography caused by mantle density variations: observation-based estimates and models derived from tomography and lithosphere thickness. *Geophys. J. Int., 205*(1), 604–621. https://doi.org/10.1093/GJI/GGW040

Stemmer, K., Harder, H., & Hansen, U. (2006). A new method to simulate convection with strongly temperature- and pressure-dependent viscosity in a spherical shell: Applications to the Earth's mantle. *Phys. Earth Plan. In., 157*(3–4), 223–249. https://doi.org/10.1016/j.pepi.2006.04.007

Stern, R. J. (2002). Subduction zones. *Rev. Geophys., 40*(4), 1012. https://doi.org/10.1029/2001RG000108

Stern, R. J. (2016). Is plate tectonics needed to evolve technological species on exoplanets? *Geosci. Front.*, 7(4), 573-580. https://doi.org/10.1016/j.gsf.2015.12.002

Stern, R. J., & Gerya, T. (2018). Subduction initiation in nature and models: A review. *Tectonophysics, 746*, 173–198. https://doi.org/10.1016/j.tecto.2017.10.014

Stern, R. J., Gerya, T., & Tackley, P. J. (2018). Stagnant lid tectonics: Perspectives from silicate planets, dwarf planets, large moons, and large asteroids. *Geosci. Front., 9*(1), 103–119. https://doi.org/10.1016/j.gsf.2017.06.004

Stevenson, D. J. (1977). Hydrogen in the Earth's core. *Nature, 268*(5616), 130–131. https://doi.org/10.1038/268130a0

Stixrude, L., & Lithgow-Bertelloni, C. (2005). Thermodynamics of mantle minerals - I. Physical properties. *Geophys. J. Int., 162*(2), 610-632. https://doi.org/10.1111/j.1365-246X.2005.02642.x

Stixrude, L., & Lithgow-Bertelloni, C. (2011). Thermodynamics of mantle minerals-II. Phase equilibria. *Geophys. J. Int, 184*, 1180–1213. https://doi.org/10.1111/j.1365-246X.2010.04890.x

Straub, S. M., & Layne, G. D. (2003). The systematics of chlorine, fluorine, and water in Izu arc front volcanic rocks: Implications for volatile recycling in subduction zones. *Geochim. Cosmochim. Ac., 67*(21), 4179–4203. https://doi.org/10.1016/S0016-7037(03)00307-7

Su, C., Liu, Y., Song, W., Fan, D., Wang, Z., & Tang, H. (2018). Thermodynamic properties of San Carlos olivine at high temperature and high pressure. *Acta Geochem., 37*(2), 171-179. https://doi.org/10.1007/s11631-018-0261-z

Su, W., Cong, B., You, Z., Zhong, Z., & Chen, D. (2002). Plastic mechanism of deformation of garnet - Water weakening. *Sci. China, Ser. D - Earth Sci-s, 45*(10), 885–892. https://doi.org/10.1360/02yd9087

Suetsugu, D., Inoue, T., Obayashi, M., Yamada, A., Shiobara, H., Sugioka, H., … Jellinek, M. (2010). Depths of the 410-km and 660-km discontinuities in and around the stagnant slab beneath the Philippine Sea: Is water stored in the stagnant slab? *Phys. Earth Planet. In., 183*(1–2), 270–279. https://doi.org/10.1016/j.pepi.2010.09.004

Suzuki, A., Ohtani, E., Morishima, H., Kubo, T., Kanbe, Y., Kondo, T., … Kikegawa, T. (2000). In situ determination of the phase boundary between wadsleyite and ringwoodite in Mg_2SiO_4. *Geophys. Res. Lett., 27*(6), 803–806. https://doi.org/10.1029/1999GL008425

Syracuse, E. M., van Keken, P. E., Abers, G. A., Suetsugu, D., Bina, C., Inoue, T., … Jellinek, M. (2010). The global range of subduction zone thermal models. *Phys. Earth Planet. In., 183*(1–2), 73–90. https://doi.org/10.1016/j.pepi.2010.02.004

REFERENCES - T

Tackley, P. J. (1993). Effects of strongly temperature-dependent viscosity on time-dependent, three-dimensional models of mantle convection. *Geophys. Res. Lett., 20*(20), 2187-2190. https://doi.org/10.1029/93GL02317

Tackley, P. J., Stevenson, D. J., Glatzmaier, G. A., & Schubert, G. (1994). Effects of multiple phase transitions in a three-dimensional spherical model of convection in Earth's mantle. *J. Geophys. Res., 99*(B8), 15877. https://doi.org/10.1029/94JB00853

Tackley, P. J. (1996). On the ability of phase transitions and viscosity layering to induce long wavelength heterogeneity in the mantle. *Geophys. Res. Lett., 23*(15), 1985-1988. https://doi.org/10.1029/96GL01980

Tackley, P. J. (1998). Self-consistent generation of tectonic plates in three-dimensional mantle convection. *Earth Planet Sc. Lett., 157*(1–2), 9–22. https://doi.org/10.1016/S0012-821X(98)00029-6

Tackley, P. J. (2000a). Self-consistent generation of tectonic plates in time-dependent, three-dimensional mantle convection simulations. Part 1: Pseudo plastic yielding. *Geochem. Geophys. Geosys., 1*(8). https://doi.org/10.1029/2000GC000036

Tackley, P. J. (2000b). Self-consistent generation of tectonic plates in time-dependent, three-dimensional mantle convection simulations. Part 2: Strain weakening and asthenosphere. *Geochem. Geophys. Geosys., 1*(8). https://doi.org/10.1029/2000GC000043

Tackley, P. J., & King, S. D. (2003). Testing the tracer ratio method for modeling active compositional fields in mantle convection simulations. *Geochem. Geophys. Geosys., 4*(4). https://doi.org/10.1029/2001GC000214

Tackley, P. J. (2008). Modelling compressible mantle convection with large viscosity contrasts in a three-dimensional spherical shell using the yin-yang grid. *Phys. Earth Planet. In., 171*(1–4), 7–18. https://doi.org/10.1016/j.pepi.2008.08.005

Tackley, P. J., Ammann, M., Brodholt, J. P., Dobson, D. P., & Valencia, D. (2013). Mantle dynamics in super-Earths: Post-perovskite rheology and self-regulation of viscosity. *Icarus, 225*(1), 50-61. https://doi.org/10.1016/j.icarus.2013.03.013

Taketoshi, N., Baba, T., Schaub, E., & Ono, A. (2003). Homodyne detection technique using spontaneously generated reference signal in picosecond thermoreflectance measurements. *Rev. Sci. Instr., 74*(12), 5226-5230. https://doi.org/10.1063/1.1628840

Tateno, S., Hirose, K., Ohishi, Y., & Tatsumi, Y. (2010). The structure of iron in earth's inner core. *Science, 330*(6002), 359-361. https://doi.org/10.1126/science.1194662

Tatsumi, Y., & Eggins, S. (1995). Subduction zone magmatism. *Blackwell Science*, Oxford, 221 pages.

Tauzin, B., Debayle, E., & Wittlinger, G. (2010). Seismic evidence for a global low-velocity layer within the Earth's upper mantle. *Nat. Geosci., 3*(10), 718–721. https://doi.org/10.1038/ngeo969

Taylor, F. B. (1910). Bearing of the tertiary mountain belt on the origin of the earth's plan. *Geol. Soc. Am. Bull., 21*(1), 179–226. https://doi.org/10.1130/gsab-21-179

Thielmann, M., & Kaus, B. J. P. (2012). Shear heating induced lithospheric-scale localization: Does it result in subduction? *Earth Planet Sc. Lett.*, 359–360, 1–13. https://doi.org/10.1016/j.epsl.2012.10.002

Thielmann, M., Kaus, B. J. P., & Popov, A. A. (2015). Lithospheric stresses in Rayleigh–Bénard convection: effects of a free surface and a viscoelastic Maxwell rheology. *Geophys. J. Int., 203*(3), 2200–2219. https://doi.org/10.1093/gji/ggv436

Thielmann, M. (2018). Grain size assisted thermal runaway as a nucleation mechanism for continental mantle earthquakes: Impact of complex rheologies. *Tectonophysics, 746*, 611–623. https://doi.org/10.1016/j.tecto.2017.08.038

Thomas, S.-M., Bina, C. R., Jacobsen, S. D., & Goncharov, A. F. (2012). Radiative heat transfer in a hydrous mantle transition zone. *Earth Planet Sc. Lett.*, 357–358, 130–136. https://doi.org/10.1016/j.epsl.2012.09.035

Thomas, S. M., Jacobsen, S. D., Bina, C. R., Reichart, P., Moser, M., Hauri, E. H., … Dollinger, G. (2015). Quantification of water in hydrous ringwoodite. *Front. Earth Sci., 2*, 38. https://doi.org/10.3389/feart.2014.00038

Tikoo, S. M., & Elkins-Tanton, L. T. (2017). The fate of waterwithin Earth and super-earths and implications for plate tectonics. *Philos. T. R. Soc.-A, 375*(2094). https://doi.org/10.1098/rsta.2015.0394

Tobie, G., Choblet, G., & Sotin, C. (2003). Tidally heated convection: Constraints on Europa's ice shell thickness. *J. Geophys. Res. E: Planets*, 108(E11). https://doi.org/10.1029/2003je002099

Tosi, N., Stein, C., Noack, L., Hüttig, C., Maierová, P., Samuel, H., … Tackley, P. J. (2015). A community benchmark for viscoplastic thermal convection in a 2D square box. *Geochem. Geophys. Geosyst., 16*(7), 2175–2196. https://doi.org/10.1002/2015GC005807

Tosi, Nicola, & Padovan, S. (2019). Mercury, Moon, Mars: Surface expressions of mantle convection and interior evolution of stagnant-lid bodies. *Mantle convection and surface expressions*, 455-489. http://arxiv.org/abs/1912.05207

Tschauner, O., Huang, S., Greenberg, E., Prakapenka, V. B., Ma, C., Rossman, G. R., … Tait, K. (2018). Ice-VII inclusions in diamonds: Evidence for aqueous fluid in Earth's deep mantle. *Science, 359*(6380), 1136-1139. https://doi.org/10.1126/science.aao3030

Tsenn, M. C., & Carter, N. L. (1987). Upper limits of power law creep of rocks. *Tectonophysics, 136*(1–2), 1–26. https://doi.org/10.1016/0040-1951(87)90332-5

Tsiganis, K., Gomes, R., Morbidelli, A., & Levison, H. F. (2005). Origin of the orbital architecture of the giant planets of the Solar System. *Nature, 435*(7041), 459–461. https://doi.org/10.1038/nature03539

Tsuchiya, T., Tsuchiya, J., Umemoto, K., & Wentzcovitch, R. M. (2004). Phase transition in $MgSiO_3$ perovskite in the earth's lower mantle. *Earth Planet Sc. Lett., 224*(3–4), 241–248. https://doi.org/10.1016/j.epsl.2004.05.017

Tucker, M. E. (2001). Sedimentary Petrology: An Introduction to the Origin of Sedimentary Rocks (3rd Ed.). *John Wiley & Sons*, 272 pages

Turcotte, D. L. (1993). An episodic hypothesis for Venusian tectonics. *J. Geophys. Res., 98*(E9), 17061. https://doi.org/10.1029/93JE01775

Turcotte, D. L. (1995). How does Venus lose heat? *J. Geophys. Res., 100*(E8), 16931. https://doi.org/10.1029/95JE01621

Turcotte, D. L., Morein, G., Roberts, D., & Malamud, B. D. (1999). Catastrophic Resurfacing and Episodic Subduction on Venus. *Icarus, 139*(1), 49–54. https://doi.org/10.1006/icar.1999.6084

Turcotte, D. L., & Schubert, G. (2002). Geodynamics (2nd Ed.) *Cambridge University Press*, 863 pages. ISBN-10 : 0521186234.

Twiss, R. J., & Moores, E. M. (1992). Structural geology. *W.H. Freeman and Company*, New York, 532 pages.

Tyler, R. H., Henning, W. G., & Hamilton, C. W. (2015). Tidal heating in a magma ocean within Jupiter's moon Io. *Astrophys. J. - Supp. Series, 218*(2), 22. https://doi.org/10.1088/0067-0049/218/2/22

REFERENCES - U

Ulmer, P., & Trommsdorff, V. (1995). Serpentine stability to mantle depths and subduction-related magmatism. *Science, 268*(5212), 858–861. https://doi.org/10.1126/science.268.5212.858

Umemoto, K., & Hirose, K. (2020). Chemical compositions of the outer core examined by first principles calculations. *Earth Planet Sc. Lett., 531*, 116009. https://doi.org/10.1016/j.epsl.2019.116009

Urey, H. C. (1955). The cosmic abundances of potassium, uranium, and thorium and the heat balances of the Earth, the Moon, and Mars. *P. Natl. A. Sci., 41*(3), 127–144. https://doi.org/10.1073/pnas.41.3.127

Utada, H., Koyama, T., Obayashi, M., & Fukao, Y. (2009). A joint interpretation of electromagnetic and seismic tomography models suggests the mantle transition zone below Europe is dry. *Earth Planet Sc. Lett., 281*(3–4), 249–257. https://doi.org/10.1016/j.epsl.2009.02.027

REFERENCES - V

Van Der Meer, D. G., Spakman, W., Van Hinsbergen, D. J. J., Amaru, M. L., & Torsvik, T. H. (2010). Towards absolute plate motions constrained by lower-mantle slab remnants. *Nat. Geosci., 3*(1), 36–40. https://doi.org/10.1038/ngeo708

Van Heck, H. J., & Tackley, P. J. (2011). Plate tectonics on super-Earths: Equally or more likely than on Earth. *Earth Plan. Sci. Lett., 310*(3-4), 252-261. https://doi.org/10.1016/j.epsl.2011.07.029

Van Hunen, J., & van den Berg, A. P. (2008). Plate tectonics on the early Earth: Limitations imposed by strength and buoyancy of subducted lithosphere. *Lithos, 103*(1–2), 217–235. https://doi.org/10.1016/j.lithos.2007.09.016

Van Hunen, J., & Moyen, J.-F. (2012). Archean Subduction: Fact or Fiction? *Ann. Rev. Earth Plan. Sci., 40*(1), 195–219. https://doi.org/10.1146/annurev-earth-042711-105255

Van Keken, P. E., King, S. D., Schmeling, H., Christensen, U. R., Neumeister, D., & Doin, M.-P. (1997). A comparison of methods for the modeling of thermochemical convection. *J. Geophys. Res. - Sol. Ea., 102*(B10), 22477–22495. https://doi.org/10.1029/97JB01353

Van Keken, P. E., Hacker, B. R., Syracuse, E. M., & Abers, G. A. (2011). Subduction factory: 4. Depth-dependent flux of H_2O from subducting slabs worldwide. *J. Geophys. Res., 116*(B1), B01401. https://doi.org/10.1029/2010JB007922

Vangelov, V. I., & Jarvis, G. T. (1994). Geometrical effects of curvature in axisymmetric spherical models of mantle convection. *J. Geophys. Res.- Sol. Ea., 99*(B5), 9345–9358. https://doi.org/10.1029/93JB03133

Vine, F. J., & Matthews, D. H. (1963). Magnetic anomalies over oceanic ridges. *Nature, 199*(4897), 947–949. https://doi.org/10.1038/199947a0

Vinet, P., Rose, J. H., Ferrante, J., & Smith, J. R. (1989). Universal features of the equation of state of solids. *J. Phys. - Cond. Matt., 1*(11), 1941.. https://doi.org/10.1088/0953-8984/1/11/002

REFERENCES - W

Walcott, R. I. (1970). Flexural rigidity, thickness, and viscosity of the lithosphere. *J. Geophys. Res., 75*(20), 3941-3954. https://doi.org/10.1029/jb075i020p03941

Walker, D. W. (1994). The design of a standard message passing interface for distributed memory concurrent computers. *Parallel Computing, 20*(4), 657-673. https://doi.org/10.1016/0167-8191(94)90033-7

Wallace, P. J. (2005). Volatiles in subduction zone magmas: Concentrations and fluxes based on melt inclusion and volcanic gas data. *J. Volcanol. Geoth. Res., 140*(1–3), 217–240. https://doi.org/10.1016/j.jvolgeores.2004.07.023

Walsh, K. J., Morbidelli, A., Raymond, S. N., O'Brien, D. P., & Mandell, A. M. (2011). A low mass for Mars from Jupiter's early gas-driven migration. *Nature, 475*(7355), 206–209. https://doi.org/10.1038/nature10201

Walsh, K. J., Morbidelli, A., Raymond, S. N., O'Brien, D. P., & Mandell, A. M. (2012). Populating the asteroid belt from two parent source regions due to the migration of giant planets-"The Grand Tack". *Meteorit. Planet. Sci., 47*(12), 1941–1947. https://doi.org/10.1111/j.1945-5100.2012.01418.x

Wang, H., Weiss, B. P., Bai, X. N., Downey, B. G., Wang, J., Wang, J., … Zucolotto, M. E. (2017). Lifetime of the solar nebula constrained by meteorite paleomagnetism. *Science, 355*(6325), 623–627. https://doi.org/10.1126/science.aaf5043

Wang, Y., Park, J. Y., Koh, Y. K., & Cahill, D. G. (2010). Thermoreflectance of metal transducers for time-domain thermoreflectance. *J. App. Phys., 108*(4), 043507. https://doi.org/10.1063/1.3457151

Way, M. J., Del Genio, A. D., Kiang, N. Y., Sohl, L. E., Grinspoon, D. H., Aleinov, I., … Clune, T. (2016). Was Venus the first habitable world of our solar system? *Geophys. Res. Lett., 43*(16), 8376–8383. https://doi.org/10.1002/2016GL069790

Weertman, J. (1970). The creep strength of the Earth's mantle. *Rev. Geophys., 8*(1), 145. https://doi.org/10.1029/RG008i001p00145

Weertman, J., & Weertman, J. R. (1975). High temperature creep of rock and mantle viscosity. *Ann. Rev. Earth. Plan. Sci.*, 3(1), 293-315.

Wegner, A.. (1915). Die Entstehung der Kontinente und Ozeane: Braunschweig. *Sammlung Vieweg*, (23), 94.

Weidenschilling, S. J., Spaute, D., Davis, D. R., Marzari, F., & Ohtsuki, K. (1997). Accretional evolution of a planetesimal swarm. *Icarus, 128*(2), 429–455. https://doi.org/10.1006/icar.1997.5747

Weller, M. B., & Lenardic, A. (2012). Hysteresis in mantle convection: Plate tectonics systems. *Geophys. Res. Lett., 39*(10), 3–7. https://doi.org/10.1029/2012GL051232

Wentzcovitch, R. M., Tsuchiya, T., & Tsuchiya, J. (2006). MgSiO3 postperovskite at D″ conditions. *P. Natl. Acad. Sci. USA, 103(3)*, 543–546. https://doi.org/10.1073/pnas.0506879103

Whitaker, R. D. (1975). An historical note on the conservation of mass. *J. Chem. Edu., 52*(10), 658–659. https://doi.org/10.1021/ed052p658

White, R. S. (1988). The Earth's Crust and Lithosphere. *J. Petrol.*, (*1*), 1–10. https://doi.org/10.1093/petrology/Special_Volume.1.1

White, R. S., McKenzie, D., & O'Nions, R. K. (1992). Oceanic crustal thickness from seismic measurements and rare earth element inversions. *J. Geophys. Res., 97*(B13), 683–702. https://doi.org/10.1029/92jb01749

Williams, C. D., & Mukhopadhyay, S. (2019). Capture of nebular gases during Earth's accretion is preserved in deep-mantle neon. *Nature, 565*(7737), 78–81. https://doi.org/10.1038/s41586-018-0771-1

Williams, Q., & Garnero, E. J. (1996). Seismic evidence for partial melt at the base of earth's mantle. *Science, 273*(5281), 1528–1530. https://doi.org/10.1126/science.273.5281.1528

Wilson, C. R., Spiegelman, M., van Keken, P. E., & Hacker, B. R. (2014). Fluid flow in subduction zones: The role of solid rheology and compaction pressure. *Earth Planet Sc. Lett., 401*, 261–274. https://doi.org/10.1016/j.epsl.2014.05.052

Wilson, J. T. (1968). Static or mobile earth: the current scientific revolution. *Proc. Am. Philos. Soc., 112*(5), 309-320.

Winter, J. D. (2010). Principles of Igneous and Metamorphic Petrology (2nd Ed.). *Harlow, UK: Pearson education*, 720 pages. https://doi.org/10.1017/CBO9780511813429

Wirth, R., Vollmer, C., Brenker, F., Matsyuk, S., & Kaminsky, F. (2007). Inclusions of nanocrystalline hydrous aluminium silicate "Phase Egg" in superdeep diamonds from Juina (Mato Grosso State, Brazil). *Earth Planet Sc. Lett., 259*(3–4), 384–399. https://doi.org/10.1016/j.epsl.2007.04.041

Wood, B. J. (1995). The effect of H_2O on the 410-kilometer seismic discontinuity. *Science, 268*(5207), 74–76. https://doi.org/10.1126/science.268.5207.74

Wood, B. J., Walter, M. J., & Wade, J. (2006). Accretion of the Earth and segregation of its core. *Nature, 441*(7095), 825-833. https://doi.org/10.1038/nature04763

Wood, B. J., Wade, J., & Kilburn, M. R. (2008). Core formation and the oxidation state of the Earth: Additional constraints from Nb, V and Cr partitioning. *Geochim. Cosmochim. Ac., 72*(5), 1415–1426. https://doi.org/10.1016/j.gca.2007.11.036

Wookey, J., Kendall, J. M., & Rümpker, G. (2005). Lowermost mantle anisotropy beneath the north Pacific from differential S-ScS splitting. *Geophys. J. Int., 161*(3), 829–838. https://doi.org/10.1111/j.1365-246X.2005.02623.x

Wookey, J., Stackhouse, S., Kendall, J. M., Brodholt, J., & Price, G. D. (2005). Efficacy of the post-perovskite phase as an explanation for lowermost-mantle seismic properties.

Wu, J., Desch, S. J., Schaefer, L., Elkins-Tanton, L. T., Pahlevan, K., & Buseck, P. R. (2018). Origin of Earth's Water: Chondritic Inheritance Plus Nebular Ingassing and Storage of Hydrogen in the Core. *J. Geophys. Res.: Planets, 123*(10), 2691–2712. https://doi.org/10.1029/2018JE005698

REFERENCES - X

Xie, S., & Tackley, P. J. (2004). Evolution of helium and argon isotopes in a convecting mantle. *Phys. Earth Plan. In., 146*(3–4), 417–439. https://doi.org/10.1016/j.pepi.2004.04.003

Xu, C., & Inoue, T. (2019). Melting of Al-Rich Phase D up to the Uppermost Lower Mantle and Transportation of H_2O to the Deep Earth. *Geochem. Geophys. Geosyst., 20*(9), 4382–4389. https://doi.org/10.1029/2019GC008476

Xu, Y., Shankland, T. J., Linhardt, S., Rubie, D. C., Langenhorst, F., & Klasinski, K. (2004). Thermal diffusivity and conductivity of olivine, wadsleyite and ringwoodite to 20 GPa and 1373 K. *Phys. Earth Planet. In, 143*(1–2), 321–336. https://doi.org/10.1016/j.pepi.2004.03.005

REFERENCES - Y

Yamasaki, T., & Seno, T. (2003). Double seismic zone and dehydration embrittlement of the subducting slab. *J. Geophys. Res.- Sol. Ea., 108*(B4), 2212. https://doi.org/10.1029/2002jb001918

Yamazaki, D., & Karato, S. (2001). Some mineral physics constraints on the rheology and geothermal structure of Earth's lower mantle. *Am. Min., 86*(4), 385–391. https://doi.org/10.2138/am-2001-0401

Yang, J., & Faccenda, M. (2020). Intraplate volcanism originating from upwelling hydrous mantle transition zone. *Nature, 579*(7797), 88–91. https://doi.org/10.1038/s41586-020-2045-y

Ye, Y., Brown, D. A., Smyth, J. R., Panero, W. R., Jacobsen, S. D., Chang, Y. Y., … Frost, D. J. (2012). Compressibility and thermal expansion of hydrous ringwoodite with 2.5(3) wt% H_2O. *Am. Min., 97*(4), 573–582. https://doi.org/10.2138/am.2012.4010

Yoder, C. F. (1979). How tidal heating in Io drives the galilean orbital resonance locks. *Nature, 279*(5716), 767–770. https://doi.org/10.1038/279767a0

Yokochi, R., & Marty, B. (2004). A determination of the neon isotopic composition of the deep mantle. *Earth Planet Sc. Lett., 225*(1–2), 77–88. https://doi.org/10.1016/j.epsl.2004.06.010

Yoshino, T., Manthilake, G., Matsuzaki, T., & Katsura, T. (2008). Dry mantle transition zone inferred from the conductivity of wadsleyite and ringwoodite. *Nature, 451*(7176), 326–329. https://doi.org/10.1038/nature06427

Yoshino, T., & Katsura, T. (2013). Electrical conductivity of mantle minerals: Role of water in conductivity anomalies. *Annu. Rev. Earth Pl. Sc., 41*, 605–628. https://doi.org/10.1146/annurev-earth-050212-124022

Youdin, A. N. (2011). On the formation of planetesimals via secular gravitational instabilities with turbulent stirring. *Astrophys. J., 731*(2), 99. https://doi.org/10.1088/0004-637X/731/2/99

Young, A. T. (1973). Are the clouds of venus sulfuric acid? *Icarus, 18*(4), 564–582. https://doi.org/10.1016/0019-1035(73)90059-6

Young, D. A., Thomsen, C., Grahn, H. T., Maris, H. J., & Tauc, J. (1986). Heat Flow in Glasses on a Picosecond Timescale. In Phonon Scattering in Condensed Matter V (pp. 49-51). *Springer*, Berlin, Heidelberg. https://doi.org/10.1007/978-3-642-82912-3_14

Young, T. E., Green, H. W., Hofmeister, A. M., & Walker, D. (1993). Infrared spectroscopic investigation of hydroxyl in β-$(Mg,Fe)_2SiO_4$ and coexisting olivine: Implications for mantle evolution and dynamics. *Phys. Chem. Miner., 19*(6), 409-422. https://doi.org/10.1007/BF00202978

Yuan, H., Zhang, L., Ohtani, E., Meng, Y., Greenberg, E., & Prakapenka, V. B. (2019). Stability of Fe-bearing hydrous phases and element partitioning in the system $MgO–Al_2O_3–Fe_2O_3–SiO_2–H_2O$ in Earth's lowermost mantle. *Earth Planet Sc. Lett., 524*, 115714. https://doi.org/10.1016/j.epsl.2019.115714

Yuan, L., Ohtani, E., Ikuta, D., Kamada, S., Tsuchiya, J., Naohisa, H., … Suzuki, A. (2018). Chemical Reactions Between Fe and H2O up to Megabar Pressures and Implications for Water Storage in the Earth's Mantle and Core. *Geophys. Res. Lett., 45*(3), 1330–1338. https://doi.org/10.1002/2017GL075720

Yuen, D. A., Cserepes, L., & Schroeder, B. A. (1998). Mesoscale structures in the transition zone: Dynamical consequences of boundary layer activities. *Earth Plan. Spac., 50*(11–12), 1035–1045. https://doi.org/10.1186/BF03352198

REFERENCES - Z

Zasova, L. V., Ignatiev, N., Khatuntsev, I., & Linkin, V. (2007). Structure of the Venus atmosphere. *Plan. Space Sci., 55*(12), 1712–1728. https://doi.org/10.1016/j.pss.2007.01.011

Zerkle, A. L. (2018). Biogeodynamics: Bridging the gap between surface and deep Earth processes. *Philos. Trans. Roy. Soc. London Ser. - A: Mat. Phys. Eng. Sci.*, 376(2132), 20170401. https://doi.org/10.1098/rsta.2017.0401

Zhang, J. S., & Bass, J. D. (2016). Sound velocities of olivine at high pressures and temperatures and the composition of Earth's upper mantle. *Geophys. Res. Lett., 43*(18), 9611-9618. https://doi.org/10.1002/2016GL069949

Zhang, T. L., Baumjohann, W., Delva, M., Auster, H. U., Balogh, A., Russell, C. T., … Lebreton, J. P. (2006). Magnetic field investigation of the Venus plasma environment: Expected new results from Venus Express. *Plan. Space Sci., 54*(13–14), 1336–1343. https://doi.org/10.1016/j.pss.2006.04.018

Zhang, T. L., Baumjohann, W., Russell, C. T., Luhmann, J. G., & Xiao, S. D. (2016). Weak, Quiet Magnetic Fields Seen in the Venus Atmosphere. *Sci. Rep., 6*(1), 1–3. https://doi.org/10.1038/srep23537

Zhang, Y., Yoshino, T., Yoneda, A., & Osako, M. (2019). Effect of iron content on thermal conductivity of olivine with implications for cooling history of rocky planets. *Earth Plan. Sci. Lett., 519*, 109–119. https://doi.org/10.1016/j.epsl.2019.04.048

Zhao, D. (2004). Origin of the Changbai intraplate volcanism in Northeast China: Evidence from seismic tomography. *Chinese Sci. Bull., 49*(13), 1401. https://doi.org/10.1360/04wd0125

Zhao, D., & Ohtani, E. (2009). Deep slab subduction and dehydration and their geodynamic consequences: Evidence from seismology and mineral physics. *Gondwana Res., 16*(3–4), 401–413. https://doi.org/10.1016/j.gr.2009.01.005

Zheng, X., Cahill, D. G., Krasnochtchekov, P., Averback, R. S., & Zhao, J. C. (2007). High-throughput thermal conductivity measurements of nickel solid solutions and the applicability of the Wiedemann-Franz law. *Acta Materialia, 55*(15), 5177-5185. https://doi.org/10.1016/j.actamat.2007.05.037

Zhong, S., McNamara, A., Tan, E., Moresi, L., & Gurnis, M. (2008). A benchmark study on mantle convection in a 3-D spherical shell using CitcomS. *Geochem. Geophys. Geosys., 9*(10). https://doi.org/10.1029/2008GC002048

Zimmermann, M. E. (2004). Rheological Properties of Partially Molten Lherzolite. *J. Petrol., 45*(2), 275–298. https://doi.org/10.1093/petrology/egg089

Acknowledgments

Reviewers of the Thesis

I would like to express my gratitude to my supervisors, Prof. Dr. Gregor J. Golabek, and Dr. Marcel Thielmann for the comments and the review of the entire thesis. I appreciate the help of Prof. Dr. Paul J. Tackley for reviewing the description of StagYY in chapter 3.6. Additionally, I would like to thank Giacomo Criniti for his comments on chapter 4, and his review on the experimental methods, Dr. Wen-Pin Hsieh for his review on the TDTR method described in chapter 4.6, Michaela J. Flanigan for the proof reading of chapter 4 and Alex Gutmann for his help with the German abstract. Finally, I would like to thank Suchetana Sarkar for proof reading every chapter, her constructive comments, and the unconditional support showed during the writing of this thesis.

Collaborators

During the past four years I have had the opportunity to collaborate with many exceptional scientists around the world. If I achieved any results, I owe it to them as well. I would like to thank Prof. Dr. Gregor J. Golabek for his supervision throughout my PhD project and Dr. Marcel Thielmann for his unwavering guidance.

I thank Prof. Dr. Paul J. Tackley for introducing me to the StagYY research group, Dr. Antoine Rozel for his patience in explaining thoroughly all the functionalities of StagYY, Dr. Fabio Crameri for his assistance with StagLab, and Dr. Patrick Sanan for helping me with the installation of StagYY in the Euler cluster at ETH.

I would like to extend my gratitude to Prof. Dr. Eiji Ohtani for all the fruitful discussions which lead to me formulating my thesis research plan, and Dr. Wen-Pin Hsieh for welcoming me in Taipei, Taiwan and introducing me to the TDTR method. I would also like to thank Keng-Hsieh Chao for his supervision with the thermal conductivity measurements.

I am grateful to Prof. Dr. Lena Noack for her comments and suggestions during the poster section at the German-Swiss Geodynamics Workshop in 2018 which were very useful in the discussion section of chapter 6.

Logistic Support

I am indebted to Susan Lausmann for helping me find a house in Bayreuth; Nicole Fischer and Anna Dinius for their support with the contracts and the documentation for the IRTG; Shinobu Okuyama and Shin Ozawa for their help with the Japanese bureaucracy and their support during my staying in Sendai; Petra Buchert and Janina Potzel for their patience with the reimbursements; Raphael Njul and Alexander Rother for the sample preparation. I would also thank Detlef Krausse for his technical support with my MAC and the microprobe analysis.

Special Thanks

Family: Alessandro, Francesco, Claudio, and Maria Grazia. Ida and Leone, Maria and Richetto. Teresa and Giuseppe, Liliana and Renzo, Angelo and Vilma, Tiziano, Daniela and Valter. Roberta and Mirko, Giovanni, Maria Chiara, Letizia. Erik and Alessandra, Niccolò, Simone, Carolina. Marco, Daniel, Marco. Gina, Sergio and Luciana. Suchetana Sarkar.

Friends: Giorgio and Benedetta, Antonio Z. and Maria Z., Marta C., Niccolò, Eleonora and Matteo, Francesca, Marco. Davide and Francesca, Michele and Chiara. Greta, Matteo, Alberto, Filippo, Marta D. and Manuele. Don Marco Marchetti.

Team Skarso: Philipp Montin, Nicolò 'Sgrimbo' Sgreva, Andrea 'Gian' Gianese, Matteo 'Pette' Pettenello, Fabiano, Simone 'Puja' Pujatti, Fabrizio and Giovanna, Gianluca Musoni.

Scout: Enrico, Martina, Francesca, Anna, Luca, Marta, Lucia, Fabiana, Mario Mantoan, Federico Pesavento, Alessandro Ipposi.

Teachers: Fabrizio Civolani, Giuseppe Fera, Cristiana Pagliarusco, Andrea Marin, Alessandra Grendene.

Source of Inspiration

Music: Giuseppe Verdi, Gioacchino Rossini, Giacomo Puccini, Pietro Mascagni, Joe Hisaishi, Nobuo Uematsu, Talking Heads, Alan Parsons Project, Franz Ferdinand, Planet Funk, Tom Waits, Bruno Conte.

Writers: J.R.R. Tolkien, Italo Calvino, Ludovico Ariosto, Frank Herbert, Philip Pullman, Mario Rigoni Stern, Dino Buzzati, Primo Levi.

Great Personalities: Marco Aurelio, Cosimo de'Medici, Enrico Dandolo, Andrea Palladio, Antonio Pigafetta, Giovanni Battista Belzoni, Giuseppe Garibaldi, Camillo Benso, Marco Cosma Manera, Alessandro and Luigi Tandura, Talamo Manfredi, Carlo Fecia di Cossato, Marc Bloch, Gaetano Salvemini, Sandro Pertini, Enrico Mattei, Adriano Olivetti, Peppino Impastato, Alejandro Jodorowsky.

Researchers: Dario Bressanini, Alessandro Barbero, Philippe Daverio, Alan Zamboni, Marco Coletti, Nicolò Zuliani.

Videogames: Hironobu Sakaguchi (Final Fantasy), Yoshitaka Amano (Final Fantasy), Hidetaka Miyazaki (Dark Souls), Akira Toriyama (Dragon Quest).

Movie Directors: Guillermo Del Toro, Akira Kurosawa, Peter Jackson, Ridley Scott.

Comic Book Artists: Mike Mignola, John Arcudi, Neil Gaiman, Alan Moore, Eiichiro Oda, Yoshihiro Togashi

(Eidesstattliche) Versicherungen und Erklärungen

(§ 9 Satz 2 Nr. 3 PromO BayNAT)

Hiermit versichere ich eidesstattlich, dass ich die Arbeit selbstständig verfasst und keine anderen als die von mir angegebenen Quellen und Hilfsmittel benutzt habe (vgl. Art. 64 Abs. 1 Satz 6 BayHSchG).

(§ 9 Satz 2 Nr. 3 PromO BayNAT)

Hiermit erkläre ich, dass ich die Dissertation nicht bereits zur Erlangung eines akademischen Grades eingereicht habe und dass ich nicht bereits diese oder eine gleichartige Doktorprüfung endgültig nicht bestanden habe.

(§ 9 Satz 2 Nr. 4 PromO BayNAT)

Hiermit erkläre ich, dass ich Hilfe von gewerblichen Promotionsberatern bzw. -vermittlern oder ähnlichen Dienstleistern weder bisher in Anspruch genommen habe noch künftig in Anspruch nehmen werde.

(§ 9 Satz 2 Nr. 7 PromO BayNAT)

Hiermit erkläre ich mein Einverständnis, dass die elektronische Fassung meiner Dissertation unter Wahrung meiner Urheberrechte und des Datenschutzes einer gesonderten Überprüfung unterzogen werden kann.

(§ 9 Satz 2 Nr. 8 PromO BayNAT)

Hiermit erkläre ich mein Einverständnis, dass bei Verdacht wissenschaftlichen Fehlverhaltens Ermittlungen durch universitätsinterne Organe der wissenschaftlichen Selbstkontrolle stattfinden können.

……
Ort, Datum, Unterschrift